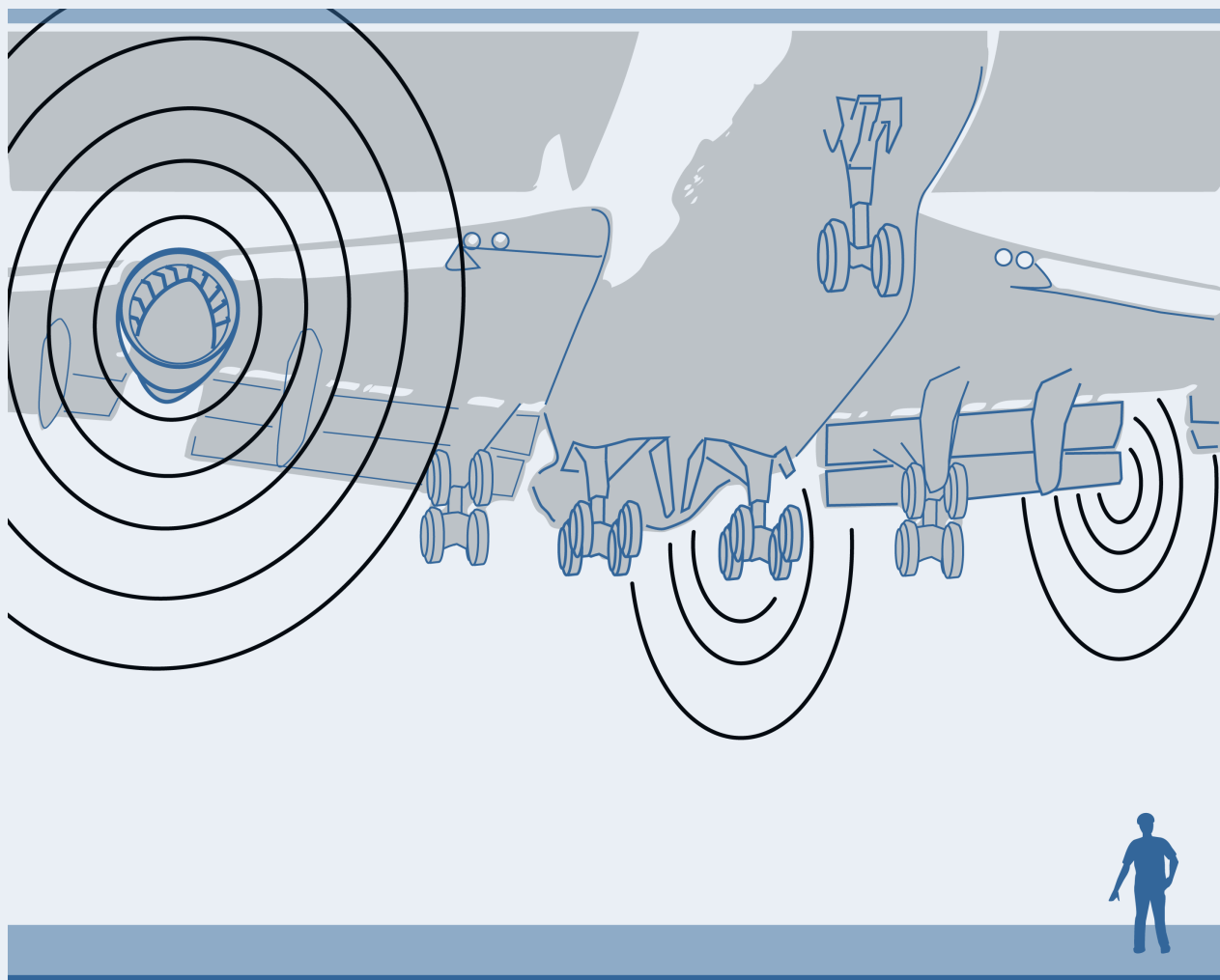




Assessment of NASA's Aircraft Noise Prediction Capability

Milo D. Dahl, editor
Glenn Research Center, Cleveland, Ohio



NASA STI Program . . . in Profile

Since its founding, NASA has been dedicated to the advancement of aeronautics and space science. The NASA Scientific and Technical Information (STI) program plays a key part in helping NASA maintain this important role.

The NASA STI Program operates under the auspices of the Agency Chief Information Officer. It collects, organizes, provides for archiving, and disseminates NASA's STI. The NASA STI program provides access to the NASA Aeronautics and Space Database and its public interface, the NASA Technical Reports Server, thus providing one of the largest collections of aeronautical and space science STI in the world. Results are published in both non-NASA channels and by NASA in the NASA STI Report Series, which includes the following report types:

- **TECHNICAL PUBLICATION.** Reports of completed research or a major significant phase of research that present the results of NASA programs and include extensive data or theoretical analysis. Includes compilations of significant scientific and technical data and information deemed to be of continuing reference value. NASA counterpart of peer-reviewed formal professional papers but has less stringent limitations on manuscript length and extent of graphic presentations.
- **TECHNICAL MEMORANDUM.** Scientific and technical findings that are preliminary or of specialized interest, e.g., quick release reports, working papers, and bibliographies that contain minimal annotation. Does not contain extensive analysis.
- **CONTRACTOR REPORT.** Scientific and technical findings by NASA-sponsored contractors and grantees.

- **CONFERENCE PUBLICATION.** Collected papers from scientific and technical conferences, symposia, seminars, or other meetings sponsored or cosponsored by NASA.
- **SPECIAL PUBLICATION.** Scientific, technical, or historical information from NASA programs, projects, and missions, often concerned with subjects having substantial public interest.
- **TECHNICAL TRANSLATION.** English-language translations of foreign scientific and technical material pertinent to NASA's mission.

Specialized services also include creating custom thesauri, building customized databases, organizing and publishing research results.

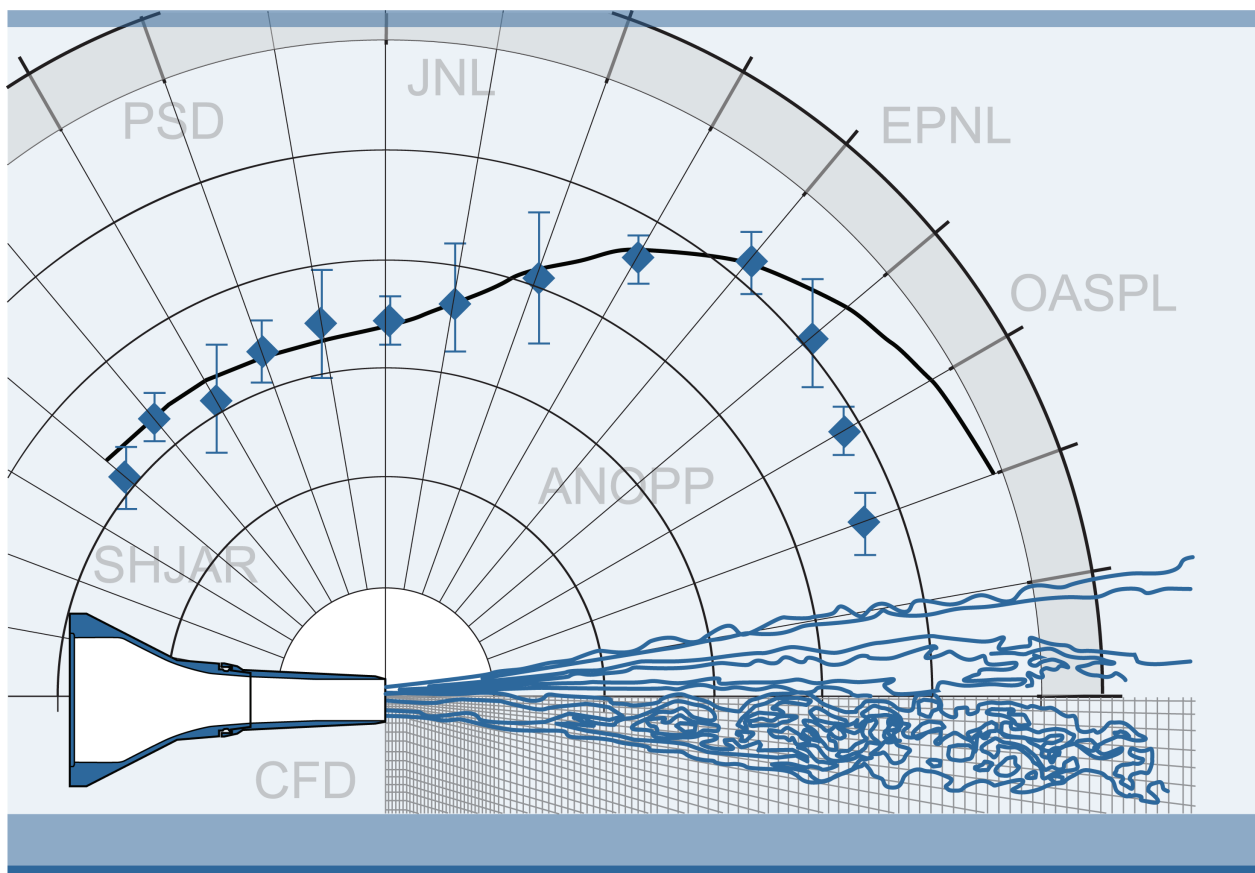
For more information about the NASA STI program, see the following:

- Access the NASA STI program home page at <http://www.sti.nasa.gov>
- E-mail your question via the Internet to help@sti.nasa.gov
- Fax your question to the NASA STI Help Desk at 443-757-5803
- Telephone the NASA STI Help Desk at 443-757-5802
- Write to:
NASA Center for AeroSpace Information (CASI)
7115 Standard Drive
Hanover, MD 21076-1320



Assessment of NASA's Aircraft Noise Prediction Capability

Milo D. Dahl, editor
Glenn Research Center, Cleveland, Ohio



National Aeronautics and
Space Administration

Glenn Research Center
Cleveland, Ohio 44135

Acknowledgments

Contributions to this study were made by members of the Aeroacoustics, Computational Aerosciences, Configuration Aerodynamics and Structural Acoustics Branches at the NASA Langley Research Center and by members of the Acoustics, Multi-disciplinary Design Analysis Optimization, and Turbomachinery and Heat Transfer Branches at the NASA Glenn Research Center. The outstanding technical efforts of both NASA civil servants and contractors in completing this work is gratefully acknowledged. They are listed as authors for each of the chapters. Thanks are also extended to the following individuals for support of this effort: Dennis L. Huff, Charlotte E. Whitfield, Fayette S. Collier, E. Brian Fite, Michael A. Marcolini, Kevin P. Shepherd, Richard J. Silcox, Joseph H. Morrison, and Zachary T. Applin.

I also thank the following people from NASA, industry, and academia for reviewing and providing feedback on this document: Constantine Baltas, Stanley F. Birch, Eugene Chien, Michael J. Czech, Michael J. Doty, Fereidoun Farassat, Marvin E. Goldstein, Yueping Guo, Alan S. Hersch, Andrew J. Kempton, Donald C. Kenzakowski, Michelle R. Kirby, Eugene A. Krejsa, Dean F. Long, Justin H. Lan, Steven Martins, Joe E. Posey, Ramons A. Reba, Todd Schultz, Robert W. Stoker, Thomas Van de Ven, Donald S. Weir, Trevor H. Wood, and Jia Yu.

Finally, I am very grateful to Laura Becker, Lorie Passe, Nancy Mieczkowski, John Jindra, and Lorraine Feher for their help and careful effort in preparing this document.

Milo D. Dahl, editor

Trade names and trademarks are used in this report for identification only. Their usage does not constitute an official endorsement, either expressed or implied, by the National Aeronautics and Space Administration.

This work was sponsored by the Fundamental Aeronautics Program at the NASA Glenn Research Center.

Level of Review: This material has been technically reviewed by expert reviewer(s).

Available from

NASA Center for Aerospace Information
7115 Standard Drive
Hanover, MD 21076-1320

National Technical Information Service
5301 Shawnee Road
Alexandria, VA 22312

Available electronically at <http://www.sti.nasa.gov>

Preface

A goal of NASA's Fundamental Aeronautics Program is the improvement of aircraft noise prediction. Within the Subsonic Fixed Wing, Subsonic Rotary Wing, and Supersonic projects, there are specific objectives to assess the accuracy of noise prediction methods. NASA is uniquely positioned to provide this publication after years of developing codes and establishing experimental databases through in-house research and with numerous industrial and university partnerships.

The purpose of this document is to provide an assessment on the current state of the art for aircraft noise prediction by carefully analyzing the results from prediction tools and from the experimental databases to determine errors and uncertainties and compare results to validate the predictions. This assessment was performed over the time period from 2006 to 2009. The state of the art in this study is restricted to prediction methods and databases developed or sponsored by NASA, although in many cases they represent the current state of the art for industry. The scope of prediction tools range from semi-empirical methods to higher fidelity models that have matured to the level where they can be used for noise prediction. The error analysis is included for both the predictions and the experimental data. Gaps are identified where more work is needed to improve the prediction methods and/or the experimental databases. The results will be used to judge the progress of future work toward narrowing these gaps and reducing the levels of error and uncertainties by quantitatively tracking the improvements.

This report begins with an introduction that gives a general background for and a discussion on the process of this assessment followed by eight topic chapters. The topic areas are aircraft system noise, engine system noise, airframe noise, fan noise, liner physics, duct acoustics, jet noise, and propulsion airframe aeroacoustics.

Contents

Preface	iii
Chapter 1—Introduction	1
Summary.....	1
1.1 Assessment Process	1
1.2 Aircraft Noise Prediction Assessment	5
Appendix A.—Nomenclature	9
A.1 Acronyms	9
A.2 Symbols	9
References	10
Chapter 2—Aircraft System Noise Prediction.....	11
Summary.....	11
2.1 Introduction.....	11
2.2 ANOPP Code.....	12
2.2.1 ANOPP Source Noise Methods.....	14
2.2.2 Installation Effects.....	17
2.2.3 ANOPP Computational Efficiency and Usage	18
2.3 ANOPP Evaluation and Demonstration of Capabilities	18
2.3.1 Vehicle Description.....	19
2.3.2 Engine Description	19
2.3.3 Trajectory Description.....	19
2.3.4 Comparison of Measurements and Predictions	21
2.3.5 Uncertainty Analysis	26
2.4 Recommendations.....	29
Appendix A.—Nomenclature	31
A.1 Acronyms	31
A.2 Symbols	31
References	32
Chapter 3—Engine System and Core Noise	35
Summary and Recommendations	35
3.1 Introduction.....	35
3.2 Core-Noise Research	36
3.2.1 Compressor Noise	36
3.2.2 Combustion Noise	37
3.2.3 Turbine Noise.....	42
3.2.4 Current Prediction Codes	42
3.3 Engine Noise Prediction Using ANOPP.....	43
3.3.1 ANOPP Static-Engine-Test Simulation.....	43
3.3.2 Sensitivity.....	44
3.4 Comparison of ANOPP–L25 Predictions and NASA-Honeywell EVNERT Engine Test- Stand Data	46
3.4.1 Comparison of Total 1/3-Octave Results	46
3.4.2 Comparison of Combustion-Noise 1/3-Octave Results.....	51
3.5 Concluding Remarks.....	58
Appendix A.—Nomenclature	59
A.1 Acronyms	59
A.2 Symbols	59
References	60
Chapter 4—Airframe Noise: A Prediction Capability Assessment	63
Summary.....	63
4.1 Introduction.....	63
4.1.1 Background	63
4.1.2 Assessment Overview	64
4.2 Prediction Methodology	64
4.2.1 Modeling Approaches	64

4.2.2	Prediction Tools	65
4.2.3	Test Facilities	65
4.2.4	Scaling Issues	65
4.2.5	Metrics.....	66
4.3	Airframe Noise Characteristics of a Gulfstream G550 Aircraft.....	66
4.3.1	Discussion of Experimental Data	66
4.3.2	Metrics and Assessment	68
4.3.3	Results and Findings	69
4.3.4	Recommendations	70
4.4	Flap-Edge Noise Measurement and Prediction.....	71
4.4.1	Test Description	71
4.4.2	Results and Findings	72
4.4.3	Metrics and Assessment	73
4.4.4	Recommendations	73
4.5	Aeroacoustic Measurement and Prediction for Boeing 777 Landing Gear Model	75
4.5.1	Discussion of Experimental Data	75
4.5.2	Results and Findings	77
4.5.3	Sensitivity Study	78
4.5.4	Recommendations	81
4.6	Prototype for Airframe Component Interaction: Tandem Cylinders	81
4.6.1	Test Descriptions.....	81
4.6.2	Computational Approach and Procedure.....	82
4.6.3	Results and Findings	83
4.6.4	Effect of Cylinder Spacing	85
4.6.5	Recommendations	88
4.7	Aeroacoustic Analysis of Simplified Landing Gear Model	88
4.7.1	Test Description	88
4.7.2	Computational Approach and Procedure.....	88
4.7.3	Results and Findings	89
4.7.4	Recommendations	90
4.8	Aerodynamic Sources of Leading-Edge Slat Noise.....	92
4.8.1	Discussion of Experimental Data	92
4.8.2	Metrics and Assessment	92
4.8.3	Results and Findings	93
4.8.4	Recommendations	98
4.9	Conclusions.....	98
4.10	Recommendations.....	99
	Appendix A.—Nomenclature	101
	A.1 Acronyms	101
	A.2 Symbols.....	101
	Appendix B.—Aircraft Noise Prediction Program.....	103
	B.1 ANOPP: Fink’s Method	103
	B.2 ANOPP: Boeing’s Method, Landing Gear Noise.....	105
	Appendix C.—CFL3D and Acoustic Analogy	107
	Appendix D.—Test Facilities	109
	D.1 Quiet Flow Facility.....	109
	D.2 Basic Aerodynamic Research Tunnel.....	110
	References	111
	Chapter 5—Fan Noise Prediction	115
	Summary.....	115
	5.1 Introduction.....	115
	5.2 Benchmark Test Cases.....	116
	5.3 Test Facility and Data Acquisition Systems	121
	5.4 Wind Tunnel Acoustic Measurements.....	121
	5.5 Rotating Rake Acoustic Measurements	122
	5.6 Uncertainty in Measurements	122

5.6.1	Wind Tunnel Aerodynamic Data Uncertainty Analysis	123
5.6.2	Wind Tunnel Sideline Acoustic Data Uncertainty Analysis	123
5.6.3	Rotating Rake Acoustic Data Uncertainty Analysis	124
5.7	Prediction and Assessment	125
5.7.1	Empirical Methods	126
5.7.2	Acoustic-Analogy-Based Methods	126
5.7.3	Computational Methods	135
5.8	Conclusions	141
5.9	Acknowledgments	141
	Appendix A.—Nomenclature	143
A.1	Acronyms	143
	Appendix B.—Additional Data-Theory Comparisons for ANOPP	145
	Appendix C.—Additional Data-Theory Comparisons for RSI Code	151
	References	155
	Chapter 6—Uncertainty in Acoustic Liner Impedance Measurement and Prediction	157
	Summary	157
6.1	Introduction	158
6.1.1	Challenge for Liner Design Improvement	158
6.1.2	Viable Liners for Turbofan Engine Nacelles	158
6.1.3	Perforated Plate Resistive Element in Multilayer Liners	159
6.1.4	Scope and Objective of This Assessment	159
6.2	Impedance Uncertainty, Quantification, and Quality Control	160
6.2.1	Statistical Process Control: A Tool for Impedance Quality Control	160
6.2.2	Specification Limits, Uncertainty Limits, and Confidence Intervals	160
6.2.3	Uncertainty Metrics	160
6.2.4	Coverage Factor for Small Sample Sizes	162
6.3	Impedance Concept and Measurement Issues	162
6.3.1	Nonlinearity Implication for Measurements and Prediction Models	162
6.3.2	Grazing Flow Implication for Measurements and Prediction Models	163
6.3.3	Test Sample Size and Scale Implications	163
6.3.4	Measurement Methodologies	164
6.3.5	Relevance of Laboratory Impedance Measurement	166
6.3.6	Implementation of Rayleigh Absorber as Validation Liner	167
6.4	Impedance Prediction Models for POHC Absorbers	167
6.4.1	Phenomenological (Semi-Empirical) Models	167
6.4.2	Semi-Empirical Models for POHC Liners	168
6.5	Database Creation for Uncertainty Assessment	176
6.5.1	Assessment Liner Geometry and Input Preparation	176
6.5.2	Quantifying Input Parameter Uncertainty	176
6.6	Results and Discussion	179
6.6.1	Graphical Format and Interpretation	179
6.6.2	Comparison of NIT and GIT Measurements With No Flow	180
6.6.3	Comparison of GIT Measurements With Flow	181
6.6.4	Comparison of Predicted and Measured Results	182
6.7	Concluding Remarks and Recommendations	197
6.8	Acknowledgments	199
	Appendix A.—Nomenclature	201
A.1	Acronyms	201
A.2	Symbols	201
	References	203
	Chapter 7—Assessment of Acoustic Propagation and Radiation Codes for Locally Reacting Liners in Flow Ducts	205
	Summary	205
7.1	Introduction	205
7.2	Statement of Problem	206
7.3	Potential Flow Formulation	207

7.3.1	Governing Differential Equations	207
7.3.2	The Linearized Acoustic Equations.....	207
7.3.3	Derivation of Scalar Wave Equations	208
7.3.4	Scalar Wave Equation in Frequency Domain.....	208
7.3.5	Acoustic Boundary Conditions.....	209
7.4	Acoustic Liner Sound Attenuation.....	210
7.5	Potential Flow Computer Codes	211
7.5.1	Quasi-Three-Dimensional Uniform-Flow Code.....	211
7.5.2	Axially Symmetric Code	213
7.5.3	Three-Dimensional Uniform-Flow Code	214
7.5.4	Three-Dimensional Code With Parabolic Approximation	216
7.6	Rotational Flow Computer Codes.....	218
7.6.1	Governing Differential Equations and Boundary Conditions.....	219
7.6.2	Quasi-Three-Dimensional Code.....	220
7.6.3	Pseudo-Time Marching Codes	222
7.7	Results and Discussion	223
7.7.1	NASA Langley Grazing Incidence Tube Simulations.....	223
7.7.2	NASA Langley Curved Duct Test Rig Simulations	230
7.7.3	NASA Glenn Advanced Noise Control Fan Simulations	232
7.8	Concluding Remarks and Recommendations	234
7.9	Acknowledgments	235
	Appendix A.—Nomenclature	237
	A.1 Acronyms	237
	A.2 Symbols.....	237
	References	239
	Chapter 8—Jet Noise Prediction.....	241
	Summary.....	241
8.1	Introduction.....	242
8.2	Discussion of Codes.....	242
8.2.1	Empirical Prediction Tool: Stone Jet Noise Module (ST2JET) Within ANOPP	243
8.2.2	Acoustic Analogy Prediction Tools.....	244
8.2.3	Reynolds-Averaged Navier-Stokes (RANS) Tool: Wind-US	248
8.3	Identification of Test Programs	250
8.4	Jet Noise Case Taxonomy.....	252
8.5	Description of Facilities.....	252
8.6	Description of Test Hardware for Data Sources	254
8.6.1	SHJAR.....	254
8.6.2	Supersonic Dual-Flow Hardware (Test Program SDF07).....	257
8.6.3	Long Duct Internal Mixer Hardware (Test Program LDIM05).....	257
8.6.4	High-Flow Cross-Facility Hardware (Test Program HFXF07)	259
8.7	Details of Measurements, Sensors, Transducers, and Placement.....	259
8.8	Acoustic Data Collection and Processing	260
8.9	Identifying Uncertainties in Acoustic Data.....	261
8.9.1	Measurement Uncertainties	261
8.9.2	Experimental Uncertainties	261
8.10	Flow Data Collection and Processing	264
8.10.1	Stereoscopic PIV System	264
8.10.2	Optical Calibration and Verification	265
8.10.3	Three-Dimensional Vector Processing.....	265
8.10.4	Flow Seeding.....	265
8.11	Identifying Uncertainties in Flow Measurements	266
8.12	Metrics	268
8.13	Description of Presentation Format for Acoustic Data	268
8.14	Empirical Code Assessment Results.....	269
8.14.1	Case Listing.....	269
8.14.2	Overall Results	269

8.15	Acoustic Analogy Code Assessment Results: Jet3D	271
8.15.1	Case Listing.....	271
8.15.2	Discussion of Jet3D Results	272
8.16	Acoustic Analogy Code Assessment Results: JeNo v1.0	276
8.16.1	Case Listing.....	276
8.16.2	Discussion of JeNo v1.0 Results	278
8.17	Conclusions.....	290
8.17.1	Empirical code.....	290
8.17.2	Acoustic Analogy Codes	291
8.17.3	Recommendations	291
Appendix A.—Nomenclature		293
A.1	Acronyms	293
A.2	Symbols	293
Appendix B.—Jet Configurations Tested in NASA-Sponsored Test Programs		295
Appendix C.—ANOPP Jet Noise Predictions and Comparison With Data.....		305
References		329
Chapter 9—Propulsion Airframe Aeroacoustic Interactions		331
Summary.....		331
9.1	Introduction.....	331
9.2	Experiments	331
9.2.1	Pylon Effects Experiment.....	333
9.2.2	Experimental Facility	333
9.2.3	Model Design and Experimental Configurations	334
9.2.4	Nozzle Operating Conditions	335
9.2.5	Acoustic Data Processing	336
9.3	Prediction Method Overview	336
9.4	Jet3D	336
9.4.1	Guidelines for Applying Jet3D.....	339
9.4.2	Sensitivity to Input Settings.....	340
9.4.3	Applications	340
9.4.4	Jet3D Challenges.....	351
9.5	Future PAA Experimental and Prediction Development	351
Appendix A.—Nomenclature		353
A.1	Acronyms	353
A.2	Symbols	353
References		354

List of Tables

Table 1.1.—Codes assessed for aircraft noise predictive capability	6
Table 1.2.—List of codes and code types arranged by chapter topic	6
Table 2.1.—Database used for “original” Heidmann method	15
Table 2.2.—Database used for “large fan” Heidmann method	15
Table 2.3.—Database used for “small fan” Heidmann method	15
Table 2.4.—ANOPP jet noise prediction methods	16
Table 2.5.—ANOPP modules used for predicting the noise from a generic Boeing 737–800 aircraft	18
Table 2.6.—Monte Carlo simulation of Boeing 737 certification effective perceived noise levels (EPNL)	27
Table 2.7.—Change in effective perceived noise level (EPNL) (dB) at approach location due to 5-percent variations in aircraft velocity and power setting	28
Table 2.8.—Change in effective perceived noise level (EPNL) (dB) at lateral sideline location due to 5-percent variations in aircraft velocity and power setting	29
Table 2.9.—Change in effective perceived noise level (EPNL) (dB) at flyover location due to 5-percent variations in aircraft velocity and power setting	29
Table 3.1.—ANOPP nondimensional performance parameters	45
Table 4.1.—G550 aircraft: characteristic dimensions	66
Table 4.2.—Trailing-edge flap noise test: test conditions	72
Table 4.3.—Trailing-edge flap noise test: characteristic dimensions	72
Table 4.4.—Experimental repeatability analysis of sound pressure levels (in decibels) observed in flap- edge beamforming	74
Table 4.5.—Major components of 6.3-percent-scale Boeing 777 landing gear	75
Table 4.6.—Test matrix for Boeing 777 landing gear noise study	77
Table 4.7.—Boeing 777 main landing gear prediction input parameters	77
Table 4.8.—Boeing 777 main landing gear component dimensions	77
Table 5.1.—Model fan stage design parameters	117
Table 5.2.—Model fan tip speed conditions used in this study	117
Table 5.3.—Aerodynamic data uncertainty analysis results	123
Table 5.4.—Analysis of uncertainty in fan noise spectra	124
Table 5.5.—Representative uncertainty levels in mode sound power levels for second harmonic of blade- passing frequency computed from measured Rotating Rake data	125
Table 5.6.—Modeling error from using hard-wall plug-flow basis function to fit shear-flow mode	125
Table 5.7.—Typical uncertainties in mode acoustic power level from all sources	125
Table 5.8.—ANOPP L25v3 HDNFAN input parameters	127
Table 5.9.—TURBO and LINFLUX grid sizes	137
Table 6.1.—Geometric parameter statistical inputs	177
Table 6.2.—Aeroacoustic parameter mean values	177
Table 6.3.—Aeroacoustic parameter standard deviations	177
Table 7.1.—Sound attenuation in decibels computed for plane wave in hard-wall duct with nonreflecting termination	224
Table 7.2.—Sound attenuation in decibels computed for least attenuated mode in soft-wall duct with nonreflecting termination	226
Table 7.3.—Wall clock time consumed on Columbia clusters computing sound attenuation with in-duct codes on baseline grid	227
Table 7.4.—Grazing incidence tube mean sound attenuation (μ) in decibels and 95% confidence interval uncertainty values ($t_n * \sigma$)	230
Table 8.1.—Assessment cases for Jet3D predictions of jet noise spectra	246
Table 8.2.—Taxonomy of test cases for assessment of jet noise prediction codes	253
Table 8.3.—Design Mach numbers of single- flow convergent-divergent nozzles	257
Table 8.4.—Analysis of uncertainty in measured jet noise spectra	262
Table 8.5.—Assessment matrix for JeNo v1.0 predictions of jet noise spectra—axisymmetric geometries	276
Table 8.6.—Assessment matrix for JeNo v1.0 predictions of jet noise spectra—nonaxisymmetric geometries	277

Table 8.7.—Test case identifier within each configuration	296
Table 9.1.—Separate-flow nozzle model areas for both cold and hot conditions and scale factors used for acoustic data processing.....	335
Table 9.2.—Bypass ratio (BPR) 5 nozzle operating conditions	335

List of Figures

Figure 1.1.—Diagram of assessment process leading to validation of computed result by comparison to experimental data, where U is uncertainty.	3
Figure 1.2.—Example of determining errors and uncertainties using a statistical approach for parameters X and dependent variable Y . (a) Raw measured and calculated data with computed means and 95% confidence intervals. (b) Computed comparison error and uncertainty band. (c) Point and line plot comparing calculated results and measured data, with “error bars.” (d) Comparison plot showing 95% confidence interval (CI) and overlap regions.	4
Figure 2.1.—ANOPP Level 25.	13
Figure 2.2.—Prediction flow within ANOPP Level 25 using CTOL source modules.	13
Figure 2.3.—ANOPP coordinate system.	14
Figure 2.4.—Analytical representation of CFM56–7B turbofan engine in Numerical Propulsion System Simulator (NPSS) (Ref. 41).	19
Figure 2.5.—Cross-sectional view of NPSS/WATE aeromechanical and flow path simulation of CFM56–7B turbofan engine (drawing to scale).	20
Figure 2.6.—SAE AIR–1845 trajectory for the B737–800/CFM56–7B at 172 300 lb. (a) Altitude. (b) Airspeed. (c) Percent net engine thrust.	21
Figure 2.7.—Noise certification measurement locations.	21
Figure 2.8.—Predicted tone-weighted perceived noise level (PNLT) time history at approach certification point.	22
Figure 2.9.—Predicted sound pressure level (SPL) at approach certification point for three different polar directivity angles, θ_e . (a) 45°. (b) 90°. (c) 135°.	22
Figure 2.10.—Predicted tone-weighted perceived noise level (PLNT) time history at lateral sideline certification point.	23
Figure 2.11.—Predicted sound pressure level (SPL) at lateral sideline certification point for three different polar directivity angles, θ_e . (a) 45°. (b) 90°. (c) 135°.	23
Figure 2.12.—Predicted tone-weighted perceived noise level (PNLT) time history for flyover (with cutback) condition.	24
Figure 2.13.—Predicted sound pressure level (SPL) at flyover (with cutback) location for three different polar directivity angles, θ_e . (a) 45°. (b) 90°. (c) 135°.	24
Figure 2.14.—Predicted contributions from each noise component to total effective perceived noise level (EPNL) at the three certification points.	25
Figure 2.15.—Comparison of predicted effective perceived noise level (EPNL) for B737–800/CFM56–7B and noise certification data of 73 certificated B737s equipped with CFM56–7B engines. Approach measurement location.	26
Figure 2.16.—Comparison of predicted effective perceived noise level (EPNL) for B737–800/CFM56–7B and noise certification data of 73 certificated B737s equipped with CFM56–7B engines. Lateral sideline measurement location.	26
Figure 2.17.—Comparison of predicted effective perceived noise level (EPNL) for B737–800/CFM56–7B and noise certification data of 73 certificated B737s equipped with CFM56–7B engines. Flyover measurement location.	26
Figure 3.1.—Coherence technique to determine combustion-noise component of far-field noise. Measurement stations C, T, and F are located in the engine combustor, core tail pipe, and far field, respectively. Signals $x(t)$, $y(t)$, and $z(t)$ are directly measurable, are functions of time t , and are the sum of coherent combustion-noise signals $u(t)$, $v(t)$, and $w(t)$ and uncorrelated signals $m(t)$, $n(t)$, and $o(t)$ resulting from other noise sources; h_{uv} and h_{vw} are impulse-response functions.	39
Figure 3.2.—Three-signal coherence technique for noise rejection, where $s(t)$ is the source signal as function of time t and h_{su} , h_{sv} , and h_{sw} are impulse-response functions. Coherent signals $u(t)$, $v(t)$, and $w(t)$ of interest are not directly measurable; their addition to mutually uncorrelated signals $m(t)$, $n(t)$, and $o(t)$ from other sources results in measurable signals $x(t)$, $y(t)$, and $z(t)$	40
Figure 3.3.—ANOPP module flow chart for static-engine test.	43
Figure 3.4.—Hard-wall case 1/3-octave surface plots comparing ANOPP predictions and EVNERT data of far-field sound from Honeywell TECH977 engine at various corrected fan speeds. SPL is sound pressure level, and f represents frequency. (a) 60 percent (approach). (b) 71 percent (cutback). (c) 87 percent (takeoff).	47

Figure 3.5.—Comparison of ANOPP predictions and EVNERT data for hard-wall case of Honeywell TECH977 engine at approach condition, 60 percent corrected fan speed. Error bands for predictions are 1 and 3 percent uncertainties in performance parameters. Error bar for data is ± 1.25 dB estimated uncertainty from calibration and instrumentation. (a) to (e) 1/3-octave sound pressure level (SPL) versus center frequency at different polar angles. (a) 30°. (b) 60°. (c) 90°. (d) 120°. (e) 150°. (f) Overall SPL (OASPL) versus polar directivity angle.	48
Figure 3.6.—Comparison of ANOPP predictions and EVNERT data for hard-wall case of Honeywell TECH977 engine at cutback condition, 71 percent corrected fan speed. Error bands for predictions are 1 and 3 percent uncertainties in performance parameters. Error bar for data is ± 1.25 dB estimated uncertainty from calibration and instrumentation. (a) to (e) 1/3-octave sound pressure level (SPL) versus center frequency at different polar angles. (a) 30°. (b) 60°. (c) 90°. (d) 120°. (e) 150°. (f) Overall SPL (OASPL) versus polar directivity angle.	49
Figure 3.7.—Comparison of ANOPP predictions and EVNERT data for hard-wall case of Honeywell TECH977 engine at takeoff condition, 87 percent corrected fan speed. Error bands for predictions are 1 and 3 percent uncertainties in performance parameters. Error bar for data is ± 1.25 dB estimated uncertainty from calibration and instrumentation. (a) to (e) 1/3-octave sound pressure level (SPL) versus center frequency at different polar angles. (a) 30°. (b) 60°. (c) 90°. (d) 120°. (e) 150°. (f) Overall SPL (OASPL) versus polar directivity angle.	50
Figure 3.8.—Treated case 1/3-octave surface plots comparing ANOPP predictions and EVNERT data of far-field sound from Honeywell TECH977 engine at various corrected fan speeds. SPL is sound pressure level, and f represents frequency. (a) 60 percent (approach). (b) 71 percent (cutback). (c) 87 percent (takeoff).	52
Figure 3.9.—Comparison of ANOPP predictions and EVNERT data for treated case of Honeywell TECH977 engine at approach condition, 60 percent corrected fan speed. Error bands for predictions are 1 and 3 percent uncertainties in performance parameters. Error bar for data is ± 1.25 dB estimated uncertainty from calibration and instrumentation. (a) to (e) 1/3-octave sound pressure level (SPL) versus center frequency at different polar angles. (a) 30°. (b) 60°. (c) 90°. (d) 120°. (e) 150°. (f) Overall SPL (OASPL) versus polar directivity angle.	53
Figure 3.10.—Comparison of ANOPP predictions and EVNERT data for treated case of Honeywell TECH977 engine at cutback condition, 71 percent corrected fan speed. Error bands for predictions are 1 and 3 percent uncertainties in performance parameters. Error bar for data is ± 1.25 dB estimated uncertainty from calibration and instrumentation. (a) to (e) 1/3-octave sound pressure level (SPL) versus center frequency at different polar angles. (a) 30°. (b) 60°. (c) 90°. (d) 120°. (e) 150°. (f) Overall SPL (OASPL) versus polar directivity angle.	54
Figure 3.11.—Comparison of ANOPP predictions and EVNERT data for treated case of Honeywell TECH977 engine at takeoff condition, 87 percent corrected fan speed. Error bands for predictions are 1 and 3 percent uncertainties in performance parameters. Error bar for data is ± 1.25 dB estimated uncertainty from calibration and instrumentation. (a) to (e) 1/3-octave sound pressure level (SPL) versus center frequency at different polar angles. (a) 30°. (b) 60°. (c) 90°. (d) 120°. (e) 150°. (f) Overall SPL (OASPL) versus polar directivity angle.	55
Figure 3.12.—Total- and combustion-noise 1/3-octave sound pressure level (SPL) versus 1/3-octave center frequency in 130° direction at different corrected fan speeds. ANOPP predictions and processed EVNERT data for Honeywell TECH977 engine configuration 35 (Ref. 57). G_{zz} refers to total noise spectrum; 2s-cip1, 2s-t551, and 3s refer to different processing techniques applied to the experimental data; and NOP refers to threshold values. (a) 48 percent (flight idle). (b) 60 percent (approach). (c) 71 percent (cutback). (d) 87 percent (takeoff).	57
Figure 4.1.—Boeing 747 aircraft in landing configuration. Four main landing gear, nose landing gear, leading-edge slats and triple-slotted, trailing-edge flaps are deployed during airport approach.	64
Figure 4.2.—ANOPP source-observer geometry. R , θ , and ϕ are measured with respect to source emission time. V_∞ is aircraft speed.	65
Figure 4.3.—Gulfstream G550 aircraft planform.	66
Figure 4.4.—NASA microphone array and Gulfstream free-field (certification) microphone layout.	67
Figure 4.5.—Representative measured sound pressure level (SPL) spectra for two configurations of Gulfstream G550 aircraft.	68
Figure 4.6.—Averaged measured sound pressure level (SPL) spectra for three selected airframe noise and clean configurations of Gulfstream G550 aircraft.	69

Figure 4.7.—Predicted sound pressure level (SPL) spectra for three selected airframe noise and clean configurations of Gulfstream G550 aircraft.	69
Figure 4.8.—Uncertainties in predicted sound pressure level (SPL) spectra due to variations in speed and azimuthal angle, ϕ , for Gulfstream G550 aircraft. Configuration is flaps at 39° with landing gear down.	69
Figure 4.9.—Difference between measured and predicted absolute sound pressure level (SPL) spectra.	70
Figure 4.10.—Difference between measured and predicted relative sound pressure level (SPL) spectra.	70
Figure 4.11.—Flap overlap and gap definitions for flap-edge noise test with model airfoil in Quiet Flow Facility (QFF).	71
Figure 4.12.—Azimuthal (ϕ) locations of Small Aperture Directional Array (SADA) microphones for far-field tests with model airfoil in Quiet Flow Facility (QFF).	71
Figure 4.13.—Flap-edge noise sound pressure level (SPL) spectra at different Mach numbers M and deflection angles. Comparison of ANOPP predictions using Fink's method and measurements from Quiet Flow Facility (QFF) experiments.	73
Figure 4.14.—Discrepancy in airframe flap-edge noise sound pressure level (SPL) spectrum at Mach number $M = 0.17$ and 39° flap between ANOPP predictions using Fink's method and measurements from Quiet Flow Facility (QFF) experiments.	73
Figure 4.15.—Boeing 777 main landing gear model. Baseline configuration, with door.	75
Figure 4.16.—Boeing 777 main gear model assembly mounted in Quiet Flow Facility (QFF) for lateral "sideline" measurements by Medium Aperture Directional Array (MADA) microphones.	76
Figure 4.17.—Boeing 777 main gear model assembly mounted in Quiet Flow Facility (QFF) for "flyover" measurements by Medium Aperture Directional Array (MADA) microphones.	76
Figure 4.18.—Quiet Flow Facility (QFF) coordinates system for landing gear noise measurements. R_e is source-to-observer distance, θ_e is polar emission angle, and ϕ_e is azimuthal emission angle.	76
Figure 4.19.—Sound pressure level (SPL) of landing gear model. Comparison of measured spectrum and total scaled (Ref. 37) ANOPP predicted spectrum with its three separate frequency component spectra using Boeing-Guo method for Mach number 0.17 at two observer locations (see Figure 4.18). (a) Flyover position, $\theta_e = 87.1^\circ$ and $\phi_e = 1.0^\circ$. (b) Forward-sideline position, $\theta_e = 59.3^\circ$ and $\phi_e = 5.17^\circ$	79
Figure 4.20.—Sound pressure level (SPL) of landing gear model. Comparison of measured spectrum and total ANOPP predicted spectrum with its separate component spectra using Fink method for Mach number 0.17 at two observer locations (see Figure 4.18). (a) Flyover position, $\theta_e = 87.1^\circ$ and $\phi_e = 1.0^\circ$. (b) Forward-sideline position, $\theta_e = 59.3^\circ$ and $\phi_e = 5.17^\circ$	79
Figure 4.21.—Sound pressure level (SPL) of landing gear model for Mach number 0.17 and given polar angle at different azimuthal angles (see Figure 4.18). (a) Comparison of measured spectra and total scaled (Ref. 37) ANOPP-predicted spectra using Boeing-Guo method. (b) Comparison of measured spectra and total ANOPP-predicted spectra using Fink method.	80
Figure 4.22.—Sound pressure level (SPL) of landing gear model for Mach number 0.17 and given azimuthal angle at different polar angles (see Figure 4.18). (a) Comparison of measured spectra and total scaled (Ref. 37) ANOPP-predicted spectra using Boeing-Guo method. (b) Comparison of measured spectra and total ANOPP-predicted spectra using Fink method.	80
Figure 4.23.—Boeing-Guo method: Combined effects for variation in Mach number and landing gear angle of attack.	81
Figure 4.24.—Tandem cylinder test configuration.	82
Figure 4.25.—Tandem cylinders installed in Basic Aerodynamic Research Tunnel (BART).	82
Figure 4.26.—Tandem cylinders installed in Quiet Flow Facility (QFF) tunnel for measurements with Medium Aperture Directional Array (MADA) microphones.	82
Figure 4.27.—Planar view of computational x,y -grid used for tandem cylinder computational fluid dynamics (CFD) simulations.	83
Figure 4.28.—Pressure coefficient C_p versus polar angle θ for the surfaces of the tandem cylinders. Comparison of results from Quiet Flow Facility (QFF) and Basic Aerodynamic Research Tunnel (BART) experiments and CFD simulations with grids of different spans. (a) Upstream cylinder. (b) Downstream cylinder.	84
Figure 4.29.—Root-mean-squared (rms) value of perturbation pressure coefficient $C_{p'}$ versus polar angle θ for the surfaces of the tandem cylinders. Comparison of results from Quiet Flow Facility (QFF) and	

Basic Aerodynamic Research Tunnel (BART) experiments and CFD simulations with grids of different resolutions and spans. (a) Upstream cylinder. (b) Downstream cylinder.....	85
Figure 4.30.—Near-field tandem cylinder sound pressure level (SPL) contours, CFD predictions, where x and y are spatial coordinates and grid dimensions and D_t is cylinder diameter.	85
Figure 4.31.—Power spectral density PSD for tandem cylinders. Comparison of CFD predictions using three grids and results from Quiet Flow Facility (QFF) experiments.	86
Figure 4.32.—Sound pressure level (SPL) spectra for tandem cylinders. Comparison of CFD predictions using three grids and measurements from Quiet Flow Facility (QFF) experiments.	86
Figure 4.33.—Error in sound pressure level (SPL) spectra predictions for tandem cylinders. Difference between CFD predictions from $MxyFz$ grid with span of 18 and experimental measurements.	86
Figure 4.34.—Root-mean-squared (rms) value of tandem cylinder surface perturbation pressure coefficient C_p versus polar angle θ at two spacings L_t/D_t , where L_t is centroid-to-centroid distance and D_t is cylinder diameter (see Figure 4.24). Comparison of CFD predictions from $MxyFz$ grid with span of 18 and measurements from Quiet Flow Facility (QFF) and Basic Aerodynamic Research Tunnel (BART) experiments.	87
Figure 4.35.—Power spectral density PSD for tandem cylinders at two spacings L_t/D_t , where L_t is centroid-to-centroid distance and D_t is cylinder diameter (Figure 4.24). Comparison of CFD predictions from $MxyFz$ grid with span of 18 and measurements from Quiet Flow Facility (QFF) experiments.	87
Figure 4.36.—Sound pressure level (SPL) spectra for tandem cylinders at centroid separation distance $L_t/D_t = 1.435$. Comparison of CFD predictions from $MxyFz$ grid with span of 18 and measurements from Quiet Flow Facility (QFF) experiments.....	87
Figure 4.37.—Error in sound pressure level (SPL) spectra predictions for tandem cylinders at centroid separation distance $L_t/D_t = 1.435$. Difference between CFD predictions from $MxyFz$ grid with span of 18 and experimental measurements.	87
Figure 4.38.—Geometry of simplified landing gear model.	88
Figure 4.39.—CFD surface grid of simplified landing gear model.	89
Figure 4.40.—Sound pressure level (SPL) spectra for landing gear in overhead position at polar angle $\theta = 88^\circ$ and azimuthal angle $\phi = -1^\circ$ (see Figure 4.18). Comparison of CFL3D predictions, using gear surface with and without the ceiling surface, and measurements from Quiet Flow Facility (QFF) experiments, nontripped and tripped cases.....	89
Figure 4.41.—Power spectral density PSD for landing gear in overhead position at polar angle $\theta = 88^\circ$ and azimuthal angle $\phi = -1^\circ$ (see Figure 4.18). Comparison of CFL3D predictions, using gear surface with and without the ceiling surface, and measurements from Quiet Flow Facility (QFF) experiments, nontripped and tripped cases.	90
Figure 4.42.—Error in CFL3D sound pressure level (SPL) spectra predictions for landing gear in overhead position at polar angle $\theta = 88^\circ$ and azimuthal angle $\phi = -1^\circ$ (see Figure 4.18). Difference between predictions, using gear surface with and without the ceiling surface, and measurements from Quiet Flow Facility (QFF) experiments, tripped case.	90
Figure 4.43.—Sound pressure level (SPL) spectra for landing gear in flyover positions (see Figure 4.18). Comparison of CFL3D predictions and measurements from Quiet Flow Facility (QFF) experiments, nontripped and tripped cases. (a) Upstream, polar angle $\theta = 58^\circ$ and azimuthal angle $\phi = -1^\circ$. (b) Downstream, polar angle $\theta = 120^\circ$ and azimuthal angle $\phi = -1^\circ$	91
Figure 4.44.—Sound pressure level (SPL) spectra for landing gear in sideline positions (see Figure 4.18). Comparison of CFL3D predictions and measurements from Quiet Flow Facility (QFF) experiments, nontripped and tripped cases. (a) On door side, polar angle $\theta = 88^\circ$ and azimuthal angle $\phi = -55^\circ$. (b) Opposite door side, polar angle $\theta = 88^\circ$ and azimuthal angle $\phi = 55^\circ$	91
Figure 4.45.—Model three-element 30P/30N high-lift aircraft wing system.	92
Figure 4.46.—Instantaneous spanwise vorticity field downstream of leading-edge slat, based on CFL3D computations. (a) Planar cut resembling cove state I. (b) Planar cut somewhat resembling cove state II.	94
Figure 4.47.—Sample snapshots of leading-edge slat spanwise vorticity field from particle imaging velocimetry (PIV) measurements (Ref. 35) with wing model configuration at 4° angle of attack in the Basic Aerodynamic Research Tunnel (BART). ω_z is spanwise vorticity, c_s is slat chord length, and V_∞ is aircraft speed. (a) Cove state I. (b) Cove state II.	94

Figure 4.48.—Time-averaged velocity magnitude profiles across leading-edge slat shear layer. (a) Locations of mixing-layer profiles A through D superposed on contour of mean spanwise vorticity. (b) Comparison of CFL3D simulation results (based on spanwise grid) for locations A through D and particle imaging velocimetry (PIV) measurements (Ref. 35). The distance ε increases from left to right, along the cuts A through D.	95
Figure 4.49.—Time-averaged two-dimensional (2D) turbulent kinetic energy TKE distribution in leading-edge slat cover region, where V_∞ is free-stream velocity. (a) Locations of mixing-layer profiles A through D superposed on particle imaging velocimetry (PIV) contours. (b) CFL3D predictions. (c) CFL3D results compared with (PIV) measurements along profiles A through D (Ref. 35), where, Tu_{2D} is the two-dimensional turbulence intensity.	96
Figure 4.50.—Peak two-dimensional turbulent intensity Tu_{2D} along leading-edge slat cove mixing-layer trajectory versus distance s from slat cusp. Comparison of CFL3D Tu_{2D} based on coarse (S1) and fine (S2) spanwise grids and particle imaging velocimetry (PIV) measurements derived from small and large fields of view (f.o.v.) (Ref. 35).	97
Figure 4.51.—Acoustic radiation due to leading-edge slat cove unsteadiness. (a) CFL3D-computed acoustic spectra (product of frequency f and power spectral density PSD) at selected probe locations between one and two chords from trailing edge noting point at Strouhal number $St = 2$, where c_s is slat chord length and V_∞ is free-stream velocity. (b) Schematic for slat noise model in Reference 81. (c) Contours of instantaneous pressure perturbations from fine-spanwise-grid simulation.	97
Figure 4.52.—Medium Aperture Directional Array (MADA) with hood removed in Quiet Flow Facility (QFF).	109
Figure 4.53.—MADA microphone arrangement.	109
Figure 4.54.—Basic Aerodynamic Research Tunnel (BART). Structure in front of test section is traverse for optical devices.	110
Figure 4.55.—Closeup: Basic Aerodynamics Research Tunnel (BART) test section with particle imaging velocimetry (PIV) camera on traverse system.	110
Figure 5.1.—The 22-in.-diameter Advanced Ducted Propulsor (ADP) Fan 1 installed in the NASA 9- by 15-Foot Low-Speed Wind Tunnel. Traversing microphone (located on white stand) is visible to left of model. Microphone moves on track parallel with axis of fan.	118
Figure 5.2.—Cross-sectional sketch of ADP Fan 1 model. ADP has 18 rotor blades, 45 fan exit guide vanes, and 63 core inlet guide vanes.	119
Figure 5.3.—The 22-in.-diameter Source Diagnostic Test (SDT) fan installed in NASA 9- by 15-Foot Low-Speed Wind Tunnel.	119
Figure 5.4.—Cross-sectional sketch of SDT fan model. SDT has 22 rotor blades and 54 fan exit guide vanes.	120
Figure 5.5.—The 22-in.-diameter Quiet High-Speed Fan 2 (QHSF 2) fan installed in NASA 9- by 15-Foot Low-Speed Wind Tunnel.	120
Figure 5.6.—Cross-sectional sketch of QHSF 2 model fan. QHSF 2 has 22 rotor blades, 50 fan exit guide vanes, 10 bypass duct struts, and 10 core duct struts.	121
Figure 5.7.—Plan view of 9- by 15-ft test section showing model-scale fan acoustic installation, 2.3-m (89-in.) sideline traversing microphone, and fixed aft microphone locations. Dimensions are in meters (inches).	122
Figure 5.8.—Rotating Rake ring assembly on 43-cm (17-in.) Advanced Ducted Propulsor (ADP) in NASA 9- by 15-Foot Low-Speed Wind Tunnel. (a) First-generation system. (b) Current-generation system.	123
Figure 5.9.—Sound pressure level (SPL) error in ANOPP predictions for all sideline emission angles for ADP fan at various tip speeds. Gray bar represents experimental uncertainty. (a) 5425 rpm. (b) 7525 rpm. (c) 8750 rpm.	128
Figure 5.10.—Sound pressure level (SPL) error in ANOPP predictions for all sideline emission angles for SDT fan at various tip speeds. Gray bar represents experimental uncertainty. (a) 7809 rpm. (b) 11 075 rpm. (c) 12 657 rpm.	129
Figure 5.11.—Sound pressure level (SPL) error in ANOPP predictions for all sideline emission angles for QHSF 2 fan at various tip speeds. Gray bar represents experimental uncertainty. (a) 9840 rpm. (b) 12 500 rpm. (c) 14 060 rpm.	130
Figure 5.12.—Computational domains for ADP fan used by TSWIFT code. (a) Rotor. (b) Stator.	131

Figure 5.13.—Flow field through ADP fan duct. Axisymmetric Mach number contours at 8750 rpm computed using TSWIFT code. External as well as internal flows included. Black lines indicate block boundaries.....	132
Figure 5.14.—Comparisons of measured and predicted turbulence intensity for three spanwise stations 2.5 in. downstream of rotor tip trailing edge of SDT fan at approach condition. Predictions made using NASA TSWIFT code; dashed curves are predicted levels raised so background level matches measured background. (a) 88 percent span. (b) 71 percent span. (c) 56 percent span.....	133
Figure 5.15.—Rotor-stator (R-S) interaction narrowband sound power level (PWL) for SDT fan at different speeds from measured stage and rotor-only PWLs: R-S = stage – rotor-only. Dashed line indicates data reliability is questioned (see Sec. 5.7.2). (a) 7809 rpm. (b) 9493 rpm. (c) 11 075 rpm. (d) 11 771 rpm. (e) 12 657 rpm.	134
Figure 5.16.—Comparison of predicted (using RSI code) and estimated narrowband sound power levels (PWLs) for SDT fan at different speeds. Estimates are rotor-stator (R-S) interaction PWLs taken from Figure 5.15. Dashed line indicates data reliability is questioned (see Sec. 5.7.2). (a) 7809 rpm. (b) 9493 rpm. (c) 11 075 rpm. (d) 11 771 rpm. (e) 12 657 rpm.	136
Figure 5.17.—Error in predicted (using RSI code) narrowband sound power levels (PWLs) for SDT fan at different speeds (Figure 5.16). Gray bar represents experimental uncertainty.	137
Figure 5.18.—Comparison of measured and predicted sound power levels (PWLs) for exhaust 2×BPF tone (second harmonic of blade-passing frequency) for ADP fan at different tip speeds. Data from Rotating Rake (RR) and sideline microphone (SL). Predictions calculated using LINFLUX code. Results are for circumferential mode –9.....	138
Figure 5.19.—Comparison of measured and predicted sound power levels (PWLs) for exhaust 2×BPF tone (second harmonic of blade-passing frequency) for SDT fan at different tip speeds. Data from Rotating Rake (RR) and sideline microphone (SL). Predictions calculated using LINFLUX code. Results are for circumferential mode –10.....	139
Figure 5.20.—Error in prediction of sound power level (PWL) for 2×BPF tone (second harmonic of blade-passing frequency) using data from Rotating Rake. Data for ADP fan is from Figure 5.18 (circumferential mode –9). Data for SDT fan is from Figure 5.19 (circumferential mode –10). Error is defined as (measured level) – (predicted level). Predictions calculated using LINFLUX code. Gray bar represents experimental uncertainty.	140
Figure 5.21.—Error in prediction of sound power level (PWL) for 2×BPF tone (second harmonic of blade-passing frequency) using data from sideline microphone. Data for ADP fan is from Figure 5.18 (circumferential mode –9). Data for SDT fan is from Figure 5.19 (circumferential mode –10). Error is defined as (measured level) – (predicted level). Predictions calculated using LINFLUX code. Gray bar represents experimental uncertainty.....	140
Figure 5.22.—Comparison of 1/3-octave measured sound pressure level (SPL) and SPL predicted from ANOPP code for ADP fan in inlet and exhaust quadrants at 5425 rpm at Mach 0.1. (a) Inlet quadrant; emission angle 46°. (b) Exhaust quadrant; emission angle 136°.....	145
Figure 5.23.—Comparison of 1/3-octave measured sound pressure level (SPL) and SPL predicted from ANOPP code for ADP fan in inlet and exhaust quadrants at 7525 rpm at Mach 0.1. (a) Inlet quadrant; emission angle 46°. (b) Exhaust quadrant; emission angle 136°.....	145
Figure 5.24.—Comparison of 1/3-octave measured sound pressure level (SPL) and SPL predicted from ANOPP code for ADP fan in inlet and exhaust quadrants at 8750 rpm at Mach 0.1. (a) Inlet quadrant; emission angle 46°. (b) Exhaust quadrant; emission angle 136°.....	146
Figure 5.25.—Comparison of 1/3-octave measured sound pressure level (SPL) and SPL predicted from ANOPP code for SDT fan in inlet and exhaust quadrants at 7809 rpm at Mach 0.1. (a) Inlet quadrant; emission angle 46°. (b) Exhaust quadrant; emission angle 136°.....	146
Figure 5.26.—Comparison of 1/3-octave measured sound pressure level (SPL) and SPL predicted from ANOPP code for SDT fan in inlet and exhaust quadrants at 11 075 rpm at Mach 0.1. (a) Inlet quadrant; emission angle 46°. (b) Exhaust quadrant; emission angle 136°.....	147
Figure 5.27.—Comparison of 1/3-octave measured sound pressure level (SPL) and SPL predicted from ANOPP code for SDT fan in inlet and exhaust quadrants at 12 657 rpm at Mach 0.1. (a) Inlet quadrant; emission angle 46°. (b) Exhaust quadrant; emission angle 136°.....	147
Figure 5.28.—Comparison of 1/3-octave measured sound pressure level (SPL) and SPL predicted from ANOPP code for QHSF 2 fan in inlet and exhaust quadrants at 9840 rpm at Mach 0.1. (a) Inlet quadrant; emission angle 46°. (b) Exhaust quadrant; emission angle 136°.....	148

Figure 5.29.—Comparison of 1/3-octave measured sound pressure level (SPL) and SPL predicted from ANOPP code for QHSF 2 fan in inlet and exhaust quadrants at 12 500 rpm at Mach 0.1. (a) Inlet quadrant; emission angle 46°. (b) Exhaust quadrant; emission angle 136°.....	148
Figure 5.30.—Comparison of 1/3-octave measured sound pressure level (SPL) and SPL predicted from ANOPP code for QHSF 2 fan in inlet and exhaust quadrants at 14 060 rpm at Mach 0.1. (a) Inlet quadrant; emission angle 46°. (b) Exhaust quadrant; emission angle 136°.....	149
Figure 5.31.—Comparison of measured narrowband sound power level (PWL) and PWL predicted using RSI code for ADP fan at various blade tip speeds. Data represent combined rotor and stator contributions. (a) 5425 rpm. (b) 6700 rpm. (c) 7525 rpm. (d) 8345 rpm. (e) 8750 rpm.....	152
Figure 5.32.—Comparison of measured narrowband sound power level (PWL) and PWL predicted using RSI code for SDT fan at various blade tip speeds. Data represent combined rotor and stator contributions. (a) 7809 rpm. (b) 9493 rpm. (c) 11 075 rpm. (d) 11 771 rpm. (e) 12 675 rpm.....	153
Figure 5.33.—Comparison of measured narrowband sound power level (PWL) and PWL predicted using RSI code for QHSF 2 fan at various blade tip speeds. Data represent combined rotor and stator contributions. (a) 9840 rpm. (b) 10 935 rpm. (c) 12 500 rpm. (d) 13 280 rpm. (e) 14 060 rpm.....	154
Figure 6.1.—Turbofan engine nacelle with wall lining.	158
Figure 6.2.—Perforate-over-honeycomb core (POHC) liner.	159
Figure 6.3.—Depiction of accuracy versus precision for parameter x , as used in this chapter. (a) High accuracy, high precision; (b) High accuracy, low precision; (c) Low accuracy, high precision; (d) Low accuracy, low precision.	161
Figure 6.4.—NASA Langley normal incidence tube (NIT). (a) Photograph. (b) Schematic.....	165
Figure 6.5.—NASA Langley grazing incidence tube (GIT). (a) Photograph. (b) Schematic. (c) Liner installed in top wall.	166
Figure 6.6.—Representative format for comparison of impedance prediction and measurement means and 95% confidence intervals.....	180
Figure 6.7.—Results from NIT impedance measurements with source excitation levels of 120 and 140 dB conducted at 100-Hz increments. (a) Resistance. (b) Reactance.	180
Figure 6.8.—Results from GIT impedance measurements with source excitation levels of 120 and 140 dB conducted at 500-Hz increments. (a) Resistance. (b) Reactance.	181
Figure 6.9.—Results from NIT and GIT impedance measurements with source excitation levels of 120 dB conducted at 100- and 500-Hz increments, respectively. (a) Resistance. (b) Reactance.	181
Figure 6.10.—Results from NIT and GIT impedance measurements with source excitation levels of 140 dB conducted at 100- and 500-Hz increments, respectively. (a) Resistance. (b) Reactance.	182
Figure 6.11.—Results from GIT impedance measurements with source excitation level of 140 dB conducted at 500-Hz increments for Mach numbers $M = 0.3$ and 0.475 . (a) Resistance. (b) Reactance.	182
Figure 6.12.—Comparison of impedance results from 14 NIT measurements and 31 Two-Parameter model (TP) simulations with no flow and 120-dB source excitation level conducted at 100-Hz increments. (a) Resistance. (b) Reactance.	183
Figure 6.13.—Comparison of impedance results from 14 NIT measurements and 31 Two-Parameter model (TP) simulations with no flow and 140-dB source excitation level conducted at 100-Hz increments. (a) Resistance. (b) Reactance.	184
Figure 6.14.—Comparison of impedance results from 10 GIT measurements conducted at 500-Hz increments and 31 Two-Parameter model (TP) simulations conducted at 100-Hz increments with no flow and 120-dB source excitation level. (a) Resistance. (b) Reactance.....	184
Figure 6.15.—Comparison of impedance results from 9 GIT measurements conducted at 500-Hz increments and 31 Two-Parameter model (TP) simulations conducted at 100-Hz increments with no flow and 140-dB source excitation level. (a) Resistance. (b) Reactance.....	185
Figure 6.16.—Comparison of impedance results from 9 GIT measurements conducted at 500-Hz increments and 31 Two-Parameter model (TP) simulations conducted at 100-Hz increments with Mach number $M = 0.3$ and 140-dB source excitation level. (a) Resistance. (b) Reactance.	185
Figure 6.17.—Comparison of impedance results from 9 GIT measurements conducted at 500-Hz increments and 31 Two-Parameter model (TP) simulations conducted at 100-Hz increments with Mach number $M = 0.475$ and 140-dB source excitation level. (a) Resistance. (b) Reactance.	186

Figure 6.18.—Comparison of impedance results from 14 NIT measurements and 31 Crandall Full-Solution model (CF) simulations conducted at 100-Hz increments with no flow and 120-dB source excitation level. (a) Resistance. (b) Reactance.	186
Figure 6.19.—Comparison of impedance results from 14 NIT measurements and 31 Crandall Full-Solution model (CF) simulations conducted at 100-Hz increments with no flow and 140-dB source excitation level. (a) Resistance. (b) Reactance.	187
Figure 6.20.—Comparison of impedance results from 10 GIT measurements conducted at 500-Hz increments and 31 Crandall Full-Solution model (CF) simulations conducted at 100-Hz increments with no flow and 120-dB source excitation level. (a) Resistance. (b) Reactance.	187
Figure 6.21.—Comparison of impedance results from 9 GIT measurements conducted at 500-Hz increments and 31 Crandall Full-Solution model (CF) simulations conducted at 100-Hz increments with no flow and 140-dB source excitation level. (a) Resistance. (b) Reactance.	188
Figure 6.22.—Comparison of impedance results from 9 GIT measurements conducted at 500-Hz increments and 31 Crandall Full-Solution model (CF) simulations conducted at 100-Hz increments with Mach number $M = 0.3$ and 140-dB source excitation level. (a) Resistance. (b) Reactance.	188
Figure 6.23.—Comparison of impedance results from 10 GIT measurements conducted at 500-Hz increments and 31 Crandall Full-Solution model (CF) simulations conducted at 100-Hz increments with Mach number $M = 0.475$ and 140-dB source excitation level. (a) Resistance. (b) Reactance.	189
Figure 6.24.—Comparison of impedance results from 14 NIT measurements and 31 Composite Empirical model (CE) simulations conducted at 100-Hz increments with no flow and 120-dB source excitation level. (a) Resistance. (b) Reactance.	189
Figure 6.25.—Comparison of impedance results from 14 NIT measurements and 31 Composite Empirical model (CE) simulations conducted at 100-Hz increments with no flow and 140-dB source excitation level. (a) Resistance. (b) Reactance.	190
Figure 6.26.—Comparison of impedance results from 10 GIT measurements conducted at 500-Hz increments and 31 Composite Empirical model (CE) simulations conducted at 100-Hz increments with no flow and 120-dB source excitation level. (a) Resistance. (b) Reactance.	190
Figure 6.27.—Comparison of impedance results from 9 GIT measurements conducted at 500-Hz increments and 31 Composite Empirical model (CE) simulations conducted at 100-Hz increments with no flow and 140-dB source excitation level. (a) Resistance. (b) Reactance.	191
Figure 6.28.—Comparison of impedance results from 9 GIT measurements conducted at 500-Hz increments and 31 Composite Empirical model (CE) simulations conducted at 100-Hz increments with Mach number $M = 0.3$ and 140-dB source excitation level. (a) Resistance. (b) Reactance.	191
Figure 6.29.—Comparison of impedance results from 10 GIT measurements conducted at 500-Hz increments and 31 Composite Empirical model (CE) simulations conducted at 100-Hz increments with Mach number $M = 0.475$ and 140-dB source excitation level. (a) Resistance. (b) Reactance.	192
Figure 6.30.—Comparison of impedance results from 14 NIT measurements and 31 Fluid Mechanical model (FM) simulations conducted at 100-Hz increments with no flow and 120-dB source excitation level. (a) Resistance. (b) Reactance.	192
Figure 6.31.—Comparison of impedance results from 14 NIT measurements and 31 Fluid Mechanical model (FM) simulations conducted at 100-Hz increments with no flow and 140-dB source excitation level. (a) Resistance. (b) Reactance.	193
Figure 6.32.—Comparison of average impedance values from Two-Parameter model (TP), Crandall Full-Solution model (CF), and Composite Empirical model (CE) simulations conducted at 100-Hz increments with no flow and 140-dB source excitation level. (a) Resistance. (b) Reactance.	193
Figure 6.33.—Comparison of average impedance values from Two-Parameter model (TP), Crandall Full-Solution model (CF), and Composite Empirical model (CE) simulations conducted at 100-Hz increments with Mach number $M = 0.3$ and 140-dB source excitation level. (a) Resistance. (b) Reactance.	194
Figure 6.34.—Comparison of average impedance values from Two-Parameter model (TP), Crandall Full-Solution model (CF), and Composite Empirical model (CE) simulations conducted at 100-Hz increments with Mach number $M = 0.475$ and 140-dB source excitation level. (a) Resistance. (b) Reactance.	194
Figure 7.1.—Turbofan engine nacelle with acoustic liner.	206

Figure 7.2.—Two types of acoustic propagation in flow ducts addressed in this chapter, showing source plane boundary Γ_s and termination plane boundary Γ_t . (a) Inlet propagation. (b) Aft-duct propagation.	206
Figure 7.3.—Finite-element discretization of two-dimensional duct.	212
Figure 7.4.—Typical two-dimensional finite-element, $[I,J]$, and local node numbering system.	212
Figure 7.5.—Finite-element discretization of three-dimensional duct.	215
Figure 7.6.—Typical three-dimensional finite-element, $[I,J,K]$, and local node numbering system.	215
Figure 7.7.—Turbofan engine showing boundary regions of axisymmetric aft-fan geometry for parabolic approximation acoustic propagation and far-field radiation code FWH3D, where \mathbf{n} is unit vector normal to outer shear layer.	218
Figure 7.8.—Sound attenuation results from 8 grazing incidence tube (GIT) measurements and 31 simulations with each sound propagation code for liner 1, no flow, and source sound pressure level of 140 dB.	228
Figure 7.9.—Sound attenuation results from 8 grazing incidence tube (GIT) measurements and 31 simulations with each sound propagation code, resonance removed, for liner 1, no flow, and source sound pressure level of 140 dB.	228
Figure 7.10.—Sound attenuation results from 8 grazing incidence tube (GIT) measurements and 31 simulations with each sound propagation code for liner 1, mean flow Mach number $M_0 = 0.25$, and source sound pressure level of 140 dB.	229
Figure 7.11.—Sound attenuation results from 8 grazing incidence tube (GIT) measurements and 31 simulations with each sound propagation code for liner 1, mean flow Mach number $M_0 = 0.40$, and source sound pressure level of 140 dB.	229
Figure 7.12.—Sound attenuation results from 8 grazing incidence tube (GIT) measurements and 6 simulations with each sound propagation code for liner 1, no flow, and source sound pressure level of 140 dB.	229
Figure 7.13.—Curved Duct Test Rig (CDTR) liner test section with straight liner installed, top removed, view looking downstream.	231
Figure 7.14.—Curved Duct Test Rig (CDTR) sound attenuation measured and predicted with two sound propagation codes; no flow, incident mode (0,0), and source sound pressure level of 130 dB.	231
Figure 7.15.—Curved Duct Test Rig (CDTR) sound attenuation measured and predicted with two sound propagation codes; no flow, incident mode (1,0), and source sound pressure level of 130 dB.	232
Figure 7.16.—Curved Duct Test Rig (CDTR) sound attenuation measured and predicted with two sound propagation codes; no flow, incident mode (0,1), and source sound pressure level of 130 dB.	232
Figure 7.17.—NASA Glenn Advanced Noise Control Fan (ANCF) rig.	233
Figure 7.18.—Internal and pseudo-duct Advanced Noise Control Fan (ANCF) computational meshes.	233
Figure 7.19.—Comparison of FWH3D and CH2DIE predictions of sound radiated from a duct for Active Noise Control Fan (ANCF); mode (2,0) and blade-passing frequency (BPF) = 533 Hz.	234
Figure 8.1.—Turbulent kinetic energy (TKE) contours downstream from a nozzle. Comparison of predictions from different CFD codes, PAB3D and Wind-US, and experimental particle image velocimetry (PIV) data.	245
Figure 8.2.—Comparison of sound pressure levels (SPLs) predicted by Jet3D for a jet from a converging nozzle using input from different CFD codes, PAB3D and Wind-US, and experimental data. Case 037 from Table 8.1. Inlet angle $\theta = 90^\circ$.	246
Figure 8.3.—Power spectral density (PSD) versus Strouhal number St of cold jet, acoustic Mach number $M_a = 0.5$, predicted by JeNo using RANS input with three turbulence models; and largest difference Δ between predictions. (a) Inlet angle $\theta = 90^\circ$. (b) $\theta = 150^\circ$.	247
Figure 8.4.—Power spectral density (PSD) versus Strouhal number St of cold jet, acoustic Mach number $M_a = 0.9$, predicted by JeNo using RANS input with three turbulence models; and largest difference Δ between predictions. (a) Inlet angle $\theta = 90^\circ$. (b) $\theta = 150^\circ$.	248
Figure 8.5.—Overall sound pressure level (OASPL) predicted by JeNo for jets at changing inlet angle θ using two different RANS code flow solutions; difference Δ in predictions is (Wind-US – Craft). (a) Acoustic Mach number $M_a = 0.5$. (b) $M_a = 0.9$.	249
Figure 8.6.—Overall sound pressure level (OASPL) predicted by JeNo for cold jets at changing inlet angle θ with ± 10 percent change in RANS code turbulent kinetic energy (TKE); and difference Δ in predictions. (a) Acoustic Mach number $M_a = 0.5$. (b) $M_a = 0.9$.	250

Figure 8.7.—Distribution of normalized turbulent kinetic energy (TKE) for 5-cm convergent nozzle; here, r is radial coordinate and x is axial distance, normalized over nozzle diameter D . Wind-US Reynolds-averaged Navier-Stokes (RANS) predictions and particle image velocimetry (PIV) measurements. (a) Acoustic Mach number $M_a = 0.5$ unheated jet (case 003, Table 8.1). (b) $M_a = 0.9$ unheated jet (case 007). (c) $M_a = 1.48$ heated jet (case 040).	251
Figure 8.8.—Small Hot Jet Acoustic Rig (SHJAR).	254
Figure 8.9.—Inside Aero-Acoustic Propulsion Laboratory (AAPL), showing Nozzle Acoustic Test Rig (NATR) and overhead far-field microphone array used in NATR acoustic testing.	255
Figure 8.10.—High Flow Jet Exit Rig (HFJER) in dual-flow mode.	256
Figure 8.11.—SHJAR nozzle system with SMC000 nozzle attached.	256
Figure 8.12.—SHJAR nozzles used in this jet noise assessment.	257
Figure 8.13.—Convergent-divergent nozzle SMC014, design Mach number $M_d = 1.18$. Dimensions are in centimeters (inches).	257
Figure 8.14.—Internally mixed, axisymmetric, dual-flow exhaust system with convergent nozzle and different bypass ratios (BPRs). S1 to S3 are splitters, PE1 is center plug, and C4 is convergent nozzle. (a) Nozzle C4S1PE1, BPR = 0.2. (b) Nozzle C4S2PE1, BPR = 1. (c) Nozzle C4S3PE1, BPR = 3.	258
Figure 8.15.—Internally mixed, axisymmetric, dual-flow exhaust system with convergent-divergent nozzle M8 shown with bypass ratio (BPR) = 0.2, splitter S1. PE2 is center plug.	259
Figure 8.16.—Internally mixed, dual-flow exhaust system with convergent nozzle and nonaxisymmetric splitters. (a) Lobed. (b) Chevron.	259
Figure 8.17.—Externally mixed dual-flow exhaust systems. Dimensions are in centimeters (inches). (a) Nozzle PAA5. (b) Nozzle PAA8. (c) Nozzle PAA11. (d) Nozzle PAA14.	260
Figure 8.18.—Sound pressure level (SPL) versus Strouhal number St at inlet angle $\theta = 90^\circ$ for different jet acoustic Mach numbers M_a . Comparison of results from current SHJAR experimental data, Reference 17, and Reference 18.	262
Figure 8.19.—Sound pressure level (SPL) versus Strouhal number St at jet acoustic Mach number $M_a = 0.5$ for inlet angles $\theta = 90^\circ$ and 150° . Comparison of values from current SHJAR experimental data and Reference 17. (a) Static temperature ratio $T_{s,r} = 0.86$ (cold). (b) $T_{s,r} = 1.76$. (c) $T_{s,r} = 2.27$.	263
Figure 8.20.—Sound pressure level (SPL) versus Strouhal number St at jet acoustic Mach number $M_a = 0.9$ for inlet angles $\theta = 90^\circ$ and 150° . Comparison of values from current SHJAR experimental data and Reference 17. (a) Static temperature ratio $T_{s,r} = 0.86$ (cold). (b) $T_{s,r} = 1.76$. (c) $T_{s,r} = 2.27$.	263
Figure 8.21.—Hot jet sound pressure level (SPL) normalized to standard day at 4.6 m (15 ft) versus Strouhal number St for different nozzle diameters D at inlet angle $\theta = 90^\circ$, Mach number $M = 0.7$, and total temperature ratio $T_{t,r} = 3.2$. (a) Comparison of values from current SHJAR experimental data and Reference 18. (b) Difference between values of Reference 18 and SHJAR data.	263
Figure 8.22.—Experimental arrangement for axial-flow stereo particle image velocimetry (PIV) measurements.	264
Figure 8.23.—Axial velocity of cold jet, acoustic Mach number $M_a = 0.5$, measured along centerline x/D using conventional particle image velocimetry (PIV), time-resolved PIV (TRPIV), laser Doppler velocimetry (LDV), and hotwire anemometry. (a) Normalized mean axial velocity, u_o/U . (b) Normalized root-mean-squared fluctuating axial velocity, $\sqrt{u'^2}/U$.	266
Figure 8.24.—Axial velocity of cold jet, static temperature ratio $T_{s,r} = 0.84$ and acoustic Mach number $M_a = 0.9$, measured along centerline x/D using particle image velocimetry (PIV) and laser Doppler velocimetry (LDV). T3 and T4 designate PIV measurements taken 1 year apart. (a) Normalized mean axial velocity u_o/U . (b) Normalized root-mean-squared fluctuating velocity $\sqrt{u'^2}/U$.	267
Figure 8.25.—Axial velocity of hot jet measured along centerline x/D using particle image velocimetry (PIV) (static temperature ratio $T_{s,r} = 2.7$ and acoustic Mach number $M_a = 0.9$) and laser Doppler velocimetry (LDV) ($T_{s,r} = 2.7$ and $M_a = 0.78$). (a) Normalized mean axial velocity u_o/U . (b) Normalized root-mean-squared fluctuating velocity $\sqrt{u'^2}/U$.	267
Figure 8.26.—Typical results for jet noise directivity analyses. (a) 1/3-octave sound pressure level (SPL) versus Strouhal number St for two inlet angles θ from SHJAR experimental data and ANOPP predictions. (b) Difference between predicted and measured SPL, with uncertainty bands. (c) Overall sound pressure level (OASPL) as function of θ .	269

Figure 8.27.—Example of source noise component and total spectra computed by ANOPP for a shock-free jet at inlet angle $\theta = 90^\circ$. 1/3-octave sound pressure level (SPL) versus Strouhal number St	269
Figure 8.28.—Average error μ in overall sound pressure level (OASPL) between ANOPP predictions and experimental data for all ANOPP assessment cases listed in Table 8.7 (Appendix B), grouped in configurations A through I with corresponding bypass ratio (BPR), azimuthal periodicity m , and Mach number M	270
Figure 8.29.—Standard deviation σ about the average overall sound pressure level (OASPL) error between ANOPP predictions and experimental data for all ANOPP assessment cases listed in Table 8.7 (Appendix B), grouped in configurations A through I with corresponding bypass ratio (BPR), azimuthal periodicity m , and Mach number M	270
Figure 8.30.—Difference in effective perceived noise level (EPNL) between ANOPP predictions and experimental data for all ANOPP assessment cases listed in Table 8.7 (Appendix B), grouped in configurations A through I with corresponding bypass ratio (BPR), azimuthal periodicity m , and Mach number M	271
Figure 8.31.—Assessment of Jet3D jet noise predictions. Case 003 (see Table 8.1) for convergent, axisymmetric nozzle: bypass ratio (BPR) = 0, Mach number $M = 0.51$, acoustic Mach number $M_a = 0.5$, and static temperature ratio $T_{s,r} = 0.955$. Comparison between Jet3D predictions and SHJAR experimental data. (a) 1/3-octave sound pressure level (SPL) versus Strouhal number St for inlet angles $\theta = 90^\circ$ and 130° . (b) Difference in SPL values, with uncertainty. (c) Overall sound pressure level (OASPL) as function of θ	272
Figure 8.32.—Assessment of Jet3D jet noise predictions. Case 007 (see Table 8.1) for convergent, axisymmetric nozzle: bypass ratio (BPR) = 0, Mach number $M = 0.98$, acoustic Mach number $M_a = 0.902$, and static temperature ratio $T_{s,r} = 0.842$. Comparison between Jet3D predictions and SHJAR experimental data. (a) 1/3-octave sound pressure level (SPL) versus Strouhal number St for inlet angles $\theta = 90^\circ$ and 130° . (b) Difference in SPL values, with uncertainty. (c) Overall sound pressure level (OASPL) as function of θ	272
Figure 8.33.—Assessment of Jet3D jet noise predictions. Case 022 (see Table 8.1) for convergent, axisymmetric nozzle: bypass ratio (BPR) = 0, Mach number $M = 0.37$, acoustic Mach number $M_a = 0.492$, and static temperature ratio $T_{s,r} = 1.767$. Comparison between Jet3D predictions and SHJAR experimental data. (a) 1/3-octave sound pressure level (SPL) versus Strouhal number St for inlet angles $\theta = 90^\circ$ and 130° . (b) Difference in SPL values, with uncertainty. (c) Overall sound pressure level (OASPL) as function of θ	273
Figure 8.34.—Assessment of Jet3D jet noise predictions. Case 025 (see Table 8.1) for convergent, axisymmetric nozzle: bypass ratio (BPR) = 0, Mach number $M = 0.68$, acoustic Mach number $M_a = 0.901$, and static temperature ratio $T_{s,r} = 1.77$. Comparison between Jet3D predictions and SHJAR experimental data. (a) 1/3-octave sound pressure level (SPL) versus Strouhal number St for inlet angles $\theta = 90^\circ$ and 130° . (b) Difference in SPL values, with uncertainty. (c) Overall sound pressure level (OASPL) as function of θ	273
Figure 8.35.—Assessment of Jet3D jet noise predictions. Case 027 (see Table 8.1) for convergent, axisymmetric nozzle: bypass ratio (BPR) = 0, Mach number $M = 1.01$, acoustic Mach number $M_a = 1.33$, and static temperature ratio $T_{s,r} = 1.759$. Comparison between Jet3D predictions and SHJAR experimental data. (a) 1/3-octave sound pressure level (SPL) versus Strouhal number St for inlet angles $\theta = 90^\circ$ and 130° . (b) Difference in SPL values, with uncertainty. (c) Overall sound pressure level (OASPL) as function of θ	274
Figure 8.36.—Assessment of Jet3D jet noise predictions. Case 034 (see Table 8.1) for convergent, axisymmetric nozzle: bypass ratio (BPR) = 0, Mach number $M = 0.3$, acoustic Mach number $M_a = 0.484$, and static temperature ratio $T_{s,r} = 2.624$. Comparison between Jet3D predictions and SHJAR experimental data. (a) 1/3-octave sound pressure level (SPL) versus Strouhal number St for inlet angles $\theta = 90^\circ$ and 130° . (b) Difference in SPL values, with uncertainty. (c) Overall sound pressure level (OASPL) as function of θ	274
Figure 8.37.—Assessment of Jet3D jet noise predictions. Case 037 (see Table 8.1) for convergent, axisymmetric nozzle: bypass ratio (BPR) = 0, Mach number $M = 0.56$, acoustic Mach number $M_a = 0.901$, and static temperature ratio $T_{s,r} = 2.702$. Comparison between Jet3D predictions and SHJAR experimental data. (a) 1/3-octave sound pressure level (SPL) versus Strouhal number St for	

inlet angles $\theta = 90^\circ$ and 130° . (b) Difference in SPL values, with uncertainty. (c) Overall sound pressure level (OASPL) as function of θ .	275
Figure 8.38.—Assessment of Jet3D jet noise predictions. Case 040 (see Table 8.1) for convergent, axisymmetric nozzle: bypass ratio (BPR) = 0, Mach number $M = 0.92$, acoustic Mach number $M_a = 1.483$, and static temperature ratio $T_{s,r} = 2.703$. Comparison between Jet3D predictions and SHJAR experimental data. (a) 1/3-octave sound pressure level (SPL) versus Strouhal number St for inlet angles $\theta = 90^\circ$ and 130° . (b) Difference in SPL values, with uncertainty. (c) Overall sound pressure level (OASPL) as function of θ .	275
Figure 8.39.—Assessment of Jet3D jet noise predictions. Case 268 (see Table 8.1) for convergent-divergent, axisymmetric nozzle: bypass ratio (BPR) = 0, Mach number $M = 1.4$, acoustic Mach number $M_a = 2.2$, and static temperature ratio $T_{s,r} = 2.53$. Comparison between Jet3D predictions and SHJAR experimental data. (a) 1/3-octave sound pressure level (SPL) versus Strouhal number St for inlet angles $\theta = 90^\circ$ and 130° . (b) Difference in SPL values, with uncertainty. (c) Overall sound pressure level (OASPL) as function of θ .	276
Figure 8.40.—Nozzles with offset stream technology used to assess the JeNo v1.0 code jet noise prediction capability. (a) Fan-wedge. (b) S-duct.	277
Figure 8.41.—Assessment of JeNo v1.0 jet noise predictions. Case 003 (see Table 8.5) for convergent, axisymmetric nozzle: bypass ratio (BPR) = 0, Mach number $M = 0.51$, acoustic Mach number $M_a = 0.5$, and static temperature ratio $T_{s,r} = 0.955$. Comparison between JeNo predictions and SHJAR experimental data. (a) 1/3-octave sound pressure level (SPL) versus Strouhal number St for inlet angles $\theta = 90^\circ$ and 130° . (b) Difference in SPL values, with uncertainty. (c) Overall sound pressure level (OASPL) as function of θ .	278
Figure 8.42.—Assessment of JeNo v1.0 jet noise predictions. Case 007 (see Table 8.5) for convergent, axisymmetric nozzle: bypass ratio (BPR) = 0, Mach number $M = 0.98$, acoustic Mach number $M_a = 0.902$, and static temperature ratio $T_{s,r} = 0.842$. Comparison between JeNo predictions and SHJAR experimental data. (a) 1/3-octave sound pressure level (SPL) versus Strouhal number St for inlet angles $\theta = 90^\circ$ and 130° . (b) Difference in SPL values, with uncertainty. (c) Overall sound pressure level (OASPL) as function of θ .	279
Figure 8.43.—Assessment of JeNo v1.0 jet noise predictions. Case 022 (see Table 8.5) for convergent, axisymmetric nozzle: bypass ratio (BPR) = 0, Mach number $M = 0.37$, acoustic Mach number $M_a = 0.492$, and static temperature ratio $T_{s,r} = 1.767$. Comparison between JeNo predictions and SHJAR experimental data. (a) 1/3-octave sound pressure level (SPL) versus Strouhal number St for inlet angles $\theta = 90^\circ$ and 130° . (b) Difference in SPL values, with uncertainty. (c) Overall sound pressure level (OASPL) as function of θ .	279
Figure 8.44.—Assessment of JeNo v1.0 jet noise predictions. Case 025 (see Table 8.5) for convergent, axisymmetric nozzle: bypass ratio (BPR) = 0, Mach number $M = 0.68$, acoustic Mach number $M_a = 0.901$, and static temperature ratio $T_{s,r} = 1.77$. Comparison between JeNo predictions and SHJAR experimental data. (a) 1/3-octave sound pressure level (SPL) versus Strouhal number St for inlet angles $\theta = 90^\circ$ and 130° . (b) Difference in SPL values, with uncertainty. (c) Overall sound pressure level (OASPL) as function of θ .	280
Figure 8.45.—Assessment of JeNo v1.0 jet noise predictions. Case 027 (see Table 8.5) for convergent, axisymmetric nozzle: bypass ratio (BPR) = 0, Mach number $M = 1.01$, acoustic Mach number $M_a = 1.33$, and static temperature ratio $T_{s,r} = 1.759$. Comparison between JeNo predictions and SHJAR experimental data. (a) 1/3-octave sound pressure level (SPL) versus Strouhal number St for inlet angles $\theta = 90^\circ$ and 130° . (b) Difference in SPL values, with uncertainty. (c) Overall sound pressure level (OASPL) as function of θ .	280
Figure 8.46.—Assessment of JeNo v1.0 jet noise predictions. Case 034 (see Table 8.5) for convergent, axisymmetric nozzle: bypass ratio (BPR) = 0, Mach number $M = 0.3$, acoustic Mach number $M_a = 0.484$, and static temperature ratio $T_{s,r} = 2.624$. Comparison between JeNo predictions and SHJAR experimental data. (a) 1/3-octave sound pressure level (SPL) versus Strouhal number St for inlet angles $\theta = 90^\circ$ and 130° . (b) Difference in SPL values, with uncertainty. (c) Overall sound pressure level (OASPL) as function of θ .	281
Figure 8.47.—Assessment of JeNo v1.0 jet noise predictions. Case 037 (see Table 8.5) for convergent, axisymmetric nozzle: bypass ratio (BPR) = 0, Mach number $M = 0.56$, acoustic Mach number $M_a = 0.901$, and static temperature ratio $T_{s,r} = 2.702$. Comparison between JeNo predictions and	

SHJAR experimental data. (a) 1/3-octave sound pressure level (SPL) versus Strouhal number St for inlet angles $\theta = 90^\circ$ and 130° . (b) Difference in SPL values, and uncertainty. (c) Overall sound pressure level (OASPL) as function of θ	281
Figure 8.48.—Assessment of JeNo v1.0 jet noise predictions. Case 040 (see Table 8.5) for convergent, axisymmetric nozzle: bypass ratio (BPR) = 0, Mach number $M = 0.92$, acoustic Mach number $M_a = 1.483$, and static temperature ratio $T_{s,r} = 2.703$. Comparison between JeNo predictions and SHJAR experimental data. (a) 1/3-octave sound pressure level (SPL) versus Strouhal number St for inlet angles $\theta = 90^\circ$ and 130° . (b) Difference in SPL values, with uncertainty. (c) Overall sound pressure level (OASPL) as function of θ	282
Figure 8.49.—Assessment of JeNo v1.0 jet noise predictions. Case 059 (see Table 8.5) for convergent-divergent, axisymmetric nozzle: bypass ratio (BPR) = 0, Mach number $M = 1.172$, acoustic Mach number $M_a = 1.047$, and static temperature ratio $T_{s,r} = 0.797$. Comparison between JeNo predictions and SHJAR experimental data. (a) 1/3-octave sound pressure level (SPL) versus Strouhal number St for inlet angles $\theta = 90^\circ$ and 130° . (b) Difference in SPL values, with uncertainty. (c) Overall sound pressure level (OASPL) as function of θ	282
Figure 8.50.—Assessment of JeNo v1.0 jet noise predictions. Case 068 (see Table 8.5) for convergent-divergent, axisymmetric nozzle: bypass ratio (BPR) = 0, Mach number $M = 1.394$, acoustic Mach number $M_a = 1.191$, and static temperature ratio $T_{s,r} = 0.73$. Comparison between JeNo predictions and SHJAR experimental data. (a) 1/3-octave sound pressure level (SPL) versus Strouhal number St for inlet angles $\theta = 90^\circ$ and 130° . (b) Difference in SPL values, with uncertainty. (c) Overall sound pressure level (OASPL) as function of θ	283
Figure 8.51.—Assessment of JeNo v1.0 jet noise predictions. Case 075 (see Table 8.5) for convergent-divergent, axisymmetric nozzle: bypass ratio (BPR) = 0, Mach number $M = 1.497$, acoustic Mach number $M_a = 1.251$, and static temperature ratio $T_{s,r} = 0.699$. Comparison between JeNo predictions and SHJAR experimental data. (a) 1/3-octave sound pressure level (SPL) versus Strouhal number St for inlet angles $\theta = 90^\circ$ and 130° . (b) Difference in SPL values, with uncertainty. (c) Overall sound pressure level (OASPL) as function of θ	283
Figure 8.52.—Assessment of JeNo v1.0 jet noise predictions. Case 083 (see Table 8.5) for convergent-divergent, axisymmetric nozzle: bypass ratio (BPR) = 0, Mach number $M = 1.659$, acoustic Mach number $M_a = 1.342$, and static temperature ratio $T_{s,r} = 0.654$. Comparison between JeNo predictions and SHJAR experimental data. (a) 1/3-octave sound pressure level (SPL) versus Strouhal number St for inlet angles $\theta = 90^\circ$ and 130° . (b) Difference in SPL values, with uncertainty. (c) Overall sound pressure level (OASPL) as function of θ	284
Figure 8.53.—Assessment of JeNo v1.0 jet noise predictions. Case 090 (see Table 8.5) for convergent-divergent, axisymmetric nozzle: bypass ratio (BPR) = 0, Mach number $M = 1.784$, acoustic Mach number $M_a = 1.403$, and static temperature ratio $T_{s,r} = 0.619$. Comparison between JeNo predictions and SHJAR experimental data. (a) 1/3-octave sound pressure level (SPL) versus Strouhal number St for inlet angles $\theta = 90^\circ$ and 130° . (b) Difference in SPL values, with uncertainty. (c) Overall sound pressure level (OASPL) as function of θ	284
Figure 8.54.—Comparison of lossless power spectral density (PSD) of jet noise versus Strouhal number St at different inlet angles θ on a $40D$ arc. NATR data and JeNo v1.0 predictions. (a) $\theta = 60^\circ$. (b) $\theta = 90^\circ$. (c) $\theta = 130^\circ$. (d) $\theta = 150^\circ$	286
Figure 8.55.—Comparison of lossless power spectral density (PSD) for offset nozzle versus Strouhal number St at different inlet angles θ on a $40D$ arc. NATR data and JeNo v1.0 predictions. (a) $\theta = 90^\circ$. (b) $\theta = 150^\circ$	286
Figure 8.56.—Comparison of lossless power spectral density (PSD) for offset S-duct nozzle and axisymmetric geometry (see Table 8.6 and Figure 8.40(b)) at different inlet angles θ on $40D$ arc. (a) Nozzle geometries. (b) NATR experimental data, $\theta = 90^\circ$ and 150° . (c) JeNo v1.0 predictions at 90° using 2.5-dimensional approximation with line-of-sight method. (d) JeNo v1.0 predictions at 150° using 2.5-dimensional approximation with line-of-sight method.	287
Figure 8.57.—Difference Δ between power spectral density (PSD) measured on thick side of S-duct nozzle and axisymmetric nozzle. (a) JeNo v1.0 prediction at inlet angle $\theta = 150^\circ$. (b) NATR experimental data at $\theta = 150^\circ$. (c) Error estimate at $\theta = 150^\circ$; difference between NATR data and prediction. (d) Error estimate at $\theta = 90^\circ$	288

Figure 8.58.—Lossless power spectral density (PSD) for offset fan-wedge nozzle and axisymmetric geometry (see Table 8.6 and Figure 8.40(a)) at different inlet angles θ on 24.46-m (80.24-ft) arc. (a) Nozzle geometries. (b) NATR experimental data. (c) JeNo v1.0 predictions at $\theta = 90^\circ$ using 2.5-dimensional approximation with line-of-sight method. (d) JeNo v1.0 predictions at $\theta = 150^\circ$ using 2.5-dimensional approximation with line-of-sight method.	289
Figure 8.59.—Difference Δ between power spectral density (PSD) measured on thick (quiet) and thin (noisy) sides of fan-wedge nozzle and axisymmetric nozzle. (a) JeNo v1.0 prediction at inlet angle $\theta = 150^\circ$. (b) NATR experimental data at $\theta = 150^\circ$. (c) Error estimate at $\theta = 150^\circ$; difference between NATR data and prediction. (d) Error estimate at $\theta = 90^\circ$	290
Figure 8.60.—Assessment of ANOPP ST2JET jet noise predictions (Table 8.7, Appendix B). Configuration A case 003 for convergent, axisymmetric nozzle: bypass ratio (BPR) = 0, Mach number $M = 0.51$, acoustic Mach number $M_a = 0.5$, and static temperature ratio $T_{s,r} = 0.955$. Comparison between ANOPP predictions and SHJAR experimental data. (a) 1/3-octave sound pressure level (SPL) versus Strouhal number St for inlet angles $\theta = 90^\circ$ and 150° . (b) Difference in 1/3-octave SPL values, with uncertainty. (c) Overall sound pressure level (OASPL) as function of θ	306
Figure 8.61.—Assessment of ANOPP ST2JET jet noise predictions (Table 8.7, Appendix B). Configuration A case 007 for convergent, axisymmetric nozzle: bypass ratio (BPR) = 0, Mach number $M = 0.98$, acoustic Mach number $M_a = 0.902$, and static temperature ratio $T_{s,r} = 0.842$. Comparison between ANOPP predictions and SHJAR experimental data. (a) 1/3-octave sound pressure level (SPL) versus Strouhal number St for inlet angles $\theta = 90^\circ$ and 150° . (b) Difference in 1/3-octave SPL values, with uncertainty. (c) Overall sound pressure level (OASPL) as function of θ	307
Figure 8.62.—Assessment of ANOPP ST2JET jet noise predictions (Table 8.7, Appendix B). Configuration A case 022 for convergent, axisymmetric nozzle: bypass ratio (BPR) = 0, Mach number $M = 0.37$, acoustic Mach number $M_a = 0.492$, and static temperature ratio $T_{s,r} = 1.767$. Comparison between ANOPP predictions and SHJAR experimental data. (a) 1/3-octave sound pressure level (SPL) versus Strouhal number St for inlet angles $\theta = 90^\circ$ and 150° . (b) Difference in 1/3-octave SPL values, with uncertainty. (c) Overall sound pressure level (OASPL) as function of θ	307
Figure 8.63.—Assessment of ANOPP ST2JET jet noise predictions (Table 8.7, Appendix B). Configuration A case 025 for convergent, axisymmetric nozzle: bypass ratio (BPR) = 0, Mach number $M = 0.68$, acoustic Mach number $M_a = 0.901$, and static temperature ratio $T_{s,r} = 1.77$. Comparison between ANOPP predictions and SHJAR experimental data. (a) 1/3-octave sound pressure level (SPL) versus Strouhal number St for inlet angles $\theta = 90^\circ$ and 150° . (b) Difference in 1/3-octave SPL values, with uncertainty. (c) Overall sound pressure level (OASPL) as function of θ	308
Figure 8.64.—Assessment of ANOPP ST2JET jet noise predictions (Table 8.7, Appendix B). Configuration A case 027 for convergent, axisymmetric nozzle: bypass ratio (BPR) = 0, Mach number $M = 1.01$, acoustic Mach number $M_a = 1.33$, and static temperature ratio $T_{s,r} = 1.759$. Comparison between ANOPP predictions and SHJAR experimental data. (a) 1/3-octave sound pressure level (SPL) versus Strouhal number St for inlet angles $\theta = 90^\circ$ and 150° . (b) Difference in 1/3-octave SPL values, with uncertainty. (c) Overall sound pressure level (OASPL) as function of θ	308
Figure 8.65.—Assessment of ANOPP ST2JET jet noise predictions (Table 8.7, Appendix B). Configuration A case 034 for convergent, axisymmetric nozzle: bypass ratio (BPR) = 0, Mach number $M = 0.3$, acoustic Mach number $M_a = 0.484$, and static temperature ratio $T_{s,r} = 2.624$. Comparison between ANOPP predictions and SHJAR experimental data. (a) 1/3-octave sound pressure level (SPL) versus Strouhal number St for inlet angles $\theta = 90^\circ$ and 150° . (b) Difference in 1/3-octave SPL values, with uncertainty. (c) Overall sound pressure level (OASPL) as function of θ	309
Figure 8.66.—Assessment of ANOPP ST2JET jet noise predictions (Table 8.7, Appendix B). Configuration A case 037 for convergent, axisymmetric nozzle: bypass ratio (BPR) = 0, Mach number $M = 0.56$, acoustic Mach number $M_a = 0.901$, and static temperature ratio $T_{s,r} = 2.702$. Comparison between ANOPP predictions and SHJAR experimental data. (a) 1/3-octave sound pressure level (SPL) versus Strouhal number St for inlet angles $\theta = 90^\circ$ and 150° . (b) Difference in 1/3-octave SPL values, with uncertainty. (c) Overall sound pressure level (OASPL) as function of θ	309
Figure 8.67.—Assessment of ANOPP ST2JET jet noise predictions (Table 8.7, Appendix B). Configuration A case 040 for convergent, axisymmetric nozzle: bypass ratio (BPR) = 0, Mach number $M = 0.92$, acoustic Mach number $M_a = 1.483$, and static temperature ratio $T_{s,r} = 2.703$. Comparison between ANOPP predictions and SHJAR experimental data. (a) 1/3-octave sound	

pressure level (SPL) versus Strouhal number St for inlet angles $\theta = 90^\circ$ and 150° . (b) Difference in 1/3-octave SPL values, with uncertainty. (c) Overall sound pressure level (OASPL) as function of θ	310
Figure 8.68.—Assessment of ANOPP ST2JET jet noise predictions (Table 8.7, Appendix B).	
Configuration B case 042 for convergent, azimuthal periodicity $m = 6$ nozzle: bypass ratio (BPR) = 0, Mach number $M = 0.972$, acoustic Mach number $M_a = 0.902$, and static temperature ratio $T_{s,r} = 0.837$. Comparison between ANOPP predictions and SHJAR experimental data. (a) 1/3-octave sound pressure level (SPL) versus Strouhal number St for inlet angles $\theta = 90^\circ$ and 150° . (b) Difference in 1/3-octave SPL values, with uncertainty. (c) Overall sound pressure level (OASPL) as function of θ	310
Figure 8.69.—Assessment of ANOPP ST2JET jet noise predictions (Table 8.7, Appendix B).	
Configuration B case 057 for convergent, azimuthal periodicity $m = 6$ nozzle: bypass ratio (BPR) = 0, Mach number $M = 0.828$, acoustic Mach number $M_a = 1.309$, and static temperature ratio $T_{s,r} = 2.571$. Comparison between ANOPP predictions and SHJAR experimental data. (a) 1/3-octave sound pressure level (SPL) versus Strouhal number St for inlet angles $\theta = 90^\circ$ and 150° . (b) Difference in 1/3-octave SPL values, with uncertainty. (c) Overall sound pressure level (OASPL) as function of θ	311
Figure 8.70.—Assessment of ANOPP ST2JET jet noise predictions (Table 8.7, Appendix B).	
Configuration C case 059 for convergent-divergent, axisymmetric nozzle: bypass ratio (BPR) = 0, Mach number $M = 1.72$, acoustic Mach number $M_a = 1.047$, and static temperature ratio $T_{s,r} = 0.797$. Comparison between ANOPP predictions and SHJAR experimental data. (a) 1/3-octave sound pressure level (SPL) versus Strouhal number St for inlet angles $\theta = 90^\circ$ and 150° . (b) Difference in 1/3-octave SPL values, with uncertainty. (c) Overall sound pressure level (OASPL) as function of θ	311
Figure 8.71.—Assessment of ANOPP ST2JET jet noise predictions (Table 8.7, Appendix B).	
Configuration C case 068 for convergent-divergent, axisymmetric nozzle: bypass ratio (BPR) = 0, Mach number $M = 1.394$, acoustic Mach number $M_a = 1.191$, and static temperature ratio $T_{s,r} = 0.73$. Comparison between ANOPP predictions and SHJAR experimental data. (a) 1/3-octave sound pressure level (SPL) versus Strouhal number St for inlet angles $\theta = 90^\circ$ and 150° . (b) Difference in 1/3-octave SPL values, with uncertainty. (c) Overall sound pressure level (OASPL) as function of θ	312
Figure 8.72.—Assessment of ANOPP ST2JET jet noise predictions (Table 8.7, Appendix B).	
Configuration C case 075 for convergent-divergent, axisymmetric nozzle: bypass ratio (BPR) = 0, Mach number $M = 1.497$, acoustic Mach number $M_a = 1.251$, and static temperature ratio $T_{s,r} = 0.699$. Comparison between ANOPP predictions and SHJAR experimental data. (a) 1/3-octave sound pressure level (SPL) versus Strouhal number St for inlet angles $\theta = 90^\circ$ and 150° . (b) Difference in 1/3-octave SPL values, with uncertainty. (c) Overall sound pressure level (OASPL) as function of θ	312
Figure 8.73.—Assessment of ANOPP ST2JET jet noise predictions (Table 8.7, Appendix B).	
Configuration C case 083 for convergent-divergent, axisymmetric nozzle: bypass ratio (BPR) = 0, Mach number $M = 1.659$, acoustic Mach number $M_a = 1.342$, and static temperature ratio $T_{s,r} = 0.654$. Comparison between ANOPP predictions and SHJAR experimental data. (a) 1/3-octave sound pressure level (SPL) versus Strouhal number St for inlet angles $\theta = 90^\circ$ and 150° . (b) Difference in 1/3-octave SPL values, with uncertainty. (c) Overall sound pressure level (OASPL) as function of θ	313
Figure 8.74.—Assessment of ANOPP ST2JET jet noise predictions (Table 8.7, Appendix B).	
Configuration C case 090 for convergent-divergent, axisymmetric nozzle: bypass ratio (BPR) = 0, Mach number $M = 1.784$, acoustic Mach number $M_a = 1.403$, and static temperature ratio $T_{s,r} = 0.619$. Comparison between ANOPP predictions and SHJAR experimental data. (a) 1/3-octave sound pressure level (SPL) versus Strouhal number St for inlet angles $\theta = 90^\circ$ and 150° . (b) Difference in 1/3-octave SPL values, with uncertainty. (c) Overall sound pressure level (OASPL) as function of θ	313
Figure 8.75.—Assessment of ANOPP ST2JET jet noise predictions (Table 8.7, Appendix B).	
Configuration D case 104C for internally mixed, convergent, axisymmetric nozzle: bypass ratio (BPR) = 0.2 and flight Mach number $M_f = 0$. For core, acoustic Mach number $M_a = 1.184$ and stagnation temperature ratio $T_{t,r} = 1.546$. For bypass, $M_a = 0.955$ and $T_{t,r} = 1.006$. Comparison between ANOPP predictions with coplanar approximation and NATR experimental data. (a) 1/3-octave sound pressure level (SPL) versus Strouhal number St for inlet angles $\theta = 90^\circ$ and 150° . (b)	

Difference in 1/3-octave SPL values, with uncertainty. (c) Overall sound pressure level (OASPL) as function of θ .	314
Figure 8.76.—Assessment of ANOPP ST2JET jet noise predictions (Table 8.7, Appendix B). Configuration D case 104F for internally mixed, convergent, axisymmetric nozzle: bypass ratio (BPR) = 0.2 and flight Mach number $M_f = 0$. For core, acoustic Mach number $M_a = 1.184$ and stagnation temperature ratio $T_{t,r} = 1.546$. For bypass, $M_a = 0.955$ and $T_{t,r} = 1.006$. Comparison between ANOPP predictions with fully mixed approximation and NATR experimental data. (a) 1/3-octave sound pressure level (SPL) versus Strouhal number St for inlet angles $\theta = 90^\circ$ and 150° . (b) Difference in 1/3-octave SPL values, with uncertainty. (c) Overall sound pressure level (OASPL) as function of θ .	314
Figure 8.77.—Assessment of ANOPP ST2JET jet noise predictions (Table 8.7, Appendix B). Configuration D case 119C for internally mixed, convergent, axisymmetric nozzle: bypass ratio (BPR) = 0.2 and flight Mach number $M_f = 0$. For core, acoustic Mach number $M_a = 2.401$ and stagnation temperature ratio $T_{t,r} = 2.581$. For bypass, $M_a = 1.523$ and $T_{t,r} = 1.042$. Comparison between ANOPP predictions with coplanar approximation and NATR experimental data. (a) 1/3-octave sound pressure level (SPL) versus Strouhal number St for inlet angles $\theta = 90^\circ$ and 150° . (b) Difference in 1/3-octave SPL values, with uncertainty. (c) Overall sound pressure level (OASPL) as function of θ .	315
Figure 8.78.—Assessment of ANOPP ST2JET jet noise predictions (Table 8.7, Appendix B). Configuration D case 119F for internally mixed, convergent, axisymmetric nozzle: bypass ratio (BPR) = 0.2 and flight Mach number $M_f = 0$. For core, acoustic Mach number $M_a = 2.401$ and stagnation temperature ratio $T_{t,r} = 2.581$. For bypass, $M_a = 1.523$ and $T_{t,r} = 1.042$. Comparison between ANOPP predictions with fully mixed approximation and NATR experimental data. (a) 1/3-octave sound pressure level (SPL) versus Strouhal number St for inlet angles $\theta = 90^\circ$ and 150° . (b) Difference in 1/3-octave SPL values, with uncertainty. (c) Overall sound pressure level (OASPL) as function of θ .	315
Figure 8.79.—Assessment of ANOPP ST2JET jet noise predictions (Table 8.7, Appendix B). Configuration E case 143C for internally mixed, convergent, axisymmetric nozzle: bypass ratio (BPR) = 1 and flight Mach number $M_f = 0$. For core, acoustic Mach number $M_a = 1.18$ and stagnation temperature ratio $T_{t,r} = 1.54$. For bypass, $M_a = 0.948$ and $T_{t,r} = 0.99$. Comparison between ANOPP predictions with coplanar approximation and NATR experimental data. (a) 1/3-octave sound pressure level (SPL) versus Strouhal number St for inlet angles $\theta = 90^\circ$ and 150° . (b) Difference in 1/3-octave SPL values, with uncertainty. (c) Overall sound pressure level (OASPL) as function of θ .	316
Figure 8.80.—Assessment of ANOPP ST2JET jet noise predictions (Table 8.7, Appendix B). Configuration E case 143F for internally mixed, convergent, axisymmetric nozzle: bypass ratio (BPR) = 1 and flight Mach number $M_f = 0$. For core, acoustic Mach number $M_a = 1.18$ and stagnation temperature ratio $T_{t,r} = 1.54$. For bypass, $M_a = 0.948$ and $T_{t,r} = 0.99$. Comparison between ANOPP predictions with fully mixed approximation and NATR experimental data. (a) 1/3-octave sound pressure level (SPL) versus Strouhal number St for inlet angles $\theta = 90^\circ$ and 150° . (b) Difference in 1/3-octave SPL values, with uncertainty. (c) Overall sound pressure level (OASPL) as function of θ .	316
Figure 8.81.—Assessment of ANOPP ST2JET jet noise predictions (Table 8.7, Appendix B). Configuration E case 156C for internally mixed, convergent, axisymmetric nozzle: bypass ratio (BPR) = 1 and flight Mach number $M_f = 0$. For core, acoustic Mach number $M_a = 2.401$ and stagnation temperature ratio $T_{t,r} = 2.581$. For bypass, $M_a = 1.53$ and $T_{t,r} = 1.053$. Comparison between ANOPP predictions with coplanar approximation and NATR experimental data. (a) 1/3-octave sound pressure level (SPL) versus Strouhal number St for inlet angles $\theta = 90^\circ$ and 150° . (b) Difference in 1/3-octave SPL values, with uncertainty. (c) Overall sound pressure level (OASPL) as function of θ .	317
Figure 8.82.—Assessment of ANOPP ST2JET jet noise predictions (Table 8.7, Appendix B). Configuration E case 156F for internally mixed, convergent, axisymmetric nozzle: bypass ratio (BPR) = 1 and flight Mach number $M_f = 0$. For core, acoustic Mach number $M_a = 2.401$ and stagnation temperature ratio $T_{t,r} = 2.581$. For bypass, $M_a = 1.53$ and $T_{t,r} = 1.053$. Comparison between ANOPP predictions with fully mixed approximation and NATR experimental data. (a) 1/3-	

octave sound pressure level (SPL) versus Strouhal number St for inlet angles $\theta = 90^\circ$ and 150° . (b) Difference in 1/3-octave SPL values, with uncertainty. (c) Overall sound pressure level (OASPL) as function of θ .	317
Figure 8.83.—Assessment of ANOPP ST2JET jet noise predictions (Table 8.7, Appendix B). Configuration F case 175C for internally mixed, convergent, axisymmetric nozzle: bypass ratio (BPR) = 3 and flight Mach number $M_\infty = 0$. For core, acoustic Mach number $M_a = 1.183$ and stagnation temperature ratio $T_{t,r} = 1.541$. For bypass, $M_a = 0.94$ and $T_{t,r} = 0.977$. Comparison between ANOPP predictions with coplanar approximation and NATR experimental data. (a) 1/3-octave sound pressure level (SPL) versus Strouhal number St for inlet angles $\theta = 90^\circ$ and 150° . (b) Difference in 1/3-octave SPL values, with uncertainty. (c) Overall sound pressure level (OASPL) as function of θ .	318
Figure 8.84.—Assessment of ANOPP ST2JET jet noise predictions (Table 8.7, Appendix B). Configuration F case 175F for internally mixed, convergent, axisymmetric nozzle: bypass ratio (BPR) = 3 and flight Mach number $M_\infty = 0$. For core, acoustic Mach number $M_a = 1.183$ and stagnation temperature ratio $T_{t,r} = 1.541$. For bypass, $M_a = 0.94$ and $T_{t,r} = 0.977$. Comparison between ANOPP predictions with fully mixed approximation and NATR experimental data. (a) 1/3-octave sound pressure level (SPL) versus Strouhal number St for inlet angles $\theta = 90^\circ$ and 150° . (b) Difference in 1/3-octave SPL values, with uncertainty. (c) Overall sound pressure level (OASPL) as function of θ .	318
Figure 8.85.—Assessment of ANOPP ST2JET jet noise predictions (Table 8.7, Appendix B). Configuration F case 188C for internally mixed, convergent, axisymmetric nozzle: bypass ratio (BPR) = 3 and flight Mach number $M_\infty = 0$. For core, acoustic Mach number $M_a = 2.385$ and stagnation temperature ratio $T_{t,r} = 2.589$. For bypass, $M_a = 1.487$ and $T_{t,r} = 1.012$. Comparison between ANOPP predictions with coplanar approximation and NATR experimental data. (a) 1/3-octave sound pressure level (SPL) versus Strouhal number St for inlet angles $\theta = 90^\circ$ and 150° . (b) Difference in 1/3-octave SPL values, with uncertainty. (c) Overall sound pressure level (OASPL) as function of θ .	319
Figure 8.86.—Assessment of ANOPP ST2JET jet noise predictions (Table 8.7, Appendix B). Configuration F case 188F for internally mixed, convergent, axisymmetric nozzle: bypass ratio (BPR) = 3 and flight Mach number $M_\infty = 0$. For core, acoustic Mach number $M_a = 2.385$ and stagnation temperature ratio $T_{t,r} = 2.589$. For bypass, $M_a = 1.487$ and $T_{t,r} = 1.012$. Comparison between ANOPP predictions with fully mixed approximation and NATR experimental data. (a) 1/3-octave sound pressure level (SPL) versus Strouhal number St for inlet angles $\theta = 90^\circ$ and 150° . (b) Difference in 1/3-octave SPL values, with uncertainty. (c) Overall sound pressure level (OASPL) as function of θ .	319
Figure 8.87.—Assessment of ANOPP ST2JET jet noise predictions (Table 8.7, Appendix B). Configuration G case 191N for externally mixed, convergent, axisymmetric nozzle: bypass ratio (BPR) = 5 and flight Mach number $M_\infty = 0$. For core, acoustic Mach number $M_a = 1.265$ and stagnation temperature ratio $T_{t,r} = 2.663$. For bypass, $M_a = 0.935$ and $T_{t,r} = 1.822$. Comparison between ANOPP predictions and NATR experimental data. (a) 1/3-octave sound pressure level (SPL) versus Strouhal number St for inlet angles $\theta = 90^\circ$ and 150° . (b) Difference in 1/3-octave SPL values, with uncertainty. (c) Overall sound pressure level (OASPL) as function of θ .	320
Figure 8.88.—Assessment of ANOPP ST2JET jet noise predictions (Table 8.7, Appendix B). Configuration G case 200C for internally mixed, convergent, axisymmetric nozzle: bypass ratio (BPR) = 5 and flight Mach number $M_\infty = 0$. For core, acoustic Mach number $M_a = 1.637$ and stagnation temperature ratio $T_{t,r} = 3.543$. For bypass, $M_a = 0.984$ and $T_{t,r} = 1.302$. Comparison between ANOPP predictions with coplanar approximation and NATR experimental data. (a) 1/3-octave sound pressure level (SPL) versus Strouhal number St for inlet angles $\theta = 90^\circ$ and 150° . (b) Difference in 1/3-octave SPL values, with uncertainty. (c) Overall sound pressure level (OASPL) as function of θ .	320
Figure 8.89.—Assessment of ANOPP ST2JET jet noise predictions (Table 8.7, Appendix B). Configuration G case 200F for internally mixed, convergent, axisymmetric nozzle: bypass ratio (BPR) = 5 and flight Mach number $M_\infty = 0$. For core, acoustic Mach number $M_a = 1.637$ and stagnation temperature ratio $T_{t,r} = 3.543$. For bypass, $M_a = 0.984$ and $T_{t,r} = 1.302$. Comparison between ANOPP predictions with fully mixed approximation and NATR experimental data. (a) 1/3-	

octave sound pressure level (SPL) versus Strouhal number St for inlet angles $\theta = 90^\circ$ and 150° . (b) Difference in 1/3-octave SPL values, with uncertainty. (c) Overall sound pressure level (OASPL) as function of θ .	321
Figure 8.90.—Assessment of ANOPP ST2JET jet noise predictions (Table 8.7, Appendix B). Configuration G case 211C for internally mixed, chevron, azimuthal periodicity $m = 8$ nozzle: bypass ratio (BPR) = 5 and flight Mach number $M_\infty = 0$. For core, acoustic Mach number $M_a = 1.614$ and stagnation temperature ratio $T_{t,r} = 3.455$. For bypass, $M_a = 0.973$ and $T_{t,r} = 1.27$. Comparison between ANOPP predictions with coplanar approximation and NATR experimental data. (a) 1/3-octave sound pressure level (SPL) versus Strouhal number St for inlet angles $\theta = 90^\circ$ and 150° . (b) Difference in 1/3-octave SPL values, with uncertainty. (c) Overall sound pressure level (OASPL) as function of θ .	321
Figure 8.91.—Assessment of ANOPP ST2JET jet noise predictions (Table 8.7, Appendix B). Configuration G case 211F for internally mixed, chevron, azimuthal periodicity $m = 8$ nozzle: bypass ratio (BPR) = 5 and flight Mach number $M_\infty = 0$. For core, acoustic Mach number $M_a = 1.614$ and stagnation temperature ratio $T_{t,r} = 3.455$. For bypass, $M_a = 0.973$ and $T_{t,r} = 1.27$. Comparison between ANOPP predictions with fully mixed approximation and NATR experimental data. (a) 1/3-octave sound pressure level (SPL) versus Strouhal number St for inlet angles $\theta = 90^\circ$ and 150° . (b) Difference in 1/3-octave SPL values, with uncertainty. (c) Overall sound pressure level (OASPL) as function of θ .	322
Figure 8.92.—Assessment of ANOPP ST2JET jet noise predictions (Table 8.7, Appendix B). Configuration G case 218C for internally mixed, lobed, azimuthal periodicity $m = 20$ nozzle: bypass ratio (BPR) = 5 and flight Mach number $M_\infty = 0$. For core, acoustic Mach number $M_a = 1.637$ and stagnation temperature ratio $T_{t,r} = 3.546$. For bypass, $M_a = 0.985$ and $T_{t,r} = 1.3$. Comparison between ANOPP predictions with coplanar approximation and NATR experimental data. (a) 1/3-octave sound pressure level (SPL) versus Strouhal number St for inlet angles $\theta = 90^\circ$ and 150° . (b) Difference in 1/3-octave SPL values, with uncertainty. (c) Overall sound pressure level (OASPL) as function of θ .	322
Figure 8.93.—Assessment of ANOPP ST2JET jet noise predictions (Table 8.7, Appendix B). Configuration G case 218F for internally mixed, lobed, azimuthal periodicity $m = 20$ nozzle: bypass ratio (BPR) = 5 and flight Mach number $M_\infty = 0$. For core, acoustic Mach number $M_a = 1.637$ and stagnation temperature ratio $T_{t,r} = 3.546$. For bypass, $M_a = 0.985$ and $T_{t,r} = 1.3$. Comparison between ANOPP predictions with fully mixed approximation and NATR experimental data. (a) 1/3-octave sound pressure level (SPL) versus Strouhal number St for inlet angles $\theta = 90^\circ$ and 150° . (b) Difference in 1/3-octave SPL values, with uncertainty. (c) Overall sound pressure level (OASPL) as function of θ .	323
Figure 8.94.—Assessment of ANOPP ST2JET jet noise predictions (Table 8.7, Appendix B). Configuration G case 230N for externally mixed, convergent, axisymmetric nozzle: bypass ratio (BPR) = 5 and flight Mach number $M_\infty = 0.1$. For core, acoustic Mach number $M_a = 1.126$ and stagnation temperature ratio $T_{t,r} = 2.46$. For bypass, $M_a = 1.566$ and $T_{t,r} = 1.17$. Comparison between ANOPP predictions and NATR experimental data. (a) 1/3-octave sound pressure level (SPL) versus Strouhal number St for inlet angles $\theta = 90^\circ$ and 150° . (b) Difference in 1/3-octave SPL values, with uncertainty. (c) Overall sound pressure level (OASPL) as function of θ .	323
Figure 8.95.—Assessment of ANOPP ST2JET jet noise predictions (Table 8.7, Appendix B). Configuration H case 235N for externally mixed, convergent, axisymmetric nozzle: bypass ratio (BPR) = 8 and flight Mach number $M_\infty = 0.01$. For core, acoustic Mach number $M_a = 1.002$ and stagnation temperature ratio $T_{t,r} = 2.447$. For bypass, $M_a = 0.812$ and $T_{t,r} = 1.114$. Comparison between ANOPP predictions and NATR experimental data. (a) 1/3-octave sound pressure level (SPL) versus Strouhal number St for inlet angles $\theta = 90^\circ$ and 150° . (b) Difference in 1/3-octave SPL values, with uncertainty. (c) Overall sound pressure level (OASPL) as function of θ .	324
Figure 8.96.—Assessment of ANOPP ST2JET jet noise predictions (Table 8.7, Appendix B). Configuration H case 241C for internally mixed, convergent, axisymmetric nozzle: bypass ratio (BPR) = 8 and flight Mach number $M_\infty = 0$. For core, acoustic Mach number $M_a = 1.366$ and stagnation temperature ratio $T_{t,r} = 3.211$. For bypass, $M_a = 0.902$ and $T_{t,r} = 1.296$. Comparison between ANOPP predictions with coplanar approximation and NATR experimental data. (a) 1/3-octave sound pressure level (SPL) versus Strouhal number St for inlet angles $\theta = 90^\circ$ and 150° . (b)	

Difference in 1/3-octave SPL values, with uncertainty. (c) Overall sound pressure level (OASPL) as function of θ .	324
Figure 8.97.—Assessment of ANOPP ST2JET jet noise predictions (Table 8.7, Appendix B). Configuration H case 241F for internally mixed, convergent, axisymmetric nozzle: bypass ratio (BPR) = 8 and flight Mach number $M_{fl} = 0$. For core, acoustic Mach number $M_a = 1.366$ and stagnation temperature ratio $T_{t,r} = 3.211$. For bypass, $M_a = 0.902$ and $T_{t,r} = 1.296$. Comparison between ANOPP predictions with fully mixed approximation and NATR experimental data. (a) 1/3-octave sound pressure level (SPL) versus Strouhal number St for inlet angles $\theta = 90^\circ$ and 150° . (b) Difference in 1/3-octave SPL values, with uncertainty. (c) Overall sound pressure level (OASPL) as function of θ .	325
Figure 8.98.—Assessment of ANOPP ST2JET jet noise predictions (Table 8.7, Appendix B). Configuration H case 253C for internally mixed, chevron, azimuthal periodicity $m = 8$ nozzle: bypass ratio (BPR) = 8 and flight Mach number $M_{fl} = 0.24$. For core, acoustic Mach number $M_a = 1.371$ and stagnation temperature ratio $T_{t,r} = 3.237$. For bypass, $M_a = 0.906$ and $T_{t,r} = 1.3$. Comparison between ANOPP predictions with coplanar approximation and NATR experimental data. (a) 1/3-octave sound pressure level (SPL) versus Strouhal number St for inlet angles $\theta = 90^\circ$ and 150° . (b) Difference in 1/3-octave SPL values, with uncertainty. (c) Overall sound pressure level (OASPL) as function of θ .	325
Figure 8.99.—Assessment of ANOPP ST2JET jet noise predictions (Table 8.7, Appendix B). Configuration H case 253F for internally mixed, chevron, azimuthal periodicity $m = 8$ nozzle: bypass ratio (BPR) = 8 and flight Mach number $M_{fl} = 0.24$. For core, acoustic Mach number $M_a = 1.371$ and stagnation temperature ratio $T_{t,r} = 3.237$. For bypass, $M_a = 0.906$ and $T_{t,r} = 1.3$. Comparison between ANOPP predictions with fully mixed approximation and NATR experimental data. (a) 1/3-octave sound pressure level (SPL) versus Strouhal number St for inlet angles $\theta = 90^\circ$ and 150° . (b) Difference in 1/3-octave SPL values, with uncertainty. (c) Overall sound pressure level (OASPL) as function of θ .	326
Figure 8.100.—Assessment of ANOPP ST2JET jet noise predictions (Table 8.7, Appendix B). Configuration H case 257C for internally mixed, lobed, azimuthal periodicity $m = 20$ nozzle: bypass ratio (BPR) = 8 and flight Mach number $M_{fl} = 0.24$. For core, acoustic Mach number $M_a = 1.376$ and stagnation temperature ratio $T_{t,r} = 3.254$. For bypass, $M_a = 0.906$ and $T_{t,r} = 1.309$. Comparison between ANOPP predictions with coplanar approximation and NATR experimental data. (a) 1/3-octave sound pressure level (SPL) versus Strouhal number St for inlet angles $\theta = 90^\circ$ and 150° . (b) Difference in 1/3-octave SPL values, with uncertainty. (c) Overall sound pressure level (OASPL) as function of θ .	326
Figure 8.101.—Assessment of ANOPP ST2JET jet noise predictions (Table 8.7, Appendix B). Configuration H case 257F for internally mixed, lobed, azimuthal periodicity $m = 20$ nozzle: bypass ratio (BPR) = 8 and flight Mach number $M_{fl} = 0.24$. For core, acoustic Mach number $M_a = 1.376$ and stagnation temperature ratio $T_{t,r} = 3.254$. For bypass, $M_a = 0.906$ and $T_{t,r} = 1.309$. Comparison between ANOPP predictions with fully mixed approximation and NATR experimental data. (a) 1/3-octave sound pressure level (SPL) versus Strouhal number St for inlet angles $\theta = 90^\circ$ and 150° . (b) Difference in 1/3-octave SPL values, with uncertainty. (c) Overall sound pressure level (OASPL) as function of θ .	327
Figure 8.102.—Assessment of ANOPP ST2JET jet noise predictions (Table 8.7, Appendix B). Configuration I case 263N for externally mixed, convergent, axisymmetric nozzle: bypass ratio (BPR) = 11 and flight Mach number $M_{fl} = 0.1$. For core, acoustic Mach number $M_a = 0.873$ and stagnation temperature ratio $T_{t,r} = 2.568$. For bypass, $M_a = 0.738$ and $T_{t,r} = 1.083$. Comparison between ANOPP predictions and NATR experimental data. (a) 1/3-octave sound pressure level (SPL) versus Strouhal number St for inlet angles $\theta = 90^\circ$ and 150° . (b) Difference in 1/3-octave SPL values, with uncertainty. (c) Overall sound pressure level (OASPL) as function of θ .	327
Figure 8.103.—Assessment of ANOPP ST2JET jet noise predictions (Table 8.7, Appendix B). Configuration I case 267N for externally mixed, convergent, axisymmetric nozzle: bypass ratio (BPR) = 14 and flight Mach number $M_{fl} = 0.1$. For core, acoustic Mach number $M_a = 0.859$ and stagnation temperature ratio $T_{t,r} = 2.53$. For bypass, $M_a = 0.686$ and $T_{t,r} = 1.071$. Comparison between ANOPP predictions and NATR experimental data. (a) 1/3-octave sound pressure level	

(SPL) versus Strouhal number St for inlet angles $\theta = 90^\circ$ and 150° . (b) Difference in 1/3-octave SPL values, with uncertainty. (c) Overall sound pressure level (OASPL) as function of θ .	328
Figure 9.1.—Propulsion airframe acoustics (PAA) classification tree.	332
Figure 9.2.—NASA Langley’s Low Speed Aeroacoustic Wind Tunnel (LSAWT). Dimensions are in centimeters. (a) Side view of test section with flow from left to right. (b) End view looking upstream with microphone array in upper right-hand side.	333
Figure 9.3.—Bypass ratio 5 nozzle with eight-chevron core nozzle and baseline fan nozzle installed in the jet engine simulator (JES) in the LSAWT.	334
Figure 9.4.—Source-to-observer conventions in Jet3D’s implementation of Lighthill’s Acoustic Analogy (LAA).	337
Figure 9.5.—Recommended shear layer grid topology for CFD predictions of jet flow.	340
Figure 9.6.—Effect of varying spatial correlation constant α_L on Jet3D predictions of sound pressure level (SPL) for baseline round bypass ratio 5 dual-stream nozzle.	341
Figure 9.7.—Effect of varying spatial correlation constant α_L on Jet3D predictions of sound pressure level (SPL) for baseline round bypass ratio 5 dual-stream nozzle with pylon.	341
Figure 9.8.—Comparison of measured data and Jet3D predictions of sound pressure level (SPL) for convergent-divergent nozzle (jet stagnation temperature $T_o \approx 955.6$ K (1720 °R), nozzle pressure ratio NPR = 3.18, and Mach number 1.4). Jet3D noise predictions are made at 13 observer locations (inlet angles). (a) 40°. (b) 50°. (c) 60°. (d) 70°.	342
Figure 9.8.—Continued. (e) 80°. (f) 90°. (g) 100°. (h) 110°.	343
Figure 9.8.—Continued. (i) 120°. (j) 130°. (k) 140°. (l) 150°.	344
Figure 9.8.—Concluded. (m) 160°.	345
Figure 9.9.—Comparison of measured data and Jet3D predictions of overall sound pressure level (OASPL) as function of inlet angle for convergent-divergent nozzle at jet stagnation temperature T_o of approximately 955.6 K (1720 °R) operating at its design nozzle pressure ratio (NPR) of 3.18 and Mach number of 1.4.	345
Figure 9.10.—Baseline separate-flow nozzle of BPR 5, configuration 1, for Jet3D jet noise prediction.	346
Figure 9.11.—Baseline separate-flow nozzle of BPR 5 with pylon, configuration 6, for Jet3D jet noise prediction.	346
Figure 9.12.—Comparison of measured data and Jet3D predictions of sound pressure level (SPL) for baseline separate-flow nozzle of BPR 5, configuration 1, at different observer locations (inlet angles). From Reference 25. (a) 52°. (b) 62°. (c) 69°. (d) 78°. (e) 88°. (f) 98°.	347
Figure 9.12.—Concluded. (g) 109°. (h) 121°. (i) 127°. (j) 134°. (k) 141°. (l) 148°.	348
Figure 9.13.—Comparison of measured data and Jet3D predictions of sound pressure level (SPL) for baseline separate-flow nozzle of BPR 5 with pylon, configuration 6, at different observer locations (inlet angles). From Reference 25. (a) 52°. (b) 62°. (c) 69°. (d) 78°. (e) 88°. (f) 98°.	349
Figure 9.13.—Concluded. (g) 109°. (h) 121°. (i) 127°. (j) 134°. (k) 141°. (l) 148°.	350
Figure 9.14.—Comparison of measured data and Jet3D predictions of effective perceived noise level (EPNL) for full-scale separate-flow nozzle of BPR 5, both configuration 1 and configuration 6 (with pylon). Standard deviation in data is ± 0.36 EPNdB.	351

Chapter 1—Introduction

Milo D. Dahl
National Aeronautics and Space Administration
Glenn Research Center
Cleveland, Ohio 44135

Summary

The NASA Aeronautics Research Mission Directorate, under its Fundamental Aeronautics Program, is developing physics-based multidisciplinary design, analysis, and optimization (MDAO) tools. At present, such tools are highly customized and focused on specific problems, configurations, and processes. Changing any of these usually requires extensive and complex redevelopment efforts to achieve new modeling solutions. The extent of these efforts can range from using analysis tools that are empirical in nature and do not handle unconventional geometries well without new experimental data, redesign, and recalibration to using highly intensive computational methods that take specialists to operate and take inordinate amounts of time to obtain a single solution set. The challenge is to create tools that have sufficient flexibility and fidelity to enable the study of the flight envelope and design space of new aircraft that may be outside of current convention. To achieve this objective, NASA needs computational tools and methods that are robust and highly accurate for performing these predictions. These tools require quantified levels of uncertainty and need to be validated with experimental data that also include established uncertainty levels. This emphasis on quantifying uncertainty establishes the credibility of the results.

The Fundamental Aeronautics Program contains four projects covering subsonic, supersonic, and hypersonic aircraft as well as subsonic rotorcraft. Each project is structured with a base of foundational research to provide knowledge for various disciplines to develop tools and technologies at the component level. These components will be integrated into subsystems and finally into full systems each with appropriate testing and validation programs. The MDAO capability will be a product of this development process. Among the disciplines defined in the program, the acoustics discipline focuses on developing improved noise prediction methods, at both the fundamental and component level, and on developing technologies to lower the overall noise radiated from the aircraft. To gauge its current capability, NASA undertook an assessment of its ability to predict the noise radiated from aircraft systems and components. The present chapter begins by outlining the process used in this assessment and describing how the errors and uncertainties were defined when comparing predicted results with measured results. This is followed by an introduction of the topics and the types of noise prediction codes assessed in the following eight chapters of this document.

Appendix A lists the acronyms and symbols found in this chapter.

1.1 Assessment Process

The process of the assessment is described in this section, and terms are defined. Validation is a term often used to denote how well the computed results agree with experimental data. This is recognized as a continual process. As more data become available, it may become necessary to make code modifications leading to more validation. In this context, an assessment is a snapshot in time of the current state of a validation process. At all times in this process, data to quantify the errors and uncertainties are gathered to document progress in prediction capability.

The assessment of NASA's current capability to predict aircraft noise is based on quantifying the differences between predictions of noise from computer codes and measurements of noise from experimental tests. The uncertainties associated with both the predictions and the measurements are also quantified. This further enhances the credibility of the assessment. The common approach of using "graphical validation" where only lines depicting predicted and measured results are placed on a plot is considered inadequate for true validation purposes (Ref. 1). An example will be given to illustrate the estimation of error and uncertainty in code prediction validation.

For the computed results, there are no methodologies for determining uncertainties that are unique to the computer codes related to aircraft noise prediction. These codes are built using common numerical methods and computing practices. Hence, we have followed well-documented practices that are found in the literature (Refs. 1 to 3), in technical guides (Refs. 4 and 5), and in engineering references (Refs. 6 to 8) for determining computational uncertainties and for determining experimental uncertainties.

The literature related to computer modeling and simulation validation uses terms like verification, validation, uncertainty, and error. Some of these terms are used interchangeably. The AIAA guide (G-077-1998, Ref. 4) on validating computational fluid dynamics simulations states that a failure to distinguish between these terms reduces the credibility of the computer modeling validation. To promote clarity and uniformity in performing this assessment of aircraft noise prediction codes, we adopted definitions for the terms given below that follow precedence in the cited literature:

(1) Verification is the process of determining if a model is implemented accurately. It includes ensuring that the controlling physical equations have been correctly implemented in a computer code, finding and removing mistakes and errors in

the numerical algorithm and in the code, making sure that the input data is accurate, and estimating the numerical solution error, as appropriate, through convergence studies.

(2) Validation is the process that gives the evidence demonstrating that the computer model is correct by comparing computed results with experimental data. The experimental data may be obtained from a variety of tests of differing complexity including fundamental experiments, subsystem tests, and complete system tests. However, it should be recognized that the complete correctness or accuracy of the computer model in all possible situations cannot be proven. Hence, validation is considered a process of determining accuracy as evidence from experiments is accumulated, which may in turn require modifications to the computer model, more validation, and so forth.

(3) Uncertainty is part of many aspects in obtaining the computed results and the experimental data. In a general definition, the AIAA guide suggests that uncertainty is a potential deficiency in any part of the computer modeling and the experimental data gathering process that is due to a lack of knowledge. Definitions for different types of uncertainties are given to help clarify the type of uncertainty being computed, for example:

Numerical Uncertainty: The uncertainty in computed results due to grid size, time steps, number of iterations, and other parameters that affect computationally based methods more than empirical methods. These uncertainties are typically estimated through code verification and convergence studies. Numerical uncertainty is assumed to be uncorrelated with model uncertainty and, if it is significant, may be combined with model uncertainty.

Model Uncertainty: The uncertainty in computed results due to initial conditions, boundary conditions, and model parameters. A deficiency or incomplete knowledge of a physical parameter, for instance, is often represented by a probability function. Thus, a statistical process is essentially used to determine model uncertainty. Estimates of the uncertainty of the code output can be obtained from variations in these conditions and parameters, otherwise known as inputs to the code, using sensitivity analysis and uncertainty analysis. Computationally based codes are assumed to be converged for this type of analysis.

(a) Sensitivity Analysis: Codes may potentially have a large number of input parameters. A sensitivity analysis reveals which input parameters most affect the output results. This analysis has the potential of identifying and, hence, reducing the number of important parameters required in follow-on studies. The following basic steps are performed:

- (i) Determine a range that each input parameter may have from experimental data or best estimate.
- (ii) Perform computations to determine the output effects for the ranges of these input parameters using one of the many techniques ranging from single input parameter adjustments while all other input parameters are held constant to a variance-based technique (Ref. 8). Depending on the number of input parameters and the method chosen, the required number of calculations may be large.

(b) Uncertainty Analysis: Once the important input parameters are determined, the following procedure is used to determine the uncertainty of code output given the uncertainty in the input parameters:

- (i) Characterize input parameter uncertainty using experimental data or best estimate. Essentially, the input parameters are described by a probability density function with mean and variance values.
- (ii) Generate a series of input values using statistical sampling methods.
- (iii) Create an ensemble set of output values using each sample set of input parameters in a computation.
- (iv) Analyze the set of code outputs to quantify the uncertainty of the computed output. Realize that the accuracy of this analysis improves as the size of the sample set, and hence the number of computational runs, increases.

A similar process was followed for experimental results. For this assessment, data came from laboratory tests, wind tunnel tests, and flight vehicle tests. Thus, the determinations of experimental uncertainty were not unique. Therefore, appropriate estimates of the experimental uncertainty were determined, which depended on the particular situation and the methodology used, as discussed in each chapter.

(4) The AIAA guide defines error as a recognizable deficiency in modeling that is not due to a lack of knowledge. The error may be categorized as acknowledged and unacknowledged. Truncation error when discretizing equations and physical approximations to simplify equations are examples of acknowledged error. Blunders and mistakes are considered to be some of the unacknowledged errors. There are many other errors that one may identify with an appropriate descriptive adjective. For this assessment, the following general definition was used:

Error: The difference between the experimental measurement and the computed result.

Implicit in this definition is that both the experimental measurements and the computed results contain errors. Thus, the defined error is a resultant of all the errors that are associated with each, including the possibility that some errors may cancel. Ultimately, the effect of this error is to show the accuracy of the computer model. Given the uncertainties associated with both computations and experiments, if the error is much larger than the combined uncertainties, then the error is considered to be dominated by modeling error, assuming that what is measured in the experiment is actually what was intended to be modeled. This definition of error applies to a single comparison, but it also may apply to a series of similar comparisons, whereby an average error can be computed.

The process outlined above is illustrated in Figure 1.1.¹ Reality is expressed by a particular component or system test

¹Figure 1.1 is based on a figure given in a presentation by H.W. Coleman at the Foundations for Verification and Validation in the 21st Century Workshop, Johns Hopkins University, Laurel, Maryland, October 22–23, 2002.

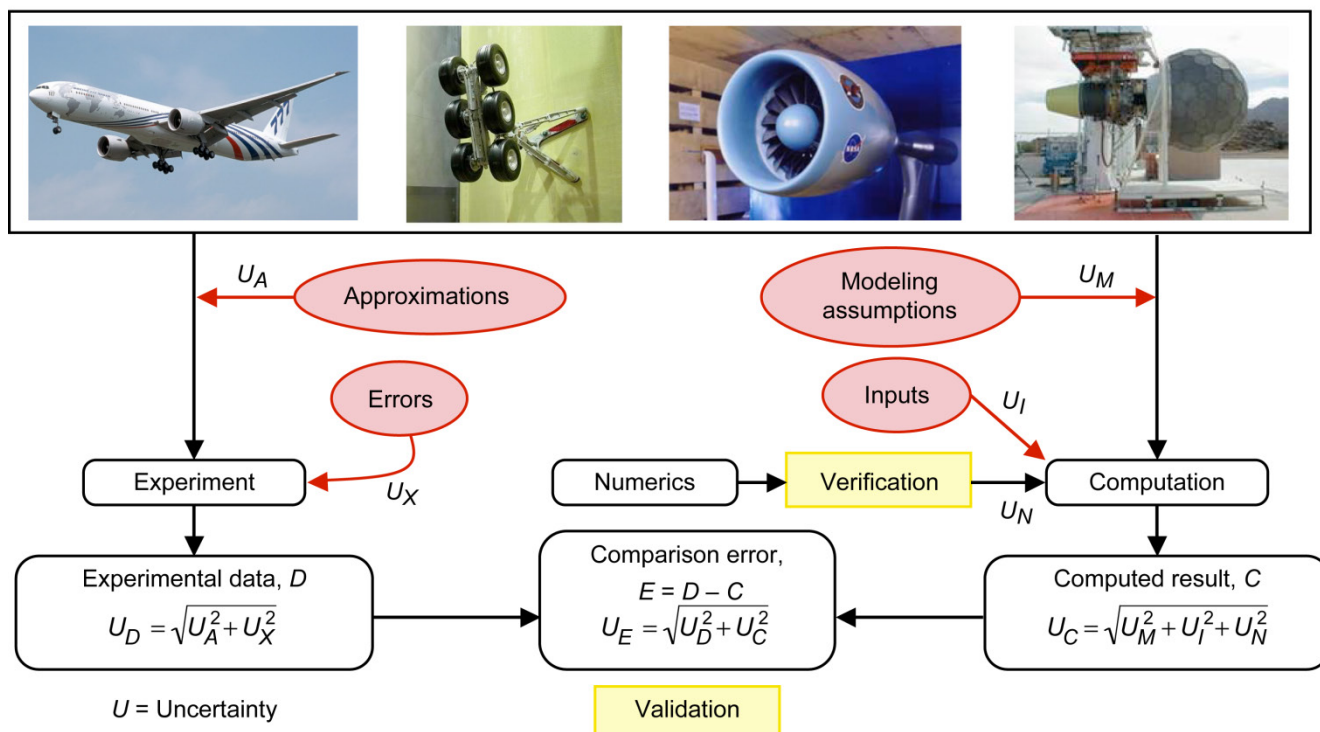


Figure 1.1.—Diagram of assessment process leading to validation of computed result by comparison to experimental data, where U is uncertainty.

configuration on which an experiment is to be conducted and for which a computer prediction is to be run. On the experimental side, certain approximations may be made as to what is being measured, and errors may be made during the experiment. For both, uncertainties U exist and are combined to obtain the total uncertainty associated with the experimental data.

Uncertainties are also found on the computational side including those associated with modeling assumptions, code inputs, and verification of the code numerical process. Modeling of the physics requires the development of mathematical equations to describe the physical processes that are thought to occur. Sometimes simplifications are made to obtain a tractable formulation. For example, complex three-dimensional geometries may be reduced to one- or two-dimensional approximations. In other cases, empirical correlations may be used to represent the physical process and enable the problem to be solved, sometimes rapidly. Computer codes require input parameters to run including initial and boundary conditions and model parameters internal to the code. Modeling and input uncertainties propagate through the code to create output uncertainties. In addition, for highly intensive computationally based codes, numerical uncertainties are defined through the verification process related to grid size, time step, iterations, and so forth, and are included in the total computational uncertainty. As indicated in Figure 1.1, the final comparison error is determined from the difference between the experimental and

computed results, and the uncertainty associated with the comparison error is computed using the uncertainties from both the experimental and computed results.

To further illustrate and explain the results computed by this assessment process, we consider some example results, as illustrated in Figure 1.2. Figure 1.2(a) shows data for both multiple measurements of a dependent variable Y at three settings for the independent parameter X and multiple calculated predictions for the same parameter. There are 20 measurement points for each X parameter. For the computations, the inputs and modeling parameters were randomly varied in 21 separate code runs to provide the calculated results. These raw data points are shown plotted on the figure slightly offset from their X -parameter value to better visualize the results. The mean values for these data and their 95% confidence intervals are shown as the small horizontal bars on the vertical lines. The confidence intervals indicate that the mean value has a 95 percent chance of being within the confidence interval given that the variance of the sample is a good estimate of the true variance value. From these results, we now have the experimental results D and the computed results C based on the mean values and their associated uncertainties U_D and U_C based on the 95% confidence intervals. The remaining parts of the figure give different presentations of the comparison between the measured data and the calculated data. Figure 1.2(c) shows a presentation of mean value comparisons where the uncertainties

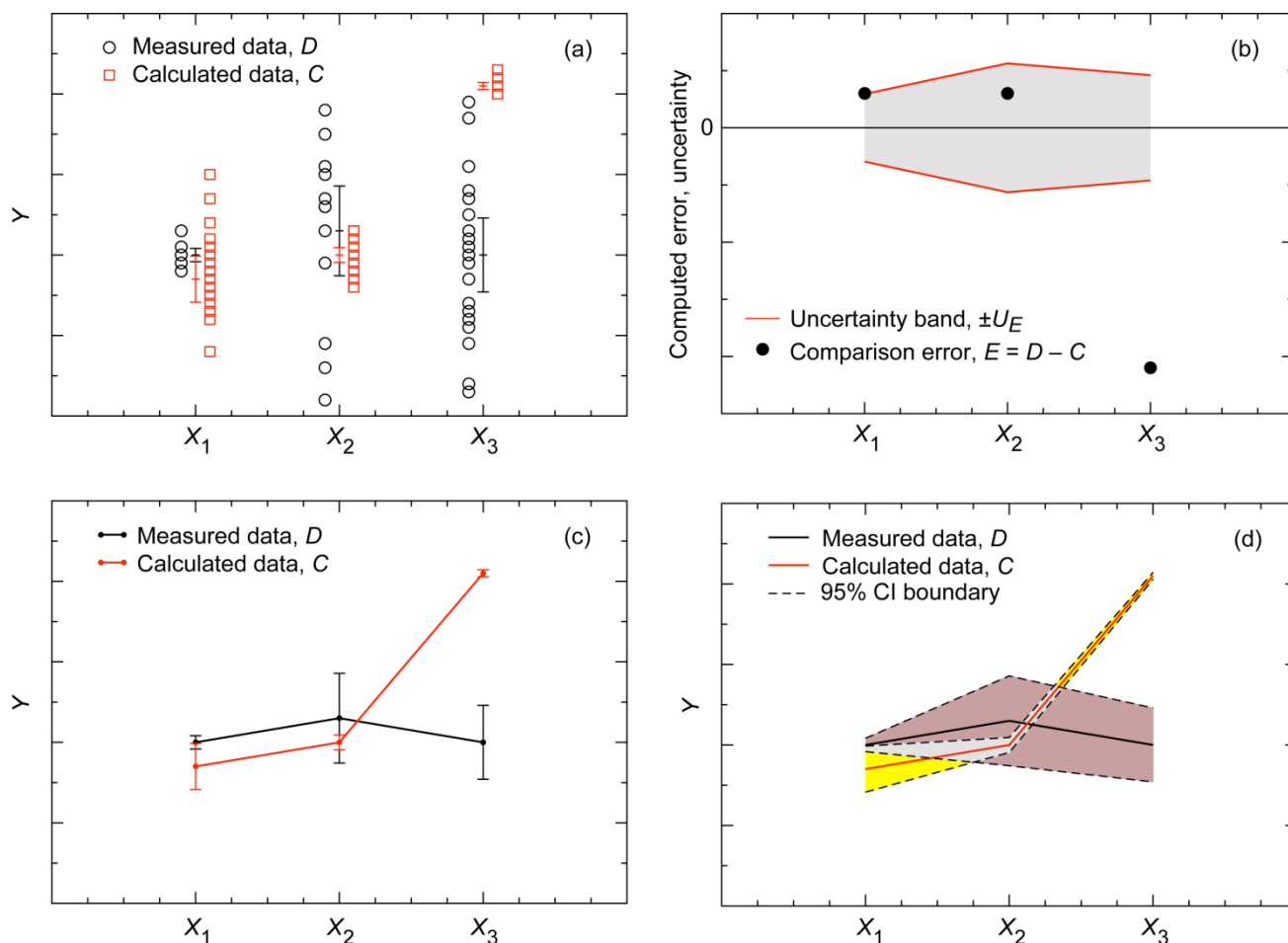


Figure 1.2.—Example of determining errors and uncertainties using a statistical approach for parameters X and dependent variable Y . (a) Raw measured and calculated data with computed means and 95% confidence intervals. (b) Computed comparison error and uncertainty band. (c) Point and line plot comparing calculated results and measured data, with “error bars.” (d) Comparison plot showing 95% confidence interval (CI) and overlap regions.

are plotted by using the classic error bars co-located with the mean data points. An alternative presentation of the same results is shown in Figure 1.2(d), where the confidence intervals are denoted by boundary lines and shading rather than using error bars. This type of plot more clearly shows the trends and overlap regions for easier assessment between the two data sets. The utility of a plot like Figure 1.2(d) becomes more apparent as the number of X points increases as in a comparison between measured and computed spectral data.

The result of combining the data shown in Figure 1.2(a) to obtain the comparison error and the combined uncertainty band is shown in Figure 1.2(b). This plot illustrates the level of comparison error, expressed as the difference between the measured mean values and the computed mean values, within a quantified level of combined uncertainty calculated from the square root of the sum of the squared uncertainties for the measured and computed results as noted in Figure 1.1. For parameter X_1 , the comparison error lies just outside the uncertainty band. For parameter X_2 , the comparison error lies

within the uncertainty band and is perhaps indicative of a “good” prediction compared with the result for parameter X_3 , where the comparison error lies well outside of the uncertainty band indicating that either the computer model is wrong or there is something wrong in the experimental measurement process. However, further explanation is required before judgment is made as to the goodness of this example assessment. The comparison error results at parameters X_1 and X_2 may be considered borderline and good, respectively, if the uncertainty band is judged to be relatively small. Then any comparison error result that lies within the uncertainty band is considered equally valid given the current known level of uncertainty in the experimentally measured data and in the computed results. Conversely, if the uncertainty band is judged to be large, then neither of the results for the X_1 and X_2 cases can be considered a good validation of the predictive capability. The results for the X_3 parameter may always be regarded as a poor validation since the error is much larger than the uncertainty.

1.2 Aircraft Noise Prediction Assessment

NASA's Aircraft Noise Prediction Program (ANOPP) (Ref. 9) represents the current capability for system-level aircraft noise prediction. As discussed in Chapters 2 and 3, the ANOPP code, initially developed in the early 1970s (Refs. 10 and 11), is a semi-empirical, computational tool that assembles source prediction modules for engine and airframe components and links them to an acoustic propagation code to obtain far-field noise levels and sound spectra. In addition, the combined noise source representation of an aircraft can be moved in time along simulated trajectories to obtain noise levels for various observers along or near this simulated flight path. ANOPP is composed of various modules that have been updated over the years as new data sets became available; however, the empirical nature of the program limits its usefulness. The ANOPP results typically show large discrepancies when attempting to predict radiated noise for aircraft designs outside of its database. Even with this limitation, ANOPP, in its current form, represents the state of the art in the ability to do rapid prediction estimates of aircraft system level noise. In addition, various subcomponents of aircraft noise may be predicted separately using the appropriate ANOPP source noise module as demonstrated in Chapters 4, 5, and 8.

The computational approaches to predicting aircraft noise that rely more on using first-principal equations than on semi-empirical source modeling, especially at the component level, use increasingly higher fidelity codes such as those categorized here as acoustic analogy and numerical methods. The acoustic analogy methods discussed in Chapters 5, 8, and 9 use a rearrangement of the governing equations. The resulting equation contains a linear operator on one side of the equation that reduces to the wave equation governing acoustic propagation at relatively large distances from the source region. On the other side of the equation are placed terms that are significant only within a relatively small region and are identified as the acoustic sources, or formally in this method, the equivalent or analogous acoustic sources. Thus, we obtain a linear, inhomogeneous equation that can be solved using a standard integral technique (Green's function method), which may involve the introduction of simplifying assumptions and approximations in order to reduce the computational effort. The problem of solving the original exact equations is replaced by a modeling requirement to determine the unknown equivalent sources. For fan noise generation, the acoustic source is usually the unsteady pressure distribution generated on the surface of a blade when a vortical disturbance velocity field interacts with the blade surface (Ref. 12). This aerodynamic source may be obtained by measurements, through computations, or by modeling. The acoustic solution is obtained by first computing the acoustic source followed by solving an integral equation for the acoustic field. Depending how the solution is structured, one can, for example, compute the blade-passage-frequency tones associated with rotor-stator interaction (Ref. 13) or compute the fan broadband noise

generated by the interaction of the fan rotor turbulent wake with the downstream stator vanes (Ref. 14). In the jet noise case, the sources are spatially distributed and identified with the turbulent fluctuations in the flow field. Computational fluid dynamics calculations using steady Reynolds-averaged Navier-Stokes (RANS) codes with turbulence models are currently being used to provide integral length and time scales that affect the functional descriptions characterizing the statistical behavior of the sources (Ref. 15). Computational methods do not require linearizing and rearranging the equations, but they are very expensive numerical methods for solving the unsteady noise generation problem directly from the governing equations (Ref. 16) or for solving the propagation problem in complex geometries given a known source (Ref. 17). Presently, computational capabilities usually limit the unsteady solution to the source region. To obtain the far-field radiated noise, techniques such as the Kirchhoff or the Ffowcs Williams-Hawkings methods are used to propagate the sound outward from near the source region (Ref. 18).

The prediction codes used in this assessment are listed in Table 1.1 with their abbreviated name followed by a brief description of the code. The codes are arranged in three categories: (1) The semi-empirical tools include all the noise prediction modules within the ANOPP code and models that predict the acoustic impedance of liner materials placed in the inlet, bypass, and exhaust ducts of aircraft engines. (2) The acoustic analogy tools compute the noise radiated from the equivalent sources of engine noise such as broadband fan noise and jet noise without and with the effects of installation hardware. These tools use turbulence and mean flow quantity inputs computed using steady RANS solvers. (3) The numerical tools include an unsteady RANS code to compute the noise generated by airframe components; a linearized Euler code to predict the engine fan tone frequencies, amplitudes, and modal content; and various codes to predict the propagation and attenuation of sound in ducts with flow and the radiation of sound to the far field from both the duct inlet and exit. Some of these codes were briefly described in the previous paragraphs. This listing does not contain all possible codes within NASA that relate to aircraft noise prediction; nor does it contain codes external to NASA in other government, industry, or academic organizations that may be similar or variations of these codes. Because of limitations on time and resources, the codes shown here were chosen as representative of the state-of-the-art or current capability in aircraft noise prediction at NASA. Many codes requiring intense computational resources such as codes using computational aeroacoustics and large eddy simulation techniques are considered to be part of ongoing research and thus not part of this assessment of aircraft noise prediction capability.

With these qualifications, the present document is an assessment of NASA's capability to predict aircraft noise and consists of eight chapters covering topics at both the system and the component levels. The chapter topics are listed in Table 1.2. In contrast to Table 1.1, the codes are listed by type according to the chapters in which they appear. Each chapter presents a discussion of the background, issues, codes, and

TABLE 1.1.—CODES ASSESSED FOR AIRCRAFT NOISE PREDICTIVE CAPABILITY

Semi-Empirical Tools	
ANOPP Level 25: Applied to components: flaps, slats, landing gear, fan, jet Applied to systems: engine, aircraft	
Liner impedance models: Two-Parameter—uses linear and nonlinear steady-flow resistance Crandall Full Solution—uses Crandall oscillatory channel flow solution Composite Empirical—contains grazing-flow effects in resistance Fluid Mechanical—one-dimensional lumped element model	
Acoustic Analogy Tools	
RSI—rotor-stator interaction code for fan broadband noise JeNo—jet noise code for free jets Jet3D—jet noise code for free jets and propulsion airframe aeroacoustics	
Numerical Tools	
CFL3D—unsteady RANS code for near-field noise sources LINFLUX—linearized Euler fan tone noise code	
Duct acoustic propagation codes: Based on convected Helmholtz equation: CH2DDS—two dimensional, uniform flow, finite element code, direct matrix solver CH3DDS—three dimensional, uniform flow, finite element code, direct matrix solver CH3DPA—three dimensional, uniform flow, parabolic approximation code Based on linearized Euler equations: LEE2DDS—two dimensional, finite element code, direct matrix solver LEE2DIS—two dimensional, finite difference code, iterative solver LEE3DIS—three dimensional, finite difference code, iterative solver	
Duct acoustic radiation codes: Based on convected Helmholtz equation: CH2DIE—two dimensional, uniform flow, finite element code with infinite outer elements Based on convected Helmholtz and Ffowcs Williams-Hawkings equations: FWH3D—three dimensional, uniform flow, parabolic approximation code with time domain integral for radiation	

TABLE 1.2.—LIST OF CODES AND CODE TYPES ARRANGED BY CHAPTER TOPIC

Chapter topic	Codes					
2. Aircraft system	ANOPP-L25					
3. Engine system	ANOPP-L25					
4. Airframe						
Flaps	ANOPP-L25					
Slats	ANOPP-L25	CFL3D				
Landing gear	ANOPP-L25	CFL3D				
5. Fan	ANOPP-L25	RSI	LINFLUX			
6. Liner physics	Two-Parameter	Crandall Full Solution	Composite Empirical	Fluid Mechanical		
7. Duct acoustics						
Propagation	CH3DPA	LEE2DDS	CH2DDS	CH3DDS	LEE2DIS	LEE3DIS
Radiation	CH2DIE	FWH3D				
8. Jet	ANOPP-L25	JeNo	Jet3D			
9. Propulsion airframe aeroacoustics	Jet3D					

experiments for that chapter topic. With the possible exception of the minimal interaction between Chapter 6 on liners and Chapter 7 on duct acoustics, the chapters are essentially independent of one another. Chapter 2, which discusses aircraft system-level noise prediction, involves the assessment of the semi-empirical ANOPP code. A discussion of the structure, content, and operation of this code is presented. Next, Chapter 3 presents a system-level assessment of the ability to predict engine noise. This involves using only the ANOPP engine noise source modules. Chapter 3 also discusses research related to engine core noise and illustrates

techniques to extract combustion noise levels from engine noise measurements. In a similar fashion, only the ANOPP airframe noise source modules are used in Chapter 4 to make noise predictions for individual components and for aircraft in flight. In addition, predictions are compared to experimental data for idealized airframe components using a high-fidelity, numerical code.

The remaining five chapters relate to the prediction of the noise radiated from the propulsive components of an aircraft. Chapter 5 assesses predictions for the noise generated by the aircraft engine fan using codes that are in each of the three

listed categories. The next two chapters relate to the noise that propagates through and out the duct in which the fan noise source resides. Chapter 6 discusses the assessment of the semi-empirical models to predict the acoustic properties of the treatment that lines the duct, and Chapter 7 assesses the ability to predict the propagation and attenuation of sound within the duct using six different numerical codes. In addition, a comparison is made between the far-field radiated noise directivity patterns predicted by two duct noise radiation codes. The final two chapters discuss the prediction of jet

noise and the changes that occur in jet noise because of the presence of a nearby airframe component. Chapter 8 assesses semi-empirical- and acoustic-analogy-type code predictions compared with measured data for many different nozzles and flow conditions. When airframe components are nearby, the interaction of aircraft noise sources with the airframe complicates the process for computing noise predictions. Using the example of a jet flow just downstream of a pylon, Chapter 9 assesses the ability to predict the resulting propulsion airframe interaction effect on the radiated noise.

Appendix A.—Nomenclature

A.1 Acronyms

ANOPP	Aircraft Noise Prediction Program (NASA)
CI	confidence interval
MDAO	multidisciplinary design, analysis, and optimization
RANS	Reynolds-averaged Navier-Stokes (code)

A.2 Symbols

C	computed result
D	experimental data
E	comparison error
U	uncertainty (see Figure 1.1)

X	independent parameter
Y	dependent variable

Subscripts:

A	approximations
C	computed result
D	experimental data
E	comparison error
I	inputs
M	modeling
N	numeric
X	experimental error

References

1. Oberkampf, William L.; and Trucano, Timothy G.: Verification and Validation in Computational Fluid Dynamics. *Prog. Aerosp. Sci.*, vol. 38, no. 3, 2002, pp. 209–272.
2. Stern, Fred, et al.: Comprehensive Approach to Verification and Validation of CFD Simulations—Part 1: Methodology and Procedures. *J. Fluids Eng.*, vol. 123, no. 4, 2001, pp. 793–802.
3. McKay, Michael D.; Morrison, John D.; and Upton, Stephen C.: Evaluating Prediction Uncertainty in Simulation Models. *Comput. Phys. Commun.*, vol. 117, no. 1, 1999, pp. 44–51.
4. AIAA Guide for the Verification and Validation of Computational Fluid Dynamics Simulation. AIAA Standards Series, AIAA G-077-1998, 1998.
5. NCSL International: American National Standard for Expressing Uncertainty—Calibration—U.S. Guide to the Expression of Uncertainty in Measurement. ANSI/NCSL Z540.2-1997, 1997.
6. Coleman, Hugh W.; and Steele, W. Glenn: *Experimentation and Uncertainty Analysis for Engineers*. Second ed., Wiley, New York, NY, 1999.
7. Taylor, John R.: *An Introduction to Error Analysis*. Second ed., University Science Books, Sausalito, CA, 1997.
8. Saltelli, A., et al.: *Sensitivity Analysis in Practice: A Guide to Assessing Scientific Models*. Wiley, Hoboken, NJ, 2004.
9. a. Zorumski, W.E.: Aircraft Noise Prediction Program Theoretical Manual. NASA TM-83199-PT-1, 1982. b. Zorumski, W.E.: Aircraft Noise Prediction Program Theoretical Manual. NASA TM-83199-PT-2, 1982.
10. Raney, J.P.: Development of a New Computer System for Aircraft Noise Prediction. AIAA-1975-536, 1975.
11. Raney, J.P.: Noise Prediction Technology for CTOL Aircraft. NASA TM-78700, 1978.
12. Ventres, C.S.; Theobald, M.A.; and Mark, W.D.: Turbofan Noise Generation—Volume 1: Analysis. NASA CR-167951, 1982.
13. Meyer, Harold D.; and Envia, Enmane: Aeroacoustic Analysis of Turbofan Noise Generation; Final Report. NASA CR-4715, 1996.
14. Nallasamy, M.; and Envia, E.: Computation of Rotor Wake Turbulence Noise. *J. Sound Vib.*, vol. 282, nos. 3–5, 2005, pp. 649–678.
15. Khavaran, Abbas; and Kenzakowski, Donald: Noise Prediction in Hot Jets. AIAA 2007-3640, 2007.
16. Tam, Christopher K.W.: Computational Aeroacoustics: An Overview of Computational Challenges and Applications. *Int. J. Comput. Fluid Dyn.*, vol. 18, no. 6, 2004, pp. 547–567.
17. Nark, Douglas M., et al.: The Development of the Ducted Fan Noise Propagation and Radiation Code CDUCT-LaRC. AIAA 2003-3242, 2003.
18. Lele, Sanjiva K.: Computational Aeroacoustics—A Review. AIAA-1997-0018, 1997.

Chapter 2—Aircraft System Noise Prediction

Casey L. Burley
National Aeronautics and Space Administration
Langley Research Center
Hampton, Virginia 23681

John W. Rawls, Jr.
Lockheed Martin Space Operations Langley Program Office
Hampton, Virginia 23681

Jeffrey J. Berton
National Aeronautics and Space Administration
Glenn Research Center
Cleveland, Ohio 44135

Michael A. Marcolini
National Aeronautics and Space Administration
Langley Research Center
Hampton, Virginia 23681

Summary

An investigation is undertaken to assess the current capability to predict aircraft noise using NASA's Aircraft Noise Prediction Program (ANOPP). NASA initiated the development of ANOPP in the early 1970s to provide the U.S. Government with the ability to independently (1) assess aircraft system noise, (2) assess aircraft component noise, and (3) evaluate aircraft noise technologies and flight procedures. To meet these goals, the prediction methodologies that have been implemented within ANOPP are predominantly empirical to semi-empirical in nature. Many of the methods predict well for conventional aircraft designs, but lack capability and fidelity required to predict for nonconventional configurations. The most accurate and robust predictions are for those configurations that assume conventional fuselage with wing-mounted engines. In this assessment predictions are made for a Boeing 737-800 with CFM56-7B engines for a certification flight procedure. The predictions are then compared with integrated noise metrics at the three certification points. A thorough validation of ANOPP was not possible because of the proprietary nature of the aircraft and engine design parameters and availability of acoustic measurements other than at the certification points.

An initial investigation is made to provide an estimate of the uncertainty in ANOPP full-aircraft noise predictions. This investigation is very limited because of lack of measured data. To perform a complete uncertainty and/or error analysis of ANOPP requires not only acoustic results, but also a full description of the engine, including engine state, and the airframe for a range of flight conditions. Since this was not available at the level of detail required, an analysis is performed to determine the uncertainty of ANOPP results for appropriate variations in aircraft velocity and throttle setting. It is found that for the variations examined, the ANOPP predictions are minimally sensitive. Because of the lack of data, it is not possible to determine the accuracy of this finding.

To improve the accuracy of community noise predictions of aircraft, such as the noise of future aircraft with advanced, unconventional noise reduction technologies, or even for the B737's certification noise levels estimated herein, NASA systems analysis tools will require significant upgrades. Some of the known issues and gaps in capabilities are identified that need to be addressed to use ANOPP in the prediction of next-generation aircraft.

2.1 Introduction

Aircraft system noise is the source noise emitted by an aircraft in flight, propagated through the atmosphere, and received by observers or sensors on the ground. The aircraft system noise includes source noise components associated with the propulsion system (such as jet, fan, compressor, combustor, propeller, and turbine noise), source noise components associated with the airframe (such as landing gear, flap, slat, and trailing-edge noise), and installation effects due to configuration (such as engine and wing

shielding and reflection). The levels of each source may vary with aircraft configuration and operating condition. The combined acoustic signature of the source components propagates through the atmosphere to the observer. The observer receives the direct signal from the aircraft as well as indirect signals modified by the local terrain and surroundings. Taken together, this is the system noise of the aircraft at an observer.

Aircraft system noise predictions are used widely throughout the aerospace community to evaluate conceptual aircraft designs, for community airport planning, and to address

community noise issues. Civilian airframe and engine makers use system noise predictions to guide design parameter selections early in conceptual product design. Governmental regulatory agencies use system noise predictions to direct noise stringency rulemaking processes that protect the public health and welfare and to allocate resources for property and land use management near airports. Military researchers are interested in system noise predictions for reasons of low observability, the health of personnel, and to be good neighbors within the civilian communities in which they operate. Government research organizations such as NASA often make aircraft system noise predictions to guide aeroacoustic research investments as well as evaluate potential for noise-reduction technologies, low-noise configurations, and low-noise procedures.

Current aircraft systems noise prediction software lies on a hierarchy that trades fidelity for range of applicability. On one end of the hierarchy are acoustic research codes based on first principles. These codes require high-fidelity aerodynamic and geometric inputs and are used to model the physics responsible for the noise generation. They tend to be somewhat limited in range of applicability in that they address narrowly focused acoustic phenomena at a component or flow physics level. The results are often not readily or easily extended to community noise metrics. These research codes are usually noncommercial, of limited availability, require expert users, and are computationally expensive. On the opposite end of this hierarchy are prediction capabilities that are of low fidelity but have a large range of application. These codes may predict multiple-event noise metrics at the airport level for an entire fleet of aircraft and are typically widely available, empirically based, and quick to execute. However, they are often validated only for current aircraft configurations, where the noise characteristics are known. NASA's aircraft system noise prediction tool, Aircraft Noise Prediction Program (ANOPP) (Refs. 1 and 2), lies somewhere between the low- and high-fidelity prediction methods, depending upon which modules are used.

NASA initiated the development of ANOPP in the early 1970s to provide the U.S. Government with the ability to independently assess aircraft system noise. NASA has continued to improve, extend, and add new prediction capabilities through validation and advanced modeling developments. ANOPP provides the capability to (1) assess aircraft system noise, (2) assess aircraft component noise, and (3) evaluate aircraft noise technologies and flight procedures. ANOPP consists of a set of modules (Refs. 1 to 3), which define the flight dynamics, noise sources of conventional takeoff and landing aircraft, and noise propagation effects, using various noise metrics. As a repository for current and future approaches to computerized study of aircraft noise, ANOPP provides maximum flexibility for updating and replacing the noise prediction methodology with state-of-the-art prediction methods. ANOPP is continually updated by incorporating more physics-based theories into the modeling such that general scaling laws are utilized to cover a wide

range of flow and geometric parameters and by incorporating new databases into the prediction schemes.

One of the initial ANOPP validations in late 1970s for full-aircraft configurations was made for the Lockheed L-1011 wide-body transport equipped with three RB.211-524B engines (Ref. 4). Predicted and measured noise comparisons were made for a range of Mach numbers (0.25 to 0.30) with engine pressure ratios ranging from 1.13 to 1.67. Comparisons of the predicted results with measurement were within several decibels in the aft quadrant, but large differences were found in the forward quadrant due to overprediction of the fan noise. Another validation study made during that time was for a McDonnell Douglas model DC-10-40 wide-body transport powered by three Pratt & Whitney JT9D-59A engines (Ref. 5). It was shown that for all power settings ANOPP consistently underpredicted the low frequency levels and overpredicted the higher frequency levels. The differences were dependent on flight condition (approach, flyover, and takeoff), but ranged from a few decibels up to 15 dB. In these early studies the noise sources were modeled in isolation and did not include any installation effects. There was no capability within ANOPP to include effects of liners. Even though the comparison between measured and predicted levels was poor, the noise trends were captured. Since that time, methods to account for installation effects (although currently considered limited) and effects of liners (albeit quite limited) have been implemented, and there have been a number of studies performed using ANOPP. ANOPP has been used as part of aircraft design optimization (Refs. 6 to 9) and assessment of current and future noise reduction technologies (Refs. 10 and 11). In addition to the subsonic aircraft (conventional takeoff and landing, CTOL) capability, a propeller analysis system (PAS) was also developed and became part of the ANOPP system (Ref. 3). Example validation efforts for this are provided in Reference 12 as well as Reference 13, for which the effect of propeller angle of attack on the noise was investigated.

Acronyms and symbols used throughout this chapter are listed in Appendix A to aid the reader.

2.2 ANOPP Code

ANOPP is a state-of-the-art aircraft noise prediction tool that relies primarily on semi-empirical methods. A schematic of the ANOPP system is shown in Figure 2.1. ANOPP consists of a set of functional modules that predict atmospheric properties, the aircraft flight path, source-to-observer geometry, source noise of the aircraft components (propulsion systems and airframe), propagation of the source noise to ground observers, and community noise metrics. The ANOPP executive is the part of the code that allows the user to interface with the other parts of ANOPP shown in Figure 2.1. This important part of the ANOPP capability not only controls the execution of modules but interprets and creates inputs for modules, provides data management for the functional

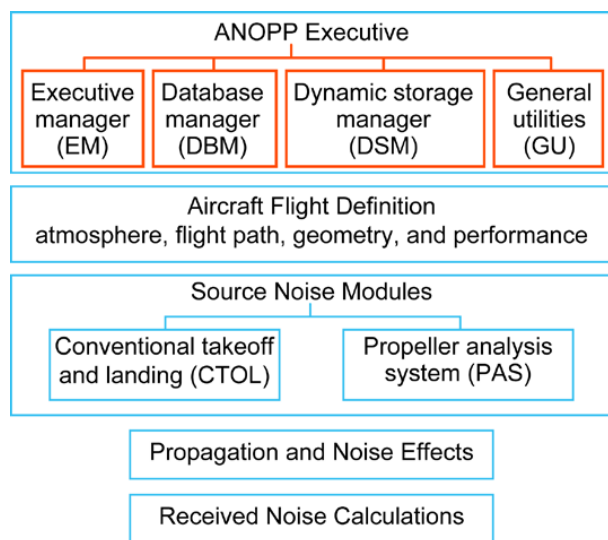


Figure 2.1.—ANOPP Level 25.

modules, and provides error handling and exit procedures to the host computer. Because of the ANOPP executive and modularity of the system, ANOPP prediction capabilities are flexible and appropriate for problems ranging from an isolated source to a full-aircraft system operating with complex flight regimes with varying conditions. The functional modules include those that can be used to set up the aircraft flight definition, the source noise modules for the CTOL, the PAS, the propagation modules, and the modules for determining noise metrics at specified far-field observer locations. A comprehensive discussion of the underlying theory, modeling, as well as ANOPP input and output is beyond the scope of this document. In summary however, the key geometric parameters and flow conditions to predict the acoustic strength and directivity required for each noise source are provided by the user and/or computed within the specific module. The details of the theory and modeling for each module can be found in Reference 2 and in the online-manual pages provided with the ANOPP code distribution. An example of the theory details provided in Reference 2 for ANOPP landing gear noise prediction can be found in Appendix B of Chapter 4, “Airframe Noise: A Prediction Capability Assessment.”

The steps shown in Figure 2.2 can summarize the prediction of aircraft noise by the ANOPP system. These steps are used to determine the noise radiated from an aircraft that follows an arbitrary flight path in the presence of an observer on the ground. During this operation, noise sources on the aircraft emit acoustic radiation computed from models that determined the power, directivity, and spectral distribution characteristics, all of which may vary with time. This source noise propagates through the atmosphere to the observer. The observer receives the noise signal from the direct ray plus a signal from a ray reflected by the local ground surface, if the observer is above the ground. The ANOPP computational process starts by first defining the aircraft flight profile. This requires that the atmosphere as well as the trajectory and operating conditions

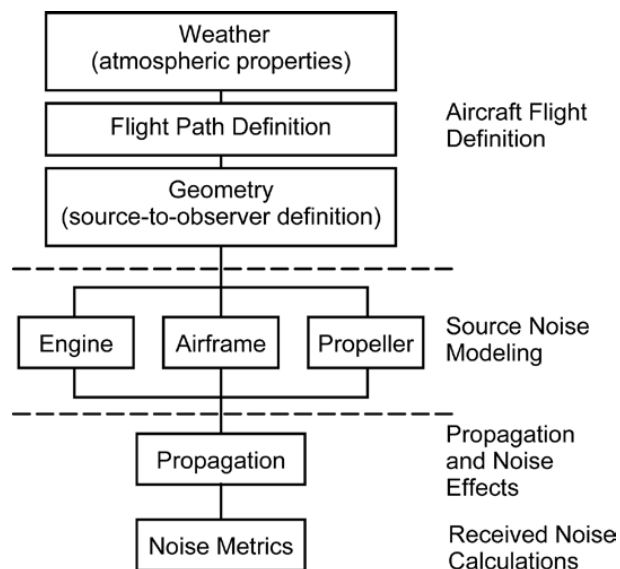


Figure 2.2.—Prediction flow within ANOPP Level 25 using CTOL source modules.

of the aircraft be defined. The Atmospheric Module (ATM) establishes the properties of the atmosphere (pressure, density, and humidity as functions of altitude). The Flight Dynamics Modules define the location and orientation of the aircraft as well as its operating state as a function of time relative to a ground fixed coordinate system. These modules also determine the engine throttle position and aircraft Mach number, which are used as control parameters for source noise predictions. The Geometry Module is then invoked to compute the time-dependent emission angles and source-to-observer distances.

Once the aircraft flight path and conditions along that path are defined, the source noise modules are then used to compute the noise from each propulsion and airframe source. ANOPP assumes that each source can be modeled as a point source. Source noise predictions are made in several coordinate systems, which are attached to the aircraft. The airframe noise predictions are made in the wind axis coordinate system. The engine noise predictions are made in the body axis system. Sources within the wind axis may be summed before propagation. Similarly sources within the body axis may be summed before propagation. Sources from the wind and body axis are propagated separately to a ground-fixed coordinate system and summed to obtain the total noise. Figure 2.3 shows the coordinate system for which the ground-fixed observers are defined. The ANOPP system internally handles the conversion between the source noise coordinate systems and the observer coordinate system. Using an assumption of acoustic superposition, the source noise spectra (mean-square pressures) are analytically summed in the vicinity of the aircraft and propagated to observers on the ground or may be summed at the ground observers.

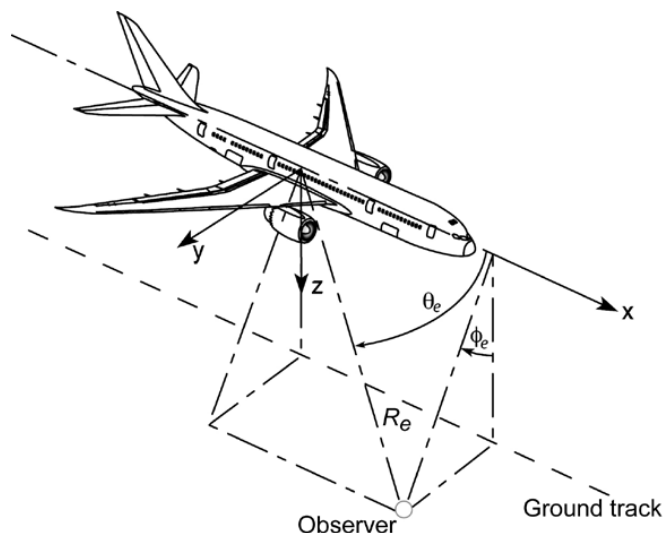


Figure 2.3.—ANOPP coordinate system.

2.2.1 ANOPP Source Noise Methods

In this section, the engine and airframe prediction capabilities contained in the ANOPP CTOL system are summarized. The ANOPP source noise prediction methods are implemented in separate modules for each of the engine and airframe noise sources. There are currently 13 source noise modules within the ANOPP CTOL system, with several of the modules including multiple methods. For instance, of the two fan noise modules in ANOPP, the fan noise module known as HDNFAN contains three methods based on the original Heidmann method. One is the original method, and the other two are enhancements for large fans and enhancements for small fans. The other fan noise module known as BFN only contains one method. The details of the methods implemented can be found in the ANOPP theory manual electronically distributed with ANOPP Level 25. This document has been significantly updated from the original ANOPP theory manual of Reference 2.

2.2.1.1 Fan

Fan noise radiates from the fan inlet and the bypass nozzle exit. The fan noise that radiates from the fan inlet is often modeled as three separate components, each associated with different noise-generation mechanisms. The first is the tone component, which is generated by steady and unsteady aerodynamic loading on rigid surfaces, such as the fan blades and the stator vanes. The second is the broadband noise component generated by unsteady aerodynamic loading associated with random flow fluctuations. These fluctuations may be caused by inflow turbulence impinging on rotor blades and stator vanes, rotor wake turbulence impinging on downstream stators, and interaction of the blade tip flow with the

turbulent wall boundary layer. The third component is often referred to as “buzz saw” noise because of its distinct sound. This noise source is also referred to as multiple pure tone noise or combination tone noise. When the fan blades rotate at supersonic tip speeds, bow shocks form at the leading edges. These shocks interact nonlinearly with each other as they propagate upstream through the inlet. Slight variations in shock strengths result in a pressure spectrum with discrete multiple pure tones at the shaft rotational frequency as well as its harmonics and subharmonics. The fan noise that radiates from the fan exhaust duct is characterized by tone and broadband components. The mechanisms that generate this noise are similar to those that generate the forward-radiated noise. The total fan noise is predicted by summing the noise from three inlet radiated noise components and two aft-radiated noise components.

The two fan noise modules implemented in ANOPP are the “Heidmann” module (HDNFAN) and the Boeing fan module (BFN). Both modules include methodologies to account for the inlet and aft radiated broadband noise, inlet and aft discrete interaction tones, and inlet combination tones. The original Heidmann method (which is one of the three options in the HDNFAN module) (Ref. 14) utilizes several acoustic relationships suggested by The Boeing Company as part of its underlying semi-empirical acoustic equation framework. This semi-empirical framework was calibrated to full-scale acoustic data obtained in the 1970s at NASA Lewis (now Glenn) Research Center under the direction of M.F. Heidmann. Two revisions have been made to the Heidmann method to improve the prediction method for fans outside the original database. Revisions made by AlliedSignal (Ref. 15) improve predictions for small turbofan engines in the 13- to 27-kN (3000- to 6000-lb) thrust range. Revisions made by GE Aircraft Engines (Ref. 16) improve predictions for large fans such as those found on the CF6-80C2, which has a rated thrust of about 270 kN (60 000 lb). The data used to develop and validate the three methods are characterized in Table 2.1 to Table 2.3. All three methods employ empirical functions to predict the sound spectra as a function of frequency and polar directivity angle. Further details of the HDNFAN module can be found later in Chapter 5, “Fan Noise Prediction,” including a description of input parameters (in Table 5.8).

The Boeing fan noise module (BFN) (Refs. 17 and 18) computes forward and aft radiated fan noise for axial flow turbofans. The module was developed using five sets of component-modeled measurements that cover a wide range of fan diameters, including narrow- and wide-chord fans, and a range of power settings that include bypass ratios greater than 8. The data used to evaluate the accuracy of the method consisted of 10 different engine data sets. These data sets included 127 individual power points, of which 48 were for bypass ratios greater than 8. Similar to the Heidmann methods, the BFN module utilizes empirical functions to predict sound spectra as a function of frequency and polar directivity angle.

TABLE 2.1.—DATABASE USED FOR “ORIGINAL” HEIDMANN METHOD

Fan	Total pressure ratio	Mass flow rate		Rotor tip Mach number	Rotor-relative tip Mach number	Number of vanes	Number of blades	Blade passage frequency, Hz	Cutoff factor	Rotor-stator spacing factor
		kg/s	lb/s							
A	1.5	430	950	1.04	1.2	90	40	2420	0.83	200
B	1.5	430	950	1.04	1.2	60	26	1570	0.80	200
C	1.6	415	915	1.39	1.52	60	26	2250	N/A	200
QF-1	1.5	396	873	0.99	1.12	12	53	3120	0.89	367
QF-3	1.4	396	873	0.99	1.12	112	53	3120	0.89	367
QF-5	1.6	385	850	0.98	1.14	88	36	2080	0.68	227
QF-6	1.2	396	873	0.67	0.88	50	42	1670	3.53	400
QF-9	1.2	403	889	0.63	0.87	11	15	556	2.38	200

TABLE 2.2.—DATABASE USED FOR “LARGE FAN” HEIDMANN METHOD

Fan	Thrust, 10 ⁴ N (10 ³ lb)	Bypass ratio	Tip speed, m/s (ft/s)	Pressure ratio
CF6	25 (57)	5	437 (1434)	1.8
E ³	14 (32)	7.7	342 (1123)	1.4
QCSEE	8 (19)	12.1	291 (956)	1.3

TABLE 2.3.—DATABASE USED FOR “SMALL FAN” HEIDMANN METHOD

Fan	Total pressure ratio	Mass flow rate, kg/s (lb/s)	Rotor tip Mach number	Rotor-relative tip Mach number	Vane to blade ratio	Blade passage frequency, Hz	Cutoff factor	Rotor-stator spacing factor
1, 2, and 3	1.5 to 1.6	45 to 91 (100 to 200)	0.3 to 1.2	1.45 to 1.53	2.0 to 2.5	3600 to 5300	0.77 to 1.15	170 to 214

2.2.1.2 Jet

The characteristics of jet noise are determined by the operating conditions of the jet and the nozzle type. ANOPP offers six prediction methods to compute jet noise. These methods are identified along with their key features in Table 2.4. The range of application for each method varies depending on the operating condition and nozzle geometry. Jet noise is often characterized by three subcomponents: jet mixing noise, broadband shock noise, and screech tones. Jet turbulent mixing noise consists of that associated with the large turbulent structures and that due to the less directional fine-scale turbulence noise. The jet mixing noise is most intense in the downstream direction and peaks near 130° as measured from the engine inlet. The broadband shock noise, on the other hand, is most intense in the upstream direction near 30°. Noise from jets with supersonic exhaust velocity contain both jet mixing noise and broadband shock noise. Modern nozzles are commonly designed such that screech tones do not occur under normal operating conditions and therefore are not modeled.

Nozzle type also plays an important role in determining the jet noise characteristics. The most basic nozzle type is the convergent circular nozzle. With the development of the turbofan bypass engine, two nozzle configurations evolved—the internally mixed nozzle and the externally mixed nozzle.

Internally mixed jets exhaust the core and bypass flow through a single downstream nozzle with the internal primary nozzle located upstream of the bypass nozzle. In some cases, the internal nozzle may incorporate a lobed forced mixer to enhance the internal mixing. Internally mixed nozzles are not explicitly modeled within ANOPP; however, the effects of internal mixing may be estimated by computing mixed flow characteristics. The more common nozzle is the “separate-flow coannular nozzle,” where the core and bypass flows exhaust through separate nozzles. The ANOPP modules STNJET and ST2JET model the separate-flow nozzle configurations, which include the coplanar nozzle, bypass nozzle that is offset (upstream) from the primary nozzle, and primary nozzle with a center plug. To add additional complexity, both the bypass nozzle and/or the primary nozzle can be fitted with exit perimeter suppression devices such as chevrons. Within ANOPP, ST2JET models the effect of chevrons as a correction to the source noise spectra of nozzles without chevrons. The following provides a short description of the noise prediction methods shown in Table 2.4:

(1) One of the first empirical jet noise prediction methods to gain widespread acceptance is the SAE-ARP 876 method (Ref. 19). SAE-ARP 876 contains several methods of which only part are implemented within ANOPP. The mixing noise

for convergent circular jets is implemented in the SGLJET module, and the broadband shock noise for convergent circular jets is implemented in the SAESHK module. The SAE method for distributed jet noise is not currently implemented within ANOPP. Both of these methods are for the prediction of single (convergent) nozzle jets.

(2) The CNLJET module also known as the “Dual Stream Coannular Jet Noise Module,” predicts the jet mixing noise for a coannular jet exhaust nozzle with inverted velocity profiles (i.e., the bypass flow is greater than the core velocity). This prediction capability is based on the method developed by Pao and Russell, References 20 and 21, respectively. The method converts the coannular jet to an equivalent single stream jet with the same thrust, mass flow rate, and energy.

(3) The TAMSHK module predicts the free-field lossless broadband shock noise for circular and rectangular nozzles. The circular jet theory, developed in References 22 and 23, is applicable to overexpanded and underexpanded jets and accounts for the effects of jet temperature and forward flight. The forward flight effects for the circular jet theory include both Doppler and convective amplification factors. The rectangular nozzle theory, developed by Tam and Reddy (Ref. 24), contains essentially the same elements as the circular jet theory. Unlike circular jet noise though, rectangular jet noise is not symmetric in the azimuthal plane. An empirical correction factor developed by Ponton et al. (Ref. 25) is used to extend the rectangular theory to azimuthal angles other than 0°. The rectangular nozzle theory is limited to nozzles with straight sidewalls and aspect ratios of 6 or less.

(4) Two ANOPP modules are associated with the work of Stone (Refs. 26 to 29). The original Stone method, STNJET, (Refs. 26 and 27) predicts the far-field mean-square acoustic pressure for single- and dual-stream circular jets for either convergent or convergent-divergent nozzles. The method predicts both jet mixing noise and broadband shock noise. The method is limited to nozzles where the core velocity is greater than the bypass velocity. In addition, only the core velocity can be supersonic. The Stone method has been modified to improve jet noise predictions for small turbofan engines in the 13- to 27-kN (3000- to 6000-lb) thrust range (Ref. 28). The Stone Jet Noise module of 2003, ST2JET, is the most comprehensive of the jet noise prediction capabilities in ANOPP. A detailed assessment of the ST2JET module is presented later in Chapter 8, “Jet Noise Prediction.” The ST2JET module predicts jet noise for circular exhaust nozzles having single or dual streams, convergent or convergent-divergent geometry, and subcritical or supercritical pressure ratio. It also accounts for the presence of center plugs and exit plane perimeter noise suppression devices. The module is based on the semi-empirical model developed by J.R. Stone of Modern Technologies Corporation (Ref. 29). The method was developed from data with bypass ratios ranging from 5.0 to 14.9 obtained from the anechoic free-jet facilities at NASA Glenn Research Center, General Electric Company, and NASA Langley Research Center as well as free-jet facilities at Lockheed. The ST2JET module is an update to the STNJET module and extends the ANOPP jet noise prediction capability to higher bypass ratio engines for a full range of nozzle configurations including jets with inverted velocity profiles.

TABLE 2.4.—ANOPP JET NOISE PREDICTION METHODS

	SAE-ARP 876 Appendix A (SGLJET)	Stone 1980 (STNJET)	Stone 2006 (ST2JET)	Pao-Russell (CNLJET)	SAE-ARP 876 Appendix B (SAESHK)	Tam (TAMSHK)
Bypass ratio	0	0 to 5	0 to 14	0.1 to 5	0	0 to 5
Circular nozzle	•	•	•		•	•
Coannular nozzle		•	•	•		
Rectangular nozzle						•
Subsonic mixing (primary)	•	•	•	•		
Supersonic mixing (primary)	•	•	•	•		
Subsonic mixing (secondary)		•	•	•		
Supersonic mixing (secondary)			•	•		
Broadband shock (primary)		•	•			
Broadband shock (secondary)			•			
Point source	•	•	•	•	•	•
Distributed source			•			
Centerbody		•	•			
Flight effects	•	•	•	•	•	
Chevrans			•			
Inverted velocity profile			•	•		

2.2.1.3 Core

Combustion noise is computed using the GECOR module. This module predicts noise from conventional combustors installed in gas turbine engines. Three methods are available within the module and are known within ANOPP as the SAE method, the small engine method, and most currently the narrowband method. The SAE method, described in Reference 19 is based on methodology proposed by R.K. Matta (Ref. 30) and produces empirical 1/3-octave band spectra as a function of frequency and polar directivity angle. It is based on core noise data from turboshaft, turbojet, and turbofan engines. The small engine method, (Ref. 28) is a revision to the SAE method for small turbofan engines in the 13- to 27-kN (3000- to 6000-lb) thrust class. The narrowband method predicts the noise generated by a combustor using empirical data and functions to compute sound spectra as a function of narrowband frequency and polar directivity angle (Ref. 31). The narrowband method follows a similar formulation to that of the ANOPP 1/3-octave band methods; however, the empirical directivity and spectrum factors are different and specific to the narrowband method.

2.2.1.4 Turbine

Prediction methods for turbine noise have historically received limited attention due to its unimportance relative to the other engine sources. Prediction of the turbine noise is also difficult to assess since direct noise measurements are nonexistent and must be determined by indirect measurements or digitally extracting from the jet noise measurements. Two modules are available in ANOPP to predict turbine noise, TUR and SMBTUR. The TUR module predicts the free-field lossless far-field noise generated by the turbine of an aircraft engine. Turbine noise is modeled as two components, broadband noise and discrete tones. The broadband noise is the result of fluctuating lift on the rotors and stators, whereas the discrete tones are caused by the interaction of rotor wakes intersecting with following stator vanes and rotors. There are two options contained in this module. The first option is a semi-empirical prediction procedure based on the method developed by Dunn and Peart as described by Krejsa and Valerino in Reference 32. The second option is a revision to the Dunn and Peart method made by AlliedSignal (Ref. 28) to improve predictions for small turbofan engines in the 13- to 27-kN (3000- to 6000-lb) thrust class. This method is called the small engine method. Both methods use essentially the same form of equations. However, the small engine method uses different constants for the broadband and tone noise acoustic power terms. Also the spectrum shape is modified for the small engine method. The broadband and tone noise components are summed to determine the overall turbine noise level.

The Smith and Bushell Turbine Noise Module or SMBTUR also predicts turbine noise, but only the broadband noise component. Similar to the TUR module, there are two options contained in this module. The first option is based on the method developed by Smith and Bushell (Ref. 33) and employs empirical functions to produce sound spectra as a function of frequency and polar directivity angle. The second option is a revision to the

Smith and Bushell method made by AlliedSignal (Ref. 28) to improve predictions for small turbofan engines in the 13- to 27-kN (3000- to 6000-lb) thrust class. Both of these options assume that the only significant noise source is the “vortex” component, which is the broadband noise due to the interaction of the rotating blades with random velocity patterns in the flow.

2.2.1.5 Airframe

ANOPP currently has two methods for computing the noise from aircraft airframe components: the “Fink” method (computed using the FNKAFM module) and the “Boeing” method; each method is detailed in Chapter 4, “Airframe Noise: A Prediction Capability Assessment.” Both methods compute the 1/3-octave noise spectra based on fundamental parameters, which define the local flow conditions and the geometry of each component. The Fink method is based on a method developed by M.R. Fink of the United Technologies Research Center for the Federal Aviation Administration (FAA) (Ref. 34). The method employs empirical functions to model the far-field noise spectrum as a function of polar directivity angle and azimuthal directivity angle. Each spectrum is the sum of all the airframe component spectra produced by the wing, tail, landing gear, flaps, and leading-edge slats.

The Boeing method also computes the noise from the airframe components; ailerons, trailing-edge flaps, leading-edge slats, and landing gear. The noise prediction methodology associated with the aerodynamic control surfaces (i.e., ailerons, flaps, and slats) was developed by Sen et al. (Ref. 35) using acoustic measurements from full- and model-scale commercial transports. The landing gear noise prediction method was developed by Guo (Ref. 36) and is based on measurements from model- and full-scale landing gear. The methods employ empirical functions to produce unattenuated 1/3-octave band acoustic spectra as a function of frequency and polar directivity angle. A Doppler frequency shift is included to account for forward flight effects. To define the airframe geometry, parameters such as wingspan, trailing-edge flap chord lengths, number of landing gear, tire sizes, and surface areas of the landing gear components must be provided by the user.

2.2.2 Installation Effects

The aircraft configuration can significantly affect the radiated noise. The aircraft engines may be installed such that the wing shields (reduces) the noise generated by the engine from ground locations during the flight operation. Alternatively, the installation of the engines under the wing may result in reflection of the noise from the fuselage and/or wing-flap surface. ANOPP currently has limited capabilities to account for these effects. The following subsections provide an overview of engine liners and the module that is available to account for noise shielding and reflection.

2.2.2.1 Liners

The Fan Noise Treatment Module (TREAT) predicts the attenuation spectra for acoustic treatment in a turbofan inlet and aft fan bypass duct. The attenuation is estimated using methods

developed by Magliozzi (Ref. 37) or Kontos et al. (Ref. 38). The attenuation spectra are applied to separate predictions of the inlet- and aft-radiated source noise produced by a source noise module, such as the Heidmann Fan Noise Module (HDNFAN), and a total attenuated fan noise prediction is produced. The method accounts for a conventional (perforate) single- or double-degree-of-freedom liner of typical design. The aft duct treatment can be either single or double layered. The inlet treatment is always assumed to be single layered. The acoustic treatment is described geometrically by the duct radius or height and the treatment length. The acoustic treatment design is simply specified by the frequency of peak attenuation. The duct flow is determined from the mass flow and flow duct area. Hence it should be noted that these models are limited and that many important details about the liner design (such as modal content of the source) and implementation factors (location of liner, number of seams, etc.) of the designs are not included. Examples of predictions of engine noise with and without the TREAT module are shown in Chapter 3, “Engine System and Core Noise.”

2.2.2.2 Wing

The Wing Geometric Effects Module computes the effects of wing shielding and reflection on the propagation of noise from the engine. The wing shielding and the wing reflection effects are modeled separately and only for specific configurations. The wing shield model assumes the source (engine) is located above the wing. The wing reflection assumes the source (engine) is below the wing-flap system. Both models ignore the presence of the fuselage. The wing shielding model employs the Fresnel diffraction theory for a semi-infinite barrier, as described in Beranek (Ref. 39) and Maekawa (Ref. 40), with modifications to treat the finite barrier presented by the aircraft wing. The wing reflection model assumes that reflection can occur only from the wing-flap system, not the fuselage. A maximum of three wing-flap panels may be included in the model, and the effect of leading-edge slats on the wing is neglected. For both the wing shielding and reflection models the wing and flap panels are assumed to be perfectly planar surfaces.

2.2.3 ANOPP Computational Efficiency and Usage

ANOPP Level 25 is written in Fortran 77 and can be run on a desktop or personal computer. For most applications, ANOPP

will easily execute on modern personal computers with no special memory or disk requirements. Typical run times for ANOPP are on the order of seconds. For complex applications, where noise is computed at hundreds of observation points, the runtimes may be only on the order of minutes, which makes ANOPP very attractive for use in system and optimization studies.

ANOPP requires that the user have a basic knowledge of aircraft aeroacoustics and propulsion systems. This is needed to properly select the appropriate prediction strategy and source noise modules. In addition the user needs to be familiar with the ANOPP executive programming language in order to customize standard input templates to solve specific problems. The ANOPP programming language is a powerful capability that provides a unified system approach to prediction of noise from a full aircraft as well as from individual aircraft components.

2.3 ANOPP Evaluation and Demonstration of Capabilities

The ANOPP prediction capabilities are demonstrated for a Boeing 737–800 with CFM56–7B engines. The following section provides a description of the vehicle, the operating condition, and flight trajectory inputs used to compute noise metrics. A careful validation whereby detailed predictions are compared with a comprehensive acoustic database was not possible because of difficulties in obtaining the required vehicle state data and availability of validation quality measurements. Full-aircraft noise data available in the public domain and suitable for validation purposes are quite limited. The predictions in this chapter are compared with certification measurements taken for a number of Boeing 737–800 with CFM56–7B engines. In addition, an initial evaluation of the sensitivity of ANOPP predictions to small changes in aircraft Mach number and engine power setting is presented.

The specific ANOPP functional modules and source noise modules used to predict the full-aircraft noise for each step indicated in Figure 2.2 are shown in Table 2.5 as all upper case identifiers. The ANOPP output for this study is the received noise that takes into account spherical spreading, atmospheric attenuation, ground effects, reflections, and lateral attenuation at certification locations. The ground was specified as soft, which is representative of the ground found at airports.

TABLE 2.5.—ANOPP MODULES USED FOR PREDICTING THE NOISE FROM A GENERIC BOEING 737–800 AIRCRAFT

Aircraft flight definition	Source noise modeling ^a	Propagation and received noise
Weather: ATM, ABS Flight path definition: SFO Source-to-observer geometry: GEO	Jet: ST2JET Fan: HDNFAN (General Electric large fan method) Acoustic liner: TREAT (General Electric acoustic liner method) Core: GECOR (SAE ARP 876 Matta method) Airframe: FNKAFM (includes landing gear, slats, flaps, trailing-edge noise sources)	Propagation: PRO Noise metrics: LEV, EFF

^aPhrases in parentheses are options used within the module.

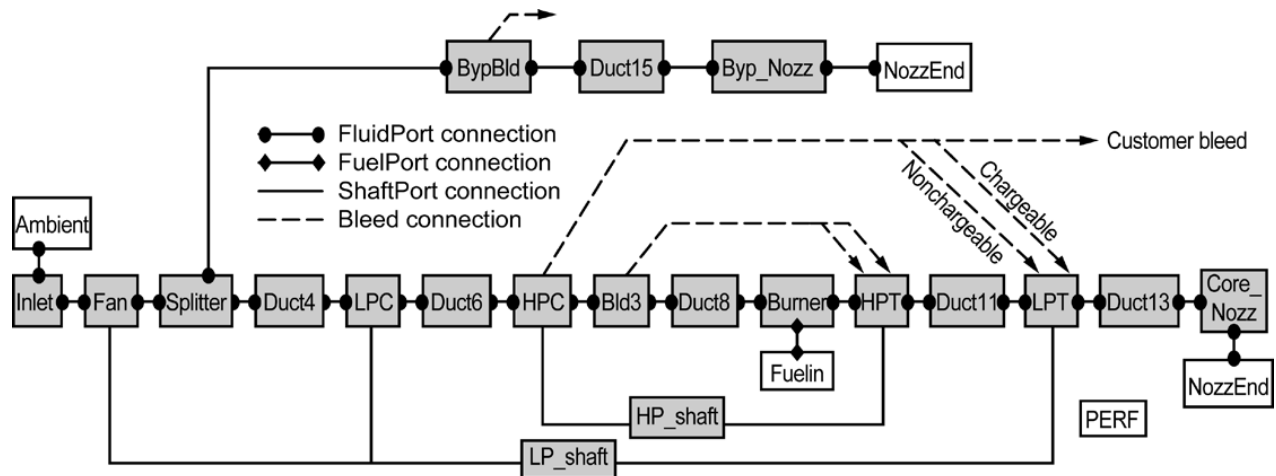


Figure 2.4.—Analytical representation of CFM56–7B turbofan engine in Numerical Propulsion System Simulator (NPSS) (Ref. 41).

2.3.1 Vehicle Description

The Boeing 737–800 is a short-to-medium-range aircraft, with a maximum range of about 5500 km (3000 nautical miles). It is equipped with two CFM56–7B engines capable of 116 kN (26 091 lb) of thrust per engine at its sea level static flat rating, with a typical cruise Mach number of 0.785. The overall length of the B737–800 is about 39 m (129 ft) with a wingspan of over 34 m (112 ft). The B737–800 can seat 162 to 189 passengers depending on the cabin class configuration. Gross airframe dimensions are required inputs for the Fink airframe noise prediction module used in this benchmarking assessment, and these inputs can be obtained from many public-domain aircraft information sources. A simple three-view drawing of the aircraft is often sufficient to provide the Fink airframe noise prediction method with proper input data.

2.3.2 Engine Description

The engine state for a range of Mach number and throttle settings is required input for ANOPP’s source noise prediction modules. Unfortunately, the propulsion system data that ANOPP needs are exceedingly difficult to obtain. Engine companies regard this information as highly proprietary company trade secrets. For this reason, propulsion data for the CFM56–7B was not available for this assessment. Fortunately, NASA has the capability to compute such propulsion data, using a thermodynamic cycle and aeromechanical engine simulation program known as the Numerical Propulsion System Simulator (NPSS, Ref. 41). The NPSS has been formally adopted by the U.S. aerospace industrial community, Government, and academia, and continues to be developed by a consortium of U.S. Government and industrial entities. Engine companies also use NPSS to create very elaborate models of their engines, since it allows for very accurate analytic predictions of the engine performance.

The CFM56–7B was analytically modeled in NPSS using data available from several reliable public-domain sources, such as FAA-type certification data sheets, manufacturer-provided airport planning documents, technical reports, Jane’s Aero Engines, and manufacturers’ Web sites. No company-proprietary data were used. Performance data were computed throughout the flight operating envelope. The various components are linked together analytically in NPSS using coding constructs known as fluid ports and mechanical ports for flow and shaft connections within the engine, respectively. The analytical linkage of the CFM56–7B is shown in Figure 2.4.

An aeromechanical, weight, and flow path analysis was also conducted using other NPSS airbreathing elements collected in the Weight Analysis of Turbine Engines (WATE) library. One result of this analysis is the two-dimensional cross section of the engine shown in Figure 2.5. The analytical NASA representation of the engine is somewhat crude when compared with higher fidelity engine-company simulations. For example, an examination of the cross section suggests that the low-pressure turbine exit, the front frame, and duct flow paths, among other components, could be modeled with greater accuracy. However, it serves well enough to provide ANOPP with its basic requirements. The CFM56–7B NPSS simulation was easily configured to write the pressures, temperatures, rotational speeds, and flow areas for each flow station within the engine to an engine state table for inclusion in the ANOPP input file.

2.3.3 Trajectory Description

The aircraft trajectory is important for accurate prediction of any time-dependent aircraft noise metric. The noise propagated through the atmosphere to the ground is dependent on the location, direction, orientation, airspeed, engine throttle setting, and operational configuration of the aircraft. These are

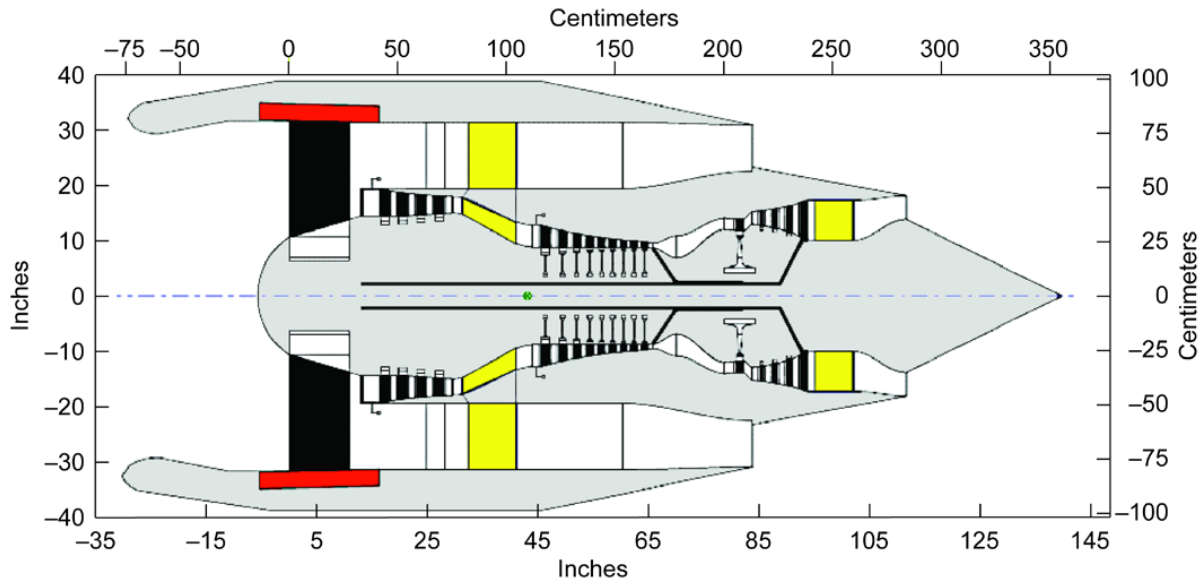


Figure 2.5.—Cross-sectional view of NPSS/WATE aeromechanical and flow path simulation of CFM56-7B turbofan engine (drawing to scale).

all functions of time and aircraft position. For an existing aircraft, these data may be obtained from measurement, where an aircraft trajectory is tracked using radar equipment, optical systems, or by other means such as from trajectory simulations. Analytical trajectory simulations require solutions of equations of motion; using aircraft aerodynamics, thrust performance, stability and control moment, weight, and atmospheric data. The aircraft aerodynamics, in the form of so-called “drag polars,” and stability and control data are needed, but are often proprietary and difficult to obtain from airframe manufacturers for the same reasons as the propulsion data described above. The aerodynamic performance of an airplane with its high-lift devices (flaps and slats) deployed during takeoff and landing is particularly sensitive. For ANOPP predictions, the aircraft trajectory can be internally calculated using ANOPP modules or computed externally and entered in as input.

The B737-800’s departure and approach trajectories were simulated using the procedures described in the Society of Automotive Engineers (SAE) Aerospace Information Report (AIR), SAE-1845 (Ref. 42). The material in this document is similar to the material in related documents published by the European Civil Aviation Conference (ECAC) Document 29 (Ref. 43). SAE-1845 describes a method where aircraft takeoff and approach trajectories may be empirically computed using aircraft and engine regression performance coefficients provided by industry. These performance coefficients are technical representations of the underlying proprietary data and hence are nonproprietary information. Engine thrust, for example, is represented by a simple regression model of lapses with airspeed, altitude, and ambient temperature with respect to a sea level static-rated thrust. These regression coefficients

and methods for using them allow rapid aircraft trajectory computations in computer codes such as the FAA’s Integrated Noise Model (INM) (Ref. 44). The empirical methods are used to compute distance, altitude, speed, and throttle setting for the various flight segments encountered during approach and departure.

The approach and departure trajectories used within ANOPP for the B737-800/CFM56-7B operating from a sea-level field are shown in Figure 2.6. The conditions are for 25 °C (77 °F) and 1.013 bar (29.92 in. Hg), with the airplane in departure configuration at its maximum takeoff gross weight of 78 150 kg (172 300 lb) and in approach configuration at its maximum landing weight of 66 360 kg (146 300 lb). The takeoff trajectory starts with the ground roll with engines at maximum takeoff rated thrust, then a rotation, followed by several climb and acceleration segments. It also includes a noise abatement throttle cutback procedure. This throttle cutback serves to reduce the noise perceived by the flyover observer and is allowed under 14 CFR Part 36 regulations (Ref. 45). After passing beyond the flyover observer, the engines are throttled up to their maximum continuous climb thrust for the remainder of the climb. Note the aircraft remains under 463 km/h (250 kn) calibrated airspeed under 3048 m (10 000 ft) per regulations. The approach has one constant-altitude, constant-calibrated-airspeed “step” that is typical of airport approach patterns. Afterwards, its descent follows a typical 3° glide slope to the runway threshold.

Certification noise levels are regulated by the requirements of the International Civil Aviation Organization (ICAO) Annex 16 noise regulations (Ref. 46) and in the United States by the Federal Aviation Regulations (FAR) Part 36 (Ref. 47). The regulations observed in this benchmarking assessment are

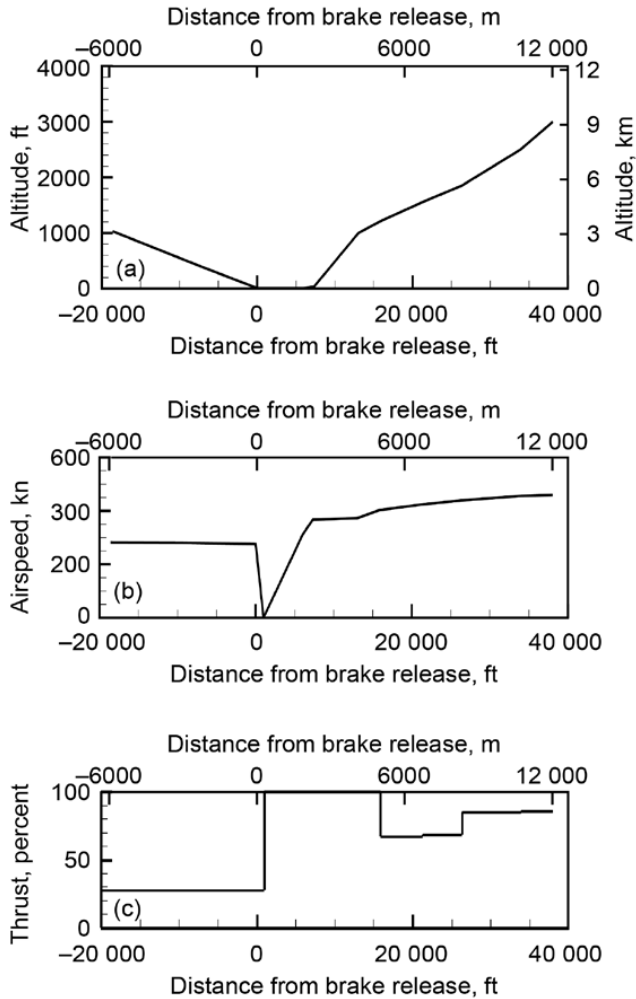


Figure 2.6.—SAE AIR-1845 trajectory for the B737-800/CFM56-7B at 172 300 lb. (a) Altitude. (b) Airspeed. (c) Percent net engine thrust.

those applicable for transport category large airplanes and jet-powered airplanes. An aircraft is flown through standardized takeoff and approach procedures, and the 1/3-octave band frequency spectrum time histories are measured at three locations identified as lateral sideline, flyover, and approach. These locations are shown in Figure 2.7. At each location the measurement microphone is located 4 ft above the ground. The certification noise metric used internationally is the effective perceived noise level (EPNL). During takeoff procedure this is measured at the flyover and lateral sideline observer points. The lateral sideline observer point is defined where the EPNL is highest along the lateral sideline reference lines symmetrically located on either side of the flight path (running parallel to the runway at a distance of 450 m, or 1476 ft). Within ANOPP, the sources are most often colocated and axisymmetric, therefore only requiring the analysis to be made on one side of the aircraft. The flyover EPNL measurement is made on one side of the aircraft. The flyover EPNL measurement is measured 6500 m (21 325 ft) from brake release on the runway centerline. (The flyover observer is also referred to as the “cutback,” “community,” “takeoff,” or “centerline” observer.) The flyover measurement most often employs a noise abatement throttle cutback procedure that is allowed under certification rules. During approach the noise is measured at the approach point, located 2291 m (7518 ft) before the point of touchdown on the runway centerline. This corresponds to 2000 m (6562 ft) from the runway threshold, where the aircraft altitude over the observer is 120 m (394 ft).

2.3.4 Comparison of Measurements and Predictions

ANOPP predictions are made for the B737-800/CFM56-7B using the source noise modules identified in Table 2.5 and the flight procedure described above. The source noise from the engine and airframe are propagated to observers located 4 ft above the ground in accordance to the specifications for

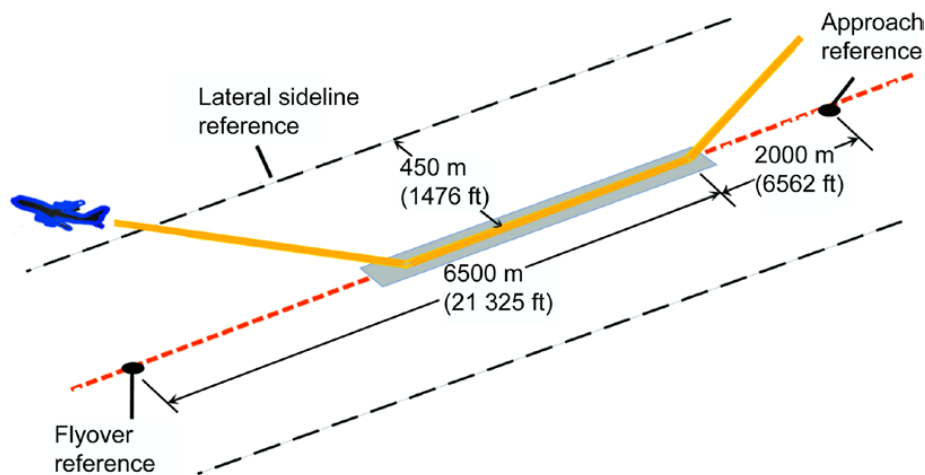


Figure 2.7.—Noise certification measurement locations.

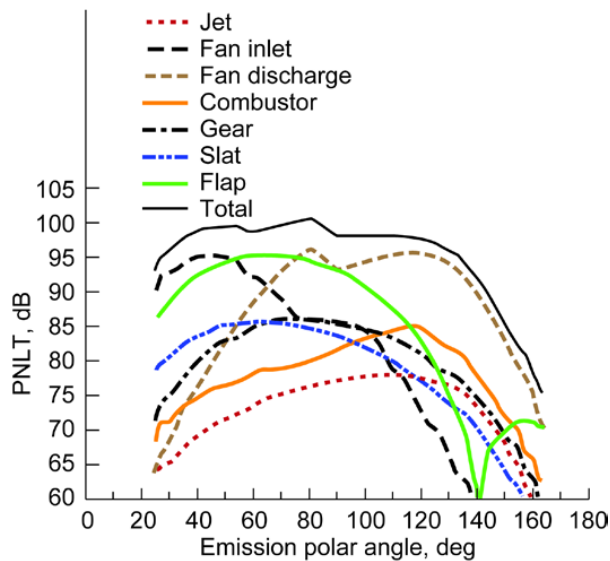


Figure 2.8.—Predicted tone-weighted perceived noise level (PNLT) time history at approach certification point.

certification measurement procedure. Noise propagation effects accounted for include spherical spreading, Doppler shift and convective amplification, atmospheric attenuation, and ground reflections based on data for grass-covered ground. The propagated acoustic spectra for each noise component are predicted at (user specified time increments) half-second intervals at each measurement location. From these spectra, ANOPP computes the perceived noise level (PNL), tone-weighted PNL (PNLT), and EPNL noise metrics for the individual sources and for the total aircraft.

The predicted PNL time histories and 1/3-octave band spectra at the certification approach, lateral sideline, and flyover observer locations are shown in Figure 2.8 to Figure 2.13. The 1/3-octave band spectra results are only shown for the three polar emission angles $\theta_e = 45^\circ$, 90° , and 135° . For the approach flight segment, the PNL time history predicted at the certification approach location is shown in Figure 2.8 and the associated 1/3-octave spectra at the three polar emission angles are shown in Figure 2.9. For polar angles prior to overhead ($\theta_e = 90^\circ$) the flap and slat noise dominates the airframe noise component. The engine sources are dominated by the fan inlet and discharge noise prior to and after the vehicle has passed overhead. The other engine noise components are minimal for the approach flight segment since the engine thrust is only at about 30 percent of the total available thrust. The PNL time history predicted at the lateral sideline certification location is shown in Figure 2.10, and the associated 1/3-octave spectra at the three polar emission angles are shown in Figure 2.11. As expected, the engine noise sources dominate, particularly the jet and fan noise. The tonal character of the fan inlet can be seen in the PNL time history by the spikes at polar angles less than 60° . The predicted results at the flyover location are shown in Figure 2.12 and

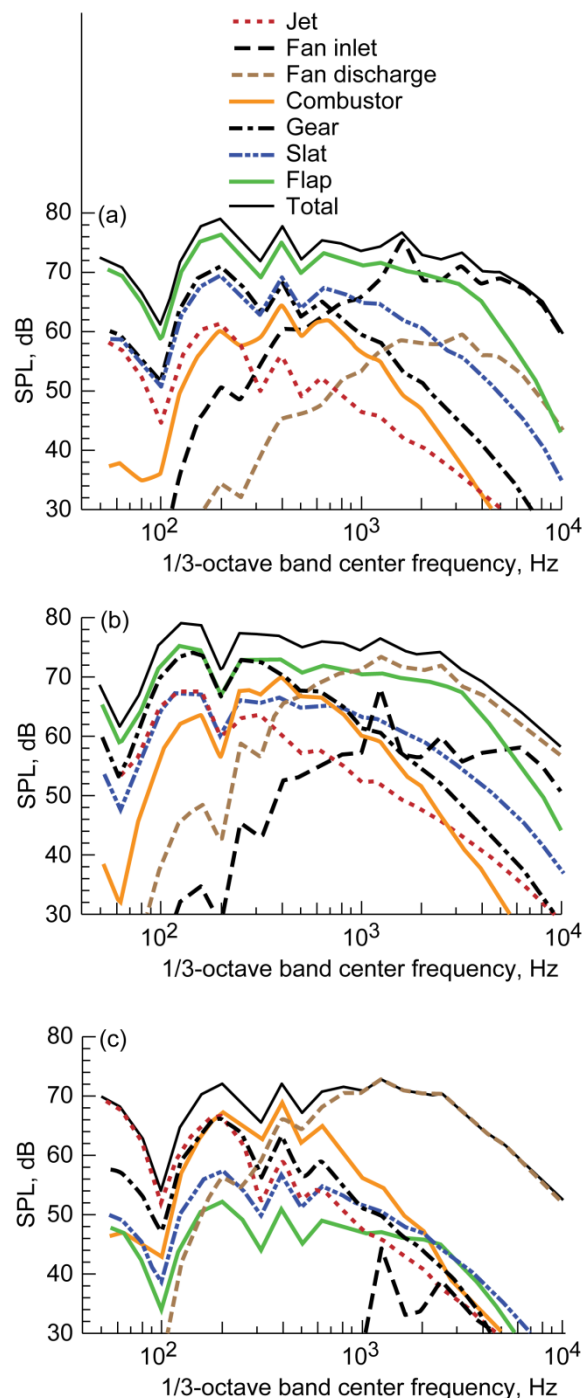


Figure 2.9.—Predicted sound pressure level (SPL) at approach certification point for three different polar directivity angles, θ_e . (a) 45° . (b) 90° . (c) 135° .

Figure 2.13. The trends are similar to those seen for the predictions at the lateral sideline location. The inlet fan noise dominates for polar angles less than $\theta_e = 90^\circ$, and the fan discharge and jet noise dominate for polar angles greater than $\theta_e = 90^\circ$.

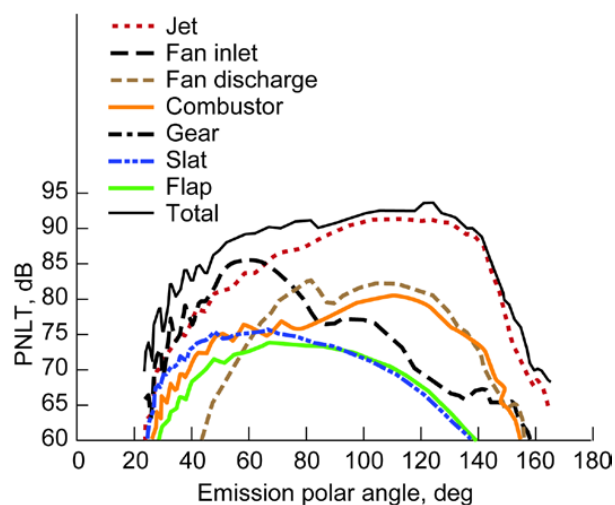


Figure 2.10.—Predicted tone-weighted perceived noise level (PNLT) time history at lateral sideline certification point.

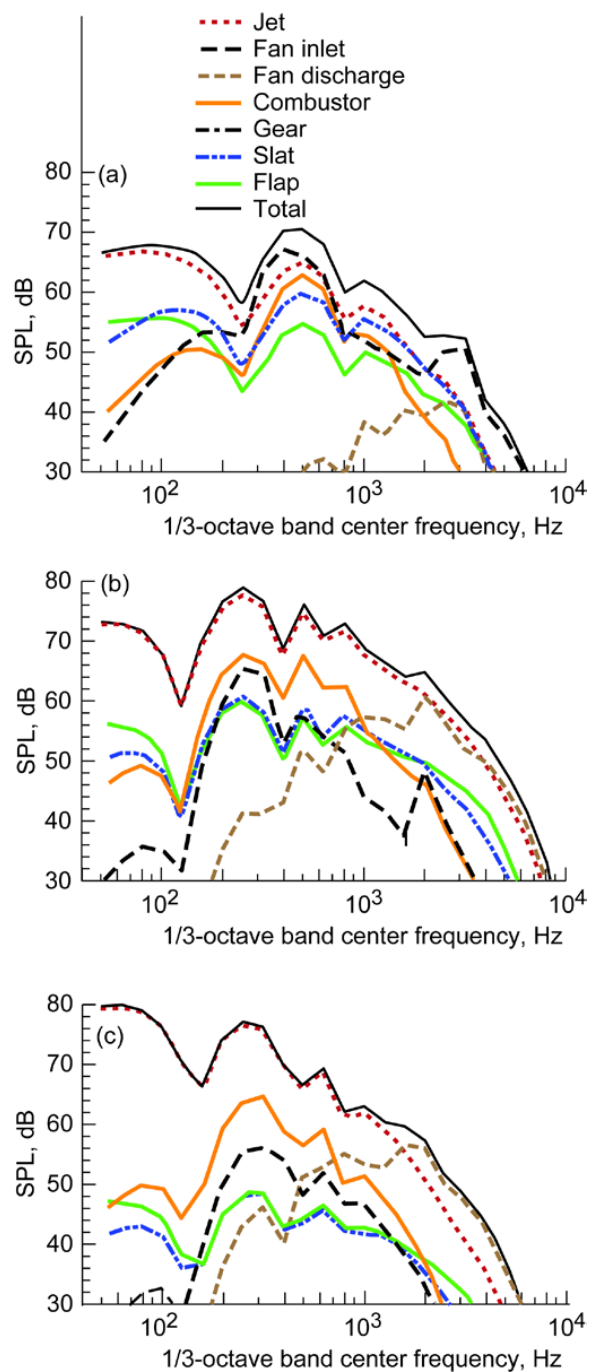


Figure 2.11.—Predicted sound pressure level (SPL) at lateral sideline certification point for three different polar directivity angles, θ_e . (a) 45° . (b) 90° . (c) 135° .

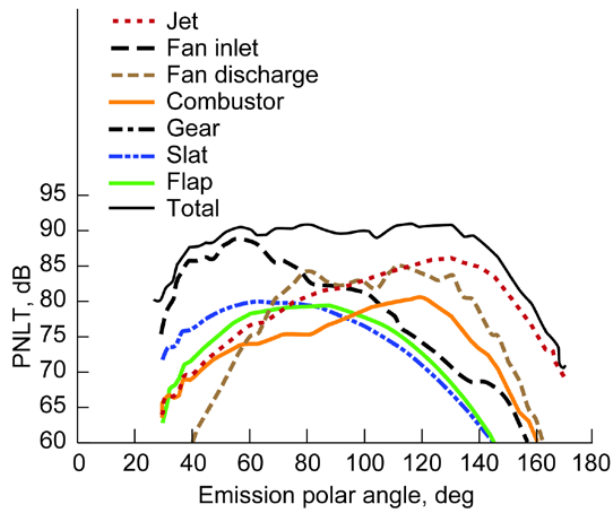


Figure 2.12.—Predicted tone-weighted perceived noise level (PNLT) time history for flyover (with cutback) condition.

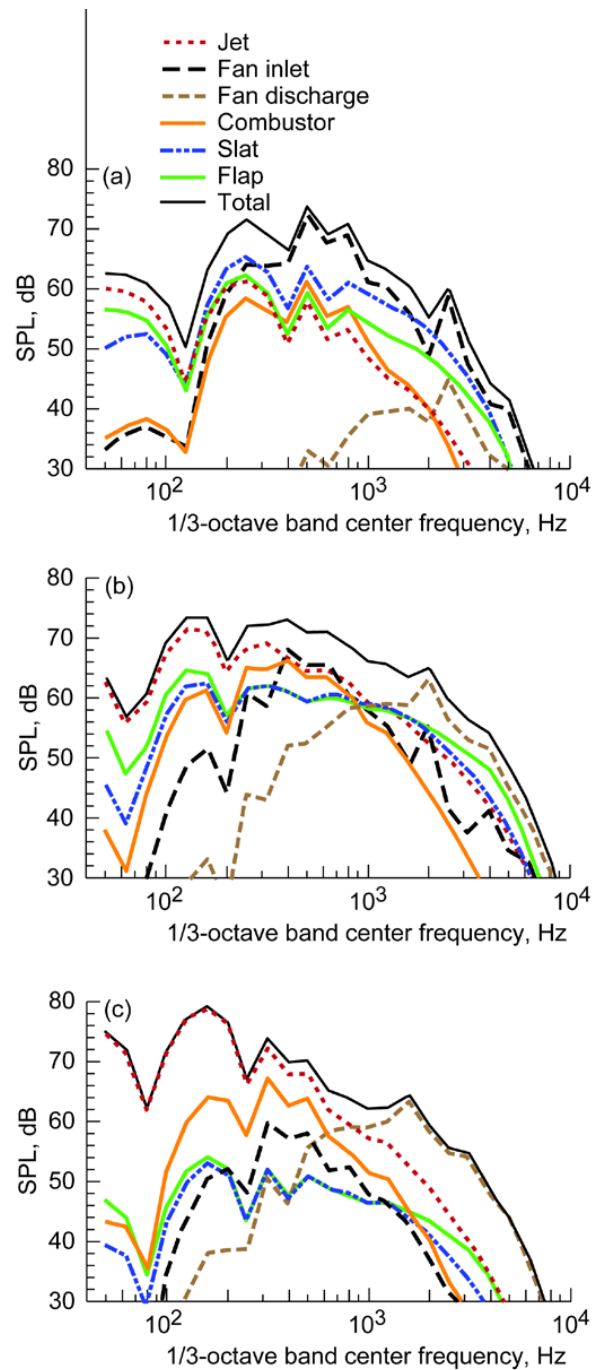


Figure 2.13.—Predicted sound pressure level (SPL) at flyover (with cutback) location for three different polar directivity angles, θ_e . (a) 45°. (b) 90°. (c) 135°.

The predicted EPNL results for each noise component contributing to the total aircraft noise are shown in Figure 2.14 for each certification measurement location. To compare the relative importance of the component noise sources on an EPNL basis, the noise from each source (fan inlet, fan discharge, jet, core, etc.) is analytically flown past each certification observer (lateral sideline, flyover, and approach). The EPNL for each source is computed as the difference between the full-system EPNL and the EPNL determined with all but the source component of interest included. (This is done on a pressure-squared basis.) This technique reduces the effect of duration and directivity discrepancies. As expected the airframe noise is nearly equivalent to the engine levels on approach and the engine sources dominate during the takeoff flight segment. The capability to identify the contribution of individual noise components provides insight into the key noise mechanisms contributing to the overall noise levels.

Identification and reduction of these sources will allow for the development of quieter aircraft designs and flight procedures.

The predicted EPNL compared with certification measurements of this vehicle are shown in Figure 2.15 to Figure 2.17. The predicted results were made assuming the highest gross weight found for this vehicle and are indicated on the plots by the red square. These measurements were obtained from the FAA Web site and are the flight certification noise measurements obtained for Boeing 737-800 with CFM56-7B. The exact details of each vehicle configuration or engine operation are not known. The cause of the large scatter in the data, particularly for the lateral sideline and flyover locations can in part be attributed to model-type variations in the engine and airplane system, which cause differences in the measured certification noise. Airplane weight and thrust performance differences by type lead to changes in trajectory and throttle history, which can produce measured noise differences of the

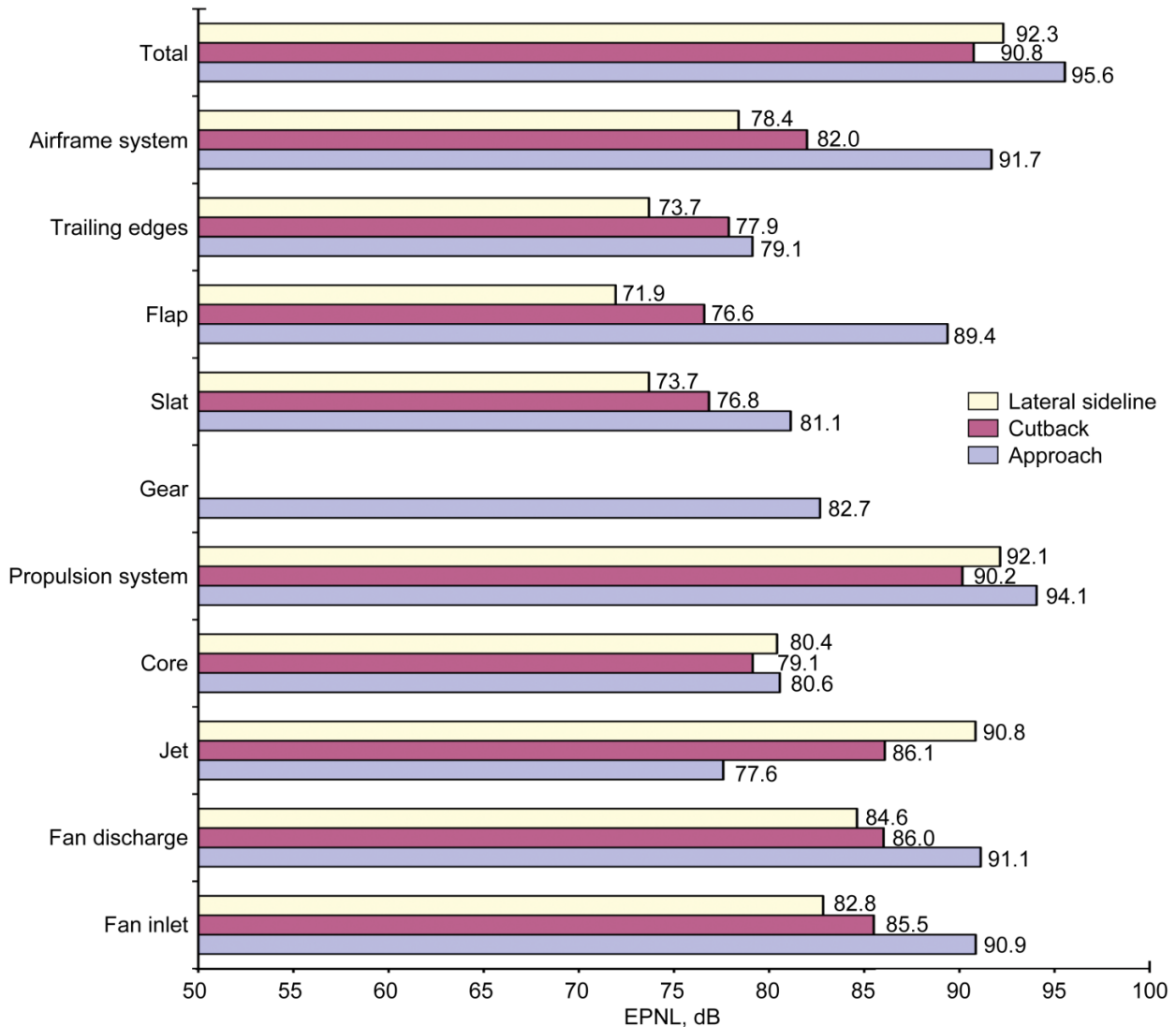


Figure 2.14.—Predicted contributions from each noise component to total effective perceived noise level (EPNL) at the three certification points.

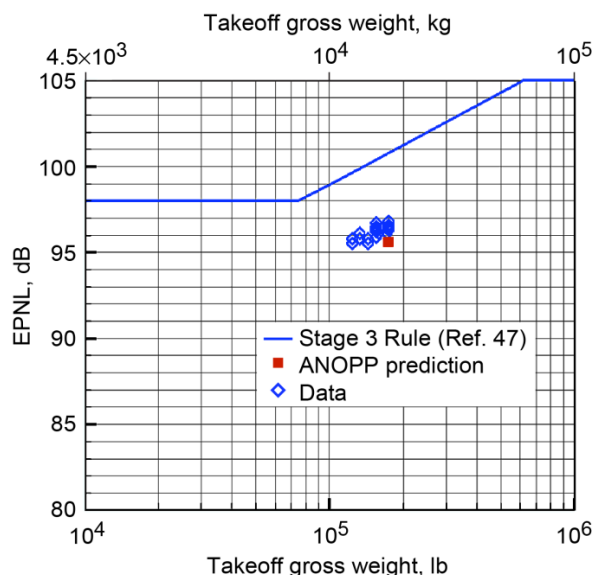


Figure 2.15.—Comparison of predicted effective perceived noise level (EPNL) for B737-800/CFM56-7B and noise certification data of 73 certificated B737s equipped with CFM56-7B engines. Approach measurement location.

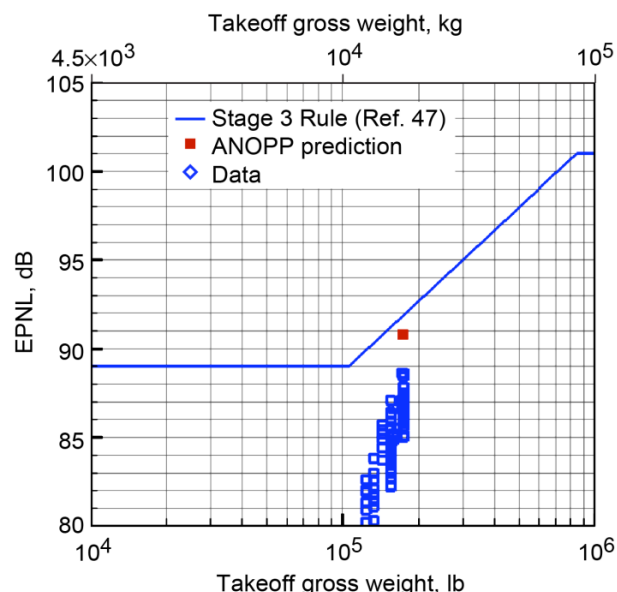


Figure 2.17.—Comparison of predicted effective perceived noise level (EPNL) for B737-800/CFM56-7B and noise certification data of 73 certificated B737s equipped with CFM56-7B engines. Flyover measurement location.

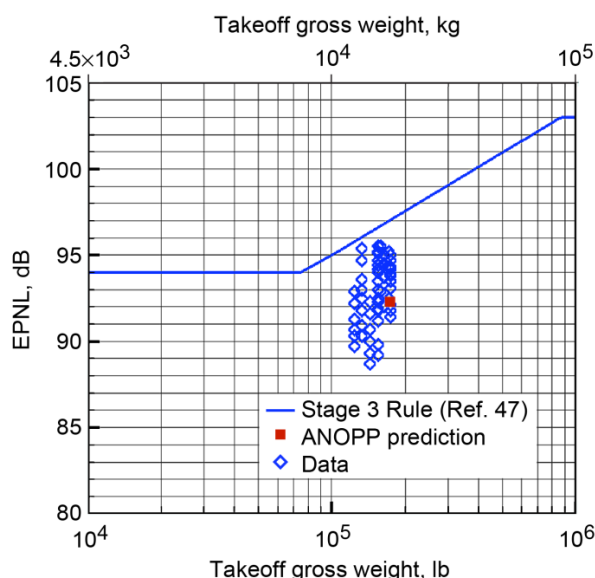


Figure 2.16.—Comparison of predicted effective perceived noise level (EPNL) for B737-800/CFM56-7B and noise certification data of 73 certificated B737s equipped with CFM56-7B engines. Lateral sideline measurement location.

first order. Differences in engine model architecture, even within a family of engine type, lead to the different engine-type ratings and may cause a substantial change in emitted noise. However, these engineering design implementations are often impossible to model without access to company-proprietary information. Also it should be noted that the manufacturers have some latitude in how the aircraft is flown in the vicinity of the flyover microphone, whereas little or no latitude exists near the other certification points. Therefore, they are likely to operate in an optimal manner that differs from the nominal takeoff procedure assumed. This could also explain the overprediction for the flyover point. The predictions shown, however, were not tweaked, but were created based on best available inputs and then directly compared with the data shown in Figure 2.15 to Figure 2.17. With many of the inputs not known exactly, the ANOPP results are considered fair to good in comparison with the data.

2.3.5 Uncertainty Analysis

An initial investigation is made to provide an estimate of the uncertainty in ANOPP full-aircraft noise EPNL predictions. This investigation is very limited because of the lack of measured data available. Performing a complete uncertainty and/or error analysis of ANOPP requires not only acoustic results, but also a full description of the engine, including engine state and airframe for a range of flight conditions. Since this is not available at the level of detail required, an analysis is performed to determine the uncertainty of ANOPP results for appropriate variations in aircraft velocity and throttle setting.

Both of these variables may directly affect the noise generation from both the engine and airframe components.

Every module in the noise prediction process will introduce some uncertainty. The purpose of this analysis is to determine the sensitivity of the EPNL prediction due to uncertainty in specific key input parameters. Therefore, the analysis is performed with the assumption that atmospheric conditions and all geometric parameters relating to the aircraft are known. Approach and takeoff profiles are simulated by intervals between fixed points where the aircraft velocity, altitude, and angle of attack are specified. The aircraft velocity is allowed to vary but the altitude and angle of attack are held fixed.

The aircraft velocity and engine power setting determine the engine performance, which is modeled in ANOPP through engine state tables. Engine state tables have two independent variables—aircraft Mach number and engine power setting—and six dependent variables: area, fuel-to-air ratio, mass flow rate, total temperature, total pressure, and rotation speed. Engine state tables are provided for each noise source. Therefore, any change in the aircraft velocity or engine power setting will be reflected in the dependent variables.

A Monte Carlo approach is used to determine the 95% confidence intervals based on a Gaussian distribution of the aircraft velocity and power setting. The aircraft velocity V and the engine power setting Π are assumed to be uncorrelated and are allowed to vary according to

$$V_i = V^* + N_{V,i} \Delta V \quad (2.1)$$

and

$$\Pi_i = \Pi^* + N_{\Pi,i} \Delta \Pi \quad (2.2)$$

where V_i is the simulated aircraft velocity, V^* is the true aircraft velocity, $N_{V,i}$ is the random number associated with the variation in aircraft velocity, and $\Delta V = 15$ ft/s is the maximum allowable variation in aircraft velocity. Similarly, Π_i is the simulated power setting, Π^* is the true power setting, $N_{\Pi,i}$ is the random number associated with the variation in power setting, and $\Delta \Pi = 5$ percent is the maximum allowable variation in power setting. Normally distributed random numbers $N_{V,i}$ and $N_{\Pi,i}$ were generated with a maximum value of 1 and a minimum value of -1 . Twenty-one simulations (i.e., predictions) are made from which the sample mean and sample standard deviation shown in Table 2.6 are computed. The Student's t -factor for the 95% confidence interval with 20 degrees of freedom is 2.086 (Ref. 48). Therefore the 95% confidence interval CI about the mean is

$$CI = \pm tS \quad (2.3)$$

where S is the sample standard deviation. The results shown in Table 2.6 state that with 95 percent confidence, the next

TABLE 2.6.—MONTE CARLO SIMULATION OF BOEING 737 CERTIFICATION
EFFECTIVE PERCEIVED NOISE LEVELS (EPNL)

Number of simulations	Approach EPNL, dB	Lateral sideline EPNL, dB	Flyover EPNL, dB
1	95.0	92.1	90.8
2	94.6	91.9	90.8
3	96.5	92.3	90.8
4	96.2	92.3	90.7
5	95.6	92.5	90.8
6	95.1	92.5	91.0
7	95.4	92.3	90.7
8	94.6	91.9	90.8
9	96.8	92.4	91.0
10	96.0	92.3	90.8
11	94.6	92.1	90.8
12	95.2	92.2	90.7
13	95.4	92.2	90.7
14	94.6	92.0	90.8
15	95.9	92.3	90.8
16	96.0	92.6	91.0
17	95.3	92.6	90.9
18	95.9	92.4	90.8
19	95.8	92.3	90.7
20	95.5	92.4	90.8
21	95.7	92.5	90.9
Sample mean	95.5	92.3	90.8
Sample standard deviation	0.6	0.2	0.1
95% confidence interval	1.3	0.4	0.2

simulation at approach will fall between ± 1.3 dB of the sample mean EPNL of 95.5 dB, the next simulation at the lateral sideline location will fall between ± 0.4 dB of the sample mean EPNL of 92.3 dB, and the next simulation at the flyover location will fall between ± 0.2 dB of the sample mean EPNL of 90.8 dB.

The noise levels are also computed for the extreme minimum and maximum values of aircraft velocity and engine power setting allowed in this analysis. This provides a minimum and maximum level of noise variation, based on these values. The results are shown in Table 2.7 to Table 2.9. The sensitivity of ANOPP predictions to small variations in these two parameters is as expected for a robust system noise capability. To fully assess the sensitivity of all ANOPP modules to all inputs was not undertaken at this time because of the lack of data available for such a study and the limited resources available to perform the thorough analysis required. However, it is recognized that there are several factors that can contribute to errors in predicting EPNL using ANOPP and some of these are as follows:

(1) ANOPP's built-in source noise prediction models are based in most part on measured results. The empirical to semi-empirical methods are hence inherently limited by the database used to develop and validate the methods. It is difficult to construct accurate analytical methods that are generically applicable to all varieties of noise sources. Fan noise, for example, is a strong function of fan design characteristics that are not necessarily captured by ANOPP's Heidmann module, which may fairly be called a generalized empirical fan noise prediction method. The prediction method is simply insensitive to airfoil geometry, positioning, and orientation; small-scale flow characteristics; specific acoustic treatment designs; and dozens of other attributes of the fan and ducts. In other words, since its framework is logically constructed and scalable, the Heidmann fan noise methodology may be a good tool to generically predict the noise for classes of fans, but it is most likely limited in its capabilities to accurately predict the noise of a specific fan design within a class. Similar arguments may be made for the other source noise prediction methods used in this benchmarking.

(2) The propulsion cycle and aeromechanical information input to source noise prediction models has some associated error. Even the best, most accurate source noise predictions will be inaccurate if the propulsion system data feeding them has inaccuracies. There is certainly some propulsion data error involved in this benchmarking activity, and the difficulty in obtaining accurate propulsion system data due to its proprietary nature was described in detail in Section 2.3.2, "Engine Description."

(3) ANOPP uses a paradigm of superposition, where multiple independent point noise sources are summed at the aircraft locale before propagating the combined signal to the ground. Real noise sources are complex, distributed sources (particularly jet noise) that are affected by the aircraft configuration and environment. The current capabilities within ANOPP do not adequately account for propulsion-source and airframe interactions, noise reflections, or complex acoustic phenomena such as refraction, diffraction, and other effects that can take place in the complex acoustic near field.

(4) Propagation modeling has some inherent error. ANOPP does capture the effects of a layered atmosphere, with procedures that correct the radiated signal for atmospheric attenuation and ground effects. Other, more complex propagation phenomena however, such as scattering, weather effects, and terrain are not adequately accounted for in the models.

(5) The trajectory simulated by the SAE AIR-1845 method may not be precisely the same as the trajectory flown by the B737 during its noise certification tests. Trajectory has a first-order influence on the outcome, and there will be some inherent error associated with this. Unfortunately, the exact details of the trajectory (vehicle orientation and engine operation) flown during certification are not available.

(6) The measured certification EPNLs to which comparisons are made have some error. For example, microphone measurements, equipment signal data processing, data corrections for ambient conditions, trajectory tracking, timing, weather, terrain, and complex propagation effects at the test site all contribute to the differences in this benchmarking. And the mathematical correction procedures specified by regulations to account for differences from the standard acoustic day accounts for some error in the published EPNLs.

TABLE 2.7.—CHANGE IN EFFECTIVE PERCEIVED NOISE LEVEL (EPNL) (dB)
AT APPROACH LOCATION DUE TO 5-PERCENT VARIATIONS
IN AIRCRAFT VELOCITY AND POWER SETTING
[Baseline represents nominal values of aircraft velocity and power setting.]

Aircraft velocity	Power setting		
	Minimum (-5 percent)	Baseline	Maximum (+5 percent)
Minimum (-4.6 m/s, or -15 ft/s)	-1.8	-0.4	1.0
Baseline	-1.3	0.0	1.3
Maximum (+4.6 m/s, or +15 ft/s)	-0.7	0.5	1.5

TABLE 2.8.—CHANGE IN EFFECTIVE PERCEIVED NOISE LEVEL (EPNL) (dB)
AT LATERAL SIDELINE LOCATION DUE TO 5-PERCENT VARIATIONS
IN AIRCRAFT VELOCITY AND POWER SETTING
[Baseline represents nominal values of aircraft velocity and power setting.]

Aircraft velocity	Power setting		
	Minimum (–5 percent)	Baseline	Maximum (+5 percent)
Minimum (–4.6 m/s, or –15 ft/s)	–0.7	0.1	0.2
Baseline	–1.0	0.0	0.1
Maximum (+4.6 m/s, or +15 ft/s)	–1.1	–0.2	–0.2

TABLE 2.9.—CHANGE IN EFFECTIVE PERCEIVED NOISE LEVEL (EPNL) (dB)
AT FLYOVER LOCATION DUE TO 5-PERCENT VARIATIONS
IN AIRCRAFT VELOCITY AND POWER SETTING
[Baseline represents nominal values of aircraft velocity and power setting.]

Aircraft velocity	Power setting		
	Minimum (–5 percent)	Baseline	Maximum (+5 percent)
Minimum (–4.6 m/s, or –15 ft/s)	0.3	0.2	0.4
Baseline	0.1	0.0	0.3
Maximum (+4.6 m/s, or +15 ft/s)	0.0	–0.1	0.2

Unfortunately, without access to proprietary data and more accurate prediction methods, we can only speculate as to the reasons for the error, or even if serendipity played a factor in the form of offsetting errors. The EPNL is a complex, high-level, multidisciplinary metric with many independent variables affecting its outcome. To truly benchmark the ANOPP capabilities, the aircraft definition and measured noise must be known and to a much higher level of accuracy than was available for this assessment.

2.4 Recommendations

To improve the accuracy of community noise predictions of aircraft, such as the noise of future aircraft with advanced, unconventional noise reduction technologies, or even for the B737's certification noise levels estimated herein, NASA systems analysis tools will require significant upgrades. Physics-based prediction tools do offer the promise of analytically developing and designing noise reduction concepts prior to testing. However, the field of first-principle, physics-based computational aeroacoustic tools is in its infancy because of the lack of knowledge required to develop accurate predictions of unsteady flow and acoustics. It will be quite some time before higher fidelity computational aeroacoustic tools become mature, accurate, robust, and fast enough to be used for noise estimates at the conceptual design level. Meeting the requirements for computing resource and computational efficiency will be key enablers for these advanced, high-fidelity solvers. Enhancements of the

empirical and semi-empirical noise tools will continue, and they will become more robust and capable. In the near term, noise prediction methods based on first principles as well as improved semi-empirical analyses will be incorporated into a software framework in order to provide a capability for assessing conventional and future nonconventional aircraft. There are undoubtedly gaps in NASA's analytical acoustic toolset that are indicated by the shortcomings in evaluating many new and unconventional concepts. In addressing these gaps, NASA's next-generation analysis tools must be flexible enough to incorporate new analytical acoustic methods as well as model the physics responsible for noise of current and future designs.

The following gaps and issues need to be addressed to more accurately predict the system noise for conventional CTOL aircraft and to allow the prediction for nonconventional aircraft:

1. Develop aircraft noise prediction strategies that are multifidelity.
 - a. Address requirements at the fundamental noise technology level up through the system design and optimization level.
 - b. Address computational needs for accuracy and efficiency.
2. Extend jet noise capabilities.
 - a. Develop methods for internally mixed jets.
 - b. Develop methods for nonaxisymmetric nozzles.
3. Develop acoustic scattering methods that are based on first principles and those appropriate for system studies.

- a. Invest in fast multipole methods and efficient algorithms.
 - b. Develop intermediate methods that can account for noise shielding and/or reflecting effects using efficient method-ologies.
4. Invest in methods to account for propulsion-airframe and airframe-airframe interaction noise sources. These need to include not only methods based on first principles to allow for application to both conventional and nonconventional aircraft

configurations, but also efficient methods that can account for the effects for system design purposes.

5. Advance atmospheric propagation methods to include effects of wind and terrain.

6. Obtain a comprehensive aircraft flight acoustic database that includes not only the noise at a number of ground measurement locations, but also the details on the engine and airframe geometries and engine operating states for the entire flight trajectory.

Appendix A.—Nomenclature

A.1 Acronyms

AIR	Aerospace Information Report (SAE)
ANOPP	Aircraft Noise Prediction Program
CTOL	conventional takeoff and landing
ECAC	European Civil Aviation Conference
EPNL	effective perceived noise level
FAA	Federal Aviation Administration
FAR	Federal Aviation Regulations
ICAO	International Civil Aviation Organization
INM	Integrated Noise Model
NPSS	Numerical Propulsion System Simulator
PAS	propeller analysis system
PNL	perceived noise level
PNLT	tone-weighted perceived noise level
SAE	Society of Automotive Engineers
SPL	sound pressure level
WATE	Weight Analysis of Turbine Engines (library)

A.2 Symbols

<i>CI</i>	confidence interval
-----------	---------------------

N	normally distributed random number, $-1 \leq N \leq 1$ (see Eqs. (2.1) and (2.2))
R	source-to-observer distance (see Figure 2.3)
S	sample standard deviation
t	Student's t -factor
V	aircraft velocity
x,y,z	ANOPP coordinate system (see Figure 2.3)
θ	polar angle (see Figure 2.3)
Π	power setting
ϕ	azimuthal angle (see Figure 2.3)

Subscripts:

e	emission
i	index
V	aircraft velocity
Π	power setting

Superscripts:

*	true
---	------

References

1. Gillian, Ronnie E.: Aircraft Noise Prediction Program User's Manual. NASA TM-84486, 1982.
2. a. Zorumski, W.E.: Aircraft Noise Prediction Program Theoretical Manual. NASA TM-83199-PT-1, 1982. b. Zorumski, W.E.: Aircraft Noise Prediction Program Theoretical Manual. NASA TM-83199-PT-2, 1982.
3. Zorumski, W.E.; and Weir, D.S.: Aircraft Noise Prediction Program Theoretical Manual: Propeller Aerodynamics and Noise. NASA TM-83199-PT-3, 1986.
4. Godby, L.: ANOPP Validation Study: Lockheed L-1011. NASA CR-159138, 1979.
5. Kapper, C.Y.: Validation of Aircraft Noise Prediction Program; Final Report. NASA CR-159047, 1979.
6. Leifsson, Leifur T., et al.: Multidisciplinary Design Optimization of Low-Airframe-Noise Transport Aircraft. AIAA-2006-230, 2006.
7. Olson, E.D.; and Mavris, D.N.: An Integrated Low-Speed Performance and Noise Prediction Methodology for Subsonic Aircraft. AIAA-2000-2070, 2000.
8. Manneville, A.; Pilczner, D.; and Spakovszky, Z.S.: Noise Reduction Assessments and Preliminary Design Implications for a Functionally-Silent Aircraft. AIAA-2004-2925, 2004.
9. Antoine, Nicolas, et al.: A Framework for Aircraft Conceptual Design and Environmental Performance Studies. AIAA-2004-4314, 2004.
10. Olson, Erik; and Mavris, Dimitri: Aircraft Conceptual Design and Risk Analysis Using Physics-Based Noise Prediction. AIAA-2006-2619, 2006.
11. Golub, Robert A.; Rawls, John W., Jr.; and Russell, James W.: Evaluation of the Advanced Subsonic Technology Program Noise Reduction Benefits. NASA/TM-2005-212144, 2005.
12. Wang, Tongqing: Validation Tests With a Scale-Model for Surface Sound Pressure Prediction of Propeller Aircraft. *J. Aerospace Power*, vol. 12, no. 4, 1997, pp. 393-396.
13. Nguyen, L. Cathy: The NASA Aircraft Noise Prediction Program Improved Propeller Analysis System. NASA CR-4394, 1991.
14. Heidmann, M.F.: Interim Prediction Method for Fan and Compressor Source Noise. NASA TM-X-71763, 1975.
15. Hough, Joe W.; and Weir, Donald S.: Aircraft Noise Prediction Program (ANOPP) Fan Noise Prediction for Small Engines. NASA CR-198300, 1996.
16. Kontos, K.B.; Janardan, B.A.; and Gliebe, P.R.: Improved NASA-ANOPP Noise Prediction Computer Code for Advanced Subsonic Propulsion Systems. NASA CR-195480, 1996.
17. Herkes, William H.; and Reed, David H.: Modular Engine Noise Component Prediction System (MCP) Technical Description and Assessment Document. NASA/CR-2005-213526, 2005.
18. Nesbitt, E.H., et al.: An Empirical Prediction of Inlet Radiated Broadband Noise From Full Scale Engines. AIAA-1998-0470, 1998.
19. SAE International: Gas Turbine Jet Exhaust Prediction. SAE ARP876, rev. E, 2006.
20. Pao, S.P.: A Correlation of Mixing Noise From Coannular Jets With Inverted Flow Profiles. NASA TP-1301, 1979.
21. Russell, J.W.: A Method for Predicting the Noise Levels of Coannular Jets With Inverted Velocity Profiles. NASA CR-3176, 1979.
22. Tam, Christopher K.W.: Broadband Shock Associated Noise From Supersonic Jets Measured By a Ground Observer. AIAA-1992-502, 1992.
23. Tam, C.K.W.: Broadband Shock-Associated Noise of Moderately Imperfectly Expanded Supersonic Jets. *J. Sound Vib.*, vol. 140, no. 1, 1990, pp. 55-71.
24. Tam, Christopher K.W.; and Reddy, N.N.: A Prediction Method for Broadband Shock Associated Noise From Supersonic Rectangular Jets. NOISE-CON 93 Proceedings, 1993, pp. 135-140.
25. Ponton, M.K.; Manning, J.C.; and Seiner, J.M.: Far-Field Acoustics of Supersonic Rectangular Nozzles With Various Throat Aspect Ratios. NASA TM-89002, 1986.
26. Stone, J.R.: Interim Prediction Method for Jet Noise. NASA TM-X-71618, 1974.
27. Stone, J.R.; and Montegani, F.J.: An Improved Prediction Method for the Noise Generated in Flight by Circular Jets. NASA TM-81470, 1980.
28. Lieber, Lysbeth: Small Engine Technology (SET)—Task 13 ANOPP Noise Prediction for Small Engines: Jet Noise Prediction Module, Wing Shielding Module and System Studies Results. NASA/CR-2000-209706, 2000.
29. Stone, J.R.; Krejsa, E.A.; Clark, B.J.; and Berton, J.J.: Jet Noise Modeling for Suppressed and Unsuppressed Aircraft in Simulated Flight. NASA/TM-2009-215524, 2009.
30. Emmerling, J.J.; Kazin, S.B.; and Matta, R.K.: Core Engine Noise Program. Supplement 1: Prediction Methods, vol. 3, FAA-RD-74-125-VOL-3-SUPPL-1, 1976.
31. Schuster, Bill; and Lieber, Lysbeth: Narrowband Model for Gas Turbine Engine Combustion Noise Prediction. AIAA 2006-2677, 2006.
32. Krejsa, Eugene A.; and Valerino, Michael F.: Interim Prediction Method for Turbine Noise. NASA TM-X-73566, 1976.
33. Bushell, K.W.; and Smith, M.J.T.: Turbine Noise—Its Significance in the Civil Aircraft Noise Problem. ASME Paper 69-WA/GT-12, 1969.
34. Fink, Martin: Airframe Noise Prediction Method. FAA-RD-77-29, 1977.
35. Sen, R.; Hardy, B.; Yamamoto, K.; Guo, Y.; and Miller, G.: Airframe Noise Subcomponent Definition and Model. NASA/CR-2004-213255, September 2004.
36. Guo, Yueping: Empirical Prediction of Aircraft Landing Gear Noise. NASA/CR-2005-213780, 2005.
37. Magliozzi, B.: V/STOL Rotary Propulsion Systems: Noise Prediction and Reduction. Volume 2: Graphical Prediction Methods, Final Report, FAA-RD-76-49-VOL-2, 1976.
38. Kontos, Karen B.; Kraft, Robert E.; and Gliebe, Philip R.: Improved NASA-ANOPP Noise Prediction Computer Code for Advanced Subsonic Propulsion Systems. Volume 2: Fan Suppression Model Development; Final Report, NASA CR-202309, 1996.
39. Beranek, Leo L.: Noise and Vibration Control. McGraw-Hill, New York, NY, 1971, pp. 174-180.
40. Maekawa, Z.: Noise Reduction By Screens. *Appl. Acoust.*, vol. 1, no. 3, 1968, pp. 157-173.
41. Lytle, John K.: The Numerical Propulsion System Simulation: An Overview. NASA/TM-2000-209915, 2000.
42. SAE International: Procedure for the Calculation of Airplane Noise in the Vicinity of Airports. AIR1845, 1986.
43. European Civil Aviation Conference: Report on Standard Method of Computing Noise Contours Around Civil Airports. ECAC/CEAC Doc 29, 2nd ed., 1997.

44. Boeker, E.R.; Dinges, E.; He, B.; Fleming, G.; Roof, C.J.; Gerbi, P.J.; Rapoza A.S.; and Hemann, J.: Integrated Noise Model (INM) Version 7.10 Technical Manual. Report No. FAA-AEE-08-01, Washington, DC, Federal Aviation Administration, January 2008.
45. Noise Standards: Aircraft Type and Airworthiness Certification. 14 CFR Part 36, 2010.
46. International Civil Aviation Organization: Catalogue of ICAO Publications 2009–2010. Group 136, Annex 16, Vol. I—Aircraft Noise, 2008.
47. Federal Aviation Administration: Noise Standards: Aircraft Type and Airworthiness Certification. AC 36-4C, July 15, 2003.
48. Coleman, Hugh W.; and Steele, W. Glenn: Experimentation and Uncertainty Analysis for Engineers. John Wiley & Sons, New York, NY, 1999.

Chapter 3—Engine System and Core Noise

Lennart S. Hultgren, Jeffrey Hilton Miles, and Philip C.E. Jorgenson
National Aeronautics and Space Administration
Glenn Research Center
Cleveland, Ohio 44135

Summary and Recommendations

Noise generated in the turbofan engine core, by sources such as the compressor, combustor, and turbine, can make a significant contribution to the overall noise signature at low-power conditions, typical of approach flight. At high engine power during takeoff, jet and fan noise have traditionally dominated over core noise. However, current design trends and expected technological advances in engine-cycle design as well as noise-reduction methods are likely to reduce noncore noise even at engine-power points higher than approach. The result of such changes will be to elevate the importance of turbomachinery core noise. Also, future airport regulations may force further noise reduction at the approach flight conditions, thus emphasizing the need for reductions in core noise.

A brief historical perspective and description of the development of the current state of the art in semi-empirical combustion noise prediction methods are given. The open issue of the relative importance of direct and indirect combustion noise is discussed. Noise-source separation techniques, which are essential in extracting the subdominant combustion noise from the total noise signatures obtained in static-engine tests, are described.

The ability of the Aircraft Noise Prediction Program (ANOPP) to predict static-engine test data is assessed with a comparison to results from such a test. The sensitivity of the predictions to uncertainties in the engine operational parameters is determined, and the effects of calibration and/or instrumentation uncertainty on the test data are estimated. There are cases where the predicted values differ from the test data by as much as 10 dB at certain frequencies. Clearly, there is room for improvement in those cases. However, considering the semi-empirical nature of the ANOPP algorithms and their inherent limitations in capturing all the physics of the noise sources, the ANOPP predictions do surprisingly well in many situations. Furthermore, when the prediction captures the dominant feature of the sound-pressure-level spectrum, the corresponding integrated measure—the overall sound pressure level—agrees with the test results within the margin of uncertainty.

Better prediction methods and models need to be developed for turbine noise—a near-term issue already of importance for today's turbofan engines. To enable future “quiet” engines, further progress must also be made in the understanding and modeling of combustion noise and its turbine transmission and interaction. The key is a robust, long-term research program comprising high-fidelity computer simulation, careful experimental measurements in real engines (including refinement of source-separation techniques) for both validation and determination of required information, and concurrent development of reduced-order models for practical noise prediction methods. The numerical work needs to employ realistic geometries and multistage turbine simulations to better understand turbine self-generated noise and transmission and conversion effects on combustion noise. Similar integrated combustor-turbine simulations are needed to separate the direct and indirect source mechanisms for combustion noise.

3.1 Introduction

Gas turbine engines for commercial subsonic aircraft have undergone many changes in their operating cycle since their first introduction in the early 1950s. The early engines were of the turbojet type, but within a decade the design had changed to the turbofan type, which provided lower fuel consumption and reduced noise and emissions. The first-generation turbofan engines had bypass ratios near unity, where the bypass ratio is defined as the ratio of the mass-flow rates in the bypass and core streams. At takeoff, the perceived jet and fan noise components were typically about 15 and 8 dB greater, respectively, than the perceived core noise; and, at approach, the perceived fan noise commonly was about 10 dB greater than the (about equal) jet and core noise components (Ref. 1). The term “core noise” covers all noise generated in the engine core: compressor, combustion, and turbine noise. The first change in the turbofan-engine design was the introduction of acoustic liners (Ref. 2). This typically reduced

the perceived fan noise at approach to a level below the jet and core noise components (Ref. 1). The next major change was the shift toward high-bypass-ratio engines, which took place during the 1970s. This change allowed as much thrust as previous engines by increasing the diameter of the jet while it reduced the jet exit velocity and as a consequence reduced the jet noise. This evolution led to the modern turbofan engine, which typically has a bypass ratio in the range of 5 to 8. For current engines, the perceived jet and fan noise are essentially on par at takeoff, and the core-noise level is about 10 to 20 dB lower (Ref. 3).

Because of the national interest in fast and efficient air transportation with minimal community impact, NASA has made large investments in noise research and noise-reduction technology. Fan noise has been studied since the mid 1960s, with its foundation based on earlier National Advisory Committee for Aeronautics (NACA) propeller- and helicopter-blade noise work. Jet noise has been investigated since the early 1950s. The reduction of fan and jet noise remains a

major NASA research objective. Steady progress was made with higher bypass ratio engines, better fan and nozzle designs, and fan-noise acoustic-treatment technologies.

Core noise was vigorously investigated starting in the early 1970s until the late 1980s, when it was concluded that its further study would have little additional impact on total engine noise and research was discontinued. However by the year 2000, it became clear that with further technology improvements, it is possible to build a much quieter turbofan engine in about a decade with fan noise, jet noise, and core noise of equal importance. Core noise would then provide a noise floor impacting any further advances in fan and jet noise reduction. It was also realized that core noise was an important contributor to airport ramp noise due to auxiliary power units (APUs). At that point, the NASA research effort to look at the core noise problem was restarted at a modest level.

In the collection by Hubbard (Ref. 4), Groeneweg et al. (Ref. 3), and Mahan and Karchmer (Ref. 5) summarize the status and understanding of turbomachinery contributions to flight vehicle noise at the beginning of the 1990s. Whereas jet and fan noise research and understanding have progressed, the state of the art in core-noise prediction has not been equally advanced. Of the core-noise components, compressor noise has received the least amount of recent modeling effort, partially because of the fact it has not been identified as a significant contributor to engine-system noise to date for high-bypass-ratio turbofan engines. For this reason, compressor-noise modeling is not emphasized here.

Low-frequency core noise up to about 1 kHz, particularly in aft quadrants, is generally attributed to combustion noise. Self-generated turbine (broadband and discrete-tone) noise normally falls in the frequency range of several kilohertz and above. High-frequency tones over 10 kHz are usually also attributed to the turbine. The discrete tones are caused by rotor wakes interacting with downstream stators and by stator potential fields interacting with upstream and downstream rotors (and stages). Turbine broadband noise is caused by rotor-stator lift fluctuations due to flow turbulence. There is also a significant broadband component in the far field associated with scattering of the discrete turbine tones by the jet shear layer(s). This so-called hay-stacking effect often dominates the broadband noise directly generated within the turbine.

Combustion noise is either of the direct or indirect type. The unsteady combustion process is the source of pressure, entropy, and vorticity fluctuations. Only the first two are commonly considered to be potential sources of far-field combustion noise. The frequency scale of these fluctuations is set by the unsteady combustion process and falls in the range of 400 to 500 Hz. A fraction of the pressure disturbances are acoustic pressure fluctuations with the balance being hydrodynamic unsteadiness. The former is referred to as “direct combustion noise.” Its spectrum is modified by the combustor geometry as well as pressure feedback on the unsteady combustion process itself. The direct combustion noise is reduced because of transmission effects during its propagation through the turbine stages. The entropy (temperature)

fluctuations are convected downstream with the local mean velocity and get converted to acoustic pressure fluctuations in the turbine and other regions of rapid flow change. This is the indirect process of turbomachinery combustion noise generation. This is potentially a very effective mechanism and occurs at all turbine stages. The indirect combustion noise occurs in the same basic frequency range as the direct, but their spectral shapes could be quite different. The relative importance of direct and indirect combustion noise is still an unresolved issue. Any quasi-steady temperature streak ingested by the turbine would have an effect similar to a fan or compressor inlet disturbance and would generate noise in the blade-passing frequency range. This possibility should be classified as a turbine self-generated noise mechanism.

In this chapter, a brief historical perspective is given, which includes a discussion of noise-source separation techniques for application to engine test-stand data, and an assessment of a current prediction method applied to a static-engine test is presented. A list of the acronyms and symbols used in this chapter is given in Appendix A to aid the reader.

3.2 Core-Noise Research

The reduction of aircraft noise has long been an important technological challenge to the commercial air transport industry. The relative importance of different propulsion noise sources has changed with the evolution of the civilian-engine design. This has been reflected in the research efforts by industry, academia, and government institutions.

3.2.1 Compressor Noise

In addition to jet noise, inlet compressor noise was found to be a significant issue at approach for the first-generation jet aircraft powered by turbojet engines. The discrete-frequency compressor whine was discovered to be more annoying to airport neighbors than the broadband exhaust noise at landing (Ref. 6). The inlet tonal noise was mainly generated by the first two stages of the axial-flow compressors used in the turbojet engines (Ref. 7). Compressor noise was actively investigated during the transition from turbojet engines to turbofan engines. (Refs. 6 to 11). The bypass ratio of the early turbofan engines was initially low, and the inlet noise issue for these engines was sometimes referred to as fan-compressor noise (Ref. 11). However, as high-bypass-ratio turbofan engines were later introduced, fan noise and not compressor noise became the dominant feature of inlet noise.

The theory developed for compressor noise based on rotor-stator interaction due to wakes, vortices, and turbulence also applies to fan and turbine noise. In the collection by Hubbard (Ref. 4), the chapter on turbomachinery noise (Ref. 3) describes the understanding in the early 1990s of compressor noise, as well as turbine and fan noise. Agarwal et al. (Ref. 12) have recently studied the compressor contribution to inlet noise. They point out that in current practice inlet noise is normally separated into fan-tone and fan-broadband components. The fan tones, occurring at the fan blade-passing frequency (BPF) and

its harmonics, are easily detected since their peak amplitude is normally well above the broadband noise level. However, if a sufficiently fine narrowband spectral analysis is carried out, the other component is often found to also contain many discrete frequencies; that is, it is not a true broadband component. The scattering of just a few compressor tones by upstream rotating blade rows, including the fan rotor, can lead to a large number of inlet tones originating from the compressor. Consequently, a significant portion of the inlet noise that is customarily identified as fan broadband noise then actually originates in the compressor. They also argue that higher fan-BPF harmonics may be dominated by contributions originating from the fan rotor wake interacting with the compressor stator rather than the interaction between the fan rotor wake and fan outlet guide vane.

It is clear that for further progress to be made in the modeling of compressor noise, the fan and compressor must be considered in an integrated fashion.

3.2.2 Combustion Noise

Major advances in combustion noise source modeling occurred during the 1970s and early 1980s and are discussed in the review chapter by Mahan and Karchmer (Ref. 5) and references therein. The approaches taken can broadly be divided into fundamental and applied research. Fundamental research activities attempt to develop first-principle theories by first considering simple situations and geometries and then successively increasing the level of complexity. Data is drawn from laboratory experiments and isolated component tests. This work has been carried out by both academic researchers and engine company investigators. Applied-research activities, in general, attempt to develop semi-empirical relations that correlate noise levels with engine operating parameters based on full-engine test data and has mainly been performed by aircraft engine companies, often with support from the Department of Transportation (DOT) Federal Aviation Administration (FAA) or NASA. Significant development of diagnostic techniques also took place during this time period.

3.2.2.1 Fundamental Research

One common fundamental-research approach (see the comprehensive review article by Strahle (Ref. 13)) is to make the simplifying assumption that combustor noise is closely related to that of an open flame. This successful avenue of research starts by developing theories and models for open-flame noise (Refs. 14 to 17) and validating those by correlating observations with variations in physical parameters. It then proceeds to more complex situations by addressing the effects of ducting on flame noise (Ref. 13) followed by combustor-rig experiments (Refs. 13, 18, and 19). There are some drawbacks to this approach: First, the combustion occurs at, or nearly at, open-air conditions and not at the pressure levels typical in engines. Second, the rigs generally exhaust directly to the atmosphere and, consequently, only information relevant to direct combustion noise is obtained. The conversion of entropy fluctuations to

noise, caused by the unsteady combustion process, requires a significant mean axial pressure gradient to be effective (Refs. 13, 20, and 21). Third, attenuation effects occurring in the turbine of an actual engine installation are not included. Despite such limitations, it is generally accepted that this approach captures the main characteristic of the direct turbomachinery combustion noise; namely, a relatively universal (Ref. 22) low-frequency (up to about 1 kHz) single-peak broadband spectrum, closely related to that of an open turbulent flame, modulated by geometry-dependent acoustic resonances (Refs. 19 and 23) and transmission effects.

In an experimental and theoretical investigation, Muthukrishnan et al., (Ref. 18) added either a convergent nozzle or an orifice plate to a combustor can used in a previous experiment (Ref. 24) and found that indirect combustion noise became the prime component as the exit Mach number (≤ 1) was increased. This result suggested that indirect combustion noise is an important, if not the dominant, contribution to low-frequency jet-engine core noise since typically the turbine (inlet) nozzle guide vanes operate at a choked, or nearly so, condition. However, as the authors pointed out, this result may depend somewhat on the fact that in the experiment the combustion took place at a fraction (10 to 20 percent) of the pressure in a real engine and the temperature fluctuations (12 percent) may have been up to six times as large as those in an actual engine situation. In addition, (Ref. 13) the nozzle exhausted into open space and not into a duct-like situation as would have been the case in an engine experiment.

Cumpsty and Marble (Refs. 25 and 26), showed good agreement between actual engine measurements and indirect-combustion-noise predictions based on a model for entropy fluctuations interacting with turbine blade rows. Cumpsty (Ref. 27), considered the interaction between a combustor and turbine and concluded that the indirect combustion noise dominates the direct.

3.2.2.2 Applied Research

Semi-empirical models for the total acoustic power are developed based on physical considerations, with model coefficients determined using isolated-component and static-engine test data. Then the far-field directivity and universal spectral distribution are obtained empirically. In the case of full-engine tests, the measured total far-field acoustic signature normally is adjusted by subtracting the low-frequency jet noise using an appropriate model to reveal the core noise. This represents a weakness since combustion noise is not always a dominant noise source at low engine-power settings.

Huff et al. (Ref. 28) reviewed the early 1970s state of the art in engine combustion-noise prediction and recommended an interim semi-empirical method to provide such a capability for the NASA Aircraft Noise Prediction Program (ANOPP) (Refs. 29 and 30). The proposed direct-combustion-noise method combined a formula developed by General Electric (Ref. 31) for the total acoustic power as a function of the engine operating condition, a Boeing (Ref. 32) obtained result for polar

directivity, and a single-peak spectral distribution based on the Society of Automotive Engineers SAE ARP876 in-flight jet-noise spectrum (Ref. 33). As recommended in the Boeing (Ref. 32) work, Huff et al. (Ref. 28) suggested using a fixed peak frequency of 400 Hz. Emmerling et al. (Ref. 34) improved the General Electric model by correlating the combustion-noise attenuation by the turbine with the design-point work extraction of the turbine and validated the resulting model using several sets of engine data. Ho and Doyle (Ref. 35) provided further validation and discussion of this model (see also Mahan and Karchmer (Ref. 5)). This simple direct combustion-noise model (Refs. 34 and 35) still forms the kernel of the ANOPP core-noise module and is referred to therein as the “SAE method.” The current ANOPP module also contains a small-engine revision (Ref. 36) of this method and a narrowband method (Ref. 23) to account for tail-pipe resonances.

Also during the latter half of the 1970s, researchers at Pratt & Whitney (Refs. 37 and 38) developed a semi-empirical prediction method for direct combustion noise. They derived models for the total acoustic power level, turbine coupling and transmission losses, and peak frequency; and they empirically determined model constants, the directivity pattern, and a universal normalized spectral distribution using a range of burner-rig and full-scale static-engine tests. Mathews et al. (Ref. 37) also measured the dynamic temperature characteristics at the exit as well as inside of a burner in a rig experiment to provide inputs for an existing Pratt & Whitney indirect combustion noise model (Ref. 39). They found experimentally that the unsteady temperature level depended mainly on the total temperature increase across the burner (roughly 9 percent at the exit) and that the corresponding length scales were approximately proportional to a burner flow-rate parameter. Based on these measurements and the prediction codes, they found that indirect combustion noise should be 18 to 22 dB lower than direct noise in the absence of turbine attenuation.

There are similarities and differences between the General Electric and Pratt & Whitney direct combustion-noise results (see also discussion in Mahan and Karchmer (Ref. 5)). In both, the total acoustic power level is proportional to the second power of the combustor pressure, the second power of the temperature rise across the combustor (the Pratt & Whitney model uses the air:fuel ratio which essentially is equivalent), and the inverse power of the combustor inlet temperature. The combustor mass-flow rate linearly affects the total acoustic power in the General Electric model, whereas in the Pratt & Whitney formula it enters through a burner flow parameter to the fourth power. The Pratt & Whitney result also depends on burner-geometry information such as the number of fuel nozzles and the burner cross-sectional area. Their formulas for turbine losses are different, but both are frequency independent. The latter fact implies that, in the absence of resonances, measured spectra for burner-rig and full-engine static tests should be quite similar. Furthermore, their directivity patterns are in good agreement, and their single-peak universal spectral distributions are similar when frequencies are normalized with the peak

frequency. The peak frequency in the General Electric model is always 400 Hz, but the corresponding Pratt & Whitney formula involves burner design and geometry parameters. In general, each of these prediction tools has shown good agreement with data from the engine manufacturer that developed the method, but not with data from other companies. The need for distinct models may be caused by differences in burner design philosophy (Ref. 40). Zuckerman (Ref. 40) summarized the history and results of the DOT/FAA sponsorship of core-noise research and provided further comments. The report also pointed out the need for continued improvements in turbine-attenuation and indirect combustion-noise source modeling.

3.2.2.3 Diagnostic Techniques

The direct measurement of turbofan-engine combustion noise is difficult because of the presence of jet noise in the frequency range of interest. Since in-flight effects reduce jet noise more than combustion noise, combustion noise can be a significant contributor to aircraft approach noise but be masked by jet noise under the corresponding static-engine test condition. To overcome this obstacle, researchers developed coherence techniques utilizing engine-internal as well as far-field measurements to identify the far-field combustion noise component. Modal analyses were also carried out to determine the source and propagation characteristics of combustion noise. As part of these efforts, NASA contracted with turbofan engine companies such as Avco Lycoming (Honeywell), General Electric Company, Pratt & Whitney, and AiResearch (Honeywell) between 1974 and 1980 to evaluate core noise.

3.2.2.3.1 Coherence Techniques

Figure 3.1 illustrates a typical three-sensor arrangement for a measurement utilizing correlation and coherence techniques to determine the combustion-noise component of the far-field noise signature. Measurement station C is located inside the combustor; station T, if present, is typically located in the core tail pipe; and station F is located in the far field. The signals $u(t)$, $v(t)$, and $w(t)$ represent the combustion-noise signals at the three stations as functions of time t . These desired signals cannot be directly obtained by themselves because of the presence of the additional-noise signals $m(t)$, $n(t)$, and $o(t)$ at the different stations. However, the downstream signals $v(t)$ and $w(t)$ are uniquely determined by the impulse-response functions h_{uv} and h_{vw} and the previous-station signals $u(t)$ and $v(t)$, respectively. The measurable signal $x(t)$, $y(t)$, or $z(t)$ at each station is the sum of the desired and corresponding additional-noise signals. The signals $m(t)$, $n(t)$, and $o(t)$ can be taken as mutually uncorrelated as well as uncorrelated with the combustion-noise signal $u(t)$, $v(t)$, or $w(t)$ at all the stations. The signal $m(t)$ is to a large extent caused by hydrodynamic pressure fluctuations (pseudo-sound) in the combustor and possibly also higher acoustic modes present in the combustor but cut off in the downstream tail pipe and can potentially be

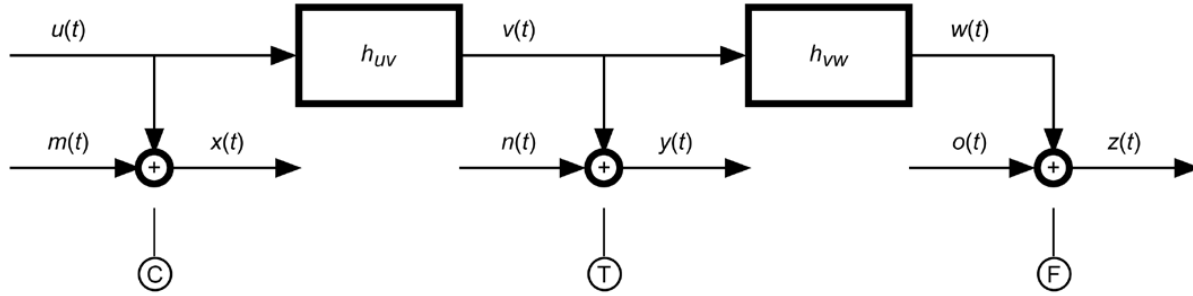


Figure 3.1.—Coherence technique to determine combustion-noise component of far-field noise. Measurement stations C, T, and F are located in the engine combustor, core tail pipe, and far field, respectively. Signals $x(t)$, $y(t)$, and $z(t)$ are directly measurable, are functions of time t , and are the sum of coherent combustion-noise signals $u(t)$, $v(t)$, and $w(t)$ and uncorrelated signals $m(t)$, $n(t)$, and $o(t)$ resulting from other noise sources; h_{uv} and h_{vw} are impulse-response functions.

quite large. The signals $n(t)$ and $o(t)$ are mainly due to acoustic pressure fluctuations from other noise sources, and particularly $o(t)$ can be dominant in the frequency range of interest because of the presence of jet noise. The goal is to determine the one-sided auto-spectrum $G_{ww}(f)$, with f denoting frequency, the combustion-noise component of the total far-field noise signature $G_{zz}(f)$. The diagnostic technique is commonly referred to as the “coherent-output-power method” when only one sensor inside the engine is utilized in combination with the far-field microphone and as the three-signal technique otherwise.

3.2.2.3.1.1 Coherent-Output-Power Method

Bendat and Piersol (Ref. 41) describe the basic formulation for the coherent-output-power method. If the sensor inside the combustor and one in the far field (Figure 3.1) are used in this technique, it follows that the coherent output spectrum is given by

$$\begin{aligned}
 G_{ww}(f) &= \frac{|G_{uw}(f)|^2}{G_{uu}(f)} \\
 &= \frac{|G_{xz}(f)|^2}{G_{uu}(f)} \\
 &= \frac{|G_{xz}(f)|^2}{G_{xx}(f) - G_{mm}(f)} \approx \frac{|G_{xz}(f)|^2}{G_{xx}(f)} \\
 &= \gamma_{xz}^2(f) G_{zz}(f)
 \end{aligned} \tag{3.1}$$

regardless of the output noise $G_{oo}(f)$. Note $G_{\alpha\alpha}$, $G_{\alpha\beta}$, and $\gamma_{\alpha\beta} = |G_{\alpha\beta}| / \sqrt{G_{\alpha\alpha} G_{\beta\beta}}$ denote the one-sided auto-spectrum, cross-spectrum, and coherence of the signals α and β , where α and β are dummy indexes. Note that the measured G_{xx} is a positive-biased estimate for the unknown input spectrum G_{uu} and, consequently, the second-to-last step in Equation (3.1) is only a valid approximation when the unknown G_{mm} can be assumed to be small compared to G_{xx} . In view of the certain presence of nonpropagating pressure fluctuations in the combustor, i.e., $G_{mm} \neq 0$, Equation (3.1) is quite likely to underpredict

the actual coherent output spectrum. Furthermore, the spectra are estimated using a finite observation time, and consequently, the signal $z(t)$ needs to be time shifted to account for the time delay of the disturbances in the computation of the cross-spectrum G_{xz} in order to yield a meaningful result.

Karchmer and colleagues (Refs. 42 to 45) showed successful application of coherence techniques to measurements obtained using a static Avco Lycoming YF-102 turbofan engine instrumented with internal as well as far-field microphones. A typical result showed the combustion coherent output power in the 120° direction (aft quadrant) to roughly have a dome-shaped spectral distribution in the range 0 to 200 Hz with the peak at about 125 Hz. At 43 percent engine speed, the peak was about 6 dB lower than the peak of the total far-field spectrum located at 120 Hz. The dome edges were about 20 dB lower at 40 and 200 Hz. Similar coherence-function results also were obtained from static tests of Pratt & Whitney JT15D (Ref. 46) and General Electric CF6-50 (Ref. 47) engines.

3.2.2.3.1.2 Three-Signal Coherence Method

Chung (Ref. 48) developed a three-signal coherence technique for microphone flow-noise rejection. Figure 3.2 shows the general block diagram for this method, where $s(t)$ is the source signal and, as before, $u(t)$, $v(t)$, and $w(t)$ are the coherent signals, $m(t)$, $n(t)$, and $o(t)$ represent mutually uncorrelated noise, and $x(t)$, $y(t)$, and $z(t)$ are the measurable signals. The coherent auto-spectra at the three measuring locations in Figure 3.2 are given by

$$G_{uu}(f) = \frac{|G_{xy}(f)| |G_{xz}(f)|}{|G_{yz}(f)|} \tag{3.2a}$$

$$G_{vv}(f) = \frac{|G_{xy}(f)| |G_{yz}(f)|}{|G_{xz}(f)|} \tag{3.2b}$$

$$G_{ww}(f) = \frac{|G_{xz}(f)| |G_{yz}(f)|}{|G_{xy}(f)|} \tag{3.2c}$$

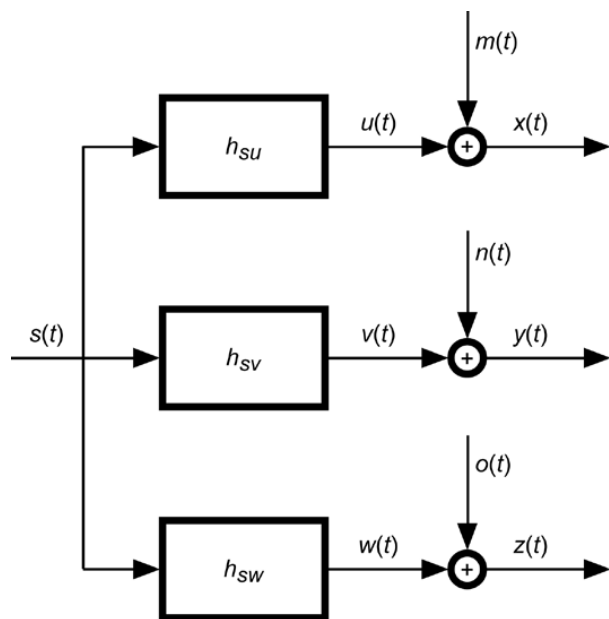


Figure 3.2.—Three-signal coherence technique for noise rejection, where $s(t)$ is the source signal as function of time t and h_{su} , h_{sv} , and h_{sw} are impulse-response functions. Coherent signals $u(t)$, $v(t)$, and $w(t)$ of interest are not directly measurable; their addition to mutually uncorrelated signals $m(t)$, $n(t)$, and $o(t)$ from other sources results in measurable signals $x(t)$, $y(t)$, and $z(t)$.

However, the three-signal method also applies to the situation shown in Figure 3.1, where the measuring stations and the signals $x(t)$, $y(t)$, and $z(t)$ are “sequential” rather than “parallel-output” measurements as in Figure 3.2. Krejsa (Ref. 49) independently considered the situation depicted in Figure 3.1 and obtained Equation (3.2c) as his far-field result. The three-signal coherence technique as applied by Krejsa (Refs. 49 to 51) eliminates the bias error in the coherent combustion-noise measurements due to nonpropagating pressure fluctuations within the engine.

The strength of the three-signal method is that it involves only measured cross-spectra. The measured cross-spectra are affected by extraneous noise only if this noise correlates between measurement locations. This can often be avoided by an appropriate spatial separation of the sensors involved; the three-signal method then provides unbiased estimates of the coherent auto-spectra. In contrast, measured auto-spectra will always include a positive definite contribution from the extraneous noise.

Krejsa compared results obtained using the earlier coherent-output-power method with those using the new three-signal method for YF-102 (Refs. 49 to 51), JT15D (Ref. 50), and CF6-50 (Ref. 50) static-engine tests (Refs. 45 to 47). He found that the older method consistently underpredicted the combustion noise spectra by several dB at low engine speeds and of the order of 10 dB at a high engine speed. Krejsa (Ref. 51) also discussed two other techniques (Refs. 52 and

53) for isolating the combustion noise using only far-field measurements, one of which introduced a model for the jet noise (Ref. 53). The three-signal coherence technique also was used by Shivashankara (Ref. 54) to study core noise in a Pratt & Whitney JT9D engine.

The three-signal coherence data for the YF-102, JT15D, and CF6-50 static-engine tests were further examined and correlated by von Glahn and Krejsa (Ref. 55). The suggested correlations utilized one, two, and four spectral segments to capture perceived peaks in the far-field core-noise spectra. Generally, the sound pressure levels at the single-segment spectrum peak, the higher frequency two-segment spectrum peak, and the two higher frequency four-segment spectrum peaks scaled with a heat-release parameter, as in the semi-empirical models described in Section 3.2.2.2, whereas the low-frequency segments scaled with the combustor exit velocity to the fourth power. They stated that the four-segment spectra provided the best overall fit to the data, but also that the two-segment spectrum appeared to be a reasonable representation of the combustion noise. However, the data comparisons do not generally show the expected 3-dB increase at the intersection of the multisegment spectra, which renders their conclusions less clear. Nevertheless, their results show that the assumption of a single-peaked far-field combustion-noise spectrum with the peak fixed at 400 Hz, as used in ANOPP, can be questioned.

It is also possible to separate core noise from jet noise using three far-field microphones since each would pick up correlated core noise and uncorrelated external noise from the jet (Refs. 54 and 56). As long as the spatial (polar angle) separation of the microphones is large enough, the jet noise at each location would be mutually uncorrelated and Equation (3.2) would apply. Mendoza et al. (Ref. 56) analyzed data from a Honeywell TECH977 static-engine test (Ref. 57) using a three-signal far-field method, among other multiple-microphone signal-processing techniques (Ref. 58). They found that the three-signal method works well in frequency regions where a single engine-internal noise source is dominant. The method did not work well for frequencies where multiple self-correlated noise sources are of comparable magnitude; for example, in the relatively limited range where combustion noise and turbine broadband noise overlap.

3.2.2.3.2 Modal and Other Analyses

In order to grasp the transmission of combustion noise to the engine-external flow region, the modal structure in the combustor and downstream passages as well as the turbine attenuation must be understood. Detailed diagnostic and analytical research efforts in these areas were carried out during the late 1970s and early 1980s.

An acoustic modal analysis was used to interpret experimental results from a full-scale (YF-102) annular combustor-rig test by Karchmer (Ref. 59) and by Krejsa and Karchmer (Ref. 60) for the tailpipe unsteady pressure field of an AiResearch QCGAT turbojet engine. The method assumed randomly occurring equal-amplitude clockwise and

counter-clockwise propagating pressure fluctuations and statistical independence between the (μ, ν) modes, where μ and ν denote the azimuthal and radial mode numbers, respectively. An optimized least-square fit of the measured cross-spectra was then used to determine the modal amplitudes. For the frequencies (≤ 1500 Hz) of interest for combustion noise, only modes with $\nu = 0$ and $0 \leq \mu \leq 4$ needed to be included in the analysis. They found that individual modes can be uniquely identified within separate frequency bands. The plane-wave (0,0) mode dominated for the lowest frequencies up to the cut-on frequency of the (1,0) mode. For higher frequencies, the most recently cut-on mode dominated the unsteady pressure field; that is, successively higher azimuthal modes dominated with increasing frequency. Karchmer (Ref. 59) concluded that the basic source generating mechanism itself has a relatively smooth spectral shape, but the geometry of the combustor is extremely effective in promoting modes that are resonant in the combustor. Krejsa and Karchmer (Ref. 60) found that the (0,0) mode was dominant up to about 800 Hz at the tail-pipe exit.

Miles and Krejsa (Ref. 61) compared an analytical model for pressure propagation and convected-entropy conversion (with assumed input entropy) with core-nozzle data obtained for a JT15D turbofan engine. The model was found to be adequate for a low nozzle-exit Mach number of about 0.2, with the effect of the convected entropy being negligible. They found that a more accurate exit-impedance model and a better description of the incoming entropy would be needed at higher nozzle exit velocities and frequencies lower than about 120 Hz. Miles et al. (Ref. 62) measured the pressure-temperature cross-spectra in a constant-area duct downstream of a General Electric J47 can combustor. Their results suggested that the pressure and temperature fluctuations correlate at the combustion source point for low frequencies and that the phase angles of the pressure and temperature are related by the convected-flow time delay. This result agrees with the earlier observation of Muthukrishnan et al. (Ref. 18) that at low frequencies indirect noise related to entropy and direct combustion noise are coherent (but become uncorrelated at moderate frequencies). Miles and Krejsa (Ref. 63) developed a one-dimensional model to calculate the relevant spectra in a ducted combustion system and compared predictions with experimental results (Ref. 62). Huff (Ref. 64) derived a simplified one-dimensional combustion-noise theory for a disk source in an infinite duct and predicted the pressure spectrum inside a CF6-50 engine (Ref. 47).

Matta and Mani (Ref. 65) developed a multistage actuator disk for low-frequency noise transmission through turbines. They found that the interaction effects of adjacent blade rows must be considered; that is, simply summing up attenuation from each blade row in isolation would have overpredicted the attenuation. A more complex finite-chord analysis also revealed that the actuator-disk theory remained valid for frequencies as high as about half the blade-passing frequency. Hence, the multistage actuator-disk theory is an adequate tool to predict direct combustion-noise attenuation by the turbine.

3.2.2.4 Low-Emission Combustors

Low-emission dual-annular combustors (DAC) under initial development in the 1990s produced significantly more noise (10 to 15 dB) than older production combustors at low-power operation, but with virtually no noise difference observed at full power (Ref. 66). Dual-annular combustors produce larger circumferential and radial variations of the total temperature in the combustor at partial-power conditions due to its firing pattern. Gliebe et al. (Ref. 66) argued that these spatially inhomogeneous, but steady, temperature distortions are effective sources for entropy fluctuations, which in turn induce pressure fluctuations (indirect noise) as they pass through the turbine and thus lead to the increased noise level. Mani (Ref. 67), on the other hand, expressed the opinion that the entropy waves are directly generated by the unsteady heat release and not as a consequence of the spatially inhomogeneous steady heat release. Nevertheless, the central point of both arguments is that the indirect-noise mechanism is responsible for the observed increase in noise.

Gliebe et al. (Ref. 66) described an actuator-disk theory for the conversion of entropy fluctuations to sound by the turbine. The analysis starts at the combustor exit and requires knowledge of the rms level and axial and circumferential integral length scales of the temperature fluctuations at that location and mean-line flow information in the turbine. An accompanying computational fluid dynamics combustor simulation provided the rms temperature level but not the length scales, which had to be estimated based on other considerations. Mani (Ref. 67) provided a linearized two-dimensional analysis of the combustor, which accounted for compressor and turbine boundary conditions and modeled the combustion zone as a flame sheet.

Gliebe et al. (Ref. 66) also developed empirical combustion-noise correlations based on earlier obtained static-test data for a selection of modern high-bypass-ratio engines. The data used was from General Electric CF6-80C2 and CFM International CFM56-5B/7B engines equipped with standard single-annular combustors (SAC) and General Electric GE90 and CFM56-5B/7B engines equipped with low-emission combustors. They adopted the multilobed spectrum ideas of von Glahn and Krejsa (Ref. 55) and found that the best fits were obtained by using a three-segment spectrum (peaks at 63, 160, and 630 Hz) for SAC engines and two spectral segments (peaks at 160 and 500 Hz) for DAC engines.

3.2.2.5 Combustion Instability

Unstable combustion is an abnormal condition that is absent from a properly designed engine. Even though it can produce considerable noise, it is not a contributor under normal operating conditions. Strahle (Ref. 13) points out that combustion noise and combustion instability are only weakly related. Combustion noise is a random noise field containing a range of frequencies, each with random amplitude and phase. While there may be acoustic feedback on the unsteady combustion process, it is not of sufficient strength to give rise to a global phase-locked

oscillation. In contrast, combustion instability is characterized by a phase-coherent, single-frequency feedback oscillation. Typically (Ref. 13), 10^{-6} to 10^{-5} of the thermal input is converted to acoustic power in a combustor, and at an instability this number rises to about 10^{-4} . The latter thermoacoustic oscillations can limit combustor life, performance, and operating conditions. Current reviews of combustion instability, or thermoacoustic oscillations in combustors, are given by Dowling and Stow (Ref. 68), Lieuwen (Ref. 69), and Keller (Ref. 70).

3.2.3 Turbine Noise

By the end of the 1960s, it was realized that the turbine contribution to the overall engine noise could no longer be ignored because of reductions in jet and fan noise (Refs. 71 and 72). Mathews et al. (Ref. 71) surveyed the early 1970s status of turbine-noise prediction and suggested research areas for further improvements in predictive capability. Krejsa and Valerino (Ref. 72) recommended an interim prediction method for turbine-noise prediction for the NASA ANOPP (Refs. 29 and 30). The ANOPP turbine-noise prediction procedures have been refined over the years, but their roots are still in the methods described in those two references (Refs. 71 and 72). Groeneweg et al. (Ref. 3) described the early 1990s understanding of turbine noise and methods for its reduction. The major turbine contributions to the far-field noise signature originate in the low-pressure turbine (LPT) and manifest as both discrete-tone and broadband noise. The tones result from the interaction between rotating and stationary blades as well as struts and occur at the BPF and its harmonics. These acoustic pressure fluctuations propagate away from the generating blade or vane row, along spinning helical paths. Turbine broadband noise is internally generated by blade lift fluctuations caused by flow turbulence as well as by scattering of the turbine tones into sideband noise (commonly referred to as “haystacks”) by the turbulence in the external exhaust shear layers. The haystacking effect represents a redistribution of some of the acoustic power from tonal to broadband noise. The overall turbine-noise acoustic power is preserved, however. The far-field turbine broadband noise spectrum is commonly dominated by this haystacking phenomenon. Up to the early 1990s, LPTs were made quieter by using acoustic treatments and so-called cutoff and modal design techniques that were coupled with corporate in-house design rules. The high solidity of the LPT stages of that era also meant that transmission losses for tones generated by early stages were significant, and commonly the second-to-last stage was the loudest.

While turbine noise is not the dominant noise source for the current generation of aircraft engines, it is quite often the most miss-predicted one, which can lead to difficulties in meeting noise guarantees for some aircraft configurations (Ref. 73). Modern engine designs, including the LPT, are different from those of the 1990s and earlier and have resulted in a greater impact of the LPT noise component on total engine noise levels. Technology advances and cycle improvements have resulted in significantly lower levels of fan and jet noise. Also,

the higher engine bypass ratios required for improved performance have resulted in larger engine diameters with lower rotational speeds, thus lowering the BPF and harmonic tone frequencies to more annoying bands where they lead to a higher effective perceived noise level, EPNL. Recent engine design and cycle changes are driven largely by cost, weight, performance, and maintainability. One result of this is a trend toward fewer LPT stages with reduced blade counts per stage. These lower airfoil counts lead to (1) higher blade loading, which produces stronger wakes and potentially increased tone intensities; (2) less stage solidity, which reduces attenuation of noise from earlier stages; and (3) a further reduction in the tone frequencies, to the point where the harmonics may now also fall into the more objectionable bands. Low cost and weight concerns have also led to a trend toward less spacing between stages as well as a decrease in the distance between the last-stage rotor and the exit struts. This decreases the decay (mixing) of wakes as well as increases the unsteady rotor-blade loading due to potential pressure fields caused by vanes and struts. In particular, the modes resulting from the interaction of the last-stage rotor and the exit struts will be stronger than for previous designs, and many of these modes are highly cut-on and are not subject to transmission losses that would occur through upstream stages (Ref. 74, personal communication).

Acoustic mode cutoff methodology, traditionally the first line of defense against tone noise, and the modal-design approach are now harder to implement because the newer LPT designs effectively increase the unsteady aerodynamic coupling of the turbine stages, which in turn introduces additional complexity in the tone generation mechanisms. Wake velocity defects are now more likely to propagate through one or more blade rows and create noise on several disks. With the trend of less attenuation per stage, the modification and/or scattering of the duct modes during their propagation through several static and rotating blade rows needs to be accounted for in the noise prediction. Furthermore, acoustic treatment is more of a challenge than it was previously. Exhaust temperatures at the design operating condition, as well as at the off-design noise generating conditions, have increased. Lightweight materials, suitable to be used for acoustic treatment and able to meet the temperature requirements, are not yet widely available.

3.2.4 Current Prediction Codes

The modular Aircraft Noise Prediction Program ANOPP was developed by NASA “to predict aircraft noise with the best currently available methods” (Ref. 75). An overview of ANOPP is presented in Chapter 2. In order to maintain and enhance the program, NASA has continued to contract with industry to evaluate ANOPP against flyover and real-engine data and to suggest improvements to its modules. These investments have over the years led to significant improvements in the capability of ANOPP.

Boeing (Ref. 76) in 1980 conducted a flyover test using a widebody 747-100 aircraft equipped with Pratt & Whitney JT9D engines. The data were acquired during level flight, using

12 ground-based microphones, with landing gear up and flaps set to minimize airframe noise, for corrected engine speeds in the 75.4 to 98.8 percent range. The tone-weighted perceived noise levels (PNLTs) were found to be consistently underpredicted in the aft direction by about 9 dB. The data also suggested a significant contribution in this quadrant from combustion noise in the 250 to 400 Hz range, with the peak occurring between 110° and 130°, for all power levels. Based on this observation, they concluded that the predictions would fit the test data better if in the combustion-noise module the peak frequency were shifted one 1/3-octave frequency band lower (from 400 to 315 Hz), and the power level were increased by about 3 dB. In addition, they stress that further development of accurate source separation techniques is an essential prerequisite for the potential improvement of component-prediction procedures.

In 1996, GE Aircraft Engines (Ref. 77) assessed ANOPP by a comparison with detailed static-engine measurements for a representative selection of high-bypass engines—CF6–80C2, E³, and QCSEE—as well as with GE in-house prediction methods. They found that the ANOPP and GE in-house predictions for combustion noise agree closely. This is not surprising since both methods are practically identical. Furthermore, they state that “it is difficult to assess the absolute accuracy of the predicted levels and peak frequency” and continue on to conclude that “the combustion noise predictions do not cause the total predicted engine noise to assume an unreasonable spectral shape or to exceed the level of total measured engine noise.”

A contract effort (Refs. 36, 78, and 79) in the mid-1990s with AlliedSignal (Honeywell) led to a substantial extension of ANOPP fan, jet, core, and turbine modules to small turbofan engines such as those typically used by smaller regional-transport and business aircraft. Acoustic measurements from static tests involving three AlliedSignal research engines were used in this effort.

Other computer codes for aircraft-noise prediction exist, but some may no longer be maintained. FOOTPR (Ref. 80) is a procedure for predicting flyover noise footprints for various engine installations and RADIUS (Ref. 80) is a tool for predicting the acoustic far-field signature of static-engine tests. These codes were created at the NASA Lewis (Glenn) Research Center as an aid during the early development stages of ANOPP, and they use common noise-source subroutines.

Another example is the HSRNOISE (Ref. 81) code, which is an outcome of noise studies by NASA and U.S. industry partners—Boeing, GE Aircraft Engines, and Pratt & Whitney—during the course of the High Speed Research (HSR) Program (1989 to 1999). The goal of this program was to advance technology for supersonic commercial transport aircraft. New models for fan and jet noise were developed for the HSR technology-concept engine (Ref. 82), a mixed-flow turbofan engine with rectangular mixer-ejector nozzles. Combustor, turbine, airframe, and other models were adopted from existing methods used either by NASA (ANOPP) or its partners. In particular, the combustion noise module is based on the method developed by Mathews and Rekos (Ref. 38).

In addition, all major engine and airframe companies have proprietary in-house noise-prediction codes with capabilities similar to those of ANOPP.

3.3 Engine Noise Prediction Using ANOPP

The NASA system tool ANOPP (Ref. 75) (Aircraft Noise Prediction Program) is a highly modular code for the engineering prediction of aircraft flyover noise as well as static-engine noise. The basic philosophy of ANOPP is to use semi-empirical prediction methods for the different engine noise sources. The methods are based on engine data with parameters based on physical understanding of dominating processes. Directivity and spectral distribution vary from component to component and with noise source mechanisms for each component, but are generally independent of engine operational conditions. The acoustic power is correlated to engine operational conditions. ANOPP also has modules for airframe noise that depend on the aircraft characteristics and flight conditions.

This section presents the application of ANOPP to predict engine test-stand acoustic data. Community noise caused by takeoff, landing, or flyover are not addressed. Level 25v3 of ANOPP is used (see also the software distribution for up-to-date documentation).

3.3.1 ANOPP Static-Engine-Test Simulation

Figure 3.3 illustrates a typical ANOPP model for a static-engine test. The first step involves defining the ambient conditions of pressure, temperature, relative humidity, density, and speed of sound using the atmospheric module (ATM). Sound attenuation by the atmosphere depends on frequency and these ambient conditions. Using these properties, the atmospheric absorption module (ABS) then constructs an absorption-coefficient table in terms of sound frequency and altitude, which is used in the propagation stage.

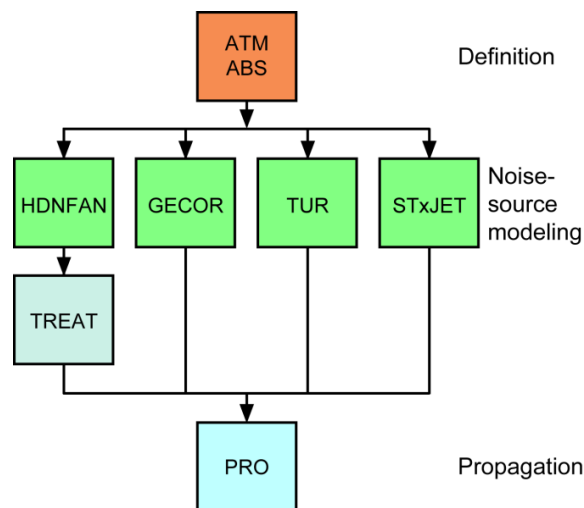


Figure 3.3.—ANOPP module flow chart for static-engine test.

The second step utilizes modules for the fan (HDNFAN), combustor (GECOR), turbine (TUR), jet (STNJET or ST2JET), and the effects of fan-noise treatment (TREAT) to predict the source noise. Each source module provides a table of the mean-square acoustic pressure in 1/3-octave frequency bands as functions of polar directivity angle and azimuthal directivity angle at a virtual observer distance. The models used in these source modules are all azimuthal-angle independent. The fan-noise-treatment module estimates the attenuation by acoustic treatment in the inlet and aft bypass duct and updates the prediction from the fan-noise module.

The third step involves propagating the noise from the source (virtual observer) location to the actual observer location. The propagation is assumed to be linear. The propagation module (PRO) sums the noise data that are generated by the noise-source modules and propagates them to the observer positions. For a static-engine test, this includes accounting for spherical spreading and characteristic impedance change, atmospheric attenuation, and ground reflection and attenuation. The first effects are a consequence of the preservation of total acoustic power in the absence of losses. The computation of the atmospheric attenuation uses the coefficient table produced by the atmospheric and atmospheric-attenuation modules in step one. In a typical static-engine test, the engine is mounted on a stand a certain distance above a hard-surface ground, and the acoustic-measurement microphones are ground mounted to minimize, if not fully remove, the ground-reflection effect.

A brief summary of the source modules used for the engine noise predictions is given here. See Chapter 2, “Aircraft System Noise Prediction” for more detail on the modules.

3.3.1.1 HDNFAN and TREAT

The HDNFAN module predicts both pure tones and broadband noise for the fan as functions of 1/3-octave frequency band and polar directivity angle using empirical relationships. The module has the option to use the original Heidmann method (Ref. 83) or extensions for small (Ref. 78) and large (Ref. 77) engines, respectively. The module accounts for six separate physical noise-generating mechanisms: inlet broadband noise, inlet rotor-stator interaction tones, inlet flow-distortion tones, combination tone noise, discharge broadband noise, and discharge rotor-stator interaction tones. In a typical static-test situation, the engine is fitted with an inflow control device to remove extraneous inflow disturbances unrepresentative of flight. Consequently, inlet flow-distortion tones were not included here. In addition to geometric and design parameters, the prediction requires as input parameters the fan rotational rate, mass flow rate, and total temperature rise across the fan. Chapter 5, “Fan Noise Prediction,” provides an assessment of the HDNFAN module as well as examples of input parameters (Table 5.8).

The TREAT module updates the fan-noise prediction by accounting for acoustic treatment. The module has the option to use methods developed by Magliozzi (Ref. 84) or Kontos et al. (Ref. 77). It requires geometry and design parameters and the operation-point inlet and aft duct mass flow rates.

3.3.1.2 GECOR

The GECOR combustion-noise module predicts broadband noise as a function of 1/3-octave frequency band and polar directivity angle with a choice of using three empirical methods. The choices are (1) the SAE method (Ref. 34), (2) a small-engine revision (Ref. 36), or (3) an intermediate narrow-band method (Ref. 23)² that includes tail-pipe modulation effects. The SAE and small-engine methods require as input parameters the combustor engine-state mass flow rate, inlet total pressure, and inlet and exit total temperatures, in addition to geometry and design parameters.

3.3.1.3 TUR

The turbine-noise module, TUR, predicts both broadband and tone noise as functions of 1/3-octave frequency band and polar directivity angle using empirical relationships (Ref. 72), with the option to use a small-engine extension (Ref. 36) of the method. In addition to geometry parameters, the module requires as input parameters the turbine shaft speed as well as exit total and static temperatures.

3.3.1.4 STNJET

The STNJET noise-source module predicts jet mixing noise and shock-associated noise for circular jets. The jets can be either single stream or coannular streams, with or without a center plug. The module has the option to use the original Stone (Refs. 85 and 86) empirical method or a small-engine extension (Ref. 36). In addition to geometry parameters, the module requires the nozzle exit flow conditions to be specified. For a subsonic single stream, with no center plug, these are the following parameters: jet total temperature and fully expanded jet density, velocity (acoustic Mach number), and Mach number.

3.3.2 Sensitivity

The influence of performance parameter uncertainties on the ANOPP total noise predictions is described here. The total mean-square pressure in a 1/3-octave frequency band b can be expressed as

$$\langle p^2 \rangle^{(b)} = \sum_{c,\ell} \langle p_{c,\ell}^2 \rangle^{(b)} \quad (3.3)$$

where the brackets represent ensemble averaging, $\langle p_{c,\ell}^2 \rangle^{(b)}$ is the contribution to the total from each source and the indices c and ℓ indicate engine component (i.e., turbine, jet, etc.) and component noise source (i.e., rotor-stator interaction tones, broadband noise, etc.), respectively. The total relative difference in the prediction caused by a parameter change can be written as a weighted sum of the relative change in the component sources:

²See ANOPP L25v3 documentation.

$$\frac{|\delta\langle P^2 \rangle^{(b)}|}{\langle P^2 \rangle^{(b)}} \leq \sum_{c,\ell} a_{c,\ell} \frac{|\delta\langle p_{c,\ell}^2 \rangle^{(b)}|}{\langle p_{c,\ell}^2 \rangle^{(b)}} \quad (3.4a)$$

$$a_{c,\ell} = \frac{\langle p_{c,\ell}^2 \rangle^{(b)}}{\langle P^2 \rangle^{(b)}} \quad (3.4b)$$

where the δ indicates a difference and $a_{c,\ell}$ is a measure of the relative contribution from an individual component source to the total mean-square pressure. Since it can be assumed that each relative difference is finite, it follows that the overall change is determined by the difference in the prediction for the dominating noise source for a given operational condition. Since the sound-pressure level (SPL) in an 1/3-octave frequency band is given by

$$SPL^{(b)} = 10 \log \left(\frac{\langle P^2 \rangle^{(b)}}{P_{\text{ref}}^2} \right) \quad (3.5)$$

it follows that the change in SPL is given by

$$\delta SPL^{(b)} = 10 \log \left(1 + \frac{\delta\langle P^2 \rangle^{(b)}}{\langle P^2 \rangle^{(b)}} \right) \quad (3.6)$$

Note that a 1-dB difference in the *SPL* corresponds to about a 26-percent change in the mean-square pressure.

For compactness of notation, let Φ denote either the mean-square pressure in a particular 1/3-octave frequency band or the mean-square pressure summed over all the bands;

that is, either $\Phi = \langle P^2 \rangle^{(b)}$ or $\Phi = \sum_b \langle P^2 \rangle^{(b)}$ along with $\xi = (\xi_1, \xi_2, \dots, \xi_k)$ denote the ANOPP parameter vector. The ANOPP parameters are of three types: The first type is the engine-performance parameters (fan shaft speed, mass flow rates, etc.) that change with the engine operation point. The second type is the engine-design parameters (geometry, design turbine temperature extraction, etc.), and they do not change with the engine operation point. The third type is the ANOPP model coefficients, and they do not change with the engine-operation point nor within a given engine class. In what follows, the engine-design and ANOPP-model parameters are assumed to be known without uncertainty. The change in Φ due to a small change in ξ is then given by $\delta\Phi = \sum_k \frac{\partial\Phi}{\partial\xi_k} \delta\xi_k$.

An upper bound on the change is given by

$$|\delta\Phi| \leq \frac{1}{2} \sum_k \left| \frac{\partial\Phi}{\partial\xi_k} \right| (\xi_k^+ - \xi_k^-) \approx \frac{1}{2} \sum_k |\Phi^{k+} - \Phi^{k-}| \quad (3.7)$$

$$\xi_k^\pm = \xi_k \pm |\delta\xi_k|$$

where $\Phi^{k\pm}$ denotes the value of Φ with only the k th parameter changed.

The sensitivity to uncertainty in the performance parameters for an ANOPP simulation is determined as follows: For a specific engine operation point, each performance parameter (see Table 3.1) is independently varied up and down by a small amount to determine the sensitivity to uncertainty in that parameter. Of course, parameters like the shaft speed in the fan and turbine modules are coupled; and mass flow rates in the fan, treatment, and combustor modules are also changed together in a proportional fashion. The absolute values of the

TABLE 3.1.—ANOPP NONDIMENSIONAL PERFORMANCE PARAMETERS

Module	Parameter	Meaning
HDNFAN	N	Fan shaft speed, Strouhal number
	MDOT	Fan mass flow rate
	DELTAT	Total temperature rise across fan
TREAT	MDOTIN	Same as HDNFAN MDOT
	MDOTAF	Mass flow rate in aft duct
GECOR	MDOT	Combustor mass flow rate
	PI	Combustor inlet total pressure
	TI	Combustor inlet total temperature
	TCJ	Combustor exit total temperature
TUR	ROTSP	Turbine shaft speed, Strouhal number
	TT	Turbine exit total temperature
	TSJ	Turbine exit static temperature
STNJET	T1	Jet total temperature
	RHO1	Fully expanded jet density
	V1	Fully expanded jet velocity, acoustic Mach number
	M1	Fully expanded jet Mach number

individual sensitivities are then added together to yield an upper bound on the prediction sensitivity to a relative uncertainty in the performance parameters. This is the procedure used below in the comparison of ANOPP predictions to engine test-stand data.

3.4 Comparison of ANOPP–L25 Predictions and NASA-Honeywell EVNERT Engine Test-Stand Data

The EVNERT (Engine Validation of Noise and Emission Reduction Technology) program (Ref. 57) was a NASA-funded test program carried out by Honeywell Aerospace (Phoenix, AZ) during the period December 2004 through August 2007. It was an ambitious program of engine validations of integrated technologies that address the reduction of engine and propulsion-airframe integration noise. As part of this program, an extensive set of acoustic far-field data was taken to characterize engine noise sources, to gain insight in their mechanisms, and to evaluate select noise-reduction concepts. The tests were carried out in the Honeywell Aerospace's San Tan outdoor engine test facility. The Honeywell TECH977 research engine, which is characteristic of small engines in the 6000- to 8000-lb thrust class, was used in these tests.

A combination of well-established industry-standard and leading-edge data acquisition, processing, reduction, and analysis techniques were used in the investigation. A wealth of information was generated that will serve noise researchers well for a considerable time and will have significant impact on the field. It is important to recognize, though, that even in a carefully executed engine-test-stand program, complete repeatability of the results cannot be expected. There is always the possibility of the temporary introduction of spurious noise sources caused by the many reconfigurations that take place during the course of a long investigation. Various degrees of agreement between predictions based on semi-empirical methods (which are based on engine-data correlations, presumably using results from many engines) and test results for a particular engine build, or between engine builds, are to be expected.

3.4.1 Comparison of Total 1/3-Octave Results

Constant-percentage-bandwidth, 1/3-octave, far-field noise data were obtained in the EVNERT program using ground-level microphones located along a circular arc from 5° to 160° with respect to the engine inlet direction, in 5° increments. The online data acquisition system also obtained narrowband data in parallel with the 1/3-octave data as well as sequentially (Ref 87, personal communication) obtained pressure-time history data at select locations. Only the 1/3-octave data will be used here, however.

A sequence of “standard” engine power settings, characterized by the corrected fan speed, was used for the many configurations investigated during the EVNERT program.

NASA was provided select engine operational parameters for the power settings for EVNERT configuration 31. The required nondimensional ANOPP performance parameters (see Table 3.1) were constructed from those. Even though, they were obtained for one particular configuration, the ANOPP nondimensional performance parameters are also representative of many of the other configurations.

Comparisons between ANOPP predictions and the EVNERT 1/3-octave data were made on an actual-day basis in the present work rather than on a standard-acoustic-day basis. This choice was based on the fact that NASA has access to the uncorrected actual-day EVNERT 1/3-octave data and converting the data would add further uncertainties to the experimental data. Consequently, the ambient (reference) conditions varied between cases (configurations and power settings) to reflect the actual conditions of the day. However, the same values of the nondimensional performance parameters were used in all cases for the ANOPP predictions carried out here.

Comparisons for configurations 25 and 31 are described in separate subsections below. Configuration 25 (October 2005) is a baseline case without any fan-noise acoustic treatment; that is, the fan flow path has all hard-wall conditions. Configuration 31 (March 2006) is identical except single-degree-of-freedom acoustic liners are installed in the inlet, aft-fan c-duct, and nozzle. Configurations 25 and 31 will now be referred to as the “hard-wall” and “treated” cases, respectively.

3.4.1.1 Hard-Wall Case

To give a visual overview of the quality of the ANOPP predictions compared to the EVNERT measured data, side-by-side 1/3-octave SPL carpet plots of predictions and test results are shown in Figure 3.4 for the approach, cutback, and takeoff conditions (60-, 71-, and 87-percent corrected fan speed). The horizontal axes are the base-10 logarithm of the center-band frequency and the directivity angle, and the vertical axis is the 1/3-octave SPL. In general, the ANOPP predictions are in qualitative agreement with the EVNERT data. As can be seen in the figure, the EVNERT engine-test SPL values are higher than the ANOPP predictions for frequencies greater than about 6 kHz in the downstream direction. This is believed to be caused by an underprediction of the turbine noise (Ref. 57). The EVNERT data is also contaminated in the 315 to 630 Hz 1/3-octave frequency bands by an abnormal noise source. Honeywell (Ref. 57) identified this noise source to be case-radiated noise by using a tarmac-array beamforming technique. They found that this unwanted noise source was present during the 2005 EVNERT configurations 13 to 28, but was not seen again after a partial engine rebuild for instrumentation in early 2006.

Figure 3.5 to Figure 3.7 show the 1/3-octave SPL spectra in the 30°, 60°, 90°, 120°, and 150° directions in parts (a) through (e) and the overall SPL (OASPL) versus polar directivity angle in part (f) for the approach, cutback, and takeoff conditions, respectively. The ANOPP predictions have

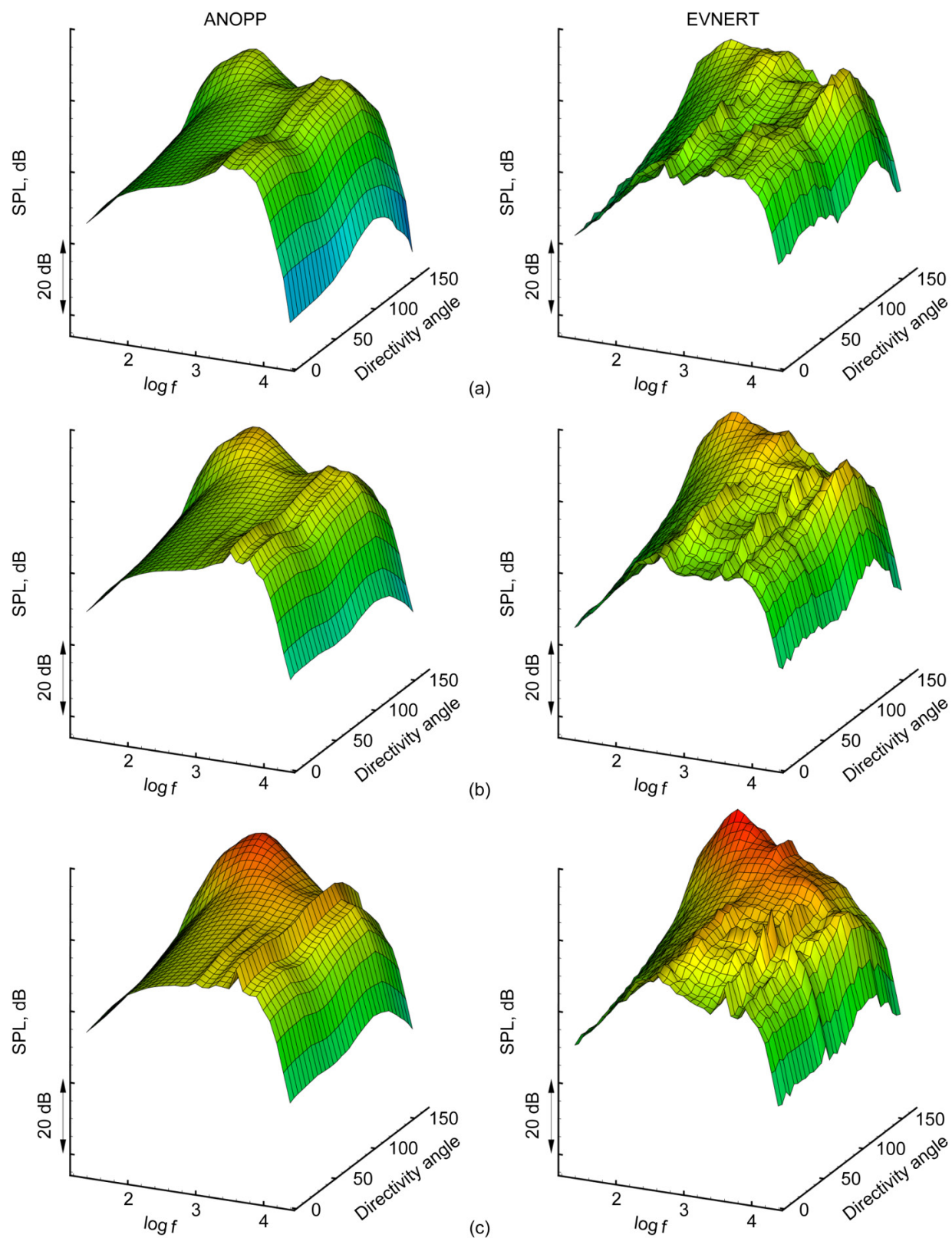


Figure 3.4.—Hard-wall case 1/3-octave surface plots comparing ANOPP predictions and EVNERT data of far-field sound from Honeywell TECH977 engine at various corrected fan speeds. SPL is sound pressure level, and f represents frequency. (a) 60 percent (approach). (b) 71 percent (cutback). (c) 87 percent (takeoff).

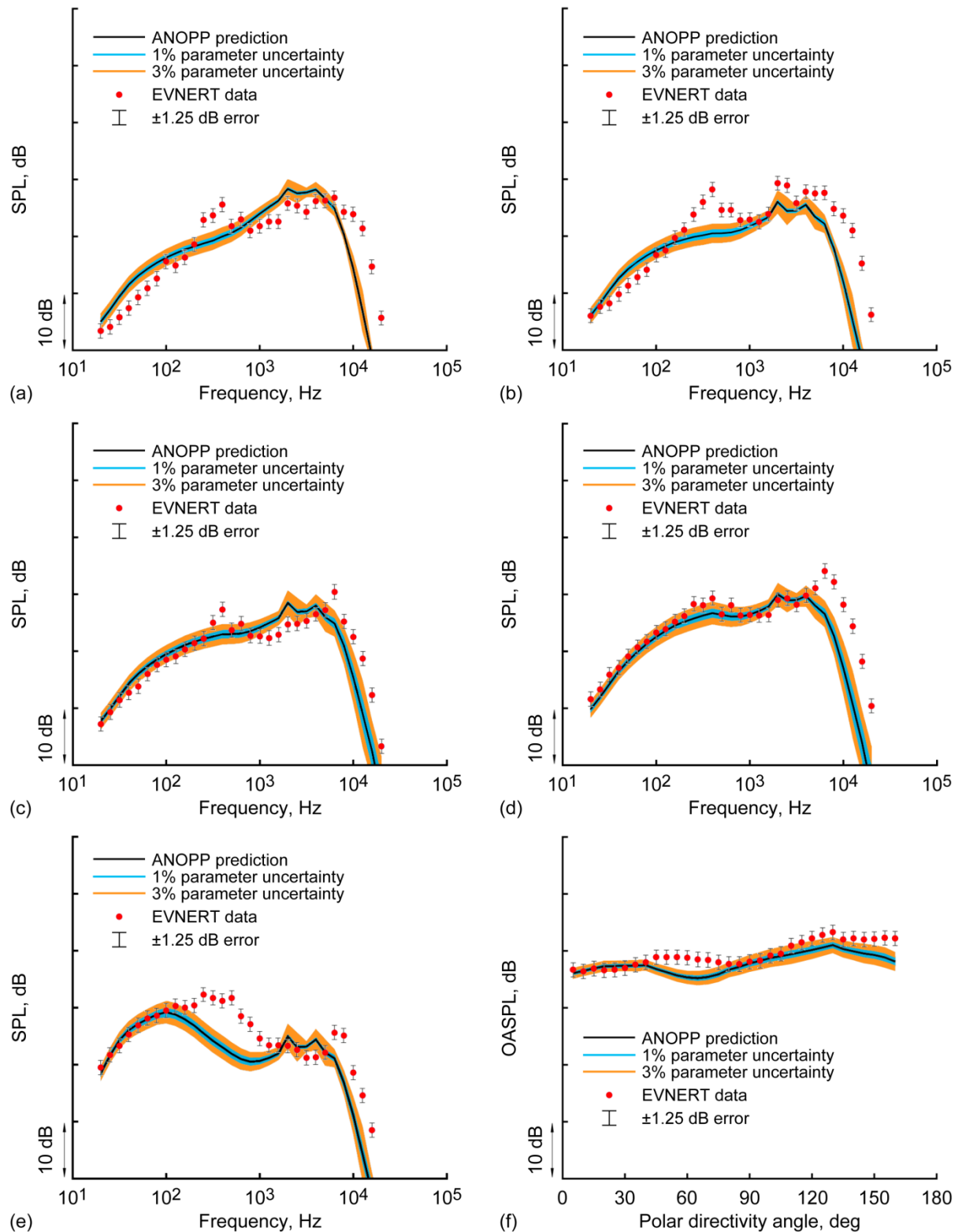


Figure 3.5.—Comparison of ANOPP predictions and EVNERT data for hard-wall case of Honeywell TECH977 engine at approach condition, 60 percent corrected fan speed. Error bands for predictions are 1 and 3 percent uncertainties in performance parameters. Error bar for data is ± 1.25 dB estimated uncertainty from calibration and instrumentation. (a) to (e) 1/3-octave sound pressure level (SPL) versus center frequency at different polar angles. (a) 30°. (b) 60°. (c) 90°. (d) 120°. (e) 150°. (f) Overall SPL (OASPL) versus polar directivity angle.

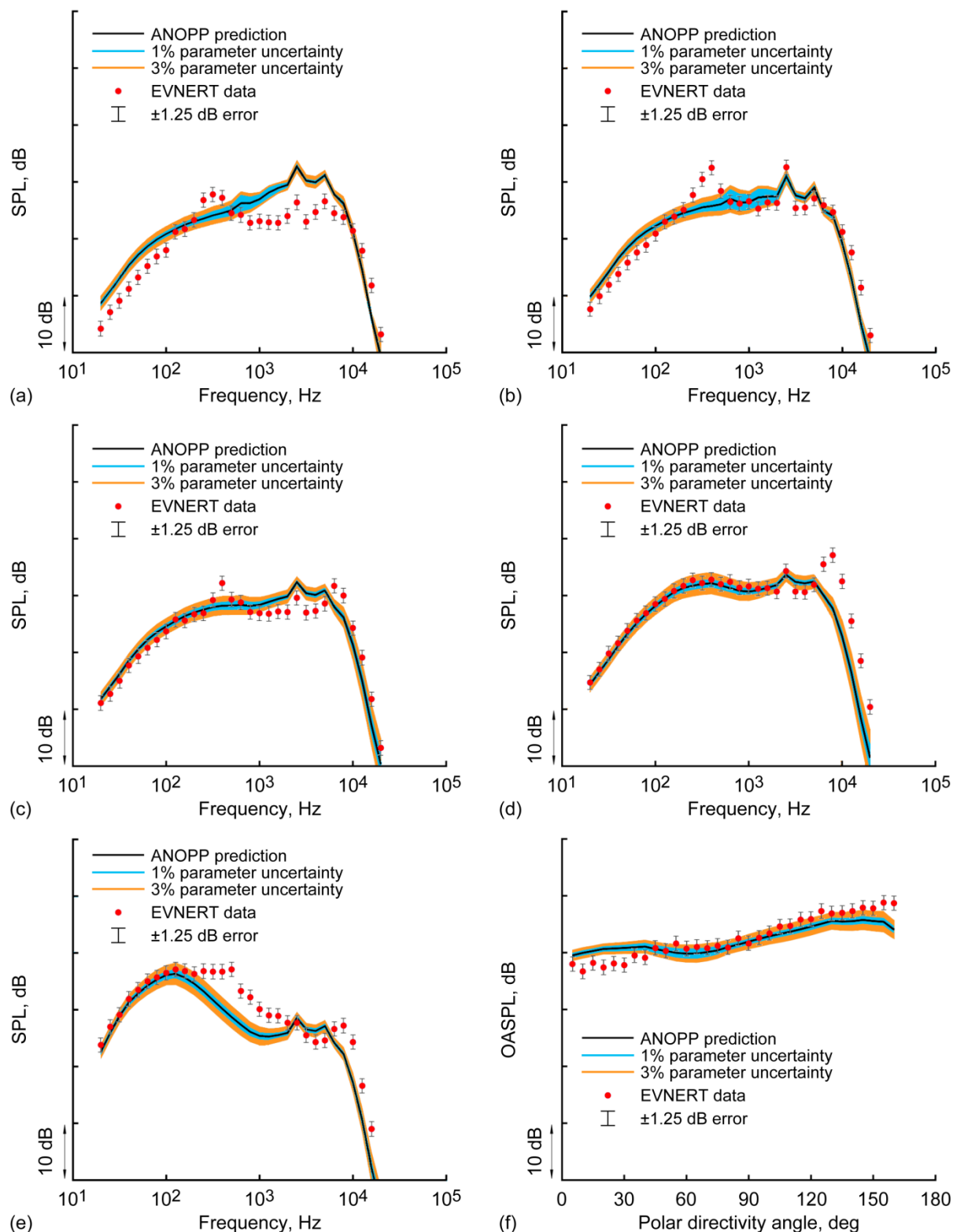


Figure 3.6.—Comparison of ANOPP predictions and EVNERT data for hard-wall case of Honeywell TECH977 engine at cutback condition, 71 percent corrected fan speed. Error bands for predictions are 1 and 3 percent uncertainties in performance parameters. Error bar for data is ± 1.25 dB estimated uncertainty from calibration and instrumentation. (a) to (e) 1/3-octave sound pressure level (SPL) versus center frequency at different polar angles. (a) 30° . (b) 60° . (c) 90° . (d) 120° . (e) 150° . (f) Overall SPL (OASPL) versus polar directivity angle.

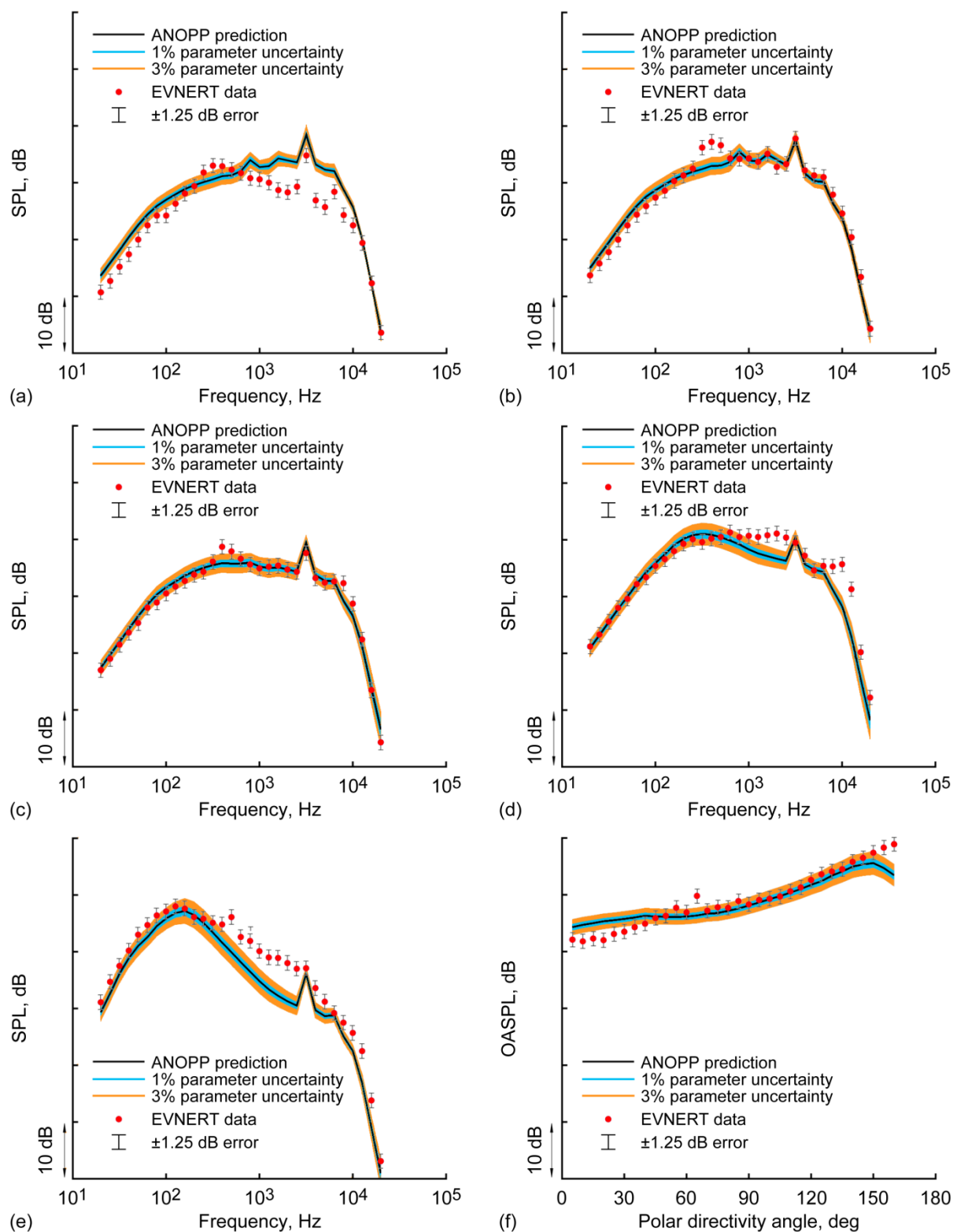


Figure 3.7.—Comparison of ANOPP predictions and EVNERT data for hard-wall case of Honeywell TECH977 engine at takeoff condition, 87 percent corrected fan speed. Error bands for predictions are 1 and 3 percent uncertainties in performance parameters. Error bar for data is ± 1.25 dB estimated uncertainty from calibration and instrumentation. (a) to (e) 1/3-octave sound pressure level (SPL) versus center frequency at different polar angles. (a) 30°. (b) 60°. (c) 90°. (d) 120°. (e) 150°. (f) Overall SPL (OASPL) versus polar directivity angle.

uncertainty bands (1 and 3 percent performance parameter uncertainty in blue and orange, respectively) and the static-engine-test data have ± 1.25 -dB bars based on estimated calibration and/or instrumentation uncertainty. The abnormal case-radiated sound and the high-frequency underprediction of the turbine noise are clearly visible in the SPL spectra shown in these figures. Nevertheless, the OASPL directivity and value are relatively well predicted for the cutback and takeoff conditions, with discrepancies mainly occurring close to the upstream and downstream directions.

3.4.1.2 Treated Case

Figure 3.8 shows 1/3-octave SPL surface plots at the approach, cutback, and takeoff conditions of 60-, 71-, and 87-percent corrected fan speeds, respectively. The figure layout is the same as that used in Figure 3.4. The ANOPP predictions are in qualitative agreement with the EVNERT data, but with some exceptions. There is high-frequency noise, probably turbine-associated, present in the EVNERT data that is not reflected in the ANOPP predictions. In addition, there is a SPL peak in the EVNERT data at the compressor shaft frequency (≈ 400 Hz at approach). It is most visible in the data for the approach conditions and decreasingly so for the higher throttle settings. This spectral peak is most likely a compressor-disk tone.³ The effect of the acoustic treatment in the inlet, c-duct, and nozzle can clearly be seen by comparing these results with those in Figure 3.4. The fan blade-passing frequency tone and its harmonics have clearly been reduced. The takeoff condition is dominated by jet noise, which somewhat masks the fan-noise attenuation due to the acoustic liners.

Figure 3.9 to Figure 3.11 show the 1/3-octave SPL spectra in the 30°, 60°, 90°, 120°, and 150° directions in parts (a) through (e) and the OASPL versus polar directivity angle in part (f) for the approach, cutback, and takeoff conditions, respectively. The uncertainty bands and bars for the prediction and data, respectively, are the same as for the hard-wall case above. The compressor-disk tone and the high-frequency underprediction of the turbine noise are clearly visible in the SPL spectra shown in these figures. The OASPL directivity and value are relatively well predicted for all conditions.

3.4.2 Comparison of Combustion-Noise 1/3-Octave Results

Data obtained for configuration 35 of the EVNERT (Ref. 57) program is used to assess the combustion-noise prediction capability of ANOPP. This engine-test configuration included engine-internal instrumentation in addition to the previously described far-field microphones. High-temperature pressure sensors with air cooling were located in a combustor

ignitor port (CIP1) and at the turbine exit (T551 and T552).⁴ Pressure-time histories at the internal sensors CIP1 and T551 and the aft-quadrant far-field microphone located in the 130° polar direction are used here. The EVNERT data acquisition system had a sampling rate of 65 536 Hz and a duration of about 70 s, leading to time histories with just over 4.5 million data points. Each time series is analyzed using a fast Fourier transform length of 8192 points (corresponding to an 8-Hz frequency resolution or bin width), Hanning windowing, and a 50-percent data-segment overlap (leading to $M = 1117$ segments). The resulting narrowband auto-spectra are then frequency summed up to yield the corresponding 1/3-octave SPL. The 1/3-octave far-field total SPL results are in full agreement with the Honeywell-provided 1/3-octave SPL data.

3.4.2.1 Source-Separation Implementation

Using the two- and three-signal coherence techniques described in Sections 3.2.2.3.1.1 and 3.2.2.3.1.2, the combustion-noise component $G_{ww}(f)$ of the far-field noise signature $G_{zz}(f)$ (see Figure 3.1) can be determined by

$$G_{ww}(f) = \gamma_{\alpha z}^2(f) G_{zz}(f), \quad \alpha = x, y \quad (3.8a)$$

where either the combustor sensor CIP1 ($\alpha = x$) or the turbine-exit sensor T551 ($\alpha = y$) is used in combination with the 130° far-field microphone, and/or it can be determined by

$$G_{ww}(f) = \frac{\gamma_{xz}(f) \gamma_{yz}(f)}{\gamma_{xy}(f)} G_{zz}(f) \quad (3.8b)$$

where signals from CIP1 sensor, T551 sensor, and the far-field microphone are utilized. These three choices will be referred to as the “2s-cip1,” “2s-t551,” and “3s” methods, respectively, in what follows. Equation (3.8a) is simply a restatement of Equation (3.1) allowing for a choice in engine-internal signal, and Equation (3.8b) follows directly from Equation (3.2c) by using the definition of coherence.

From a purely theoretical point of view, $0 \leq \gamma_{\alpha\beta} \leq 1$, with $\gamma_{\alpha\beta} = 0$ meaning that the two signals $\alpha(t)$ and $\beta(t)$ are completely uncorrelated and $\gamma_{\alpha\beta} = 1$ indicating perfectly correlated signals. In practice, only estimates $\hat{\gamma}_{\alpha\beta}$ of the coherence can be obtained using finite data series. The estimated coherence will, in fact, be nonzero even for completely uncorrelated signals (Refs. 88 and 89); that is, only the interval

$$\varepsilon < \hat{\gamma}_{\alpha\beta} \leq 1 \quad (3.9)$$

is meaningful, where

$$\varepsilon^2 = 1 - (1 - I)^{1/(N-1)} \quad (3.10)$$

³According to Reference 87 (personal communication), these tones are commonly seen in propulsion engines, auxiliary power units, and automobile turbochargers. They can be attributed to the geometric characteristics of the compressor system.

⁴The sensor labels here follow the naming convention in Reference 57.

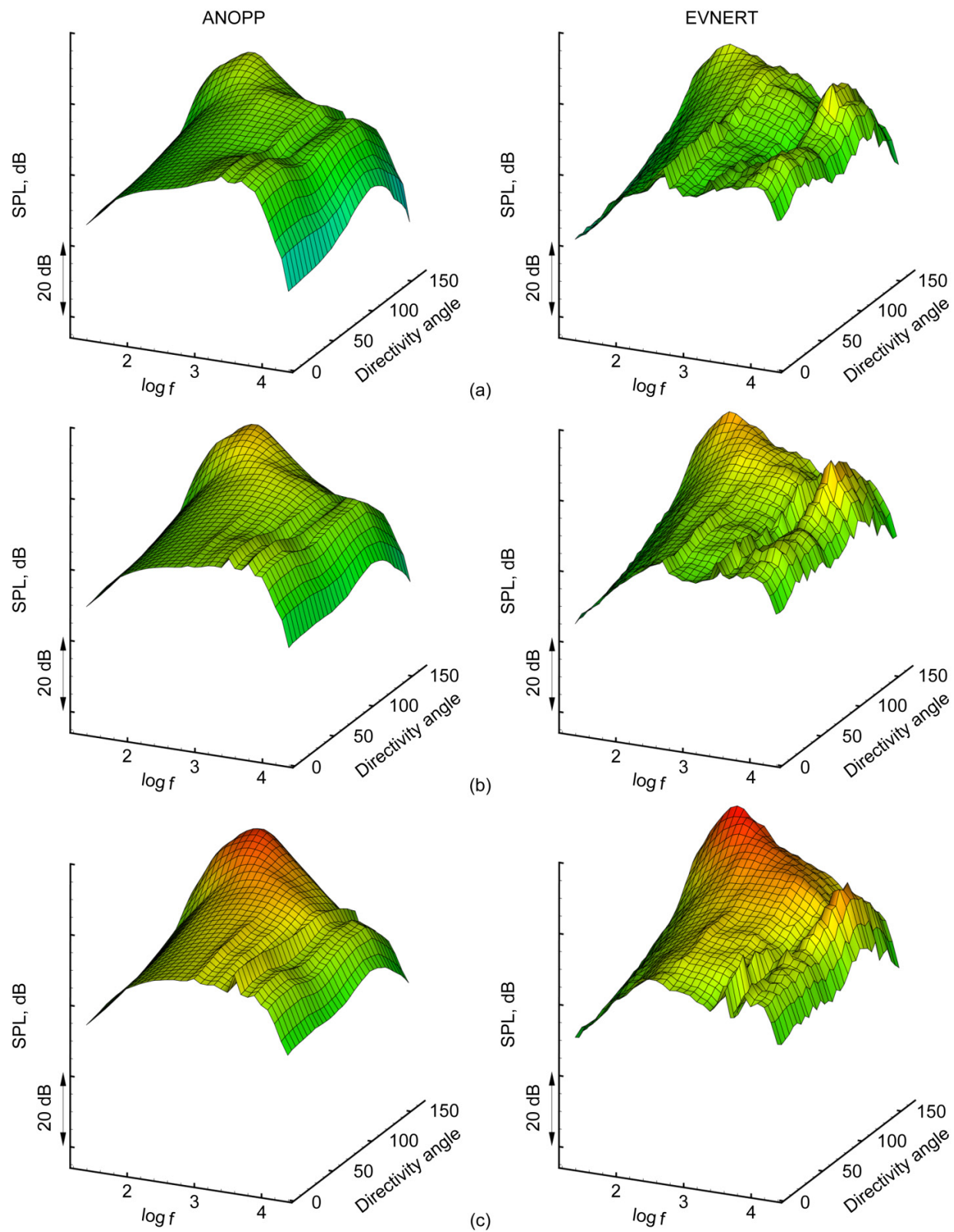


Figure 3.8.—Treated case 1/3-octave surface plots comparing ANOPP predictions and EVNERT data of far-field sound from Honeywell TECH977 engine at various corrected fan speeds. SPL is sound pressure level, and f represents frequency. (a) 60 percent (approach). (b) 71 percent (cutback). (c) 87 percent (takeoff).

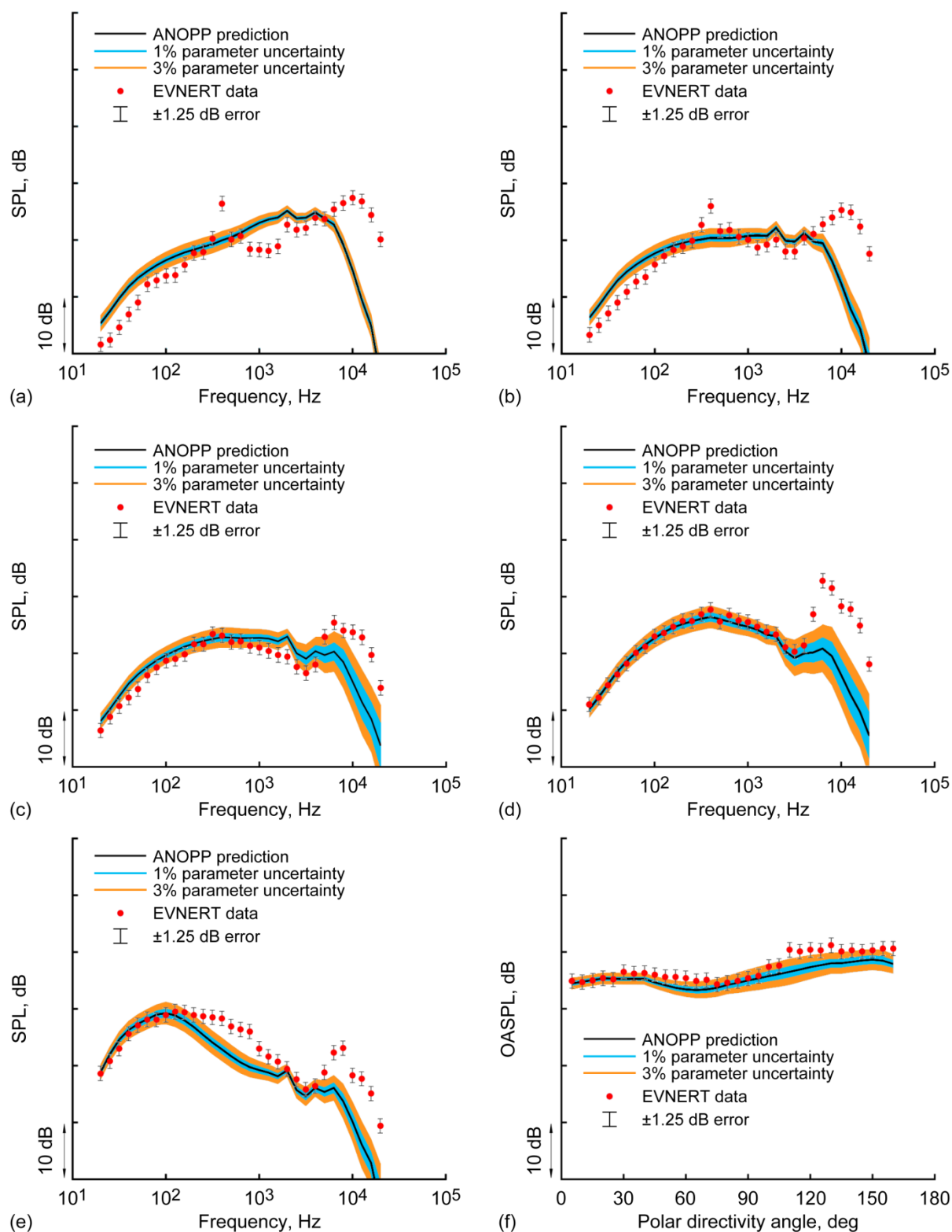


Figure 3.9.—Comparison of ANOPP predictions and EVNERT data for treated case of Honeywell TECH977 engine at approach condition, 60 percent corrected fan speed. Error bands for predictions are 1 and 3 percent uncertainties in performance parameters. Error bar for data is ± 1.25 dB estimated uncertainty from calibration and instrumentation. (a) to (e) 1/3-octave sound pressure level (SPL) versus center frequency at different polar angles. (a) 30°. (b) 60°. (c) 90°. (d) 120°. (e) 150°. (f) Overall SPL (OASPL) versus polar directivity angle.

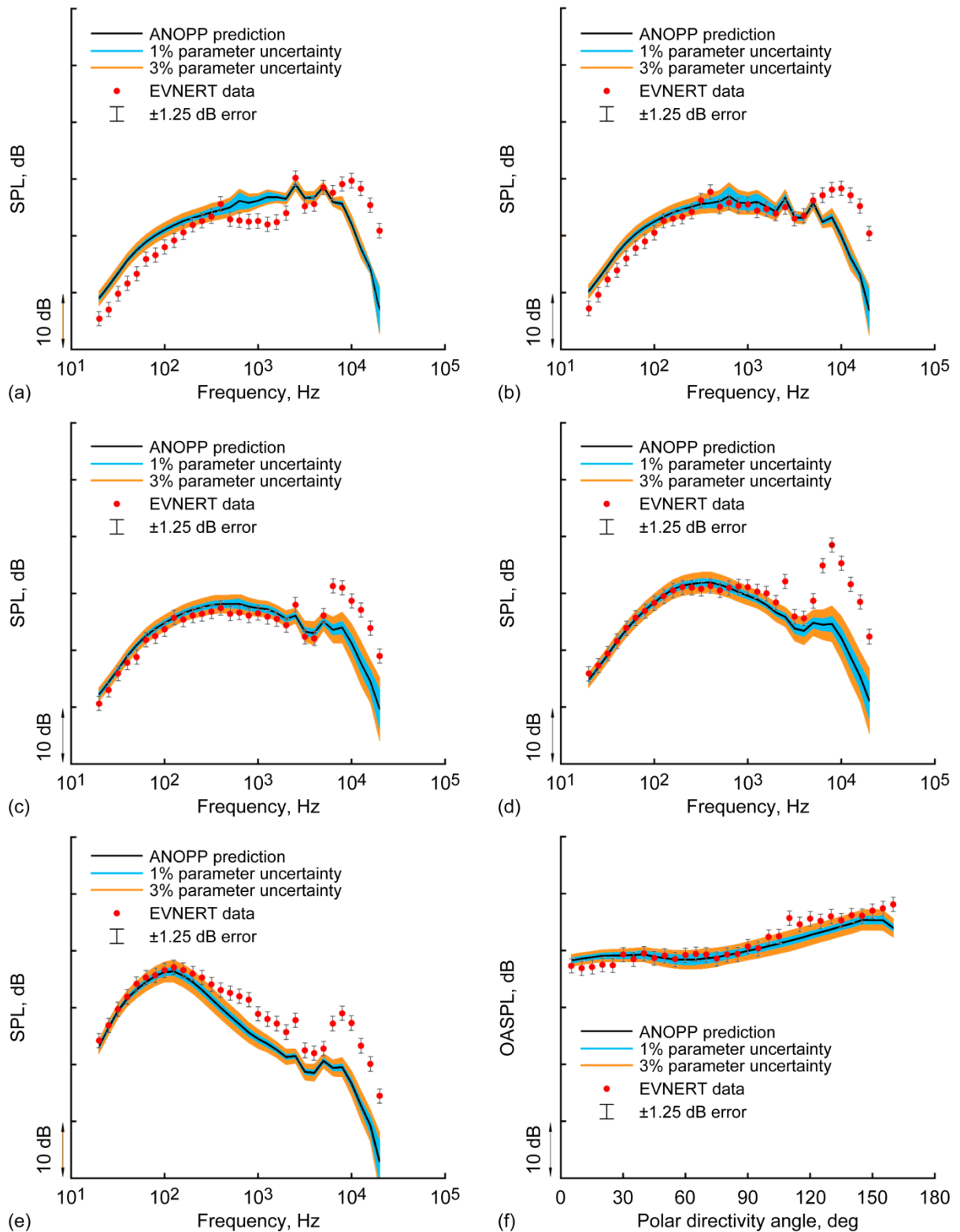


Figure 3.10.—Comparison of ANOPP predictions and EVNERT data for treated case of Honeywell TECH977 engine at cutback condition, 71 percent corrected fan speed. Error bands for predictions are 1 and 3 percent uncertainties in performance parameters. Error bar for data is ± 1.25 dB estimated uncertainty from calibration and instrumentation. (a) to (e) 1/3-octave sound pressure level (SPL) versus center frequency at different polar angles. (a) 30° . (b) 60° . (c) 90° . (d) 120° . (e) 150° . (f) Overall SPL (OASPL) versus polar directivity angle.

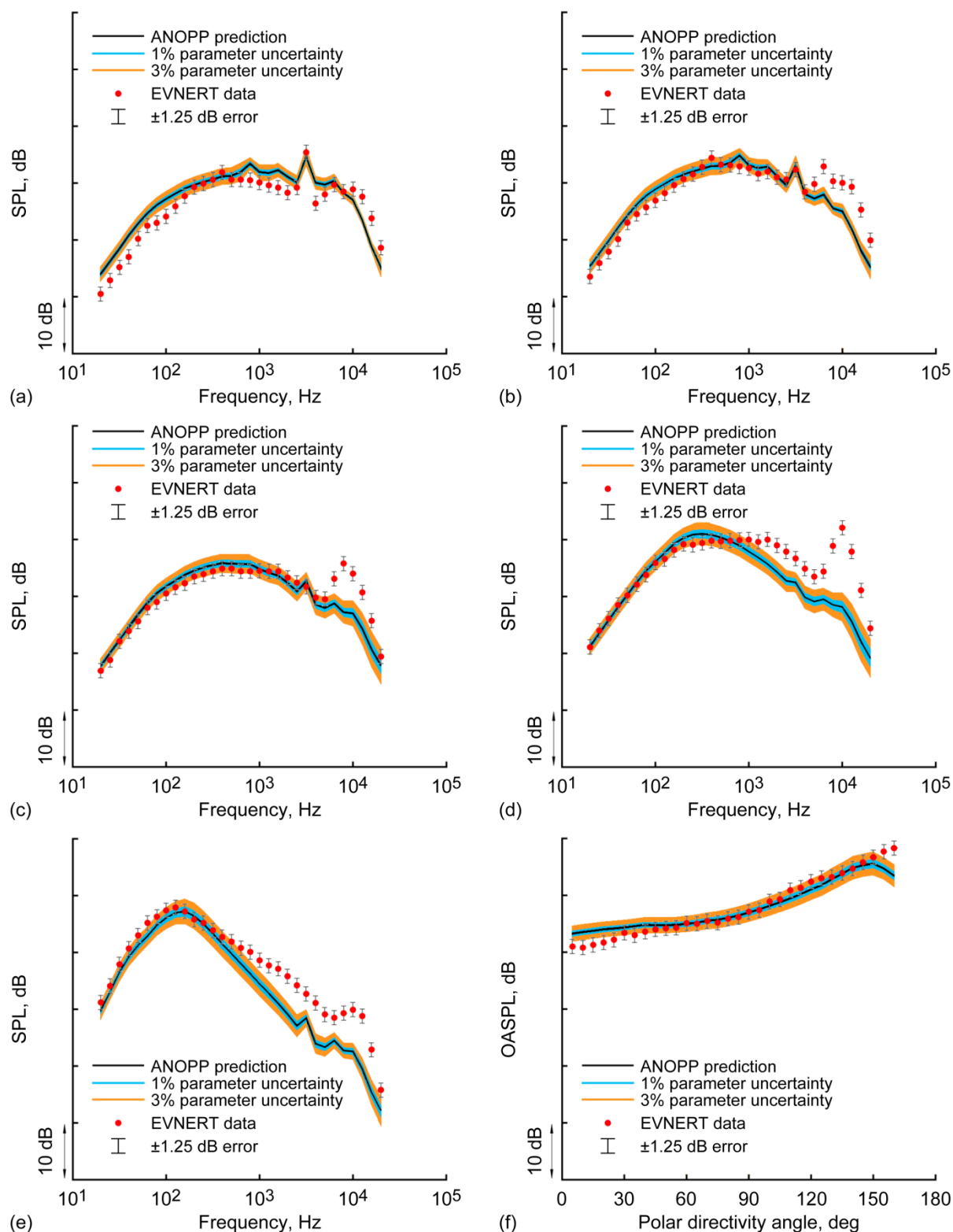


Figure 3.11.—Comparison of ANOPP predictions and EVNERT data for treated case of Honeywell TECH977 engine at takeoff condition, 87 percent corrected fan speed. Error bands for predictions are 1 and 3 percent uncertainties in performance parameters. Error bar for data is ± 1.25 dB estimated uncertainty from calibration and instrumentation. (a) to (e) 1/3-octave sound pressure level (SPL) versus center frequency at different polar angles. (a) 30° . (b) 60° . (c) 90° . (d) 120° . (e) 150° . (f) Overall SPL (OASPL) versus polar directivity angle.

I is the percent confidence interval if the true $\gamma_{\alpha\beta}^2$ is zero, and N is the number of independent data segments used in obtaining $\hat{\gamma}_{\alpha\beta}^2$. Welch (Ref. 90) showed, in the context of estimating auto power spectra, that N can be replaced by $9M/11$. Miles (Ref. 89) suggested that a better estimate for the coherence threshold value, or noise floor, ε can be obtained by purposely unaligning the two time series. That is, a time delay is deliberately introduced to make the two time series uncorrelated. The estimated unaligned coherence does not depend on any particular assumptions about the underlying statistical properties of the time series and accounts for any data-segment overlap and algorithms used in the analysis. The unaligned result captures the coherence of any discrete tones present in the signals and also provides an estimate of the minimum observable broadband coherence. Miles (Refs. 89 and 91) found that Equation (3.10) with $N = M$ provided a good estimate of the noise floor. Following Miles, the estimated coherence threshold for the present study is $\varepsilon = 0.00518$. If the estimated coherence exceeds the threshold the two time series are coupled. If it is less than the threshold, the signals are random and appear independent for that particular number of segments.

In the two-signal (coherent-output-power) method calculations carried out here, the estimated coherence $\hat{\gamma}_{\alpha\beta}(f)$ is replaced by the threshold value ε if it falls below that value for a particular narrowband frequency. That is, the estimated narrowband combustion-noise component $\hat{G}_{ww}(f)$ is simply set to $\varepsilon^2 \hat{G}_{zz}(f)$ for the frequency in question. Otherwise it is given by the equivalent of Equation (3.8a). The narrowband estimate is then frequency summed to yield the corresponding 1/3-octave result for the far-field combustion-noise component.

Mathematically, it follows from Equation (3.9) that

$$\varepsilon^2 < \frac{\hat{\gamma}_{xz} \hat{\gamma}_{yz}}{\hat{\gamma}_{xy}} < \varepsilon^{-1} \quad (3.11)$$

The upper limit of this inequality is an unphysical result in view of Equation (3.8b) and the fact that \hat{G}_{ww} cannot be larger than \hat{G}_{zz} . Clearly, an additional discriminator is needed to ensure a physically realistic three-signal combustion-noise estimate. This is provided by the following necessary condition for Equation (3.2) to be valid:

$$\Theta \equiv \arg [G_{xz} \text{conj}(G_{yz}) / G_{xy}] = 0 \quad (3.12)$$

The standard deviation (in radians) of the estimate for the cross-spectrum phase angle $\Theta_{\alpha\beta} = \arg(G_{\alpha\beta})$ is given by (Refs. 41 and 91).

$$\sigma_{\alpha\beta} = \sin^{-1} \sqrt{(1 - \gamma_{\alpha\beta}^2) / 2\gamma_{\alpha\beta}^2 N} \quad (3.13)$$

Note that the standard deviation is zero for perfectly correlated signals and increases as the coherence is diminished. Consequently, in the three-signal method calculations carried out here, the estimated narrowband combustion-noise component for a particular narrowband frequency $\hat{G}_{ww}(f)$ is set to $\varepsilon^2 \hat{G}_{zz}(f)$ if any of the estimated coherence values $\hat{\gamma}_{xz}$, $\hat{\gamma}_{yz}$, or $\hat{\gamma}_{xy}$ fall below the threshold value ε or if the estimated phase angle

$$\hat{\Theta} > \hat{\sigma}_{xz} + \hat{\sigma}_{yz} + \hat{\sigma}_{xy}$$

where

$$\hat{\sigma}_{\alpha\beta} = \sin^{-1} \sqrt{\frac{[1/\max(\hat{\gamma}_{\alpha\beta}^2, \varepsilon^2)] - 1}{2N}} \quad (3.14)$$

and $\alpha, \beta = x, y, z$. Otherwise it is given by the equivalent of Equation (3.8b), utilizing the estimated values for the functions on the right-hand side. The narrowband estimate is then summed up to yield the corresponding 1/3-octave result for the combustion-noise contribution to the far-field noise signature.

3.4.2.2 Statistical Uncertainty

The textbook by Bendat and Piersol (Ref. 41) gives a summary of statistical random error formulas for single input/output systems. From these, it follows that the statistical uncertainties for the present coherent-power-method estimates are given by

$$\mathcal{E}_r[\hat{G}_{zz}(f)] = \frac{1}{\sqrt{N}} \quad (3.15a)$$

$$\mathcal{E}_r[\hat{G}_{\alpha\beta}(f)] = \frac{1}{\gamma_{\alpha\beta} \sqrt{N}} \quad (3.15b)$$

$$\mathcal{E}_r[\hat{\gamma}_{\alpha\beta}^2(f)] = \frac{\sqrt{2}[1 - \gamma_{\alpha\beta}^2(f)]}{\gamma_{\alpha\beta}(f)\sqrt{N}} \quad (3.15c)$$

$$\mathcal{E}_r[\hat{G}_{ww}(f)] = \frac{[2 - \gamma_{\alpha\beta}^2(f)]^{1/2}}{\gamma_{\alpha\beta}(f)\sqrt{N}} \quad (3.15d)$$

where \mathcal{E}_r denotes the relative error or uncertainty. To evaluate these, the unknown true coherence $\gamma_{\alpha\beta}$ is replaced by its computed value $\hat{\gamma}_{\alpha\beta}$. Equation (3.15a) is the well known result that the uncertainty in an auto-spectrum estimation decreases as the inverse square root of the number averages used. This result shows that for the present computations, the statistical uncertainty of the total-noise auto-spectrum is about 3.3 percent, which is an order of magnitude smaller than the 33 percent (1.25 dB) estimated measurement uncertainty.

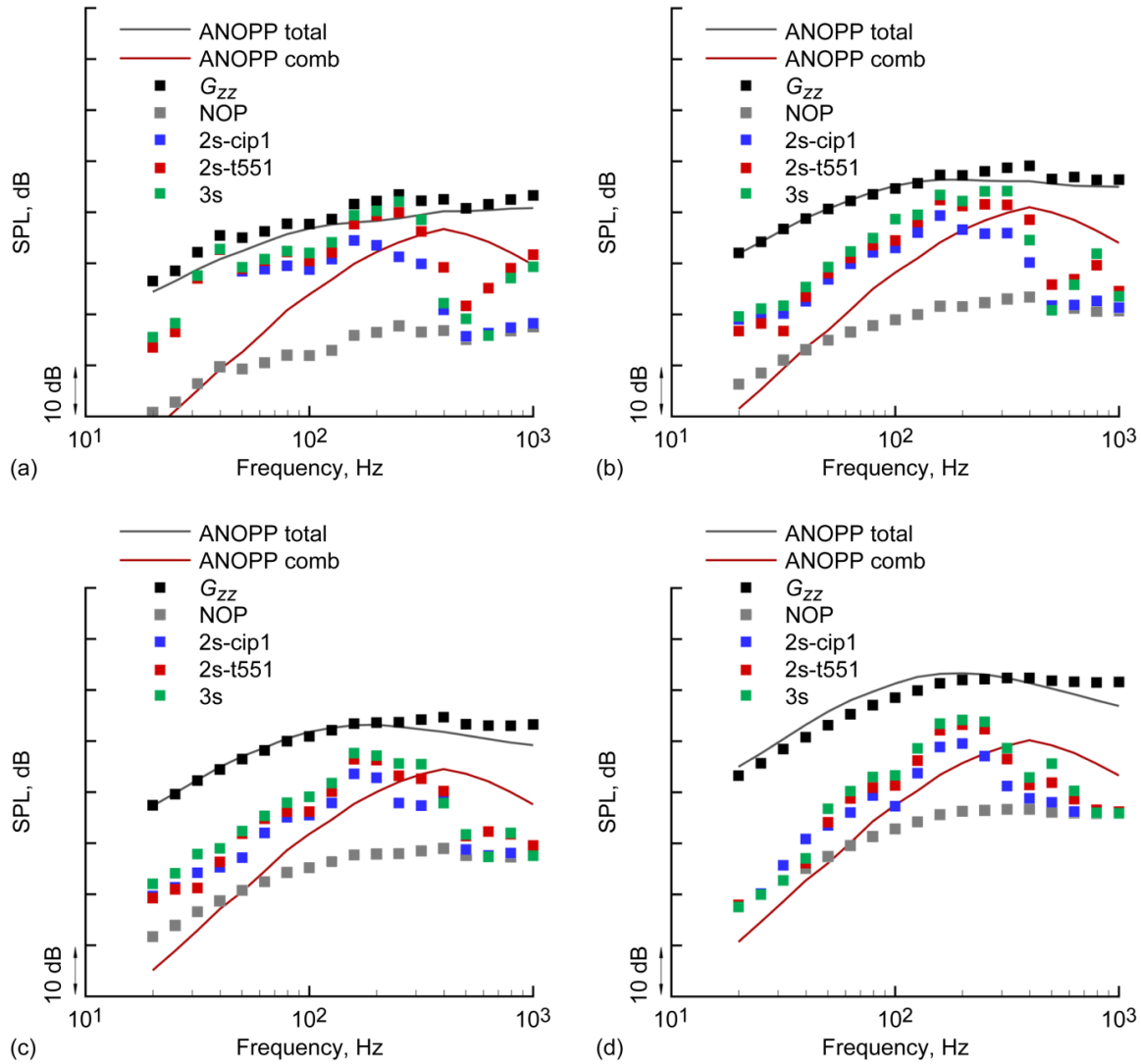


Figure 3.12.—Total- and combustion-noise 1/3-octave sound pressure level (SPL) versus 1/3-octave center frequency in 130° direction at different corrected fan speeds. ANOPP predictions and processed EVNERT data for Honeywell TECH977 engine configuration 35 (Ref. 57). G_{zz} refers to total noise spectrum; 2s-cip1, 2s-t551, and 3s refer to different processing techniques applied to the experimental data; and NOP refers to threshold values. (a) 48 percent (flight idle). (b) 60 percent (approach). (c) 71 percent (cutback). (d) 87 percent (takeoff).

Equation (3.15c) shows that the uncertainty in the coherence vanishes as the signals become correlated. This indicates that computed coherence values are more accurate than the quantities used in its evaluation. It is also important to realize that the estimate Equation (3.15d) also assumes that the input signal (see Figure 3.1) does not contain a noise component; that is, $m(t) = 0$ when $\alpha(t) = x(t)$ or $n(t) = 0$ for $\alpha(t) = y(t)$.

Using logarithmic differencing, it follows that the statistical uncertainty in the three-signal method can be expressed as

$$\begin{aligned} \varepsilon_r[\hat{G}_{ww}(f)] \leq & \frac{1}{2} \varepsilon_r[\hat{\gamma}_{xz}^2(f)] \\ & + \frac{1}{2} \varepsilon_r[\hat{\gamma}_{yz}^2(f)] + \frac{1}{2} \varepsilon_r[\hat{\gamma}_{xy}^2(f)] \\ & + \varepsilon_r[\hat{G}_{zz}(f)]. \end{aligned} \quad (3.16)$$

For perfectly correlated signals, both Equations (3.15d) and (3.16) reduce to the equivalent of Equation (3.15a). As the signals become uncorrelated, Equations (3.15d) and (3.16) indicate a relative uncertainty of $\sqrt{2/\varepsilon^2 N}$ and $(3/2)\sqrt{2/\varepsilon^2 N}$, respectively. Using the present number of data segments, the statistical uncertainty in the combustion-noise estimate is about 3 percent when the signals are highly correlated and becomes roughly 80 and 120 percent (depending on source-separation method) as they become poorly correlated. This suggests that the three-signal method is less robust than the two-signal methods when the coherence is small.

3.4.2.3 Results

The far-field signal $z(t)$ must be time shifted to account for the physical propagation delay between the engine-internal sensors and the 130° microphone. Following Miles (Ref. 91), the corresponding time series is shifted by 5800 points, which corresponds to an 88.5-ms time delay. Figure 3.12 shows the results of the source-separation procedures at the four engine power settings of 48-, 60-, 71-, and 87-percent corrected fan speed (flight-idle, approach, cutback, and takeoff conditions) for the 1/3-octave center frequency range of 20 to 1000 Hz. The solid lines represent the ANOPP 1/3-octave SPL predictions for the total (dark grey) and combustion (red-brown) noise. The symbols correspond to results computed from the experimental time histories as described above. The black squares, labeled G_{zz} , represent the total noise signature, which is reasonably well predicted by the ANOPP results. The grey squares, labeled NOP, correspond to the threshold value for the coherent output power and any combustion-noise result

below these values would not be meaningful using the present number of data segments and source-separation techniques. The blue, red, and green squares correspond to the combustion noise detected using the three methods 2s-cip1, 2s-t551, and 3s, respectively.

By comparing the results for the three different cases, the effect of the positive-bias error inherent in the two-signal method, not unexpectedly, leads to an underprediction of the peak value when the combustor-internal sensor CIP1 is used. The two-signal method utilizing the turbine-exit sensor T551 and the three-signal method both clearly detect a single combustion noise peak, but indicate that the 400-Hz combustion-peak location used in ANOPP is not adequate for this particular engine. The peak occurs at least two 1/3-octave bands lower. The ANOPP peak value also appears to be at least 3 dB too low.

3.5 Concluding Remarks

Within the limitations of static-engine measurements, the ANOPP total-noise predictions agree well with the EVNERT data, considering their semi-empirical base. In the near term, better prediction methods and models need to be developed for the nondominant turbine noise. The source-separation methods applied here to the EVNERT data show that the ANOPP combustion-noise predictions are not adequate for the particular engine used in the test. To enable future “quiet” aircraft engines, progress must be made in the understanding and modeling of the now subdominant combustion noise and its transmission and/or interaction with the turbine.

Appendix A.—Nomenclature

A.1 Acronyms

ANOPP	Aircraft Noise Prediction Program
APU	auxiliary power unit
BPF	blade-passing frequency
DAC	dual-annular combustors
DOT	Department of Transportation
EPNL	effective perceived noise level
EVNERT	Engine Validation of Noise and Emission Reduction Technology
FAA	Federal Aviation Administration
HSR	High Speed Research (Program)
LPT	low-pressure turbine
NACA	National Advisory Committee for Aeronautics
OASPL	overall sound pressure level
PNLT	tone-weighted perceived noise level
SAC	single-annular combustors
SAE	Society of Automotive Engineers
SPL	sound pressure level

A.2 Symbols

a	measure of relative contribution (from individual component source to total mean-square pressure)
I	percent confidence interval
f	frequency
G	one-sided spectrum
h	impulse-response function
M	number of 50-percent-overlapped segments
$m(t), n(t), o(t)$	uncorrelated signals from other sources than the one of interest
N	number of independent data segments

P	unsteady pressure
p	contribution to unsteady pressure from individual noise source
$s(t)$	source signal (see Figure 3.2)
SPL	sound pressure level
t	time
$u(t), v(t), w(t)$	not directly measurable coherent signals (see Figure 3.1 and Figure 3.2)
$x(t), y(t), z(t)$	directly measurable signals (see Figure 3.1 and Figure 3.2); sum of not directly measurable coherent signal and uncorrelated signal from other sources.
$\alpha(t), \beta(t)$	generic signals (could mean s, u, v, w, x, y , or z)
γ	coherence
ε	small number >0 from Equation (3.9)
\mathcal{E}	error or uncertainty
Θ	phase angle
μ	azimuthal mode number
ν	radial mode number
ξ	ANOPP parameter vector
$\hat{}$	estimate of quantity
$\langle \rangle$	ensemble average

Subscripts:

c	engine component
r	relative
ref	reference
ℓ	engine-component noise source
α, β	generic signals (could mean s, u, v, w, x, y , or z)

References

1. Aircraft Noise Abatement: Hearings Before the Subcommittee on Aeronautics and Space Technology of the Committee on Science and Astronautics U.S. House of Representatives. Ninety-third Congress, Second Session (Hearings of December 5, 6, and 18, 1973, appear as Appendix XIII), no. 44, U.S. Government Printing Office, Washington, DC, 1974.
2. Blumenthal, V.L.; Russell, R.E.; and Streckenbach, J.M.: A Positive Approach to the Problems of Aircraft Noise. AIAA-1973-1157, 1973.
3. Groeneweg, John F., et al.: Turbomachinery Noise. *Aeroacoustics of Flight Vehicles: Theory and Practice*, H.H. Hubbard, ed., vol. 1, ch. 3, NASA RP-1258, WRDC TR-90-3052, 1991, pp. 151-209.
4. Hubbard, H.H.: *Aeroacoustics of Flight Vehicles: Theory and Practice*, vols. 1 and 2. NASA RP-1258, WRDC TR-90-3052, 1991.
5. Mahan, J. Robert; and Karchmer, Allen: Combustion and Core Noise. H.H. Hubbard, ed., *Aeroacoustics of Flight Vehicles: Theory and Practice*, vol. 1, ch. 9, NASA RP-1258, WRDC TR-90-3052, 1991, pp. 483-517.
6. Tyler, J.M.; and Sofrin, T.G.: Axial Flow Compressor Noise Studies. *SAE Trans.*, vol. 70, 1962, pp. 309-332.
7. Bragg, S.L.; and Bridge, R.: Noise From Turbojet Compressors. *J. R. Aeronaut. Soc.*, vol. 68, no. 637, 1964, pp. 1-10.
8. Hetherington, R.: Compressor Noise Generated By Fluctuating Lift Resulting From Rotor-Stator Interaction. *AIAA J.*, vol. 1, no. 2, 1963, pp. 473-474.
9. Griffiths, J.W.R.: The Spectrum of Compressor Noise of a Jet Engine. *J. Sound Vib.*, vol. 1, no. 2, 1964, pp. 127-140.
10. Lowson, M.V.: Reduction of Compressor Noise Radiation. *J. Acoust. Soc. Am.*, vol. 43, 1968, pp. 37-50.
11. Benzakein, M.J.: A Study of Fan-Compressor Noise Generation. NASA SP-207, 1969, pp. 257-274.
12. Agarwal, Naval; Ganz, U.; and Premo, J.W.: Compressor Noise Contribution to Inlet Noise. AIAA-2004-2913, 2004.
13. Strahle, Warren C.: Combustion Noise. *Prog. Energy Combust. Sci.*, vol. 4, no. 3, 1978, pp. 157-176.
14. Strahle, W.C.: On Combustion Generated Noise. *J. Fluid Mech.*, vol. 49, pt. 2, 1971, pp. 399-414.
15. Strahle, W.C.: Some Results in Combustion Generated Noise. *J. Sound Vib.*, vol. 23, no. 1, 1972, pp. 113-125.
16. Shivashankara, B.N.; Strahle, Warren C.; and Handley, John C.: Evaluation of Combustion Noise Scaling Laws by an Optical Technique. *AIAA J.*, vol. 13, no. 5, 1975, pp. 623-627.
17. Mahan, J.R.: A Critical Review of Noise Production Models for Turbulent, Gas-Fueled Burners; Final Report. NASA CR-3803, 1984.
18. Muthukrishnan, M.; Strahle, W.C.; and Neale, D.H.: Separation of Hydrodynamic, Entropy, and Combustion Noise in a Gas Turbine Combustor. *AIAA J.*, vol. 16, no. 4, 1978, pp. 320-327.
19. Strahle, Warren C.; and Muthukrishnan, M.: Correlation of Combustor Rig Sound Power Data and Theoretical Basis of Results. *AIAA J.*, vol. 18, no. 3, 1980, pp. 269-274.
20. Ffowcs Williams, J.E.; and Howe, M.S.: Generation of Sound by Density Inhomogeneities in Low Mach Number Nozzle Flows. *J. Fluid Mech.*, vol. 70, pt. 3, 1975, pp. 605-622.
21. Marble, F.E.; and Candel, S.M.: Acoustic Disturbance From Gas Non-Uniformities Convected Through a Nozzle. *J. Sound Vib.*, vol. 55, no. 2, 1977, pp. 225-243.
22. Tam, Christopher K.W., et al.: Combustion Noise of Auxiliary Power Units. AIAA-2005-2829, 2005.
23. Schuster, Bill; and Lieber, Lysbeth: Narrowband Model for Gas Turbine Engine Combustion Noise Prediction. AIAA-2006-2677, 2006.
24. Strahle, Warren C.; Muthukrishnan, M.; and Neale, Douglas H.: Coherence Between Internal and External Noise Generated By a Gas Turbine Combustor. *AIAA J.*, vol. 15, no. 7, 1977, pp. 1018-1024.
25. Cumpsty, N.A.; and Marble, F.E.: Interaction of Entropy Fluctuations With Turbine Blade Rows; A Mechanism of Turbojet Engine Noise. *Proc. R. Soc. Lond. A*, vol. 357, 1977, pp. 323-344.
26. Cumpsty, N.A.; and Marble, F.E.: Core Noise From Gas Turbine Exhausts. *J. Sound Vib.*, vol. 54, no. 2, 1977, pp. 297-309.
27. Cumpsty, N.A.: Jet Engine Combustion Noise: Pressure, Entropy and Vorticity Perturbations Produced By Unsteady Combustion or Heat Addition. *J. Sound Vib.*, vol. 66, no. 4, 1979, pp. 527-544.
28. Huff, R.G.; Clark, B.J.; and Dorsch, R.G.: Interim Prediction Method for Low Frequency Core Engine Noise. NASA-TM-X-71627, 1974.
29. Zorumski, W.E.: Aircraft Noise Prediction Program Theoretical Manual, Part 1. NASA TM-83199-PT-1, 1982.
30. Zorumski, W.E.: Aircraft Noise Prediction Program Theoretical Manual, Part 2. NASA TM-83199-PT-2, 1982.
31. Motsinger, R.: Prediction of Engine Combustor Noise and Correlation With T64 Engine Low Frequency Noise. General Electric Technical Report R72AEG313, 1972.
32. Dunn, D.G.; and Peart, N.A.: Aircraft Noise Source and Contour Estimation. NASA CR-114649, 1973.
33. Society of Automotive Engineers International: Gas Turbine Jet Exhaust Noise Prediction. SAE ARP876 Rev. E, 2006.
34. Emmerling, J.J.; Kazin, S.B.; and Matta, R.K.: Core Engine Noise Control Program. Volume 3: Prediction Methods. Supplement 1: Extension of Prediction Methods; Final Report. FAA-RD-74-125-VOL-3-SUPPL-1, 1976.
35. Ho, P.Y.; and Doyle, V.L.: Combustion Noise Prediction Update. AIAA-1979-588, 1979.
36. Hough, J.W.; and Weir, D.S.: Small Engine Technology (SET)—Task 13 ANOPP Noise Prediction for Small Engines: Jet, Core, and Turbine Module Revisions. AlliedSignal Engines Technical Report No. 21-9655, internal report, 1997.
37. Mathews, D.C.; Rekos, N.F., Jr.; and Nagel, R.T.: Combustion Noise Investigation. FAA RD-77-3, 1977.
38. Mathews, D.C.; and Rekos, N.F., Jr.: Prediction and Measurement of Direct Combustion Noise in Turbopropulsion Systems. *J. Aircraft*, vol. 14, no. 9, 1977, pp. 850-859.
39. Pickett, G.F.: Core Engine Noise Due To Temperature Fluctuations Convecting Through Turbine Blade Rows. AIAA-1975-528, 1975.
40. Zuckerman, R.S.: Core Engine Noise Reduction—Definition and Trends. Technical Report AIAA-1977-1273, 1977.
41. Bendat, Julius S.; and Piersol, Allan G.: *Engineering Applications of Correlation and Spectral Analysis*. Wiley-Interscience, New York, NY, 1980.
42. Karchmer, A.M.; and Reshotko, M.: Core Noise Source Diagnostics on a Turbofan Engine Using Correlation and Coherence Techniques. NASA TM-X-73535, 1976.

43. Reshotko, Meyer, et al.: Core Noise Measurements on a YF-102 Turbofan Engine. *J. Aircraft*, vol. 14, no. 7, 1977, pp. 611–612.
44. Karchmer, A.M.: Identification and Measurement of Combustion Noise From a Turbofan Engine Using Correlation and Coherence Techniques. NASA TM-73747, 1977.
45. Karchmer, A.M.; Reshotko, M.; and Montagnais, B.J.: Measurement of Far Field Combustion Noise From a Turbofan Engine Using Coherence Functions. AIAA 1977-1277 (NASA TM-73748), 1977.
46. Reshotko, M.; and Karchmer, A.M.: Core Noise Measurements From a Small, General Aviation Turbofan Engine. NASA TM-81610, 1980.
47. Doyle, V.L.; and Moore, M.H.: Core Noise Investigation of the CF6-50 Turbofan Engine. NASA CR-159749, 1980.
48. Chung, J.Y.: Rejection of Flow Noise Using a Coherence Function Method. *J. Acoust. Soc. Am.*, vol. 62, 1977, pp. 388–395.
49. Krejsa, E.A.: New Technique for the Direct Measurement of Core Noise From Aircraft Engines. AIAA-81-1587 (NASA TM-82634), 1981.
50. Krejsa, E.A.: Application of 3-Signal Coherence to Core Noise Transmission. AIAA-1983-0759 (NASA TM-83333), 1983.
51. Krejsa, E.A.: Combustion Noise From Gas Turbine Aircraft Engines Measurement of Far-Field Levels. NASA TM-88971, 1987.
52. Parthasarathy, S.P.; Cuffel, R.F.; and Massier, P.F.: Separation of Core Noise and Jet Noise. AIAA J., vol. 18, no. 3, 1980, pp. 256–261.
53. Tester, B.J.; and Fisher, M.J.: Engine Noise Source Breakdown: Theory, Simulation and Results. AIAA-1981-2040, 1981.
54. Shivashankara, B.N.: High Bypass Ratio Engine Noise Component Separation by Coherence Technique. *J. Aircraft*, vol. 20, no. 3, 1983, pp. 236–242.
55. von Glahn, U.; and Krejsa, E.: Correlation of Core Noise Obtained By Three-Signal Coherence Techniques. NASA TM-83012, 1982.
56. Mendoza, J.M.; Nance, D.K.; and Ahuja, K.K.: Source Separation From Multiple Microphone Measurements in the Far Field of a Full Scale Aero Engine. AIAA-2008-2809, 2008.
57. Weir, Don: Engine Validation of Noise and Emission Reduction Technology Phase I. NASA/CR-2008-215225 (Honeywell Report No. 21-13843), 2008.
58. Hsu, J.S.; and Ahuja, K.K.: A Coherence-Based Technique To Separate Internal Mixing Noise From Farfield Measurements. AIAA-98-2296, 1998.
59. Karchmer, Allen M.: Acoustic Modal Analysis of a Full Scale Annular Combustor. NASA TM-83334 (AIAA-83-0760), 1983.
60. Krejsa, E.A.; and Karchmer, A.M.: Acoustic Modal Analysis of the Pressure Field in the Tailpipe of a Turbofan Engine. NASA TM-83387, 1983.
61. Miles, J.H.; and Krejsa, E.A.: Pressure Transfer Function of a JT15D Nozzle Due to Acoustic and Convected Entropy Fluctuations. *J. Acoust. Soc. Am.*, vol. 72, no. 6, 1982, pp. 2008–2019.
62. Miles, J.H.; Wasserbauer, C.A.; and Krejsa, E.A.: Cross Spectra Between Temperature and Pressure in a Constant Area Duct Downstream of a Combustor. NASA TM-83351 (AIAA-1983-0762), 1983.
63. Miles, J.H.; and Krejsa, E.A.: A Theoretical Model for the Cross Spectra Between Pressure and Temperature Downstream of a Combustor. NASA TM-83671, 1984.
64. Huff, R.G.: Simplified Combustion Noise Theory Yielding a Prediction of Fluctuating Pressure Level. NASA TP-2237, 1984.
65. Matta, R.K.; and Mani, R.: Theory of Low Frequency Noise Transmission Through Turbines. NASA CR-159457, 1979.
66. Gliebe, P., et al.: Aeroacoustic Prediction Codes. NASA/CR-2000-210244, 2000.
67. Mani, R.: Issues in Combustion Noise. Center for Turbulence Research Annual Research Briefs 2007, 2007, p. 255.
68. Dowling, Ann P.; and Stow, S.R.: Acoustic Analysis of Gas Turbine Combustors. *J. Propul. P.*, vol. 19, no. 5, 2003, pp. 751–764.
69. Lieuwen, T.: Modeling Premixed Combustion—Acoustic Wave Interactions: A Review. *J. Propul. P.*, vol. 19, no. 5, 2003, pp. 765–781.
70. Keller, Jacob J.: Thermoacoustic Oscillations in Combustion Chambers of Gas Turbines. AIAA J., vol. 33, no. 12, 1995, pp. 2280–2287.
71. Mathews, D.C.; Nagel, R.T.; and Kester, J.D.: Review of Theory and Methods for Turbine Noise Prediction. AIAA-1975-540, 1975.
72. Krejsa, E.A.; and Valerino, M.F.: Interim Prediction Method for Turbine Noise. NASA TM-X-73566, 1976.
73. Nesbitt, Eric: Towards a Quieter Low Pressure Turbine: Design Characteristics and Prediction Needs. *International J. Aeroacoustics*, vol. 10, no. 1, 2011, pp. 1–15.
74. Mathews, D.C.: Pratt & Whitney Aircraft, East Hartford, CT (retired), personal communication, 2008.
75. Gillian, R.E.: Aircraft Noise Prediction Program User's Manual. NASA TM-84486, 1982.
76. Shivashankara, B.N.: Aircraft Noise Prediction Program Validation. NASA CR-159333, 1980.
77. Kontos, K.B.; Janardan, B.A.; and Gliebe, P.R.: Improved NASA-ANOPP Noise Prediction Computer Code for Advanced Subsonic Systems. NASA CR-195480, Vol. 1, 1996.
78. Hough, Joe W.; and Weir, Donald S.: Aircraft Noise Prediction Program (ANOPP) Fan Noise Prediction for Small Engines. NASA CR-198300, 1996.
79. Hough, J.W.; Royalty, C.M.; and Weir, D.S.: ANOPP Combustion, Turbine, and Jet Noise Prediction Comparisons for Small Engines and a New Inlet Acoustic Treatment Design Module TREAT; Final Report. NASA CR-201587, 1997.
80. Clark, B.J.: Computer Program to Predict Aircraft Noise Levels. NASA TP-1913, 1981.
81. Rawls, J.W., Jr.; and Yeager, J.C.: High Speed Research Noise Prediction Code (HSRNOISE) User's and Theoretical Manual. NASA/CR-2004-213014, 2004.
82. Pratt & Whitney and General Electric Aircraft Engines: Critical Propulsion Components. NASA/CR-2005-213584/VOL1, 2005.
83. Heidmann, M.F.: Interim Prediction Method for Fan and Compressor Source Noise. NASA TM-X-71763, 1979.
84. Magliozzi, B.: V/STOL Rotary Propulsion Systems Noise Prediction and Reduction. Volume 2—Graphical Prediction Methods; Final Report. FAA-RD-76-49-VOL-2, 1976.
85. Stone, J.R.: Interim Prediction Method for Jet Noise. NASA TM-X-71618, 1974.

86. Stone, J.R.; and Montegani, F.J.: An Improved Prediction Method for the Noise Generated by Circular Jets. NASA TM-81470, 1980.
87. Weir, D.S.: Honeywell Aerospace, Phoenix, AZ, personal communication, 2007.
88. Brillinger, D.R.: Time Series: Data Analysis and Theory. Holden-Day, San Francisco, CA, 1981.
89. Miles, Jeffrey H.: Aligned and Unaligned Coherence: A New Diagnostic Tool. NASA/TM—2006-214112 (AIAA-2006-0010), 2006.
90. Welch, P.: The Use of Fast Fourier Transform for the Estimation of Power Spectra: A Method Based On Time Averaging Over Short, Modified Periodograms. IEEE Trans. Audio Electroacoust., vol. 15, no. 2, 1967, pp. 70–73.
91. Miles, J.H.: Spectral Separation of the Turbofan Engine Coherent Combustion Noise Component. NASA/TM—2008-215157 (AIAA-2008-50), 2008.

Chapter 4—Airframe Noise: A Prediction Capability Assessment

Jay H. Casper, David P. Lockard, Casey L. Burley, Meelan M. Choudhari, William M. Humphreys,
Florence V. Hutcheson, Mehdi R. Khorrami, and Craig L. Streett
National Aeronautics and Space Administration
Langley Research Center
Hampton, Virginia 23681

Summary

Presented herein are the comprehensive findings of a 2006 investigation to determine NASA's capability to predict airframe noise levels for aircraft that are configured for airport approach. During landing operations, the prominent components of airframe noise are the landing gear, along with the leading-edge slats and trailing-edge flaps of the aircraft's high-lift system. The present assessment includes far-field predictions for these airframe components and their validation with experimental measurement. The test cases are chosen from previously identified experiments involving wind tunnel models and flight testing of operational aircraft. In a number of these cases, noise levels are predicted with semi-empirical methods that are based on rudimentary source models with considerable reliance upon an experimental database. The remaining predictions are from first principles, in which the acoustic source is simulated by computational fluid dynamics. While these latter methods are too computationally intensive to be considered practical prediction tools, the wealth of detailed information they yield can provide insight into the further development of existing modeling techniques. The present chapter contains a comprehensive overview of several investigations into airframe noise measurement and prediction, for both scale models and operational aircraft. Results and findings are discussed, and recommendations for extending the current state of the art for airframe noise prediction are provided.

4.1 Introduction

Airframe noise has been defined by Crighton as “the nonpropulsive noise of an aircraft in flight” (Ref. 1). The generation of such noise is driven by an aircraft's geometry, resulting in acoustic sources associated with flow features such as boundary layer flow past trailing edges, incident turbulence, and wakes. Because of significant noise reduction in the propulsion systems of commercial aircraft during the past five decades, today's airport noise levels are considerably influenced by airframe noise. In addition, it has been determined that compliance with increasingly stringent noise regulations cannot be achieved through reductions in the propulsion system alone (Ref. 1). As a result, the Federal Aviation Administration (FAA) requires planning and testing for airframe noise measurements to demonstrate compliance in its aircraft noise certification process (Ref. 2).

An aircraft's radiated noise is most influenced by airframe sources during airport approach, when its engines are operating at reduced thrust, and the airframe itself is configured for landing. During landing operations, the aircraft's wings are in high-lift configuration, and its landing gear is lowered, as illustrated in Figure 4.1. Flyover measurements (e.g., Refs. 3 to 11) and wind tunnel tests (e.g., Refs. 12 to 19) have revealed that the prominent sources of airframe noise are associated with the leading-edge slats, trailing-edge flaps, and landing gear of commercial transports.

4.1.1 Background

By 1970, as a result of research commissioned by the U.S. Air Force (Refs. 20 and 21), significant interest had arisen in airframe noise radiated by commercial transport aircraft.

Measured noise levels for gliders and light aircraft, when scaled to commercial transports of the day, suggested that airframe noise levels during airport approach were of sufficient amplitude that compliance with ongoing FAA regulations would not be possible by engine noise control alone. At that same time, substantial reduction in propulsion noise was occurring with the introduction of the high-bypass turbofan engine, chosen by the U.S. Air Force to power its C-5 Galaxy transport. With the expectation of continued reduction in engine noise levels, airframe noise was perceived as the “ultimate noise barrier” (Ref. 22).

NASA initiated a flight research program in 1972 to investigate the nature and relative importance of airframe noise sources. During the following 10 years, NASA was involved in a significant effort that included full-scale flight testing, wind tunnel experiments, and the development of prediction tools. Flight testing involved the measurement of airframe noise levels for sailplanes, turboprops, and jet aircraft (Refs. 3 to 9). Wind tunnel research included anechoic testing of model-scale aircraft (Refs. 12 and 13), as well as fundamental studies to characterize acoustic source mechanisms (Refs. 23 to 26). This considerable body of experimental research spurred improved testing techniques (e.g., Refs. 27 to 29) and established an airframe noise database that was coordinated with the development of prediction methods (Refs. 30 to 32). Airframe noise research subsided during the 1980s, along with cutbacks in funding for aircraft noise research in general. Aircraft noise research at NASA was refocused in 1993, with the initiation of the Advanced Subsonic Transport (AST) Program, and continued through the Quiet Aircraft Technology (QAT) Program until 2005. Today, airframe noise research is conducted under the auspices of the Subsonic Fixed Wing



Figure 4.1.—Boeing 747 aircraft in landing configuration. Four main landing gear, nose landing gear, leading-edge slats and triple-slotted, trailing-edge flaps are deployed during airport approach.

(SFW) project within NASA’s Fundamental Aeronautics Program (FAP). Efforts within the past decade have included important tests for aircraft configurations and component-level studies, throughout a considerable range of scale, to identify acoustic sources and implement noise reduction technology (Refs. 10, 11, 14 to 19, and 33 to 41).

4.1.2 Assessment Overview

The present chapter contains the findings of a 2006 study to assess NASA’s current capabilities in airframe noise prediction. This assessment includes calculations of acoustic radiation for airframe component models and an operational aircraft as well as comparison of the predictions with measurements obtained during various test programs. Also included are descriptions of the prediction methodologies, test facilities, and relevant experimental techniques and procedures.

The presentation of this chapter is organized as follows. In Section 4.2, airframe noise prediction methodology is discussed, including an introduction to the predictive and experimental tools that are relevant to the present study. Section 4.3 contains a description of a recent flight test (Ref. 11) involving a Gulfstream G550 aircraft, with associated airframe noise predictions. Test descriptions for various model-scale airframe components, and corresponding computational results, are presented in Sections 4.4 through 4.8. Two of the models are airfoil sections: a NACA 63₂-215 section with a part-span flap (Ref. 34), and a 30P/30N section with a leading-edge slat (Ref. 35). The remaining models include two small-scale landing gears (Refs. 36 and 37) and a pair of tandem cylinders (Refs. 38 and 39). In Section 4.9, findings are summarized, and recommendations are made for improving current prediction methods and for future research. Lastly, Appendix A lists acronyms and symbols used in this chapter, and Appendix B to Appendix D contain pertinent details for the analytical and experimental tools that were employed to produce the results herein.

4.2 Prediction Methodology

Two significantly different approaches to problem modeling are represented by the acoustic predictions within this

chapter. These approaches are discussed below, including their relative strengths and weaknesses. The corresponding prediction methods for each of these modeling approaches are briefly described, with details contained in Appendix B and Appendix C. In each of the case studies (Secs. 4.3 to 4.8), a corresponding experiment is conducted to produce validation data for predictive comparison. The facilities employed to obtain these test results are identified, while more thorough descriptions can be found in Appendix D and associated references. Scaling issues and metrics (e.g., data variability, uncertainty) are also addressed.

4.2.1 Modeling Approaches

The first approach to airframe noise prediction involves the use of lower-order, semi-empirical source models. The term “lower order” here is used in the informal sense, to imply that the basis for the model’s formulation does not account for every important aspect of the problem. Therefore, these models typically rely upon experimental measurement for such critical characteristics as amplitude scaling or spectral shape. Computational efficiency is the primary advantage in the application of prediction methods based on lower-order models. However, an empirically based prediction method cannot be reliably applied to aircraft configurations that differ significantly from those contained within the method’s derivative database.

A second, and more fundamental, approach to modeling airframe noise relies on first principles. Specifically, an acoustic source is determined by solution of mathematical equations that accurately describe all significant aspects of the physical problem. In the present work, this “physics-based” approach requires that the source be simulated with a computational fluid dynamics (CFD) calculation. Such fundamental modeling avoids the constraints imposed by a preexisting database, but does not presently yield a practical approach on a routine basis, because of the computational effort involved. Typically, unsteady CFD calculations for noise prediction require the attention of expert users, tedious and time-consuming grid generation, and access to supercomputers for weeks, if not months, depending upon the problem of interest. However, results obtained within this fundamental approach contain considerably more information than predictions based on lower-order models, and thereby lend support to further research in noise reduction techniques and tool development.

Today, lower-order, semi-empirical models continue to provide the prediction methods of choice with respect to design and technology development, because of their rapid execution and relative ease of application. As such, they are representative of the current state of the art, and half of the predictions in the present chapter are obtained with methods of this type. Also, note that the previously stated weakness in semi-empirical modeling has not heretofore been an issue, in that the basic configuration for transport aircraft has not been significantly altered since the advent of the jet airliner in the 1950s. However, within NASA, there has been a growing interest in unconventional configurations, which are clearly

outside the realm of the current practical prediction methodology. Section 4.10 provides recommendations for the improvement of present prediction methods, including the extension of their application beyond conventional aircraft.

4.2.2 Prediction Tools

Half of the airframe noise predictions (Secs. 4.3 to 4.5) in the present chapter are obtained with the Aircraft Noise Prediction Program (ANOPP) (Ref. 42), developed at NASA Langley Research Center. An overview of ANOPP is presented in Chapter 2, “Aircraft System Noise Prediction.” ANOPP contains two airframe noise modules, both of which incorporate lower order, semi-empirical models. One module represents a prediction scheme developed by Fink (Ref. 32) for the FAA, and the other a method developed for NASA at Boeing Aircraft Company (Refs. 43 and 44). The specific formulations used to conduct the present study are provided in Appendix B. ANOPP uses the coordinate system shown in Figure 4.2, where R represents the propagation distance, and θ and ϕ are the polar and azimuthal directivity angles, respectively. An additional convention used throughout the present work is the Strouhal number, which has the general form $St = fL/V_\infty$, where f is frequency, L is a characteristic length, and V_∞ is the aircraft speed. Moreover, to be consistent with ANOPP’s documentation, airspeed is represented in Appendix B by the product $M_\infty a_\infty$, where the factors respectively denote the aircraft Mach number and the ambient sound speed.

In Sections 4.6 to 4.8, the physics-based approach is taken to predict aerodynamic noise to the far field. Conceptually, a CFD code that solves the Navier-Stokes equations can be used to model an aerodynamic source that produces sound as well as its propagation to any required point in the far field. However, such a straight-forward CFD approach to airframe noise prediction is, at present, computationally prohibitive. As such, the physics-based approach to airframe noise prediction currently results in a hybrid, two-step process: The acoustic source is simulated with a near-field CFD calculation, which is then used as input to an acoustic analogy to propagate the noise to the far field. In the present chapter, the near-field flow is computed with CFL3D (Refs. 45 and 46), and the propagated noise is obtained by integrating the Ffowcs Williams-Hawkins (FW-H) equation (Ref. 47). More information on these prediction tools can be found in Appendix C and the references therein.

4.2.3 Test Facilities

The testing and noise analysis associated with a full-scale, operational aircraft are discussed in Section 4.3. Airframe noise data were obtained during a flight test conducted at NASA’s Wallops Flight Facility at Wallops Island, Virginia. A brief description of this facility and the pertinent measurements are contained in Section 4.3, while further details can be found in Reference 11.

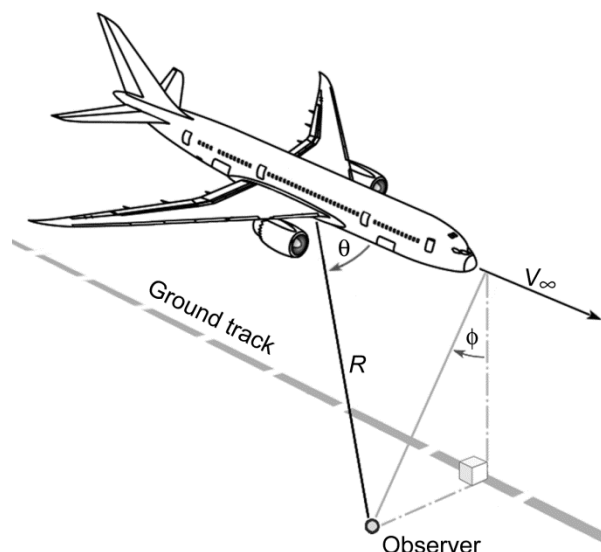


Figure 4.2.—ANOPP source-observer geometry. R , θ , and ϕ are measured with respect to source emission time. V_∞ is aircraft speed.

All of the scaled model testing reported herein was conducted in two wind tunnel laboratories at NASA Langley Research Center: the Basic Aerodynamic Research Tunnel (BART) and the Quiet Flow Facility (QFF). The BART is a flow diagnostic facility that specializes in the acquisition of fundamental flow-field data (Ref. 48), and the QFF has an anechoic test section that is designed to obtain aerodynamic noise measurements (Ref. 49). These two experimental facilities are more fully described in Appendix D.

4.2.4 Scaling Issues

The ANOPP predictions are compared with measurements from both wind tunnel and flight tests in the present chapter. Although ANOPP was developed to compute noise (of all types) associated with full-scale aircraft in flight, predictions obtained with ANOPP’s airframe noise modules should scale with geometric dimension and flow speed (see Appendix B). Therefore, in concept ANOPP can be used to compute aerodynamic noise from aircraft of arbitrary size, including small-scale wind tunnel models. However, at least two potential issues arise when predicting noise from small-scale models with methods that are calibrated with flight test data. First, wind tunnel experiments may not include interaction effects, which are implicitly included in such semi-empirical models. Also, it is not clear how such small-scale predictions should be corrected to account for important differences that can occur between geometrically similar cases of significantly disparate Reynolds number.

Despite the issues involved in the use of wind tunnel experiments to develop aircraft noise prediction tools (as stated above), model tests are far less expensive to conduct than tests with operational aircraft. Therefore, considerably more

airframe noise data is available from model tests than from flight tests. Moreover, the bulk of available flight test data was obtained during the 1970s, when equipment and procedures were much less mature than today. Separation of the individual noise sources from flight tests is difficult, whereas wind tunnel tests often focus on individual components. Therefore, much of the current development in improved prediction methods, as well as the determination of potential noise reduction techniques, is based on wind tunnel data. The relevance of the small-scale tests is substantiated through comparisons with flight test data and measurements in those wind tunnels that simulate flight Reynolds numbers. Given the importance of both wind tunnel and flight tests, data from aircraft flyovers and ground-based testing are compared with ANOPP predictions.

4.2.5 Metrics

Unless otherwise noted, all acoustic results herein are presented in 1/3-octave sound pressure levels (SPLs), with the reference pressure taken as 20 μ Pa. “Error” is defined as the difference between a prediction and its associated experimental value. Only a limited uncertainty analysis has been performed: Data variability has been documented for experimental and computational test cases, contingent upon the availability of a sufficiently large database; for ANOPP predictions only, a limited analysis has been performed involving sensitivity to input parameters.

4.3 Airframe Noise Characteristics of a Gulfstream G550 Aircraft

An airframe noise flight test program was jointly conducted by NASA and Gulfstream Aerospace Corporation at NASA’s Wallops Flight Facility (WFF), from October 2 through November 1, 2006. The primary objective of this flight test was to acquire baseline airframe noise measurements for a regional jet class transport, using both a ground-based microphone array and individual microphones. The flight tests were executed in two phases, with each phase lasting approximately 10 days. Acoustic data for a Gulfstream G550 aircraft, on approach to landing, were acquired in Phase I. At least 24 combinations of aircraft configurations and test conditions were flown. The test matrix, ranging from cruise to landing configurations, was designed to provide an acoustic characterization of both the full aircraft and individual airframe components. Noise sources were isolated by selectively deploying components (flaps, main landing gear, nose gear, spoilers, etc.) and altering the airspeed, glide path, and engine settings. A subset of the Phase I test matrix was repeated during Phase II with a smaller Gulfstream G450 aircraft. The Phase I and II tests confirmed that the airframe is a major contributor to the noise from regional jets during landing operations. Full details of the flight test program and post processing of the acoustic data have been documented in

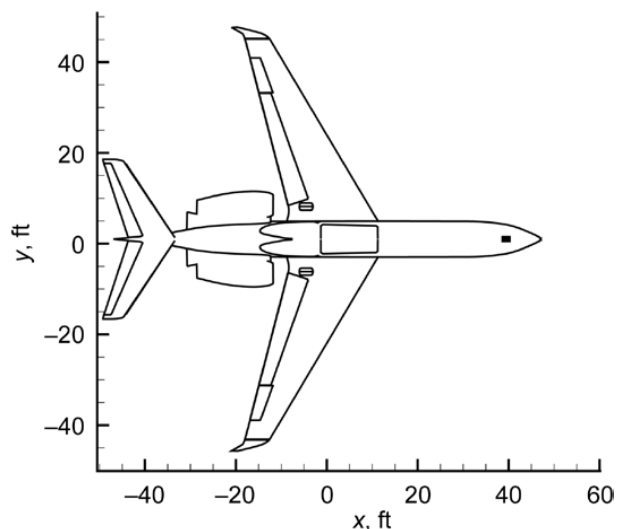


Figure 4.3.—Gulfstream G550 aircraft planform.

Reference 11 and will not be repeated here. Only the salient features are presented in the present chapter.

4.3.1 Discussion of Experimental Data

For the present study, only the Phase I data acquired with the G550 are used to assess current airframe noise prediction capabilities. Gulfstream’s G550 is a T-tail, twin-engine jet aircraft marketed as a corporate class transport. However, with one of the largest wingspans in its class, the scale of the G550 airframe approaches that of a regional jet, particularly in regard to the study of airframe noise. The aircraft’s planform is sketched in Figure 4.3, with relevant dimensions given in Table 4.1.

TABLE 4.1.—G550 AIRCRAFT:
CHARACTERISTIC DIMENSIONS

Overall length, m (ft).....	29.39 (96.42)
Height, m (ft).....	7.87 (25.83)
Wingspan, m (ft).....	28.5 (93.5)
Gross wing area, m ² (ft ²)	105.63 (1137)
Mean aerodynamic chord, m (ft)	4.22 (13.86)
Flap span per side, m (ft).....	7.8 (25.58)
Flap area per side, m ² (ft ²).....	8.8 (94.7)
Tail plane span, m (ft)	10.72 (35.17)
Tail plane area, m ² (ft ²).....	22.75 (244.86)
Max. gross takeoff weight, kg (lb).....	41 300 (91 000)

The test was conducted on WFF’s Runway 4, the longest of the facility’s three available runways, with a length of 2667 m (8750 ft) and a width of 45.7 m (150 ft). This runway was selected to meet several essential criteria for successful test completion. The most critical elements under consideration were: (a) the availability of a large flat overrun section, where the NASA microphone array and Gulfstream free-field

microphones could be placed adjacent to each other, along the aircraft approach direction, (b) the length of the runway to minimize potential risks during low-altitude, low-speed fly-over at low engine power settings, and (c) the enforcement of a minimum distance between the installed microphones and any nearby roads, to reduce the impact on background noise levels from local traffic.

The airframe noise test involved extensive noise measurements using NASA's 167-microphone array system, as well as Gulfstream's isolated, pole-mounted (certification) microphones. The layout of the microphone array and the individual microphones are shown in Figure 4.4, as installed on the overrun segment near the approach of Runway 4. The microphone array measurements are useful for noise source localization studies; noise source maps for the G550 from the Phase I flight test are presented in Reference 11. For the present discussion, the pole-mounted microphone data are more appropriate because the absolute noise levels for the various test configurations can be directly compared with the predictions. The mounting, operation, and processing of the data collected from the pole-mounted microphones were accomplished by Gulfstream engineers. Analysis of the individual microphone data followed the standard procedure typical of the aircraft certification process within the industry.

Measured acoustical data (raw data) were adjusted for the effects of amplitude stability (calibration drift), microphone pressure response, microphone free-field-to-incidence correction, wind screen insertion loss, ambient barometric pressure correction, and system noise response. These computations were accomplished using a special version of Gulfstream's noise certification analysis software.

Identification and determination of data errors and uncertainties for full-scale acoustic measurements is a challenging task. Unlike a highly controlled wind tunnel environment, flight tests occur in uncontrolled surroundings wherein the local atmospheric conditions do not remain constant. Although local conditions, up to an altitude of 152.5 m (500 ft), were recorded every hour using a combination of a weather balloon and a ground station, significant local atmospheric variations could occur within a short time period. The dominance of the errors introduced by the atmospheric effects (sound propagation, absorption, etc.) may mask other typical sources of error (e.g., instrumentation errors). To partially bracket the uncertainties introduced in the measured noise levels, repeat flights for each test condition were executed. For very few select configurations, repeat runs on a different day were performed to document day to day variability in the recorded noise levels.

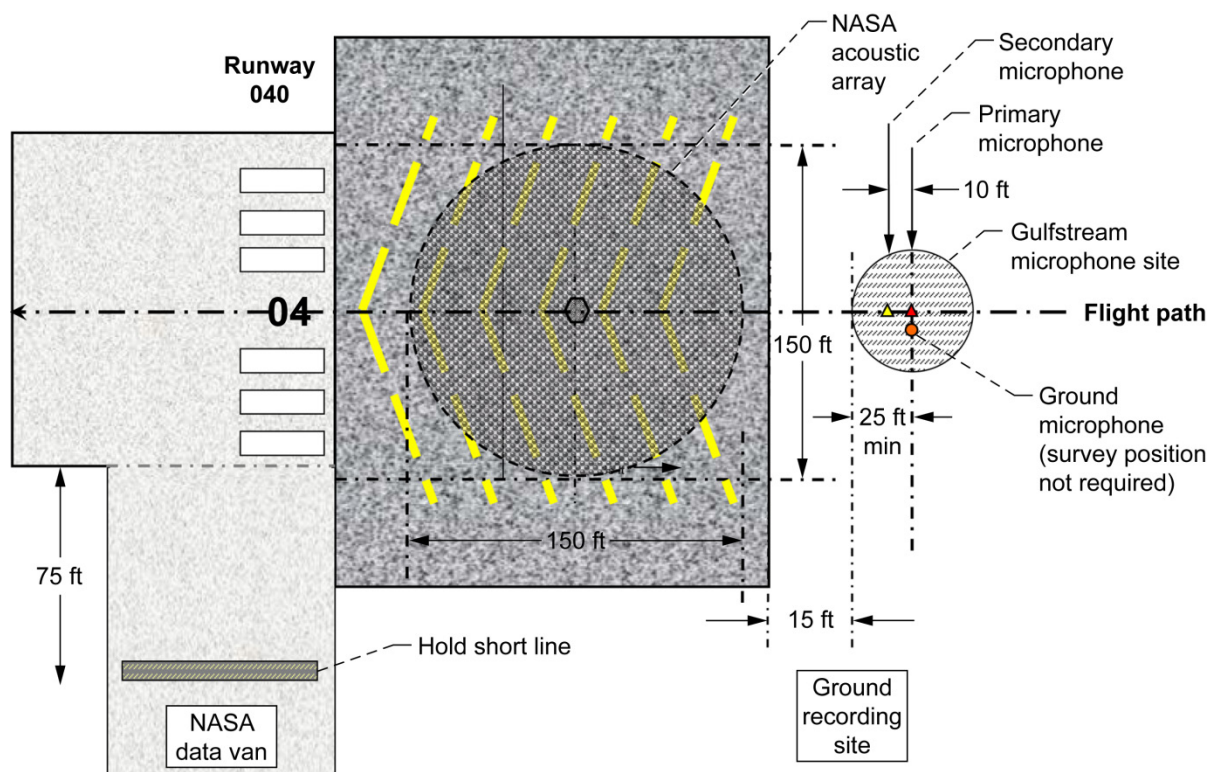


Figure 4.4.—NASA microphone array and Gulfstream free-field (certification) microphone layout.

In addition to the fully deployed (landing) and clean (cruise) configurations, Phase I covered numerous other configurations that were designed to isolate the noise sources associated with individual components (flap, nose gear, main gear, etc.). For each configuration, noise measurements were obtained at three distinct speeds with multiple runs at each speed in order to ensure that statistically meaningful data were obtained. Only a few select configurations at the nominal speed of 147 kn, for the time duration corresponding to an averaged emission (or polar overhead) angle $\theta = 86^\circ$, are used for the purposes of the present assessment. The selection of the candidate configurations was based on the desire to consider the more prominent airframe noise sources. The four selected configurations are (1) flaps deflected at 39° and gear down (landing configuration), (2) flaps deflected at 39° and gear up, (3) flaps retracted and only main gear down, and (4) flaps retracted and gear up (clean configuration). Note that the G550 wing has no leading-edge slat; therefore, slat noise is irrelevant to the current study.

4.3.2 Metrics and Assessment

As the primary NASA tool available for full-scale airframe noise prediction, ANOPP was utilized to perform the study. For the present full-scale noise assessment of regional jets, two distinct metrics are employed. The first metric involves comparison of the predicted absolute noise levels for the selected configurations and the levels obtained from the pole-mounted microphones. As an alternative criterion, the second assessment metric is based on comparison of relative noise levels, which are obtained as follows: The mean-square acoustic pressure for the clean (cruise) and each “dirty” (deflected surfaces) configuration under consideration are subtracted (dirty minus clean); the SPLs associated with these relative pressures are then calculated. This relative noise metric also partially eliminates any ambiguity attributed to the presence of residual engine noise or the background environmental noise within the measured signal.

Processing of the pole-mounted microphone data to extract the noise levels was accomplished by Gulfstream engineers. The processed data contain the appropriate corrections to account for absorption and propagation effects due to the variation in the local atmospheric conditions as well as variations in aircraft speed and altitude from the nominal values. Assuming a spherical spreading of the radiated noise and a V_∞^6 velocity dependence for the noise levels, the post-processed 1/3-octave band spectra have been normalized to a common altitude of 120 m (394 ft) and aircraft speed of 147 kn. However, the corresponding minor shift in the frequencies (less than 2 percent in most instances) was omitted during the normalization step.

Good data repeatability was demonstrated in Reference 11 where the variability in the measured SPLs was highlighted. The highest levels of variation in the measured SPL mostly shows up in the higher frequencies (above 3 to 4 kHz) where

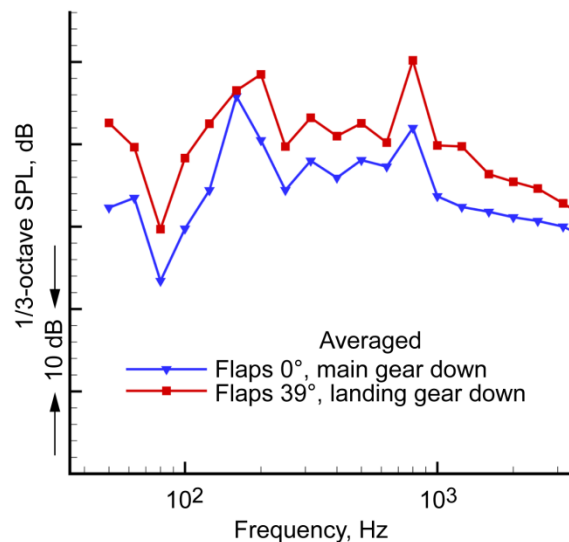


Figure 4.5.—Representative measured sound pressure level (SPL) spectra for two configurations of Gulfstream G550 aircraft.

the levels are typically 10 to 15 dB below the peak and variation of the atmospheric conditions is the dominant factor. Thus, presentation of the results and comparison with the predicted sound levels are attempted for frequencies up to the 1/3-octave band level 35 (3150 Hz center-frequency). Figure 4.5 compares the measured spectra for the full-dirty configuration (flaps-39 with landing-gear-down) with the spectra with only the main gear deployed. The primary (80 Hz) and secondary (250 Hz) dips as well as the low-frequency peak (160 to 200 Hz) in the spectra are caused by the destructive or constructive superposition of ground-reflected waves on the sound levels measured by the pole-mounted microphones. The prominent peak at 800 Hz is associated with a tone emanating from the main landing gear. At the time of this writing, its source has been identified, and a remedy for its elimination has been found. Therefore, for the purpose of comparison with predicted SPLs, the main gear tone has been removed from the spectra, and the corresponding frequency band is assigned a level that is linearly interpolated using the levels from the adjacent bands.

The SPLs for the four selected conditions are plotted in Figure 4.6. Each curve represents the averaged value of all the accepted runs conducted for that particular configuration. Notice the absence of the main gear tone. Comparison of the levels for the landing (square symbols) and clean (circular symbols) configurations indicates that deploying the flaps and undercarriage results in an increase of 6 to 10 dB in the low-to mid-frequency range. Given that all the flights were executed with an approach-idle engine setting, Figure 4.6 shows residual engine noise not to be a factor within the frequency range displayed. Moreover, the main landing gear contributes less to the total noise than the flaps.

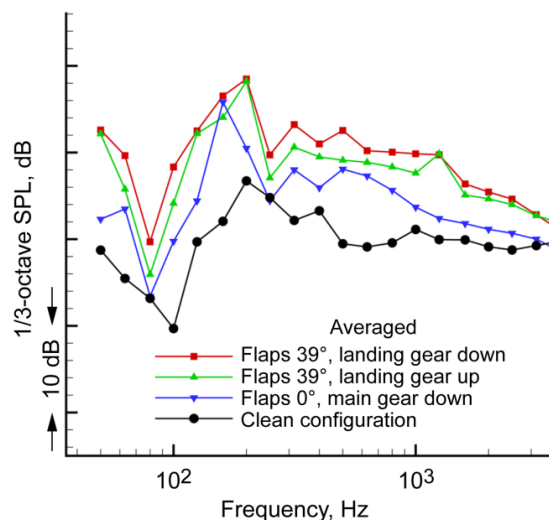


Figure 4.6.—Averaged measured sound pressure level (SPL) spectra for three selected airframe noise and clean configurations of Gulfstream G550 aircraft.

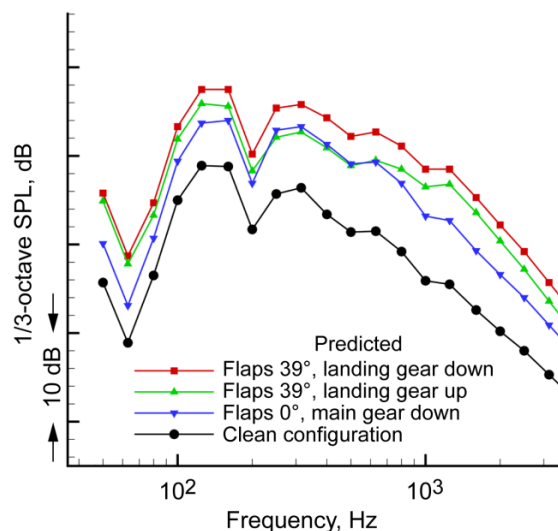


Figure 4.7.—Predicted sound pressure level (SPL) spectra for three selected airframe noise and clean configurations of Gulfstream G550 aircraft.

4.3.3 Results and Findings

ANOPP (Ref. 42), NASA's foremost aircraft noise prediction tool, was used for predicting the full-scale airframe noise levels for the G550 aircraft. Some of the aerodynamic parameters required as input to the Boeing model (Refs. 43 and 44) could not be obtained for this study. Thus, only the airframe noise module based on Fink's model (Refs. 32 and 42) was employed to compute the noise levels. In contrast to acoustic measurements in ground-based facilities, in flight the aircraft represents a moving noise source. To partially simulate the moving source behavior, several other ANOPP modules were utilized in addition to the airframe noise module. Listed in the sequence used in the prediction process, these modules were Atmospheric, Atmospheric Absorption, Steady Flyover, Geometry, Airframe Noise, and Propagation. Noise levels were predicted for a reference altitude of 120 m (394 ft), an aircraft speed of 147 kn, an azimuthal (sideline) angle of 0° , a polar (overhead) angle of 86° , and acoustic standard day conditions (21°C (70°F) and 70 percent relative humidity).

The predicted SPLs for the four selected configurations are shown in Figure 4.7. In the low- to mid-frequency range, the spectra are similar in shape to the measured values. In particular, the frequencies corresponding to the peak SPL are well predicted. Note that by choosing a receiver located at the same height as the pole microphone, the low-frequency peaks and valleys caused by ground reflection are also captured. For frequencies above 800 Hz, however, the predicted spectra show a much steeper drop in SPL, with the decay becoming most rapid above 2 kHz. The effects of variations in aircraft speed and azimuthal angle (ϕ) on the predicted noise were also determined. The azimuthal variation was chosen as it directly corresponds to the aircraft's roll angle as it passes over the measurement location. Figure 4.8 displays the effects of ± 5 percent variation in the nominal speed (147 kn) on the SPL

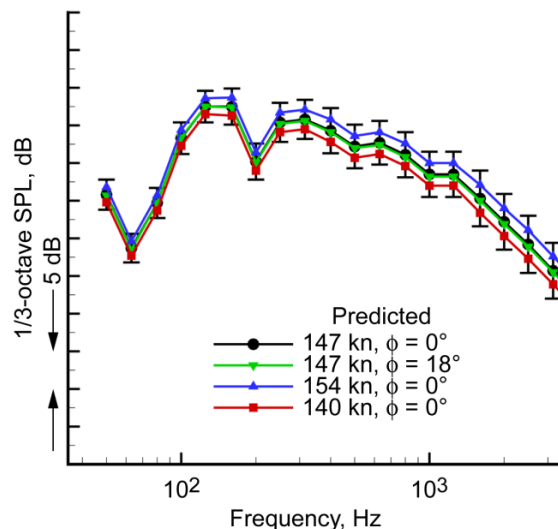


Figure 4.8.—Uncertainties in predicted sound pressure level (SPL) spectra due to variations in speed and azimuthal angle, ϕ , for Gulfstream G550 aircraft. Configuration is flaps at 39° with landing gear down.

for the landing configuration. The curves with square (red) and delta (blue) symbols bracket the extent of the variation in the SPL relative to the baseline (circular symbols) values. Also plotted in Figure 4.8 is the change in sound pressure levels predicted for the sideline angle of $\phi = 18^\circ$. From a geometrical point of view, this situation would be equivalent to the $\phi = 0$ case while the aircraft moving over the microphones undergoes a roll (banked) angle of 18° . Selecting such a large azimuth angle is a consequence of the insensitivity of the Fink model to small changes in ϕ . Moreover, the ϕ -dependency of the Fink model is symmetric and, therefore, the result is the same for $\phi = 342^\circ$.

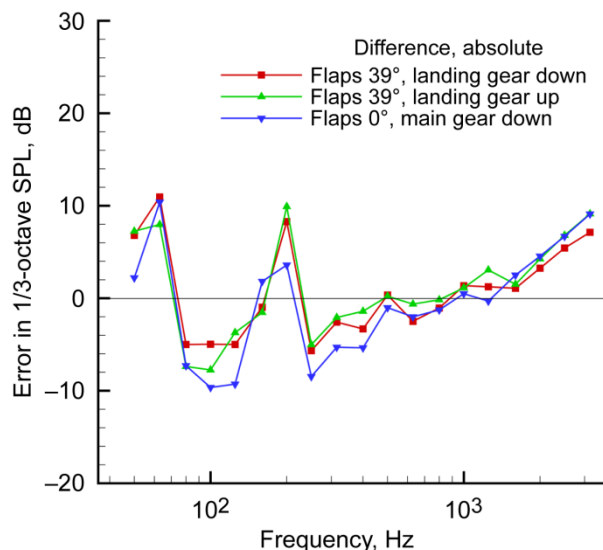


Figure 4.9.—Difference between measured and predicted absolute sound pressure level (SPL) spectra.

To assess the predicted absolute SPLs, a direct comparison between the measured (Figure 4.6) and computed values (Figure 4.7) is attempted. Subtracting the computed levels from the measured data, the differences in SPL are plotted in Figure 4.9 for the three airframe noise configurations. Positive values indicate that the simulated pressures underpredict the measurements, and negative values indicate overprediction. The underprediction and overprediction of the noise is on the order of 10 dB for frequencies below 300 Hz, but the variations become significantly smaller for higher frequencies up to 3 kHz. The trend towards larger errors for frequencies above 3 kHz must be viewed with suspicion due to engine noise and other forms of background noise inherent in the measured data. Nevertheless, the large errors at low to moderate frequencies clearly demonstrate the inadequacies of the present ANOPP airframe noise module to predict the full-scale absolute noise levels. Given the 1- to 2-dB uncertainties in most pole-mounted microphone measurements, predicted pressure levels that are within plus or minus 1 to 2 dB of the measured results would be considered ideal. Certainly, the observed 5- to 10-dB errors of the present assessment are considerably larger and point to the need for improved prediction methods.

Results from the second assessment metric (based on changes relative to the clean configuration) are displayed in Figure 4.10. As before, positive values indicate underprediction and negative values, overprediction of the measured SPLs. Note that the trends are similar to those observed for the absolute level errors (Figure 4.9). The error for the flap at 0°, main gear down configuration shows very large oscillations at 80 and 250 Hz. These extreme levels are caused by subtraction of pressures with very similar magnitudes (see data represented by circles and triangles in Figure 4.6) and have no physical meaning. The curve for the flaps at 39° and gear down configuration (square symbols) shows the least

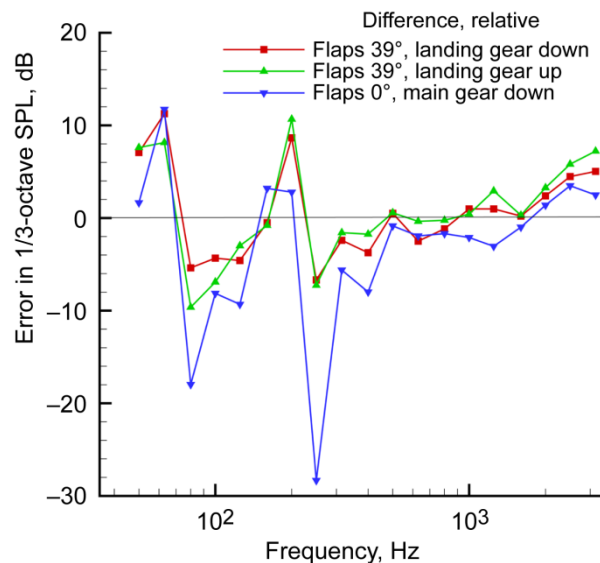


Figure 4.10.—Difference between measured and predicted relative sound pressure level (SPL) spectra.

deviation from the 0-SPL line, indicating better agreement between the computed and measured SPL when all airframe noise sources are included. Once more, the errors in the relative noise levels at high frequencies (above 3 kHz) must be viewed with caution because of the presence of residual engine and high background noise levels. Comparing the results presented in Figure 4.9 and Figure 4.10, it is clear that ANOPP does a good job of predicting the relative SPL or the absolute levels in the mid-frequency range (500 to 2500 Hz). Nevertheless, the ultimate goal of having the capability to predict the SPL within 1 to 2 dB over the entire frequency range of interest eludes us. In this regard, the errors in the relative SPL (Figure 4.10) are still too high.

4.3.4 Recommendations

The large errors in the predicted absolute and relative noise levels observed here are disappointing and point out the inherent risk of using empirically based predictive methods outside the range of the database from which they were originally derived. Fortunately, the overall magnitudes of the predicted changes in noise spectra are, for the most part, of the right order, and differ from the measured changes mostly by ± 8 dB. As indicated repeatedly in this chapter, for improvements in airframe noise prediction to occur, more details regarding the physical processes of noise generation in these complex, highly nonlinear flow fields must be elucidated, using coordinated experimental and computational studies. Empiricism in the predictive tools should be limited to more fundamental levels with the incorporation of configuration-sensitive, local flow-field analyses. The ability to analyze airframe-noise-related flows at such intricate levels will require further investment in the development of advanced experimental and computational methods.

4.4 Flap-Edge Noise Measurement and Prediction

The component-based approach employed by Fink to predict total aircraft noise is now commonly used (Refs. 43, 44, and 50 to 52). Because individual components cannot be flight tested in isolation, difficulties in separating the contributions of all the sources leave some ambiguity when attempting to calibrate models for individual components. Ground-based testing allows components to be tested in isolation under controlled circumstances providing unambiguous data for calibration and model development. However, interactions effects, which are implicitly included in data from flight tests, must be explicitly accounted for if wind tunnel data are used for calibration. Furthermore, the physics in wind tunnels is not always representative of flight. Small-scale models typically result in much lower Reynolds numbers unless pressurized tunnels (Ref. 53) are employed. Very low Reynolds numbers can result in anomalous transition characteristics and thereby affect the flow and radiated noise. Transition strips and grit-covered models are often used to simulate the effects of high-Reynolds-number flow. Although these techniques can be effective, the eventual connection back to flight is important (Ref. 54).

Because wind tunnel testing is being used as a source of data for the development of aircraft noise prediction methods, it is important to include comparisons between ANOPP predictions and acoustic measurements at model scale. Flap-edge noise spectra obtained from a QFF experiment are compared with predicted spectra, using ANOPP's airframe noise modules. The acquisition and processing of the experimental data is described below, followed by predictions and comparisons. Additional information about the QFF can be found in Appendix D.

4.4.1 Test Description

The test model used in the QFF experiment (Ref. 34) was a NACA 63₂-215 main-element airfoil with an attached half-span Fowler flap of 12.2-cm (4.8-in.) chord. The chord and span of the main-element airfoil were 40.6 cm (16 in.) and 91.4 cm (36 in.), respectively. The flap was attached by an adjustable set of "U" brackets to minimize bracket interference with the ideal flap flow field. The model was held in place by vertical plates, which were rigidly mounted to the side-plate supports of the nozzle. The main element angle was set at 16°, which corresponds to a free-field angle of attack of 8.53°. Two flap angles, 29° and 39°, were tested. The relative positions of the main-element trailing edge and the leading edge of the flap are determined by measures of "gap" and "overlap," as defined in Figure 4.11. Normalized with respect to the main-element chord length, the gap and overlap for the 29° flap angle were 0.0227 and 0.0242, respectively. For the 39° flap angle, these parameters were, respectively, 0.0231 and 0.0132.

The far-field acoustics of the model were measured in the QFF using the Small Aperture Directional Array (SADA), which is discussed in Appendix D. The SADA was located 5 ft (1.5 m) from the center of the main element trailing edge, and in

a plane perpendicular to, and centered on, the span of the model. This SADA position corresponds to zero azimuthal angle ($\phi = 0$). The noise measurements were obtained for mean-flow Mach numbers of 0.07, 0.11, and 0.17 and for different flap side edge configurations, with the SADA positioned at 12 azimuthal positions, as shown in Figure 4.12. Note that, given the small QFF phased-array aperture, and thus limited solid collecting angle, "de-correlation" effects in the phased array data at high frequencies are expected to be very limited. The data chosen for comparison to prediction are SADA measurements from Reference 34, obtained for the baseline flap-edge configuration, on the pressure side of the model, at $\phi = 107^\circ$ (Figure 4.12).

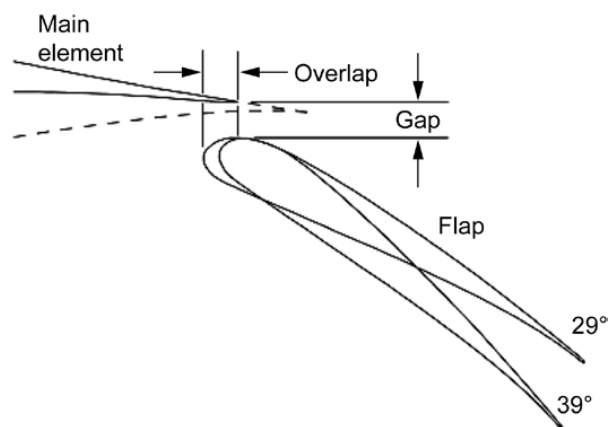


Figure 4.11.—Flap overlap and gap definitions for flap-edge noise test with model airfoil in Quiet Flow Facility (QFF).

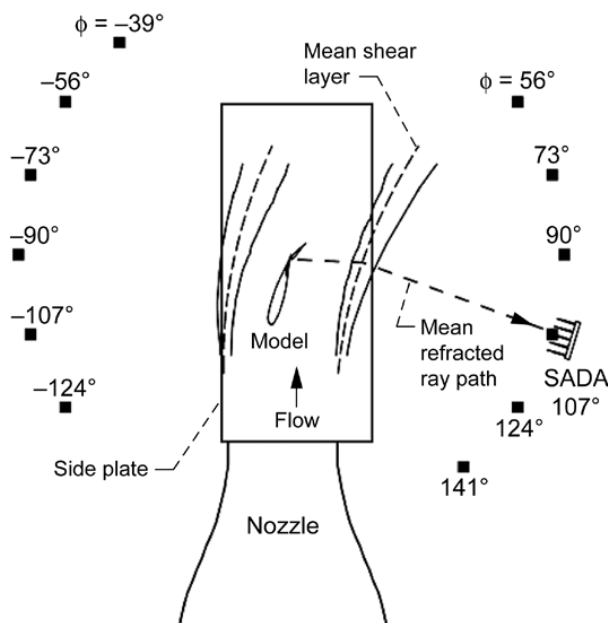


Figure 4.12.—Azimuthal (ϕ) locations of Small Aperture Directional Array (SADA) microphones for far-field tests with model airfoil in Quiet Flow Facility (QFF).

Signals from the array microphones were band-pass filtered over a pass band of 300 to 50 kHz and digitized using a 14-bit transient data recorder. A conventional beamforming approach (Refs. 55 and 56), employing matrices of cross-spectra between the array microphones, was used to electronically “steer” the array to chosen noise source locations. The spatial resolution (or sensing area over noise source regions) was controlled independently of frequency and steering-direction over broad frequency ranges. The array processing accounted for mean amplitude and phase changes due to refracted sound transmission through the shear layer to the individual microphones of the array. For each test case, the cross-spectral matrix had a corresponding background matrix subtracted from it to remove extraneous system noise (measured microphone and sensor noise for zero tunnel flow speed). Spectral data were determined for each narrowband frequency (34.88 Hz resolution bandwidth) of interest. The 1/3-octave band spectra were formed from the narrow-band spectra.

4.4.2 Results and Findings

The 1/3-octave band flap-edge noise spectra obtained for the test conditions listed in Table 4.2 were used for comparison to ANOPP predictions. Predicted spectra were obtained with the airframe noise module in ANOPP that implements Fink’s flap-noise model (Refs. 32 and 42). As ANOPP was initially developed to calculate noise levels for an aircraft in flight, relative to a stationary observer on the ground, Doppler frequency shifting is included as a default program condition. However, such phenomena do not occur during a typical wind tunnel measurement, where the model and microphone positions are in the same reference frame. Therefore, in order to appropriately compare ANOPP results with test measurements, the effects of Doppler shifting are excluded from the prediction methodology. For instance, the Strouhal number for the present test case is $St = fA_f / M_\infty a_\infty b_f$ (subscript f denotes flap), which does not include the Doppler factor, $1 - M_\infty \cos \theta$ (Eq. (4.17) in Appendix B). Note that the flap chord is the characteristic length in this case, and is determined by the ratio, A_f/b_f , of the surface area to the span.

TABLE 4.2.—TRAILING-EDGE FLAP NOISE TEST:
TEST CONDITIONS

[See Figure 4.11 and Figure 4.12.]

Flap model configuration tested.....	Flat edge flap (baseline)
Flap chord, cm (ft)	12.2 (0.4)
Flap span, cm (ft)	45.7 (1.5)
Flap deflection angles, deg.....	29, 39
Main element angle of attack, deg ^a	8.53
Mach numbers.....	0.07, 0.11, 0.17
Distance from flap side edge to SADA, m (ft) ^b	1.52 (5)
SADA elevation angle (emission angle), deg ^b	107
SADA Azimuthal angle (emission angle), deg ^b	0

^aAfter wind tunnel correction.

^bSADA: Small Aperture Directional Array in Quiet Flow Facility (QFF).

The trailing-edge flap noise test characteristic dimensions listed in Table 4.3 were used as input to Fink’s trailing-edge flap model. Note that the observer polar directivity angle (θ) that is required as input to this module, is defined with respect to the wing axis and measured from the wing leading edge. Hence, the SADA elevation angle ($\phi = 107^\circ$) in the QFF experiment corresponds to a polar directivity angle of 81.53° in the ANOPP module.

TABLE 4.3.—TRAILING-EDGE FLAP NOISE TEST:
CHARACTERISTIC DIMENSIONS

Flap area, cm ² (ft ²)	557.4 (0.6)
Flap span, cm (ft)	45.7 (1.5)
Flap deflection angles, deg	29, 39
Mach numbers	0.07, 0.11, 0.17
Distance from source to observer, m (ft)	1.52 (5)
Polar directivity angle, θ , deg	81.53
Azimuthal directivity angle, ϕ , deg	0
Number of slots for trailing-edge flap	1

In Figure 4.13 the predicted spectra are compared with the QFF data. It is seen that the SPLs are very well predicted over a broad frequency range for the 39° flap, while the levels are overpredicted for most of the frequency range for the 29° flap case. It is also observed that agreement between the predictions and experimental data improves with decreasing Mach number. The discrepancy (Δ dB) between the experimental and predicted spectra is plotted in Figure 4.14, for the 39° flap and a Mach number of 0.17. For this case, which is most representative of an aircraft flap during approach conditions, the Δ dB is less than 4 dB from 1.5 to 25 kHz. Below 1.5 kHz, the discrepancy rises to a maximum of 6.3 dB.

A sensitivity study was performed over a limited set of parameters for the 39° flap, at a Mach number of 0.17. The Mach number was varied ± 1 percent (maximum error in the Mach number setting that could have occurred in the QFF experiment) and the wing angle of attack was varied by ± 5 percent (after wind tunnel correction was applied). Variations in the wing angle of attack only meant a change of $\pm 0.42^\circ$ of the polar directivity angle θ , because the wing angle of attack is not a parameter used in the Fink method to define the acoustic amplitude and spectral shape. The effect from these parameter variations on the SPLs is shown as error bars in Figure 4.13.

The effect of flap deflection angle on the predicted spectral level was also examined. It was found that the Fink method is relatively insensitive to changes in flap deflection angle. As shown in Figure 4.13, the experimental data indicate a difference in noise level, between the 29° and 39° flap of less than 4 dB below 1.5 kHz (for the three speeds tested). Above 2 kHz, the difference in noise level rises up to 8 dB. Additional predictions were performed for a 19° and a 49° flap deflection angle. The results indicated that increasing the flap deflection angle leads to a small increase in noise level that is uniform across the frequency range of interest (0.05 to 40 kHz). Thus,

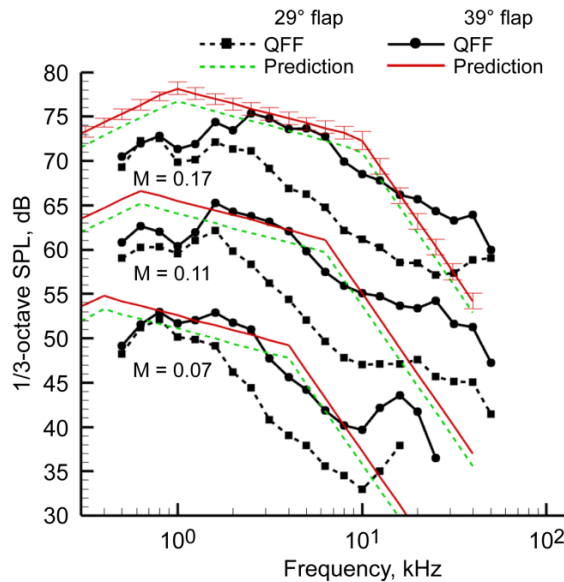


Figure 4.13.—Flap-edge noise sound pressure level (SPL) spectra at different Mach numbers M and deflection angles. Comparison of ANOPP predictions using Fink's method and measurements from Quiet Flow Facility (QFF) experiments.

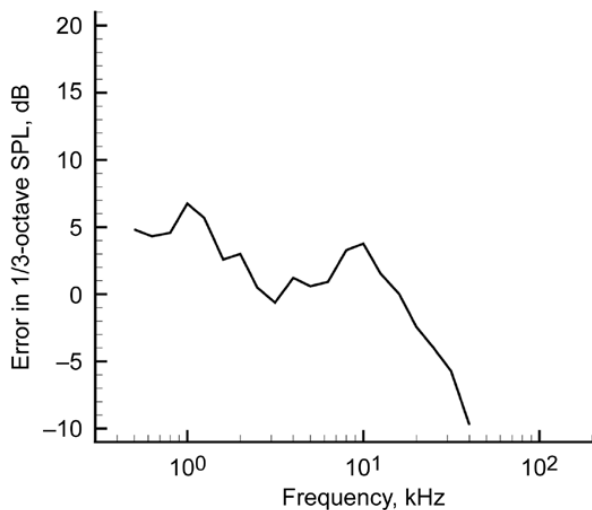


Figure 4.14.—Discrepancy in airframe flap-edge noise sound pressure level (SPL) spectrum at Mach number $M = 0.17$ and 39° flap between ANOPP predictions using Fink's method and measurements from Quiet Flow Facility (QFF) experiments.

increasing the flap deflection angle from 19° to 49° , in 10° increments, results in successive increases in noise level of 3 dB (19° to 29°), 1.5 dB (29° to 39°), and 0.5 dB (39° to 49°).

4.4.3 Metrics and Assessment

A limited study was conducted to determine the repeatability of SPLs derived from beamform analyses of phased-

array data acquired in 1997 for a flap noise model in the QFF (the last time such repeat data were available in the facility). A series of 16 repeat sets of phased-array data acquired for a baseline flat side-edge flap were processed using standard frequency-domain, delay-and-sum beamforming across a range of 1/3-octave center frequencies spanning 315 to 40 000 Hz. These data sets represent repeat testing for a flap deflection of 39° and a wind tunnel Mach number of 0.17. Otherwise, relevant test conditions and array orientations for this repeatability study are identical to those in Table 4.2.

The results of the analysis are displayed in Table 4.4 where the peak SPL value observed in the beamforming presentation (centered on the flap side edge) for each frequency trial is tabulated. Also shown is the percent error in the peak of the pressure squared for each frequency. This error was derived from the standard deviation of the squared pressures obtained from measurements for each trial. The maximum observed repeatability error was 4.36 percent for the 25 kHz 1/3-octave frequency band with a typical error of approximately 2 to 3 percent for the majority of the frequency bands. Therefore, a visual representation of the variation in the experimental spectra shown in Figure 4.13 would be within the displayed symbol sizes.

Note that while the repeatability analysis was conducted using standard beamforming, it is reasonable to assume that an analysis using DAMAS deconvolution (Ref. 57) would yield similar results. When applied to leading- and trailing-edge noise sources, DAMAS was shown to give almost identical integrated SPLs across a wide frequency range when compared with results from beamform analyses. Given the duality between the two processing methods, it is expected that the repeatability errors would be similar. Finally, the present study only addresses simple repeatability of measurements. Topics for further research would include the identification of bias errors and a theoretical analysis involving a formal propagation of errors.

4.4.4 Recommendations

The Fink method was found to follow Strouhal scaling and, hence, allows for noise prediction of model-scale-size flaps. The predictions compared well with the experimental model-scale data for the higher flap deflection angle tested. The method was found, however, to be relatively insensitive to change in flap deflection angle, and thus overpredicted the noise level for the lower flap deflection angle tested. It is recommended that this ANOPP flap-noise prediction model be improved, to the extent possible, using the available database of model-scale measurements. One must keep in mind, however, that this database was generated from experiments at a relatively low Reynolds number and on a geometry that may be only partially representative of that encountered in engineering practice. While there are experimental databases that suggest the magnitude of the effects of these issues, they are judged inadequate in terms of absolute noise level measurements to be useful in this initial assessment.

TABLE 4.4.—EXPERIMENTAL REPEATABILITY ANALYSIS OF SOUND PRESSURE LEVELS (IN DECIBELS) OBSERVED IN FLAP-EDGE BEAMFORMING

Trial	1/3-Octave Frequency Band, Hz										
	315	400	500	630	800	1000	1250	1600	2000	2500	3150
1	74.53	73.79	72.64	73.63	74.08	71.69	72.25	74.39	73.26	74.70	74.17
2	74.27	73.79	72.63	73.43	73.79	71.60	72.10	74.39	73.36	74.67	74.06
3	74.70	73.99	72.99	73.28	73.91	71.40	72.21	74.22	73.18	74.59	74.12
4	74.25	73.69	72.79	73.32	73.86	71.42	72.09	74.27	73.16	74.60	74.05
5	74.28	73.62	72.50	73.36	73.72	71.69	72.03	74.02	73.38	74.59	74.10
6	74.08	73.63	72.57	73.37	73.76	71.36	71.86	74.15	73.16	74.40	73.98
7	74.46	73.79	72.42	73.09	73.91	71.65	71.87	74.26	73.20	74.63	74.16
8	74.03	73.30	72.41	73.30	73.90	71.45	72.12	74.17	73.00	74.57	73.98
9	74.18	73.72	72.31	73.20	73.84	71.52	72.24	74.13	73.20	74.72	74.05
10	74.23	73.63	72.69	73.28	73.84	71.56	72.08	74.16	73.29	74.56	74.19
11	74.19	73.68	72.60	73.28	73.82	71.47	72.06	73.94	73.19	74.55	74.15
12	74.21	73.62	72.55	73.37	73.95	71.54	72.08	74.27	73.37	74.48	74.16
13	74.11	73.44	72.27	73.34	73.78	71.46	72.02	74.31	73.20	74.51	74.16
14	74.26	73.65	72.66	73.14	73.62	71.40	71.99	74.12	73.17	74.45	73.98
15	73.99	73.48	72.40	73.11	73.64	71.35	71.99	74.08	73.16	74.59	74.09
16	74.16	73.67	72.66	73.21	73.93	71.45	71.83	74.18	73.13	74.51	73.89
Mean	74.24	73.66	72.57	73.29	73.83	71.50	72.05	74.19	73.21	74.57	74.08
STDV ^a	0.18	0.16	0.18	0.13	0.12	0.11	0.13	0.12	0.10	0.09	0.09
% Error ^b	4.32	3.63	4.29	3.09	2.72	2.59	2.88	2.82	2.28	1.99	2.01

Trial	1/3-Octave Frequency Band, Hz										
	4000	5000	6300	8000	10 000	12 500	16 000	20 000	25 000	31 500	40 000
1	73.21	73.91	73.72	70.18	68.68	67.50	65.57	65.17	64.37	63.87	65.78
2	73.13	73.81	73.64	70.19	68.60	67.34	65.41	64.97	64.08	63.63	65.50
3	73.21	73.92	73.71	70.21	68.63	67.34	65.48	65.09	64.22	63.74	65.60
4	73.12	73.79	73.64	70.01	68.42	67.25	65.31	64.92	64.00	63.55	65.42
5	73.04	73.73	73.54	70.04	68.43	67.17	65.31	64.89	64.03	63.58	65.49
6	73.06	73.79	73.53	69.97	68.47	67.21	65.29	64.87	63.99	63.53	65.40
7	73.09	73.81	73.58	70.04	68.46	67.20	65.33	64.88	63.95	63.55	65.40
8	73.09	73.77	73.55	70.04	68.42	67.27	65.36	64.97	64.03	63.57	65.38
9	73.22	73.81	73.76	70.24	68.61	67.37	65.50	65.11	64.21	63.79	65.57
10	73.12	73.90	73.76	70.13	68.52	67.29	65.36	64.97	64.09	63.60	65.39
11	73.11	73.64	73.58	70.09	68.43	67.20	65.32	64.85	64.00	63.47	65.34
12	73.15	73.66	73.55	70.03	68.49	67.20	65.27	64.86	63.92	63.47	65.35
13	73.07	73.69	73.51	69.93	68.35	67.12	65.20	64.74	63.85	63.36	65.28
14	72.94	73.65	73.48	69.85	68.33	66.99	64.99	64.48	63.59	63.18	65.07
15	73.00	73.72	73.47	69.92	68.32	67.01	65.21	64.70	63.80	63.35	65.24
16	73.09	73.66	73.49	69.81	68.38	67.08	65.02	64.61	63.76	63.34	65.18
Mean	73.10	73.77	73.59	70.04	68.47	67.22	65.31	64.88	63.99	63.54	65.40
STDV ^a	0.08	0.09	0.10	0.13	0.11	0.13	0.15	0.18	0.19	0.18	0.17
% Error ^b	1.73	2.15	2.30	2.93	2.52	3.08	3.52	4.15	4.36	4.13	3.93

^aSTDV is standard deviation of the pressure squared values expressed in decibels.

^bThe % Error is 100 times the standard deviation in the pressure squared divided by the mean pressure squared.

4.5 Aeroacoustic Measurement and Prediction for Boeing 777 Landing Gear Model

While most often used to predict the noise for a vehicle in flight, ANOPP can also be used to study a noise source associated with an individual component, such as an aircraft landing gear. In this mode, the sound is propagated to stationary observers located on a spherical surface that is centered at the source. To compare ANOPP predicted noise levels with wind tunnel data, when the source and microphone locations are fixed relative to each other, the effects of Doppler frequency shifting were removed by modifying the code. For example, the Strouhal number for the present test cases is $St = fd/M_\infty a_\infty$ which excludes the Doppler factor, $1 - M_\infty \cos \theta$ (Eq. (4.23), Appendix B). The characteristic length d is the wheel diameter.

To facilitate the assessment of ANOPP's ability to predict landing gear noise, an extensive experimental study was conducted using the Medium Aperture Directional Array (MADA) in the QFF to acquire detailed noise spectra and directivity data for a high-fidelity, 6.3-percent-scale Boeing 777 main landing gear. The MADA and QFF are discussed in more detail in Appendix D. Straightforward individual microphone processing and DAMAS array processing were employed to compile unique flyover and sideline directivity databases for a range of free-stream Mach numbers that are relevant to airport approach conditions. Comprehensive corrections were applied to the test data to account for shear layer ray path and amplitude variations. This allowed proper beamforming at different measurement orientations, as well as directivity presentations in free-field emission coordinates. For the purposes of the assessment, the experimental spectral and directivity data were compared with predicted noise spectra and contours using the two ANOPP airframe noise modules. Details of the experimental data acquisition and processing and comparison with the ANOPP predicted noise follow.

4.5.1 Discussion of Experimental Data

The test model used for the assessment was a 6.3-percent-scale high-fidelity Boeing 777 main gear assembly that was previously tested as part of an overall semi-span model (Ref. 16). The high-complexity gear was composed of a six-wheel bogie and a generally faithful representation of full-scale strut, oleo, braking, and hydraulic hardware. The exact configuration of the model used in the assessment is shown in Figure 4.15. The major component sizes for the model are listed in Table 4.5. The model was fabricated with load-bearing metal components and detailed stereo lithography components. Standard electrical wiring and pressure tubing (ranging from 1.2 to 2.0 mm, or 0.05 to 0.08 in.) were used to roughly simulate the hydraulic lines and cables. These were generally a little larger than scale. This is expected to have shifted the high-frequency content of the scale-model noise down slightly. The attached door for the baseline

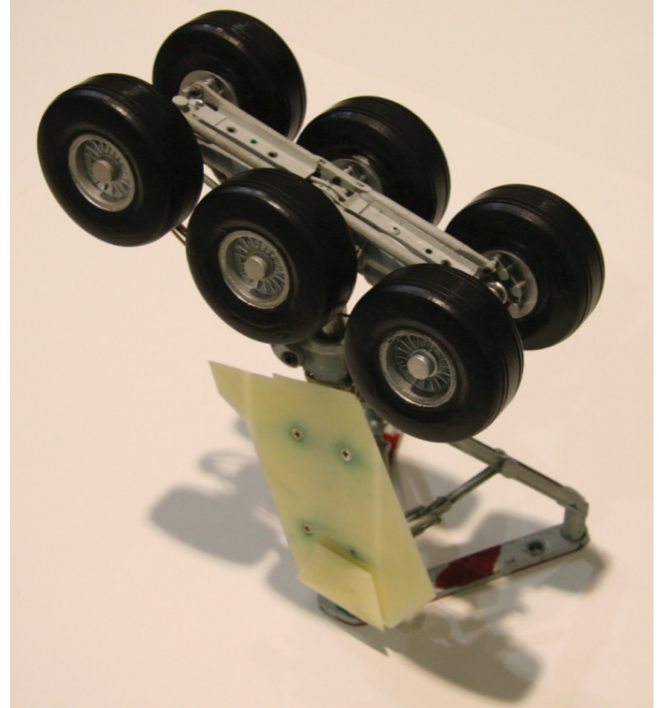


Figure 4.15.—Boeing 777 main landing gear model. Baseline configuration, with door.

TABLE 4.5.—MAJOR COMPONENTS OF 6.3-PERCENT-SCALE BOEING 777 LANDING GEAR

Model height, cm (in.)	30.5 (12)
Side-to-side width, cm (in.)	12.7 (5)
Length of oleo, cm (in.)	21.6 (8.5)
Diameter of oleo, cm (in.)	2.5 (1)
Strut component widths, cm (in.)	1.3 (0.5)
Wheel width, cm (in.)	3.2 (1.25)
Wheel diameter, cm (in.)	8.3 (3.25)
Truck length, cm (in.)	20.3 (8)

configuration in Figure 4.15 had approximate dimensions of 10.2 by 12.7 cm (4 by 5 in.) and a thickness of 3 mm (1/8 in.).

Figure 4.16 shows the model mounted to a treated portion of one of the QFF side-plates. The intent of the treatment was to create an acoustically compliant surface near the model while maintaining a flat boundary for the flow. The surface was created by stretching a thin Kevlar (DuPont) fabric over an open-backed ribbed frame, thus reducing acoustic surface reflections. Figure 4.16 represents the set-up for model “sideline” measurements with the boom-mounted MADA. For model “flyover” measurements, a removable 60-cm- (23.5-in.-) wide side-plate was especially constructed and mounted along a 0.9-m (3-ft) side edge of the nozzle, as illustrated in Figure 4.17. This setup (Figure 4.17) enables “flyover” measurements, with the array positioned “underneath” the landing gear model. The flyover side-plate was correspondingly covered with Kevlar fabric over an open-backed ribbed frame.



Figure 4.16.—Boeing 777 main gear model assembly mounted in Quiet Flow Facility (QFF) for lateral “sideline” measurements by Medium Aperture Directional Array (MADA) microphones.

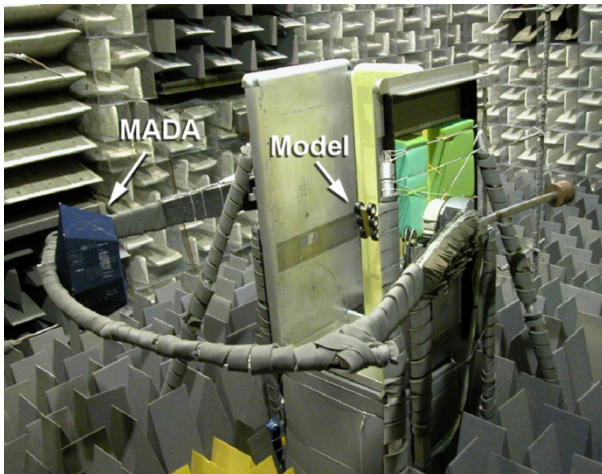


Figure 4.17.—Boeing 777 main gear model assembly mounted in Quiet Flow Facility (QFF) for “flyover” measurements by Medium Aperture Directional Array (MADA) microphones.

For either orientation of the landing gear model, the coordinate system shown in Figure 4.18 was employed during analysis of the directivity data. The reference center of the landing gear was defined to be the center of the truck assembly. The coordinate system, defining the x-axis as being aligned with the direction of flight and the z-axis directed under the flight path, corresponds to the coordinate system used in ANOPP. Using this coordinate system, observer locations can be specified by an observer distance R_e and two angles with θ_e denoting the polar flyover angle and ϕ_e denoting the azimuthal sideline angle. The “e” subscript indicates that these are emission coordinates determined from

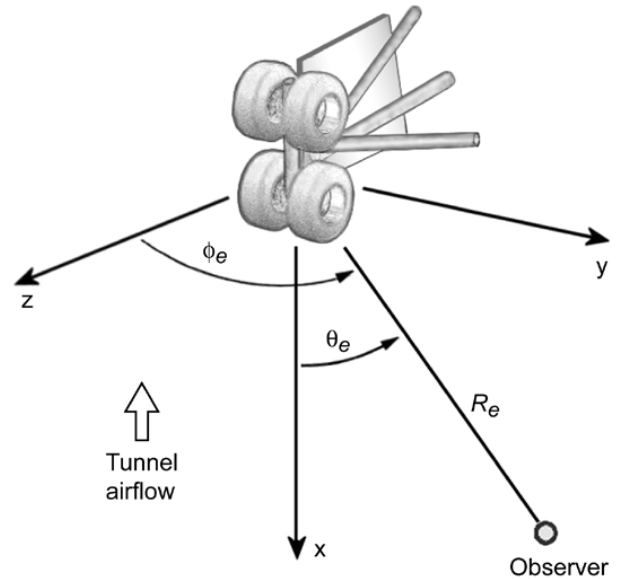


Figure 4.18.—Quiet Flow Facility (QFF) coordinates system for landing gear noise measurements. R_e is source-to-observer distance, θ_e is polar emission angle, and ϕ_e is azimuthal emission angle.

tunnel, array, and landing gear mounting geometries, along with corresponding shear-layer acoustic refraction corrections. Reference 36 reports an extensive analysis used to derive equivalent emission coordinates in order to provide measurements in a coordinate system that can be used for free-field correlations.

Signals from the array microphones were band-pass filtered over a pass band of 300 Hz to 50 kHz and digitized using a 14-bit transient data recorder. Postprocessing of the acquired array data included single microphone auto-spectrum analysis (using four microphones from the MADA identified in Appendix D and Ref. 36), conventional frequency-domain delay and sum beamforming, and DAMAS deconvolution. The processing accounted for mean amplitude and phase changes due to refracted sound transmission through the shear layer to the individual MADA microphones. A key feature of the beamforming and DAMAS processing was that the spatial resolution was controlled independently of steering frequency and direction over a broad frequency range.

The test matrix for the assessment is summarized in Table 4.6. A baseline landing gear configuration was employed with the side-mounted door and all detail hardware attached. The Mach numbers tested ranged from 0.11 to 0.17, corresponding to a Reynolds-number range of 2.1×10^5 to 33×10^5 , based on wheel diameter. Although the nominal Mach number for a landing aircraft is around 0.2, the main landing gear experiences a slightly lower flow speed due to the circulation around the wing and flaps. Therefore, the tested Mach numbers are similar to what would be experienced by landing gear in flight. However, the test Reynolds numbers are only 6.3 percent of what would be experienced in flight.

Finally, a range of polar and azimuthal angles was chosen for acquisition such that a sizeable portion of the hemispherical directivity of the gear could be obtained and compared with ANOPP predictions.

TABLE 4.6.—TEST MATRIX FOR BOEING 777
LANDING GEAR NOISE STUDY

Model configuration tested	Baseline (with side door)
Model mounting, views.....	Flyover, sideline
Mach numbers.....	0.11, 0.13, 0.15, 0.17
Reynold's numbers (based on wheel diameter).....	2.1×10^5 to 3.3×10^5
Polar angular range (emission angles), deg	55 to 135
Azimuthal angular range (emission angles), deg.....	-106 to 94

4.5.2 Results and Findings

The Boeing prediction method had been developed using full-scale landing gear noise data, whereas Fink's method incorporated both model- and full-scale data during its development to define the noise spectral shape and amplitude. Note that difficulties in the matching of model- and full-scale landing-gear data have been encountered by other researchers (Refs. 41 and 58). However, the current comparisons between the predictions and the 6.3-percent-scale model data do not exhibit similar discrepancies. The Fink method (Refs. 32 and 42) is a pure Strouhal scaling approach that allows prediction of arbitrary landing gear size. The Boeing-Guo method (developed by Guo, Ref. 44) is also largely based on a

Strouhal scaling approach. However, the use of “complexity factors” to ensure agreement with full-scale landing gear data, and the inclusion of a narrowband (versus 1/3 octaves) spectrum function in the source definition, prevent the prediction of arbitrary landing gear sizes. Therefore, a scaling method was developed to correctly compare Guo's full-scale landing gear predictions with model-scale data. This scaling method is described in Reference 37.

The inputs to both prediction methods are extracted from the description of a full-scale Boeing 777 main landing gear provided in Reference 59, and given here in Table 4.7 and Table 4.8. Fink's method only requires as input the number of wheels and their diameter, the length of the main strut, and the free-stream Mach number. The Boeing-Guo method, which accounts for significantly more geometric detail, requires the entries in both tables as input.

TABLE 4.7.—BOEING 777 MAIN LANDING GEAR
PREDICTION INPUT PARAMETERS^a

Free-stream Mach number	0.17
Source-to-observer distance, m (ft).....	24.3 (79.5)
Angle of attack, deg	0.0
Wheel track angle, deg.....	13.0
Number of tires	6
Tire diameter, cm (in.)	127.0 (50.0)
Tire width, cm (in.).....	50.8 (20.0)

^aFull scale (Ref. 59).

TABLE 4.8.—BOEING 777 MAIN LANDING
GEAR COMPONENT DIMENSIONS^a

Main gear components	Length, cm (in.)	Diameter or width, cm (in.)	Thickness, cm (in.)
Shock strut	388.6 (153.0)	40.6 (16.0)	-----
Upper hydraulic rod	76.2 (30.0)	30.5 (12.0)	-----
Lower hydraulic rod	88.9 (35.0)	7.6 (3.0)	-----
Axle	266.7 (105.0)	21.6 (8.5)	-----
Axle connection	304.8 (120.0)	33.0 (13.0)	-----
Front hydraulic rod	137.2 (54.0)	19.3 (7.6)	-----
Lower front side bar	127.0 (50.0)	17.8 (7.0)	15.2 (6.0)
Lower aft side bar	127.0 (50.0)	17.8 (7.0)	15.2 (6.0)
Upper front side bar	137.2 (54.0)	20.3 (8.0)	15.2 (6.0)
Upper aft side bar	137.2 (54.0)	20.3 (8.0)	15.2 (6.0)
Horizontal front side bar	121.9 (48.0)	10.2 (4.0)	10.2(4.0)
Horizontal aft side bar	109.2 (43.0)	10.2 (4.0)	10.2 (4.0)
Upper torque bar	147.3 (58.0)	12.7 (5.0)	7.6 (3.0)
Lower torque bar	162.6 (64.0)	12.7 (5.0)	7.6 (3.0)
Rear wheel steering	63.5 (25.0)	6.4 (2.5)	-----
Rear wheel hydraulic	50.8 (20.0)	12.7 (5.0)	-----

^aFull scale (Ref. 59).

Figure 4.19 compares “scaled” Boeing-Guo predictions with experimental measurement at two different observer locations; Figure 4.19(a) is for the flyover position and Figure 4.19(b) is for the forward-sideline position. The total scaled spectrum and its three separate frequency component spectra are shown. At both locations, the high-frequency component overpredicts by about 2 to 5 dB at frequencies beyond 10 kHz. At frequencies less than 1250 Hz, the predictions underpredict the data. The peak in the total spectrum is around 5 kHz, but the curve is relatively flat between 1 and 10 kHz. The variation in the peaks of the low-, mid-, and high-frequency components produces the extended flat portion of the total, which is not borne out by the experimental data. At the forward-sideline location (Figure 4.19(b)) the overall spectrum is higher than at flyover location (Figure 4.19(a)), with the low- and mid-frequency components responsible for most of the increase. As the azimuthal angle increases, the contribution of the low- and mid-frequency components increases. For both the flyover and forward-sideline locations, the high-frequency component is responsible for the overprediction beyond 5 kHz.

Figure 4.20 is similar to Figure 4.19, but the predictions are from the Fink method. In Figure 4.20(a), at the flyover location, the predictions compare reasonably well over the full frequency range, but the high frequencies are overpredicted by 1 to 3 dB. At this observer location, the wheel component totally dominates the predictions. In contrast, the component breakdown from the Guo method in Figure 4.19(a) is relatively balanced. Clearly, the breakdown of at least one of the methods does not correspond with the actual physics. At the forward-sideline location shown in Figure 4.20(b), the prediction is too low beyond 5 kHz and up to 6 dB too high for lower frequencies. Between the flyover and forward-sideline locations, the contribution of the wheels is nearly identical. The increase in the spectrum is achieved by a dramatic increase in the strut component (namely due to the directivity function), and most of the increase is at low frequency.

The Fink and scaled Boeing-Guo predictions are compared with noise measurements for a range of azimuthal directivity angles in Figure 4.21. Both methods assume azimuthal symmetry and thus produce the same results at positive and negative azimuthal angles, as indicated in the figures. Note that both prediction methods are based on data from landing gear that included a door, as does the scale model tested. Measured spectra for both the positive and negative azimuthal angles show the degree of asymmetry of the noise for the model. At $\phi_e = -59.1^\circ$ for the observer on the door side, the noise is lower in level compared with that on the side opposite the door at $\phi_e = -57.8^\circ$, and the high-frequency levels are similar to those at the flyover location $\phi_e = -1.0^\circ$. The door and wheels appear to be responsible for 3 to 5 dB of shielding at high frequencies. Neither the Guo nor Fink model predicts this shielding effect.

More details regarding azimuthal directivity and the effect of the door are found in Reference 36.

In Figure 4.22, the Fink and “scaled” Boeing-Guo predictions are compared with measurements for a range of flyover polar angles. The measured spectral shape is quite similar for the three angles. Although both the Fink and Guo predictions for the three angles are also similar in shape, the Fink predictions are in better overall agreement with the measurements. The measurements show a reduction of 5 dB between $\theta_e = 56.0^\circ$ and $\theta_e = 87.1^\circ$, which is also observed in the Boeing-Guo predictions. However, the amplitude of the Boeing-Guo predictions is around 5 dB too high at higher frequencies. Almost no change is observed in the Fink predictions for these angles, but a reduction of around 3 dB is observed between $\theta_e = 87.1^\circ$ and $\theta_e = 122.1^\circ$. At low frequencies, the experimental data shows a similar decrease, but almost no change at higher frequencies. Neither model appears to adequately model the polar variation in amplitude, which is at least partially caused by convective amplification.

4.5.3 Sensitivity Study

The sensitivity of the Boeing-Guo and Fink landing-gear noise predictions to the Mach number and angle of attack was studied for the case with a nominal 0.17 Mach number. The observer for this sensitivity study was located at polar and azimuthal directivity angles, $\theta_e = 87.1^\circ$ and $\phi_e = -1.0^\circ$, respectively. The Mach number was varied by ± 1 percent (equivalent to the maximum Mach number error that could have occurred in the QFF experiment) about the mean value of 0.17. The landing gear angle of attack was varied by ± 5 percent about the mean value of 13° . Only the Mach number sensitivity was considered for the Fink landing-gear noise model, as this model does not account for the angle of attack.

The effects of Mach number on the predicted levels for the Fink and Boeing-Guo methods were less than 0.3 and 0.4 dB, respectively, at all frequencies. The smallest differences were observed at the lower frequencies (on the order of 0.1 dB) and increased to a maximum at the higher frequencies. For the Boeing-Guo method, the level variations due to changes in the angle of attack were about ± 0.1 dB at all frequencies. The combined (maximum) effects of Mach number and landing gear angle of attack for the Boeing-Guo method are shown in Figure 4.23. The variation in levels ranged from ± 0.3 dB at the lower frequencies to about ± 0.45 dB at the highest frequency. The two semi-empirical models follow expected V_∞^6 trends with respect to changes in Mach number, and these changes are substantial for just a 1-percent variation. The Mach number variation across the face of the gear is likely to be much larger than 1 percent for a gear mounted on a wing and experiencing flight conditions. Hence, accounting for this variation could significantly improve the ability to predict flight articles.

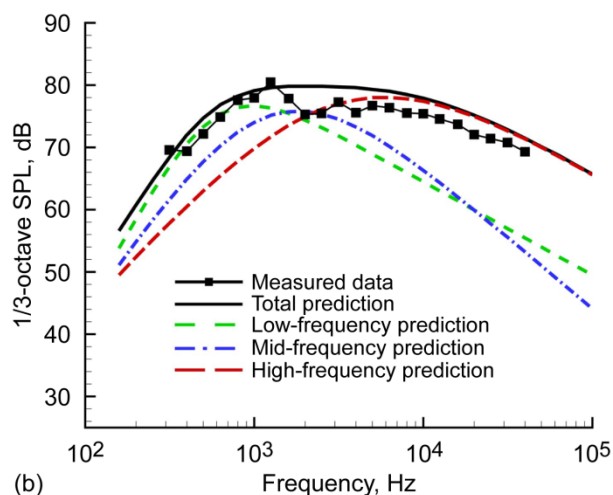
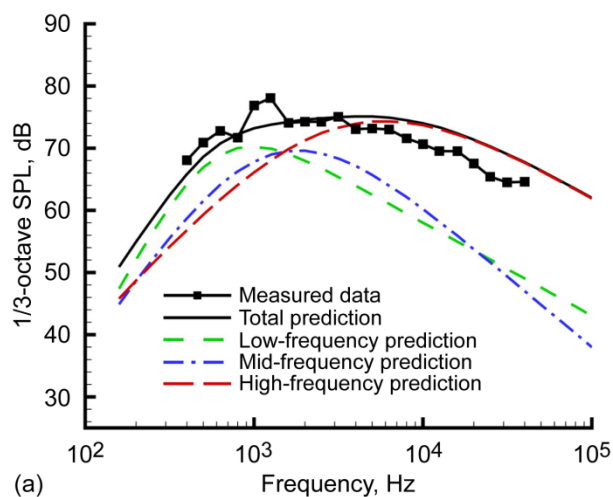


Figure 4.19.—Sound pressure level (SPL) of landing gear model. Comparison of measured spectrum and total scaled (Ref. 37) ANOPP predicted spectrum with its three separate frequency component spectra using Boeing-Guo method for Mach number 0.17 at two observer locations (see Figure 4.18). (a) Flyover position, $\theta_e = 87.1^\circ$ and $\phi_e = 1.0^\circ$. (b) Forward-sideline position, $\theta_e = 59.3^\circ$ and $\phi_e = 5.17^\circ$.

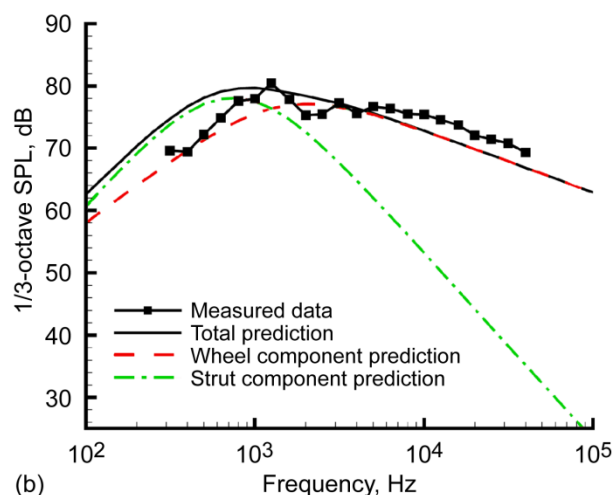
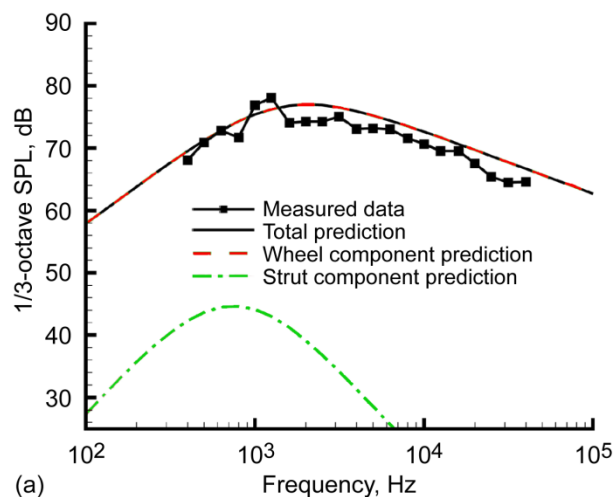


Figure 4.20.—Sound pressure level (SPL) of landing gear model. Comparison of measured spectrum and total ANOPP predicted spectrum with its separate component spectra using Fink method for Mach number 0.17 at two observer locations (see Figure 4.18). (a) Flyover position, $\theta_e = 87.1^\circ$ and $\phi_e = 1.0^\circ$. (b) Forward-sideline position, $\theta_e = 59.3^\circ$ and $\phi_e = 5.17^\circ$.

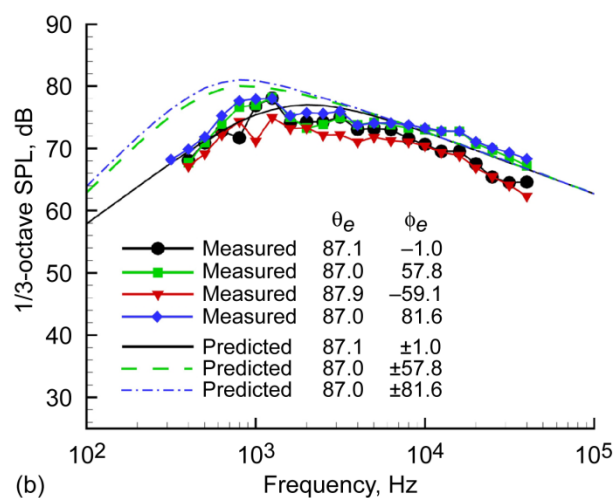
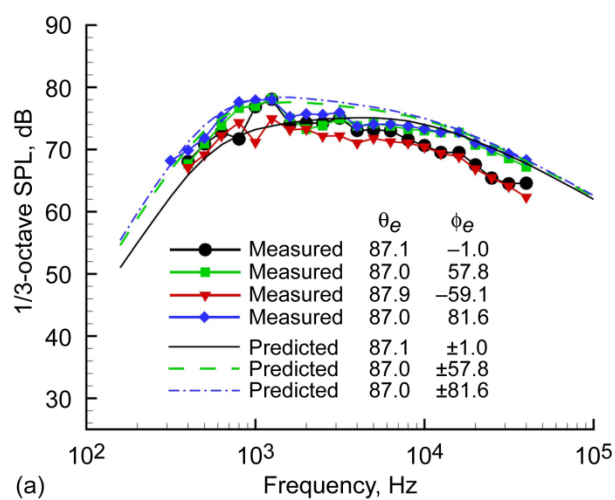


Figure 4.21.—Sound pressure level (SPL) of landing gear model for Mach number 0.17 and given polar angle at different azimuthal angles (see Figure 4.18). (a) Comparison of measured spectra and total scaled (Ref. 37) ANOPP-predicted spectra using Boeing-Guo method. (b) Comparison of measured spectra and total ANOPP-predicted spectra using Fink method.

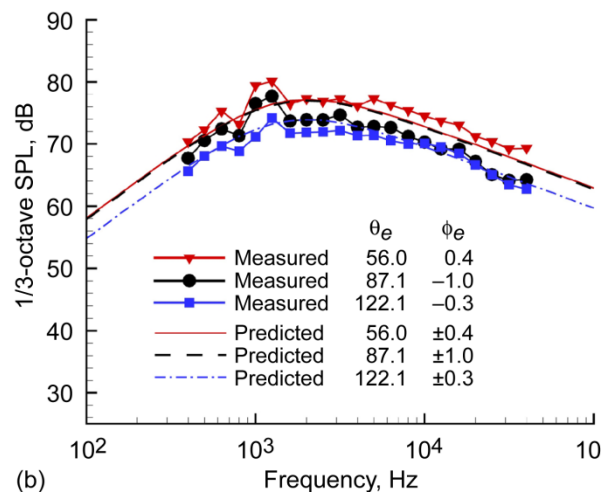
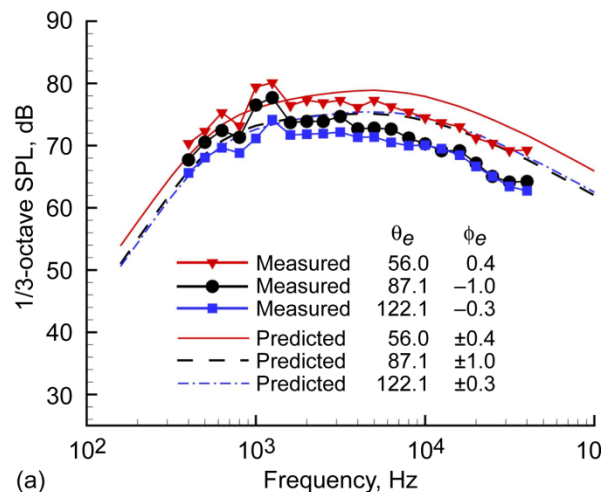


Figure 4.22.—Sound pressure level (SPL) of landing gear model for Mach number 0.17 and given azimuthal angle at different polar angles (see Figure 4.18). (a) Comparison of measured spectra and total scaled (Ref. 37) ANOPP-predicted spectra using Boeing-Guo method. (b) Comparison of measured spectra and total ANOPP-predicted spectra using Fink method.

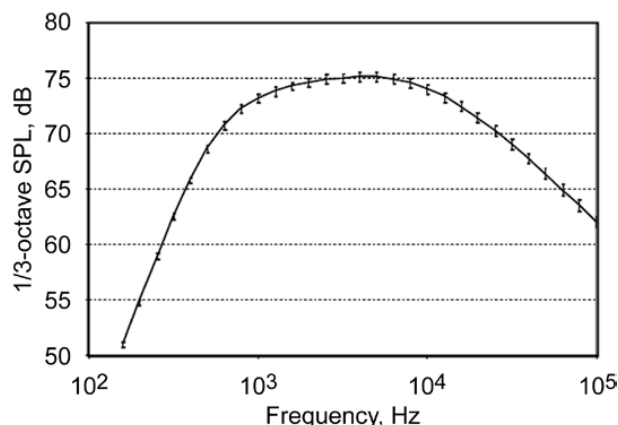


Figure 4.23.—Boeing-Guo method: Combined effects for variation in Mach number and landing gear angle of attack.

4.5.4 Recommendations

NASA's ANOPP offers two empirically based methods to predict landing gear noise: the Fink method and the Boeing-Guo method. The Boeing-Guo method was developed almost exclusively using full-scale landing gear data. The Fink method was developed using both model- and full-scale data. Both methods have previously been shown to compare well with full-scale noise data. Application of these methods to a model-scale landing gear was investigated by comparing predictions from each method with measurements for a high-fidelity, 6.3-percent-scale Boeing 777 main landing gear. The Fink method was found to follow Strouhal scaling and, hence, employed the scale model geometry as input. The Boeing-Guo method was found not to strictly follow Strouhal scaling and hence could not employ the scale model geometry as input. Hence, full-scale landing gear geometry was used as input to the Guo method, and the predicted results were then scaled to represent model-scale noise. Without this additional scaling, the Guo method cannot be used to compare with model-scale data. In this respect, Fink's method is more general.

The measured polar and azimuthal directivity spectra reveal distinctive directivity patterns, with higher levels of noise directed forward and away from the door side of the landing gear. The Fink and "scaled" Boeing-Guo predictions show good comparisons for flyover polar angles and fair comparisons for overall directivity, particularly at the larger azimuthal angles. These comparisons suggest that noise measured for high-fidelity, scale-model landing gear is representative of that found for full-scale landing gear, as the prediction methods were developed and compared well with full-scale data. It is recommended that both ANOPP prediction methods be improved using the newly available extensive database of model-scale noise measurements. One obvious area of needed improvement lies in the models' insensitivity to the presence or absence of the door, particularly in the prediction of azimuthal directivity.

4.6 Prototype for Airframe Component Interaction: Tandem Cylinders

The remaining test cases in the present assessment (Secs. 4.6 to 4.8) involve the more fundamental, physics-based modeling approach described in Section 4.2.1. As such, the near-field flow (including the acoustic source) is simulated with the Navier-Stokes code CFL3D (see Appendix C). The source simulation data is then used as input to an analytical formulation to propagate the noise to a predetermined observer location. The first such case involves a benchmark problem, two cylinders in tandem to an oncoming flow, for which the availability of detailed experimental data enables a thorough examination of the simulation's capability to capture the relevant physics in the processes of noise generation and propagation.

4.6.1 Test Descriptions

Experimental data have been obtained in the BART and QFF wind tunnel facilities at NASA Langley (see Appendix D). The test configuration comprises two cylinders of equal diameter (D_t), aligned in the streamwise direction. The configuration under consideration is shown in Figure 4.24. The separation distance between the cylinder centroids, L_t , and all other test parameters involving length are normalized with respect to D_t . The angle θ is measured from the upstream stagnation point and is positive in the clockwise direction.

Two experiments (Refs. 38 and 39) have been performed in the BART, providing steady and unsteady surface pressure data, detailed flow-field measurements using particle image velocimetry (PIV), and hot-wire measurements in the wake of the downstream cylinder. During Phase 1, the free-stream velocity was set to 56.1 m/s (184 ft/s), corresponding to a Mach number of 0.166. Each cylinder measured 44.45 mm (1.75 in.) in diameter, and spanned the test-section height (Figure 4.25), for an aspect ratio of $b/D_t = 16$ where b is the length of the span. The test Reynolds number, based on cylinder diameter, was 1.66×10^5 . Before the Phase 2 test runs, in order to accommodate more tubing and wiring for additional transducers, two new cylinders were manufactured, measuring 57.15 mm (2.25 in.) in diameter, thereby altering the value of b/D_t to 12.44. To maintain the Phase 1 Reynolds number, the tunnel speed was set to 43.89 m/s (144 ft/s), with a corresponding Mach number of $M = 0.129$. To ensure a fully turbulent shedding process, the boundary layers on the upstream cylinder were tripped between azimuthal locations of 50° and 60° from the leading stagnation point. The measured surface pressure distribution for the large cylinder centroid separation case was nearly identical to that measured by previous investigators for a single, isolated cylinder at a Reynolds number greater than 8 million (Ref. 60).

Upon conclusion of the Phase 2 BART test, the tandem-cylinders model was removed and altered in length to mount in the QFF for acoustic measurements (Refs. 61 and 62). The model was supported above the open-jet nozzle by two vertical side plates that were mounted to the short sides of the nozzle (Figure 4.26). The cylinders spanned the 0.914-m (3-ft) section, yielding an aspect ratio of $b/D_t = 16$. To simulate the BART results as closely as possible, the trip arrangement on the front cylinder was duplicated, and the speed in the tunnel was adjusted until the shedding frequency was matched. The nominal Mach number for the test was 0.127 (43.4 m/s) with a dynamic pressure of 1145 Pa (0.166 psi). In addition to replicating the BART measurements of the steady and unsteady surface pressures, the acoustic radiation was measured using three pole-mounted microphones. Further details of the QFF test are reported in Reference 61.

4.6.2 Computational Approach and Procedure

The flow about tandem cylinders was simulated in free air, without any wind tunnel walls. All input parameters were based on wind tunnel test conditions during Phase 1 testing in the BART facility. The free-stream Mach number in the computations was 0.166, and the Reynolds number was 1.66×10^5 , based on cylinder diameter. The separation distance between the centroids of the inline cylinders was $L_t = 3.7D_t$ (Figure 4.24). For this spacing, the flow is supercritical and both cylinders experience large-scale shedding. The experiments were run at different speeds, so the data have been corrected to an equivalent speed, with the QFF Mach number of 0.127 chosen as the reference to which the CFD calculations were scaled.

The calculations incorporate the shear stress transport (SST) $k-\omega$ turbulence model of Menter (Refs. 63 and 64), which was developed for steady flow. Because of the overly diffusive nature of the turbulence model, proper growth of unsteady phenomena can be inhibited. To remedy this shortcoming, a quasi-laminar approach, as described in Khorrami, et al. (Ref. 65), has been adopted. Following this approach, the flow field is assumed to be quasi-laminar, except for a narrow strip surrounding the cylinder surfaces where the SST turbulence model is used. Outside of this strip, the production term associated with the turbulence model is switched off. For computational convenience, the distance from the cylinder at which the switch occurs was set based on a set number of grid points from the surface. Because of the azimuthal nonuniformity in the grid stretching, the switch occurs between $0.01D_t$ and $0.04D_t$, which includes the entire boundary layer within the region of attached flow. For different grid spacings, the number of points from the surface was changed to maintain the switching at the same physical distance. All of the simulations were run without specifying a transition location. The turbulence model in the Reynolds-averaged Navier-Stokes (RANS) region was run in a fully turbulent mode and allowed to transition on its own.

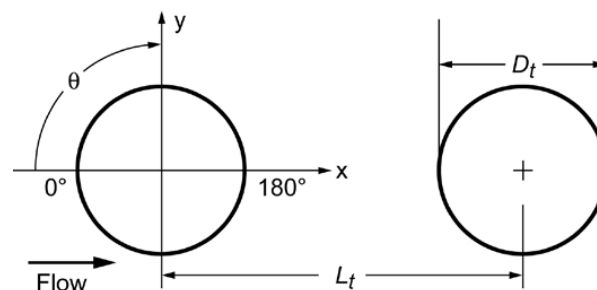


Figure 4.24.—Tandem cylinder test configuration.

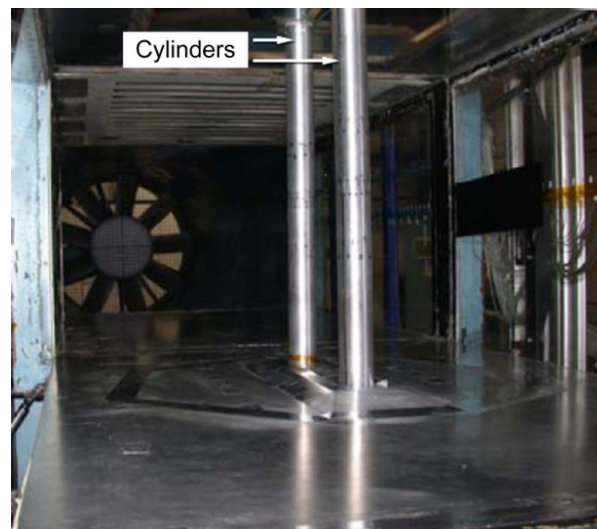


Figure 4.25.—Tandem cylinders installed in Basic Aerodynamic Research Tunnel (BART).

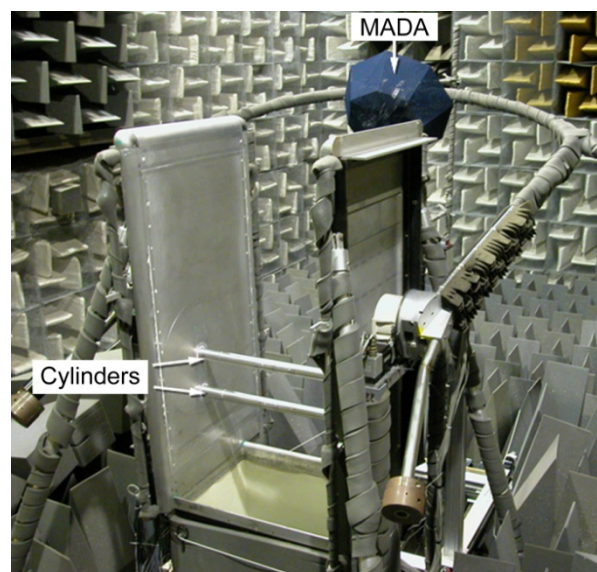


Figure 4.26.—Tandem cylinders installed in Quiet Flow Facility (QFF) tunnel for measurements with Medium Aperture Directional Array (MADA) microphones.

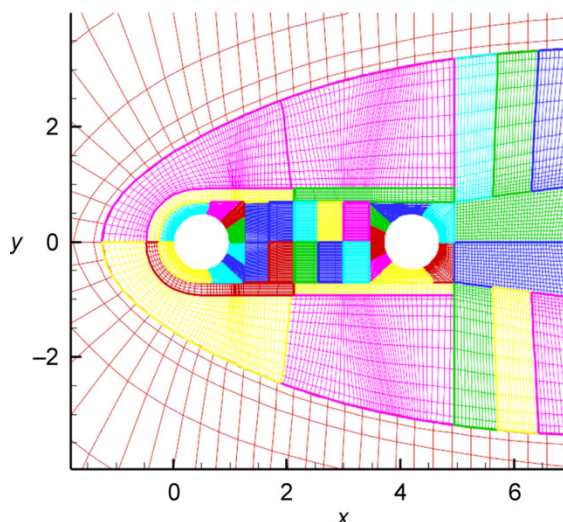


Figure 4.27.—Planar view of computational x,y -grid used for tandem cylinder computational fluid dynamics (CFD) simulations.

Tandem cylinder grids were generated by replicating a 404 000-point, block-structured, planar x,y -grid in the spanwise direction. The planar grid is shown in Figure 4.27. The total grid count for a span of 6 was 80 million. This grid is denoted as $Fxyz$. Care was taken so that the first point off the solid surfaces was at $y^+ < 1$. The reference length in the grid was the cylinder diameter, D_t . Hence, a span of 3 means 3 diameters. Periodic boundary conditions were imposed in the spanwise direction. A Riemann condition was applied at the outer boundaries, except for a small region in the wake where extrapolation was employed. The no-slip condition with an adiabatic thermal condition was applied on all solid surfaces. Details about the boundary conditions can be found in the CFL3D user's manual (Ref. 45). Simulations based on medium-level grids (derived from the finest grid by removing every other grid point in each direction) were performed to allow an assessment of the grid convergence of the computed solutions. This family of grids is denoted as $Mxyz$. A span of 18, which is more representative of the experiment, has been examined with a 30-million-point grid. Although the planar resolution on the medium mesh was reasonable, the spanwise resolution did not seem to be sufficient. Therefore, a series of grids with the same spanwise resolution as the fine grid were generated. These grids, denoted as $MxyFz$, have nearly isotropic cell spacing in the wake region between the cylinders. Again, a spanwise extent of 18 was examined, with 60 million points in the grid. A constant, nondimensional time step of $\Delta t a_\infty / D_t = 0.051$ or $\Delta t V_\infty / D_t = 0.0855$ (corresponding to approximately 520 time steps per period for the primary

shedding frequency) was used for all simulations, where V_∞ is the free-stream velocity. Limited calculations were also performed with double and half the time step without any appreciable differences in the first- and second-moment statistics, although the required effort to obtain sufficient samples makes it problematic to be definitive about such statements.

The simulation procedure includes several steps. First, a steady-state computation was used to set up the basic mean flow, followed by an unsteady calculation with random suction and blowing applied to different spanwise and azimuthal sections of both cylinder surfaces in order to accelerate the onset of three-dimensional unsteady flow structures. The forcing did not exceed 3 percent of the free-stream velocity. The forcing was turned off after significant unsteadiness was observed, typically 200 time steps into the unsteady calculation. The simulations were then run for 5000 to 10 000 time steps to allow the transient flow field to wash out before collecting time records. Data were collected every other time step.

The radiated noise is calculated using the FW-H approach (Refs. 47 and 66) described in Appendix C. The acoustic calculation uses unsteady, CFD simulation data on a surface surrounding the source. The FW-H noise calculations involve unsteady data collected on 32 total subsurfaces composing the impenetrable data surface, which lies on the cylinders. Only the pressure is needed on an impenetrable surface. Calculations with permeable surfaces away from the cylinders showed good agreement with those using the solid-surface data (Ref. 61). The 32 subsurfaces are a natural consequence of the block-structured grid used for the CFD calculations. Each subsurface is a boundary of one of the blocks comprising the grid. The complete time record of over 12 000 samples was subdivided into five segments of 4096 samples with 50 percent overlap. A Hamming filter was applied to each segment. The FW-H code was used to calculate the noise at the exact locations of the pole-mounted microphones in the experiment. To account for differences in flow speed between the calculation and the experiments, frequencies were Strouhal scaled, and the acoustic power corrected by assuming proportionality to $St^2 V_\infty^6$, where $St = f D_t / V_\infty$.

4.6.3 Results and Findings

Extensive aerodynamic comparisons between the simulations and experiments can be found in References 61 and 65. Figure 4.28 presents the pressure coefficient results for the upstream and downstream cylinders. The pressure coefficient, C_p , is defined as $C_p = (p - p_\infty) / (\frac{1}{2} \rho V_\infty^2)$, where p , ρ , and V are local values for the pressure, density, and speed of the airflow, respectively, and the subscript ∞ denotes a free-stream value. Figure 4.28(a) shows that the base pressure on

the upstream cylinder from the $M_{xy}F_z$ grid matches slightly better with the QFF experimental data, whereas the M_{xyz} and F_{xyz} results match better with the BART data. As the simulations were performed in free air, one might expect that the CFD should match the open-jet QFF results. On the downstream cylinder, there is very little difference among the various computed solutions, but the discrepancy with experiment is considerably larger. Solution variations among the different grids are more substantial when comparisons are based on perturbation pressure (denoted p'), which is determined from the Reynolds decomposition, $p = \bar{p} + p'$, where \bar{p} denotes the mean (time-averaged) value of the pressure field. Such variations are shown in Figure 4.29, where the comparison quantity is the root-mean-squared (rms) value of the coefficient of perturbation pressure, $C_{p'} = p' / (\frac{1}{2} \rho V_\infty^2)$. On the upstream cylinder (Figure 4.29(a)), the fluctuations on the $M_{xy}F_z$ grid are considerably lower than on the other two grids and match extremely well with the experimental data. The levels on the finest grid F_{xyz} are the highest, but the F_{xyz} grid only has a span of 6, and there is a complex interaction between grid resolution and spanwise extent on the fluctuation levels. Note that the range for the downstream cylinder in Figure 4.29(b) is much larger than for the upstream cylinder. In general, the computations pick up the location of the peak fluctuations around $\theta = 45^\circ$ because of the impingement of the wake on the downstream cylinder.

From a noise perspective, the downstream cylinder is going to dominate the radiation because the pressure fluctuations are 10 to 15 dB higher than those on the upstream cylinder. The near-field SPL contours in Figure 4.30 resemble the directivity from a dipole source just upstream of the downstream cylinder. Although CFD seems to have directly captured some of the radiated noise, this is still very much in the near field. The wavelength of the primary shedding frequency is larger than the size of the computational domain. The FW-H equation was used to make predictions of the noise at a microphone located at the downstream (x, y) location of the rear cylinder at $(9.11D_t, 32.49 D_t)$. In the experiment, a 64-channel, 16-bit transient data recorder controlled by a workstation was used to acquire the data at a sampling rate of 25 600 samples per second. High- and low-pass filters, set respectively at 5 Hz and 10 kHz, were used to condition the outputs from each microphone channel. The noise spectra were obtained by partitioning each time signal into 1000 non-overlapping segments of 8192 samples, and each time history segment was Fourier transformed using a Hamming window for signal conditioning. The resulting frequency resolution was 3.125 Hz.

A comparison between the predictions using the three grids and the experimental results is shown using a narrowband analysis in Figure 4.31. All of the data have been scaled to an equivalent 1-Hz bin width, so the presentation is in power

spectral density. Both the experiment and predictions show a pronounced tone at low frequency. The prediction is only off by less than 20 Hz from what was observed in the experiment (178 Hz in the experiment and 160 Hz in the simulation). The F_{xyz} result was obtained by replicating the data from the span of 6 calculations 3 times to produce a span of 18, matching the length of the other calculations and the experiment. However, this results in an artificial spanwise correlation that produces more noise below 2000 Hz than the M_{xyz} grid. The elevated

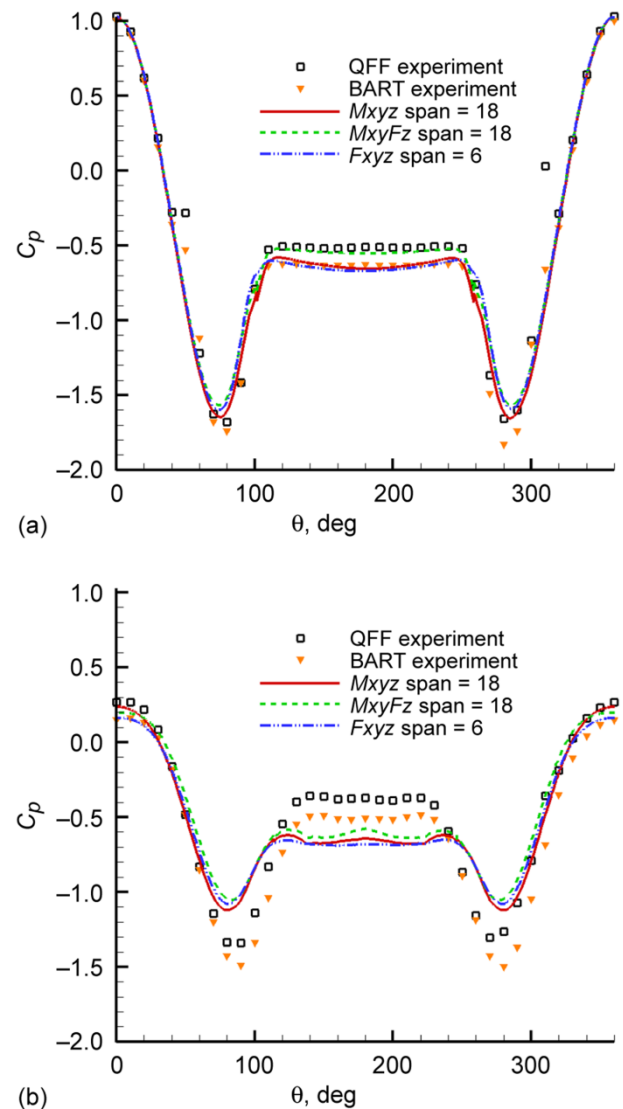


Figure 4.28.—Pressure coefficient C_p versus polar angle θ for the surfaces of the tandem cylinders. Comparison of results from Quiet Flow Facility (QFF) and Basic Aerodynamic Research Tunnel (BART) experiments and CFD simulations with grids of different spans. (a) Upstream cylinder. (b) Downstream cylinder.

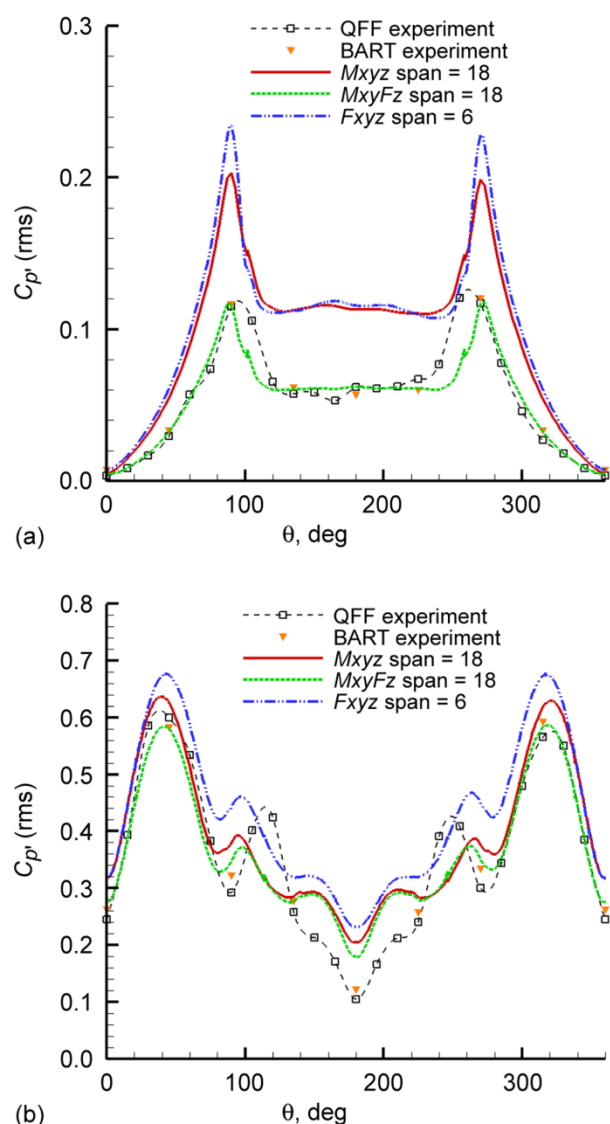


Figure 4.29.—Root-mean-squared (rms) value of perturbation pressure coefficient C_p' versus polar angle θ for the surfaces of the tandem cylinders. Comparison of results from Quiet Flow Facility (QFF) and Basic Aerodynamic Research Tunnel (BART) experiments and CFD simulations with grids of different resolutions and spans. (a) Upstream cylinder. (b) Downstream cylinder.

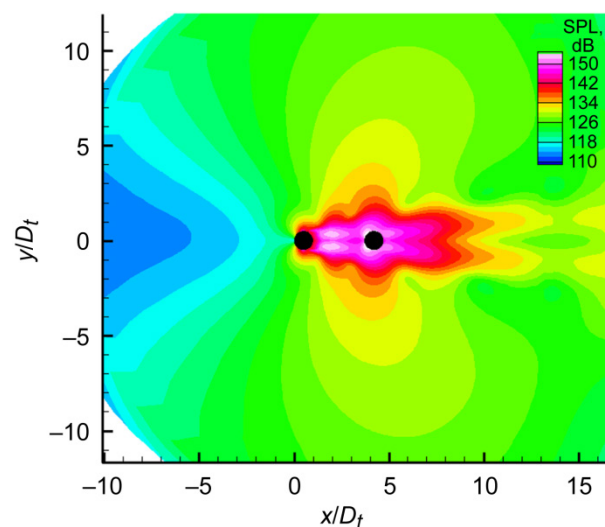


Figure 4.30.—Near-field tandem cylinder sound pressure level (SPL) contours, CFD predictions, where x and y are spatial coordinates and grid dimensions and D_t is cylinder diameter.

levels are also evident in the 1/3-octave results shown in Figure 4.32. Bars are included in the plot representing the scatter between runs in the experiment and between different averaging segments in the predictions. The time record available from the CFD was short, so only five segments of 4096 samples were used to obtain an average. The band shows the maximum and minimum values that were observed in the five segments. Although the CFD shows large variations, even the experiment shows considerable scatter because of the highly intermittent nature of the shedding process. Figure 4.33 shows the difference between the prediction from the M_{xyzFz} grid and the experiment. Because the shedding frequency from the CFD and experiment were slightly different and the tone was near the edge of a 1/3-octave bin, the error plot shows large peaks at these frequencies. Other than missing the shedding frequency by about 20 Hz, the CFD prediction is actually in good agreement with the experiment.

4.6.4 Effect of Cylinder Spacing

Simulations and experiments have also been performed at other cylinder spacings. A detailed comparison between the results for a subcritical spacing of $1.435D_t$ is in Reference 62. In the subcritical state, large-scale shedding is suppressed. This state was experimentally observed with a cylinder centroid-to-centroid spacing of $1.435D_t$, resulting in a more difficult flow field to simulate. Not only must the simulations correctly predict the reduced shedding, many frequencies must be resolved as they nearly equally contribute to the overall character of the flow. Often, however, the noise engineer is most interested in how the flow field and radiated noise change as a result of modifications to the geometric configuration. Thus, the computations are examined to assess how well

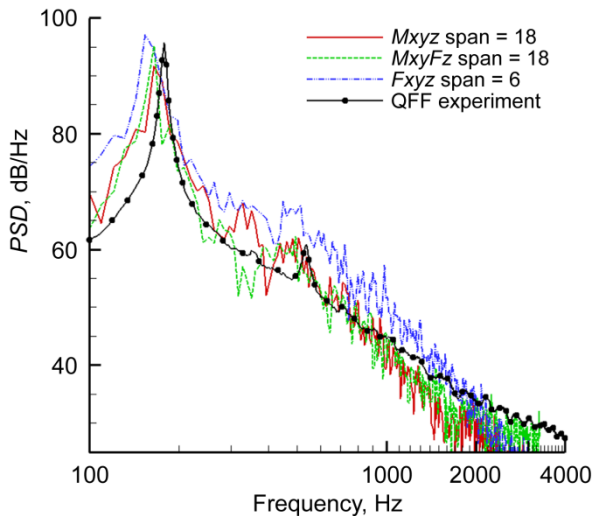


Figure 4.31.—Power spectral density PSD for tandem cylinders. Comparison of CFD predictions using three grids and results from Quiet Flow Facility (QFF) experiments.

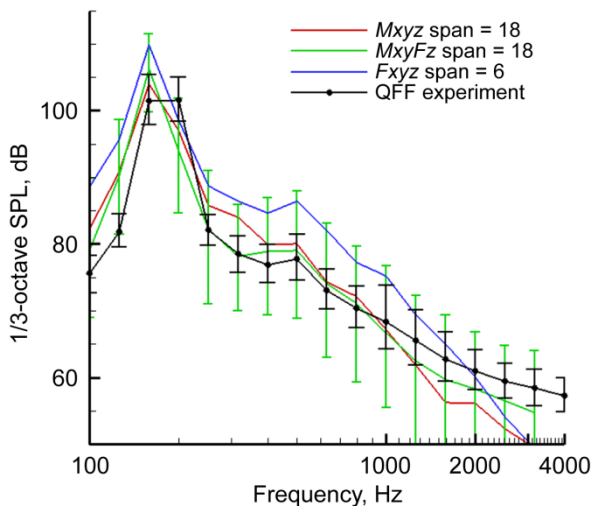


Figure 4.32.—Sound pressure level (SPL) spectra for tandem cylinders. Comparison of CFD predictions using three grids and measurements from Quiet Flow Facility (QFF) experiments.

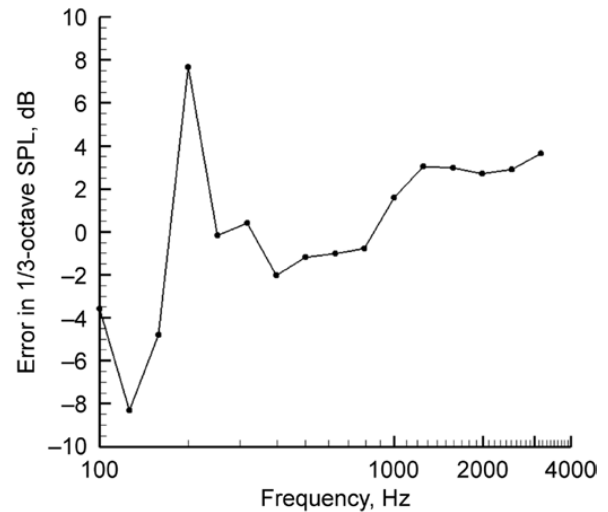


Figure 4.33.—Error in sound pressure level (SPL) spectra predictions for tandem cylinders. Difference between CFD predictions from $MxyFz$ grid with span of 18 and experimental measurements.

the predictions respond to varying the spacing from supercritical ($L_t/D_t = 3.7$) to subcritical ($L_t/D_t = 1.435$). The levels of peak surface pressure on the downstream cylinder in both cases are used in the evaluation. Using the calculation on the $MxyFz$ grid with a span of 18 as a reference, a comparison of experimental rms surface-pressure fluctuations for the two cylinder centroid separation distances is shown in Figure 4.34. The peak rms levels are different by a factor of 2 to 3 between the two configurations, and the CFD has picked up this effect. All of the CFD solutions from the different grids correctly capture the trend. Acoustic results for the different cylinder centroid separation distances are compared in Figure 4.35. Both the experimental and CFD results show that the tone and broadband amplitudes are significantly lower for the smaller spacing. A decrease of 20 dB represents an order of magnitude in reduction for the fluctuating pressure. Clearly, the CFD has predicted the correct trend in the far-field acoustics even though the details of the spectrum at the smaller spacing have not been captured. The spectral peak in the simulations is still 10 dB above the rest of the spectrum, whereas the peak is barely discernible in the experiments. Figure 4.36 presents the 1/3-octave SPL comparison between the simulations and experiment for the $1.435D_t$ spacing, and Figure 4.37 presents the corresponding error. Although the error exceeds 12 dB around the frequency of the peak in the predicted pressure spectra, the CFD has still correctly captured the dramatic reduction in the noise levels between the $3.7D_t$ and $1.435D_t$ spacing cases. For some applications, capturing the trends is sufficient, but higher fidelity in predicting absolute noise levels is needed.

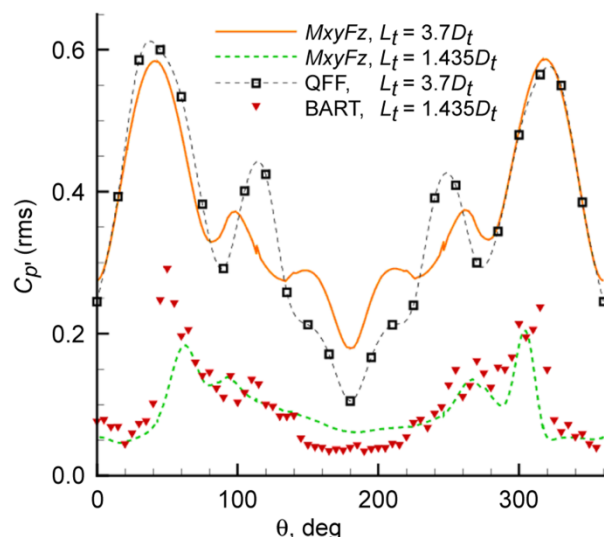


Figure 4.34.—Root-mean-squared (rms) value of tandem cylinder surface perturbation pressure coefficient $C_{p'}$ versus polar angle θ at two spacings L_t/D_t , where L_t is centroid-to-centroid distance and D_t is cylinder diameter (see Figure 4.24). Comparison of CFD predictions from *MxyFz* grid with span of 18 and measurements from Quiet Flow Facility (QFF) and Basic Aerodynamic Research Tunnel (BART) experiments.

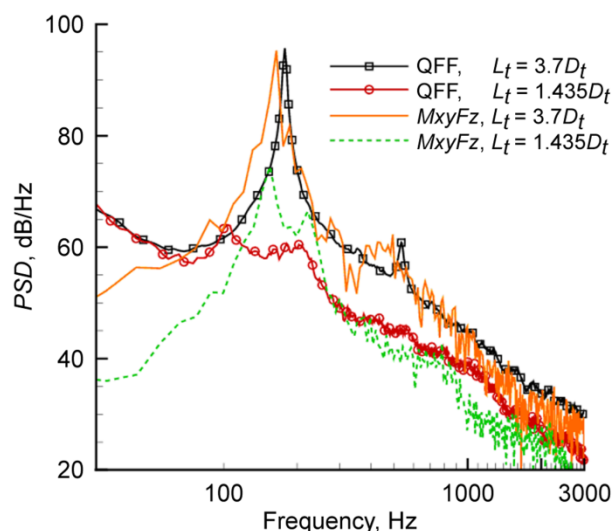


Figure 4.35.—Power spectral density PSD for tandem cylinders at two spacings L_t/D_t , where L_t is centroid-to-centroid distance and D_t is cylinder diameter (Figure 4.24). Comparison of CFD predictions from *MxyFz* grid with span of 18 and measurements from Quiet Flow Facility (QFF) experiments.

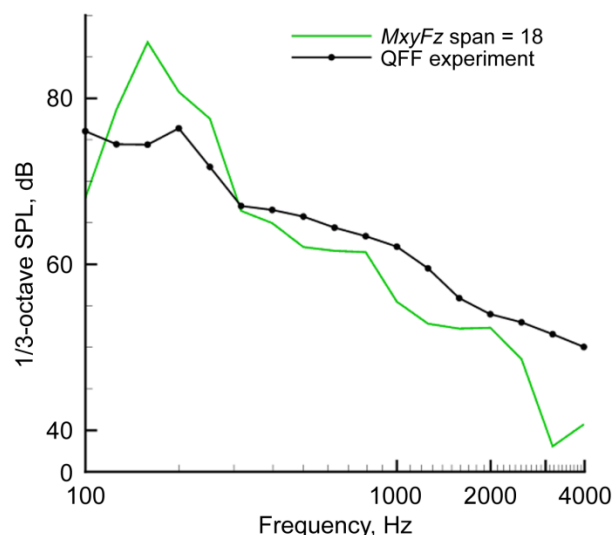


Figure 4.36.—Sound pressure level (SPL) spectra for tandem cylinders at centroid separation distance $L_t/D_t = 1.435$. Comparison of CFD predictions from *MxyFz* grid with span of 18 and measurements from Quiet Flow Facility (QFF) experiments.

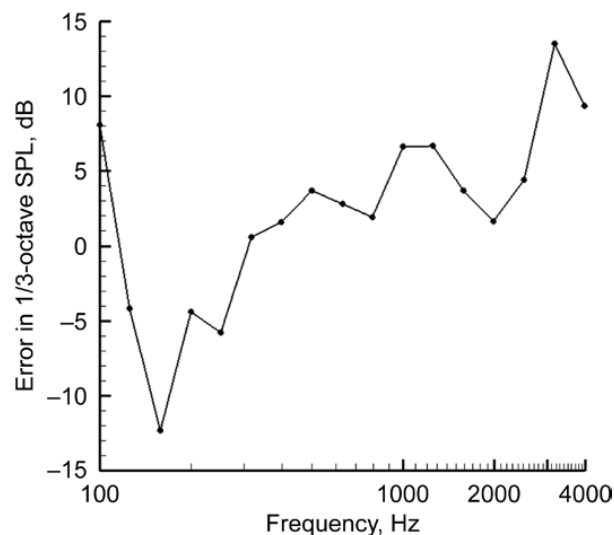


Figure 4.37.—Error in sound pressure level (SPL) spectra predictions for tandem cylinders at centroid separation distance $L_t/D_t = 1.435$. Difference between CFD predictions from *MxyFz* grid with span of 18 and experimental measurements.

4.6.5 Recommendations

The tandem cylinder problem has proven to be an excellent and challenging dataset to test the ability of CFD to accurately predict the near-field aerodynamics and the resulting noise. Although reasonable results were obtained with the $M_{xy}F_z$ grid with a span of 18, the noise results for the F_{xyz} grid and a span of 6 overpredicted amplitudes. Unfortunately, the computational cost is prohibitive for a span of 18 on the F_{xyz} grid. Much faster flow solvers are needed to predict airframe noise when very complicated physics is responsible for the noise generation. Furthermore, robustness and the ability to model complex geometries are very important. It is imperative that resource investment be made in the development of fast, highly accurate flow solvers with robustness and geometric flexibility. Ideally, such solvers would adapt in an unsteady manner to the relevant flow features to maintain a desired level of accuracy. Benchmark problems like the tandem cylinders provide a means to assess the accuracy and efficiency of new methods.

4.7 Aeroacoustic Analysis of Simplified Landing Gear Model

Wind tunnel tests and computer simulations are conducted to study the aerodynamic noise generated by a Mach 0.2 flow over a simplified landing gear without small-scale parts, such as hydraulic lines and fasteners. An integral of the FW-H equation predicts the noise at far-field observer locations from surface-pressure data provided by an unsteady computational fluid dynamics calculation. The subsequent analysis includes the identification of geometric and aerodynamic characteristics that are responsible for various features in the computed noise spectra.

4.7.1 Test Description

The geometry of the test model, shown in Figure 4.38, approximately represents a 10-percent-scale Boeing 757 main landing gear. The model assembly is composed of four wheels, two side struts, an oleo, a side door, yokes, a pin, and other structures that join the system together. Tests were initiated in the Low-Turbulence Pressure Tunnel (LTPT) at NASA Langley, with the landing-gear model mounted on a three-element airfoil section (Ref. 67). The LTPT is a pressurized facility that enables model testing at increased Reynolds numbers while maintaining a constant Mach number (see Ref. 68 for facility details). The test conditions for the initial CFD analysis (Ref. 69), and those to follow, correspond to a free-stream Mach number of 0.2 at a static temperature of 302.9 K (85.5 °F), and a free-stream stagnation pressure 284 kPa (2.8 atm). Under these conditions, the Reynolds number is 1.23 million, relative to the landing-gear wheel diameter of 0.094 m (3.7 in.).

Most of the data from the LTPT test are unavailable, but acoustic measurements for the simplified landing-gear model were recently obtained in the QFF (see Appendix D). Although

a comprehensive report on this QFF test is yet to be published, a few results are presented herein for prediction validation. Because of obvious similarities with the Boeing 777 model test in Section 4.5, aerodynamic noise associated with the present landing gear model was measured using the same setup and procedures described in References 36 and 37. The Reynolds number for the QFF test, based on wheel diameter, was 370 000.

4.7.2 Computational Approach and Procedure

Noise sources for this simplified landing gear have been simulated with CFL3D (Refs. 43 and 46) and a detached-eddy simulation (DES) (Ref. 70) methodology as proposed by Spalart (Refs. 71 and 72), coupled to a FW-H equation solver (Refs. 47 and 66) discussed in Appendix C. The DES model essentially reduces the level of eddy viscosity in regions away from solid surfaces when the grid is sufficiently fine. For the CFD simulations, the landing-gear model was mounted on a flat plate that represents the pressure surface of the aircraft wing. The flow calculations were run fully turbulent at a Reynolds number of 1.23×10^6 , based on the landing-gear wheel diameter. The structured grid consisted of 155 blocks possessing a total of 13.3 million grid points. Figure 4.39 shows a coarsened grid distribution on the surface of the model. A Riemann condition was applied at the outer boundaries, except for a small region in the wake where extrapolation was employed. The no-slip condition with an adiabatic thermal condition was applied on all solid surfaces. Details of these boundary conditions can be found in the CFL3D User's Manual (Ref. 45), and additional information in regard to the computations can be found in References 73 and 74.

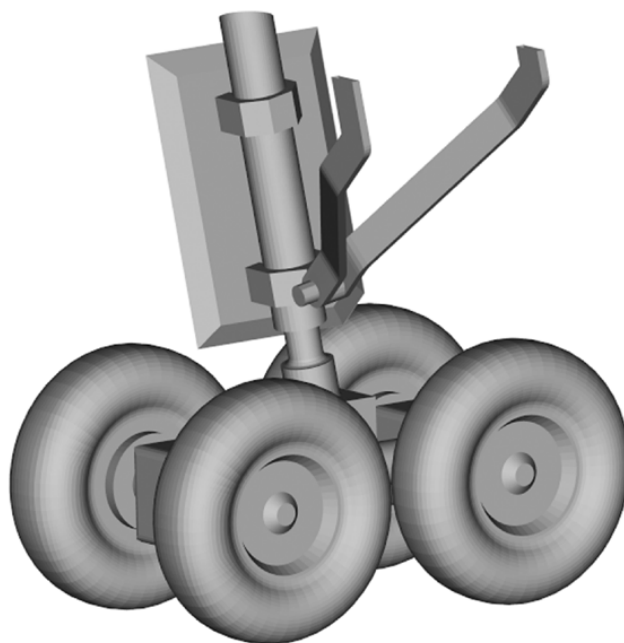


Figure 4.38.—Geometry of simplified landing gear model.

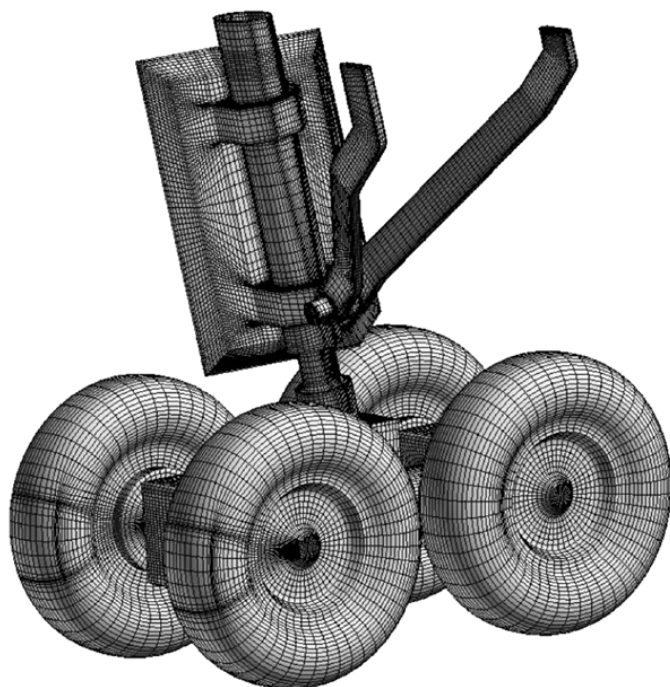


Figure 4.39.—CFD surface grid of simplified landing gear model.

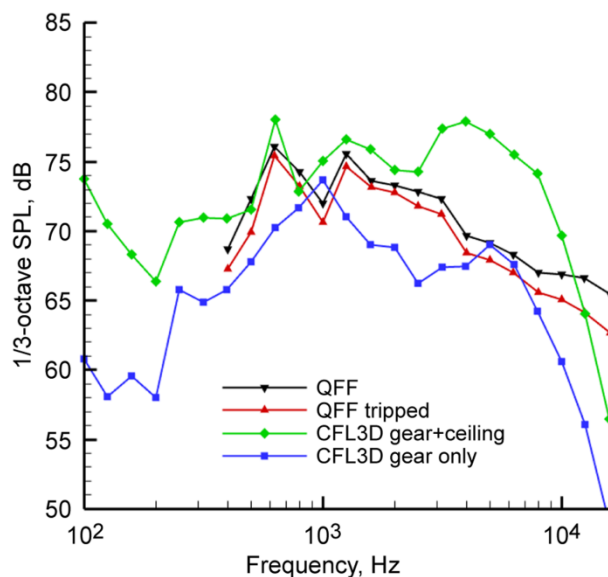


Figure 4.40.—Sound pressure level (SPL) spectra for landing gear in overhead position at polar angle $\theta = 88^\circ$ and azimuthal angle $\phi = -1^\circ$ (see Figure 4.18). Comparison of CFL3D predictions, using gear surface with and without the ceiling surface, and measurements from Quiet Flow Facility (QFF) experiments, nontripped and tripped cases.

The noise calculations involve unsteady flow data collected on 181 total subsurfaces comprising all the solid surfaces in the calculation. Only the pressure is required on impenetrable surfaces. One hundred forty-seven subsurfaces were on the gear itself, and thirty-four were on the plate above the gear. The subsurfaces are a natural consequence of the block structured grid used for the CFD calculation. Each subsurface is a boundary of 1 of the 155 blocks comprising the grid. Over 12 000 nondimensional time samples were collected from the DES simulation. The computations were sampled at every fourth time step, with $\Delta t a_\infty / d = 0.02$, where the tire diameter, d , was used as the reference length. All of the acoustic results represent an average over five segments with 50 percent overlap. Each segment consisted of 4096 samples. The observer was located 100 wheel diameters away from the model. To compare with the experimental data, the CFD results were scaled to a propagation distance of 1.52 m (5 ft, or 16.2 wheel diameters) and $M = 0.17$, by assuming that the acoustic power is proportional to V_∞^6 / R^2 .

4.7.3 Results and Findings

The predictions are compared with the experimental values at five observer locations: overhead, two flyover positions, and two sideline positions. The comparison for the nominally overhead position ($\theta = 88^\circ$, $\phi = -1^\circ$) is presented in Figure 4.40. The experimental data from the QFF includes both the nontripped and tripped cases. For the tripped case, the gear was coated in a fine grit to simulate the effects of higher Reynolds number. The amplitude of the noise is 1 to 3 dB lower with the grit, but the shapes of the curves are very similar. The results from the tripped case should be more similar to the computational results because the Reynolds number in the simulations was considerably higher. Two predictions using the CFL3D data are included: one using all solid surfaces (gear+ceiling), and one using only the surfaces on the gear. The grid is heavily patched in the vicinity of the ceiling, and disturbances passing through these interfaces are distorted and often artificially amplified. The noise levels obtained using only the ceiling is nearly identical to that from the gear+ceiling. The hump in the gear+ceiling spectra between 2 to 8 kHz is most likely caused by the artificial amplification. However, at lower frequencies, the gear+ceiling calculation is in much better agreement with the experiment relative to the gear-only prediction. The experiment employed a Kevlar sheet to prevent reflections from the mounting plate, which is the same as the ceiling in the computations. However, Kevlar is not completely acoustically transparent. Furthermore, most of the noise radiated from the ceiling in the computations is from the interaction of flow structures with the surface and not simple acoustic reflection. Therefore, it is hard to ascertain which of the calculations more faithfully represents the experiment.

A thorough perusal of the calculations indicates that the shed wake from the side bars is the source of the peak SPL at 700 Hz in Figure 4.40. The peak at approximately 1300 Hz is

due to the wake from the main oleo. Most of the noise near 1000 Hz is coming from the gear boxes and connectors. A narrowband presentation of the same data is given in Figure 4.41. Although there is not much change in the overall level of agreement, the differences in the peak frequencies are now evident. Beyond 10 000 Hz, the CFD data drops off rapidly. Because of the lack of resolution in the grid, the high frequencies are excessively damped. At full scale, the dropoff would begin around 1000 Hz, which is well below the maximum frequency at which landing gear contribute to the overall aircraft noise. The error in the overhead predictions is presented in Figure 4.42. The QFF tripped case is taken as the baseline for comparison purposes. The gear+ceiling calculation is within 2 dB of the experiment up to 2000 Hz, whereas the gear-only computation has errors between 3 and 6 dB. Beyond 10 000 Hz, the errors for both calculations approach 10 dB.

Experimental data and predictions for polar angles of $\theta = 58^\circ$ (upstream) and 120° (downstream) are shown in Figure 4.43. Only the predictions using the CFD solutions from the gear alone are presented. In contrast to the experimental data, the CFD predicts only slightly lower levels downstream than upstream. However, Figure 4.44 shows that the CFD predicts the correct trend for the observers at $\phi = -55^\circ$ (door side) and 55° (opposite the door), with higher levels opposite the door. It is interesting that the CFD prediction for $\phi = 55^\circ$ is in much better agreement with the data than $\phi = -55^\circ$ and picks up the first two peaks. The door may be reflecting some of the signal from the interactions occurring near the ceiling resulting in a signal that is similar to the one seen in Figure 4.43(a) for the overhead position.

4.7.4 Recommendations

The CFD grid used in the computations was large when the calculation was performed, but much finer grids could be used today. Furthermore, the grid was heavily patched, especially in the vicinity of the ceiling. The patches resulted in obvious errors and large oscillations as strong disturbances passed through. Refining the grid should improve considerably the predictions and remove the ambiguity about the importance of flow interactions with the ceiling. However, a reasonable grid for a DES-type calculation would require on the order of 150 million points. Running CFL3D with 150 million points on 493 cores on an SGI Altix ICE computer (using 3 of the 4 cores on each Intel X5355 2.66 GHz processor), results in 175 GB of total memory usage (365 MB per core). The code executes 1000 time steps in 70 hours. Completion of 50 000 time steps would require 145 days. Although feasible, such a calculation is quite large by today's standards, and the grid count is still insufficient to resolve the small scales generated around landing gear. Furthermore, the number of time steps would need to be increased by a couple of orders of magnitude to produce the same number of samples for averaging as are typically used in experiments.

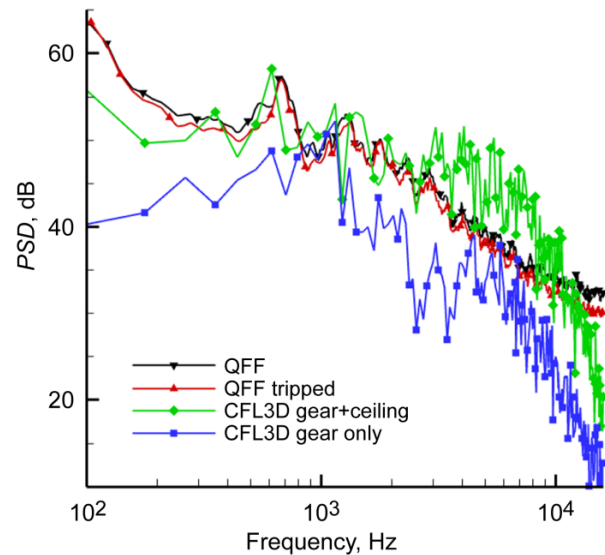


Figure 4.41.—Power spectral density *PSD* for landing gear in overhead position at polar angle $\theta = 88^\circ$ and azimuthal angle $\phi = -1^\circ$ (see Figure 4.18). Comparison of CFL3D predictions, using gear surface with and without the ceiling surface, and measurements from Quiet Flow Facility (QFF) experiments, nontripped and tripped cases.

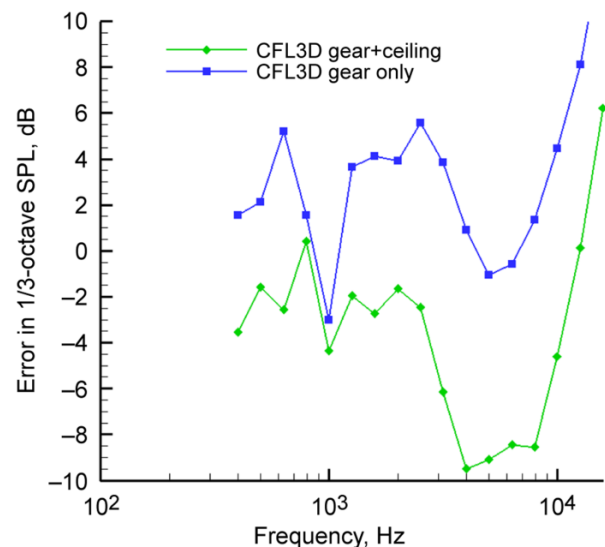
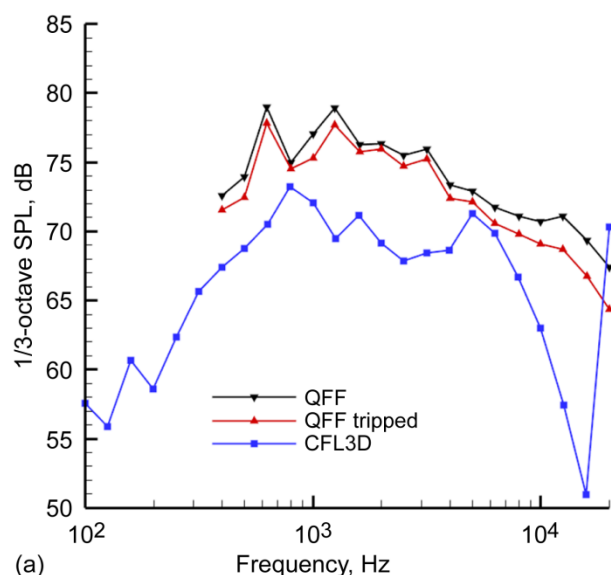
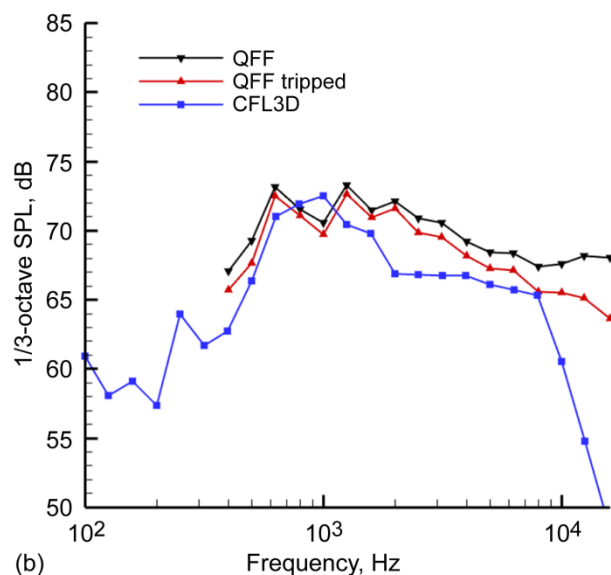


Figure 4.42.—Error in CFL3D sound pressure level (SPL) spectra predictions for landing gear in overhead position at polar angle $\theta = 88^\circ$ and azimuthal angle $\phi = -1^\circ$ (see Figure 4.18). Difference between predictions, using gear surface with and without the ceiling surface, and measurements from Quiet Flow Facility (QFF) experiments, tripped case.

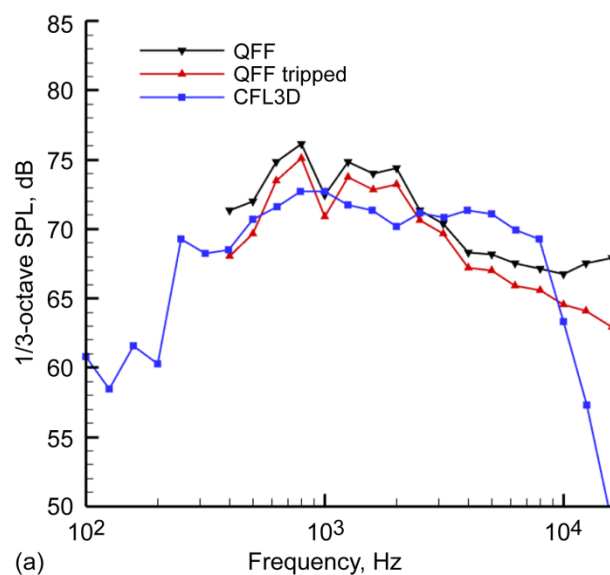


(a)

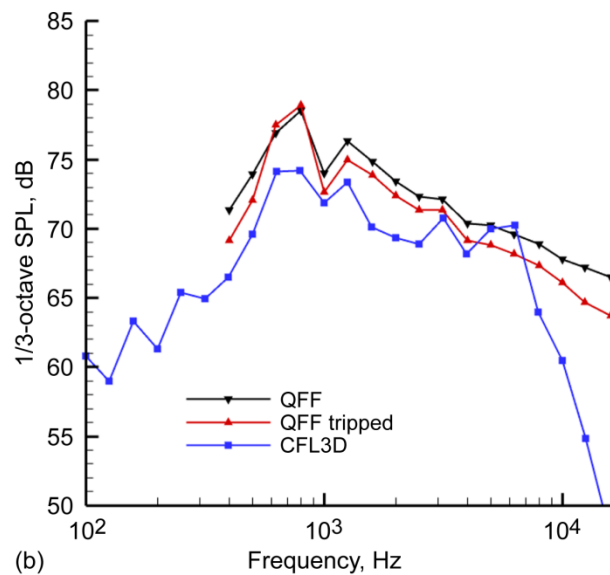


(b)

Figure 4.43.—Sound pressure level (SPL) spectra for landing gear in flyover positions (see Figure 4.18). Comparison of CFL3D predictions and measurements from Quiet Flow Facility (QFF) experiments, nontripped and tripped cases. (a) Upstream, polar angle $\theta = 58^\circ$ and azimuthal angle $\phi = -1^\circ$. (b) Downstream, polar angle $\theta = 120^\circ$ and azimuthal angle $\phi = -1^\circ$.



(a)



(b)

Figure 4.44.—Sound pressure level (SPL) spectra for landing gear in sideline positions (see Figure 4.18). Comparison of CFL3D predictions and measurements from Quiet Flow Facility (QFF) experiments, nontripped and tripped cases. (a) On door side, polar angle $\theta = 88^\circ$ and azimuthal angle $\phi = -55^\circ$. (b) Opposite door side, polar angle $\theta = 88^\circ$ and azimuthal angle $\phi = 55^\circ$.

Improvements in the turbulence model are also needed. The DES computation (Ref. 74) is a vast improvement over the original unsteady RANS computation reported in Reference 73. Nonetheless, there is still considerable room for improvement. The effects of the RANS region on the unsteady surface fluctuations, caused by impinging wakes, are still largely unknown. Experimentally, although the acoustic field has been mapped out, no near-field data have been obtained for the landing gear. A dataset with both near- and far-field information is needed to more clearly understand the flow phenomena and validate predictions.

Both the above computational study and the previous experimental one focused entirely on the noise generated by the flow field in the near vicinity of the landing gear itself. In a number of experimental studies of landing gear configurations mounted on wings with trailing-edge flaps deployed, microphone phased-array maps (Refs. 19 and 75) suggest that the collective unsteady wake of the gear, impinging on the leading edge and passing over the trailing edge of the flap, can produce significant radiated noise, presumably through a scattering process. Existing experimental and computational data should be examined in order to form a conclusion regarding the further study of this mechanism.

4.8 Aerodynamic Sources of Leading-Edge Slat Noise

In addition to trailing-edge flaps and landing gear (as previously discussed), leading-edge slats are also considered to be significant sources of aircraft noise during airport landing operations. The present study is focused on three-dimensional simulations of the slat cove flow within a computational domain of limited spanwise extent. The results indicate that accounting for the three-dimensionality of flow fluctuations leads to considerable improvement in the accuracy of the unsteady, near-field solution. Validation data is provided by particle-image velocimetry measurements from a test conducted on a generic high-lift model in the BART facility.

4.8.1 Discussion of Experimental Data

The 30P/30N model tested in the BART at NASA Langley represents a generic, three-element, zero-sweep high-lift configuration with slat and flap deflections of 30° each (Figure 4.45). The slat chord, c_s , and flap chord, c_f , of the model are equal to 14.48 and 30 percent, respectively, of the stowed chord, c , of 0.457 m (18 in.). For the approach configuration, the slat gap is 2.95 percent; the flap gap is 1.27 percent;

and the slat and flap overhang settings are equal to -2.95 and 0.25 percent, respectively. (Ref. 76 provides a definition of these rigging parameters.) At the test Mach number of $M = 0.17$, the Reynolds number Re_c based on the stowed chord of the BART model, corresponds to 1.7 million. While this Reynolds number is substantially lower in comparison to full-scale applications, the BART experiment is still suitable for validating numerical predictions of the slat cove noise sources as described in Reference 77.

The BART measurements (Ref. 35) consist of steady surface pressure measurements plus extensive two-dimensional PIV data within the midspan plane of the model. To assess the accuracy of unsteady near-field predictions, calculations are performed for the configuration corresponding to a 4° angle of attack in BART, which approximates the mean slat loading for a free-flight configuration at a 5.5° angle of attack.

4.8.2 Metrics and Assessment

Previous studies (Refs. 78 and 79) have shown that many features of the unsteady slat cove flow may be inferred via planar (i.e., two-dimensional) computations that neglect both the local three-dimensionality of the unsteady flow structures within the slat cove and the large-scale three-dimensional effects due to the sidewalls of the tunnel. The origin of the dominant flow structures is linked to the Kelvin-Helmholtz instability of the shear layer emanating from the slat cusp. The two-dimensional computations capture the growth and evolution of large-scale coherent structures within the shear layer (including shear layer roll-up and vortex pairing) as well as their interaction with the slat surface. Following their impingement on the slat pressure surface, these vorticity structures either are advected past the slat trailing edge or migrate back to the slat cusp within the recirculating zone. Hybrid acoustic predictions, based on a combination of the two-dimensional near-field simulations and the FW-H equation, have been found to be consistent with the measured slat noise data in terms of both spectral shape and Mach number scaling (Refs. 78 and 80). However, the spectral intensity was overpredicted by greater than 10 dB in certain cases (Ref. 78). More importantly, the two-dimensional near-field simulations predicted excessively energetic slat-cove flow structures, resulting in poor agreement with certain major aspects of the measured unsteady flow data (Ref. 80).

The present assessment focuses on the comparison of BART measurements (Ref. 35) with three-dimensional simulations that account for the local three-dimensionality of the unsteady slat cove flow field. Because of limited



Figure 4.45.—Model three-element 30P/30N high-lift aircraft wing system.

computational resources, the spanwise width of the computational domain is set at 37.3 percent of the slat chord; that is, 2.5 percent of the actual span. Given the complexity of the slat cove flow structures contributing to broadband noise radiation, the metrics chosen for this comparison correspond to

- (1) Instantaneous spanwise vorticity distributions (compared visually with BART PIV data)
- (2) First- and second-moment statistics of the velocity field
- (3) The nature of the near-field acoustic radiation (compared with a DLR model (Ref. 81), based on ground test data)

Quantitative error measures have been employed in regard to (2); however, similar measures are not appropriate for (1) or (3), and therefore the comparisons between computations and measurements are purely qualitative.

4.8.3 Results and Findings

A general description of the computational methodology has already been discussed in Section 4.2.2; additional details may be found in Reference 77. Briefly, the CFL3D code is used with a zonal turbulence model to solve the unsteady, thin-layer Navier-Stokes equations for the 30P/30N configuration. The two-equation SST model of Menter (Refs. 63 and 64) is used to capture the mean flow behavior in regions away from the slat cove region, whereas the turbulence production term in the turbulence transport equations has been switched off within the cove region to eliminate the excessive diffusive effects of the turbulence model on the resolved unsteady flow structures. The design of the cross-sectional grid is based on prior experience, but limited grid sensitivity studies have been performed in regard to spanwise grid resolution and time step. Only the results obtained with the finest spanwise grid are typically used for this assessment, which focuses on the broadband sources of unsteadiness in the slat cove region. Additional sources of noise, such as vortex shedding from the finite thickness slat trailing edge, are not included in this assessment.

The simulations were performed using characteristic boundary conditions at the far-field boundaries in the cross-sectional plane (which are positioned at a minimum of 10 chord lengths away from the center of the model), except for extrapolation from the interior at the downstream boundary. Periodic boundary conditions were employed across the spanwise boundaries of the computational domain. No-slip conditions were imposed at the solid surfaces, along with an adiabatic wall thermal boundary condition.

Two representative snapshots of the spanwise vorticity, within a spanwise cut through the computational domain, are shown in Figure 4.46(a) and (b). Similar images based on the planar PIV data from Reference 35 are shown in Figure 4.47. The PIV measurements indicate a regular train of vortical structures along the slat shear layer. There is occasional entrainment of the vortical structures into the recirculation

zone, which is the defining characteristic of “cove state I” in Figure 4.47(a); however, the majority of the vortices convect directly past the trailing edge, with no recirculation (“cove state II” in Figure 4.47(b)). The three-dimensional predictions in Figure 4.46 resemble the planar PIV data, indicating both states of the measured cove flow field. However, an inspection of several other three-dimensional computational snapshots suggests that the role of the recirculating vortices may be somewhat overemphasized within the narrow domain simulation, perhaps, because of its lack of large-scale three-dimensional (i.e., model installation) effects.

Time-averaged vorticity is used to derive what is referred to as the “shear-layer trajectory” in the slat cove. The notion of this trajectory is depicted in Figure 4.48(a), where it appears as a narrowband of time-averaged vorticity contours between the cusp and the reattachment point upstream of the trailing edge. Then, pictorially, the shear-layer trajectory is the curve segment that runs along the “center” of this band of contours, along a contour defined by local vorticity maxima. This curve segment is numerically determined by a collection of grid points that results from a search for local vorticity maxima, as directed along paths including points interior and exterior to the recirculation zone. The discrete distance s along the trajectory is determined by numerical arclength.

A comparison between the computed and measured mean shear-layer profiles at selected stations along the aft part of the shear layer trajectory is shown in Figure 4.48(b). The distance ϵ in Figure 4.48(b) is measured along each of the four line segments (A, B, C, and D) in Figure 4.48(a) and is set to zero at the point of maximum mean velocity slope in the shear layer. The maximum slope of the computed velocity profiles agrees well with the measured data; however, computations underpredict the velocity differential across the mixing layer, again, presumably because of a lack of large-scale three-dimensional effects.

Contours of the measured and predicted distributions of two-dimensional turbulent kinetic energy (TKE) are shown in Figure 4.49(a) and (b), respectively. This two-dimensional TKE is defined by the quantity $(\langle u', u' \rangle + \langle v', v' \rangle)/2$, where u' and v' are the Cartesian components of the two-dimensional velocity perturbation field, and the angular brackets represent the inner product operator. The peculiar “inverted λ ” shape of the PIV-based contours of TKE distribution near the reattachment location is also captured within the three-dimensional simulation. However, in comparison with the PIV data, the computations indicate somewhat higher levels of turbulence intensity ($Tu_{2D} = \sqrt{TKE}$) within the recirculation zone, as illustrated in Figure 4.49(c). Besides that, the TKE distribution based on the current three-dimensional time-accurate calculations is in good overall agreement with PIV data and, also, the steady-state predictions based on RANS calculations with a two-equation turbulence model active throughout the flow (i.e., including the cove region). The TKE from previous two-dimensional simulations showed significantly higher levels (Refs. 81 to 83) than either of these results.

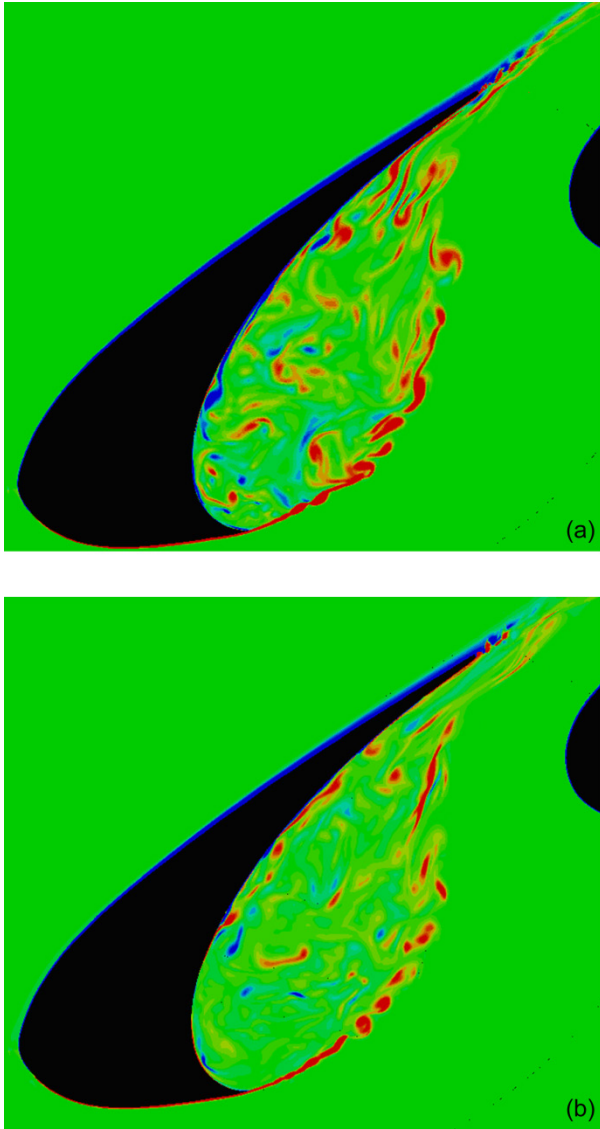


Figure 4.46.—Instantaneous spanwise vorticity field downstream of leading-edge slat, based on CFL3D computations. (a) Planar cut resembling cove state I. (b) Planar cut somewhat resembling cove state II.

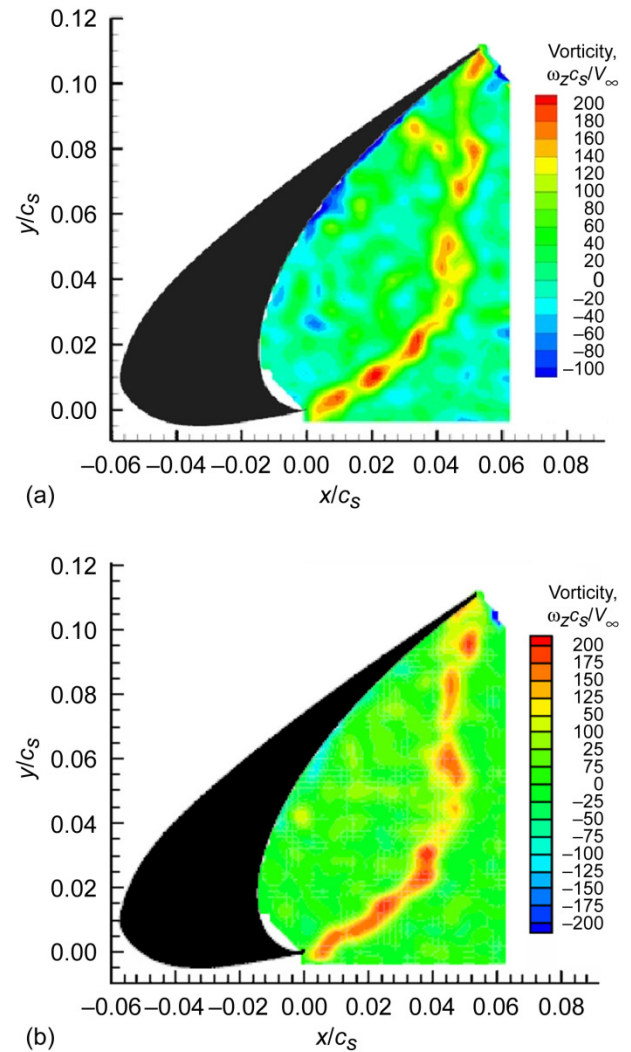


Figure 4.47.—Sample snapshots of leading-edge slat spanwise vorticity field from particle imaging velocimetry (PIV) measurements (Ref. 35) with wing model configuration at 4° angle of attack in the Basic Aerodynamic Research Tunnel (BART). ω_z is spanwise vorticity, c_s is slat chord length, and V_∞ is aircraft speed. (a) Cove state I. (b) Cove state II.

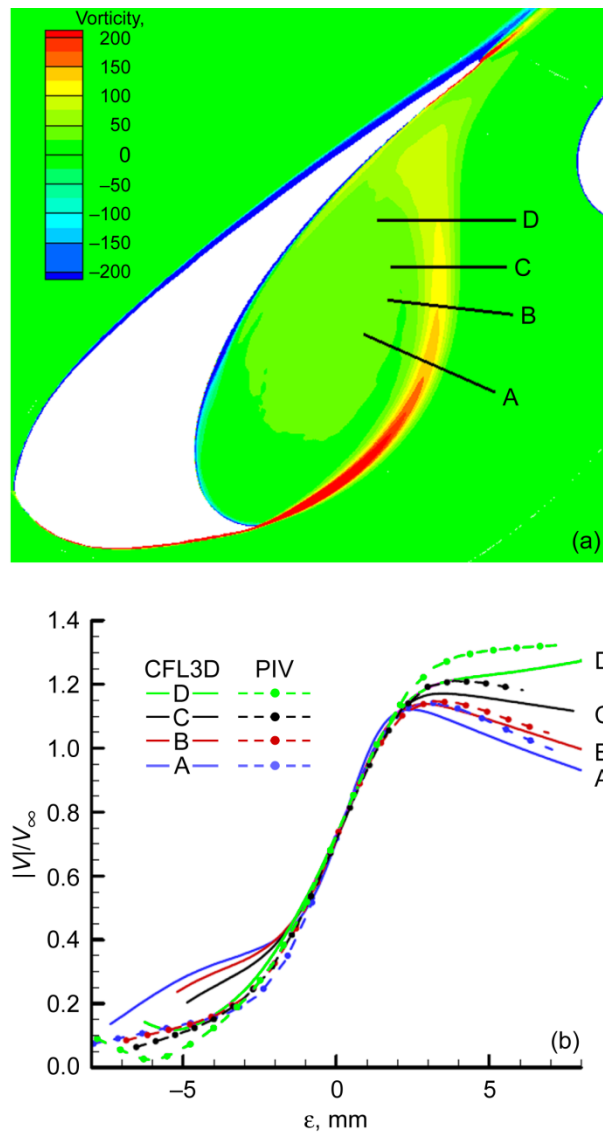


Figure 4.48.—Time-averaged velocity magnitude profiles across leading-edge slat shear layer. (a) Locations of mixing-layer profiles A through D superposed on contour of mean spanwise vorticity. (b) Comparison of CFL3D simulation results (based on spanwise grid) for locations A through D and particle imaging velocimetry (PIV) measurements (Ref. 35). The distance ϵ increases from left to right, along the cuts A through D.

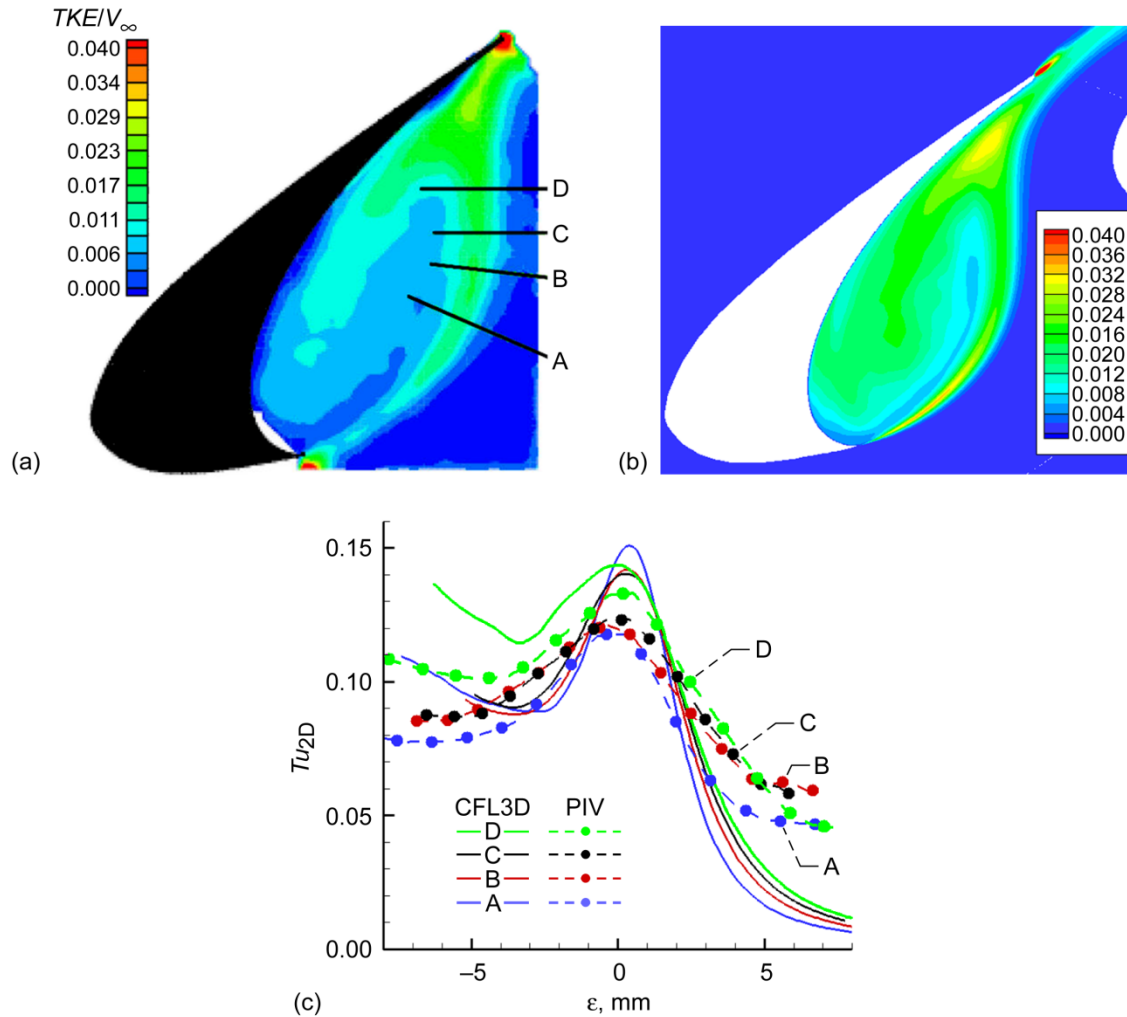


Figure 4.49.—Time-averaged two-dimensional (2D) turbulent kinetic energy TKE distribution in leading-edge slat cover region, where V_∞ is free-stream velocity. (a) Locations of mixing-layer profiles A through D superposed on particle imaging velocimetry (PIV) contours. (b) CFL3D predictions. (c) CFL3D results compared with (PIV) measurements along profiles A through D (Ref. 35), where Tu_{2D} is the two-dimensional turbulence intensity.

In Figure 4.50, the peak two-dimensional turbulence intensity across the slat mixing layer is plotted against the distance s from the slat cusp along the mean shear-layer trajectory. Within the upstream portion of the shear-layer trajectory ($s < 40$ mm, or 1.6 in.), the measured PIV data based on a large field of view (f.o.v.) encompassing the entire slat cove indicate quite significant discrepancies with the numerical predictions. The relatively thin mixing layer near the cusp is poorly resolved by the large f.o.v. and is the likely cause of the observed differences. A portion of the mixing-layer evolution close to the slat cusp was included within a smaller f.o.v. (i.e., higher resolution) PIV measurement that is also included in Figure 4.50. The higher resolution PIV data seem to capture the fluctuation amplitudes near the predicted overshoot ($s \approx 10$), which is presumably associated with shear-layer

transition from laminar to turbulent behavior. Unfortunately, the higher resolution data did not extend sufficiently far downstream to capture all of the shear-layer development.

Some preliminary insights concerning slat noise characteristics can also be gleaned from the subject computations. The frequency spectra of the computed pressure fluctuations at selected probe locations at distances between 1 and 2.5 slat chords away from the slat trailing edge are shown in Figure 4.51(a). The ordinate in the figure is the frequency multiplied by the power spectral density PSD . With the frequency plotted on a log scale, the product $f \times PSD$ visually gives equal weighting to the energy at each frequency. Probes below the slat (at approximately 1.8 and 2.5 slat chords from the slat trailing edge) are to the rear of the overhead direction, whereas those above the slat (at approximately 1.1 slat chords

from the trailing edge) are in the forward arc. The acoustic spectra across the range of frequencies plotted in the figure closely resemble the spectrum of pressure fluctuations near the reattachment location, emphasizing the prominence of this region in contributing to the slat's broadband noise sources. The peak Strouhal number of the acoustic spectra in Figure 4.51(a) lies within the Strouhal number range, $1 \leq St \leq 3$, similar to the previous measurements of subscale high-lift configurations (Ref. 81). Beyond this peak (up to about 14 kHz), the rolloff in the computed acoustic spectra is not unlike the $1/f^2$ decay predicted by Guo's analytical model (Ref. 50). However, simulations on a domain of greater spanwise extent would be required to confirm this high-frequency rolloff.

Based partly on experimental measurements, Dobrzynski and Pott-Pollenske (Ref. 81) modeled the directivity of the broadband slat noise sources as that of an acoustic dipole that is normal to the slat surface near the trailing edge (Figure 4.51(b)). The orientation of the computed contours of the instantaneous pressure perturbations (Figure 4.51(c)) resembles the near-field propagating pressure waves from an acoustic dipole. However, far-field predictions are necessary to enable definitive comparisons with the above model, particularly in view of the multiple acoustic conversion mechanisms relevant to slat noise generation, such as scattering near the slat trailing edge and the gap region.

In summary, the favorable comparison with the planar PIV data represents a substantial improvement over previous two-dimensional computations (Refs. 78 to 80), revealing the importance of three-dimensional fluctuations in determining

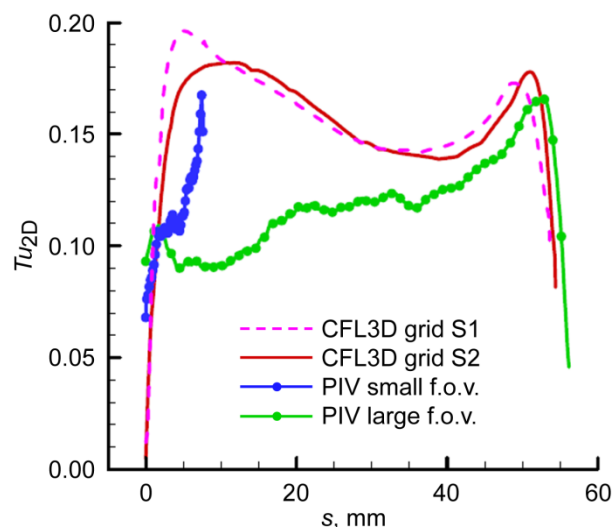
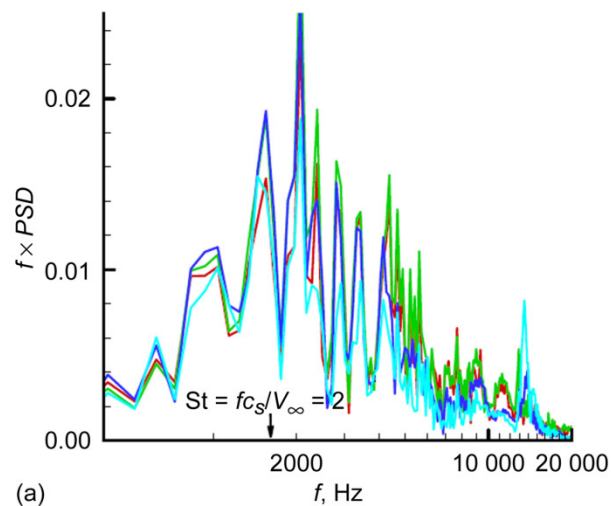
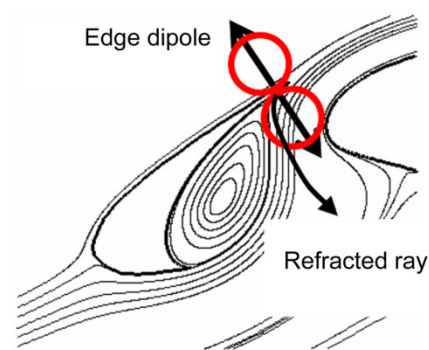


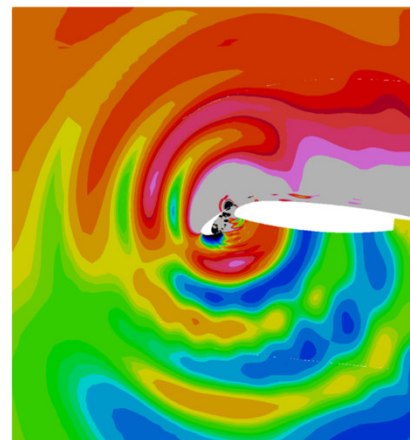
Figure 4.50.—Peak two-dimensional turbulent intensity Tu_{2D} along leading-edge slat cove mixing-layer trajectory versus distance s from slat cusp. Comparison of CFL3D Tu_{2D} based on coarse (S1) and fine (S2) spanwise grids and particle imaging velocimetry (PIV) measurements derived from small and large fields of view (f.o.v.) (Ref. 35).



(a)



(b)



(c)

Figure 4.51.—Acoustic radiation due to leading-edge slat cove unsteadiness. (a) CFL3D-computed acoustic spectra (product of frequency f and power spectral density PSD) at selected probe locations between one and two chords from trailing edge noting point at Strouhal number $St = 2$, where c_s is slat chord length and V_∞ is free-stream velocity. (b) Schematic for slat noise model in Reference 81. (c) Contours of instantaneous pressure perturbations from fine-spanwise-grid simulation.

the unsteady dynamics within the cove region. The computed acoustic characteristics (in terms of the frequency spectrum and spatial distribution) within short distances from the slat resemble the previously reported, subscale measurements of slat noise (Ref. 81).

4.8.4 Recommendations

A more definitive assessment of the computational model will be enabled by acoustic measurements of the same configuration. Furthermore, additional measurements of the slat cove flow including the surface pressure fluctuations, especially just upstream of the slat trailing edge where the slat cove shear layer reattaches to the slat pressure surface, would be a crucial factor in evaluating the accuracy of both the computed frequency spectra and the spanwise coherence of the broadband noise sources in this acoustically significant region. Spanwise distribution of the acoustic sources has a direct impact on the far-field acoustic intensity, as the intensity is proportional to the spanwise coherence length.

Off-surface measurements using a hot wire would help overcome the limited spatial resolution of the current PIV data, especially near the slat cusp, and will also provide an additional means of validating the frequency spectra of computed fluctuations. Acquisition of three-dimensional PIV data across selected spanwise planes will contribute to a more complete assessment of the near-field computations by elucidating the spanwise structure of the slat flow fluctuations.

After demonstrating that the relevant metrics of the unsteady slat cove flow can be adequately predicted with such numerical simulations, the latter can be used to complement the typically sparse flow-field details available from experimental measurements. The simulation data can be used to develop and calibrate models for the spatio-temporal correlations used in low-order physics-based methods for airframe noise prediction. A promising approach of this type would involve the modeling of an acoustic source with fluctuation metrics derived from a stationary RANS computation along with a suitable model for the appropriate coherence functions. The sound can then be propagated to the far field by some method of choice; for example, by applying an acoustic analogy to a tailored Green's function (Ref. 82), or solving the linearized Euler equations (Ref. 83).

A major drawback of the computation used during the present assessment corresponds to the limited spanwise extent of the computational domain. Appropriately validated computations of this type can still be used, even in their present form, to help refine the lower-order models for noise prediction (Refs. 82 and 83) and/or to help develop physics-based noise reduction concepts. However, it is still desirable to extend such computations to larger spanwise domains, so that reliable acoustic predictions can be made without requiring additional ad hoc assumptions. Increasing the computational efficiency by resorting to high-order accurate, yet robust, flow solvers (e.g., Ref. 84) should help accelerate the accomplishment of that goal; again, it is imperative that resource investment be made in this area.

There are two additional complications to the physics of slat-noise generation that must be investigated. One such complication can result from the wing's leading-edge sweep, which could contribute to a spanwise velocity component that is large relative to that of the slat-cove flow in the plane normal to the leading edge. When this occurs, the cove flow no longer continually recirculates within the cove region (Figure 4.47(a)), and instead traverses a helical path to the outer tip of the slat. Such a phenomenon suggests that the flow in the cove shear layer is highly skewed, which could influence the structure of the fluctuations generated therein. Secondly, the potential effects of support brackets must be considered. In particular, the interaction of a strong spanwise cove flow with a bluff-body-like bracket geometry could have a measureable impact on slat noise radiation.

4.9 Conclusions

An investigation is undertaken to assess the current capability to predict airframe noise levels for aircraft that are configured for airport approach. During landing operations, the leading-edge slats and trailing-edge flaps of the aircraft's high-lift system as well as the landing gear are the primary sources of airframe noise. The present assessment includes far-field predictions for these airframe components and their validation with experimental measurement. The test cases are chosen from previously identified experiments involving wind tunnel models as well as from flight testing of operational aircraft. In most of these cases, the generation and propagation of airframe noise are predicted with NASA's Aircraft Noise Prediction Program (ANOPP). The remaining predictions are from first principles, in which the acoustic source is simulated by computational fluid dynamics. Although such methods cannot be considered practical prediction tools, the wealth of detailed information they yield regarding the physics of airframe noise sources can provide insight into the development of the next generation of prediction tools.

Assessment metrics are defined to quantify the extent to which the computations and measurements are reliable and compare favorably. Predicted and measured results are subjected to various analyses to determine parametric ranges of applicability for each of the applied techniques. As the source models within ANOPP are largely empirical, comparisons of predictions with measurements of both total airframe noise and the noise from individual components ranged from acceptable to poor. For instance, in Section 4.4, "Flap-Edge Noise Measurement and Prediction," Fink's method was unable to adequately predict the noise increment due to an altered flap deflection (Figure 4.13). In Section 4.5, "Aeroacoustic Measurement and Prediction for Boeing 777 Landing Gear Model," both Fink's and Boeing's landing-gear source models were found lacking in regard to their insensitivity to the presence of a bay door (Figure 4.21).

However, as stated by Gillian (Ref. 85), ANOPP's primary function is "to predict aircraft noise with the best currently available methods." Furthermore, the notion of a "best"

available method is predominantly influenced by the ability to use that method in a highly efficient manner. As of this writing, all such methods are based upon lower-order models and heavily reliant upon empiricism. Therefore, ANOPP (or any other present-day noise prediction tool) cannot be expected to provide design-level information on a case-by-case basis. Rather, ANOPP's primary benefit lies in its ability to determine overall noise trends for full aircraft studies.

Nonetheless, such disappointing results as those cited above indicate that the next generation of prediction methods must be responsive, in a fundamental way, to any geometric variation that alters the unsteady flow field. Also indicated is a need to pursue empirical relationships on a more basic level than previously investigated. Recommendations to achieve such advances in the present state of the art are given below.

4.10 Recommendations

The methods discussed within this chapter fall under the general classification of empirical prediction, wherein little information regarding the details of the actual physical processes that generate the noise is incorporated and predictions are based on correlations of experimental data. Although useful for rapid predictions in current engineering environments, the inability of the methods to predict even the change in noise due to an altered flap deflection—a most basic engineering parameter variation—demonstrates that such methods are not only prone to failure but also that an engineer may not know when the prediction is likely to fail.

Research in noise prediction methods must increasingly focus on utilizing more detailed descriptions of the noise-generating physics. Examples of the development of such descriptions are discussed in References 86 to 88, involving coordinated experimental and computational studies on a range of simple geometries (called building-block problems). Indeed, the computational tools discussed in this chapter form a major component of such studies, but significant improvements are yet required for these tools to reliably and efficiently predict all required mechanisms of noise generation.

For engineering predictions, however, one can envision semiempirical tools, wherein the empiricism corresponds to aerodynamic noise sources on a more fundamental level. As an example, if empirical correlations could be developed for the noise amplitude and spectrum with respect to a set of generic flow-field features (e.g., the vorticity distribution of a shear layer in a separated flow), then such a semi-empirical method could begin with a computation of the steady flow field about the flap edge of a wing design under investigation. This computed flow field would then be examined for the corresponding correlation variables, and the noise predicted. The sensitivity of the noise prediction to engineering parameters would thus be contained in the computation of the steady flow field.

The suggested development effort requires a coordinated deployment of advanced experimental and computational tools in a series of fundamental studies that are carefully chosen and conducted, and for which sufficient time and resources are allotted. In order to make significant progress in the ability to accurately predict airframe noise for a wide range of configurations and flow conditions, it is clear that sufficient resources be invested in advancing the state of the art for numerical simulation and measurement of the unsteady flow fields that generate airframe noise. Specific recommendations include

1. Intensify development of numerical simulation tools, including Reynolds averaged Navier-Stokes (RANS), unsteady RANS (URANS), large-eddy simulation (LES), detached-eddy simulation (DES), and appropriate hybrids thereof. In addition, an efficient method for constructing tailored Green's functions should be developed. RANS and tailored Green's function development combined with improved models for the space-time coherence of the acoustic source would enable relatively rapid, medium-fidelity airframe noise predictions that could be calibrated and augmented using higher-fidelity, hybrid RANS/LES computations.

2. Continue development of hardware and processing methods for phased arrays and related measurement technologies, with such goals as higher sensor count, greater efficiency, and lower cost. Such development should include improvement to beamforming, deconvolution, and coherence detection algorithms, advanced methods to account for reflections and flow diffraction, and parallel distributed processing of array signals for real-time presentation of noise levels and directivity. Ideally, such methods should be capable of simultaneous, nonintrusive measurement of fluctuating flow fields associated with multiple noise sources.

3. Conduct a portfolio of fundamental, "building-block" numerical simulations, in conjunction with detailed multi-instrumented experiments. Such a program is intended to generate an archival database of space-time correlation functions for flow-field fluctuations associated with aerodynamic noise sources, for eventual use in advanced prediction methods.

4. Intensify pertinent research in such areas as flow control, circulation control, and morphing structures to facilitate the development of noise reduction technology.

In closing, it is timely to comment on the outlook for extending the present prediction methodology beyond the realm of conventional aircraft configuration. At first glance, such an outlook is a contradiction in terms, as noted by Whitfield (Ref. 89):

Current aircraft system noise prediction tools (such as ANOPP) rely on current knowledge. Their ability to extrapolate to unconventional configurations is not to be trusted.

Nonetheless, the aeroacoustic research community increasingly looks to unconventional aircraft to achieve long-term noise reduction goals. As stated by Posey, et al. (Ref. 90), with direct relevance to non-engine aircraft noise,

... as jet noise has decreased, noise from the fan and other engine components, as well as from flow over the airframe, has become unmasked, making further noise reduction much more difficult. Thus, a very large reduction in community noise due to an aircraft flyover will probably require an unconventional aircraft design that relies not only on a quiet engine design, but also on propulsion/airframe integration that minimizes noise production and shields the ground from the residual noise.

Such is the apparent conundrum, given the necessity to develop tomorrow's quiet aircraft through unconventional

design, while available noise prediction tools are presently unfit for the task. Clearly, methods that bring more of the physics into the prediction, and rely less on low-order modeling, are more extensible to unconventional configurations. However, only direct numerical simulation methods avoid modeling altogether. Every other methodology is limited by either the experimental database on which it is calibrated or the model itself, when physical attributes are not determined from first principles. For the foreseeable future, direct numerical simulation will not be a viable option due to its unacceptable consumption of computational resources when applied to problems involving turbulent flow on a full-scale aircraft. Therefore, more fundamental approaches to model development, such as those based on judiciously chosen "building blocks" (Recommendation 3 above), will be the primary means of improving prediction accuracy and extending the methodology to unconventional configurations.

Appendix A.—Nomenclature

A.1 Acronyms

ANOPP	Aircraft Noise Prediction Program
AST	Advanced Subsonic Transport (Program)
BART	Basic Aerodynamic Research Tunnel
CFD	computational fluid dynamics
DES	detached-eddy simulation
FAA	Federal Aviation Administration
FAP	Fundamental Aeronautics Program
f.o.v.	field of view
FW–H	Ffowcs Williams-Hawkings
LES	large-eddy simulation
LTPT	Low-Turbulence Pressure Tunnel
MADA	Medium Aperture Directional Array
PIV	particle image velocimetry
PSD	power spectral density
QAT	Quiet Aircraft Technology (Program)
QFF	Quiet Flow Facility
RANS	Reynolds-averaged Navier-Stokes
rms	root-mean-squared
SADA	Small Aperture Directional Array
SST	shear stress transport (model)
SFW	Subsonic Fixed Wing (project)
SPL	sound pressure level
TKE	turbulent kinetic energy
URANS	unsteady Reynolds-averaged Navier-Stokes
WFF	Wallops Flight Facility

A.2 Symbols

a	speed of sound
A	planform area
A_G	empirically derived constant in Equation (4.28), Appendix B
B_G	empirically derived constant in Equation (4.28), Appendix B
b	span length
C	coefficient (e.g., pressure coefficient)
c	chord length
D	diameter
\mathcal{D}	directivity function
d	aircraft tire diameter
F	noise spectrum function
F_{xyz}	computational mesh with fine grid-point spacing in x,y,z-coordinates

f	frequency
K	constant in Equation (4.19), Appendix B
L	length
\mathcal{L}	total length of all main struts
l	strut length
M	Mach number
M_{xyz}	computational mesh with medium-level grid-point spacing in x,y,z-coordinates
M_{xyFz}	computational mesh with medium-level grid-point spacing in x,y-coordinates and fine grid-point spacing in z-coordinate
n	number of wheels on aircraft
P	spectral component of acoustic pressure in Equations (4.24) and (4.25), Appendix B
p	aerodynamic pressure
PSD	power spectral density
q	empirical constant from Equation (4.28), Appendix B, that defines spectral shape
R	source-to-observer distance
Re	Reynolds number
S	aggregate surface-integration-effects parameter in Equation (4.25), Appendix B
St	Strouhal number
s	distance along slat shear layer trajectory
TKE	turbulent kinetic energy
Tu	turbulence intensity
t	time
u,v	velocity components in the x- and y-directions
V	velocity
W	aircraft maximum takeoff gross weight
x, y, z	Cartesian coordinates, in the streamwise, spanwise, and normal directions, respectively
α	quantity from Equation (4.27), Appendix B
β	flow energy conversion efficiency parameter in Equation (4.25), Appendix B
γ	empirically derived constant in Equation (4.28), Appendix B
δ	boundary layer thickness
ε	distance across shear layer
η	complexity factor, Equation (4.26), Appendix B
θ	polar angle
μ	dynamic viscosity
Π	acoustic power
ρ	density of air

σ	empirically derived constant in Equation (4.28), Appendix B
ϕ	azimuthal angle
ω	vorticity
∂	deflection angle

Subscripts:

e	emission
f	flap
H	high-frequency component
h	horizontal tail surface
L	low-frequency component
M	mid-frequency component
O	overall

p	pressure
ref	reference
s	slat
t	tandem cylinder
v	vertical tail surface
w	wing
z	z-axis component
2D	two-dimensional
∞	aircraft or free stream

Superscripts:

*	normalized (nondimensional)
'	perturbation quantity

Appendix B.—Aircraft Noise Prediction Program

Most of the acoustic predictions in the present work are obtained with semi-empirical methods in the Aircraft Noise Prediction Program (ANOPP) (Ref. 42). ANOPP was developed for general aircraft noise prediction, including the effects of an aircraft's characteristics, engines, and operations as well as atmospheric and ground effects. As such, ANOPP is organized into modules that account for the flight operation of interest, describe the source-to-observer geometry, model the required noise-generating mechanism(s), propagate the noise through the atmosphere, and calculate the quantity of the noise received by the observer. Two airframe noise modules are available in ANOPP, each containing several component source models that can either be applied in isolation or summed to compute the total nonpropulsive noise for a given aircraft configuration. Only those airframe source models that are used in the present test cases are described below in a straightforward manner, with minimal discussion of theory or development. For a more thorough discussion of all available airframe noise source models, see Reference 42.

B.1 ANOPP: Fink's Method

The earlier of the two airframe noise modules in ANOPP contains acoustic source models developed by Fink (Ref. 32) for the Federal Aviation Administration (FAA). In Fink's "noise component method," total airframe noise is calculated as an acoustic sum of component sources. It is, therefore, assumed that all component sources are mutually incoherent. In the development of his model, Fink formulated the noise contribution for each airframe component with an appropriate scaling law, and determined amplitudes by matching available experimental data.

In ANOPP, the far-field noise associated with an airframe component source is computed in terms of a nondimensional, mean-square acoustic pressure. All of Fink's component models can be expressed in the general form

$$\langle p^2 \rangle^* = \frac{\Pi^*}{4\pi R^{*2}} \frac{\mathcal{D}(\theta, \phi) F(\text{St})}{(1 - M_\infty \cos \theta)^4} \quad (4.1)$$

In Equation (4.1), Π^* is a nondimensional acoustic power, \mathcal{D} is a directivity function, F is a spectral shape function, and M_∞ is the aircraft Mach number. The nondimensional variable R^* represents the physical propagation distance R normalized by the aircraft wingspan, and θ and ϕ represent the polar and azimuthal directivity angles, respectively; these dimensions are illustrated in Figure 4.2 (see Sec. 4.2.2). The argument St is a Strouhal number, defined by

$$\text{St} = \frac{fL}{M_\infty a_\infty} (1 - M_\infty \cos \theta) \quad (4.2)$$

where f is frequency, a_∞ is the ambient sound speed, and L is a characteristic length scale of the airframe noise source. Note that the independent variables in Equations (4.1) and (4.2) are interpreted with respect to the visual position of the aircraft at signal emission time.

A prediction for an aircraft's total airframe noise is ultimately a sum of the mean-square pressures, in Equation (4.1), that correspond to the individual airframe components described in the following three subsections. Although the methodology is presented within a nondimensional framework, the output from ANOPP is easily directed either to mean-square acoustic pressure in English or SI units or to a sound pressure level (SPL) in decibels, relative to a suitable reference pressure.

B.1.1 Clean Airframe Noise

The lower limit of an aircraft's airframe noise is generated by its "clean" (cruise) configuration. In Fink's method, the noise radiated by a "clean airframe" is composed entirely of trailing-edge sources; that is, those of the wings and tail surfaces. The theoretical basis for Fink's clean airframe noise model is attributed to the trailing-edge noise analyses in References 91 and 92. For a conventionally constructed aircraft, the acoustic power associated with the wing's trailing-edge noise is

$$\Pi^* = (4.464 \times 10^{-5}) M_\infty^5 \delta_w^* \quad (4.3)$$

where δ_w^* is a normalized boundary-layer thickness at the trailing edge, determined by a turbulent flat-plate model,

$$\delta_w^* = 0.37 \frac{A_w}{b_w^2} \left[\frac{\mu_\infty b_w}{\rho_\infty M_\infty a_\infty A_w} \right]^{1/5} \quad (4.4)$$

The quantities A_w and b_w are the area and span of the wing, respectively, while ρ_∞ and μ_∞ are the respective density and dynamic viscosity of the ambient medium.

The trailing-edge acoustic power for a horizontal tail surface (h) is similar to that of a clean wing,

$$\Pi^* = (4.464 \times 10^{-5}) M_\infty^5 \delta_h^* \left[\frac{b_h}{b_w} \right]^2 \quad (4.5)$$

$$\delta_h^* = 0.37 \frac{A_h}{b_h^2} \left[\frac{\mu_\infty b_h}{\rho_\infty M_\infty a_\infty A_h} \right]^{1/5} \quad (4.6)$$

The symbols δ_h^* , A_h , and b_h correspond to the horizontal tail surface in the same way as their wing counterparts in Equations (4.3) and (4.4). The noise directivity function for the wing or horizontal tail surface is given by

$$\mathcal{D}(\theta, \phi) = 4 \cos^2 \phi \cos^2(\theta/2) \quad (4.7)$$

Following the symbolic convention in Equations (4.3) to (4.7), the acoustic power formulation for a vertical tail surface (v) is

$$\Pi^* = (4.464 \times 10^{-5}) M_\infty^5 \delta_v^* \left[\frac{b_v}{b_w} \right]^2 \quad (4.8)$$

$$\delta_v^* = 0.37 \frac{A_v}{b_v^2} \left[\frac{\mu_\infty b_v}{\rho_\infty M_\infty a_\infty A_v} \right]^{1/5} \quad (4.9)$$

Because of its perpendicular orientation with respect to the planes of the wing and horizontal tail surfaces, the noise directivity function for a vertical tail surface is

$$\mathcal{D}(\theta, \phi) = 4 \sin^2 \phi \cos^2(\theta/2) \quad (4.10)$$

For conventionally constructed aircraft, the spectral shape function $F(\text{St})$ for trailing-edge noise associated with a clean airframe component is

$$F(\text{St}) = 0.613 \left[\frac{10\text{St}}{(10\text{St})^{1.5} + 0.5} \right]^4 \quad (4.11)$$

$$\text{St} = \frac{f \delta^* b}{M_\infty a_\infty} (1 - M_\infty \cos \theta) \quad (4.12)$$

where the values of the span b and the boundary layer thickness δ^* correspond to any one of the three clean airframe components discussed above. Equations (4.3) to (4.12) yield the necessary input to Equation (4.1) to compute the far-field, mean-square acoustic pressure for each clean airframe component. A prediction for the total noise associated with the clean airframe is produced by summing these individual mean-square pressures.

B.1.2 Trailing-Edge Flap Noise

Unlike the leading-edge slats, the additional noise radiated by the extension of trailing-edge flaps is not directly related to the clean wing noise. Instead, Fink regarded the flap panels as immersed in the turbulent wake of the main wing element and any additional upstream flap elements. Thus, trailing-edge flap noise is interpreted as the result of unsteady lift fluctuations due to incident turbulence. This model was entirely determined by scaling and curve-fitting available flight data (Refs. 5, 7, and 93).

For a flap system (f) with one or two slots, the additional acoustic power can be expressed as

$$\Pi^* = (2.787 \times 10^{-4}) M_\infty^6 \frac{A_f}{b_f^2} \sin^2 \partial_f \quad (4.13)$$

where A_f , b_f , and ∂_f are the flap's area, span, and deflection angle, respectively. The spectral shape for a system of single- or double-slotted flaps is described by the piecewise continuous function,

$$F(\text{St}) = \begin{cases} 0.0480 \text{ St} & (\text{St} < 2) \\ 0.1406 \text{ St}^{-0.55} & (2 \leq \text{St} \leq 20) \\ 216.49 \text{ St}^{-3} & (\text{St} > 20) \end{cases} \quad (4.14)$$

For triple-slotted flaps, the overall acoustic power is

$$\Pi^* = (3.509 \times 10^{-4}) M_\infty^6 \frac{A_f}{b_f^2} \sin^2 \partial_f \quad (4.15)$$

which represents an increase in power by 1 dB to account for the added flap complexity. The piecewise spectrum function for triple-slotted flaps is

$$F(\text{St}) = \begin{cases} 0.0257 \text{ St} & (\text{St} < 2) \\ 0.0536 \text{ St}^{-1/16} & (2 \leq \text{St} \leq 75) \\ 17.078 \text{ St}^{-3} & (\text{St} > 75) \end{cases} \quad (4.16)$$

For either trailing-edge flap case, the Strouhal number and noise directivity function are, respectively,

$$\text{St} = \frac{f A_f}{M_\infty a_\infty b_f} (1 - M_\infty \cos \theta) \quad (4.17)$$

$$\mathcal{D}(\theta, \phi) = 3(\sin \partial_f \cos \theta + \cos \partial_f \sin \theta \cos \phi) \quad (4.18)$$

With the appropriate acoustic power and spectrum function from one of Equations (4.13) through (4.16), and the directivity in Equation (4.18), the flap's contribution to the far-field acoustic pressure is then calculated with Equation (4.1).

B.1.3 Landing Gear Noise

The development of a general noise model for an aircraft's landing gear is a particularly daunting task. The geometry of a given landing gear can be quite complex, containing many parts that vary significantly in shape, size, and flow orientation. Fink's landing gear noise model is heavily reliant upon the experimental work of Heller and Dobrzynsky (Ref. 94). For instance, Fink incorporates the same Strouhal scaling, in which the landing gear tire diameter is chosen as the characteristic length scale. Heller and Dobrzynsky justified this scaling by noting "fairly constant" ratios of the tire diameter to the strut diameter, exposed strut length, wheel lateral spacing, and

tire width, for landing gear on certain classes of aircraft (Ref. 94). Also, Fink's model does not account for cavity noise due to landing gear bay doors remaining open, because the results in Reference 94 suggested that the noise radiated by an isolated cavity was mostly overwhelmed by that of the landing gear itself. Finally, Fink used the measured spectra in Reference 94 as a starting point for his own formulation, and approximated them with arbitrary empirical equations. Fink's formulation, described below, is based on a characterization of the landing gear noise spectrum as the sum of two spectra, one representing a noise source that is independent of the azimuthal angle ϕ and another that varies as $\sin^2\phi$. Thus, Fink concluded that the prediction process for landing gear noise could be reasonably simplified by assuming that only two noise sources were significant: those arising from the wheels and the struts.

In Fink's airframe noise component method, the wheels and the strut of a landing-gear assembly each radiate an individual acoustic power, according to

$$\Pi_{\text{wheels}}^* = K n M_\infty^6 \left(\frac{d}{b_w} \right)^2 \quad (4.19a)$$

$$\Pi_{\text{strut}}^* = 2.753 \times 10^{-4} M_\infty^6 \left(\frac{d}{b_w} \right)^2 \frac{l}{d} \quad (4.19b)$$

where n is the number of wheels per landing gear, d is the tire diameter, and l is the strut length. The constant K is 4.349×10^{-4} for $n = 1$ or 2 , and 3.414×10^{-4} for $n = 4$. Note that the ratio of exposed strut length to tire diameter is included in Equation (4.19b) to better predict noise from landing gear that may be significantly outside the presumed aircraft class; for example, those with a long-strut nose gear or a short-strut tail wheel. The directivity functions for the wheels and strut noise are

$$\mathcal{D}(\theta, \phi)|_{\text{wheels}} = \frac{3}{2} \sin^2 \theta \quad (4.20a)$$

$$\mathcal{D}(\theta, \phi)|_{\text{strut}} = 3 \sin^2 \theta \sin^2 \phi \quad (4.20b)$$

For one- or two-wheel landing gear, the wheel and strut noise spectra can be written

$$F(\text{St})|_{\text{wheels}} = \frac{13.59 \text{St}^2}{(\text{St}^2 + 12.5)^{9/4}} \quad (4.21a)$$

$$F(\text{St})|_{\text{strut}} = \frac{5.325 \text{St}^2}{\text{St}^8 + 30} \quad (4.21b)$$

while the corresponding spectra for a four-wheel landing gear are

$$F(\text{St})|_{\text{wheels}} = \frac{0.557 \text{St}^2}{(0.25 \text{St}^2 + 1)^{3/2}} \quad (4.22a)$$

$$F(\text{St})|_{\text{strut}} = \left(\frac{1.280 \text{St}}{\text{St}^2 + 1.06} \right)^3 \quad (4.22b)$$

The Strouhal number, in Equations (4.21) and (4.22) is referenced to the tire diameter:

$$\text{St} = \frac{f d}{M_\infty a_\infty} (1 - M_\infty \cos \theta) \quad (4.23)$$

The appropriate wheel and strut noise contributions are individually input to Equation (4.1), and then summed to compute the mean-square acoustic pressure for the landing gear in the far field.

B.2 ANOPP: Boeing's Method, Landing Gear Noise

More recent airframe noise models (Refs. 43 and 44) have been developed by The Boeing Company and are incorporated into a separate ANOPP module. In some respects, Boeing's approach to airframe noise is similar to Fink's. Most importantly, the total noise is calculated as a sum of component-wise noise contributions that are generated by mutually incoherent sources. In addition, experimental measurement plays a critical role in Boeing's semi-empirical method. However, the process and formulations are significantly different, as will become apparent below.

The application of Boeing's airframe noise model in the present assessment involves the prediction of acoustic spectra for a model-scale Boeing 777 main landing gear. The relatively sparing use of this ANOPP module within the present assessment is, in part, due to difficulties with its implementation. These difficulties have arisen largely in two areas: unavailability of required input parameters and scaling issues, when wind tunnel models are involved (See Sec. 4.5.2, "Results and Findings."). Therefore, these models will need to be reconsidered at a later date to determine their full effectiveness.

Boeing's landing gear noise model, developed by Guo (Ref. 44), is based on fundamental aerodynamic noise theory, statistical scaling laws derived from the theory, and correlations of these laws with full-scale landing gear noise tests. The method decomposes the landing gear noise into three spectral components. The low-frequency spectral component represents the noise generated by large-scale structures such as wheels. The mid- and high-frequency spectral components correspond to the main struts and the small-scale details such as hydraulic lines, respectively. The spectral shape, amplitude, and directivity of each component were derived separately, and each contains factors to allow modeling of the details of each spectral component in an attempt to include more

physics. The Boeing-Guo method requires significantly more detailed information to define the landing gear assembly than does Fink's method, thus providing a higher fidelity prediction capability. These inputs include all the basic flow and geometric parameters used in Fink's model: the number of wheels, wheel diameter, and main strut length. In addition, the Boeing-Guo model requires the wheel width, axle diameters, bogie length and width, as well as details on all other struts, shock struts, vertical bars, axles, torque bars, junction rods, and door details. Furthermore, and more importantly unlike Fink's model, the Boeing-Guo model was developed in terms of a narrow-band spectrum, which is converted to 1/3 octaves as the last step. This has ramifications regarding frequency scaling as will be indicated later. The general form of the far-field, mean-square acoustic pressure formulation is

$$\langle p^2 \rangle = \frac{\rho_\infty^2 a_\infty^4 M^6 \mathcal{D}_O(\theta_e)}{R_e^2 (1 - M_\infty \cos \theta_e)^4} (P_L + P_M + P_H) \quad (4.24)$$

where the parameters common to all three spectral components have been factored out, and those specific to a particular component are represented by the P terms. The subscripts L , M , and H denote the low-, mid-, and high-frequency components, respectively. The overall directivity $\mathcal{D}_O(\theta_e)$ is in addition to the directivity function defined within each P term and is included to account for the effects of the landing gear installation. The propagation distance R_e and angle θ_e are defined in Figure 4.18. To simulate wind tunnel conditions, the factor $(1 - M_\infty \cos \theta_e)^4$ is required to account for convective amplification, but was erroneously excluded from the method (Ref. 95). This factor has been incorporated for the predictions reported herein. Each P takes the form

$$P = \beta S \mathcal{D}(\theta_e, \phi_e) F(\text{St}) \quad (4.25)$$

where β is the flow energy conversion efficiency parameter, which models the efficiency of the process whereby the steady flow motion of the landing gear parts generates unsteady flow that radiates noise. Currently, this parameter can only be determined by matching prediction with data. In Equation (4.25), S is the aggregate surface-integration-effects parameter and is related to the aggregate surface area of the landing gear parts for each frequency component. For the low-frequency component it is computed directly from the wheel dimensions. For the mid-frequency component it is computed by summing the surface areas of all main strut elements. For the high-frequency component, that approach is not practical because of the large number of small parts, which have various shapes and orientations. Hence, S_H is modeled using an empirically defined length scale and "complexity factor" η which has the following form for a main landing gear:

$$\eta = 1 + 0.15 \left[\frac{W}{W_{\text{ref}}} \frac{\mathcal{L}}{\mathcal{L}_{\text{ref}}} \frac{n}{n_{\text{ref}}} - 1 \right] \quad (4.26)$$

The terms W , \mathcal{L} , and n are the maximum takeoff gross weight of the aircraft, the total length of all the main struts, and the number of wheels, respectively. The subscript "ref" indicates reference values, determined from full-scale data (Ref. 59). The functions $\mathcal{D}(\theta_e, \phi_e)$ and $F(\text{St})$ are the component specific directivity and spectrum functions, respectively. The general form of the directivity function is

$$\mathcal{D}(\theta_e, \phi_e) = (1 + \alpha_1 \cos^2 \theta_e)^2 (1 + \alpha_2 \sin^2 \phi_e) \quad (4.27)$$

where α_1 and α_2 are unique for each of the three frequency domains. The values for the low-, mid-, and high-frequency domains, respectively, are $\alpha_1 = (0.2, 0.6, 1.0)$ and $\alpha_2 = (3.0, 2.0, 0.1)$. The spectrum function $F(\text{St})$ is a narrowband power spectral density function and has the following form:

$$F(\text{St}) = A_G \frac{\text{St}^\sigma}{(B_G + \text{St}^\gamma)^q} \quad (4.28)$$

where σ , γ , and q are empirical constants that define the spectral shape; and A_G and B_G are derived constants that set the peak value of the spectrum to unity at an empirically derived Strouhal number or the peak Strouhal number. For each of the three frequency-component spectra, a unique set of σ , γ , q , A_G , and B_G was determined for each peak Strouhal number by analyzing full-scale test data (Ref. 95). The Strouhal number St is determined using the characteristic length scale associated with the frequency range for which $F(\text{St})$ is being evaluated. The characteristic length scale for the low-frequency component spectrum is the wheel diameter; whereas, the characteristic length scale for the mid- and high-frequency component spectra are computed using the aggregate surface area parameter, an average length, and an empirical scale factor. Complete details on the development of these factors and parameters are fully documented in References 59 and 95.

Because F is defined as a narrowband spectral function, its shape is not invariant with respect to St , which undercuts the generality of using Strouhal scaling on which it is based. This effect, combined with the empirical function η used to define S_H , makes the Boeing-Guo method, at present, only appropriate for full-scale landing gear. However, the model does attempt to incorporate as much physics as possible to reduce configuration dependence, but does not eliminate empiricism. Note that this method compares very well with full-scale landing gear measurements (Refs. 44 and 95) and is considered an improvement over existing semi-empirical prediction capabilities for full-scale Boeing 737 and 777 landing gear predictions.

Appendix C.—CFL3D and Acoustic Analogy

The acoustic predictions for the tandem cylinders and the simplified landing gear model in Sections 4.6 and 4.7, respectively, are modeled from first principles, beginning with the fundamental theory of aerodynamic sound proposed by Lighthill (Ref. 96). With the introduction of his “acoustic analogy,” followed by important extensions to solid surfaces (Ref. 96) in arbitrary motion (Ref. 47), Lighthill established a philosophy by which the noise associated with most problems of interest could be accurately predicted, provided that the “equivalent forces” and stresses representing the sources of sound could be accurately modeled. Within this approach to noise prediction, the objective is to model the actual flow mechanisms that give rise to the sources and propagation of radiated sound, thereby leading to the simulation of these sources with solutions of an appropriate set of fluid dynamics equations (e.g., unsteady Reynolds-averaged Navier-Stokes (URANS), large eddy simulation (LES), etc.). Such methods cannot presently be considered practical prediction tools, due to the turnaround times involved in their application. However, the wealth of detailed information they yield regarding the physics of airframe noise sources can provide insight into the development of the next generation of prediction tools.

Despite continued advances in computational resources and numerical algorithms, it is still prohibitively expensive, and often infeasible, to attempt to resolve wave propagation from near-field sources to far-field observers. Integral techniques that can predict the far-field signal based solely on near-field input are a means to overcome this difficulty. Here, the Ffowcs Williams-Hawkins (FW-H) equation (Ref. 47) solvers described by Lockard (Ref. 66) are used to predict the acoustic signature at various observer locations using unsteady flow data from the computational fluid dynamics (CFD) calculation. The FW-H equation is a rearrangement of the exact continuity and Navier-Stokes equations into a form with a wave equation on the left-hand side and a number of source terms on the right. Hence, the Navier-Stokes equations still need to be solved to determine the values for the source terms, but only where nonlinear and viscous effects are important; all of the linear propagation outside of this region can be determined by the FW-H equation. The solution to the FW-H equation is typically obtained using the free-space Green’s function. The resulting solution requires a surface integral and a volume integral over all space outside of the surface, but the solution is often well approximated by the surface integral alone. To perform the integrations, the time histories of all the flow variables are needed, but no spatial derivatives are explicitly required. The FW-H method has typically been applied by having the integration surface coincide with solid bodies, but the method is still applicable when the surface is off the body and penetrable. The codes used in this work are valid for both cases.

Certain flows exist where the volume integral cannot be ignored, such as those containing significant refraction of waves by shear layers and wakes or direct radiation of sound

by turbulence. As long as the integration surface is placed outside of all regions where the volume source terms are large, the volume integral contribution can be neglected. In airframe noise problems where the flow speed is generally around Mach 0.2, most of the noise is generated by the interaction unsteadiness with solid surfaces. Refraction and the direct generation of noise by turbulence are generally much smaller effects. However, the common practice is to ignore the volume integral but compare the FW-H noise predictions obtained using the solid body as a surface with those from surfaces at varying distances away from the body. The predictions should agree if the volume source terms are negligible and the underlying CFD is sufficiently accurate. In addition, calculations using penetrable data surfaces are subject to additional sources of error caused when nonacoustic disturbances pass through the surface. Whether the error can be ignored is problem dependent and difficult to formally prove. However, the true radiated sound from airframe noise problems is often much larger than that of the spurious signal generated by disturbances passing through penetrable surfaces. Singer (Ref. 98) and Brentner and Farassat (Ref. 99) have shown that for different surfaces in the near field of solid bodies, the FW-H correctly calculates the radiated sound, whereas the linear Kirchhoff method produces erroneous results. Nonetheless, a rigorous description of the error incurred when wakes pass through penetrable FW-H surfaces is needed.

For three-dimensional flows with arbitrary motion, the time-domain FW-H formulations developed by Farassat (Ref. 100) are efficient and amenable to numerical computations. In retarded time formulations, the time of reception is known, and the time of emission is calculated. For arbitrary motion, the retarded time calculation requires a numerical root-finding technique. Alternatively, source time algorithms start with the source or emission time and then determine the reception time. For stationary observers, this involves a simple calculation. For a given source time, the arrival time at the observer is typically different for each source point on the mesh describing the FW-H surface. Therefore, the noise signal at the observer must be interpolated from the accumulated signals from all the source points. The forward-time algorithm has the advantage of only requiring the surface data from a single source time to calculate a contribution to the noise. Therefore, it can be directly coupled to CFD codes to compute the noise as the CFD computation proceeds and obviate the need to store all of the surface data. However, stored data allow for the scrutiny of the surface data and for additional observer locations to be included after the CFD computation finishes.

Some simplifications to the retarded-time formulation can be applied for airframe noise problems based on restrictions of the surface motion (Ref. 66) that obviate the need to numerically determine the retarded time. Furthermore, frequency-domain versions of the FW-H (Ref. 66) have been developed that are very efficient when only a limited number of frequencies are important. Additionally, the frequency-domain version is

applicable to two-dimensional problems where time-domain methods formally require an infinite time integration to account for all sources in the third spatial dimension.

The unsteady surface data for the FW-H solver is obtained from simulations with CFL3D (Refs. 45 and 46), a CFD code developed at NASA Langley Research Center. CFL3D uses a finite-volume formulation for the three-dimensional, time-dependent, thin-layer Reynolds-averaged Navier-Stokes (RANS) equations. The code employs a third-order upwind difference for the convection terms that is nominally second-order accurate on nonuniform grids. The viscous terms are discretized with second-order central differences. Time is advanced with a second-order backward difference. When running in time-accurate mode, the solution is converged within each physical time step by applying a dual time-stepping algorithm with multiple sub-iterations. Nominally, 20 to 30 sub-iterations per time step are required, but the number will vary depending on the grid and length of the time interval. CFL3D outputs the sub-iteration residual, lift, and drag after each sub-iteration, and the number of sub-iterations are chosen to ensure that the lift and drag have leveled off within each time step and that the residual has dropped by 2 to 3 orders of magnitude. However, the convergence of the turbulence quantities is typically worse than for the flow equations themselves.

Airframe-noise source regions usually involve unsteadiness in high Reynolds number, separated flows. Direct numerical simulations and LES of such flows are prohibitive because of the near-wall grid resolution requirements. Hybrid models that attempt to transition from an LES away from the geometry to a traditional turbulence model in the near wall region greatly reduces the grid requirement, but are still an active area of research. Even with hybrid models, the computations are resource intensive, requiring months on large Beowulf clusters or supercomputers.

The simulation procedure includes several steps. First, a steady-state computation is used to set up the basic mean flow, followed by an unsteady calculation with random suction and blowing applied to different sections of solid surfaces in order to accelerate the onset of three-dimensional, unsteady flow structures. In practice, the forcing does not exceed 3 percent of the free-stream velocity. Forcing is turned off after large-scale unsteadiness is observed, typically 200 time steps into the unsteady calculation. The simulations are then run for 5000 to 10 000 time steps to allow initial transients in the flow field to dissipate, before collecting time records. Averaged flow quantities are produced by time-averaging over 20 000 to 50 000 time steps.

Appendix D.—Test Facilities

All but two of the prediction assessments in the present chapter are based on experiments conducted in two wind tunnels: the Quiet Flow Facility and the Basic Aerodynamic Research Tunnel, both at NASA Langley Research Center. This appendix gives general descriptions for these test facilities and relevant measurement techniques. In the prediction assessments, additional details that apply to the specific test cases are mentioned as necessary.

D.1 Quiet Flow Facility

The Quiet Flow Facility (QFF) is an open-jet wind tunnel that is specifically designed for anechoic testing. The facility is equipped with a 0.61- by 0.914-m (2- by 3-ft) rectangular open-jet nozzle, oriented vertically in a 407.8-m³ (14 400-ft³) chamber. The shorter sides of the nozzle are bounded by fixed side plates, to which various test articles can be mounted. The QFF is capable of sustaining a maximum free-stream Mach number of 0.17.

Acoustic spectra and directivity data in the QFF are obtained using the Medium Aperture Directional Array (MADA). The MADA consists of 41 B&K Model 4138 0.318-cm (1/8-in.) microphones with 0.64 cm (1/4-in.) preamplifiers, mounted on an acoustically treated frame and covered with a hood of thin woven nylon fabric to reduce microphone self-noise due to recirculating air currents within the QFF. The hooded array is boom-mounted and faces the model region. Figure 4.52 is a photo of the MADA with the front hood removed to show the overall mounting. The schematic in Figure 4.53 shows the arrangement of the array microphones as viewed from the source region. The MADA microphones are arranged in five concentric circles, each with eight equally spaced microphones, and one microphone mounted in the center (also serving as the phase center of the array). The inner four circles and the single central microphone correspond to the geometric arrangement for the Small Aperture Directional Array (SADA), used for legacy datasets (e.g., Ref. 55). The circles are irregular in the sense that the horizontal- and vertical-arm microphone spacings are slightly larger than those in the diagonal arms. The pivotal boom is attached to the fixed side plates and allows positioning of the array at a large range of polar and azimuthal angles, with respect to the test model. For the single-microphone analyses described in this chapter (e.g., Sec. 4.5; also, Refs. 36 and 37), the four MADA microphones shown circled in Figure 4.53 are used independently. At a nominal source distance of 1.5 m (5 ft), these microphones span polar and azimuthal ranges of approximately 10° in solid angle from the center of the boom rotation.

In the course of each experiment, the SADA and MADA are carefully calibrated to check for deviations between experimental and theoretical array responses. Thus, injection calibrations that consist of inserting a known signal simultaneously

into all microphone channels are performed to detect microphone sensitivity and phase drift. A series of point source tests is also performed by placing a calibrator source (intended to provide an omnidirectional sound source) in the test section at operational working distance from the array. Noise measurements are obtained across a broad frequency range and are compared with corresponding theoretical array responses.

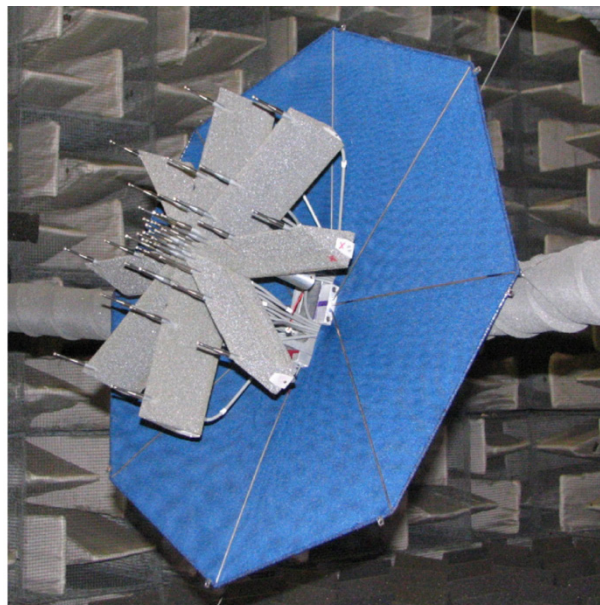


Figure 4.52.—Medium Aperture Directional Array (MADA) with hood removed in Quiet Flow Facility (QFF).

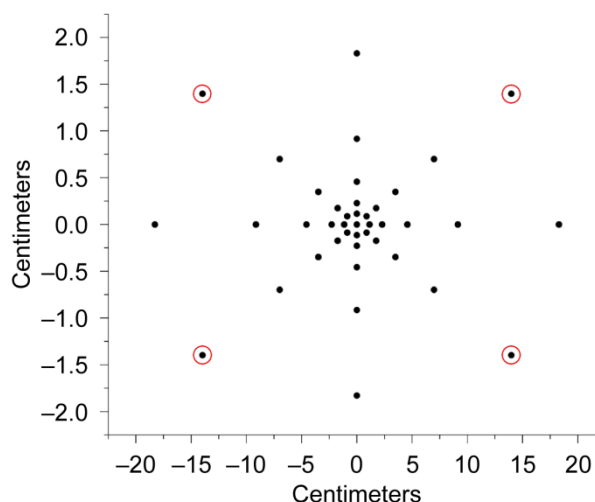


Figure 4.53.—MADA microphone arrangement.

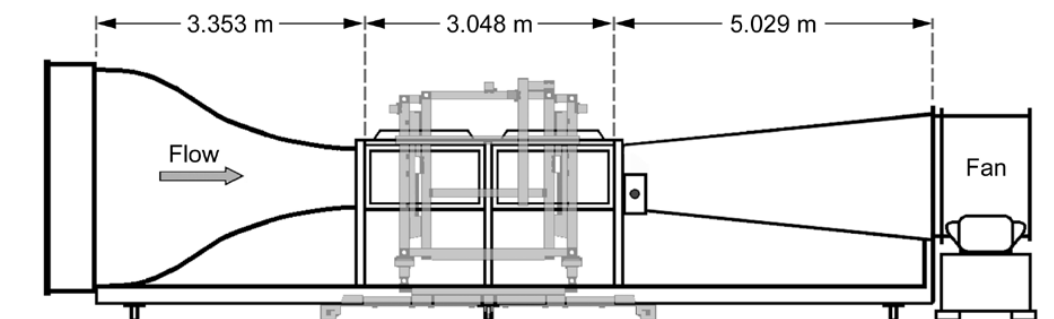


Figure 4.54.—Basic Aerodynamic Research Tunnel (BART). Structure in front of test section is traverse for optical devices.

D.2 Basic Aerodynamic Research Tunnel

The Basic Aerodynamics Research Tunnel (BART) is a flow diagnostic facility that specializes in the acquisition of flow-field data to support the development and validation of computational fluid dynamics (CFD) models and techniques (Ref. 48). As such, this facility enables a researcher to undertake studies that require flow-field and surface measurements of high spatial and temporal resolution. The BART is equipped with highly automated data acquisition and control systems to efficiently process large experimental datasets, as well as large amounts of mass storage to maintain the facility database. This test facility and several instrumentation techniques are briefly described below. More detailed information can be found in References 48 and 101.

The BART is an atmospheric, open-return wind tunnel with a closed test section that measures 0.711 m (2.33 ft) in height, 1.016 m (3.33 ft) in width, and 3.048 m (10 ft) in length. A tunnel schematic is sketched in Figure 4.54. During operation, air is drawn into the tunnel inlet by a 9-blade, 11-stator fan, which is powered by a 92-kW (125-hp), alternating-current motor that is coupled to a magnetic clutch. An electronic controller maintains the fan speed within 0.1 percent of full scale (less than 1 rpm variation). The tunnel flow is first conditioned by a 10-cm- (4-in.-) thick honeycomb that has a 0.64-cm (1/4-in.) cell size, followed by four antiturbulence screens that are 20 mesh-per-inch with 64 percent porosity (ratio of open area to total area). The flow is then accelerated through an 11:1 contraction before entering the test section. The maximum flow speed at the test section entrance is approximately 65 m/s (213 ft/s), with turbulence intensity varying from 0.03 percent at 15 m/s (49 ft/s) to 0.09 percent at maximum tunnel speed.

Optical access to the model and surrounding flow is provided by plexiglass (or glass, if required) windows in the test section walls and ceiling that are as large as structurally possible. Traditional diagnostic techniques available at the BART facility include titanium dioxide solution to reveal surface streaklines, five-hole probe surveys to record instantaneous velocity fields, pitot pressure surveys, and hot-wire anemometry. Within the more advanced techniques, a

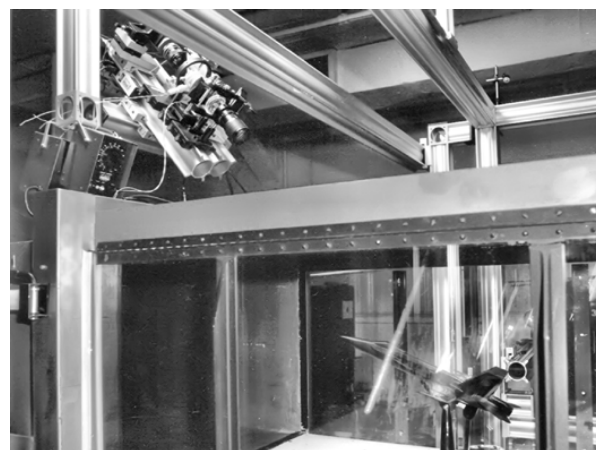


Figure 4.55.—Closeup: Basic Aerodynamics Research Tunnel (BART) test section with particle imaging velocimetry (PIV) camera on traverse system.

three-component laser Doppler velocimeter is capable of obtaining accurate velocity measurements in flow fields with reverse flows, as well as large shear gradients and velocity fluctuations.

With particular relevance to the present assessment, flow-field velocity measurements were taken with a two-dimensional digital particle image velocimetry (PIV) system (Refs. 35 and 38). The PIV system was deployed with either one or two high-resolution video cameras with a sensor size of 1360 by 1024 pixels. Using a 50-mm (2-in.) lens, the field of view was approximately 80 by 60 mm (3.2 by 2.4 in.) for a single camera. With a second camera, two fields of view were overlapped to produce an expanded 156×60-mm field of view. The cameras were mounted to a traverse system (Figure 4.55) surrounding the tunnel, along with the laser and light-sheet optics. A 1.5-mm- (0.06-in.-) thick light sheet was generated using a pulsed, frequency-doubled, 200-mJ Nd-YAG laser, operated at 5 Hz. The experimental flow was seeded by dispersing particles with a theatrical fog machine throughout the entire room housing the tunnel. Further experimental details for the test cases associated with the present assessment are reported in References 35 and 38.

References

1. Crighton, David G.: *Airframe Noise. Aeroacoustics of Flight Vehicles: Theory and Practice*, NASA RP-1258-VOL-1 (WRDC-TR-90-3052-VOL-1), H.H. Hubbard, ed., 1991, pp. 391-447.
2. U.S. Department of Transportation: *Noise Standards: Aircraft Type and Airworthiness Certification*. FAA Advisory Circular No. 36-4C, July 15, 2003.
3. Healy, G.J.: *Measurement and Analysis of Aircraft Far-Field Aerodynamic Noise; Final Report*. NASA CR-2377, 1974.
4. Gibson, J.S.: *Non-Engine Aerodynamic Noise Investigation of a Large Aircraft*. NASA CR-2378, 1974.
5. Lasagna, P.L.; and Putnam, T.W.: *Preliminary Measurements of Aircraft Aerodynamic Noise*. AIAA-1974-572, 1974.
6. Burley, R.R.: *Preliminary Measurement of the Airframe Noise From an F-106B Delta Wing Aircraft at Low Flyover Speeds; Establishment of Lower Limit for Noise Level of Supersonic Transport Aircraft*. NASA TM-X-71527, 1974.
7. Putnam, T.W.; Lasagna, P.L.; and White, K.C.: *Measurements and Analysis of Aircraft Airframe Noise*. AIAA-1975-510, 1975.
8. Bauer, A.B.; and Munson, A.G.: *Airframe Noise of the DC-9-31; Final Report*. NASA CR-3027, 1978.
9. Lasagna, P.L., et al.: *Landing Approach Airframe Noise Measurements and Analysis*. NASA TP-1602, 1980.
10. Stoker, Robert, et al.: *Airframe Noise Source Locations of a 777 Aircraft in Flight and Comparisons With Past Model-Scale Tests*. AIAA-2003-3232, 2003.
11. Khorrami, Mehdi, et al.: *Preliminary Analysis of Acoustic Measurements From the NASA-Gulfstream Airframe Noise Flight Test*. AIAA-2008-2814, 2008.
12. Shearin, J.G.; and Block, P.J.: *Airframe Noise Measurements on a Transport Model in a Quiet Flow Facility*. AIAA-1975-509, 1975.
13. Shearin, J.G.: *Airframe Noise of a Small Model Transport Aircraft and Scaling Effects*. NASA TP-1858, 1981.
14. Hayes, Julie A., et al.: *Airframe Noise Characteristics of a 4.7 Percent Scale DC-10 Model*. AIAA-1997-1594, 1997.
15. Guo, Y.P.; Joshi, M.C.; Bent, P.H.; and Yamamoto, K.J.: *Surface Pressure Fluctuations on Aircraft Flaps and Their Correlation with Far-Field Noise*. *J. Fluid Mechanics*, vol. 415, 2000, pp. 175-202.
16. Stoker, Robert W.; and Sen, Rahul: *An Experimental Investigation of Airframe Noise Using a Model-Scale Boeing 777*. AIAA-2001-987, 2001.
17. Soderman, Paul, et al.: *Airframe Noise Study of a CRJ-700 Aircraft Model in the NASA Ames 7- by 10-Foot Wind Tunnel No. 1*. AIAA-2002-2406, 2002.
18. Guo, Y.P.; and Joshi, M.C.: *Noise Characteristics of Aircraft High Lift Systems*. *AIAA J.*, vol. 41, no. 7, 2003, pp. 1247-1256.
19. Horne, W. Clifton, et al.: *Aeroacoustic Study of a 26%-Scale Semispan Model of a Boeing 777 Wing in the NASA Ames 40- by 80-Foot Wind Tunnel*. NASA/TP-2004-212802, 2004.
20. Hotz, E.R., et al.: *Measurements of the Radiated Noise from Sailplanes*. AFFDL-TM-70-3-FDDA, 1970.
21. Kroeger, R.A.; Gruschka, H.D.; and Helvey, T.C.: *Low Speed Aerodynamics for Ultra-Quiet Flight*. AFFDL-TR-71-75, 1972.
22. Gibson, J.S.: *The Ultimate Noise Barrier—Far Field Radiated Aerodynamic Noise*. *Proceedings of the International Conference on Noise Control Engineering*, Washington, DC, 1972, pp. 332-337.
23. Fink, Martin R.: *Experimental Evaluation of Theories for Trailing Edge and Incidence Fluctuation Noise*. *AIAA J.*, vol. 13, no. 11, 1975, pp. 1472-1477.
24. Fink, M.R.: *Investigation of Scrubbing and Impingement Noise*. NASA CR-134762, 1975.
25. Fink, M.R.; and Schlinker, R.H.: *Airframe Noise Component Interaction Studies; Final Report*. NASA CR-3110, 1979.
26. Paterson, Robert W.; and Amiet, Roy K.: *Acoustic Radiation and Surface Pressure Characteristics of an Airfoil Due To Incident Turbulence*. NASA CR-2733, 1976.
27. Soderman, Paul T.; and Noble, Stephen C.: *Directional Microphone Array for Acoustic Studies of Wind Tunnel Models*. *J. Aircraft*, vol. 12, no. 3, 1975, pp. 168-173.
28. Ahtye, W.F.; and Kojima, G.K.: *Correlation Microphone for Measuring Airframe Noise in Large-Scale Wind Tunnels*. AIAA-1976-553, 1976.
29. Kendall, J.M.: *Airframe Noise Measurements by Acoustic Imaging*. AIAA-1977-55, 1977.
30. Revell, J.D.: *On the Calculation of Aerodynamic Noise Generated by Large Aircraft at Landing Approach*. *J. Acoust. Soc. Am.*, vol. 55, no. S1, 1974, p. S73.
31. Hardin, J.C., et al.: *Prediction of Airframe Noise*. NASA-TN-D-7821, 1975.
32. Fink, M.R.: *Airframe Noise Prediction Method*. FAA RD-77-29, 1977.
33. Choudhari, Meelan M., et al.: *Aeroacoustic Experiments in the NASA Langley Low-Turbulence Pressure Tunnel*. NASA/TM-2002-211432, 2002.
34. Brooks, Thomas H.; and Humphreys, William H., Jr.: *Flap-Edge Aeroacoustic Measurements and Predictions*. *J. Sound Vib.*, vol. 261, no. 1, 2003, pp. 31-74.
35. Jenkins, Luther; Khorrami, Mehdi; and Choudhari, Meelan: *Characterization of Unsteady Flow Structures Near Leading-Edge Slat: Part I: PIV Measurements*. AIAA-2004-2801, 2004.
36. Humphreys, William; and Brooks, Thomas: *Noise Spectra and Directivity for a Scale-Model Landing Gear*. AIAA-2007-3458, 2007.
37. Burley, Casey, et al.: *ANOPP Landing Gear Noise Prediction Comparisons to Model-Scale Data*. AIAA-2007-3459, 2007.
38. Jenkins, Luther, et al.: *Characterization of Unsteady Flow Structures Around Tandem Cylinders for Component Interaction Studies in Airframe Noise*. AIAA-2005-2812, 2005.
39. Jenkins, Luther, et al.: *Measurements of Unsteady Wake Interference between Tandem Cylinders*. AIAA-2006-3202, 2006.
40. Streett, Craig, et al.: *Aerodynamic Noise Reduction for High-Lift Devices on a Swept Wing Model*. AIAA-2006-212, 2006.
41. Elkoby, Ronen, et al.: *Airframe Noise Results From the QTD II Flight Test Program*. AIAA-2007-3457, 2007.
42. Zorumski, W.E.: *Aircraft Noise Prediction Program Theoretical Manual*. NASA TM-83199, pt. 2, 1982.
43. Golub, Robert A., et al.: *Airframe Noise Sub-Component Definition and Model*. NASA/CR-2004-213255, 2004.
44. Guo, Yueping: *Empirical Prediction of Aircraft Landing Gear Noise*. NASA/CR-2005-213780, 2005.

45. Krist, Sherrie L.; Biedron, Robert T.; and Rumsey, Christopher L.: CFL3D User's Manual (Version 5). NASA/TM—1998-208444, 1998.
46. Rumsey, C.L.; Biedron, R.T.; and Thomas, J.L.: CFL3D: Its History and Some Recent Applications. NASA TM—112861, 1997.
47. Ffowcs Williams, J.E.; and Hawkins, D.L.: Sound Generation by Turbulence and Surfaces in Arbitrary Motion. *Philos. Trans. Roy. Soc. London Ser. A*, vol. 264, 1969, pp. 321–342.
48. Sellers, William L., III; and Kjelgaard, Scott O.: The Basic Aerodynamics Research Tunnel—A Facility Dedicated to Code Validation. AIAA—1988–1997, 1988.
49. Hubbard, Harvey H.; and Manning, James C.: Aeroacoustic Research Facilities at NASA Langley Research Center: Description and Operational Characteristics. NASA TM—84585, 1983.
50. Guo Yueping: A Discrete Vortex Model for Slat Noise Prediction. AIAA—2001–2157, 2001.
51. Guo, Y.P.; Yamamoto, K.J.; and Stoker, R.W.: Component-Based Empirical Model for High-Lift System Noise Prediction. *J. Aircraft*, vol. 40, no. 5, 2003, pp. 914–922.
52. Bertsch, Lothar; and Dobrzynski, Werner: Tool Development for Low-Noise Aircraft Design. AIAA—2008–2995, 2008.
53. Stoker, Robert W.; Underbrink, James R.; and Neubert, Guy R.: Investigations of Airframe Noise in Pressurized Wind Tunnels. AIAA—2001–2107, 2001.
54. Pott-Pollenske, Michael, et al.: Validation of a Semiempirical Airframe Noise Prediction Method through Dedicated A319 Flyover Noise Measurements. AIAA—2002–2470, 2002.
55. Humphreys, William M., Jr., et al.: Design and Use of Microphone Directional Arrays for Aeroacoustic Measurements. AIAA—1998–471, 1998.
56. Brooks, Thomas F.; and Humphreys, William M., Jr.: Effect of Directional Array Size on the Measurement of Airframe Noise Components. AIAA—1999–1958, 1999.
57. Brooks, Thomas F.; and Humphreys, William M., Jr.: A Deconvolution Approach for the Mapping of Acoustic Sources (DAMAS) Determined From Phased Microphone Arrays. *J. Sound Vib.*, vol. 294, no. 4, 2006, pp. 856–879.
58. Remillieux, Marcel, et al.: Aeroacoustic Study of a 26%-Scale, High-Fidelity, Boeing 777 Main Landing Gear in a Semi-Anechoic-Wind-Tunnel Test Section. AIAA—2007–3453, 2007.
59. Guo, Y.: An Improved Landing Gear Noise Prediction Scheme. NASA Informal Contractor Report, NAS1–NNI04AA11B, Task NNL06AB63T.
60. Roshko, Anatol: Experiments on the Flow Past a Circular Cylinder at Very High Reynolds Number. *J. Fluid Mech.*, vol. 10, no. 3, 1961, pp. 345–356.
61. Lockard, David, et al.: Tandem Cylinder Noise Predictions. AIAA—2007–3450, 2007.
62. Lockard, David, et al.: Aeroacoustic Simulations of Tandem Cylinders with Subcritical Spacing. AIAA—2008–2862, 2008.
63. Menter, F.R.: Two-Equation Eddy-Viscosity Turbulence Models for Engineering Applications. *AIAA J.*, vol. 32, no. 8, 1994, pp. 1598–1605.
64. Menter, F.R.: Zonal Two-Equation $k-\omega$ Turbulence Models for Aerodynamic Flows. AIAA—1993–2906, 1993.
65. Khorrami, Mehdi, et al.: Simulations of Bluff Body Flow Interaction for Noise Source Modeling. AIAA—2006–3203, 2006.
66. Lockard, David: A Comparison of Ffowcs Williams-Hawkins Solvers for Airframe Noise Applications. AIAA—2002–2580, 2002.
67. Stoker, Robert W.; Underbrink, James R.; and Neubert, Guy R.: Investigations of Airframe Noise in Pressurized Wind Tunnels. AIAA—2001–2107, 2001.
68. McGhee, R.J.; Beasley, W.D.; and Foster, J.M.: Recent Modifications and Calibration of the Langley Low-Turbulence Pressure Tunnel. NASA TP–2328, 1984.
69. Li, Fei; Khorrami, Mehdi; and Malik, Mujeeb: Unsteady Simulations of a Landing-Gear Flow Field. AIAA—2002–2411, 2002.
70. Squires, K.D., et al.: Progress on Detached-Eddy Simulation of Massively Separated Flows. AIAA—2002–1021, 2002.
71. Spalart, Phillippe R.: Young-Person's Guide to Detached-Eddy Simulation Grids. NASA/CR—2001–211032, 2001.
72. Spalart, P.R.: Strategies for Turbulence Modelling and Simulations. *Int. J. Heat Fluid Flow*, vol. 21, no. 3, 2000, pp. 252–263.
73. Lockard, David P.; Khorrami, Mehdi; and Li, Fei: Aeroacoustic Analysis of a Simplified Landing Gear. AIAA—2003–3111, 2003.
74. Lockard, David; Khorrami, Mehdi; and Li, Fei: High Resolution Calculation of a Simplified Landing Gear. AIAA—2004–2887, 2004.
75. Oerlemans, Stefan; and Pott-Pollenske, Michael: An Experimental Study of Gear Wake/Flap Interaction Noise. AIAA—2004–2886, 2004.
76. Klausmeyer, Steven M.; and Lin, John C.: Comparative Results From a CFD Challenge Over a 2D Three-Element High-Lift Airfoil. NASA TM—112858, 1997.
77. Choudhari, Meelan M.; and Khorrami, Mehdi R.: Effect of Three-Dimensional Shear-Layer Structures on Slat Cove Unsteadiness. *AIAA J.*, vol. 45, no. 9, 2007, pp. 2174–2186.
78. Khorrami, Mehdi R.; Singer, Bart A.; and Berkman, Mert E.: Time-Accurate Simulations and Acoustic Analysis of Slat Free Shear Layer. *AIAA J.*, vol. 40, no. 7, 2002, pp. 1284–1291.
79. Khorrami, Mehdi; Choudhari, Meelan; and Jenkins, Luther: Characterization of Unsteady Flow Structures Near Leading-Edge Slat. Part II: 2D Computations. AIAA—2004–2802, 2004.
80. Choudhari, Meelan, et al.: Slat Cove Noise Modeling: A Posteriori Analysis of Unsteady RANS Simulations. AIAA—2002–2468, 2002.
81. Dobrzynski, W.; and Pott-Pollenske, M.: Slat Noise Source Studies for Farfield Noise Prediction. AIAA—2001–2158, 2001.
82. Agarwal, Anurag; and Morris, Philip: Broadband Noise From the Unsteady Flow in a Slat Cove. AIAA—2004–854, 2004.
83. Ewert, Roland: Broadband Slat Noise Prediction Based on CAA and Stochastic Sound Sources From a Fast Random Particle-Mesh (RPM) Method. *Comput. Fluids*, vol. 37, no. 4, 2008, pp. 369–387.
84. Imamura, T., et al.: Three-Dimensional Unsteady Flow Computations Around a Conventional Slat of High-Lift Devices. *AIAA J.*, vol. 46, no. 5, 2008, pp. 1045–1053.
85. Gillian, R.E.: Aircraft Noise Prediction Program User's Manual. NASA TM–84486, 1982.
86. Macaraeg, M.G.: Fundamental Investigations of Airframe Noise. AIAA—1998–2224, 1998.

87. Streett, C.L., et al.: In Search of the Physics: The Interplay of Experiment and Computation in Airframe Noise Research; Flap-Edge Noise. AIAA-2003-979, 2003.
88. Khorrami, Mehdi R., et al.: In Search of the Physics: The Interplay of Experiment and Computation in Slat Aeroacoustics. AIAA-2003-980, 2003.
89. Whitfield, Charlotte E.: NASA's Quiet Aircraft Technology Project; Final Report. ICAS 2004-6.10.1 (I.L.), 2004.
90. Posey, Joe; Tinetti, Ana; and Dunn, Mark: The Low-Noise Potential of Distributed Propulsion on a Catamaran Aircraft. AIAA-2006-2622, 2006.
91. Ffowcs Williams, J.E.; and Hall, L.H.: Aerodynamic Sound Generation By Turbulent Flow in the Vicinity of a Scattering Half Plane. *J. Fluid Mech.*, vol. 40, pt. 4, 1970, pp. 657-670.
92. Chase, David M.: Sound Radiated By Turbulent Flow off a Rigid Half-Plane as Obtained From a Wavevector Spectrum of Hydrodynamic Pressure. *J. Acoust. Soc. Am.*, vol. 52, no. 3, pt. 2, 1972, pp. 1011-1023.
93. Fethney, P.: An Experimental Study of Airframe Self-Noise. AIAA-1975-511, 1975.
94. Heller, H.H.; and Dobrzynski, W.M.: Sound Radiation From Aircraft Wheel-Well/Landing Gear Configurations. AIAA-1976-552, 1976.
95. Guo, Yueping: A Semi-Empirical Model for Aircraft Landing Gear Noise Prediction. AIAA-2006-2627, 2006.
96. Lighthill, M.J.: On Sound Generated Aerodynamically. I. General Theory. *Proc. Royal Soc. London Series A*, vol. 211, 1952, pp. 564-587.
97. Curle, N.: The Influence of Solid Boundaries on Aerodynamic Sound. *Proc. Royal Soc. London Series A*, vol. 231, 1955, pp. 505-514.
98. Singer, B.A., et al.: Simulation of Acoustic Scattering From a Trailing Edge. *J. Sound Vib.*, vol. 230, no. 3, 2000, pp. 541-560.
99. Brentner, Kenneth S.; and Farassat, F.: Analytical Comparison of the Acoustic Analogy and Kirchhoff Formulation for Moving Surfaces. *AIAA J.*, vol. 36, no. 8, 1998, pp. 1379-1386.
100. Farassat, F.: Linear Acoustic Formulas for Calculation of Rotating Blade Noise. *AIAA J.*, vol. 19, no. 9, 1981, pp. 1122-1130.
101. Jenkins, Luther N.: An Experimental Investigation of the Flow Over the Rear End of a Notchback Automobile Configuration. SAE Technical Paper Series 2000-01-0489, 2000.

Chapter 5—Fan Noise Prediction

Edmane Envia
National Aeronautics and Space Administration
Glenn Research Center
Cleveland, Ohio 44135

Daniel L. Tweedt
AP Solutions Inc.
Cleveland, Ohio 44135

Richard P. Woodward, David M. Elliott, E. Brian Fite,
Christopher E. Hughes, Gary G. Podboy, and Daniel L. Sutliff
National Aeronautics and Space Administration
Glenn Research Center
Cleveland, Ohio 44135

Summary

This chapter presents the results of an assessment of aircraft engine fan noise prediction capability at NASA. Representative codes in the empirical, acoustic-analogy-based, and computational categories were exercised and assessed against a set of benchmark acoustic data obtained from wind tunnel tests of three model-scale fans representing the ultra-high-, high-, and moderate-bypass-ratio designs. The chosen codes were the Aircraft Noise Prediction Program (ANOPP), representing an empirical capability; RSI, representing an acoustic-analogy-based capability; and LINFLUX, representing a computational aeroacoustics capability. The selected benchmark fans cover a wide range of fan pressure ratios and tip speeds, and are representative of modern turbofan engine designs. The assessment results indicate that ANOPP can predict 1/3-octave fan noise spectra to within 4 dB of the measurement uncertainty band for ultra-high- and high-bypass-ratio fans except at the extreme aft emission angles, but the discrepancy between data and theory is considerably larger for the moderate-bypass-ratio fan. The RSI code can predict the rotor-stator interaction broadband noise power level spectra to within 4 dB of the experimental uncertainty band for the high-bypass-ratio fan. The comparisons for the other two fans could not be carried out owing to lack of appropriate experimental data for those fans. The LINFLUX code can predict rotor-stator interaction tone noise power levels to within experimental uncertainties for the ultra-high-bypass-ratio fan, but deviates by as much as 7.6 dB outside the experimental uncertainty band for the high-bypass-ratio fan. LINFLUX results could not be computed for the moderate bypass-ratio-fan, since the mean flow solutions did not converge for that fan.

5.1 Introduction

The term fan noise is used here to denote the noise associated with the fan stage of a turbofan engine, which is produced by a number of different source mechanisms. For the most part, fan noise is produced through the interaction of unsteady flow perturbations with the fan rotor blades and fan exit guide vanes. These mechanisms include the interaction of inflow distortions and the inlet boundary layer with the fan rotor and the interaction of fan rotor flow perturbations (blade viscous wakes, tip clearance flow, etc.) with the bypass and core stators. The interaction can also be self-generated (often called self-noise) as in the case of noise produced by scattering of fan blade boundary layer turbulence at the blade trailing edge, noise due to local separation of the flow on the airfoil, or noise associated with vortex shedding at the blade trailing edge. Depending on the nature of the unsteady perturbations involved, the interaction sources generate discrete frequency tones, broadband noise, or in most cases, both. Fan noise can also be produced by the steady part of the flow within the fan stage. Examples include the interaction of the fan with the

steady potential (i.e., pressure) field of the engine struts and the multiple pure tones (MPT) of the fan (also called buzz-saw noise) that are produced as a result of spatial non-uniformities in the rotor-locked pressure field. The fan-strut interaction produces discrete tones at the harmonics of the blade-passing frequency, while buzz-saw is produced at the multiples of fan shaft rotational frequency. It has been suggested that the fluctuating Reynolds stress (i.e., volume quadrupole) of the turbulent flow within the fan stage is also an important source of fan noise at high frequencies and high fan loading conditions. The strengths of fan noise sources depend on the fan rotational speed. As an example, the MPT noise is only significant when the fan tip speed is supersonic. At subsonic tip speeds, the rotor-locked pressure field is evanescent and contributes very little to the total noise signature of the fan. As the fan tip speed varies across the operating regime of the engine, the proportions of the contributions from various sources change. Measurements of fan noise from model-scale rigs and full-scale engines have provided indications of the relative importance of some of the fan noise sources as a function of the fan tip speed, but because of the overlapping

nature of the sources it is not always possible to differentiate between them.

Since the fan is a significant source of noise in a modern aircraft engine, it is important to assess the ability of the current codes to predict its noise contribution accurately. There is a variety of fan noise prediction methods, but in general, these methods can be grouped into three main categories: empirical, acoustic-analogy-based, and computational.

In the first category, experimental data are used to construct correlations between appropriate fan noise metrics and operating parameters. The correlations are often constructed for overall fan noise levels (i.e., the sum of contributions from all sources) since it is often not possible to conclusively isolate contributions of various noise sources from the total measured fan noise signature. These methods are widely used, principally, as part of system-level prediction codes for engine design evaluation studies. While it takes significant experience and skill to discern the appropriate correlation relationships from the mass of available information, once constructed, these methods are relatively easy to use, requiring a readily available set of input parameters. Codes based on empirical models tend to require minimal computer resources and run times, typically producing answers on a 1/3-octave spectral basis in a matter of seconds. ANOPP is the only empirical code currently in the NASA fan noise prediction inventory. As described in Chapter 2, "Aircraft System Noise Prediction," ANOPP calculates fan noise through its HDNFAN module, which predicts fan noise inclusive of all fan noise sources. ANOPP, more generally, can be used to predict overall aircraft noise for the purposes of estimating aircraft community noise impact using the effective perceived noise level (EPNdB) metric.

As the name suggests, the methods in the second category are based on the acoustic analogy theory developed by Lighthill (Ref. 1). In this theory, the aerodynamic and acoustic aspects of the problem are treated separately. Mathematically, this is done by a rearrangement of the exact equations of the motion so that a linear wave equation is obtained whose left-hand side describes the propagation of sound and its right-hand side represents a known aerodynamic source that generates the sound. The aerodynamic source is to be measured, computed, or otherwise modeled independently. The solution to the wave equation is given formally in terms of integrals that describe convolution of the source distribution and the acoustic propagation characteristics. Depending on the level of approximations involved in the description of the fan geometry and/or flow conditions, the solution can be expressed either in closed form or may require the use of a quadrature scheme to evaluate the solution integrals. Such models have been developed for a number of fan noise sources, but most have been developed to predict the so-called rotor-stator interaction noise, which is produced as a result of the impingement of the fan rotor wakes on the fan exit guide vanes. The level of expertise needed to use this class of codes is more than the empirical models and often requires access to,

or knowledge of, fairly detailed aerodynamic and geometric input parameters from independent measurements or computations. As such, acoustic-analogy-based codes tend to require more computer resources and run times, typically producing answers in a matter of minutes for tone noise and in a matter of hours for broadband noise. There are a number of NASA fan noise codes that fall in the acoustic analogy category. These include V072 (Refs. 2 and 3) and TFaNS (Refs. 4 to 7), which are used for rotor-stator interaction tone noise prediction; RSI (Ref. 8) and BFaNS (Refs. 9 to 11), which are used for rotor-stator interaction broadband-noise prediction; and Superpose (Ref. 12), which is used for rotor buzz-saw noise prediction.

The third category of fan noise prediction methods encompasses those approaches that—like the acoustic-analogy-based methods—start with the exact equations of motion, but require little or no approximations regarding the fan geometry or its flow field. The resulting coupled system of unsteady flow equations, therefore, retain their complexity and can only be solved numerically through the use of appropriate computational algorithms. These methods, generically called computational aeroacoustics (CAA) methods, include linearized frequency-domain methods as well as nonlinear time-domain methods. With recent advances in computing power and computational algorithms, CAA codes are beginning to gain a place in the toolbox of fan noise prediction methods. The use of CAA tools typically requires a high level of expertise and familiarity with the tools themselves and with computer hardware and software used to implement them. Depending on the particular code and application, these codes require significant computer resources, typically requiring tens of hours of computation time for tone noise prediction and tens of days for broadband noise prediction. NASA codes in this category include two Euler codes, LINFLUX (Refs. 13 to 15) and BASS (Refs. 16 to 20). LINFLUX is a linearized, frequency-domain, tone-noise prediction code, and BASS is a nonlinear, time-domain, broadband-noise prediction code. Both codes are currently used for rotor-stator interaction noise prediction.

In this chapter, a representative code in each category that is available in the public domain will be discussed and assessed against a set of benchmark fan noise data. In each case, a brief description of the code will be given including a discussion of the input parameters and the output produced by the code. It should be emphasized that the list of codes considered here is representative, not exhaustive. Each selected code typifies the current state of the art at NASA in each category and represents the capabilities of similar codes elsewhere that fall in that category. A list of acronyms and symbols used in this chapter is given in Appendix A.

5.2 Benchmark Test Cases

The selected test cases for this study include an ultra-high-bypass-ratio fan stage, the NASA-Pratt & Whitney Advanced Ducted Propulsor (ADP) Fan 1; a high-bypass-ratio fan stage,

the NASA-General Electric Source Diagnostic Test (SDT) fan; and a moderate-bypass-ratio fan stage, the NASA-Honeywell Quiet High Speed Fan 2 (QHSF 2). Again, the benchmark cases selected are not meant to be exhaustive, but representative. All three fans were tested in the NASA Glenn Research Center 9- by 15-Foot Low-Speed Wind Tunnel (9×15 LSWT) over the last decade. In all cases, sideline as well as in-duct acoustic measurements were acquired and have been used for the comparison purposes in this study. Owing to the limitations of the codes, only data from the so-called hard-wall configurations, which do not include acoustic treatment inside the fan duct, have been considered in this study.

Table 5.1 shows select design parameters for these three model fans. The fan design conditions represent a significant

value range. The ADP fan has a subsonic design tip speed in contrast to the supersonic design tip speeds for the SDT and QHSF 2 fans. Note the change in the fan bypass ratio, pressure ratio, and tip speed for these fans. The design point corrected inlet weight flows⁵ are similar for all three. The somewhat lower weight flow for the ADP fan is partly due to the higher rotor hub:tip radius ratio and consequent reduced flow area for that fan. All three fans have a 22-in.-diameter rotor and were tested at a number of fan tip speeds. For the purposes of this study, five fan tip speed conditions have been considered for each fan which include speeds that are representative of the three noise certification points; namely, approach, cutback and takeoff, and two additional intermediate tip speeds. The fan tip speeds investigated in this study are listed in Table 5.2.

TABLE 5.1.—MODEL FAN STAGE DESIGN PARAMETERS

Parameter	Fan stage ^a		
	ADP	SDT	QHSF 2
Fan speed, rpm	8750	12 656	15 625
Corrected tip speed, m/s (ft/s)	256 (840)	370 (1215)	449 (1474)
Stage pressure ratio	1.29	1.47	1.82
Rotor hub-to-tip radius ratio	0.43	0.30	0.35
Bypass ratio	13.3	8.9	3.8
Corrected specific weight flow, kg/m ² -s (lbm/ft ² -s)	180.2 (36.9)	204.1 (41.8)	213.4 (43.7)
Inlet corrected weight flow, kg/s (lbm/s)	38.9 (85.7)	45.6 (100.5)	44.9 (98.9)
Rotor blade count	18	22	22
Fan exit guide vane count	45	54	50
Core inlet guide vane count	63	None	None
Bypass and core duct support struts	None	None	10

^aADP is Advanced Ducted Propulsor, SDT is Source Diagnostic Test, and QHSF 2 is Quiet High Speed Fan 2.

TABLE 5.2.—MODEL FAN TIP SPEED CONDITIONS USED IN THIS STUDY

Fan ^a	Condition	Corrected speed, rpm	Design speed, percent
ADP	Approach	5 425	62.0
	---	6 700	76.6
	Cutback	7 525	86.0
	---	8 345	95.4
SDT	Takeoff	8 750	100.0
	Approach	7 809	61.7
	---	9 493	75.0
	Cutback	11 075	87.5
QHSF 2	---	11 771	93.0
	Takeoff	12 657	100.0
	Approach	9 840	63.0
	---	10 935	70.0
QHSF 2	Cutback	12 500	80.0
	---	13 280	85.0
	Takeoff	14 060	90.0

^aADP is Advanced Ducted Propulsor, SDT is Source Diagnostic Test, and QHSF 2 is Quiet High Speed Fan 2.

⁵ Corrected flow is the mass flow that would pass through the fan if the inlet pressure and temperature were at the standard day conditions (i.e., pressure = 101.4 kPa (14.696 lbf/in.²) and temperature = 288 K (518.7 °R)).

A photograph of the ADP fan (Refs. 21 and 22), installed in the 9×15 LSWT, is shown in Figure 5.1. ADP has a relatively low stage pressure ratio of 1.29 and a subsonic design corrected tip speed of 256 m/s (840 ft/s), which avoids the generation of multiple pure tones. A three-dimensional exposed view of the fan stage is depicted in Figure 5.2. The fan stage has 18 rotor blades, 45 radial bypass stator vanes, and 63 radial core stator vanes (the core is passive). It has the highest design bypass ratio (13.3) of the three fans considered in this chapter. Figure 5.3 shows a photograph of the SDT fan (Refs. 23 and 24) installed in the 9×15 LSWT. A three-dimensional exposed view of SDT is shown in Figure 5.4. The fan stage has 22 rotor blades (this rotor is called R4) and 54

radial stator vanes. The SDT fan has a design corrected tip speed of 370.3 m/s (1215 ft/s) and a stage pressure ratio of 1.47. Figure 5.5 shows a photograph of the QHSF 2 (Refs. 25 and 26) model installed in the 9×15 LSWT. The three-dimensional exposed view of this fan is depicted in Figure 5.6 showing its relatively close rotor-stator spacing and its swept stator. The QHSF 2 has the highest design tip speed (449.3 m/s, or 1474 ft/s) of the three model fans in this study. It has 22 rotor blades, 50 swept stator vanes, 10 bypass struts, and 10 struts in its passive core. Its bypass ratio of 3.8, well below that of the other two model fans, is considered moderate.



Figure 5.1.—The 22-in.-diameter Advanced Ducted Propulsor (ADP) Fan 1 installed in the NASA 9- by 15-Foot Low-Speed Wind Tunnel. Traversing microphone (located on white stand) is visible to left of model. Microphone moves on track parallel with axis of fan.

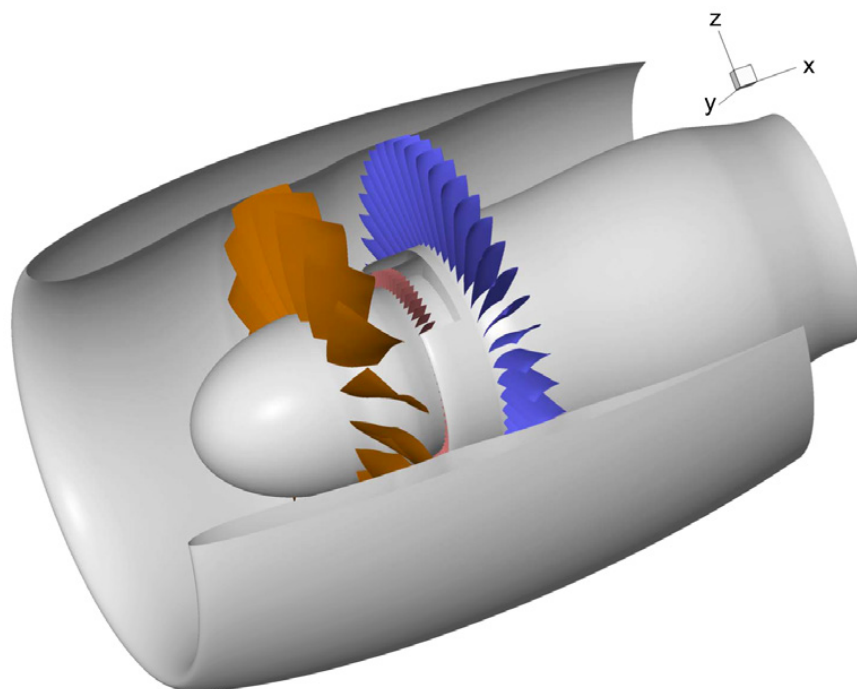


Figure 5.2.—Cross-sectional sketch of ADP Fan 1 model. ADP has 18 rotor blades, 45 fan exit guide vanes, and 63 core inlet guide vanes.



Figure 5.3.—The 22-in.-diameter Source Diagnostic Test (SDT) fan installed in NASA 9- by 15-Foot Low-Speed Wind Tunnel.

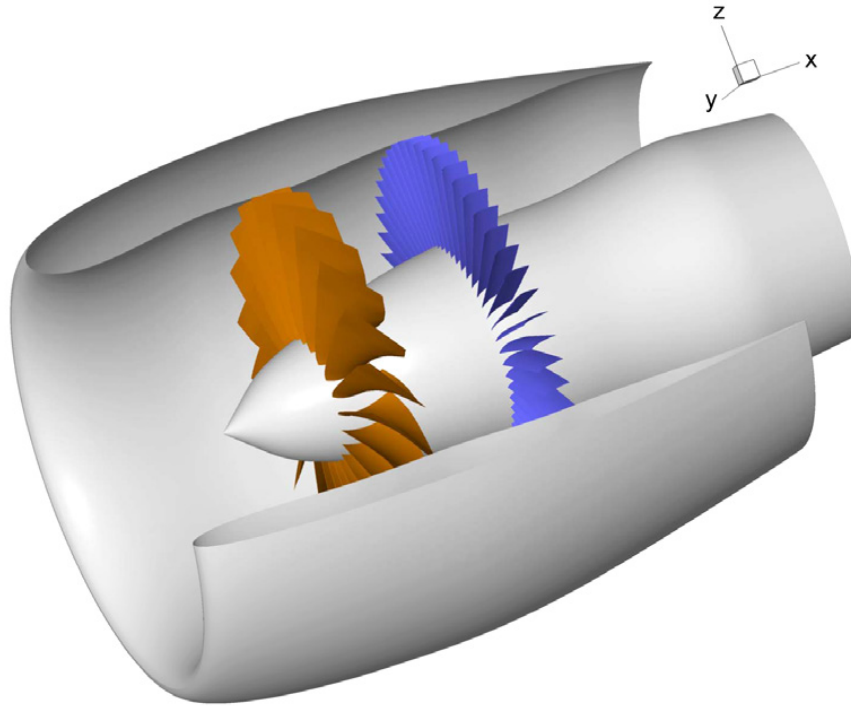


Figure 5.4.—Cross-sectional sketch of SDT fan model. SDT has 22 rotor blades and 54 fan exit guide vanes.



Figure 5.5.—The 22-in.-diameter Quiet High-Speed Fan 2 (QHSF 2) fan installed in NASA 9- by 15-Foot Low-Speed Wind Tunnel.

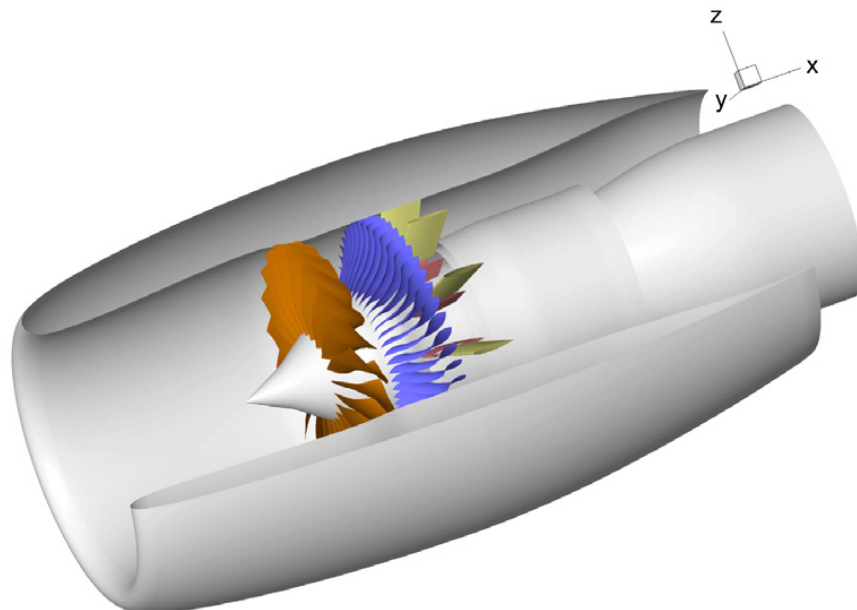


Figure 5.6.—Cross-sectional sketch of QHSF 2 model fan. QHSF 2 has 22 rotor blades, 50 fan exit guide vanes, 10 bypass duct struts, and 10 core duct struts.

5.3 Test Facility and Data Acquisition Systems

The 9×15 LSWT is a continuous-flow, anechoic wind tunnel facility located at the NASA Glenn Research Center (Ref. 27), and is part of the 8- by 6-Foot Supersonic Wind Tunnel complex. The 9×15 LSWT is capable of producing test section Mach numbers up to 0.23, as well as being used for static propulsion system performance testing. Acoustic-treatment-filled boxes are installed on the test section flow surfaces, making the test section nominally anechoic down to 250 Hz (Refs. 28 to 31). Flow conditioning systems upstream of the test section reduce incoming turbulence and velocity distortion levels to very low values, making this facility ideally suited for establishing baseline acoustic levels and for noise source isolation testing of simulated propulsion systems. Figure 5.7 is a schematic showing a plan view of the 2.7- by 4.6-m (9- by 15-ft) test section and the location of the installed model-scale fan hardware and the sideline acoustic measurement system (i.e., the traversing microphone and the fixed aft microphones). The fan models were all powered by the NASA Glenn Ultra High Bypass (UHB) Drive Rig propulsion simulator. A four-stage air turbine driven by high-pressure, high-temperature air through tubes in the support strut generates the power to drive the fan model through a common shaft connection. The UHB Drive Rig can deliver a maximum of 3766 kW, or 5050 shaft horsepower, at 16 850 rpm with air supplied at 1.6 MPa (230 psia) and 260 °C (500 °F).

5.4 Wind Tunnel Acoustic Measurements

Model fan acoustic sideline measurements in the 9×15 LSWT are acquired using a traversing microphone probe at 2.27-m (89.3-in.) sideline distance from the fan axis (see Figure 5.7). Data is taken from 48 positions at 2.5° intervals. Additionally, to obtain more angular coverage in the aft quadrant, three fixed microphone probes are placed in the rear of the test section. Together, the traversing probe and the fixed microphones cover 51 measurement locations. All acoustic data is obtained at the tunnel Mach number of 0.1, which is sufficient to establish acoustic flight effects (Ref. 32). The emitted angles corresponding to the 51 microphone locations at 0.1 Mach number range from 25° to 158° from the fan stacking axis with 0° being the forward position upstream of the fan. The microphones used in the measurements are all 0.6 cm (1/4 in.) in diameter.

Acoustic data in the 9×15 LSWT were acquired with two different sampling rates: 240 and 24 kHz. Both were acquired with a sample size of 4096, resulting in bandwidths of approximately 5.9 and 59 Hz, respectively. Allowing for the Nyquist limit and filter rolloff effects, typically, the range 0 to 8 kHz for the bandwidth of 5.9 Hz, and the range 0 to 80 kHz for the bandwidth of 59 Hz were used for analysis purposes. Corrections to the data have been made for microphone response, cable response, bullet nose cover receptivity, filter response, atmospheric attenuation, and spherical

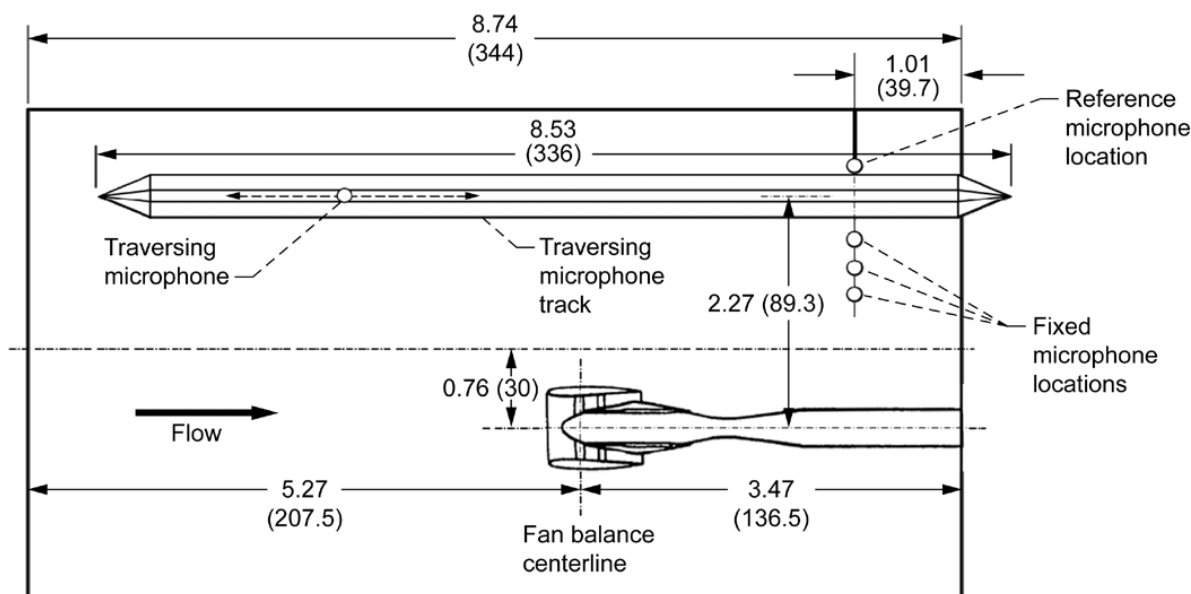


Figure 5.7.—Plan view of 9- by 15-ft test section showing model-scale fan acoustic installation, 2.3-m (89-in.) sideline traversing microphone, and fixed aft microphone locations. Dimensions are in meters (inches).

spreading.⁶ Finally, for the purposes of comparison with predictions, the measured spectra shown here are presented at a distance of 0.3-m (1-ft) from the fan stacking axis without loss due to atmospheric absorption.

5.5 Rotating Rake Acoustic Measurements

An experimental measurement system was developed and implemented by NASA Glenn in the 1990s to measure turbofan duct acoustic modes. The system is a continuously rotating radial microphone rake that is inserted into the duct (see Figure 5.8). The Rotating Rake (Refs. 33 and 34) provides a complete map of the acoustic duct modes present in the fan duct and has been used on a variety of test articles including a low-speed concept test rig, several high-speed model-scale fans in the wind tunnel, and even on a full-scale production turbofan engine on an engine test stand. The Rotating Rake has been critical in developing and evaluating a number of noise reduction concepts as well as providing experimental databases for verification of fan noise prediction codes.

Rotating Rake data is obtained from radially distributed high-response transducers mounted on a rake. Transducers used are 1.6 mm (0.062 in.) in diameter with a 34-kPa (5-psi) delta dynamic range. For inlet measurements, 12 to 14 transducers are typically distributed in equal radial increments

starting near the outer wall to the duct centerline at the throat. For exhaust measurements, six to eight transducers are typically distributed in equal radial increments starting near the outer wall to the near inner wall at the duct exit plane.

The key concept of the Rotating Rake is that by slowly rotating the microphone rake, say, at 1/200 of the speed of the fan shaft, a Doppler shift is imparted to a given duct spinning mode that is uniquely related to its circumferential mode index. This allows the decomposition of the measured pressure profile into a collection of circumferential modes. The radial modes are then obtained by solving a least-squares-curve fit to each of these circumferential modes using the Bessel functions as the radial basis modes. The acoustic power level (PWL) for each radial mode is computed based on physical conditions directly from the mode pressure. Strictly speaking, this is valid only for a hard-wall cylindrical duct with a uniform (i.e., plug) flow through the duct and has implications for the accuracy of the fitted solution. The theory and implementation of the Rotating Rake with historical examples is documented in Reference 33.

5.6 Uncertainty in Measurements

The measurement values obtained from both of the facilities described above contain uncertainties that are documented in this section. The uncertainty analysis for measurements taken in the 9×15 LSWT facility includes both aerodynamic data and acoustic data. For the Rotating Rake facility, the uncertainty analysis is determined for the mode acoustic power levels computed from mode measurements.

⁶Information regarding specific procedure used for correcting 9×15 LSWT data may be obtained by contacting the NASA Glenn Acoustics Branch.

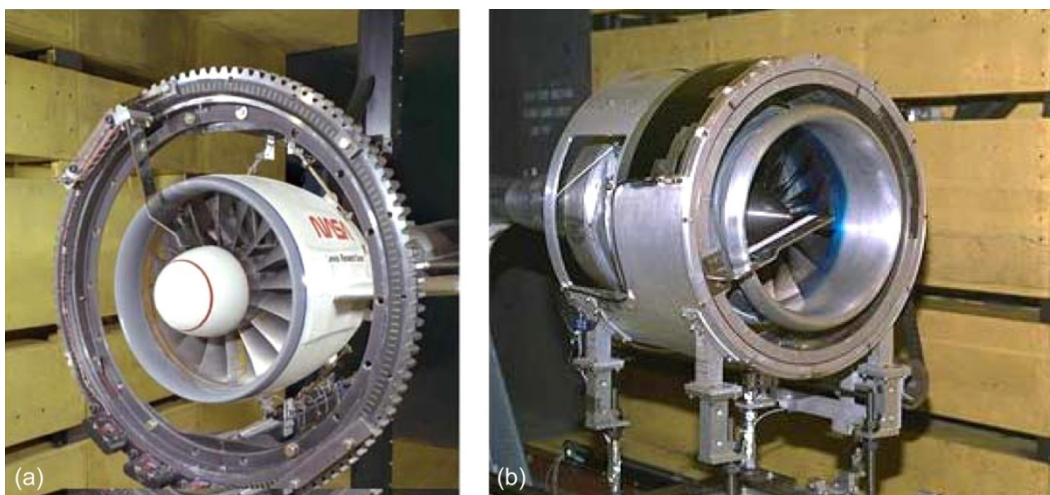


Figure 5.8.—Rotating Rake ring assembly on 43-cm (17-in.) Advanced Ducted Propulsor (ADP) in NASA 9- by 15-Foot Low-Speed Wind Tunnel. (a) First-generation system. (b) Current-generation system.

5.6.1 Wind Tunnel Aerodynamic Data Uncertainty Analysis

An error analysis using the standard ASME (American Society of Mechanical Engineers) measurement analysis techniques (Refs. 35 to 37) was conducted on the aerodynamic values used for reducing experimental far-field and Rotating Rake acoustic data. The measurement uncertainties of the data were first identified including the random and bias errors. A confidence level of 95 percent was then used corresponding to two standard deviations in a Gaussian error distribution with the number of degrees of freedom at least equal to 30. The random and bias errors from the uncorrelated sources were combined either linearly or in quadrature to produce an overall characterization for each variable. The computed uncertainties for aerodynamic variables important for acoustic data reduction are shown in the Table 5.3. It should be noted that these uncertainties are for a single point measurement and are based on manufacturer's specifications of the various measurement system components.

TABLE 5.3.—AERODYNAMIC DATA UNCERTAINTY ANALYSIS RESULTS

Variable name	±Uncertainty
Tunnel total pressure, kPa (psia)	0.05 (0.0074)
Tunnel static pressure, kPa (psia)	0.05 (0.0074)
Tunnel total temperature, K (°R)	0.69 (1.25)
Tunnel static temperature, K (°R)	0.69 (1.25)
Tunnel Mach number	0.0016
Tunnel percent humidity, percent	0.022
Fan speed, rpm	4
Corrected fan speed, rpm	5
Inlet and exit duct Mach number	0.0004
Fan exit temperature, K (°R)	0.69 (1.25)

5.6.2 Wind Tunnel Sideline Acoustic Data Uncertainty Analysis

The acoustic data system in the 9×15 LSWT consists of the following hardware from end to end: Brüel & Kjær (B&K) Type 4939 0.6-cm (1/4-in.) microphones; B&K 0.6- to 1.3-cm (1/4- to 1/2-in.) adapter cabling; B&K Type 2807 power supply; Stewart high-pass filters; DSP Technologies, Inc., analogue-to-digital and low-pass filter boards; and a Concurrent (Masscomp Computer Corporation) computer. The primary component, the B&K Type 4939 microphone, was calibrated by B&K before use and has an uncertainty shown in Table 5.4. This uncertainty is given for three representative frequencies corresponding to 300 Hz (low), 3000 Hz (medium), and 30 000 Hz (high). Every component introduces an amplitude uncertainty, which is eliminated by generating a calibration factor for the entire system at the beginning of every run using a known source. The calibration source is a B&K 4220 250-Hz, 124-dB pistonphone. The B&K pistonphone's computed uncertainty is shown in Table 5.4.

For atmospheric attenuation, the ANSI S1.26–1995 Method for Calculation of the Absorption of Sound by the Atmosphere (Ref. 38) claims an uncertainty of ±10 percent for the regime in which data is acquired in the 9×15 LSWT. The uncertainty levels for the ambient conditions of temperature and humidity were determined as ±0.69 °C (1.25 °F) and ±0.022 percent relative humidity (based on the instrument manufacturer's specifications), respectively. Other errors in measurement include distance to the microphone from the assumed source and the uncertainty of the fan-model-corrected rpm, which is the controlling set point for the fan model. These uncertainty values are ±1.3 cm (0.5 in.) per 254 cm (100 in.) and ±5 rpm corrected, respectively.

TABLE 5.4.—ANALYSIS OF UNCERTAINTY IN FAN NOISE SPECTRA

Source	Uncertainty, <i>e</i> , dB			Basis for determining uncertainty (Sec. 5.6.2)
	Nominal frequency, Hz			
	300	3000	30 000	
Atmospheric attenuation	0.00001	0.001	0.1	±0.69 °C (1.25 °F), ±2 percent relative humidity, hot and humid day
Distance	0.04	0.04	0.04	±1.3 cm (0.5 in.) error in 254 cm (100 in.)
Set point	0.1	0.1	0.1	< ±0.25 percent error in rpm
Pistonphone	0.15	0.15	0.15	Brüel & Kjær (B&K) 4220, 124 dB, 250 Hz
Spectral response calibration	0.0	0.01	0.16	Certified by B&K calibration facility
1/3-octave-band averaging	0.33	0.1	0.01	Chi-squared analysis of 1/3-octave integration (five narrowbands minimum) at 90% confidence
— or —				
Narrowband averaging	0.61	0.61	0.61	Chi-squared analysis of 194-average narrowband at 90% confidence
Total ^a	0.59	0.39	0.61	1/3-octave spectra
	0.86	0.87	1.07	Narrowband spectra

^aTotal uncertainty is summed according to $10\log_{10}\left[1 + \sum(10^{e/10} - 1)\right]$.

Lastly, an error uncertainty is determined for the integration of the acquired data for averaging analysis purposes for both narrowband and 1/3-octave-band analysis. A chi-square analysis was done for 194-average narrow bands at a 90% confidence interval for the narrow-band uncertainty. A chi-square analysis was also done for a minimum of 5 narrowbands at 90% confidence interval for the 1/3-octave-band uncertainty. The uncertainty varies in the 1/3-octave-band analysis according to frequency because of the fact that fewer narrowbands are used in the lower frequencies, and the number of narrow bands combined to form single 1/3-octave bands increases as frequency increases. The overall data measurement uncertainty was determined for three different frequency ranges and two noise-band-averaging methods. The results are shown in Table 5.4.

The above analysis addresses the uncertainty in measured amplitude of the data. The measured frequency uncertainty is based on the uncertainty in the revolutions per minute of the fan model in the 9×15 LSWT. The calculated uncertainty of the fan model in the wind tunnel is ±5 corrected revolutions per minute. The highest uncertainty can be calculated for the lowest speed of interest here, which is 5425 rpm. This gives an uncertainty in the measured frequency of ~0.09 percent.

The list of uncertainties considered here, while not exhaustive, represents all the important measurement uncertainty factors. Finally, it should be noted again that these uncertainty levels were calculated based on manufacturer specifications of the various components of the measurement system.

5.6.3 Rotating Rake Acoustic Data Uncertainty Analysis

The uncertainty in the mode acoustic PWL computed from the Rotating Rake mode measurements arises from three basic components: instrumentation and calibration, data reduction, and modeling error.

The instrumentation and calibration error arises from the errors associated with transducer and the telemetry transmission. The transducer uncertainty was determined by referencing to a pistonphone that was calibrated to a known transducer and the uncertainty assumed to be that of the pistonphone. The uncertainty induced by transmission through the telemetry system was obtained by placing a known signal across the telemetry and comparing this known signal with the telemetry output.

The data reduction uncertainty arises from the uncertainty in the inputs to the equation used for computation of mode power. Propagation of uncertainties through this equation may be calculated in the standard manner by analyzing the partial derivatives of the power equation with respect to all of the relevant parameters. The parameters that have a significant effect on mode PWL are mode pressure, duct Mach number, and mode cutoff ratio based on the corrected revolutions per minute. Errors in geometry (e.g., variations in blade and vane manufacturing, installation, etc.) are small for the three fans considered, particularly regarding their influence on the noise generation mechanisms considered in this study.⁷ As such, the influence of the geometric errors on mode PWL has been

⁷This is not always true. Case in point is the buzz-saw noise resulting from small differences in blade manufacturing and installation. Buzz-saw noise is not considered in this study.

TABLE 5.5.—REPRESENTATIVE UNCERTAINTY LEVELS IN MODE SOUND POWER LEVELS FOR SECOND HARMONIC OF BLADE-PASSING FREQUENCY COMPUTED FROM MEASURED ROTATING RAKE DATA

[Data from Source Diagnostic Test (SDT) fan.]

Circumferential mode number	Uncertainty level, dB		
	Approach	Cutback	Takeoff
–8	1.26	1.10	1.47
18	0.27	0.51	0.91
–10	0.21	0.87	0.34

ignored here. The resulting uncertainties in rotor-stator interaction mode measurements that would arise for the SDT fan at three representative speeds points are shown in Table 5.5. These are considered the representative levels and shall be used in subsequent analysis.

The uncertainty in modeling error is a result of using basis functions for plug flow when shear flow basis functions may be more appropriate. The shear flow basis functions can be computed using the methodology described in Reference 39. Table 5.6 shows the error that would result from fitting a plug-flow basis function to a mode shape arising in shear flow. In this example, the computed zeroth-order radial acoustic mode in a duct with shear flow is used as measured values and fitted (i.e., approximated) by the zeroth-order radial acoustic mode when plug flow is assumed to be present in the duct. The last column on the right shows the percent error in acoustic pressure that occurs at the selected radial locations when making a plug flow assumption for a duct flow that physically is a shear flow. Clearly, the mismatch can lead to sizable discrepancies (3.2 dB in terms of mode amplitude). The modeling error depends on the particular mode under consideration, which means that an accurate estimate of the modeling error would require an exhaustive assessment of all rotor-stator interaction modes present in the measured fan tone data for all of the fans and tip speeds under consideration here. Since such modal data is not available for all configurations and tip speeds of interest here, it was decided to use the uncertainty shown in Table 5.6 as the representative uncertainty for modeling error.

The overall uncertainty is then the square root of the sum of the squares of the component uncertainties as shown in Table 5.7. Thus for each fan and operating point, an uncertainty can be computed for any given mode at each harmonic. This uncertainty can be expected to vary. In the absence of actual data for all modes and for all fans,⁸ it is proposed that the number obtained here for the case analyzed for SDT (i.e., ± 4.3 dB) be applied to the other fans as well. As such, this represents the uncertainty in mode PWL for an arbitrary mode in either inlet or exhaust.

⁸Individual mode power distributions for the ADP fan are not available.

TABLE 5.6.—MODELING ERROR FROM USING HARD-WALL PLUG-FLOW BASIS FUNCTION TO FIT SHEAR-FLOW MODE^a

Radial location ^b	Shear flow mode	Plug flow curve fit	
	Pressure, Pa (psi)	Pressure, Pa (psi)	Percent error ^c
0.000	0.000	0.000	0.0
0.040	0.000	0.000	0.0
0.106	0.002 (2.9×10^{-7})	0.001 (1.5×10^{-7})	0.1
0.206	0.029 (4.2×10^{-6})	0.010 (1.5×10^{-6})	1.5
0.341	0.196 (2.8×10^{-5})	0.069 (1.0×10^{-5})	9.7
0.500	0.691 (1.0×10^{-4})	0.260 (3.8×10^{-5})	32.9
0.659	1.260 (1.8×10^{-4})	0.590 (8.6×10^{-5})	51.1
0.794	1.310 (1.9×10^{-4})	0.901 (1.3×10^{-4})	31.2
0.894	0.925 (1.3×10^{-4})	1.077 (1.6×10^{-4})	11.6
0.960	0.507 (7.3×10^{-5})	1.140 (1.7×10^{-4})	48.3
		Average error: ^d 18.6 percent	
		Mode amplitude pressure	
		Pa (psi)	dB
		0.909 (1.3×10^{-5})	91.8
		0.536 (7.8×10^{-5})	88.6

^aNumber of radial nodes in mode is zero.

^bNormalized by duct radius.

^cPercent error calculated as $\frac{|\text{pressure}(\text{shear}) - \text{pressure}(\text{plug})|}{\text{max. pressure}(\text{shear})} \times 100$

^dAverage error calculated as $\frac{1}{10} \sum_i \text{percent error}_i$, where i is an index representing the radial locations.

TABLE 5.7.—TYPICAL UNCERTAINTIES IN MODE ACOUSTIC POWER LEVEL FROM ALL SOURCES

Uncertainty source	Uncertainty, e , dB	$10^{(e/10)} - 1$
Calibration	0.5	0.122
Telemetry	0.4	0.096
Data reduction	1.5	0.413
Modeling	3.2	1.089
Sum of component uncertainties		1.720
Total uncertainty = $10 \log_{10}(1+1.720) = 4.3$ dB		

5.7 Prediction and Assessment

In this section, the results of the assessment exercise are presented. The presentation is organized according to the categorization discussed earlier; namely, that we begin with the empirical results, followed by the acoustic-analogy-based results, and conclude with the computational aeroacoustics results. In each case, comparisons of the predicted levels and

the measured levels are presented. All comparisons include the calculated uncertainty of the experimental measurements as appropriate. In the interest of brevity, representative data-theory comparisons are shown in the main text, but all the rest are included in Appendix B and Appendix C. Depending on the particular fan noise code evaluated, the results are presented in terms of sound pressure level (SPL) or sound power level (PWL). The input requirements of each code are listed and discussed as appropriate.

5.7.1 Empirical Methods

As a representative code in the empirical methods category, the version (i.e., Level) 25 of the Aircraft Noise Prediction Program (ANOPP) was chosen to assess the accuracy of the empirical methods for predicting fan noise. ANOPP represents the state of the art at NASA in empirical methods for aircraft noise prediction. It can be used to predict the noise on the component basis as well as at the system level. Much literature has been devoted to describing the inner workings of ANOPP (see Refs. 40 to 44 for an in-depth understanding of ANOPP), so no details will be given here about the code. For the purposes of this study, the fan noise module in ANOPP, called HDNFAN (Ref. 45), was used to predict the sideline noise radiation for the test-bed fans. The HDNFAN fan noise prediction module, designated Level 25, version 3 (L25v3), was developed using data from a number of fans,⁹ but this database does not include data from the model fans used in this study. HDNFAN predicts fan noise spectrum on a 1/3-octave-level basis inclusive of all fan noise sources and for both inlet and exhaust and includes the effects of acoustic transmission through the blade rows, scattering from the inlet and exhaust lips, and shear layer refraction in the exhaust stream.

ANOPP requires a host of geometric, environmental, and operational parameters as input. Table 5.8 lists these input parameters for each fan under consideration here. The ANOPP calculations for each of the three fans were carried out at the three fan tip speeds corresponding to the nominal approach, cutback, and takeoff conditions listed in Table 5.2. The actual revolutions per minute shown in Table 5.8 correspond to the corrected revolutions per minute listed in Table 5.2. The calculations and comparisons with the data were carried out for all emission angles as “lossless” on a 0.3-m (1-ft) radius centered on the fan pitch axis.

A sampling of the data-theory comparisons is presented in Appendix B in Figure 5.22 to Figure 5.30 for typical inlet and exhaust quadrant emission angles, namely 46° and 136°, respectively. The figures are organized as a function of fan tip speed for ADP, SDT, and QHSF 2, respectively. As shown in Table 5.4, the measured SPL data have a frequency-dependant 1/3-octave uncertainty level of less than 1 dB over the entire

range of frequencies of interest. However, for the sake of simplicity the uncertainty level is assumed to be a constant ± 1 -dB band for the entire frequency range as indicated by the error bars on the measured levels shown in these figures. It should be noted that the microphone measurements for both the inlet and exhaust below 2 kHz are contaminated by rig noise caused by the scrubbing of the exhaust flow over the drive rig assembly. This extraneous noise source has been robustly characterized in a recent investigation whose results have been documented in Reference 46. As a result, the portion of the data that is shown in Figure 5.22 to Figure 5.30 in Appendix B that is below 2 kHz should be ignored.

In Figure 5.9 to Figure 5.11, the results for all sideline (emission) angles have been summarized in the form of the decibel error in predicting the measured levels. Therefore, each point represents the difference between the measured and predicted SPL on a 1/3-octave basis. The gray band spanning the ± 1 -dB range represents the experimental uncertainty. Results below the 2-kHz band are not shown because of drive rig noise contamination.

On average, the data-theory agreement falls well outside of the experimental uncertainty band for all three fans when all frequencies and angles are considered. In the extreme aft angles, in particular, ANOPP tends to underpredict the measured levels by sizable margins. However, with the exception of a few isolated frequency bands, the data-theory deltas are within ± 4 dB of the experimental uncertainty margin for ADP and SDT for nearly all frequency and angle combinations. The deltas also tend to be clustered together and follow the same general trends for nearly all frequencies. The same is not true for QHSF 2 for which the deltas are outside the ± 4 -dB range (especially for the 12 500 rpm case) and there is far more scatter in the deltas. As noted in Table 5.8, the ANOPP predictions were all generated using the “GE revised method” within HDNFAN module and represent the best comparisons of all available options in ANOPP L25v3.

In summary, the data-theory comparisons indicate that ANOPP predictions are within ± 4 dB of the measurement uncertainty band for most fan tip speed, 1/3-octave frequency band, and emission angle combinations for the ADP and SDT fans. However, the data-theory discrepancy is considerably larger for the QHSF 2 fan.

5.7.2 Acoustic-Analogy-Based Methods

As a representative code in this category, the most recent version of the RSI (i.e., rotor-stator interaction) code was chosen to predict broadband noise generated by the interaction of rotor turbulence impinging on the downstream stator in the bypass duct. The underlying theory for this code has been described in detail in Reference 8 and will not be repeated here. The RSI code computes in-duct narrowband distribution of PWL as a function of frequency. It computes the PWL upstream and downstream of the stator. The upstream portion contributes to the fan inlet noise, and the downstream portion is the main source of the fan exhaust

⁹The fan noise module was developed using Marcus Heidmann’s method with revisions by General Electric (GE) Aircraft Engines for hard-wall modern fans including CF6, CFM56, E³, and QCSEE (see Ref. 45).

TABLE 5.8.—ANOPP L25V3 HDNFAN INPUT PARAMETERS
[Using GE revised method.]^a

Input parameter ^b	Fan ^c								
	ADP			SDT			QHSF 2		
	Approach	Cutback	Takeoff	Approach	Cutback	Takeoff	Approach	Cutback	Takeoff
Ambient temperature, K (°R)	297.3 (535.2)	296.4 (533.5)	297.1 (534.8)	295.7 (532.2)	295.5 (531.9)	295.3 (531.5)	297.4 (535.3)	297.2 (534.9)	297.4 (536.3)
Ambient pressure, kPa (lb/ft ²)	97.67 (2039.9)	97.63 (2039.0)	97.59 (2038.3)	98.44 (2056.0)	98.30 (2053.1)	98.25 (2052.0)	99.46 (2077.2)	99.35 (2075.0)	99.32 (2074.3)
Ambient speed of sound, m/s (ft/s)	345.6 (1134.1)	345.1 (1132.2)	345.5 (1133.6)	340.3 (1116.4)	340.3 (1116.4)	340.3 (1116.4)	345.6 (1134.1)	345.6 (1133.7)	346.0 (1135.2)
Ambient density, kg/m ³ (slug/ft ³)	1.182 (0.00229)	1.182 (0.00229)	1.182 (0.00229)	1.167 (0.00226)	1.167 (0.00226)	1.167 (0.00226)	1.197 (0.00233)	1.197 (0.00233)	1.197 (0.00233)
Blade count	18	18	18	22	22	22	22	22	22
Vane count	45	45	45	54	54	54	50	50	50
Revolutions per minute (actual)	5510	7630	8885	7910	11 205	12 810	9995	12 690	14 295
Inlet cross-sectional area, m ² (ft ²)	0.200 (2.15)	0.200 (2.15)	0.200 (2.15)	0.222 (2.39)	0.222 (2.39)	0.222 (2.39)	0.215 (2.32)	0.215 (2.32)	0.215 (2.32)
Design relative tip Mach number	0.86	0.86	0.86	1.20	1.20	1.20	1.52	1.52	1.52
Axial rotor-stator spacing (in rotor tip chords)	1.42	1.42	1.42	3.14	3.14	3.14	2.32	2.32	2.32
Fan inlet flow, kg/s (lb/s)	11.16 (24.60)	17.70 (39.02)	20.66 (45.54)	25.46 (56.14)	36.82 (81.17)	42.75 (94.24)	27.03 (59.60)	34.84 (76.8)	39.96 (88.1)
Fan inlet total temperature, K (°R)	297.3 (535.2)	296.4 (533.5)	297.1 (534.8)	295.7 (532.2)	295.5 (531.9)	295.3 (531.5)	297.4 (535.3)	279.2 (534.9)	297.4 (536.3)
Fan exit total temperature, K (°R)	306.0 (550.8)	31.5 (564.3)	320.4 (576.7)	310.3 (558.6)	325.6 (586.1)	335.6 (604.0)	320.7 (577.3)	337.1 (605.8)	349.1 (628.4)
GE flight cleanup (takeoff, cutback = 1; approach = 2)	2	1	1	2	1	1	2	1	1

^aGE is General Electric Company.

^bSource-to-observer distance set to 0.3 m (1 ft).

Fan reference diameter set to 0.56 m (1.83 ft).

Flight Mach number set to 0.0 to avoid “flyover” Doppler frequency shift in output spectra.

Prediction method flag set to GE revised method.

Inlet guide vane index set to 1 (no vanes).

Inlet flow distortion index set to 1 (no distortion).

Fan inlet broadband switch set to “true.”

Fan inlet R/S discrete tone switch set to “true.”

Fan inlet combination tone switch set to “false.”

Fan inlet distortion tone switch set to “false.”

Fan discharge broadband switch set to “true.”

Fan discharge rotor-stator discrete tone set to “true.”

^cADP is the NASA-Pratt & Whitney Advanced Ducted Propulsor Fan 1; SDT, the NASA-General Electric Source Diagnostic Test fan; and QHSF 2, the NASA-Honeywell Quiet High Speed Fan 2.

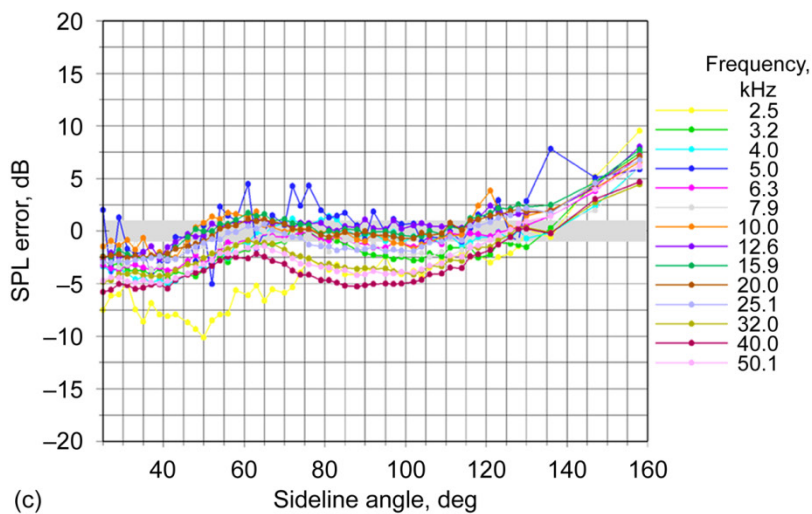
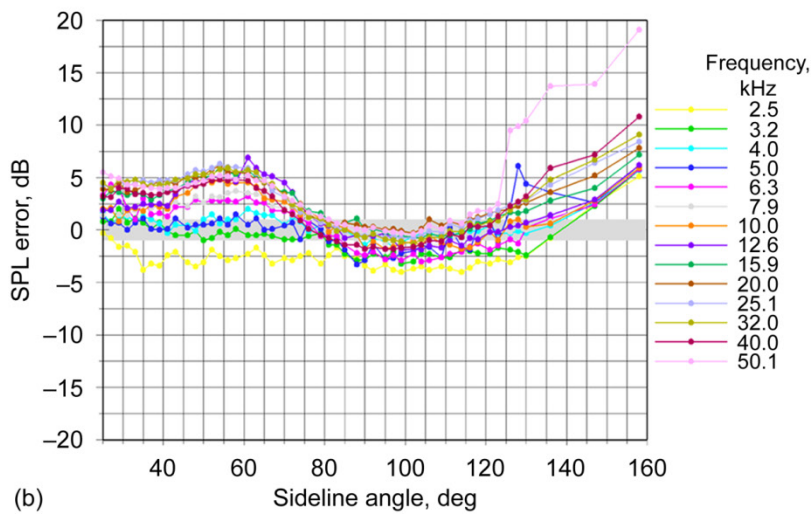
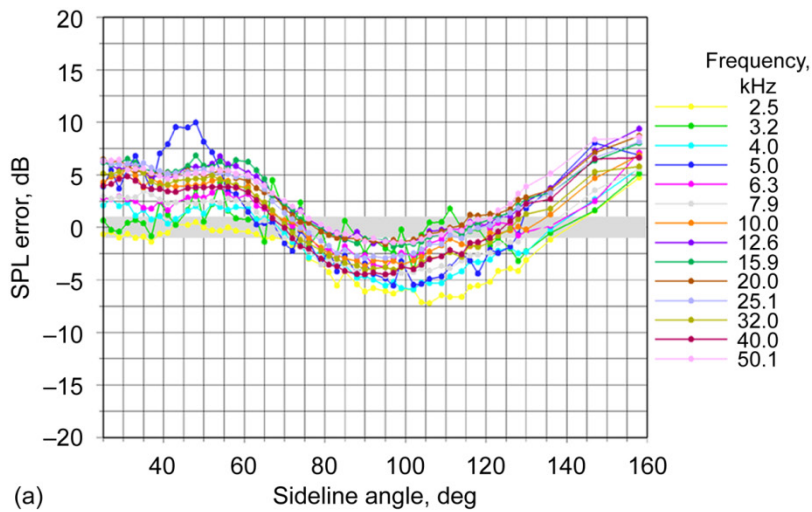


Figure 5.9.—Sound pressure level (SPL) error in ANOPP predictions for all sideline emission angles for ADP fan at various tip speeds. Gray bar represents experimental uncertainty. (a) 5425 rpm. (b) 7525 rpm. (c) 8750 rpm.

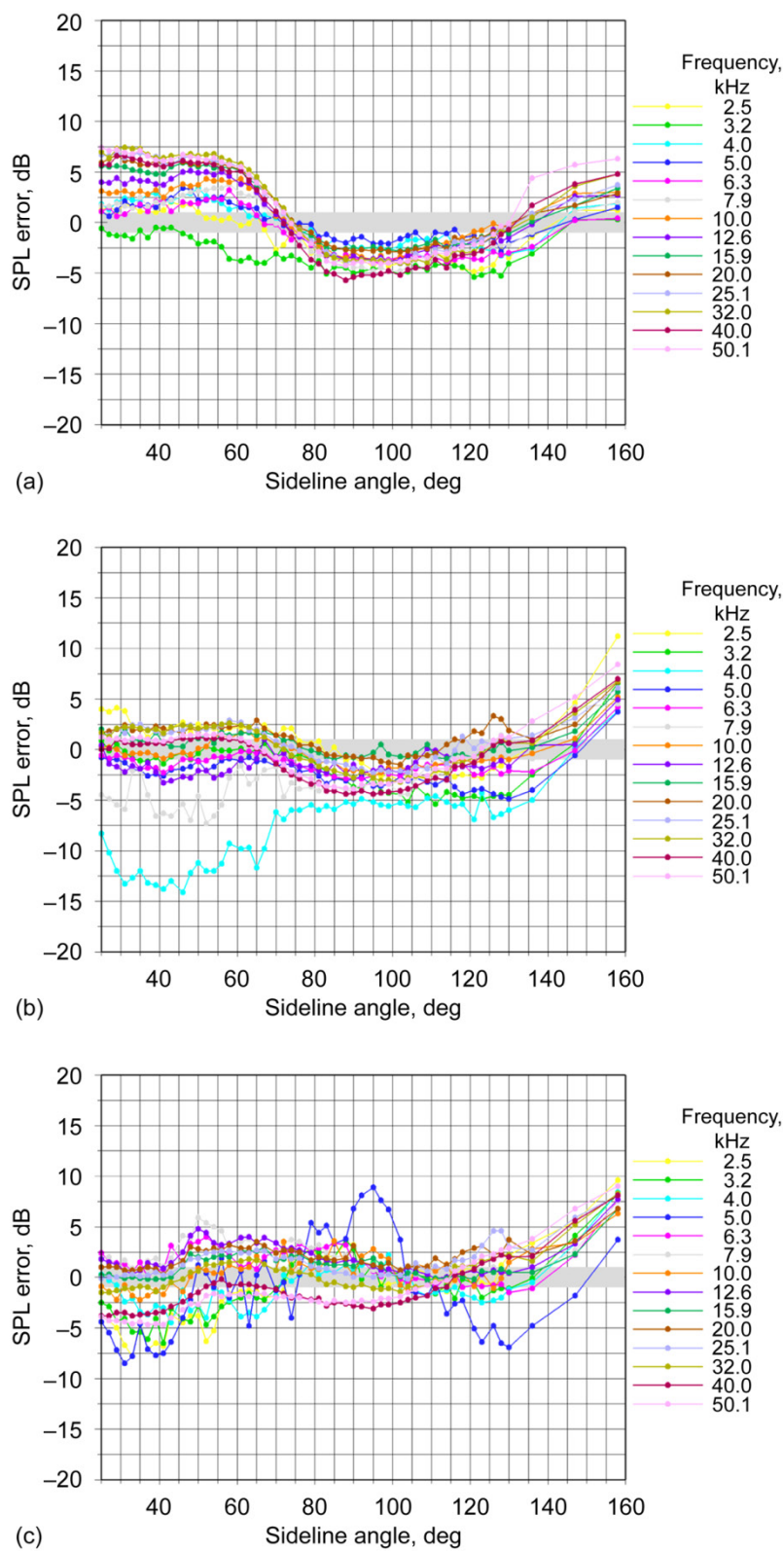


Figure 5.10.—Sound pressure level (SPL) error in ANOPP predictions for all sideline emission angles for SDT fan at various tip speeds. Gray bar represents experimental uncertainty. (a) 7809 rpm. (b) 11 075 rpm. (c) 12 657 rpm.

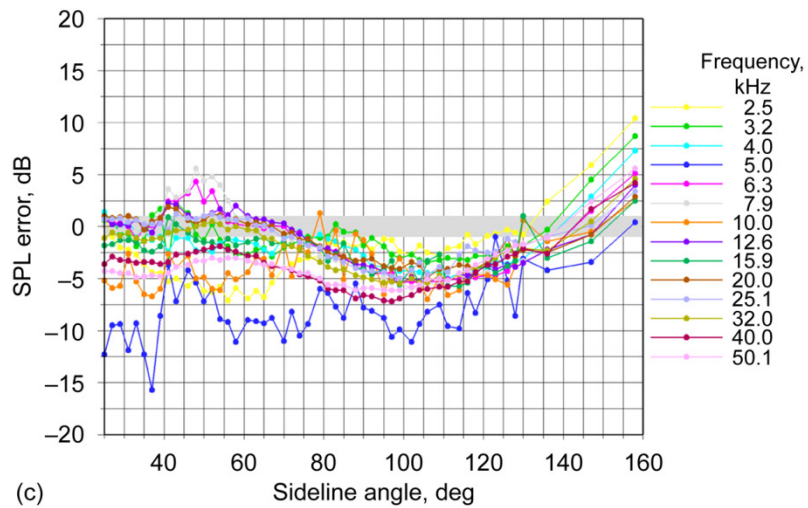
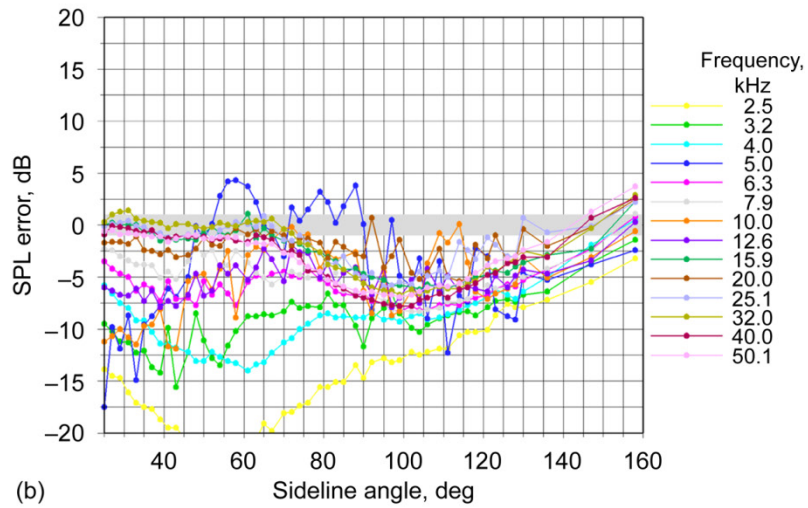
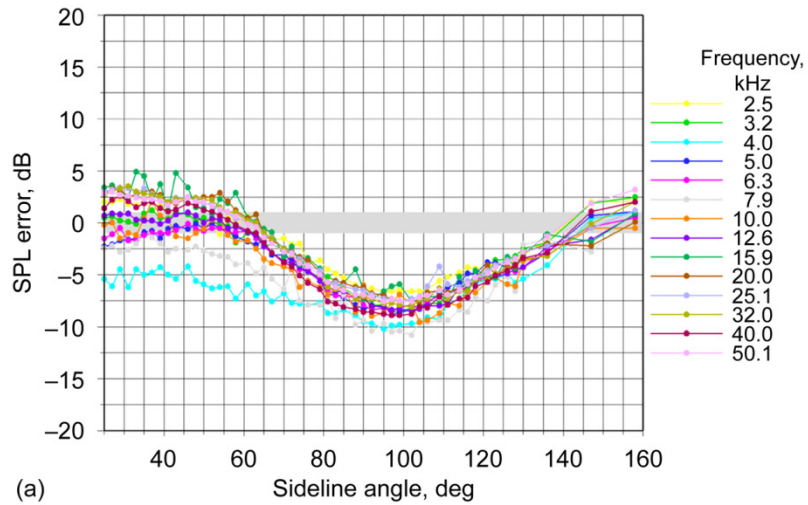


Figure 5.11.—Sound pressure level (SPL) error in ANOPP predictions for all sideline emission angles for QHSF 2 fan at various tip speeds. Gray bar represents experimental uncertainty. (a) 9840 rpm. (b) 12 500 rpm. (c) 14 060 rpm.

noise. It should be noted that the predicted upstream PWL does not include the effects of acoustic transmission loss through the rotor and, therefore, would overestimate the upstream level noise. It should also be noted here that the measured PWL, which is calculated by integrating the measured sideline SPL over a sphere enclosing the fan model, includes contributions from the rotor-stator interaction source as well as the rotor-only source(s) (i.e., the contribution of the rotor by itself). As such, a direct comparison of the RSI code PWL predictions to the measured PWL is not fruitful. However, if rotor-stator interaction PWL contribution could be estimated, then meaningful comparisons could be carried out.

Like similar codes, RSI requires a description of the basic blade row geometry, mean flow quantities, and impinging turbulence characteristics as input for computing broadband noise spectra. Specifically, RSI requires the radial variations of the vane chord and stagger angle, radial distributions of the axial and tangential components of the mean flow, radial distributions of the root-mean-squared (rms) turbulence intensity, and the integral length scales of turbulence. Turbulence information is sometimes available from experiments or more typically is heuristically modeled to provide the best fit of the predicted noise spectra to the measured levels. An alternative approach is to compute the turbulence characteristics using Reynolds-averaged Navier-Stokes (RANS) calculations, since measuring the turbulence integral length scales is not an easy task especially in high-speed flow environments. The RANS code utilized in this study is TSWIFT, which is a derivative of a code developed at NASA Glenn over the past several years (see Ref. 47). For each fan under consideration in this study, the TSWIFT code was used to compute the flow field at all tip speeds of interest. This represents a large and detailed investigation of the fan aerodynamics for the three fans used in this study and served as an invaluable resource for generating the input for this assessment.

Shown in Figure 5.12 are the three-dimensional computational blocks for the rotor and stator (in this case for the ADP fan). The full simulation includes additional blocks enclosing not only the two blade rows, but also the entire flow path inside the nacelle as well as the external flow field within the tunnel. The blocks are a mix of axisymmetric and full three-dimensional flow-field volumes. In Figure 5.13 axisymmetric Mach number contours computed using the TSWIFT code for the ADP fan at the takeoff condition (i.e., 8750 rpm) are shown as an example of the level of detail that is available from these simulations. All geometric, mean flow, and turbulence information needed to run the RSI code were obtained by interrogating the rotor, stator, and the rotor-stator intermediate blocks. As described in Reference 8 the turbulence and kinetic energy information are used to construct both an analytic description of the rms turbulence intensity across the blade pitch and to estimate the integral length scales of turbulence using the isotropic assumption. In the RSI code a distinction is made between the distributions of the turbulence intensity within the background flow and within the rotor wake flow (see Ref. 8). Background turbulence refers to that portion of turbulence that was not generated by the rotor blades, but originated upstream of the fan and was drawn into the fan disc. It should be noted that we define the background turbulence region as spanning the entire blade pitch and that its level is uniform across the blade pitch. Any excess level above the background produced downstream of the fan blade is considered to be the wake turbulence contribution. Because the RSI predictions are sensitive to the input turbulence information, it is desirable to check the accuracy of the computed turbulence characteristics from the TSWIFT code by comparing them with the experimental data.

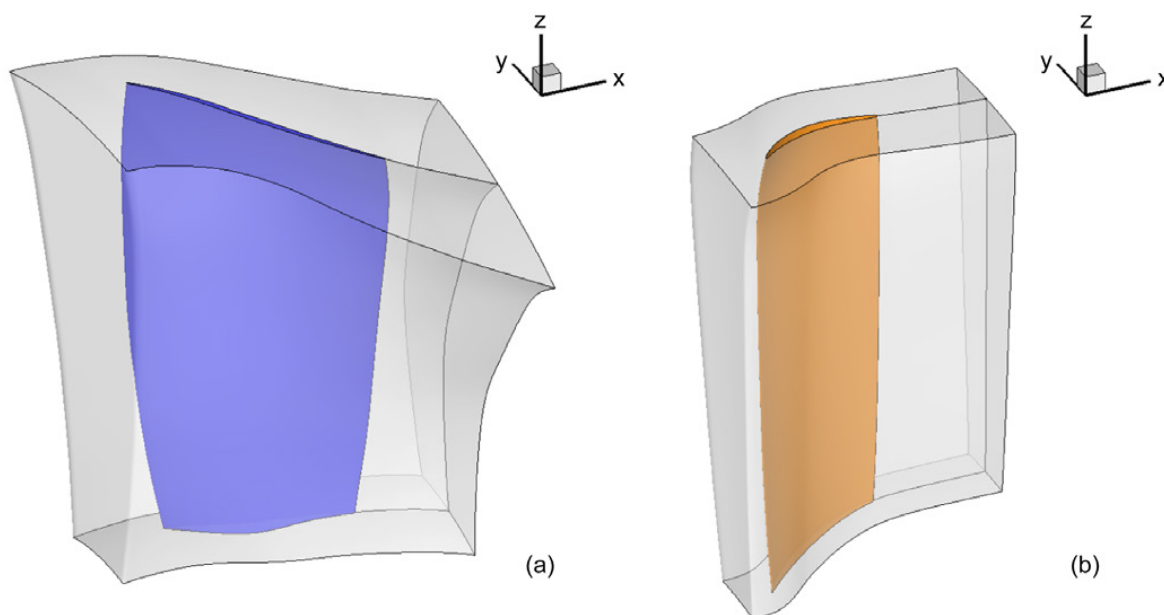


Figure 5.12.—Computational domains for ADP fan used by TSWIFT code. (a) Rotor. (b) Stator.

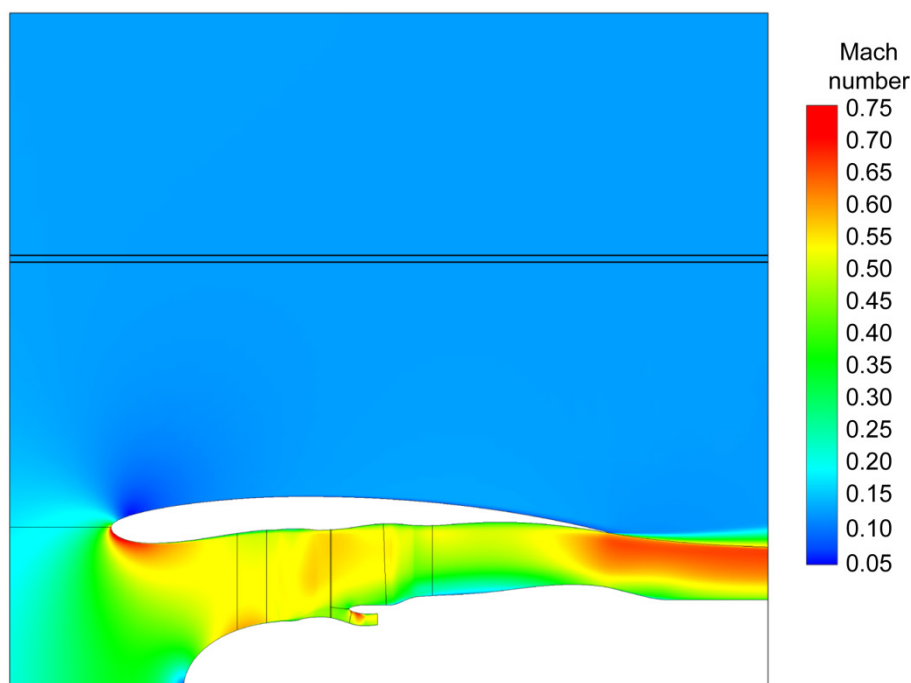


Figure 5.13.—Flow field through ADP fan duct. Axisymmetric Mach number contours at 8750 rpm computed using TSWIFT code. External as well as internal flows included. Black lines indicate block boundaries.

In Figure 5.14 comparisons of the predicted and measured total turbulence intensity 6.4 cm (2.5 in.) downstream of the fan rotor tip trailing edge are plotted at three spanwise stations. The results correspond to the approach condition (7809 rpm) for the SDT fan and are the most reliable available data for this purpose. The comparisons are shown for three spanwise stations; namely, 88 percent shown in the top plot for the outboard region, 71 percent span shown in the middle plot for an intermediate region, and 56 percent shown in the bottom plot for an inboard region. Note that the locations of the inboard and outboard stations were selected to avoid the disturbed flow regions near the inner and outer walls where it is hard to make a distinction between the background turbulence and wake turbulence. The intermediate station was chosen since it falls between the other two. Whereas the TSWIFT code seems to predict reasonable levels of turbulence within the wake region, it predicts much lower levels for the background turbulence by as much as 90 percent. The cause of this shortfall is not entirely clear at this point and warrants further investigation. In the meantime, for the purposes of this study, the measured background turbulence level, which turns out to be about 1.5 m/s (5 ft/s) at all spanwise stations and all the measured conditions,¹⁰ was used as the input for the

background turbulence level for all RSI test cases. Otherwise, the RANS results were used “as is,” meaning that the distribution of the wake turbulence intensity as well as the integral length scale were used from the RANS simulation results without any change. It should be emphasized that in the TSWIFT code, the background turbulence level is set a priori on the outer boundaries of the computational domain¹¹ and remains essentially unaffected in absolute terms (not percent basis) by the flow through the fan rotor. Therefore, the computed wake turbulence level (as we have defined it here) would have not changed had a 5-ft/s background level been used in TSWIFT simulations in the first place.

Finally, it should be noted that the turbulence information used here was extracted at the exit plane of the rotor block since TSWIFT uses a mixing plane strategy to couple the rotor and the stator and, as such, smears the turbulence information at the inlet plane of the stator block. To ensure accuracy, the rotor block exit plane was placed very close to the stator leading edge (approximately 1.3 cm (0.5 in.)).

The PWL predictions from the RSI code for all cases considered in this chapter are compared with the measured PWL and the results are shown in Figure 5.31 to Figure 5.33 in Appendix C. Note that the measured PWL spectra include

¹⁰Note that on a percent basis, the background turbulence intensity level changes as a function of spanwise station and fan tip speed.

¹¹The 1990s vintage measurements reported 0.25-percent free-stream turbulence level at Mach number = 0.1 (i.e., ~0.09 m/s, or ~0.28 ft/s).

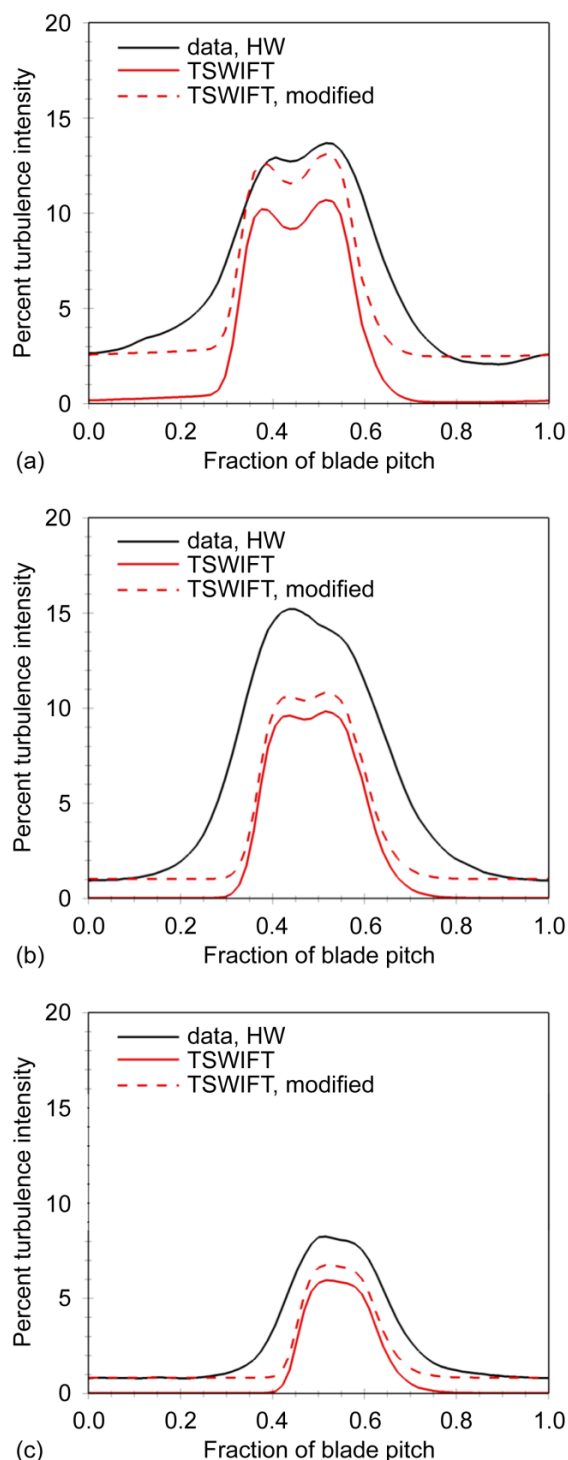


Figure 5.14.—Comparisons of measured and predicted turbulence intensity for three spanwise stations 2.5 in. downstream of rotor tip trailing edge of SDT fan at approach condition. Predictions made using NASA TSWIFT code; dashed curves are predicted levels raised so background level matches measured background. (a) 88 percent span. (b) 71 percent span. (c) 56 percent span.

only broadband contribution since tone content was removed from the measured data.¹² The RSI predictions were calculated for 50 frequency values, roughly covering the range between 1 and 50 kHz. The actual RSI acoustic power level predictions at each frequency value are shown as open red circles in these figures. There is some scatter in predictions because RSI couples a two-dimensional stripwise unsteady aerodynamic response to a three-dimensional acoustic modal description. Because there is an inherent mismatch between the cutoff phenomena in two- and three-dimensional unsteady responses, there sometimes occurs exaggerated two-dimensional aerodynamic response near a two-dimensional mode cutoff condition that would not have occurred for a three-dimensional mode. The result is a somewhat erratic PWL variation as a function of frequency. This is more noticeable at lower frequencies where fewer modes propagate at each frequency, and therefore the power sum is more sensitive to the variations in each mode level. To mitigate the effect of the cutoff mismatch, in this study, a polynomial curve was fitted through the predicted points to smooth out the scatter.¹³

It should be noted that the predicted PWL spectra shown here include only the exhaust contribution since stator inlet noise is negligible compared with the stator exhaust noise (Ref. 23). From the information in Table 5.4, an error band of ± 1 dB is assigned to the measured PWLs. The reader is reminded that the measurements below 2 kHz are contaminated by the extraneous drive rig noise mentioned in the previous section, “5.7.1 Empirical Methods.” Furthermore, the RSI acoustic power level predictions do not include the rotor-only contribution. In contrast, the measured PWL data (henceforth referred to as “stage PWL”) include both the rotor-stator interaction noise PWL and rotor-only noise PWL.

To gauge the relative magnitude of the rotor-only contribution, we have plotted in Figure 5.15 the measured rotor-only PWL for the SDT fan along with the stage PWL. Note that the stage PWL data are the same as those plotted in Figure 5.32 (Appendix C). The rotor-only PWL data were acquired for the SDT fan (but not the other two fans) by removing the stator and independently supporting the nacelle and the centerbody (see Ref. 49). With both sets of PWL spectra available, one can calculate the rotor-stator interaction contribution by spectral subtraction of the two (i.e., antilogarithmic difference converted back to decibels). The result, shown in blue, represents only an estimate because rotor transmission loss effects are still present in the difference spectra. Nonetheless, these estimates provide a better benchmark for evaluating the RSI predictions than the stage PWL data do. Naturally, the

¹²The tone extraction procedure is somewhat subjective without the use of time-domain averaging, which is only possible if long time series data were acquired together with the once-per-revolution signal from the fan rotor. Such data are not available for all fan configurations investigated here.

¹³A more elegant and mathematically robust fix may be that suggested by Atassi and Hamad in Reference 48, which ameliorates the cutoff mismatch.

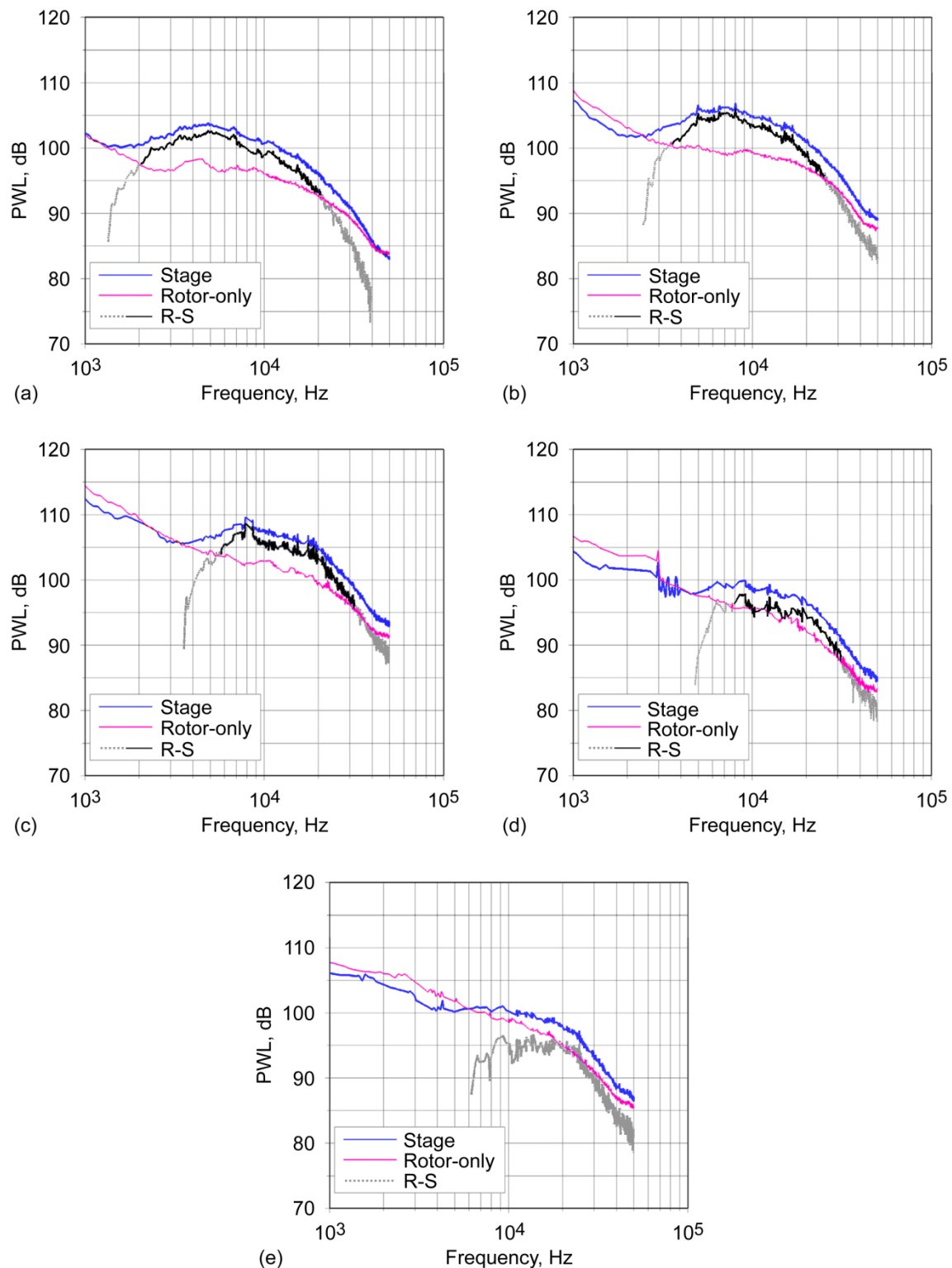


Figure 5.15.—Rotor-stator (R-S) interaction narrowband sound power level (PWL) for SDT fan at different speeds from measured stage and rotor-only PWLs: R-S = stage – rotor-only. Dashed line indicates data reliability is questioned (see Sec. 5.7.2). (a) 7809 rpm. (b) 9493 rpm. (c) 11 075 rpm. (d) 11 771 rpm. (e) 12 657 rpm.

benchmarking will be limited to the SDT data, but even this limited assessment is still useful.

It should be noted that the rotor-only PWL data include a higher proportion of drive rig noise contamination because of the high-speed swirling flow exiting the duct and impinging on the drive rig. The contamination levels are higher—since the absolute exit velocities are higher—for the rotor-only configuration compared with the stage configuration for the same fan tip speed. The difference is clearly evident by examining the crossover point where rotor-only noise power levels exceed the stage power levels as the tip speed increases. As a result, the range of frequencies where the rotor-stator interaction PWL estimates are valid decreases as the fan tip speed increases. Specifically, at the lowest tip speed (i.e., 7809 rpm) the spectral differencing results are valid starting at 2 kHz, while for the highest tip speed (i.e., 12 657 rpm) they are valid starting at 6 kHz.

Another important aspect of the spectral differencing has to do with the interpretation of the difference when the rotor-only PWLs are close to the stage PWLs, even if the rotor-only noise levels are less than the stage noise levels. Given the ± 1 -dB measurement uncertainty band, when the constituent spectra are within 2 dB of each other, the resulting difference is suspect. In order to ensure unambiguous results, we have chosen to use 3 dB as the criterion to accept the difference as reliable. Put differently, we accept the rotor-stator interaction PWL as free from ambiguity only when the difference PWL is equal to or larger than the rotor-only PWL. In Figure 5.15, where this criterion is not met, the rotor-stator interaction PWL is shown as a dotted line. An examination of the results in these figures indicates that the frequency range where the rotor-stator interaction PWL is reliable shrinks as the tip speed increases until eventually, at the highest fan tip speed, the resulting spectrum is entirely unreliable.

Although somewhat limited, these rotor-stator interaction estimates can still serve to assess the validity of the RSI predictions. The RSI acoustic power level predictions are compared with the estimated rotor-stator interaction acoustic power level in Figure 5.16. As before, only the reliable portion of the estimated rotor-stator interaction PWL spectrum is shown as a solid line. Where comparisons are possible, the data-theory agreement is fair at low tip speeds, but deteriorates with increasing tip speed.

The results of the data-theory comparisons for the SDT fan are summarized in Figure 5.17. Generally speaking, the RSI predictions overestimate the level of measured sound power level generated by rotor-stator interaction noise by as much as 4 dB beyond the uncertainty margin. Surprisingly, the data-theory agreement is better when the RSI predictions are compared with the measured stage PWL as shown in Figure 5.32 (Appendix C). In addition to the shortcoming of the RSI code, it is also entirely possible that the procedure used to isolate the measured rotor-stator interaction noise described earlier may be partially responsible for the relatively poor data-theory agreement summarized in Figure 5.17. Therefore, the principal conclusion here is that rotor-only

source contribution must be modeled in order to get a better assessment of the accuracy of the RSI code for predicting fan broadband noise.

5.7.3 Computational Methods

As an example of computationally intensive methods, the LINFLUX code (see Ref. 15) was selected for this assessment exercise. The choice was dictated for two main reasons. First, LINFLUX has been in use since the late 1990s and has been rigorously exercised and even used in design work. Second, computational codes tend to require significant user experience to be reliably used for analysis and design purposes. At NASA, LINFLUX has been extensively used and is the tool of choice when high-fidelity predictions are required.¹⁴ NASA has been developing a more advanced code in this category (i.e., BASS, see Ref. 20), but it is still in the late development stages and not yet ready for routine use.

LINFLUX is a frequency-domain, three-dimensional, linearized inviscid description of the unsteady flow. In this study it was used to compute the rotor-stator interaction tones generated as a result of the mean perturbations in the fan rotor wake impinging on the stator. The underlying mean flow (also three-dimensional and inviscid) is representative of the flow through a realistic stator. The required nonlinear mean flow can be computed using any suitable inviscid code, but for the purposes of this study a serial version of the TURBO inviscid steady aerodynamic code was used. Both LINFLUX and TURBO use an implicit and finite-volume description of the flow, which makes for better consistency in describing and analyzing both the mean and perturbation components of the flow. A detailed description of the LINFLUX code (and to some extent the version of the TURBO code used here) can be found in Reference 15 and other works cited in that document. The LINFLUX code calculates perturbation density, momenta, and internal energy everywhere in the domain subject to specified wake perturbation input, which are supplied in terms of the fan blade-passing harmonic content. In this study, these were generated from the TSWIFT simulations discussed earlier. The TSWIFT simulations were used to supply the inflow conditions for the mean flow calculations. These include the radial profiles of the circumferentially averaged total pressure, total temperature, and the swirl angle at the inflow plane of the computational domain for TURBO. The harmonic content of the wake perturbation were also computed from the TSWIFT solutions by extracting wake perturbation velocities at the exit plan of the rotor block and Fourier decomposing them.

In addition to the field solution, LINFLUX also calculates the tone SPL and PWL upstream and downstream of the stator.¹⁵ Since the computational inflow and outflow boundaries fall well short of the Rotating Rake measurement stations,

¹⁴The well-known NASA tone noise prediction codes V072 and TFaNS were not assessed, since LINFLUX, by comparison, has been shown to produce more robust results in both trend and absolute sense.

¹⁵LINFLUX does not account for rotor transmission effects.

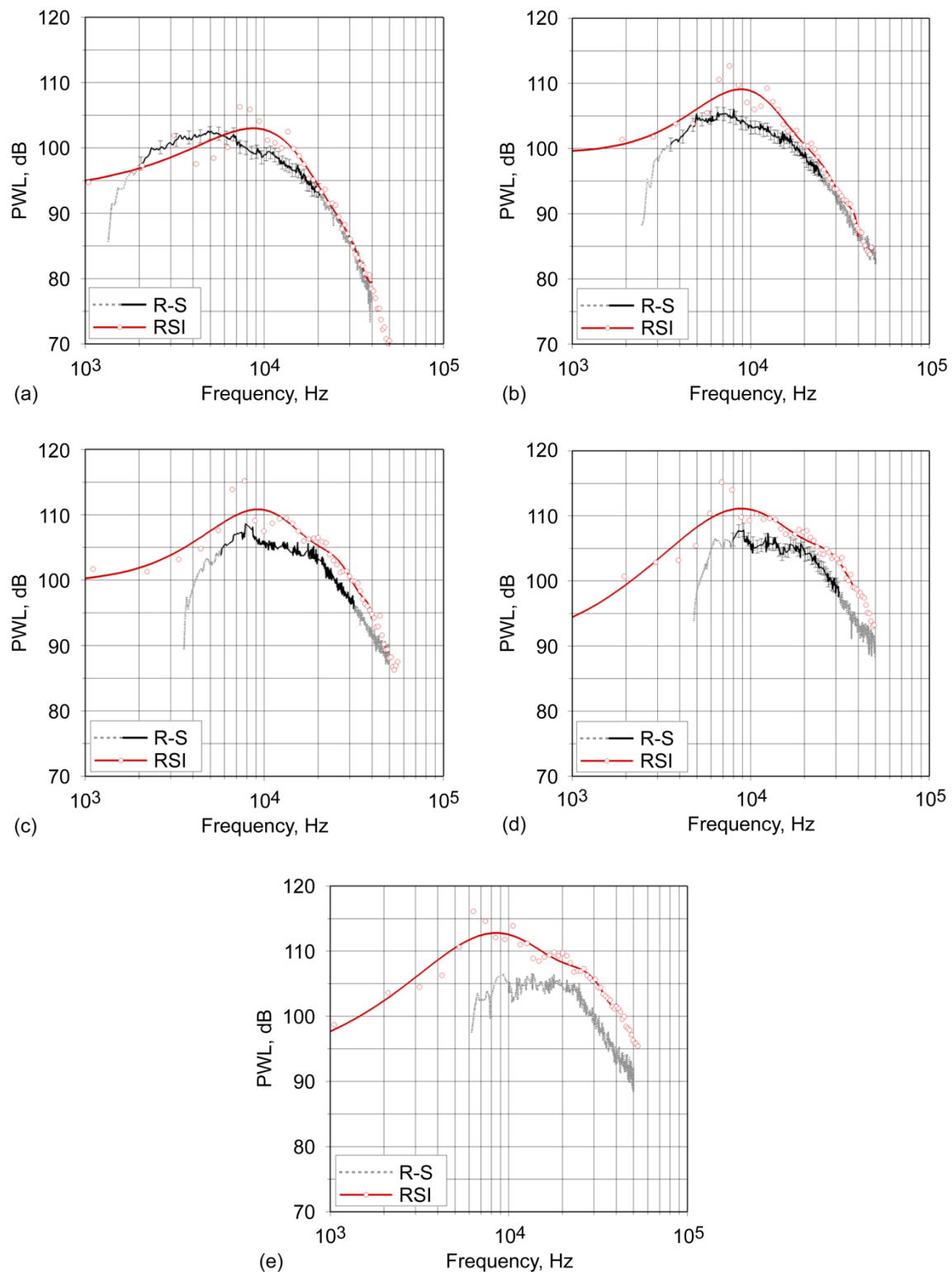


Figure 5.16.—Comparison of predicted (using RSI code) and estimated narrowband sound power levels (PWLs) for SDT fan at different speeds. Estimates are rotor-stator (R-S) interaction PWLs taken from Figure 5.15. Dashed line indicates data reliability is questioned (see Sec. 5.7.2). (a) 7809 rpm. (b) 9493 rpm. (c) 11 075 rpm. (d) 11 771 rpm. (e) 12 657 rpm.

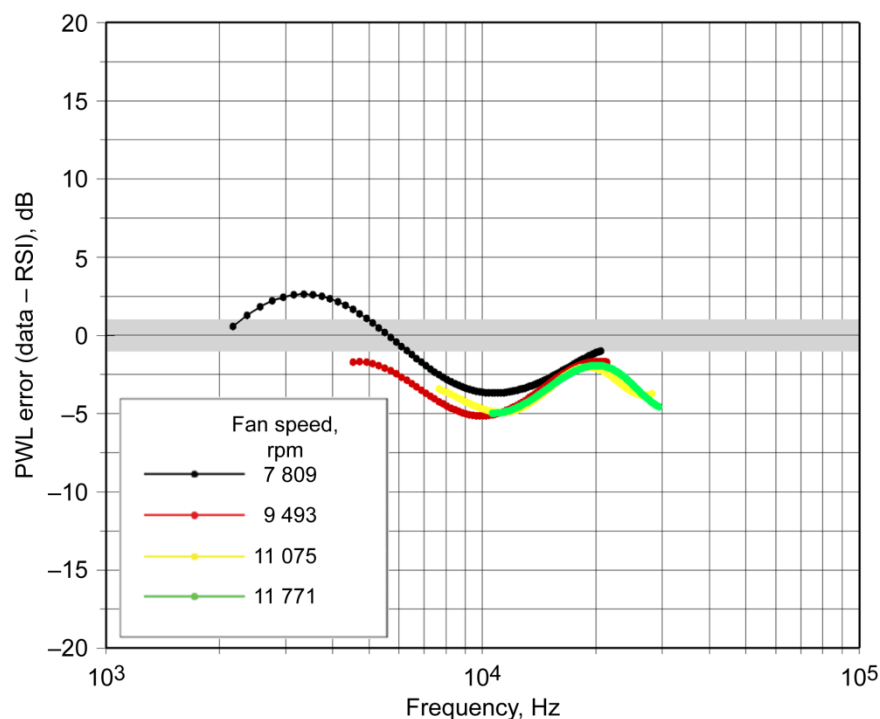


Figure 5.17.—Error in predicted (using RSI code) narrowband sound power levels (PWLs) for SDT fan at different speeds (Figure 5.16). Gray bar represents experimental uncertainty.

the data-theory comparisons shown here are on the acoustic power level basis, which is thought to be conserved, at least for the nonswirling flow downstream of the stator.

Both the mean and perturbation flows are discretized on a regular H-mesh topology, which needs to be dense enough to resolve the perturbations of interest. Therefore, the size of the grid depends on the frequency content under consideration. In this study, the goal was to resolve rigorously the second harmonic of the blade-passing frequency (i.e., $2 \times \text{BPF}$) tone.¹⁶ The documentation for the LINFLUX code calls for a minimum of 40 grid points per acoustic wavelength to adequately resolve the perturbations. Each grid extends axially one vane chord upstream and one vane chord downstream to allow the mean flow to become axisymmetric at the inflow and outflow planes. In the radial direction nearly the same number of grid points were used in all cases because the vane span (measured vertically) is nearly the same for all three stators. In the tangential direction, the grid spans one blade passage because LINFLUX uses the known interblade phase angle as a means of relating the boundary conditions on one side of the passage to those on the other side. The grid sizes used for the three fans in this study are listed in Table 5.9. The larger axial grid size for QHSF 2 is a consequence of the swept geometry of the stator for this fan, which necessitates a larger axial domain if the one vane chord upstream and downstream “rule” were to be enforced. Finally, the

differences in the tangential direction are due to differences in the vane counts. In the interest of reducing the number of grids that had to be generated and the mean flow fields that had to be computed for each fan, the grid corresponding to the highest fan tip speed (and hence highest frequency) was chosen as the common grid for all speeds for that fan.

TABLE 5.9.—TURBO AND LINFLUX GRID SIZES

Fan ^a	Axial	Radial	Tangential
ADP	181	49	43
SDT	181	51	37
QHSF 2	211	51	39

^aADP is the NASA-Pratt & Whitney Advanced Ducted Propulsor Fan 1; SDT, the NASA-General Electric Source Diagnostic Test fan; and QHSF 2, the NASA-Honeywell Quiet High-Speed Fan 2.

In all cases, the TURBO and LINFLUX calculations were run to convergence (i.e., at least 4 orders of magnitude reduction in the maximum residual). This involved running the TURBO simulations at least 40 000 iterations and the LINFLUX calculations a minimum of 5000 iterations unless the solution converged sooner. The characteristics of the converged mean flowfields were closely examined in each case to ensure that the flow was well behaved especially near the blade surface. This turned out to be possible only for the ADP and SDT fans, but not the QHSF 2 fan. For the latter fan, the flow develops a small recirculation zone near the leading edge on the pressure side and/or near the trailing edge on the suction side of the vane. An

¹⁶Blade-passing frequency tone is cut off for all three fans, given their blade/vane ratios.

examination of the TSWIFT simulation results indicates that the same phenomena are present in the viscous solutions and, hence, they are not artifacts of the inviscid calculations. When such recirculation zones are present in the mean flow, the perturbation calculations do not behave well and sometimes do not even converge. As a result, the QHSF 2 results are not included in this chapter, but might be included in a separate report if they can be converged through reasonable changes in the inflow conditions.

The results of the data-theory comparisons for the 2×BPF tones of the ADP and SDT fans are shown in Figure 5.18 and Figure 5.19. The comparisons shown here are only for the downstream-radiated noise (i.e., the exhaust noise), since the three-dimensional rotor acoustic transmission loss through the fan rotor cannot be accounted for using the LINFLUX code at the present time. Figure 5.18 shows the variations in the level of the acoustic power at the 2×BPF as a function of the tip speed for the ADP fan, and Figure 5.19 shows the results for the SDT fan. Acoustic power levels based on SPL measurements from both the Rotating Rake system (designated RR data) and the 9×15 wind tunnel sideline microphone system (designated SL data) are shown in both figures. As indicated

in Table 5.4 and Table 5.7, the uncertainty margin in measuring the sideline acoustic data is ± 1 dB, and for the Rotating Rake system it is ± 4.3 dB. Both sets of uncertainties are indicated in the figures also.

Note that, in general, there are noticeable differences between the acoustic power levels obtained via the Rotating Rake and sideline microphone systems. This is in part due to the fact that while the Rotating Rake system can measure a specific circumferential mode at a given frequency (i.e., the rotor-stator Tyler-Sofrin interaction mode with a circumferential mode number of -9 at 2×BPF for ADP), the sideline measurements include—in addition to the Tyler-Sofrin mode—extraneous modes generated at 2×BPF. The extraneous modes, which are always produced in a fan rig, are a result of manufacturing and installation imperfections that prevent precise phasing amongst corresponding wakes from various fan blades and amongst unsteady pressure responses from various vanes. The end result is imperfect cancellations and reinforcements giving rise to circumferential modes that do not obey the Tyler-Sofrin rule based on the blade and vane counts (see Ref. 50). Fortunately, in most cases the extraneous modes are much less energetic than the Tyler-Sofrin mode(s), and in aggregate, they contribute only

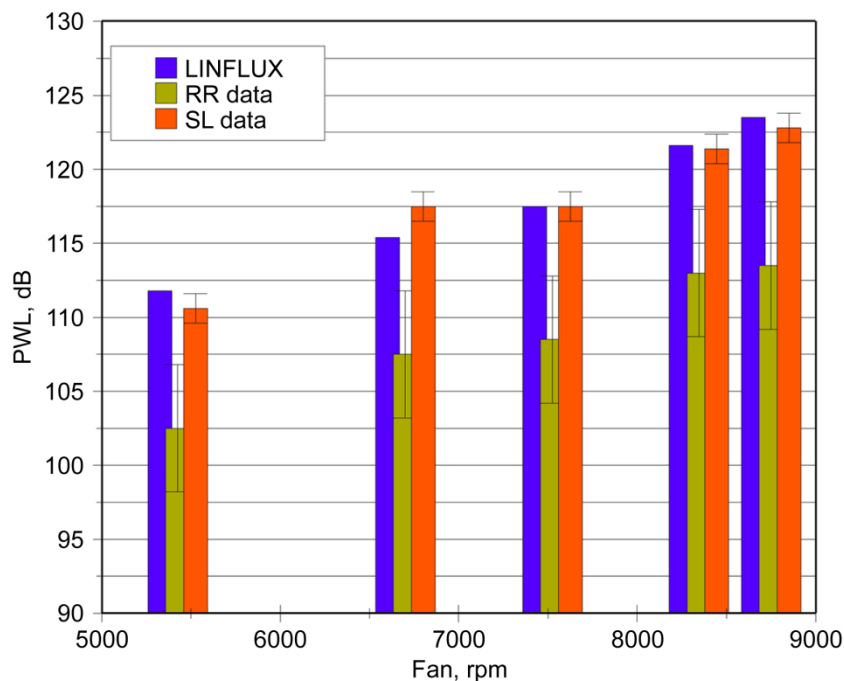


Figure 5.18.—Comparison of measured and predicted sound power levels (PWLs) for exhaust 2×BPF tone (second harmonic of blade-passing frequency) for ADP fan at different tip speeds. Data from Rotating Rake (RR) and sideline microphone (SL). Predictions calculated using LINFLUX code. Results are for circumferential mode -9 .

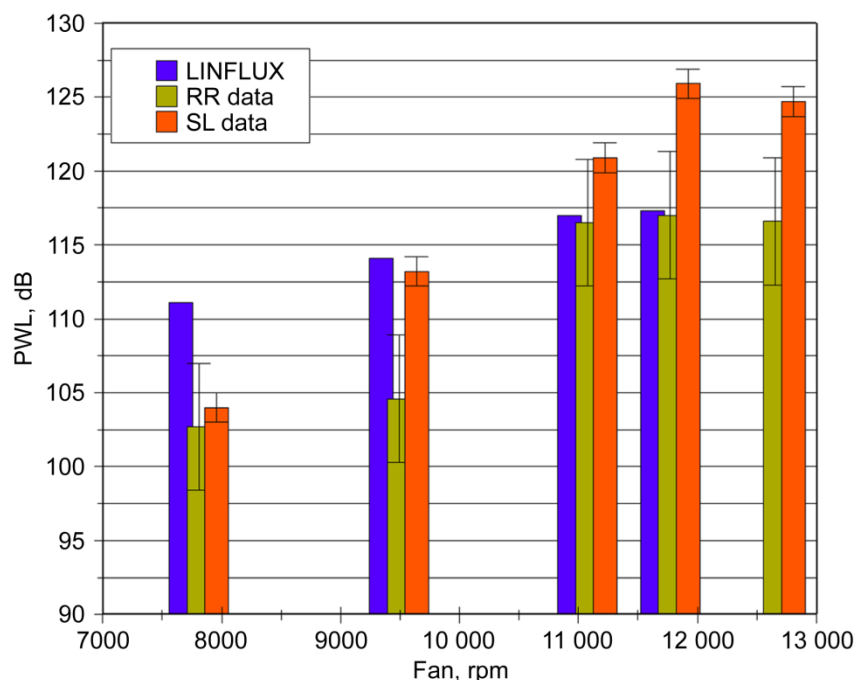


Figure 5.19.—Comparison of measured and predicted sound power levels (PWLs) for exhaust 2×BPF tone (second harmonic of blade-passing frequency) for SDT fan at different tip speeds. Data from Rotating Rake (RR) and sideline microphone (SL). Predictions calculated using LINFLUX code. Results are for circumferential mode −10.

a modest extra amount of acoustic power beyond that contained in the Tyler-Sofrin mode(s). For example, for SDT fan, where detailed Rotating Rake mode data are available, it turns out that the extraneous modes typically contribute less than 2 dB to the total acoustic power at 2×BPF. Therefore, the sizable discrepancies between the PWLs for the Rotating Rake and sideline data cannot be entirely explained by the presence of the extraneous modes. This makes a conclusive determination of the LINFLUX prediction accuracy problematic since the measured data are somewhat suspect. However, given the relatively large uncertainties in the Rotating Rake data compared with the sideline data, it is likely that the sideline data is a better measure of the acoustic power at the target frequencies. Nonetheless, in the interest of completeness, data-theory comparisons for both measurements systems are included here.

Returning to Figure 5.18 and Figure 5.19, it is typically the case that there is good agreement between the predictions from LINFLUX and the sideline data for the ADP fan for all tip speed conditions. The agreement for the SDT fan is not as good and generally comparable to that using the Rotating Rake data. In contrast, the data-theory agreement for the Rotating Rake data is quite poor for both fans. The results of the prediction error analysis are presented in Figure 5.20 for the data based on the Rotating Rake measurement system, and

in Figure 5.21 for the data based on the sideline measurement system. In both figures, the gray bar signifies the experimental uncertainty. In the case of the Rotating Rake data (Figure 5.20) for the majority of the cases, the prediction error lies well outside of the uncertainty band (by as much as 5.7 dB for the ADP fan at takeoff condition). In contrast, the margin of error is much smaller and mostly within the uncertainty band for the ADP fan when the predictions are compared with the sideline data. The error for the SDT fan is large even when compared with the sideline data (by as much as 7.6 dB for the 11 771-rpm tip speed condition). Therefore, taking the sideline data as the benchmark, there is excellent agreement between data and theory for the ADP fan mostly within the uncertainty band, but a rather poor agreement for the SDT fan with errors as large as 7.6 dB outside of the sideline measurements uncertainty band.

Finally, additional studies were carried out to investigate the dependence of the LINFLUX predictions on the grid size. The results of these studies indicate that the solutions presented here are grid independent such that halving the grid size for the ADP fan (i.e., using a 181×25×43 grid) changed the predictions by less than 1 dB. It should be noted that this conclusion is based on running both TURBO and LINFLUX on the coarser mesh for all five ADP fan speeds.

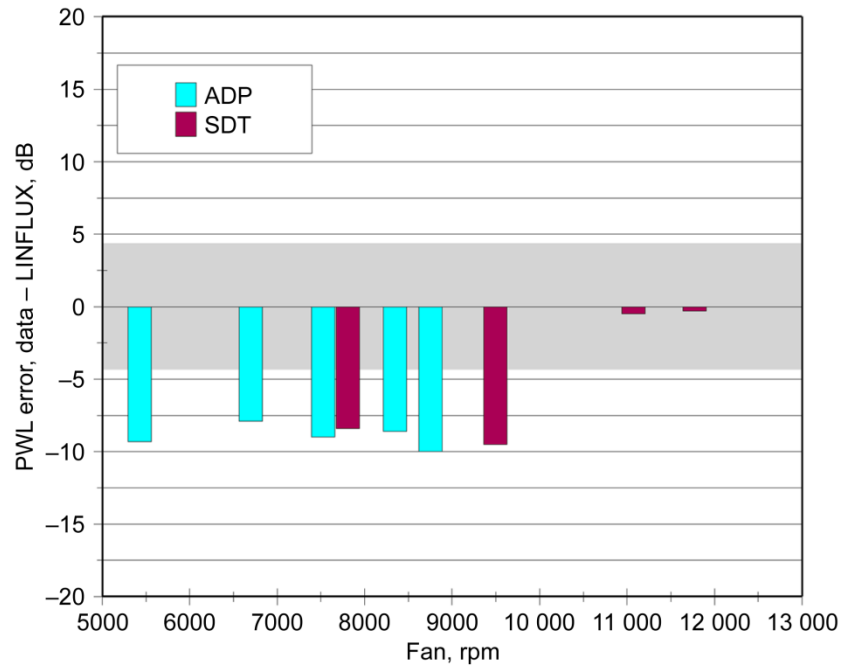


Figure 5.20.—Error in prediction of sound power level (PWL) for 2x BPF tone (second harmonic of blade-passing frequency) using data from Rotating Rake. Data for ADP fan is from Figure 5.18 (circumferential mode -9). Data for SDT fan is from Figure 5.19 (circumferential mode -10). Error is defined as (measured level) - (predicted level). Predictions calculated using LINFLUX code. Gray bar represents experimental uncertainty.

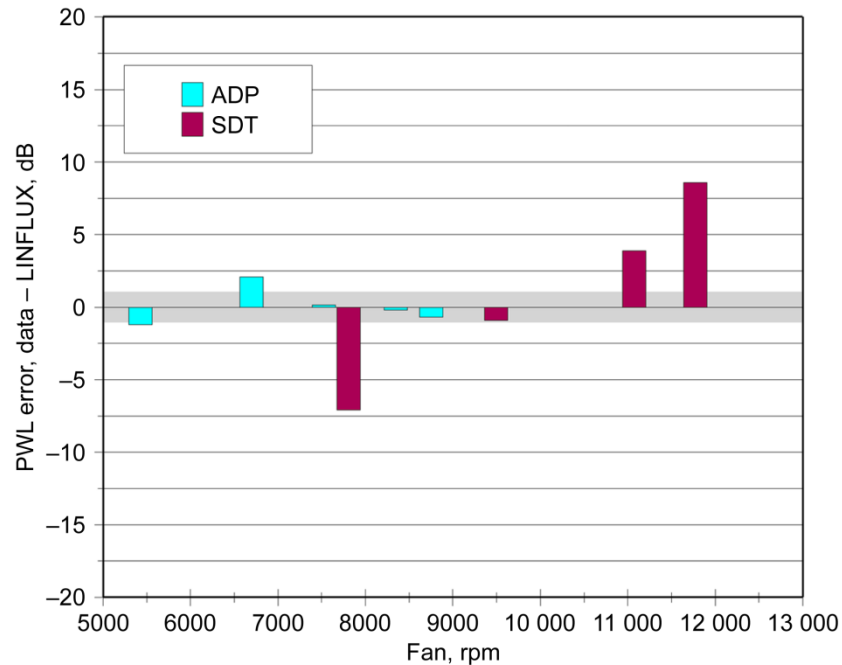


Figure 5.21.—Error in prediction of sound power level (PWL) for 2x BPF tone (second harmonic of blade-passing frequency) using data from sideline microphone. Data for ADP fan is from Figure 5.18 (circumferential mode -9). Data for SDT fan is from Figure 5.19 (circumferential mode -10). Error is defined as (measured level) - (predicted level). Predictions calculated using LINFLUX code. Gray bar represents experimental uncertainty.

5.8 Conclusions

NASA fan prediction codes in the empirical, acoustic-analogy-based, and computational categories were exercised and assessed against a set of benchmark fan acoustic data. The codes included ANOPP (an empirical code), RSI (an acoustic-analogy-based code), and LINFLUX (a computational aeroacoustics code). The benchmark fans cover a wide range of fan bypass ratios, pressure ratios, and tip speeds. The assessment results indicate that the ANOPP code can predict the fan noise spectrum to within 4 dB of the measurement uncertainty band on a 1/3-octave basis for the ultra-high- and high-bypass-ratio fans. The RSI code can predict rotor-stator interaction broadband noise spectrum to within 4 dB of experimental uncertainty band for the high-bypass ratio fan. The LINFLUX code can predict interaction tone power levels to within experimental uncertainties at low and moderate fan tip speeds, but could deviate by as much as 7.6 dB outside the experimental uncertainty band at the highest tip speeds in some cases.

The results of this assessment report will guide the course of the future developments in the area of fan noise modeling and prediction at NASA. In the short term, the goal is to continue to improve the RSI code while also adopting and/or developing a rotor-only noise prediction capability that can be

combined with RSI to provide an improved fan broadband noise prediction tool set. In parallel, work is underway to develop a rotor acoustic transmission capability that can be used in conjunction with both the RSI and LINFLUX codes to improve inlet noise prediction. In the meantime, the ongoing work in developing a numerically based approach to predicting rotor-stator interaction broadband noise has been completed, and initial code validation exercises are underway. It is hoped that, when it is ready, this code (currently called BASS) together with LINFLUX will represent the state of the art in fan noise prediction for subsonic-tip-speed fans. In the long term, the aim is to revisit supersonic rotor noise and improve the Superpose code to tackle MPT noise. As for ANOPP, NASA continues to maintain and improve it, but plans are in place to eventually supplant this code with a multifidelity capability that accounts for source distribution and source noncompactness as well as installation, reflection, refraction, and scattering effects.

5.9 Acknowledgments

Edmane Envia thanks Dr. Christopher J. Miller for his invaluable suggestions for improving the quality of the mean flow solutions used in the LINFLUX assessment studies.

Appendix A.—Nomenclature

A.1 Acronyms

ADP	Advanced Ducted Propulsor
ANOPP	Aircraft Noise Prediction Program
ASME	American Society of Mechanical Engineers
BPF	blade-passing frequency
CAA	computational aeroacoustics
GE	General Electric
LSWT	Low-Speed Wind Tunnel

MPT	multiple pure tones
PWL	power level
QHSF 2	Quiet High Speed Fan 2
RANS	Reynolds-averaged Navier–Stokes
rms	root-mean-squared
SDT	Source Diagnostic Test
SPL	sound pressure level
UHB	ultrahigh bypass

Appendix B.—Additional Data-Theory Comparisons for ANOPP

In this appendix, Figure 5.22 to Figure 5.30 present additional comparisons between experimental and theoretical (using the Aircraft Noise Prediction Program (ANOPP) code) sound pressure level (SPL) data for the NASA-Pratt & Whitney Advanced Ducted Propulsor (ADP) Fan 1, the

NASA-General Electric Source Diagnostic Test (SDT) fan, and NASA-Honeywell Quiet High Speed Fan 2 (QHSF 2) model fans at typical inlet and exhaust emission angles of 46° and 136° , respectively.

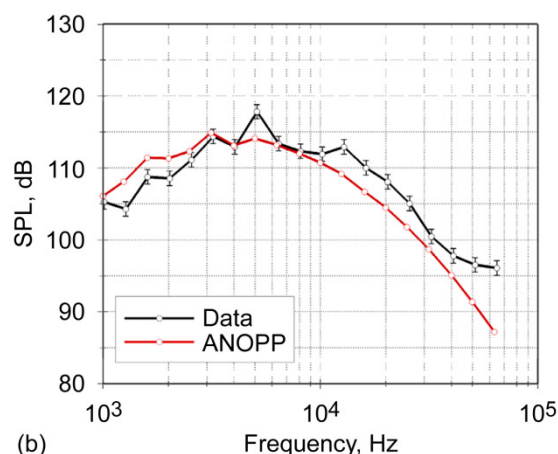
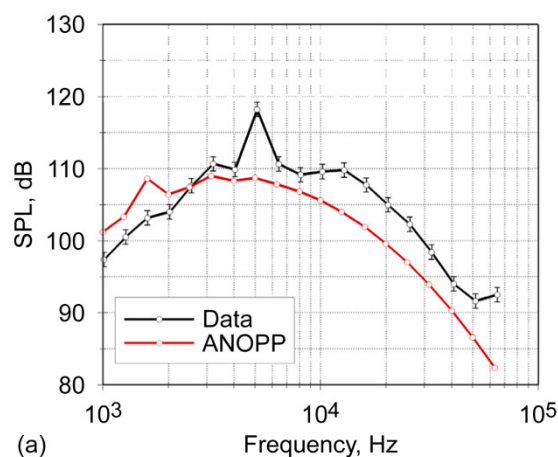


Figure 5.22.—Comparison of 1/3-octave measured sound pressure level (SPL) and SPL predicted from ANOPP code for ADP fan in inlet and exhaust quadrants at 5425 rpm at Mach 0.1. (a) Inlet quadrant; emission angle 46° . (b) Exhaust quadrant; emission angle 136° .

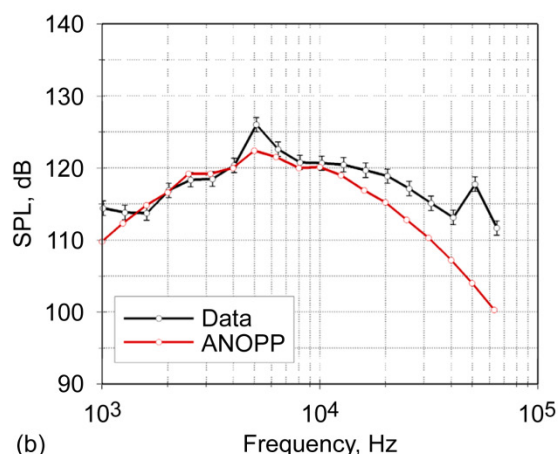
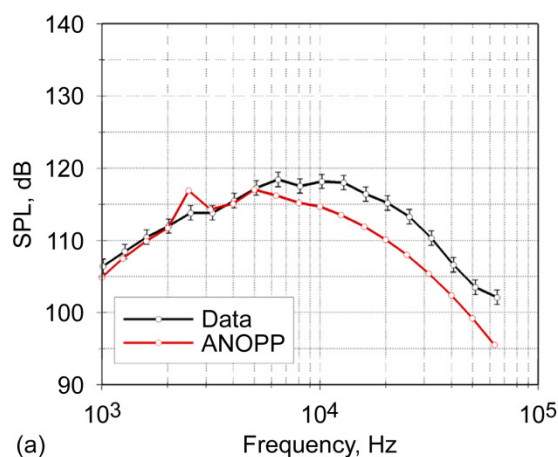


Figure 5.23.—Comparison of 1/3-octave measured sound pressure level (SPL) and SPL predicted from ANOPP code for ADP fan in inlet and exhaust quadrants at 7525 rpm at Mach 0.1. (a) Inlet quadrant; emission angle 46° . (b) Exhaust quadrant; emission angle 136° .

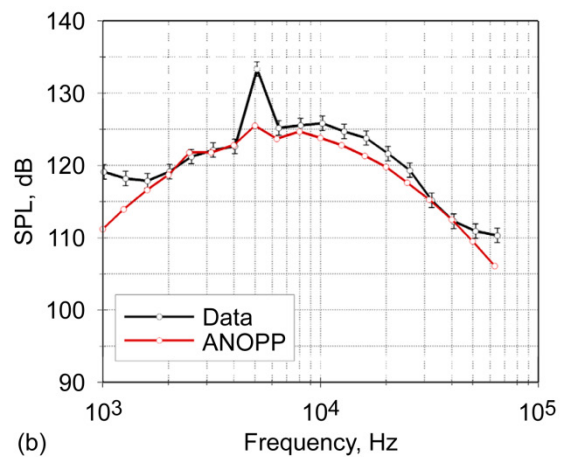
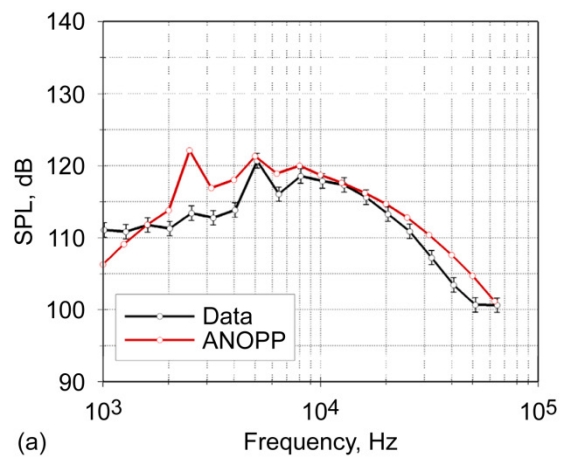


Figure 5.24.—Comparison of 1/3-octave measured sound pressure level (SPL) and SPL predicted from ANOPP code for ADP fan in inlet and exhaust quadrants at 8750 rpm at Mach 0.1. (a) Inlet quadrant; emission angle 46°. (b) Exhaust quadrant; emission angle 136°.

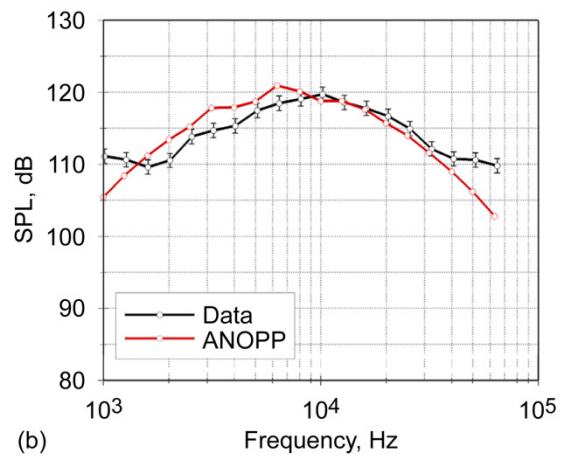
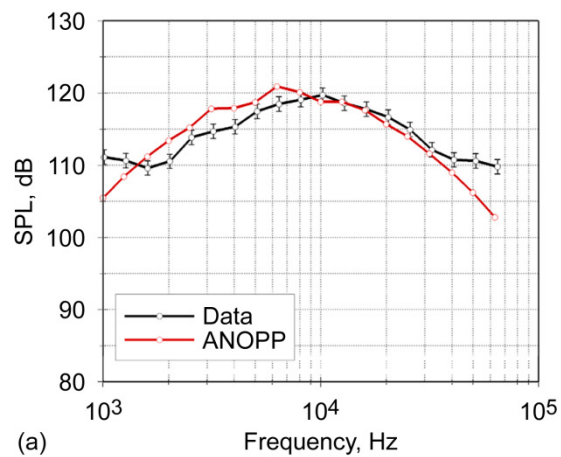


Figure 5.25.—Comparison of 1/3-octave measured sound pressure level (SPL) and SPL predicted from ANOPP code for SDT fan in inlet and exhaust quadrants at 7809 rpm at Mach 0.1. (a) Inlet quadrant; emission angle 46°. (b) Exhaust quadrant; emission angle 136°.

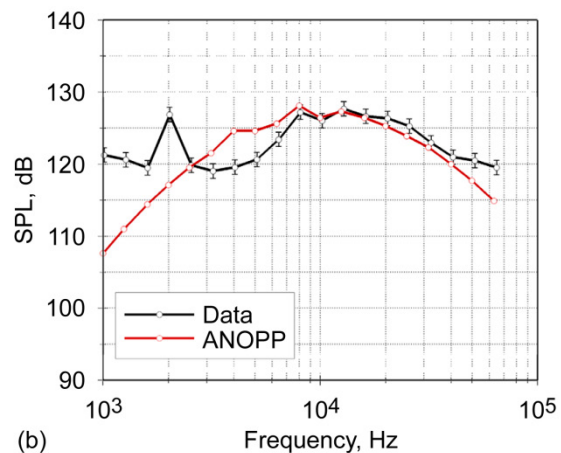
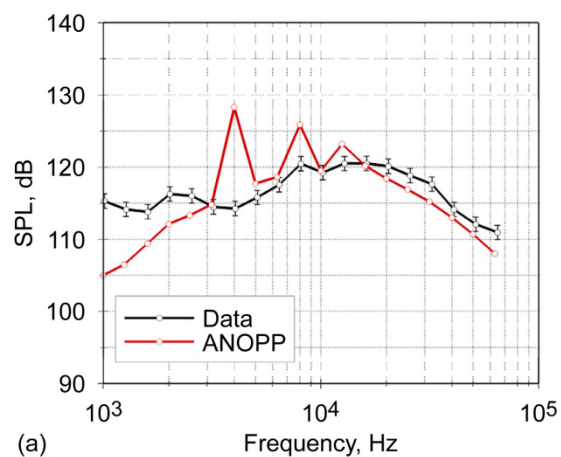


Figure 5.26.—Comparison of 1/3-octave measured sound pressure level (SPL) and SPL predicted from ANOPP code for SDT fan in inlet and exhaust quadrants at 11 075 rpm at Mach 0.1. (a) Inlet quadrant; emission angle 46°. (b) Exhaust quadrant; emission angle 136°.

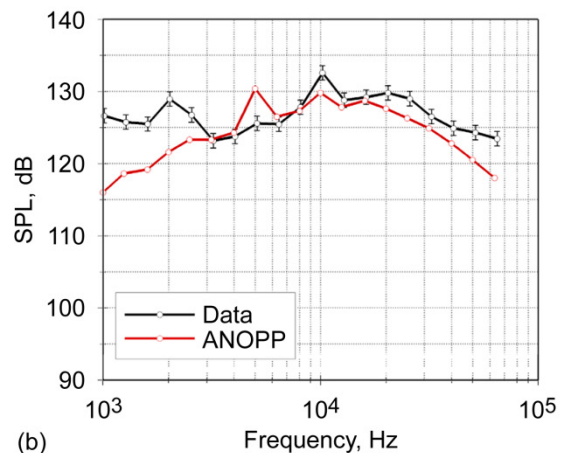
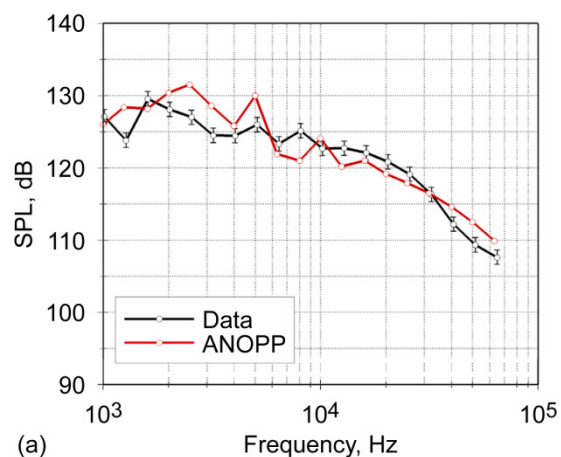
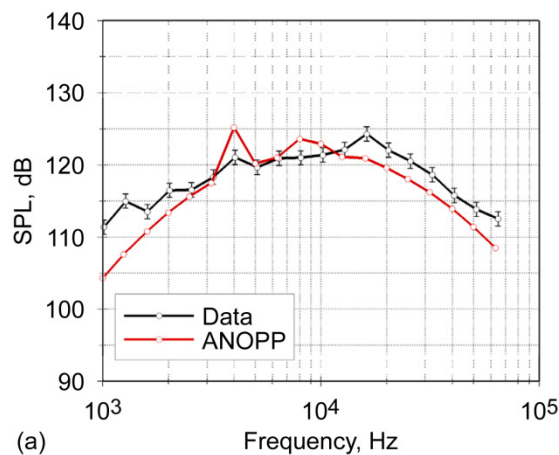
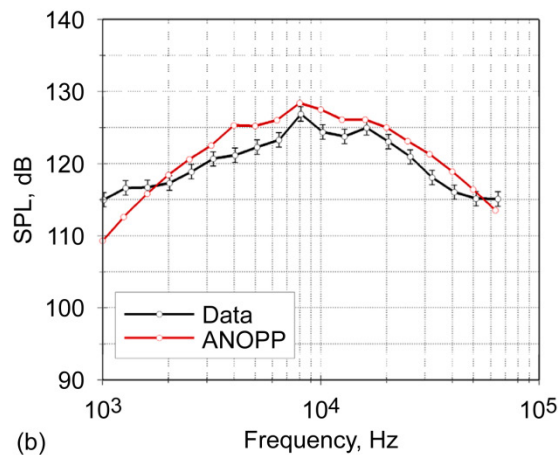


Figure 5.27.—Comparison of 1/3-octave measured sound pressure level (SPL) and SPL predicted from ANOPP code for SDT fan in inlet and exhaust quadrants at 12 657 rpm at Mach 0.1. (a) Inlet quadrant; emission angle 46°. (b) Exhaust quadrant; emission angle 136°.

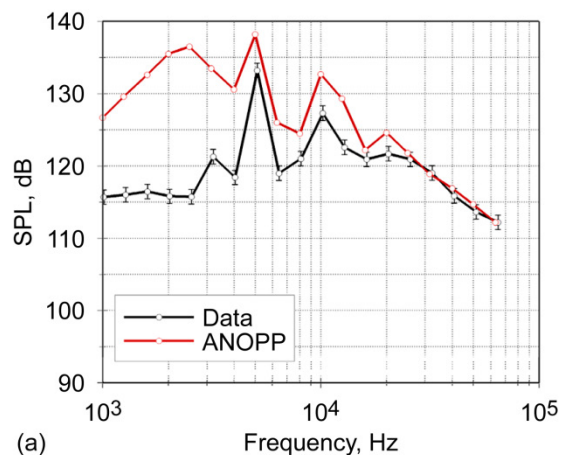


(a)

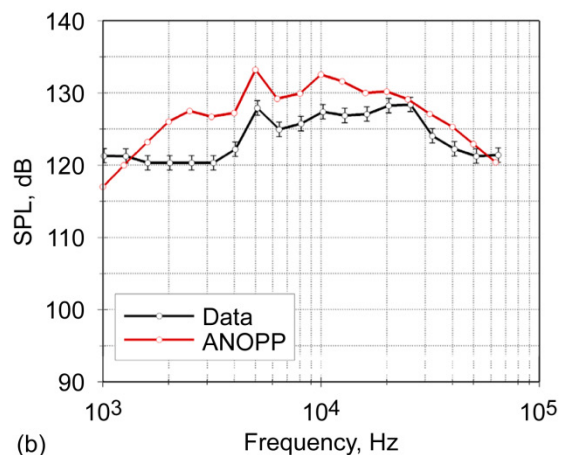


(b)

Figure 5.28.—Comparison of 1/3-octave measured sound pressure level (SPL) and SPL predicted from ANOPP code for QHSF 2 fan in inlet and exhaust quadrants at 9840 rpm at Mach 0.1. (a) Inlet quadrant; emission angle 46°. (b) Exhaust quadrant; emission angle 136°.



(a)



(b)

Figure 5.29.—Comparison of 1/3-octave measured sound pressure level (SPL) and SPL predicted from ANOPP code for QHSF 2 fan in inlet and exhaust quadrants at 12 500 rpm at Mach 0.1. (a) Inlet quadrant; emission angle 46°. (b) Exhaust quadrant; emission angle 136°.

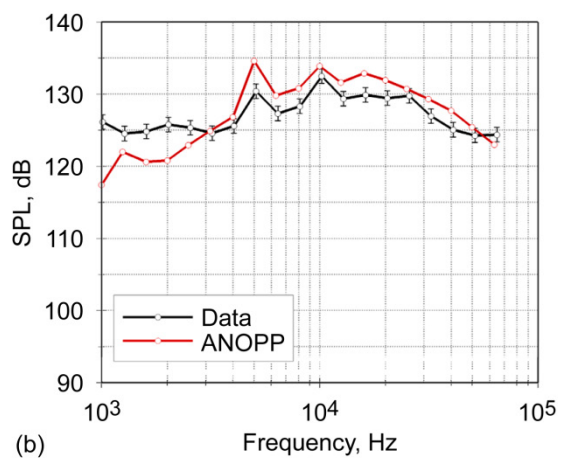
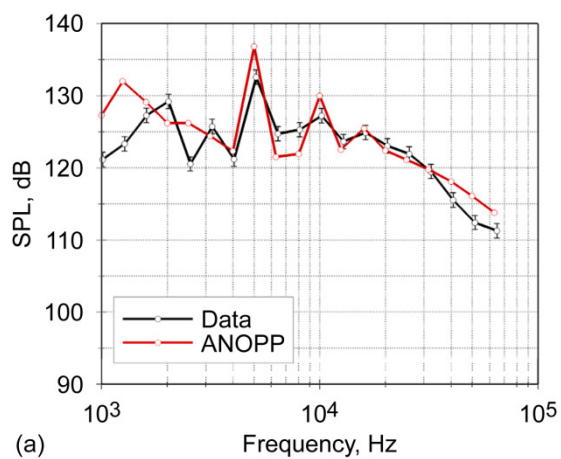


Figure 5.30.—Comparison of 1/3-octave measured sound pressure level (SPL) and SPL predicted from ANOPP code for QHSF 2 fan in inlet and exhaust quadrants at 14 060 rpm at Mach 0.1. (a) Inlet quadrant; emission angle 46°. (b) Exhaust quadrant; emission angle 136°.

Appendix C.—Additional Data-Theory Comparisons for RSI Code

In this appendix, Figure 5.31 to Figure 5.33 present additional comparisons between experimental and theoretical (using RSI code) narrowband sound power level (PWL) data for the NASA-Pratt & Whitney Advanced Ducted Propulsor

(ADP) Fan 1, the NASA-General Electric Source Diagnostic Test (SDT) fan, and NASA-Honeywell Quiet High Speed Fan 2 (QHSF 2) model fans at various blade tip speeds.

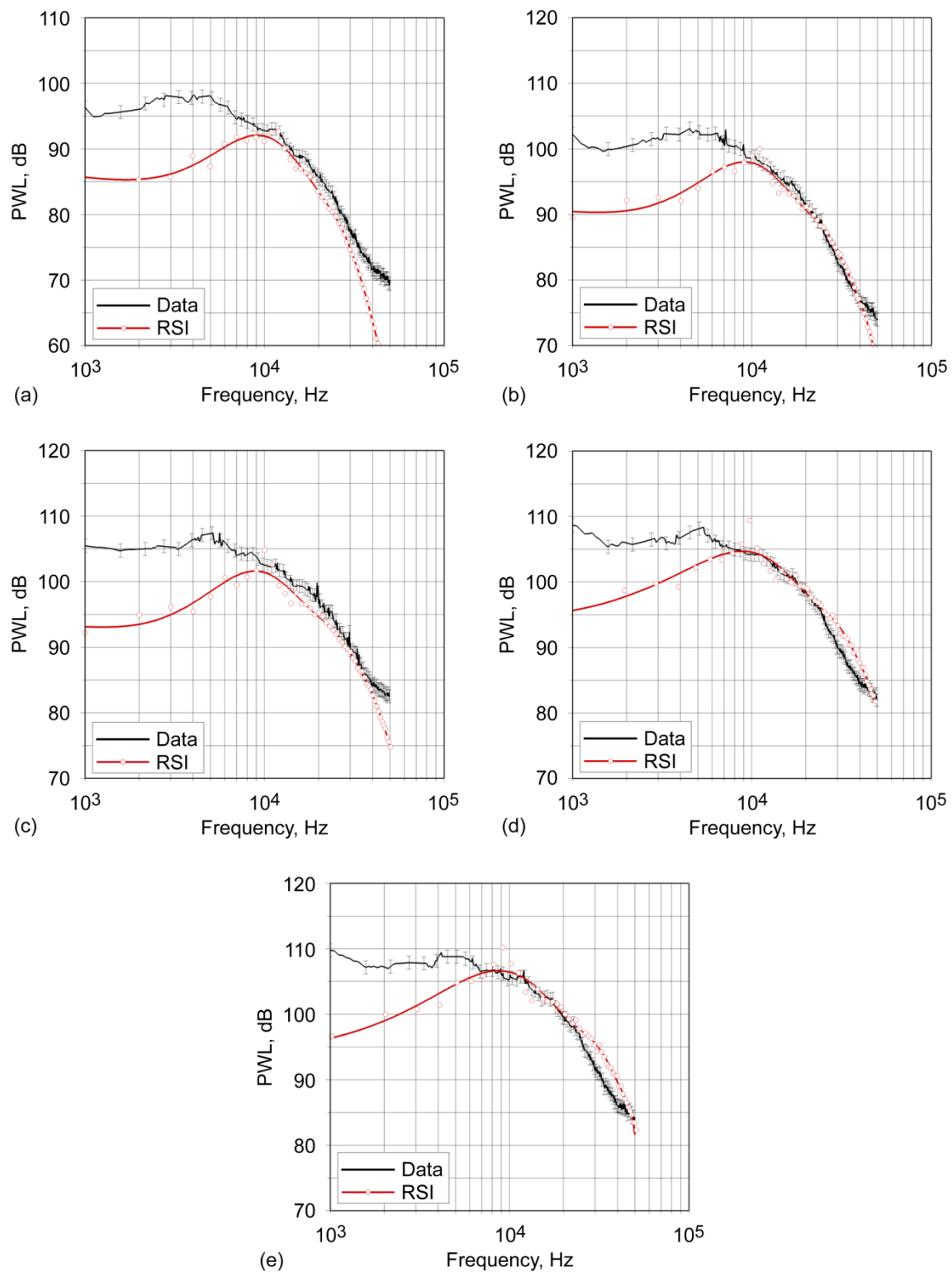


Figure 5.31.—Comparison of measured narrowband sound power level (PWL) and PWL predicted using RSI code for ADP fan at various blade tip speeds. Data represent combined rotor and stator contributions. (a) 5425 rpm. (b) 6700 rpm. (c) 7525 rpm. (d) 8345 rpm. (e) 8750 rpm.

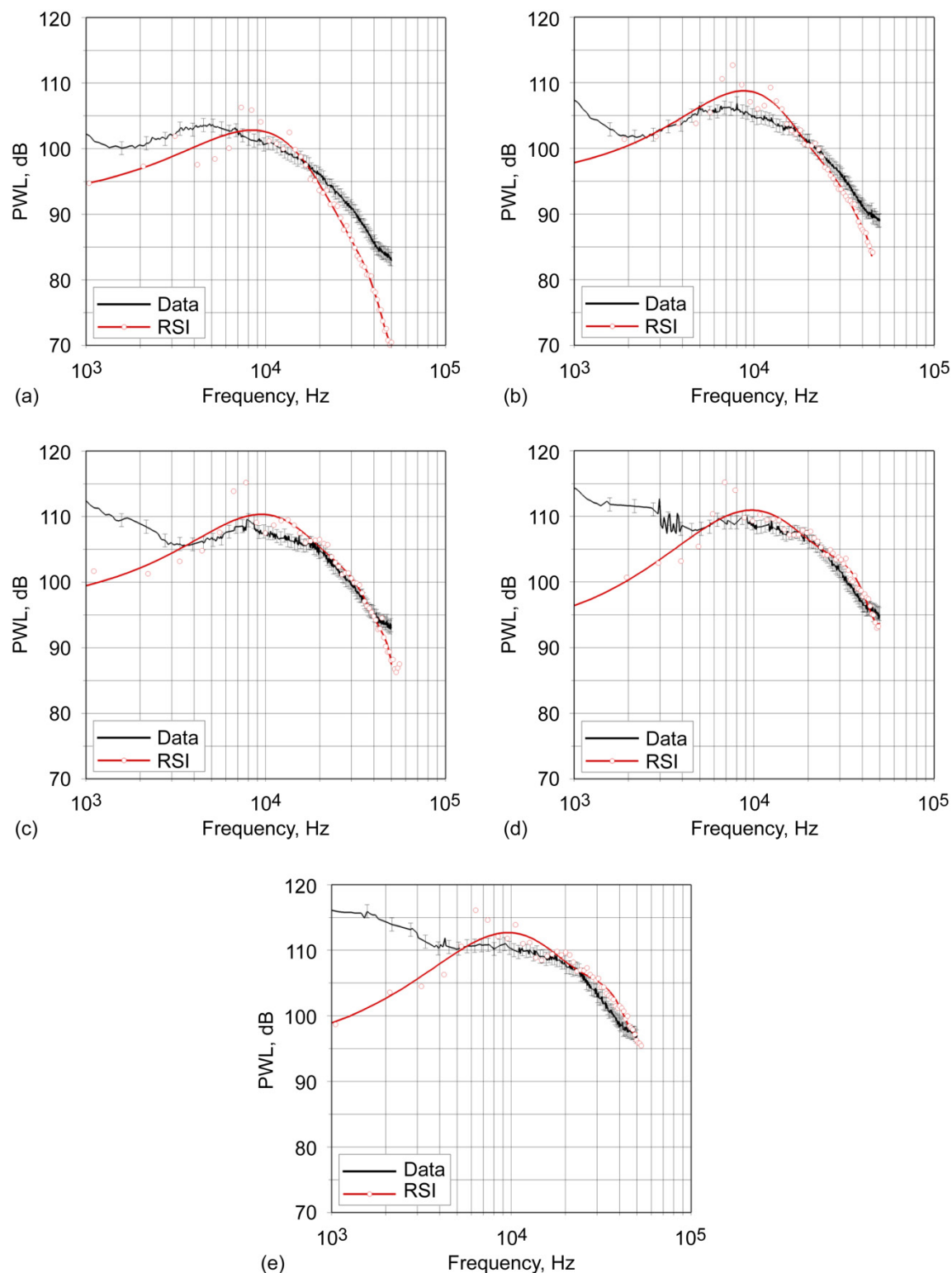


Figure 5.32.—Comparison of measured narrowband sound power level (PWL) and PWL predicted using RSI code for SDT fan at various blade tip speeds. Data represent combined rotor and stator contributions. (a) 7809 rpm. (b) 9493 rpm. (c) 11 075 rpm. (d) 11 771 rpm. (e) 12 675 rpm.

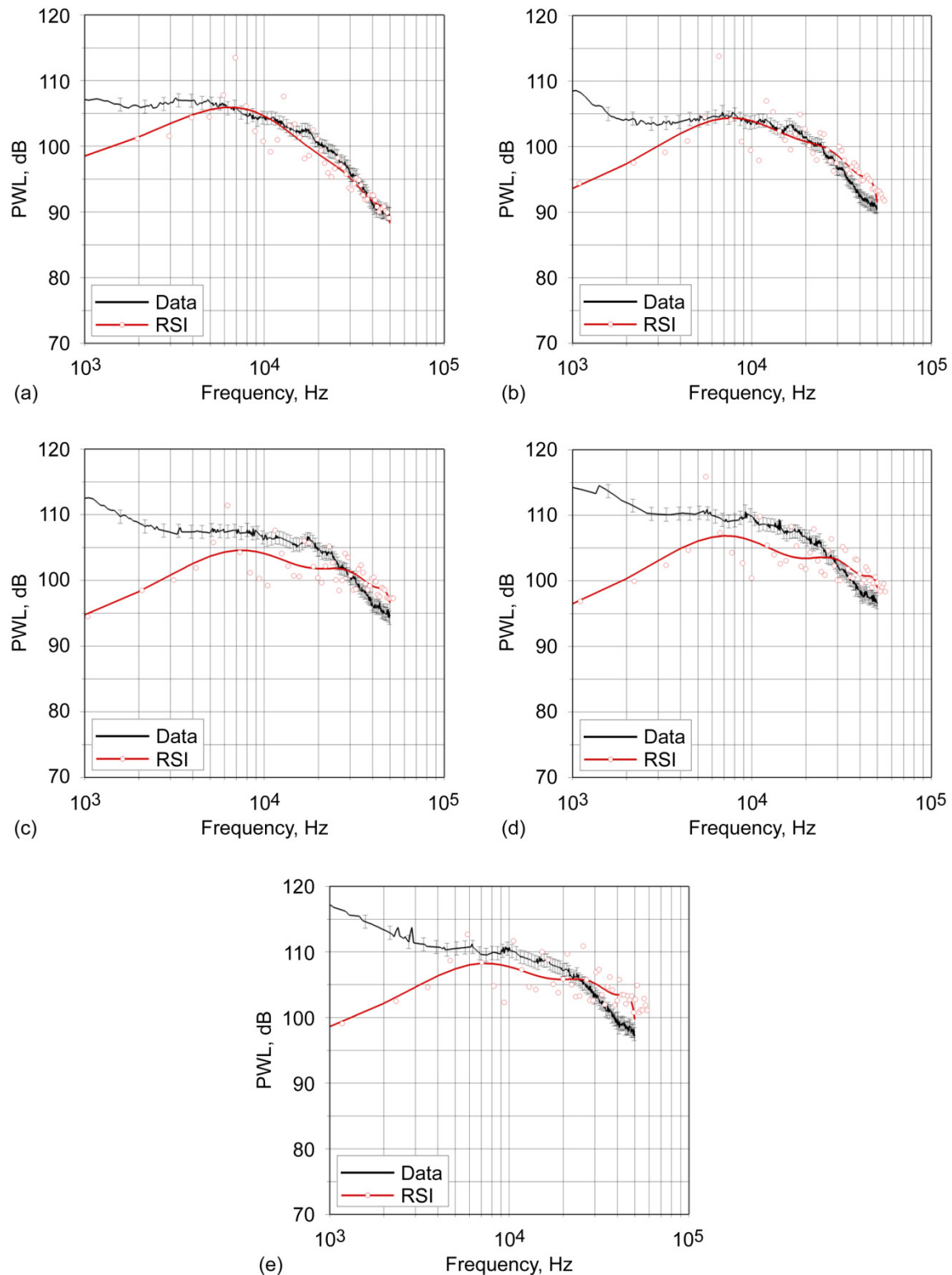


Figure 5.33.—Comparison of measured narrowband sound power level (PWL) and PWL predicted using RSI code for QHSF 2 fan at various blade tip speeds. Data represent combined rotor and stator contributions. (a) 9840 rpm. (b) 10 935 rpm. (c) 12 500 rpm. (d) 13 280 rpm. (e) 14 060 rpm.

References

1. Lighthill, Michael J.: On Sound Generated Aerodynamically. I. General Theory. *Proc. Royal Soc. London Series A*, vol. 211, 1952, pp. 564–587.
2. Topol, David A.; and Mathews, Douglas C.: Rotor Wake/Stator Interaction Noise Prediction Code. NASA Contract Report NAS3–25952, 1993.
3. Meyer, Harold D.; and Envia, Edmane: Aeroacoustic Analysis of Turbofan Noise Generation. NASA CR–4715, 1996.
4. Topol, David A.: TFaNS Tone Noise Design/Prediction System, Volume I: System Description, CUP3D Technical Documentation and Manual for Code Developers. NASA/CR—1999-208882, 1999.
5. Topol, David A.; and Eversman, Walter: TFaNS Tone Noise Design/Prediction System, Volume II: User's Manual, TFaNS Vers 1.4. NASA/CR—1999-208883, 1999.
6. Topol, David A.: TFaNS Tone Noise Design/Prediction System, Volume III: Evaluation of System Codes. NASA/CR—1999-208884, 1999.
7. Topol, David A.: TFaNS—Tone Noise Design/Prediction System, User's Manual, TFaNS Version 1.5. NASA/CR—2003-212380, 2003.
8. Nallasamy, M.; and Envia, E.: Computation of Rotor Wake Turbulence Noise. *J. Sound Vib.*, vol. 282, nos. 3–5, 2005, pp. 649–678.
9. Morin, Bruce L.: Broadband Fan Noise Prediction System for Turbofan Engines, Volume 1: Set_BFaNS User's Manual and Developer's Guide. NASA/CR—216898/VOL1, 2010.
10. Morin, Bruce L.: Broadband Fan Noise Prediction System for Turbofan Engines, Volume 2: BFaNS User's Manual and Developer's Guide. NASA/CR—216898/VOL2, 2010.
11. Morin, Bruce L.: Broadband Fan Noise Prediction System for Turbofan Engines, Volume 3: Validation and Test Cases. NASA/CR—216898/VOL3, 2010.
12. Gliebe, P.; Mani, R.; Shin, H.; Mitchell, B.; Ashford, G.; Salamah, S.; and Connell, S.: Aeroacoustics Prediction Codes (Section 5, Fan MPT Noise Model Development). NASA/CR—2000-210244, 2000.
13. Montgomery, Matthew D.; and Verdon, Joseph M.: A Three-Dimensional Linearized Unsteady Euler Analysis for Turbomachinery Blade Rows. NASA Contractor Report 4770, 1997.
14. Chuang, H.A.; and Verdon, J.M.: A Numerical Simulator for Three-Dimensional Flows Through Vibrating Blade Rows. NASA/CR—1998-208511, 1998.
15. Verdon, Joseph M.: Linearized Unsteady Aerodynamic Analysis of the Acoustic Response to Wake/Blade-Row Interaction. NASA/CR—2001-210713, 2001.
16. Hixon, R.; Nallasamy, M.; and Sawyer, S.: Parallelization Strategy for an Explicit Computational Aeroacoustics Code. AIAA–2002–2583, 2005.
17. Nallasamy, M.; Hixon, R.; Sawyer, S.; and Dyson, R.: A Time Domain Analysis of Gust-Cascade Interaction. AIAA–2003–3134, 2003.
18. Nallasamy, M.; Hixon, R.; and Sawyer, S.: Computed Linear/Nonlinear Acoustic Response of a Cascade for Single/Multi Frequency Excitations. AIAA–2004–2998, 2004.
19. Hixon, Ray; Sescu, Adrian; Sawyer, Scott: Validation of a CAA Code Using a Benchmark Wake-Stator Interaction Problem. AIAA–2009–3340, 2009.
20. Sescu, Adrian; Hixon, Ray; Nallasamy M.; and Sawyer, Scott: Prediction of Noise from Realistic Rotor-Wake/Stator-Row Interaction Using Computational Aeroacoustics. AIAA–2009–3339, 2009.
21. Jeracki, Robert J.: Comprehensive Report of Fan Performance From Duct Rake Instrumentation on 1.294 Pressure Ratio, 8.06 ft/sec Tip Speed Turbofan Simulator Models. NASA/TM—2006-213863, 2006.
22. Dittmar, James H.; Elliott, David M.; and Bock, Lawrence A.: Some Acoustic Results from the Pratt and Whitney Advanced Ducted Propulsor—Fan 1. NASA/TM—1999-209049, 1999.
23. Woodward, Richard P., et al.: Fan Noise Source Diagnostic Test—Far-Field Acoustic Results. AIAA–2002–2427, 2002.
24. Hughes, C. E.: Aerodynamic Performance of Scale-Model Turbofan Outlet Guide Vanes Designed for Low Noise. AIAA–2002–374, 2002.
25. Dittmar, James H.; Elliott, David M.; and Fite, E. Brian: The Noise of a Forward Swept Fan. NASA/TM—2003-212208, 2003.
26. Weir, Donald: Design and Test of Fan/Nacelle Models Quiet High-Speed Fan. NASA/CR—2003-212370, 2003.
27. Yuska, Joseph A.; Diedrich, James H.; and Clough, Nestor: Lewis 9- by 15-Foot V/STOL Wind Tunnel. NASA TM X–2305, 1971.
28. Arrington, E. Allen; and Gonzalez, Jose C.: Flow Quality Improvements in the NASA Lewis Research Center 9- by 15-Foot Low Speed Wind Tunnel; Final Report. NASA CR—195439, 1995. Available from the NASA Center for Aerospace Information.
29. Dahl, Milo D.; and Woodward, Richard P.: Comparison Between Design and Installed Acoustic Characteristics of NASA Lewis 9- by 15-Foot Low-Speed Wind Tunnel Acoustic Treatment. NASA TP–2996, 1990.
30. Dahl, Milo D.; and Woodward, Richard P.: Acoustical Evaluation of the NASA Lewis 9- by 15-Foot Low Speed Wind Tunnel. NASA TP–3274, 1992.
31. Woodward, Richard P., et al.: Background Noise Levels Measured in the NASA Lewis 9- by 15-Foot Low-Speed Wind Tunnel. NASA TM–106817 (AIAA–95–0720), 1995.
32. Chestnutt, David: Flight Effects of Fan Noise. NASA CP–2242, 1982.
33. Sutliff, Daniel L.: Turbofan Duct Mode Measurements Using a Continuously Rotating Microphone Rake. *Int. J. Aeroacoustics*, vol. 6, no. 2, 2007, pp. 147–170.
34. Sutliff, Daniel L.: Rotating Rake Mode Measurements Over Passive Treatment in a Ducted Fan. NASA/TM—2006-214493, 2006.
35. Dieck, Ronald H.: Measurement Uncertainty: Methods and Applications. Fourth ed., ISA, Research Triangle Park, NC, 2007.
36. Meyer, Stuart L.: Data Analysis for Scientists and Engineers. John Wiley & Sons, New York, NY, 1986.
37. Taylor, John R.: An Introduction to Error Analysis: The Study of Uncertainties in Physical Measurements. Second ed., University Science Books, Sausalito, CA, 1997.
38. ANSI S1.26–1995: Method for Calculation of the Absorption of Sound by the Atmosphere. Washington, DC, 1995. <http://webstore.ansi.org/RecordDetail.aspx?sku=ANSI%2fAS+A+S1.26-1995+%28R2009%29> Accessed May 5, 2010.
39. Dahl, Milo; and Sutliff, Daniel: Numerical Technique for Analyzing Rotating Rake Mode Measurements in a Duct With Passive Treatment and Shear Flow. AIAA–2007–3679, 2007.

40. Gillian, R.E.: Aircraft Noise Prediction Program User's Manual. NASA TM-84486, 1982.
41. Zorumski, W.E.: Aircraft Noise Prediction Program Theoretical Manual. NASA TM-83199-PT-1, 1982.
42. Wilson, Mark R.: An Introduction to High Speed Aircraft Noise Prediction. NASA CR-189582, 1992.
43. Kontos, K.B.; Janardan, B.A.; and Gliebe, P.R.: Improved NASA-ANOPP Noise Prediction Computer Code for Advanced Subsonic Propulsion Systems. Volume 1: ANOPP Evaluation and Fan Noise Model Improvement. NASA CR-195480, 1996.
44. Kontos, Karen B.; Kraft, Robert E.; and Gliebe, Philip R.: Improved NASA-ANOPP Noise Prediction Computer Code for Advanced Subsonic Propulsion Systems. Volume 2: Fan Suppression Model Development. NASA CR-202309, 1996.
45. Heidmann, Marcus F.: Interim Prediction Method for Fan and Compressor Source Noise. NASA TM X-71763, 1979.
46. Brown, Clifford A.; and Schifer, Nicholas A.: Low Frequency Noise Contamination in Fan Model Testing. ASME GT2008-50850, 2008, pp. 849-862.
47. Chima, Rodrick V.: Swift—Multiblock Analysis Code for Turbomachinery. User's Manual and Documentation. Version 300, 2003. <http://www.grc.nasa.gov/WWW/5810/rvc/docs.htm> Accessed May 5, 2010.
48. Atassi, H.; and Hamad, G.: Sound Generated in a Cascade by Three-Dimensional Disturbances Convected in a Subsonic Flow. AIAA-1981-2046, 1981.
49. Hughes, Christopher, et al.: Fan Noise Source Diagnostic Test—Rotor Alone Aerodynamic Performance Results. AIAA-2002-2426, 2002.
50. Tyler, J.M.; and Sofrin, T.G.: Axial Flow Compressor Noise Studies. SAE Trans. v70, 1962, pp. 308-332.

Chapter 6—Uncertainty in Acoustic Liner Impedance Measurement and Prediction

Tony L. Parrott and Michael G. Jones
National Aeronautics and Space Administration
Langley Research Center
Hampton, Virginia 23681–2199

Summary

For nearly five decades, passive acoustic liners have been the mainstay for attenuation of tone-dominated fan noise propagated through aircraft engine nacelles, both in the inlet and the aft-fan duct. For the most part, these liners consist of one- to three-layer perforate-over-honeycomb structures. Besides the desire to attain a target attenuation spectrum, several environmental and structural considerations drive liner design. Early in the history of liner development, the convergence of these considerations led to the resistive-facesheet resonator as the key functional element. From the acoustician's viewpoint, such structures are locally reacting; that is, lateral wave propagation in the liner is prohibited. This means that the normal incidence acoustic impedance becomes the key design parameter governing sound attenuation in the duct airway. As such, an impedance boundary condition on the acoustic wave propagation process allows the nuances of the duct propagation problem to be isolated. This is especially relevant to understanding how uncertainties in the propagation process interact with uncertainties in the duct boundary conditions (i.e., liner impedance).

This chapter focuses on prediction and measurement uncertainties of the local-reacting impedance boundary condition, as employed in duct propagation models to predict acoustic attenuation spectra for nacelle liners. Given an attenuation spectrum target, the liner designer is tasked with providing a realizable, optimal liner design. Over the past five decades, numerous semi-empirical impedance prediction models have been proposed by academia and aircraft industry researchers. During this time, NASA Langley Research Center has focused mainly on the development of impedance measurement technology. This separation between measurement technology and modeling has placed Langley's measurement capability in the role of validating prediction models generated by its industry and academia partners. Clearly, such validations need to be supported by accompanying statements concerning error bounds or limits. The basis for the current assessment consists of 95% confidence interval estimates of impedance measurements for a representative single-layer perforate-over-honeycomb core (POHC) test liner.

There are a wide variety of acoustic liners available today; thus it is not possible to make general statements about sources of error in their performance or the quantification thereof. Instead, this study addresses a conventional, single-layer POHC-type liner. A POHC liner typifies the issues that arise when attempting to apply uncertainty analysis to liner design and fabrication as it relates to quality control on the end product; that is, installed liner impedance. To accomplish this, statistical process control (SPC) concepts are used where confidence intervals for predicted and measured impedances for this POHC test liner represent the variability in the liner development process (i.e., the “voice of the process”) that is being monitored using SPC. It is argued that with sufficient validation, prediction models can serve to quantify uncertainty metrics of liner fabrication processes for compliance with the “voice of the customer”; that is, the end-user-imposed confidence interval that contains the target design impedance.

In general, confidence intervals for the measurements and model predictions do not center on the same mean values, which is indicative of systematic error (in either or both the measurement process and prediction model). Also, the prediction model confidence intervals for the resistance component vary greatly and do not always encompass those for the measurements. Although systematic error is present for the reactance component, it is contained within the model confidence intervals. As expected, confidence intervals grow monotonically with frequency for all models.

There is a strong connection between this chapter and Chapter 7, “Assessment of Acoustic Propagation and Radiation Codes for Locally Reacting Liners in Flow Ducts,” which focuses on the prediction and measurement of sound propagation through engine nacelles. It is noteworthy that, over some bandwidths, small uncertainty in the impedance boundary condition may correlate with large uncertainty in the predicted attenuation. Conversely, in other bandwidths, a small uncertainty in the predicted attenuation may correlate with relatively large uncertainty in the liner impedance. Clearly, the relationship between confidence intervals on the impedance and the predicted attenuation is not uniform with frequency and is likely to be highly dependent on the duct configuration and/or source.

One of the main achievements of this assessment is to propose the applicability of the SPC paradigm to deliver an installed liner impedance spectrum to within accompanying customer-specified uncertainty limits. This assessment also highlights current capabilities and limitations of impedance measurement processes and prediction models. Finally, it provides guidance toward future model development and measurement process enhancements needed to improve the state of the art in acoustic liner design and measurement.

6.1 Introduction

Beginning in the 1960s, attention became focused on tone-dominated engine noise radiated to airport communities from turbofan-powered aircraft (Ref. 1). In the late 1960s, the potential for reducing tone noise with passive acoustic treatments (see Figure 6.1), as applied to a turbofan nacelle, was dramatically demonstrated via flight tests conducted using a Boeing 707-320C powered by JT3D-7 engines. Results from this flight test showed that acoustic liners could achieve tonal noise reduction on landing approach (dominant tone reduction of 32 dB at 2.7 kHz) (Ref. 2). The liner structure consisted of a honeycomb core bonded between a porous facesheet and an impervious back plate. Such structures are resonant absorbers, with the facesheet porosity controlling the peak absorption and the honeycomb depth controlling the absorption peak frequency. As such, they are well suited for tonal noise reduction. The flight test results clearly demonstrated that suppression of noise radiated from the JT3D-7 inlet was enhanced by using two treated splitter rings and treated support struts to increase the effective treatment-length-to-duct-height ratio (L/H). (Geometric L/H was approximately 3.25 for the JT3D-7 inlet.) Approximately three decades later, tests were conducted in the 9- by 15-ft Low-Speed Wind Tunnel at the NASA Glenn Research Center with the Advanced Ducted Propulsor (22-in. ADP fan rig), a very large bypass ratio turbofan engine (Ref. 3). The single-layer liner used in this test was representative of 1992 liner technology, and the ADP engine had an L/H of approximately 0.5 (a factor of 6.5 less than that of the JT3D-7 flight test engine). When scaled up to a 267-kN (60 000-lb) thrust engine, a noise reduction of 5.2 dB was computed for a 457-m (1500-ft) flyover approach at Mach 0.1. Maximum single-tone reduction (at a full-scale frequency of about 600 Hz) was estimated to be about 10 dB, and broadband noise attenuation ranged from 2 to 3 dB. The L/H ratio is the key metric for estimating the effectiveness of liners to reduce the amount of noise radiated from the engine nacelle. As L/H increases, the corresponding noise reduction also increases. It is a testimonial to the advancing liner technology over the three decades separating these two tests that, in spite of an L/H reduction by a factor of 6.5, significant tonal and broadband noise reductions were achieved.

Acronyms and symbols used in this chapter are listed in Appendix A to aid the reader.

6.1.1 Challenge for Liner Design Improvement

The progress in improving liner efficiency over the past four decades, as described above, places in perspective the challenge of achieving even greater liner efficiency in the face of decreasing L/H and the changing character of turbofan noise spectra (broadband noise increase and spectrum shift to lower frequencies). Success is contingent on advances in materials technology, liner fabrication processes, liner architecture, liner impedance prediction models, and—perhaps most critically—the validation of such models via impedance

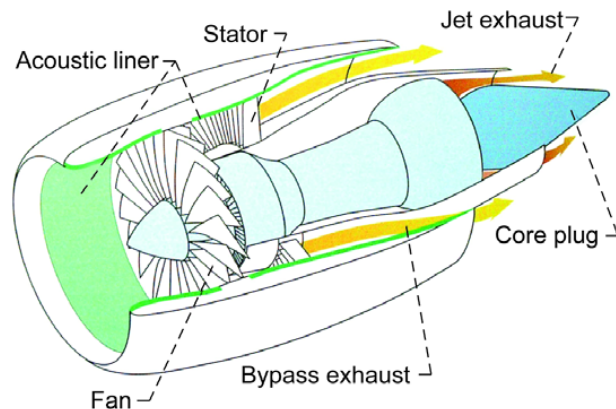


Figure 6.1.—Turbofan engine nacelle with wall lining.

measurements. As mentioned previously, the L/H ratio for a lined duct is a key metric for estimating relative performance. Historically, an off-optimum liner design could still achieve a desired noise reduction provided there was sufficient L/H available. As L/H becomes more restricted, off-optimum design becomes less tolerable. The continuing evolution of the high-bypass engine, along with greater political pressure to reduce the noise footprint in spite of the persistent increase in the number of airport operations, combine to provide great stimulus to improve liner efficiency. Notwithstanding past turbofan noise source reductions credited to improvements in fan blade design, passive liner technology continues to be an important tool for reducing turbofan noise emission. Consistent with the foregoing issues, the implication is that future liner design will become far less forgiving than was the case historically. Thus there is a need for more efficient designs that provide more attenuation per L/H , as well as an increased emphasis on ensuring that a target design is realized in the operational engine nacelle. To that end, the objective of the uncertainty analysis described in this chapter lays out a framework for assessing the effects of environmental and geometric parameters on liner design.

6.1.2 Viable Liners for Turbofan Engine Nacelles

For application in turbofan engines, viable liner designs must function in harsh aeroacoustic environments to provide efficient noise attenuation while complying with stringent mechanical and environmental constraints. Historically, these constraints have ruled out bulk absorbers such as foam and fiberglass, which are excellent choices for broadband attenuation, but are unsuitable for nacelle environments due to fluid retention, debris contamination, lack of load-bearing capacity and maintenance concerns (Refs. 1 and 4). Instead, liner designers were compelled to explore other acoustic dissipation mechanisms. To that end, the thin, porous facesheet (typically realized as a perforate) over honeycomb core (POHC, see Figure 6.2) liner offers a suitable alternative, as it is a lightweight, load-bearing, low-maintenance structural component. It is derived from its purely structural counterpart that consists of a

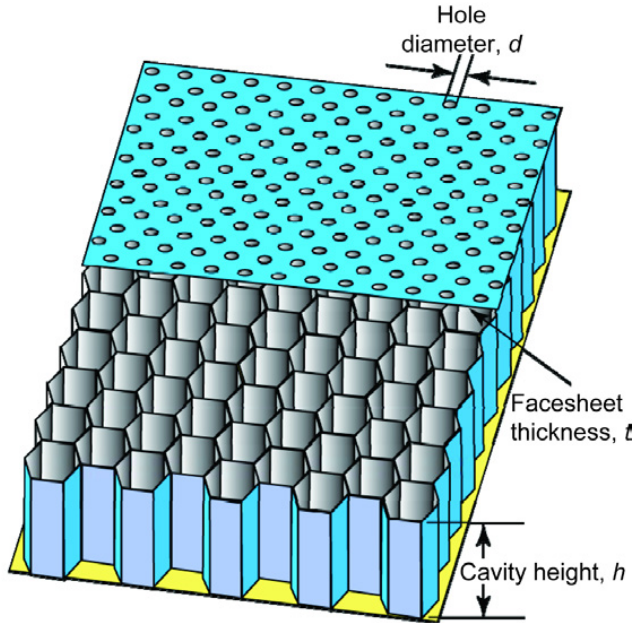


Figure 6.2.—Perforate-over-honeycomb core (POHC) liner.

honeycomb core bonded between two thin, impervious facesheets, with consequent low area density and high bending stiffness. By making one of the facesheets porous, it is transformed into a local-reacting acoustic absorber for incident waves on the porous side; that is, acoustic waves interior to the structure are restricted from propagating lateral to the facesheet surface. This local reaction aspect provides an enormous simplification for calculating the duct airway sound attenuation because an impedance boundary condition suffices to couple the acoustically absorbing structure to the wave propagation process in the duct airway. Fortuitously, this “tried and tested” load-bearing structure provides the mechanical properties to make it an excellent choice for duct liner treatments. The structure can be fabricated using a wide variety of facesheet materials to provide the desired porosity; for example, fibermetals, woven wire mesh combined with perforates, or stand-alone perforates (as illustrated in Figure 6.2). New fabrication methodologies for manufacturing perforates, such as electron-beam and laser-beam drilling, have developed in recent years to supplement the more traditional technologies such as shear-punched and pin mandrel-formed holes.

6.1.3 Perforated Plate Resistive Element in Multilayer Liners

In its simplest form, a POHC absorbing structure provides significant attenuation over a relatively narrow bandwidth, making it an excellent noise reduction choice for tone-dominated, low-bypass turbofan engines. These sandwich-type structures can also be stacked into multiple layers to enhance attenuation bandwidth via additional degrees of freedom, to

allow tuning of the absorption spectrum. Multiple layers can extend attenuation bandwidth by at least one octave. For current high-bypass engines, up to three-layer liners are in use. While these multilayer systems have greater bandwidth than the single-layer resonant structure, they are also more complex to fabricate, and their increased weight translates into greater cost and reduced payload. Two recent developments offer the possibility of improved bandwidth while retaining the structural simplicity and mechanical advantages of the single-layer liner. The first involves the insertion of multiple porous septa (cellular caps) into individual honeycomb cells at selected depths (Ref. 5). The second involves the implementation of a specified porosity (e.g., laser-drilled perforations) in the honeycomb cell walls (Refs. 6 and 7). These two innovations portend the advent of a “designer bulk absorber,” wherein anisotropic, bulk acoustic properties can be specified (e.g., flow resistivity). This means that liners can be designed to range from local reacting to extended reacting in two independent directions. Further, because the fundamental resistance element in such liners is a thin porous material, acoustic property modeling builds on existing empirical impedance prediction models. As previously noted, the modeling of such liners is likely to be more computationally intense than for the single-layer, local-reacting liner. However, in view of the continuing decline of computational costs, bandwidth control to optimally attenuate both tonal and broadband noise may become feasible in the future.

6.1.4 Scope and Objective of This Assessment

In summary, for about five decades, continuing advances in materials technology have provided an increasing number of choices for resistive elements in nacelle liner treatments. These have included fibermetal products (originally targeted to industrial filtering processes), woven wire meshes, synthetic meshes, and metal foams. Although many of these advances continue to be explored for potential usage in liner designs, the perforated facesheet continues to be a commonly employed resistance element, mainly because of its structural simplicity and strength, mechanical durability, easily quantifiable geometric properties, and low cost. Consequently, the aircraft industry has accumulated an extensive database, whereby semi-empirical impedance prediction models have been developed for liner design. Because of the continuing relevance of the POHC liner, in both its single-layer and multilayer configurations, and because of time constraints, the scope of this assessment will be limited to a single-layer POHC test liner configuration. This absorbing structure is representative of the issues encountered in an uncertainty analysis. The main objective of this assessment is to provide a statistical approach for assessing the quality of an impedance “product” in the same manner as statistical process control is used for a manufacturing process. In the next section, the metrics of uncertainty are discussed, along with their implication for the measurement and prediction of liner impedance spectra.

6.2 Impedance Uncertainty, Quantification, and Quality Control

This section addresses the metrics used to quantify impedance uncertainty and the relevance of such metrics to the task of applying statistical process control technology to achieving target liner impedance spectra in an operational aircraft engine to within a specified range of uncertainty.

6.2.1 Statistical Process Control: A Tool for Impedance Quality Control

A single realization of a liner design in an operational engine is subject to random and systematic errors that result in frequency-dependent deviation of the installed impedance from the targeted values. The limiting of such errors to an interval centered on the target impedance is traditionally the task of manufacturing quality control. Traditional quality control is based on a statistical sampling of the final product and thus does not detect an out-of-compliance condition until after it occurs. Statistical process control (SPC) monitors the inherent variability of a manufacturing process at critical points (“voice of the process”) to provide a warning of an impending out-of-compliance condition (Refs. 8 and 9). The power of SPC is to provide a basis to intervene in the manufacturing processes at critical points to prevent production of out-of-compliance units. This approach to quality control would achieve an installed liner impedance under operational conditions to within some specified total error. The user-specified variation of the end product from the target (“voice of the customer”) is what makes SPC an attractive approach for impedance quality control. It fits well with the SPC concept because the statistical sampling of the installed liner impedance is impractical on a routine basis. It is the judicious sampling of the manufacturing process that is the critical aspect of SPC, and that makes it an attractive conceptual framework for specifying installed impedance uncertainty in operational aircraft engines. As with SPC applied to widget production, the task is to anticipate an impending out-of-compliance condition at selected stages in the design and fabrication process. To some degree, manufacturing process monitoring is already being implemented in current acoustic liner production. What may be missing, however, is a robust statistical database for the various subprocesses which constitute the voice of the process and that may be used in conjunction with a user-defined uncertainty limit such as a confidence interval centered on the desired impedance. For a liner impedance spectrum, such confidence intervals are frequency dependent. The most critical (and potentially useful) aspect of applying the SPC paradigm to assure performance compliance is the creation of a laboratory-validated, semi-empirical impedance prediction model that serves as a kind of proxy for impedance measurements on the installed product (assumed inaccessible on a routine basis). Thus, in what follows, we apply uncertainty analyses to

impedance predictions and measurements for the POHC single-layer liner.

6.2.2 Specification Limits, Uncertainty Limits, and Confidence Intervals

The goal of SPC, for liner implementation on an operational engine, is to estimate the confidence with which an installed impedance complies with an end-user-defined uncertainty range centered on the target impedance. When quantified in terms of a probabilistic statement this uncertainty range is generally called a confidence interval because it estimates the level of confidence that the implemented impedance will fall within the stated uncertainty interval. Because it is not practical to “measure” the impedance of the finished product (i.e., installed impedance), a semi-empirical impedance prediction model provides the basis for estimating not only impedance mean values but also the standard deviation about the mean. These two statistical quantities are crucial to estimating compliance of the process with a user-specified uncertainty limit. Thus SPC is a statistical tool and for its successful application relies on a sufficiently robust statistical database. Both the statistical database and the selected semi-empirical liner impedance prediction model are crucial for the successful application of SPC to estimating installed impedance uncertainty.

The success of a quality control program, in the SPC context, depends upon a validated impedance prediction model and an informed customer specification limit. Model validation is done in a laboratory environment and is the basis for employing the model as a kind of proxy for the voice of the process. Given a creditable voice of the process, an informed customer specification limit on a target impedance spectrum translates into an optimal choice (both technically and economically) for the entity ultimately responsible for compliance of an aircraft engine noise certification requirement. Without realistic specification limits, presumably determined from allowable uncertainty contributed by the turbofan noise to the aircraft footprint, the liner producer simply does not know how “tight” the process input parameters need to be! Thus, since there are no a priori specification limits provided for the POHC liner studied in this assessment, the focus is on the credibility of the voice of the process. This takes the form of comparisons of semi-empirical impedance prediction models and laboratory measurements. These comparisons are done in terms of an uncertainty analysis on statistical datasets of measured impedance spectra and Monte Carlo simulations applied to impedance prediction models.

6.2.3 Uncertainty Metrics

An unbiased measurement repeated N times on a hypothetical, statistically stable, parent population exhibits random fluctuations about the mean of the N sample values. For unimodal (e.g., Gaussian) statistical distributions, the sample mean approaches that of the parent population mean

(sometimes denoted “true value”), as N increases without limit. In practice, the sample mean, as well as other statistical parameters of interest, is always an estimate of the parent population counterpart. Real measurement processes (and predictive models) may impose unknown bias error (also called systematic error) on the sample statistics to cause a nonrandom shift in sample statistical parameters relative to their true values. This fact constitutes the major challenge for uncertainty analysis as systematic error is not known a priori and is thus not easily separated out from random error. Conceptually, at least, the total error in a single measurement (or prediction) comprises an unknown combination of systematic and random errors (Ref. 10). Again, because the true value is unknown, the total error is also unknown. However difficult the distinction between systematic and random errors may be in practice, these distinctions are nevertheless helpful. Hence, systematic errors are said to be due to assignable causes, and random errors are said to be due to unassignable causes.

Systematic and random errors are sometimes differentiated by the terms accuracy and precision that, in conventional usage, are synonymous. In the technical context here, accuracy denotes closeness to the true value and precision denotes the degree of clustering around a mean value (not necessarily the true value). In this document, we find it convenient to use all

of these descriptors. There are four combinations of precision and accuracy as illustrated in Figure 6.3. Generally, improving measurement methodology increases accuracy, whereas improving measurement technique increases precision. The reader will note that increasing accuracy or precision corresponds to an improved measurement, but not in the same manner. Correspondingly, a decrease in systematic error or random error corresponds to an improved measurement. Thus, these descriptors bear an inverse relationship to each other. While the above definitions have been discussed in terms of measurements, we also intend to apply them to impedance model predictions.

As will be discussed in Section 6.3.5, “Relevance of Laboratory Impedance Measurement,” a propagation model must be employed to measure (educe) the impedance of a test liner. This indirect measurement process affords ample opportunity for accuracy and precision errors to arise. To help mitigate these errors, at least for the impedance measurement technologies employed at the NASA Langley Research Center, studies have been conducted via well-understood absorbing structures (validation liners) consisting of parallel, capillary-like channels embedded in a rigid matrix (Ref. 11). The impedance behavior of such structures is nearly linear (impedance independent of excitation level and mean flow speed), making the impedance predictable from first principles. This

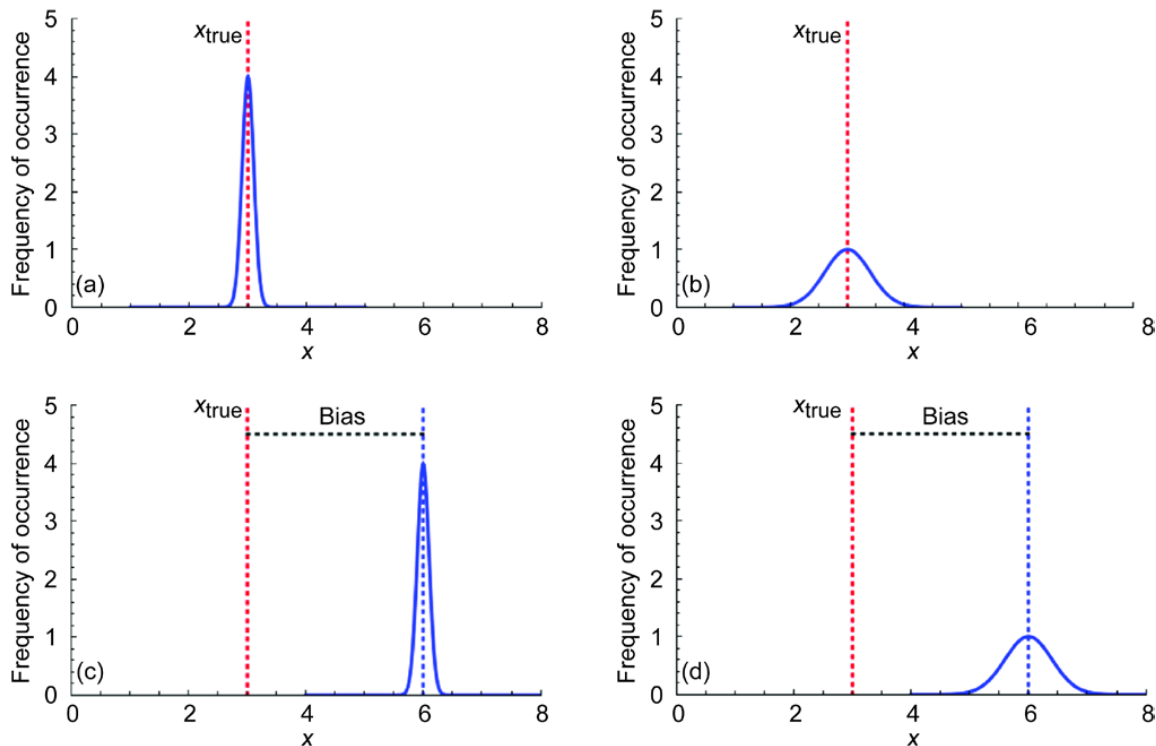


Figure 6.3.—Depiction of accuracy versus precision for parameter x , as used in this chapter. (a) High accuracy, high precision; (b) High accuracy, low precision; (c) Low accuracy, high precision; (d) Low accuracy, low precision.

prediction capability allows very accurate and precise impedance spectra to be determined. This capability allows these liners to be used to establish a baseline uncertainty for validating the impedance measurement methodologies and processes at Langley (Ref. 12), which have been used to validate both normal incidence and grazing incidence impedance measurement processes (Refs. 13 and 14).

For the purposes of this study, the metric for uncertainty is chosen to be the 95% confidence interval (Ref. 10). These intervals are calculated from the statistics generated by repeated impedance measurements and predictions. Calculation of 95% confidence intervals, as used here, assumes input parameter statistics to be Gaussian distributed. The precision part (random error) of the uncertainty analysis consists of simply comparing 95% confidence intervals for impedance measurements and predictions. The accuracy part (systematic error) of the uncertainty analysis consists of comparing the measured and predicted mean values. These confidence intervals are deemed to have a 95-percent probability of containing the “truth.” For the purposes of this study, the truth is assumed to be the mean values that would be attained with a large number (parent population) of measurements or predictions. Correspondingly, there is a 95-percent confidence that the next measurement (or simulation, in the case of prediction models) will fall within the 95% confidence interval. Any difference between the measured and predicted mean values is deemed to be systematic error (due to assignable causes). The confidence interval widths are deemed to arise from unassignable causes (random variability). These definitions are the bases for all the commentary on the many data charts to follow in Section 6.6, “Results and Discussion.”

6.2.4 Coverage Factor for Small Sample Sizes

When estimating a confidence interval for a small sample size taken from a normally distributed parent population, a coverage factor is introduced to account for the fact that the sample probability density function follows a Student’s *t*-distribution for small sample sizes (Ref. 10). Because sufficiently large sample sizes (number of tests or simulations) are generally impractical, especially in experimental work, the underlying assumption of parent population normality cannot be confirmed. In the present task, this situation arises both in the use of the nonlinear data reduction equation for the impedance measurement methodologies and in the prediction models. The impedance prediction models presented in this assessment involve nonlinear equations and are thus almost guaranteed to generate non-Gaussian output distributions for sufficiently large excursions of the inputs from their respective means. This is true even when the input distributions (probability distributions of the input parameters used in the prediction model) are Gaussian and large sample sizes are employed. To allay the concern for the usage of a coverage factor under these circumstances, a Monte Carlo process was used to acquire a large number of simulations (impedance predictions). Excellent agreement between the coverage

factor-based confidence intervals and those calculated directly from the Monte Carlo simulations is achieved.

6.3 Impedance Concept and Measurement Issues

Mathematically, acoustic impedance can be defined as the ratio of the frequency transforms of the acoustic pressure and acoustic particle velocity (hereinafter called the acoustic velocity when appropriate) at a point of interest in an acoustic field (Ref. 15). As a result of the directional nature of acoustic velocity, the acoustic impedance is also directional. Thus, at the surface of a local-reacting liner, the normal incidence impedance boundary condition is relevant at all incidence angles, even at grazing incidence. This is a result of the pressure being a scalar and the acoustic velocity being a vector constrained to be normal to the surface. Conversely, if the normal incidence impedance for a purportedly local-reacting material is found not to hold at grazing incidence, then the material (liner) is judged to depart from the local reaction assumption. Few materials (or absorbing structures) are ideally locally reacting; however, many approximate this condition. This is generally the case for POHC liners in operational nacelle liner treatments, even though cell-to-cell drainage slots are present in the circumferential direction. Departure from a local reaction assumption at grazing incidence is a source of systematic error for conventional POHC liners. If an absorbing structure is locally reacting, and its impedance is independent of the aeroacoustic environment, then the impedance is an intrinsic property of that structure. However, the nonlinear acoustic response of a typical POHC liner and its sensitivity to grazing flow makes its impedance a joint property of the structure and aeroacoustic environment. The fundamental indirectness of acoustic impedance measurement is a key contributor to the difficulty of making these measurements in the presence of high acoustic excitation levels and grazing flows. As mentioned previously in Section 6.2.3, “Uncertainty Metrics,” Langley employs a validation liner to provide a measure of confidence in the various measurement methodologies. This liner exhibits a high degree of linearity and insensitivity to grazing flow and is discussed further in Section 6.3.6, “Implementation of Rayleigh Absorber as Validation Liner.” It consists of a number of parallel tubes embedded in a ceramic matrix that are oriented normal to the surface (Refs. 11 and 13). Historically, such structures have been called Rayleigh absorbers (Ref. 16).

6.3.1 Nonlinearity Implication for Measurements and Prediction Models

As noted above, the classical impedance boundary condition breaks down for POHC liners because the impedance increases with increasing acoustic excitation. The nonlinearity poses an issue for using the classical frequency-domain concept of impedance as an experimental characterization of a perforate, because the impedance is no longer a unique

property of the perforate: it is also dependent on the excitation spectrum. Under the current physics-based modeling paradigm, this excitation-spectrum dependence is manifested entirely by the total root-mean-squared (rms) velocity through the perforate (both acoustically and turbulence driven). Thus the shape of the excitation test spectrum is not relevant so long as the resulting rms acoustic velocity is kept invariant. Researchers have found it advantageous to use both broadband and isolated tones as excitation sources. Broadband excitation is less labor intensive and equipment demanding (compression driver limitations). Detailed excitation spectrum control is lost with broadband excitation, and extraction of broadband acoustic signals in the presence of grazing-flow noise becomes more challenging. Discrete tone excitation avoids the control and signal extraction issues but tends to be labor intensive. At Langley, the authors have chosen to employ single-tone-dominated excitation spectra for impedance prediction model validation investigations and broadband excitation for system diagnostic testing. Separations of at least 20 dB between the target and spurious tones are easily achieved. This choice allows different test liners to be compared on a frequency-by-frequency basis with greater control of excitation level. Tonal excitation also allows more in-depth investigations of the assumptions that undergird the impedance prediction models now used by industry. Such investigations are yet to be performed in a systematic manner.

6.3.2 Grazing Flow Implication for Measurements and Prediction Models

For conventional POHC liners, the facesheet aspect ratio (thickness to hole diameter) t/d ranges from about 0.2 to 1.5, in which case grazing flow over the liner dominates the resistance, with a contribution roughly proportional to the Mach number. This effect can easily overwhelm the viscous and acoustic nonlinearity contributions and tends to subdue the nonlinear response to high acoustic excitation levels. Grazing flow tends to have comparatively little effect on the perforate mass reactance (a limiting reduction to not less than one-half its no-flow value at high flow speeds). It thus follows that the challenge for a perforate impedance prediction model is to accurately account for the grazing-flow effect. There are two prevailing theories regarding the basis of the grazing-flow effect. The first assumes it to be driven by the interaction of the acoustically driven oscillatory orifice flow with the grazing-flow boundary layer. The second assumes the dominant grazing-flow effect to be the combination, on an energy basis, of acoustic excitation with pseudo-excitation due to turbulence. There is considerable connectivity between the two approaches (Refs. 17 to 19).

Although high-speed grazing flows and high acoustic excitation levels complicate frequency-domain impedance prediction models for perforates, their continued use for a POHC liner has provided notable success in advancing passive liner technology for application in turbofan engines. Ongoing advances in perforate manufacturing technology have allowed

a t/d of up to at least 5 to be attained (i.e., a microperforate), wherein viscous resistance becomes a significant contributor to the total resistance.

It should also be noted that a more rigorous way to characterize a nonlinear duct liner boundary condition is via a time-domain impedance operator that relates the instantaneous acoustic velocity at the liner surface to the excitation pressure (Ref. 20). Sporadic research on this approach has produced mixed results. To exploit this approach, time-domain models of the source and the duct airway propagation process are required. Although the time-domain impedance boundary condition remains a topic of research interest, the frequency-domain approach remains the basis for most impedance prediction models relevant to liner design.

6.3.3 Test Sample Size and Scale Implications

When conducting tests in a laboratory environment, one must be mindful that there are some characteristics of the full-scale environment (in this case, an aircraft engine nacelle) that cannot be fully simulated. For instance, it is important to attempt to maintain a sufficiently large test sample such that the measured results are representative of those that would be expected in the full-scale environment. This was not a problem for the samples used to validate the impedance prediction processes with the two Langley waveguides (normal incidence tube (NIT) and grazing incidence tube (GIT)), as these samples contain hundreds of small-diameter channels distributed across their surfaces, such that any edge effects (e.g., partially blocked channels) represent a very small portion of the total surface area. Similarly, it is expected that microperforate samples, with their high hole densities, should be representative of larger surfaces used in the full-scale environment. However, for the assessment liner used in the current investigation, there are two key concerns. The first is associated with hole blockage, and the second is due to partial cells along the edges of liner test samples.

A number of holes in the facesheet are at least partially blocked by the interface between the honeycomb core and the facesheet. Of course, this is not unique to test samples, as honeycomb cores are an integral part of all POHC liners. However, this blockage can cause some variation in the number of holes per cell, thereby causing a variation in local or cell-to-cell impedance. If the size of the sample (assumed taken from the parent material) is sufficiently large, these variations will average out over the entire surface, and will be representative of the full-scale liner (ignoring, for the moment, the changes in impedance along the axial length of the liner due to nonlinearity effects). However, for sufficiently small samples, random variations of impedance will be measured with nominally identical samples.

The effect described above is particularly troublesome along the test sample edges. Unavoidable partial cells that occur at the liner edges at full scale represent a small percentage of the entire liner surface, but may represent a substantial percentage of the surface for small samples. If only one test

sample is employed, this leads to a systematic error in the impedance measurement with respect to the full-scale liner. One way to avoid this issue is to perform measurements on a statistically significant number of nominally identical test samples, each fabricated by randomly orienting the honeycomb core with respect to the perforate hole pattern.

A consideration of the issues listed above led to the choices of dimensions for the NIT and GIT samples. These choices represent a compromise between the issues regarding representative sample size and a desire to study the effects of plane-wave sources (no higher-order modes) on these liners up to a frequency of 3 kHz. In the comparisons between measured and predicted impedances presented later in this chapter, the effects described above manifest themselves as a systematic error because only one sample is evaluated. This error can be viewed in two ways. In one sense, the test sample can be considered as not representative of the full-scale environment, in that it does not present the same average impedance across its surface as would be observed in the engine. Alternatively, the prediction model can be viewed as not including all of the detailed geometry of the test sample. Regardless, this sample is viewed as sufficiently representative of the full-scale environment to allow useful comparison.

Impedance spectra for full-scale liners are generally desired over a frequency range of at least 0.4 to 4 kHz. One way of achieving this goal, while maintaining the capability to use only plane-wave sources, is to reduce the dimensions of the acoustic waveguide. Of course, this further exacerbates the effects of sample size, as described above. Another way to extend the frequency range is to incorporate higher-order modes into the measurement and analysis methods. Schultz, et al. (Ref. 12), conducted an analytical uncertainty analysis, in which extremely tight 95% confidence intervals on the measured impedances were computed in a 25.4- by 25.4-mm (1- by 1-in.) normal incidence tube up to frequencies above 6 kHz.

It is often useful to conduct model-scale testing, such as tests with a fan rig that is a scaled version of the full-scale engine, as it allows testing at greatly reduced expense. However, it is not a trivial matter to fabricate liners to reduced scale, as each of the geometric components should be reduced by the same scale factor. In addition, this requires the test regime (frequency range) in the fan rig to be scaled as well, thereby requiring the frequency range to be translated to higher frequencies. For example, if 1/5-scale models are used, the 0.4 to 4 kHz, full-scale frequency range is translated to a 2 to 20 kHz range. To support this type of testing, component liners must also be tested over this scale-model frequency range. This extension has not been pursued at Langley, as the emphasis has instead been placed on methods that use the full-scale frequency range at laboratory scale. One attempt to extend the frequency range in this manner was developed by Schultz, et al. (Ref. 21). They used a modal decomposition method with their 25.4- by 25.4-mm (1- by 1-in.) normal incidence tube to extend the frequency range to 13.5 kHz. The results they acquired with a plane-wave source (out to about

6 kHz) were excellent, while the data acquired, with higher-order modes present, exhibited some effects of mode scatter.

6.3.4 Measurement Methodologies

Impedance measurement methodologies are divided into two categories: (1) those that are invasive to the test sample and (2) those that are noninvasive. Invasive methods run the risk of perturbing the structure and acoustic field, thus introducing systematic error that can be notoriously difficult to isolate and correct. Noninvasive methods provide a global impedance measurement, but have the disadvantage of requiring an acoustic field model to mediate between acoustic pressure measurements and the surface impedance of the test sample. At Langley, global methods have been used almost exclusively. In the following subsections, two invasive and two noninvasive methods are described. The two invasive methods are included because they offer capabilities that cannot be achieved with the two noninvasive methods currently employed by Langley. In contrast with the noninvasive methods employed by Langley, these two methods offer the potential for direct impedance measurements in full-scale engine nacelles. Of the two invasive methods, the in situ method has been used to a much greater extent than the T-tube method.

6.3.4.1 Invasive Methods

The in situ method (ISM), originally investigated by Dean (Ref. 22) and later by Kraft, et al. (Ref. 23) requires pressure measurements at the backing cavity surface and at a representative location on the facesheet surface. The facesheet measurement can be measured with a single, flush-mounted microphone or by means of a traversing probe. In any case, a large systematic error can be incurred if the facesheet pressure is not measured with care. This is particularly true for perforates because of the hydrodynamic near field of oscillatory orifice flows. The advantages of the ISM are (1) it does not require a model for the acoustic field, external to the liner, to mediate between pressure measurements and the local impedance of the targeted cell, (2) measurements can be conducted in difficult environments, such as an operational engine, and (3) it requires no supporting test duct (waveguide). Disadvantages are (1) the measured impedance is local to a cell and may not be representative of a global impedance (e.g., POHC liners where hole counts, and thus blockage, vary from cell-to-cell), (2) the intrinsic cell impedance is almost certainly disturbed to some unknown degree by the intrusive microphones, (3) the precision required for microphone installation requires mechanical skill, is tedious and time consuming, and (4) an assumption must be made about the acoustic field within the measurement cell.

The ISM has acquired a reputation for being labor and skill intensive, along with having a lack of accuracy, precision, and robustness. This has prompted Langley to avoid this methodology. In spite of the large systematic and random error reported for this method, (Ref. 23) its capability of measuring a point-like impedance, albeit contaminated by hydrodynamic

effects, is of interest for studying the details of the near-field impedance variability at microscale and for validating direct numerical simulation of such flows via the Navier-Stokes equations (Ref. 24).

The T-tube method (TTM) described by Dean and Feder (Ref. 25) employs a normal incidence tube mounted normal to a flow duct. A small test sample with no back plate is mounted flush with the flow duct wall, such that grazing flow sweeps across its face while sound is incident on the open back side (thus the invasive nature of this method). The total impedance of the test sample plus that of the duct environment is measured by standard means in the normal incidence tube (see next section). Its chief merit is that it requires no inflow acoustic measurements, as do the waveguide methods (see next section). Another merit of the TTM is that it gives a global impedance (in contrast with a point-like impedance from the ISM) over a facesheet geometry suitable for a normal incidence tube. This feature avoids the systematic error that arises from averaging out nonlinear effects along a test sample length, typically required in a waveguide measurement. Aside from being an invasive method (i.e., removal of the back plate), the big disadvantage of the TTM is the inclusion of the generally unknown radiation impedance looking into the flow duct. This constitutes a very significant source of systematic error unless carefully “calibrated out.” This issue notwithstanding, the TTM can be useful as a means of measuring impedance changes due to grazing flow and can serve as complement to the waveguide methods.

6.3.4.2 Noninvasive Waveguide Methods

Noninvasive methods require a field propagation model to mediate between complex acoustic excitation pressures measured well away from the test sample surface in a control volume adjacent to the test sample. These methods generally provide an average surface impedance over the test sample surface, making this method a global determination of impedance. However, they require detailed modeling of each of the boundary conditions of the computational domain used to represent in the test environment. For the grazing-flow environment, the boundary conditions used in the Langley methodology include (1) the source plane, which can contain one or more modes, (2) the exit plane, either an impedance or pressure condition, (3) rigid boundaries along the two sidewalls, the bottom wall, and the portion of the upper wall that does not contain the test liner, (4) the complex acoustic pressure field along the wall opposite the liner, and (5) the surface impedance of the test liner.

The overriding advantage of the waveguide method, as seen from the Langley perspective, is that it provides the only possibility of measuring the global impedance of an intact, test liner sample in a simulated environment representative of an operational engine environment. Clearly, none of the invasive methods discussed above can do this. However, the invasive methods remain of interest because they may have a role to play in certain impedance prediction model development

issues. NASA Langley employs two hardware implementations of noninvasive, impedance measurement: a deterministic, two-microphone method (TMM) (Refs. 26 to 28) as implemented in a normal incidence tube (NIT, see Figure 6.4), and an over-determined, multimicrophone method (MMM) that employs a microphone array embedded in the walls of a grazing incidence waveguide with or without grazing flow (grazing incidence tube, GIT, see Figure 6.5).

Error sources specific to the TMM and MMM are well documented in the literature (Refs. 12, 26, and 27). Here, we focus on error sources that are likely to arise when results using the two methodologies are compared for the specific apparatuses employed at Langley, the NIT and GIT. The NIT accommodates a test sample size of 50.8 by 50.8 mm (2 by 2 in.). The GIT accommodates sample sizes that can range from 50.8 by 50.8 mm (2 by 2 in.) to 50.8 by 406.4 mm (2 by 16 in.). Although the GIT can accommodate the same sample size as the NIT, data quality suffers because the decaying wave field adjacent to a 50.8 by 50.8 mm (2 by 2 in.) sample in the GIT cannot be well resolved, at least with the current arrangement of microphone locations. This means that test sample interchangeability between the NIT and GIT is not a suitable way to compare sample impedance data for normal and grazing incidence. Instead, two test samples, one 50.8 by 50.8 mm (2 by 2 in.) and the other 50.8 by 406.4 mm (2 by 16 in.), are fabricated to nominally the same specifications. Any random variability between such samples appears as a

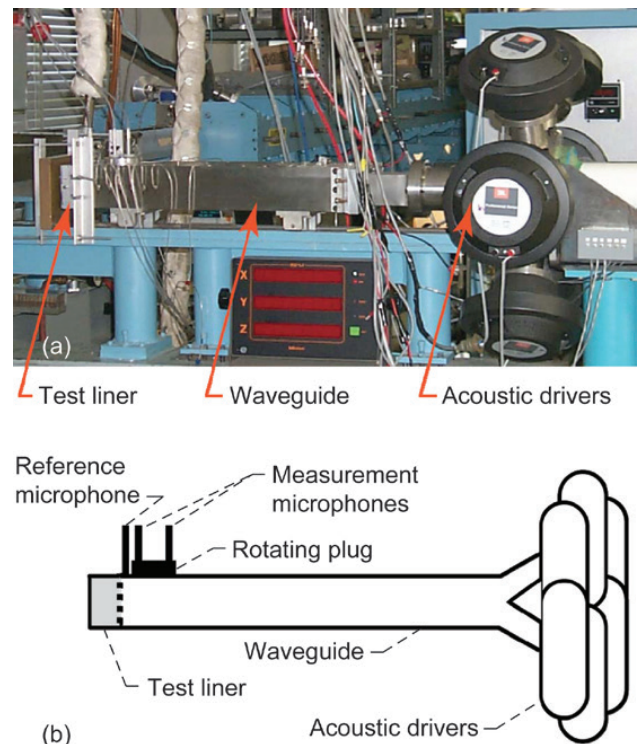


Figure 6.4.—NASA Langley normal incidence tube (NIT).
(a) Photograph. (b) Schematic.

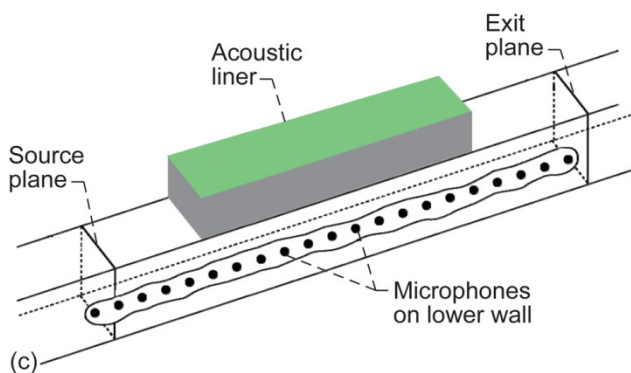
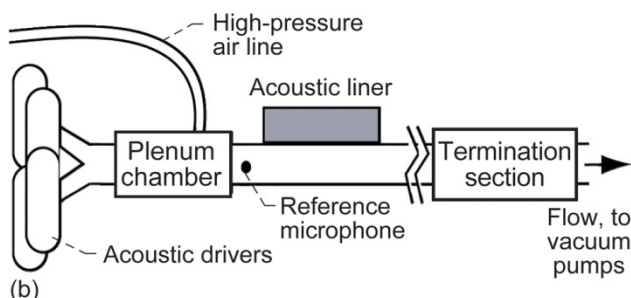
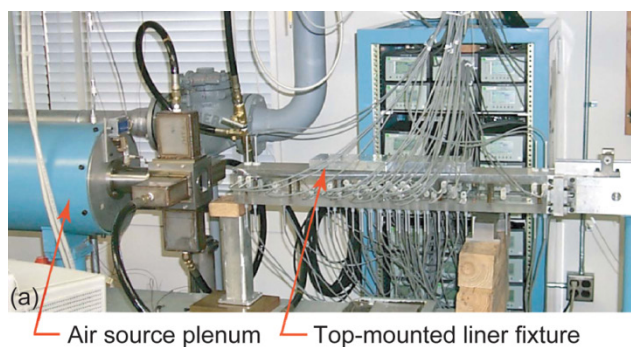


Figure 6.5.—NASA Langley grazing incidence tube (GIT). (a) Photograph. (b) Schematic. (c) Liner installed in top wall.

systematic error, unless a statistically significant number of nominally identical samples are tested. This is believed not to be a significant source of error for the validation test samples. However, random error may be aliased into a systematic error when POHC test liner results are compared for the two methodologies on a paired, sample-to-sample basis.

The TMM, as implemented at Langley, has been demonstrated to provide high-quality normal-incidence impedance measurements from 400 to 3000 Hz, over a range of normalized resistance and reactance values of 0 to 10 and -10 to 10, respectively. However, a potentially significant source of systematic error for the GIT is related to the global nature of the impedance measurement when performed on a nonlinear test liner. Significant attenuations can occur over the standard test liner length. This can cause the acoustic resistance to decrease from the leading to trailing edge. Because

the MMM assigns an average (smeared) impedance over the entire liner length, a significant systematic error can be incurred. One strategy for dealing with this error consists of dividing the liner into multiple axial segments that are sufficiently small to render a uniform-impedance assumption (different impedance for each segment) acceptable. A preliminary effort has been made to implement this strategy (Ref. 29).

For the GIT, grazing flow complicates the field model and the source and exit plane boundary conditions on the control volume. These source and exit boundary conditions constitute a daunting measurement challenge, especially in the presence of flow. In addition to these ancillary boundary conditions, the flow field profile throughout the control volume adjacent to, and centered on, the test liner (Figure 6.5(c)) is an input parameter. These issues notwithstanding and for the reasons stated previously, NASA Langley has chosen to invest great effort in the development of this impedance measurement technology as implemented in the GIT (Refs. 26 to 28, 13, 30, and 31). The GIT is currently being upgraded to provide acoustic excitation levels up to 150 dB over a frequency range of 400 to 6000 Hz, grazing flow up to a Mach number of 0.6, and sound propagation with and against the grazing flow (simulates aft and inlet conditions).

6.3.5 Relevance of Laboratory Impedance Measurement

As previously stated, the key motivation for implementing the waveguide-based methodology is to simulate, insofar as is feasible, a test liner subjected to realistic aeroacoustic environments and to determine its impedance in this environment. Thus, it is intended for a waveguide propagation model to capture the salient features of the aeroacoustic environment. This requires input parameters on a control volume with some, as yet unknown, level of accuracy and precision. Whereas an analytical data reduction equation connects a transfer function measurement to the test sample impedance for no-flow, normal-incidence impedance measurements, an iterative numerical algorithm is required for grazing flow. Wave propagation in the waveguide has been modeled by the convected Helmholtz equation (CHE) and the linearized Euler equations (LEE) (Refs. 14, 31, and 32). The CHE model captures the full three-dimensional aspects of the aeroacoustic field in the control volume, centered on the test liner, for uniform mean flows. Alternatively, the current implementation of the LEE model can capture the effects of the boundary layer, but only in a two-dimensional aeroacoustic environment. The iterative scheme requires that an initial impedance be arbitrarily set to a convenient value, and then iterated upon until the computed complex acoustic pressures at the microphone locations converge to the corresponding measured acoustic pressures, in a mean square sense, to within a specified tolerance (thus the over-determined character of this methodology relative to the TMM as applied in the NIT). The liner impedance for which the measured and predicted

acoustic pressures converge is taken to be the measured impedance. These codes have been validated (Ref. 14) via an implementation of the Rayleigh absorber described previously. The data reduction equations for the CHE and LEE propagation models are discussed in Chapter 7 on duct acoustics.

It is important to note that the sole justification for the large effort, over the past four decades, to experimentally evaluate liner response in realistic environments at laboratory scale has been driven by the liner nonlinearity and the need to describe these effects via semi-empirical impedance prediction models. Should advances in materials science and fabrication technologies allow the development of linear liners that are suitable for aircraft nacelles, the need for simulating harsh aeroacoustic environments at laboratory scale will cease, with the consequence that impedance prediction models can be enormously simplified. Some indication of that trend is evidenced in the high t/d perforates available via laser hole drilling. However, the current focus remains on liners that exhibit significant nonlinearity. To that end, the uncertainty analysis employed here focuses on a representative perforate.

6.3.6 Implementation of Rayleigh Absorber as Validation Liner

From what has been said previously, it is clear that the indirect nature of impedance measurement (eduction) is complicated by the addition of high-speed grazing flows combined with intrinsic liner nonlinearity. It is therefore important that the aforementioned impedance measurement methodologies be verified via a liner whose impedance can be predicted from first principles. This has been accomplished at NASA Langley by implementing the so-called Rayleigh absorber concept (Ref. 16), an absorber that dissipates acoustic energy by means of acoustic boundary layers in a geometrically well defined internal structure (e.g., narrow, capillary-like channels (Ref. 16)). As alluded to previously, the NASA Langley implementation of the Rayleigh absorber is achieved by densely packed, parallel cylindrical channels in an impervious ceramic matrix material (Ref. 11). The material is precision cut to conform to test liner dimensions for the NIT (active face 50.8 by 50.8 mm, or 2 by 2 in.) and GIT (50.8 by 406.4 mm, or 2 by 16 in.). The channels are rigidly terminated at lengths up to about 82 mm (3.2 in.) to give a channel length-to-diameter ratio up to 130. The various implementations of the Rayleigh absorber will henceforth be called validation liners.

Accurate impedance prediction of the validation liner depends critically upon ascertaining the channel propagation constant and characteristic impedance. The theory for performing this calculation is classical and is thoroughly reviewed by Tijdeman (Ref. 33). Any acoustic nonlinearity or grazing-flow effect on the impedance of such an absorber can arise only at the liner surface where the channels interface with the aeroacoustic field. It is intuitively clear that the scale of dissipation at this interface must be small compared with the interior dissipation. Thus acoustic nonlinearity and grazing-flow effects are

minimized, but not entirely eliminated by the small scale of the individual channel openings and relative large composite open area ratio (better than 50 percent, compared with conventional POHC liners). Numerous comparisons between predictions and measurements in both the NIT and GIT have justified the use of this implementation of the Rayleigh absorber as a validation liner (Refs. 13 and 14).

6.4 Impedance Prediction Models for POHC Absorbers

For the purposes of this discussion, first-principles acoustic impedance prediction models for POHC liners are those for which the impedance can be related to the acoustic energy dissipation physics in the perforate via the fluid dynamic equations of motion of the unsteady flow. It is also assumed that the structure is mechanically rigid, but possibly heat conducting, and that no empirical parameters are needed; that is, only tabulated physical constants are to be used. The only absorbing structure that qualifies for this kind of prediction model in the work at Langley is the ceramic tubular material implementation of the so-called Rayleigh absorber, as discussed in the previous section. The application of first-principles models to realistic absorbers, such as POHC liners, gives rise to nonlinear, differential equations that require several simplifications and approximations to achieve a computationally practical result. Thus, as a practical matter, there has been a bias toward phenomenological, or semi-empirical, models with concomitant heavy reliance upon empirically determined parameters.

6.4.1 Phenomenological (Semi-Empirical) Models

Phenomenological acoustic impedance prediction models are based on easily measured parameters that are relevant to the phenomenon of interest, as per the relationship between acoustic resistance and direct current (DC) flow resistance. Unlike first-principles models, which imply a detailed description of the phenomenon of interest, phenomenological models make use of dimensional analysis to identify dimensionless groupings of parameters. These parameter groups are then used to provide guidance for experimental testing to flesh out the details of the phenomenon: for example, the classical Reynolds number dependence of laminar to turbulent transition in pipe flow. Phenomenological models are also denoted as semi-empirical. For acoustic impedance modeling, the empirical parameters are usually determined from a combination of nonacoustic and acoustic measurements. Historically, the acoustic resistance part of the impedance prediction models can be related to the modeling concepts used to study flow losses through metering orifices and percolation through porous media of interest in fluid filtering and seepage flow in aquifers (Refs. 34 and 35). This is possible because of the commonality between the fluid flow regimes in these structures, such as the transition from laminar to turbulent flow at a critical Reynolds number based upon a characteristic length

scale (micropore diameter for foam-like structures, fiber diameter for fibrous materials, or hole diameter for perforates). It is this commonality of flow regimes at the microscale that allows impedance prediction models for perforates to employ generally the same phenomenological framework as do micropore structures. Although the physics of flow losses in porous materials is generally well understood, a semi-empirical impedance prediction model must be employed if the nonlinear contribution to resistance is important. This happens when, at the hole scale, acoustic excitation pressure p is such that the terms $v(\partial v/\partial x)$ and $\partial v/\partial \tau$ become comparable in the fluid dynamic equation of motion

$$\rho \left(\frac{\partial v}{\partial \tau} + v \frac{\partial v}{\partial x} \right) + \frac{\partial p}{\partial x} = 0 \quad (6.1)$$

that describes the acoustic velocity v through the perforate where ρ is the constant ambient density. This criterion for significant nonlinearity in perforates is discussed at length by Melling (Ref. 36) and Kraft (Ref. 37). The importance of resistance nonlinearity for a POHC liner depends not only on acoustic excitation level and frequency, but also upon perforate geometry (e.g., hole aspect ratio, t/d , and open-area ratio, σ). Generally, the nonlinear contribution to resistance is reduced by increasing the hole aspect ratio and the open area ratio, which reduces particle velocity in the perforate holes for a given excitation. It should be noted that the terms “open area ratio” and “porosity” are often used interchangeably, with porosity generally expressed as a percentage and open area ratio expressed as a fraction.

It is expected that semi-empirical models will continue to play a major role in POHC impedance prediction for the foreseeable future. However, there are three caveats to this forecast. One is that viscous losses within micropores, which contain holes with large hole aspect ratios, may be exploited to dominate nonlinear losses and thus exhibit insignificant response to grazing flow (Ref. 5). Second, advances in computational technology may permit first-principles models to be employed in routine liner design. A third possibility is that electromechanical liner technology (Ref. 38) may emerge to make the design of targeted liner impedance spectra less critical. However, even for the self-adjusting or “smart liner,” it will be necessary to achieve a mean impedance spectrum, about which an onboard intelligence implements adjustments in response to a changing environment. In the interim, the refinement of semi-empirical impedance prediction models to meet targeted impedance spectra to within an appropriate specification range will continue to be sought. The objective of this assessment is to lay a foundation for discriminating among the merits of such competing models.

6.4.2 Semi-Empirical Models for POHC Liners

Perforates used in POHC liners are assumed to satisfy the lumped-element and quasi-steady-flow assumptions. Thus, a

measurement of DC flow resistance (a nonacoustic parameter) is generally assumed to translate into an effective dynamic, or acoustic, resistance (both linear and nonlinear contributions). The empiricism of such models limits their range of applicability. For example, one model may hold for facesheet thicknesses less than the hole diameter ($t/d < 1$), whereas another model may hold for facesheet thicknesses greater than the hole diameter ($t/d > 1$). They may also employ parameter groupings derived from dimensional analysis, as previously mentioned. The lumped-element model holds when the local fluid motion associated with a perforate hole can be regarded as moving as a unit: that is, there is no wave motion on the scale of the fluid motion affected by the hole. This would include the fluid contained within the hole and the induced flow-field distortion in the vicinity of the hole. The mathematical criterion for lumped-element modeling is that the product of the acoustic wavenumber and the effective hole length be much less than unity (Ref. 15). Thus, the lumped-element assumption implies that the perforate has zero thickness. For a single-layer impedance prediction model, this assumption has been observed to generate significant systematic errors in the antiresonance region. Another important assumption for many perforate acoustic impedance models is that the rms acoustic velocity can be equated to a DC (or steady) flow velocity. This rests upon the quasi-steady-flow assumption and is key to modeling the nonlinear part of the resistance in a frequency domain sense. This assumption is violated if the excitation time scale becomes too small (high frequencies), such that flow profiles within an orifice do not develop to near a steady-state condition.

For conventional POHC liners, as currently used in aircraft engine nacelles, the perforate hole aspect ratio t/d ranges from about 0.5 to 1.5. Consequently, the nonlinear contribution to resistance dominates the viscous contribution. For this range of hole aspect ratio, grazing flow has a large effect on the nonlinear resistance because it significantly perturbs the entire, oscillatory flow field associated with the hole. As an aside, it should be intuitively clear that as hole aspect ratio increases, response sensitivity to grazing flow decreases. Correspondingly, the viscous contribution to resistance increases to the point that it can dominate the total resistance when the hole aspect ratio reaches about 50, as is the case for the Rayleigh absorber previously discussed. From these remarks, it should be clear that a viable impedance prediction model for POHC liners must deal with both nonlinearity and grazing-flow effects, in addition to the more classical viscous dissipation contribution to resistance. Aside from their mechanical advantages, perforates offer more precise control of governing parameters (e.g., porosity and hole geometry) than do micropore-type structures. (In this context, “micropore” is intended to convey the concept of a rigid, porous matrix that supports randomly dispersed, tortuous fluid paths as provided by reticulated foams, granulated materials, or compacted fibers—micropores excluded.) The added complication of nonlinearity and grazing-flow effects notwithstanding, the impedance prediction models for POHC

liners allow them to employ generally the same phenomenological framework as do micropore structures.

Another limiting feature of any semi-empirical POHC impedance prediction model is that the various empirical parameters are specific to the perforate fabrication process (e.g., shear punching, pin-mandrel forming, or electron-beam drilling). Further, the accuracy and precision of their predictions are conditioned upon the variability (i.e., quality) of the perforate fabrication process and the test data used to support the model empiricism. This is one reason for the propensity of industry to treat such models as proprietary in order to preserve their competitive status. When such models are used outside their empirical support base, the utmost caution should be exercised. With these caveats in mind, the models discussed here have been selected to focus on POHC structures consisting of punched aluminum facesheets bonded to honeycomb core via a sheet reticulation bonding process (Ref. 39). The authors believe that the chosen POHC test liner (assessment liner) for this project is representative of this fabrication class. However, it does not necessarily follow that the assessment liner complies with all the assumptions underlying the empiricism in the various prediction models. Also, it should be noted that none of the empirical parameters have been adjusted to bring about improved agreement with the measured results.

In what follows, four semi-empirical impedance prediction models are presented that are believed to represent those currently used by industry. The model descriptions are intended to capture their salient features, and are not to be construed as a critical analysis of their differences and similarities. The names given to these models, described in the subsequent sections, are the Two-Parameter (TP) model, the Crandall Full-Solution (CF) model, the Composite Empirical (CE) model, and the Fluid Mechanical (FM) model.

6.4.2.1 Two-Parameter Model (TP)

The TP and CF impedance prediction models share a commonality in that they parse the liner impedance (normalized by ρc , where ρ is the ambient density and c is the ambient speed of sound) as follows

$$\zeta = \theta + i\chi = \theta_{\text{lin}} + \theta_{\text{nonlin}} + \theta_{\text{gf}} + i\{\chi_{\text{fs}} - \cot(kh)\} \quad (6.2)$$

where θ_{lin} and θ_{nonlin} are the viscous and nonlinear contributions to the facesheet resistance, respectively. The grazing-flow contribution is given by θ_{gf} . The reactance is given by the expression in brackets, from the facesheet mass reactance and cavity compliance via the terms χ_{fs} and $\cot(kh)$, respectively. Note that an $e^{i\omega\tau}$ time convention is used (where ω is the angular frequency and τ is time) throughout this paper, and all impedances are normalized by ρc .

A lumped-element assumption for a perforate allows the acoustic oscillatory flow through the perforate to be treated as locally incompressible and quasi-steady. Thus, a DC flow resistance measurement on the perforate provides the basis for

an empirical model of the acoustic resistance. No dynamic information related to the mass reactance is available by this means. If the honeycomb cell depth (backing cavity) h is sufficiently small relative to the acoustic wavelength, it can also be treated as a lumped compliance element, or a Helmholtz resonator. If this is not the case, then it is modeled as a rigidly terminated transmission line. The cell reactance is then given by $\chi_{\text{cav}} = -\cot(kh)$, where k is the wavenumber and h is the cell depth. This is the cell reactance model used in this document. It holds for excitation frequencies that are low enough that cross modes are not supported in an individual cell, which is generally not a serious limitation. For perforates in which the viscous contribution to resistance is small, viscous losses in the honeycomb core may become evident as systematic errors that add a small resistance to the total resistance of the liner.

The simplest of the four models evaluated in this document is the so-called Two-Parameter impedance prediction model. It gets its name from parsing the DC flow resistance R_f into linear and nonlinear contributions, most simply expressed as

$$R_f = A + B \cdot V_{\text{inc}} \quad (6.3)$$

Experimentally, R_f is determined using $R_f = \Delta P / V_{\text{inc}}$, where V_{inc} is the measured incident flow velocity through the test specimen and ΔP is the measured pressure drop across the specimen. Such measurements should be conducted over an incident velocity range commensurate with that expected for acoustic excitation. The constants A and B can be determined directly by fitting Equation (6.3) to the measured values of R_f and V_{inc} . This purely empirical curve fit constitutes the simplest characterization of thin facesheet resistance behavior. It is not restricted to perforates, but must be repeated for each facesheet structure of interest (e.g., fibermetal sheet). Because of its intensely empirical nature, this form of the two-parameter flow resistance characterization is not pursued further in this document.

Alternatively, a semi-empirical model for the flow resistance can be inferred from the one-dimensional momentum equation (Ref. 35) for the pressure loss in a porous material. From Green's analysis (Ref. 35), the pressure gradient in a porous material can be characterized by an equation of the form

$$-\frac{dP}{dx} = \alpha\mu V + \beta\rho V^2 \quad (6.4)$$

where μ is the ambient dynamic viscosity, x corresponds to the direction of interest, and α and β are used to characterize the internal geometry of the material. These coefficients relate to the pressure losses due to viscosity and fluid inertia, respectively. Inertia-related pressure loss arises from flow path tortuosity. At sufficiently low Reynolds numbers based on a suitable characteristic length, the pressure gradient is controlled entirely by the first term. At higher flow speeds, the

inertial effects come into play to eventually dominate the pressure gradient. In smooth pipe flow, this behavior corresponds to the transition from laminar to turbulent flow and occurs abruptly at a Reynolds number of about 2300. In porous materials, the transition is gradual with increasing Reynolds number, which necessitates the usage of both terms to characterize the pressure losses in a porous material.

The above model for the pressure gradient (or flow resistance) through a porous material has served as the inspiration for flow resistance characterization of perforated plates. For perforates, the internal geometry is macroscopically regular and well defined, in contrast with porous foams or fibrous materials. Nevertheless, flow path regularity of perforates does not remove the gradual laminar-to-turbulent transition response with respect to Reynolds number as might be expected based on pipe flow. Thus, the pressure loss (flow resistance) across perforates generally tends to behave more like a high-inertia-dominated porous material than a collection of parallel pipe flows. This tendency is believed associated with geometric irregularities at the perforate hole subscale and their effect on flow losses generated by vorticity.

As noted above and in contrast with conventional porous materials (e.g., foams or loosely packed particles), the inertia-related pressure losses for a perforated plate arise mainly from vorticity that is generated exterior to the perforate holes (i.e., exiting jet-like flows). The character of these flows is controlled by the hole Reynolds number, discharge coefficient, and hole aspect ratio. Other microscopic details of the hole geometry may also be involved, such as roughness and hole edge curvature. From the above background, it should be clear that a semi-empirical model for a thin perforate plate, in the paradigm described above, is likely to involve ingredients from pipe flow theory and orifice metering theory. In that vein, a two-parameter flow resistance model for perforated plates of thickness t is given by

$$\theta_f = \frac{R_f}{\rho c} = \frac{a\mu t}{2\rho c(\sigma C_D)d^2} + \frac{\kappa_i + \kappa_e}{2c(\sigma C_D)^2} V_{\text{inc}} \quad (6.5)$$

where the empirical constant a is assigned a value of 64. As suggested above, the first term in Equation (6.5) has its roots in Hagen-Poiseuille pipe flow (Refs. 34 and 40) or in Darcy's law governing seepage through porous media (Ref. 35). The second term can also be derived from orifice metering theory (Ref. 34). Empirical constants ($\kappa_i + \kappa_e$) account for entrance and exit end effects, whereas the discharge coefficient, C_D , accounts for vorticity-associated losses both at the hole walls and exterior to the holes. The quantity ($\kappa_i + \kappa_e$) is taken as unity and a default value for C_D is 0.76 for a sharp-edged orifice. In addition to being dependent on Reynolds number and hole geometry, the discharge coefficient is greatly affected by grazing flow and is therefore a source of systematic and random error in any impedance prediction model. It may also depend weakly on porosity (via hole separation) because of

interference between entry and exit flows through adjacent holes.

In the TP model for resistance, the effect of grazing flow is taken into account by the Rice-Heidelberg model as given by

$$\theta_{gf} = \frac{R_{gf}}{\rho c} = \frac{M_{C/L}}{\sigma\{2 + 1.256(\delta_1/d)\}} \quad (6.6)$$

where R_{gf} is the grazing-flow resistance, $M_{C/L}$ is the free-stream (centerline) Mach number, and δ_1 is the boundary layer displacement thickness. Again, this is a single-hole model that accounts for multiple holes via mass conservation via the open area ratio, σ , as shown in Equation (6.5). The fact that grazing flow affects the discharge coefficient means there should be a direct modification of the contribution from Equation (6.3) when grazing flow is present. This is a significant shortcoming of the TP model as well as the CF model described in the next section. In practice, it is likely a moot issue for many conventional perforates as applied in nacelle ducts because the resistance increase due to grazing flow is the dominant contributor to total resistance. When the quantity δ_1/d is near unity and the grazing-flow effect is dominant, the total perforate resistance from Equation (6.6) is instead approximated by

$$\theta_{gf} = \frac{M_{C/L}}{3\sigma} \quad (6.7)$$

In summary, the complete normalized resistance component is given by

$$\theta = \frac{a\mu t}{2\rho c(\sigma C_D)d^2} + \frac{\kappa_i + \kappa_e}{2c(\sigma C_D)^2} v_{\text{rms}} + \theta_{gf} \quad (6.8)$$

where θ_{gf} is provided by Equation (6.6) or (6.7), depending on the magnitude of grazing-flow velocity. Note that V_{inc} has now been replaced by the rms acoustic velocity, v_{rms} . The presence of v_{rms} forces the calculation of the impedance to use an iterative procedure (described in greater detail below). It is also of interest to note that the nonlinear term scales on the inverse of the square of the open area ratio, whereas the linear and grazing-flow terms scale on the first power of the inverse of the open area ratio. This accentuates the role of the open area ratio when the nonlinear term is a significant contributor relative to the other two terms.

As previously noted, the POHC liner compliance is supplied by the cavity, and is modeled as

$$\chi_{\text{cav}} = -\cot(kh) \quad (6.9)$$

The remaining contributor to the acoustic reactance is the normalized mass reactance due to the perforate facesheet, and is taken to be

$$\chi_{fs} = \frac{k(t + \varepsilon d)}{\sigma C_D} \quad (6.10)$$

where εd is the hole length end correction and

$$\varepsilon = \frac{0.85(1 - 0.7\sqrt{\sigma})}{1 + 305M_{C/L}^3} \quad (6.11)$$

A discussion of this end correction is provided in Reference 41. Early literature (Ref. 36) suggests a value of 0.85 for the no-flow, linear end correction for a single (isolated) orifice. The factor $(1 - 0.7\sqrt{\sigma})$ was provided by Ingard (Ref. 42) to account for open area ratio, and the grazing-flow effect $(1 + 305M_{C/L}^3)$ is due to Rice (Ref. 19). In summary, the complete acoustic reactance is given by

$$\chi = -\cot(kh) + \frac{k(t + \varepsilon d)}{\sigma C_D} \quad (6.12)$$

This is the only component of the model in which the interaction among neighboring holes is taken into account, albeit implicitly, via the end correction, εd . The total acoustic impedance ζ is given by the combination of Equations (6.8) and (6.12).

6.4.2.2 Crandall Full-Solution Model (CF)

The distinguishing feature for the next model (Ref. 43) is the use of a purely analytical solution for oscillatory flow in a circular channel to produce both Poiseuille-type and frequency-dependent viscous losses. Melling (Ref. 36) cites Crandall as the first to give this problem a modern treatment, thus the name for this model. A disadvantage of this approach is that both the resistance and mass reactance components internal to the hole use Bessel functions to describe the in-hole velocity profile. This is handled by defining two different hole end corrections, one for resistance and one for reactance. The model introduces a purely empirical dependence of discharge coefficient C_D upon the t/d ratio and perforate open area ratio σ . The discharge coefficient is employed in the nonlinear resistance contribution as well as the perforate mass reactance. Hole interaction is included via the factor $(1 - 0.7\sqrt{\sigma})$ in mass reactance, and via the factor $(1 - \sigma^2)$ in the nonlinear resistance. Aside from these differences, this model is very similar in its phenomenological basis to the TP model described earlier. However, there is no explicit use of DC flow resistance data. Also, similar to the TP model, the grazing-flow effects are simply superimposed via the Rice-Heidelberg model.

The full equation for normalized liner acoustic impedance is given as

$$\zeta = \theta_0 + \theta_{0,\omega} + S_R v_{rms} + \theta_{gf} + i[\chi_m + \chi_{me} + S_m v_{rms} - \cot(kh)] \quad (6.13)$$

The contributing terms are described below with their individual derivations.

For a single tone source, as was used in the current investigation, the total (incident plus reflected) sound pressure level *SPL* at the surface of the liner with a known impedance ζ is used to compute the rms acoustic velocity v_{rms} as

$$v_{rms} = \frac{P_{ref} 10^{SPL/20}}{\rho c |\zeta|} \quad (6.14)$$

where the reference pressure P_{ref} has a value of 20 μPa (2.9×10^{-9} psi). For multitone or broadband sources, the measured overall *SPL* and the frequency-dependent surface impedance $\zeta(f)$ are used to determine the frequency-dependent acoustic velocity $v_{rms}(f)$ similar to that shown in Equation (6.14). These frequency-dependent components are then combined to determine the rms acoustic velocity used in the current model. Because of the nature of Equation (6.14), an iterative approach must be used to simultaneously determine v_{rms} and ζ .

The effective mass end correction, εd , has different contributions to the resistance and reactance terms. Let

$$\zeta_{0,\omega} = (\theta_0 + \theta_{0,\omega}) + i(\chi_m + \chi_{me}) \quad (6.15)$$

where θ_0 and $\theta_{0,\omega}$ represent the frequency-independent and frequency-dependent components of the normalized linear acoustic resistance, respectively; χ_m is the normalized mass reactance; and χ_{me} is the corresponding mass reactance due to the end correction. The real and imaginary components of $\zeta_{0,\omega}$ are computed as follows:

$$(\theta_0 + \theta_{0,\omega}) = \text{Re} \left\{ \frac{i \omega (t + \varepsilon_{Re} d) / (c \sigma)}{F(k_\mu r)} \right\} \quad (6.16)$$

$$(\chi_m + \chi_{me}) = \text{Im} \left\{ \frac{i \omega (t + \varepsilon_{Im} d) / (c \sigma)}{F(k_\mu r)} \right\} \quad (6.17)$$

where r is the hole radius ($r = d/2$) and ε_{Re} is given by

$$\varepsilon_{Re} = \frac{1 - 0.7\sqrt{\sigma}}{1 + 305M_{C/L}^3} \quad (6.18)$$

and ε_{Im} is given by

$$\varepsilon_{Im} = 0.85 \varepsilon_{Re} \quad (6.19)$$

Equation (6.13) can now be rewritten as

$$\zeta = \zeta_{0,\omega} + S_R v_{\text{rms}} + \theta_{gf} + i\{S_m v_{\text{rms}} - \cot(kh)\} \quad (6.20)$$

The derivations for nonlinear resistance slope, S_R , and nonlinear mass reactance slope, S_m , are given by

$$S_R = \frac{133.6541}{\rho c} \left(\frac{\rho}{2 C_D^2} \frac{1 - \sigma^2}{\sigma^2} \right) \quad (6.21)$$

$$S_m = -0.00207 \frac{k}{\sigma^2} \quad (6.22)$$

and the normalized grazing-flow-induced acoustic resistance, θ_{gf} , is provided by Equation (6.6). It should be noted that Equations (6.21) and (6.22) are empirically derived formulas, with units of seconds per meter. Thus, the numerical coefficient for S_R is dimensionless, and the numerical coefficient for S_m has units of seconds. Finally, $F(k_\mu r)$ is defined (Ref. 33) as

$$F(k_\mu r) = 1 - \frac{2J_1(k_\mu r)}{k_\mu r J_0(k_\mu r)} \quad (6.23)$$

where J_0 and J_1 are zero- and first-order Bessel functions, and k_μ is the wavenumber of the viscous Stokes wave computed from

$$k_\mu^2 = -i \frac{\omega \rho}{\mu} \quad (6.24)$$

Finally, the discharge coefficient is a function of t/d . For $t/d \leq 1$, it is given by

$$C_D = 0.80695 \sqrt{\sigma^{0.1} / e^{-0.5072(t/d)}} \quad (6.25)$$

However, for perforated plates with $t/d > 1$, the discharge coefficient will vary based on skin material and perforation method. A sufficient database is necessary to establish an adequate empirical equation in each case. For example, the following relation is used for electro-deposited nickel-based microperforate plates.

$$C_D = 0.584854 \sqrt{\sigma^{0.1} / e^{-1.151(d/t)}} \quad (6.26)$$

6.4.2.3 Composite Empirical Model (CE)

The Composite Empirical model (CE) (Ref. 44, private communication) blends resistance contributions from a DC flow resistance model with grazing-flow effects due to an effective acoustic velocity (in turn, due to the turbulent boundary layer) in a way that the TP and CF models do not. The grazing-flow resistance appears as a cross-term derived by invoking contributions from the DC flow resistance and the effective acoustic velocity (calculated as root-square-sum of the purely acoustic particle velocity), as well as an equivalent particle velocity generated by the turbulent flow. The detailed structure of this model is as follows:

$$\zeta = \theta_{DC} + \theta_{AC} + 1.25\theta_I v_{\text{eff}} C_{D,\omega} + i(\chi_m + \chi_{me} + \chi_{cav}) \quad (6.27)$$

where θ_{DC} is the steady flow resistance, and θ_{AC} and θ_I are the frequency-dependent and inertial contributions to the resistance, respectively. v_{eff} is an effective rms acoustic velocity, $C_{D,\omega}$ is a discharge coefficient correction for unsteady flow, χ_m is the internal mass reactance, χ_{me} is the attached mass reactance, and χ_{cav} is the classical cavity reactance given by Equation (6.9). Expressions for the above impedance components are

$$\theta_{DC} = 1.75 \left(\frac{32\mu t}{\rho c \sigma d^2} \right) \quad (6.28a)$$

$$\theta_{AC} = 2.82 \sqrt{\frac{\mu \omega}{\rho}} \left(\frac{t/d + 1}{c \sigma} \right) \quad (6.28b)$$

$$\theta_I = \left\{ \frac{1}{2c(\sigma C_D)^2} \right\} \quad (6.28c)$$

$$C_{D,\omega} = 1 - \exp \left[- \left(\frac{0.53 v_{\text{eff}}}{\sigma f d} \right)^{1.2} \right] \quad (6.29)$$

$$v_{\text{eff}} = \sqrt{v^2 + 0.2 \mathcal{B} C_D^2 \sigma^2 V_{gf}^2} \quad (6.30a)$$

$$\mathcal{B} = 0.05 + 0.11(d/\delta_2) \quad (6.30b)$$

where v is the acoustic velocity at a given frequency, V_{gf} is the grazing-flow speed, and δ_2 is the boundary layer momentum thickness. For a given incident sound excitation level (in decibels), the effective rms acoustic velocity can also be computed as

$$v_{\text{eff}} = \frac{P_{\text{ref}} \cdot 10^{SPL/20}}{\rho c |\zeta|} \quad (6.31)$$

and can be used to determine the impedance via an iterative process. The mass reactance terms are given by

$$\chi_m + \chi_{me} = 1.11 \left(\frac{\omega}{c} \right) \left\{ t + \frac{0.85d(1 - 0.9\sqrt{\sigma})}{e^z} \right\} \quad (6.32)$$

where

$$z = 0.275 \left(\frac{\omega}{c} \right)^2 + \frac{0.035 v_{\text{eff}}}{\sigma f d} + 8.65 \left(\frac{V_{gf}}{c} \right)^2 + 0.8192 \left(\frac{V_{gf}}{c} \right) \quad (6.33)$$

and the cavity reactance χ_{cav} is given by Equation (6.9).

6.4.2.4 Fluid Mechanical Model (FM)

The Fluid Mechanical model (FM) (Ref. 45) employs an orifice-centered control volume to describe the acoustically driven unsteady flow into the orifice-cavity system. Although the model employs five empirically determined parameters, it is also the most “first principles based” of the four models considered in this investigation. To keep the model one-dimensional, equations employing conservation of mass and momentum (the component normal to the surface) are used to parse the flow into inviscid-core and boundary-layer components. Viscous scrubbing losses and inertial losses are restricted to the boundary-layer and inviscid-core flows, respectively. Consequently, the resulting time-domain equation of motion for fluid momentum is nonlinear in velocity, arising from momentum flux terms at the control volume surfaces. Five simplifications are employed to make the differential equation amenable to solution for a time-harmonic excitation. Thus, the following empirical parameters are introduced:

- (1) \mathcal{K}_{ss} and \mathcal{K}_{ac} steady-state and acoustic viscous loss parameters, respectively
- (2) C_D orifice discharge coefficient
- (3) \mathcal{H} orifice nonlinear inertial length

Parameters \mathcal{K}_{ss} and \mathcal{K}_{ac} are dependent upon t/d , the orifice thickness-to-diameter ratio, and C_D is dependent upon a nondimensional orifice velocity (like a Reynolds number) and frequency. The parameter \mathcal{H} is an orifice inertial length parameter that is unknown and must be modeled experimentally (Ref. 46), and the ratio \mathcal{H}/d is strongly dependent upon acoustic excitation and frequency. All of these model parameters have been derived using POHCs with the following conditions:

$$\begin{aligned} 0.4 &\leq t \leq 129 \text{ mm} \quad (0.02 \leq t \leq 5.1 \text{ in.}) \\ 0.8 &\leq d \leq 1.6 \text{ mm} \quad (0.03 \leq d \leq 0.06 \text{ in.}) \\ 0.5 &\leq t/d \leq 16 \\ 0.0039 &\leq \sigma \leq 0.0156 \\ 75 &\leq SPL \leq 140 \text{ dB} \end{aligned}$$

Therefore, application of this model outside these parameter ranges should be used with caution.

The resistance component of the FM model is given by

$$\theta = \sqrt{\left(\frac{1-C_D}{C_D}\right)\left(\frac{p_{pk}}{\rho c^2 \sigma^2}\right) + \left(\frac{\theta_L}{2}\right)^2} + \left(\frac{\theta_L}{2}\right) \quad (6.34)$$

where p_{pk} is the peak acoustic excitation pressure at the surface of the liner and

$$\theta_L = \frac{\mu t}{\rho c d^2 \sigma} \left(\mathcal{K}_{ss} + \mathcal{K}_{ac} \sqrt{\frac{\omega d^2 \rho}{\mu}} \right) \quad (6.35)$$

The reactance component for a resonator with a cavity length of h is given by

$$\chi = \frac{\omega \mathcal{H}}{\sigma c} - \cot(kh) \quad (6.36)$$

As mentioned previously, \mathcal{K}_{ss} and \mathcal{K}_{ac} are related to viscous losses and have a simple dependency upon the ratio of plate thickness to orifice diameter, t/d , given by

$$\mathcal{K}_{ss} = 13 + 10.23 \left(\frac{t}{d} \right)^{-1.44} \quad (6.37a)$$

and

$$\mathcal{K}_{ac} = 3 + 2.32 \left(\frac{t}{d} \right)^{-1} \quad (6.37b)$$

The orifice nonlinear inertial length, \mathcal{H} , is given by

$$\mathcal{H} = \mathcal{D} \left\{ 1 - (1 - \mathcal{H}_{\text{res}}) \exp \left[-\mathcal{M} \left(\frac{f}{f_{NL}} - 1 - f_0 \right)^4 \right] \right\} \quad (6.38)$$

where the single hole orifice inertial length for low sound pressure level (SPL), \mathcal{D} , is

$$\mathcal{D} = \left(t + \frac{0.85d}{1 + 1.25\sqrt{\sigma}} \right) \left\{ 1 + \frac{0.0263(\mathcal{N} - 1)}{1 + 0.2554(\mathcal{N} - 1)} \right\}^{-2} \quad (6.39)$$

and \mathcal{N} is the number of holes in the perforated plate (facesheet). Nondimensional parameters \mathcal{M} , and \mathcal{V} are defined as

$$\begin{aligned} \mathcal{M} = & \left\{ 0.011 + 2.086 \left(\frac{t}{d} \right) \right\} \mathcal{V}^{-\eta_0} \\ & + 13.06 \left\{ 1 - \exp \left[-64.9 \left(\frac{t}{d} \right)^{4.365} \right] \right\} \end{aligned} \quad (6.40a)$$

$$\eta_0 = 0.0325 \left(\frac{t}{d} \right)^{-3.7} + 3.4 \quad (6.40b)$$

and

$$\mathcal{V} = \sqrt{\frac{p_{pk}}{\rho v_{\text{ref}}^2}} \quad (6.40c)$$

where

$$v_{\text{ref}} = 2\pi f_L \left(t + \frac{0.85d}{1+1.25\sqrt{\sigma}} \right) \quad (6.40d)$$

The three frequency parameters, f_0 , f_L , and f_{NL} , are given by

$$f_0 = \left\langle \frac{1.34 \left(\frac{t}{d} \right)}{\mathcal{V} \left\{ 1 + 18.81 \left(\frac{t}{d} \right) \right\}} \right\rangle + 0.264 \left\{ 1 - e^{-4.49(t/d)} \right\} - 0.436 \quad (6.41a)$$

$$f_L = \frac{c}{2\pi} \left\{ 1 + \frac{0.0263(\mathcal{N} - 1)}{1 + 0.2554(\mathcal{N} - 1)} \right\} \times \sqrt{\frac{\sigma}{h} \left(t + \frac{0.85d}{1+1.25\sqrt{\sigma}} \right)^{-1}} \quad (6.41b)$$

and

$$f_{NL} = f_L \left\{ 1 + \left\langle 0.785 - 0.76 \left\{ 1 - \exp \left[-3.63 \left(\frac{t}{d} \right) \right] \right\} \right\rangle \times \left\{ 1 - \exp \left[-3.63 \left(\frac{t}{d} \right)^{0.6} \mathcal{V}^2 \right] \right\} \right\} \quad (6.41c)$$

The nonlinear inertial length at the resonance condition is given by

$$\mathcal{H}_{\text{res}} = \frac{1 + 0.7254 \left(\frac{t}{d} \right)^{-1.227} \mathcal{V}^{\eta_1}}{1 + 1.018 \left(\frac{t}{d} \right)^{-1.411} \mathcal{V}^{\eta_1}} \quad (6.42)$$

where

$$\eta_1 = 3.419e^{-0.1174(t/d)} \quad (6.43)$$

C_D is determined by curve fitting to data taken at the resonant frequency of the liner. First, a curve fit to C_D at resonance, $C_{D,\text{res}}$, is determined for selected resonators to get

$$C_{D,\text{res}} = \frac{1 + m_{\text{res}} \mathcal{V}^2}{1 + n_{\text{res}} \mathcal{V}^2} \quad (6.44)$$

where

$$m_{\text{res}} = \frac{1 + 110.5e^{0.647(t/d)}}{1 + 0.109e^{0.647(t/d)}} \quad (6.45a)$$

$$n_{\text{res}} = \frac{1 + 168.5e^{0.647(t/d)}}{1 + 0.109e^{0.647(t/d)}} \quad (6.45b)$$

Further curve fits for a range of selected resonators have been obtained to construct the general discharge coefficient, which is given by

$$C_D = \frac{C_{D,\text{res}} + m_0 f_{\text{non}}^2}{1 + n_0 f_{\text{non}} + m_0 f_{\text{non}}^2} \quad (6.46)$$

where f_{non} is a nondimensional frequency given by

$$f_{\text{non}} = \frac{f_{NL}}{f} - 1 \quad (6.47)$$

and the curve-fitting parameters m_0 and n_0 for C_D include

$$m_0 = m_1 + m_2 e^{-m_3 \mathcal{V}} \quad (6.48)$$

where

$$m_1 = 18.81 \left(\frac{t}{d} \right) - 57.11 \left\{ 1 - e^{-0.18(t/d)} \right\} \sqrt{\frac{t}{d}} \quad (6.49a)$$

$$m_2 = \exp \left[\frac{33.5 \left(\frac{t}{d} \right) - 78 \left(\frac{t}{d} \right)^2 + 131 \left(\frac{t}{d} \right)^3 + 917 \left(\frac{t}{d} \right)^4}{1 + 148 \left(\frac{t}{d} \right)^4} \right] \quad (6.49b)$$

$$m_3 = 43.2 \left(\frac{t}{d} \right) - 147.1 \left\{ 1 - e^{-0.19(t/d)} \right\} \sqrt{\frac{t}{d}} \quad (6.49c)$$

and

$$n_0 = \frac{n_1 + n_2 \mathcal{V}}{1 + n_3 \mathcal{V}} \quad (6.50)$$

where

$$n_1 = \frac{-3.44 - 0.182 \left(\frac{t}{d} \right)}{1 + 0.342 \left(\frac{t}{d} \right)} \quad (6.51a)$$

$$n_2 = \frac{18.23 + 1.33 \left(\frac{t}{d} \right)}{1 + 0.151 \left(\frac{t}{d} \right)} \quad (6.51b)$$

$$n_3 = \frac{38}{1 + 1.3 \times 10^{-7} \left(\frac{t}{d} \right)^2} \quad (6.51c)$$

6.4.2.5 Grazing-flow Contribution to Resistance: Comparison of Models

The grazing-flow contribution to perforate resistance is included in the TP and CF models via the Rice-Heidelberg grazing-flow resistance model (Refs. 41 and 43). It is simply superimposed onto the respective no-flow models as

$$\theta_{gf} = \frac{M_{C/L}}{\sigma(2 + 1.256(\delta_1/d))} \quad (6.52)$$

where θ_{gf} is the grazing-flow resistance, $M_{C/L}$ is the free-stream Mach number (at duct centerline), σ is the open area ratio (porosity) of the perforate, δ_1 is the boundary layer displacement thickness, and d is the hole diameter. The porosity in the denominator accounts for the difference between a single hole and the entire perforate, but it does not account for hole-to-hole interactions. The boundary layer correction term, involving δ_1/d , is based on empirical correlations with data and is attributed to Hersch (Ref. 46). It is of interest to note that in the limiting case as δ_1 approaches 0, θ_{gf} reduces to exactly one-half the free-stream Mach number (with due accounting for porosity):

$$\lim_{\delta_1 \rightarrow 0} \theta_{gf} \rightarrow \frac{1}{2} \frac{M_{C/L}}{\sigma} \quad (6.53)$$

The above limiting value is 20 percent less than that predicted by a purely theoretical, inviscid flow dissipation model of Baumeister (Ref. 47). His model is based on the hypothesis that the grazing flow sweeps nearly all the orifice jet kinetic energy into the mean flow when the orifice jet velocity is nearly the same as the mean-flow velocity. Under this circumstance, the Baumeister model predicts a grazing-flow contribution to resistance of

$$\theta_{gf} = \frac{1}{1.6} \frac{M_{C/L}}{\sigma} \quad (6.54)$$

Thus, under the inviscid flow model restrictions, the dominant term in the Rice-Heidelberg model can be viewed as being due to an inviscid flow dissipation mechanism. The term involving boundary layer displacement δ_1 can be interpreted as a correction on an inviscid flow dissipation mechanism. As a matter of consistency, the Rice-Heidelberg grazing-flow resistance tends to 0 in the limit of increasing δ_1/d .

A worrisome issue arises with the “tacked-on” nature of the Rice-Heidelberg model to account for the grazing-flow resistance in the TP and CF models. The discharge coefficient C_D in the TP and CF models is inferred from DC flow resistance measurements. When such measurements are conducted with grazing flow, the discharge coefficient will typically be substantially different from the corresponding value observed in the absence of grazing flow. This dependence of the discharge

coefficient on the grazing flow is not captured in the TP and CF models. As a result, the grazing-flow effect is isolated to the Rice-Heidelberg contribution. Correspondingly, the counterpart of a discharge coefficient does not appear in the inviscid dissipation part of the Rice-Heidelberg model. For those cases where the grazing-flow contribution dominates the resistance, this decoupling of the grazing-flow effect and acoustics may not appreciably affect the total resistance for conventional perforates. However, for low to modest grazing-flow speeds, the respective contributions to the acoustic resistance by acoustics and the grazing flow may be sufficiently close to cause measurable systematic error. Similarly, the respective contributions of acoustics and grazing flow to the acoustic resistance are nearly the same for microperforates, which have a relatively large facesheet thickness-to-hole diameter ratio (t/d). Thus, significant systematic error can be incurred for these types of liners as well.

The CE model avoids the issue discussed above. In this model, the acoustic and fluid dynamic effects are integrated, and the discharge coefficient appears explicitly in the inertial loss and grazing-flow resistance terms. Green (Ref. 35) provides the phenomenological basis for the flow losses through a general porous medium, and Eversman (Ref. 17) describes the inclusion of grazing flow for thin porous materials suitable for the resonant liners of interest here. The grazing-flow resistance is assumed to derive from a pseudo-acoustic pressure given by

$$\Delta p_{rms} = K \left(\frac{1}{2} \rho V^2 \right) \quad (6.55)$$

where K is an empirical function of the grazing-flow boundary layer, facesheet geometry and effective roughness. This pseudo-acoustic pressure, Δp_{rms} , combines with the acoustic excitation pressure in a root-sum-squared fashion to define an increment in the total rms particle velocity through the perforate. This is an essential difference between the CE model and the other two (TP and CF) models.

6.4.2.6 Summary of Salient Features of Models

In this section, we contrast some of the similarities and distinctions among the above four models.

Similarities:

(1) Each acoustic resistance model for the perforate facesheet is physics based and employs lumped-element and quasi-steady flow assumptions to model unsteady flow losses. This is justified because all dissipation is confined to a layer, centered at the perforate thickness midspan, with thickness much smaller than the shortest wavelength of interest.

(2) These assumptions allow an effective lumped-element resistance, R_{eff} , to be calculated from a knowledge of the DC flow resistance and a prescribed unsteady velocity through the perforate, as follows:

$$R_{\text{eff}} = \frac{\int_0^T R_f(v)v(\tau)^2 d\tau}{\int_0^T v(\tau)^2 d\tau} \quad (6.56)$$

where T is the period of the longest wavelength of interest. Each of the four models employ an iterative scheme to determine a velocity time history consistent with a flow resistance model and specified acoustic excitation.

(3) Based on a Fok's formula (Ref. 36), hole-to-hole interactions are assumed to be weak for conventional POHC liners. As such, both multihole effects and hole-to-hole interactions are included via the facesheet porosity parameter for the resistance component.

(4) Grazing-flow effects are decoupled from viscous and inertial resistance contributions.

(5) The cavity is purely compliant and therefore provides no dissipation.

Distinctions:

(1) TP (Two-Parameter): The TP model is the simplest of the four models included in this study. It makes minimum use of empirical parameters, the most prominent being the Hagen-Poiseuille laminar flow friction factor, a , and orifice discharge coefficient, C_D , to predict frequency-independent linear and nonlinear contributions to resistance, respectively. A modest hole-interaction effect is included in the reactance, where the hole end correction is decreased by the factor $(1 - 0.7\sqrt{\sigma})$ (see Eq. (6.11)).

(2) CF (Crandall Full-Solution): The CF model includes a frequency-dependent viscous resistance contribution via the full Navier-Stokes solution (due to Crandall) for oscillatory flow in a circular channel. Separate end corrections are used for resistance and reactance. Also, orifice thickness-to-hole diameter ratio and porosity dependence are incorporated into the discharge coefficient parameter.

(3) CE (Composite Empirical): The CE model integrates effects of grazing flow on resistance by adding a turbulent boundary-layer-driven excitation onto the acoustic excitation on an energy basis.

(4) FM (Fluid Mechanical): The FM model employs a first-principles-based application of the mass and momentum equations to an orifice-centered control volume. These equations are manipulated and combined into a time-domain, nonlinear, differential equation. Five assumptions are applied to solve this equation. This solution characterizes the unsteady orifice flow for harmonic acoustic excitation. The solution procedure gives rise to five empirical parameters that must be evaluated experimentally via acoustic impedance measurements. Unlike the other three models, it does not include grazing-flow effects.

6.5 Database Creation for Uncertainty Assessment

This section describes the creation of a statistical database for both the input parameters and the processing of those parameters through the prediction model.

6.5.1 Assessment Liner Geometry and Input Preparation

During the late 1990s, a study was conducted by four organizations (NASA, Boeing, GE, and Goodrich) to compare impedance measurement methodologies (Ref. 48). The facesheet geometry (see Table 6.1) for the single-layer baseline liner used in that study was considered to be at or near the median for each geometric parameter (hole diameter, facesheet thickness, and porosity). This same liner configuration was chosen as the assessment liner for the current investigation, such that results from this study could be compared with those from previous studies conducted by each of these organizations. This assessment liner was fabricated in two configurations (50.8- by 50.8-mm and 50.8- by 406.4-mm active surface areas) to allow testing in the NASA Langley normal incidence tube (NIT) and grazing incidence tube (GIT), respectively. Each configuration was fabricated from the same parent material, using the same fabrication processes. In the several graphics that follow, statistical metrics (95% confidence intervals) are presented. The 50.8- by 50.8-mm configuration was tested 14 times in the NIT at each test condition. Similarly, the 50.8- by 406.4-mm configuration was tested 8 to 10 times in the GIT at each test condition of interest to provide meaningful statistical metrics. Repeat runs were conducted at different times of the year, and the assessment liner of interest was removed and reinstalled between tests.

6.5.2 Quantifying Input Parameter Uncertainty

In what follows, a brief description is provided of how each input parameter was measured along with a description of how the uncertainty in that parameter was determined. For those parameters that were measured at least once per test (between 8 and 14 times), the mean and standard deviation were computed in the classical manner. For parameters that were determined to be independent of any particular test, the methods chosen for estimating their means and standard deviations are included with the description below. The resultant means and standard deviations for the geometrical parameters associated with the assessment liner are provided in Table 6.1. Limited tests with other liners showed very similar results. Because of time constraints, this was the only liner tested a sufficient number of times to support meaningful statistical estimates. Thus, only the results for this liner are

discussed in the remainder of this chapter. The aeroacoustic parameter mean values and standard deviations for the assessment liner are provided in Table 6.2 and Table 6.3, respectively.

6.5.2.1 Geometric Parameters

As mentioned earlier, each configuration (50.8 by 50.8 mm and 50.8 by 406.4 mm) was fabricated from the same parent material. Thus, it was assumed that the geometric parameters have the same values for either configuration. For convenience, these parameters were measured on the smaller samples. The following parameters were measured at 10

randomly selected locations across the sample surface. The corresponding means and standard deviations computed from these measurements are provided in Table 6.1.

(1) Facesheet thickness (t): The thickness was measured using a computer-aided system that allows the user to move a probe until it makes contact with a surface and then records the location in a three-dimensional coordinate system. The facesheet thickness was determined by taking the difference between the results from measurements taken in this manner from both sides of the facesheet.

(2) Cavity depth (h): The cavity depth was measured with the same contact probe system described above.

TABLE 6.1.—GEOMETRIC PARAMETER STATISTICAL INPUTS^a

Facesheet thickness, t , mm (in.)		Hole diameter, d , mm (in.)		Cavity depth, h , mm (in.)		Open area ratio, σ	
Mean	StDev	Mean	StDev	Mean	StDev	Mean	StDev
0.813 (0.032)	0.025 (9.8×10 ⁻⁴)	0.965 (0.038)	0.000	38.176 (1.50)	0.076 (3×10 ⁻³)	0.089	0.002

^aMean indicates mean value and StDev, the standard deviation.

TABLE 6.2.—AEROACOUSTIC PARAMETER MEAN VALUES

Test case	Test rig ^a	Average Mach number, M_{ave}	Sound pressure level, SPL , dB	Static pressure, P_s , Pa (psi)	Static temperature, T_s , K (°R)	Discharge coefficient, C_D	Boundary-layer displacement thickness δ_1 , mm (in.)	Boundary-layer momentum thickness, δ_2 , mm (in.)
1	NIT	0.000	120.0	101 601 (14.736)	295.8 (532.4)	0.771	0.00	0.00
2	NIT	0.000	140.0	101 438 (14.712)	295.4 (531.7)	0.771	0.00	0.00
3	GIT	0.000	122.3	101 701 (14.751)	295.8 (532.4)	0.771	0.00	0.00
4	GIT	0.000	140.5	101 686 (14.748)	295.8 (532.4)	0.771	0.00	0.00
5	GIT	0.252	121.3	101 687 (14.495)	295.3 (531.5)	0.771	0.05 (0.002)	1.75 (0.07)
6	GIT	0.251	140.7	101 933 (14.784)	295.2 (531.4)	0.771	0.05 (0.002)	1.75 (0.07)
7	GIT	0.400	120.2	101 839 (14.771)	293.8 (528.8)	0.771	0.05 (0.002)	1.75 (0.07)
8	GIT	0.400	140.6	101 823 (14.768)	293.8 (528.8)	0.771	0.05 (0.002)	1.75 (0.07)

^aThe NASA Langley normal incidence tube (NIT) or grazing incidence tube (GIT).

TABLE 6.3.—AEROACOUSTIC PARAMETER STANDARD DEVIATIONS

Test case	Test rig ^a	Average Mach number, M_{ave}	Sound pressure level, SPL , dB	Static pressure, P_s , Pa (psi)	Static temperature, T_s , K (°R)	Discharge coefficient, C_D	Boundary-layer displacement thickness δ_1 , mm (in.)	Boundary-layer momentum thickness, δ_2 , mm (in.)
1	NIT	0.0000	0.2	611 (0.089)	0.8 (1.4)	0.135	0.000	0.000
2	NIT	0.0000	0.4	810 (0.118)	1.3 (2.3)	0.135	0.000	0.000
3	GIT	0.0000	1.6	387 (0.056)	0.9 (1.6)	0.135	0.000	0.000
4	GIT	0.0000	1.1	485 (0.070)	0.6 (1.1)	0.135	0.000	0.000
5	GIT	0.0012	0.9	790 (0.115)	0.3 (0.5)	0.135	0.004 (0.00016)	0.102 (0.004)
6	GIT	0.0012	0.8	862 (0.125)	0.2 (0.4)	0.135	0.004 (0.00016)	0.102 (0.004)
7	GIT	0.0007	1.6	783 (0.114)	0.2 (0.4)	0.135	0.001 (0.00004)	0.102 (0.004)
8	GIT	0.0006	1.2	754 (0.109)	0.2 (0.4)	0.135	0.001 (0.00004)	0.102 (0.004)

^aThe NASA Langley normal incidence tube (NIT) or grazing incidence tube (GIT).

(3) Hole diameter (d): A set of precision pins was used to determine the hole diameter of each of the 10 randomly selected holes. The outer diameter of the largest pin that would fit through a hole was used as the diameter. All holes were observed to have the same diameter. It should be noted that this assumes the holes to be perfectly round. If they are not, the precision pins provide a measure of the minimum width of the hole opening.

(4) Open area ratio (σ): This parameter is a function of the hole diameter and the distances between adjacent rows and columns of holes (staggered rows to form equilateral hole patterns). The mean and standard deviation of the hole diameters were computed based on measurements described above. The distance between adjacent rows and columns was determined using the contact probe system described above. The open area ratio mean was then computed using

$$\sigma = \frac{\pi d^2}{4s_r s_c} \quad (6.57)$$

where s_r and s_c are the row and column separation distances, respectively. The mean open area ratio is taken to be the value computed using the mean values of the corresponding parameters (d , s_r and s_c). Also, since these parameters are assumed to be uncorrelated, the standard deviation is given by

$$StDev(\sigma) = \left\langle Mean^2(\sigma) \left\{ \left(\frac{2}{d} \right)^2 Var(d) + \left(\frac{1}{s_r} \right) Var(s_r) + \left(\frac{1}{s_c} \right) Var(s_c) \right\} \right\rangle^{0.5} \quad (6.58)$$

where $Mean$, $StDev$, and Var represent the mean, standard deviation, and variance of the selected parameter.

6.5.2.2 Aeroacoustic Parameters

These parameters are associated with the aeroacoustic environment in which a test was conducted. The following provides a description of how each parameter is “measured” in the NASA Langley NIT and GIT.

(1) Static pressure (P_s):

- (a) The atmospheric pressure in the test facility is recorded prior to each test in the NIT; this is taken to be the static pressure for the NIT tests.
- (b) A pitot-static probe mounted in the center of the GIT, downstream of the test window, is used to record the static pressure at the beginning of each test. It is of interest to note that at a centerline Mach number of 0.3, the static pressure gradient in the hard-wall section has been reported as 1733 Pa/m (0.08 psi/ft). This corresponds to a variation of about 704 Pa (0.102 psi) over a distance equal to the assessment

liner length, comparable to a range of standard deviations in static pressures from Table 6.3 of 387 to 862 Pa (0.056 to 0.125 psi) (Ref. 13).

(2) Static temperature (T_s):

- (a) The static temperature for NIT tests is taken to be the room temperature in the test facility.
- (b) The static temperature in the GIT is recorded with the pitot-static probe mentioned above.

(3) Centerline and average Mach numbers (M_{CL} and M_{ave}):

- (a) The Mach number in the NIT is 0.
- (b) When flow is turned on in the GIT, the prediction models require either a centerline Mach number or a cross-section-averaged Mach number. Since the flow profile changes lengthwise along the liner, the centerline Mach number also changes, and to a lesser extent, the cross-section-averaged Mach number changes. Thus, when a prediction code requires a centerline Mach number as input, this is determined by averaging the centerline Mach number at three locations: just upstream of the liner leading edge, at the length-wise mid-span, and just downstream of the trailing edge. The downstream location, centerline Mach number is used as the facility set point, and is indexed to the average of the three centerline Mach numbers via a curve fit. When the cross-section-averaged Mach number is required, the same procedure is adopted, except that cross-section-averaged Mach numbers replace the centerline Mach numbers.

(4) Boundary layer displacement thickness (δ_1):

- (a) The boundary layer displacement thickness in the NIT is 0.
- (b) For the GIT tests, this parameter was assumed to be correlated with the centerline Mach number as determined in the earlier test (Ref. 49). This parameter was not measured during each test, but was assumed to be solely a function of the target M_{CL} . As such, the variability was taken to be the range of boundary layer displacement thickness over the length of the liner (i.e., difference between values computed at the upstream and downstream planes). This range was assumed to span the full range of uncertainty for this parameter, $\pm 3 \cdot StDev(\delta_1)$.

(5) Boundary layer momentum thickness (δ_2):

This parameter was handled in the same manner as described above for boundary layer displacement thickness.

(6) Discharge coefficient (C_D):

During the late 1990s, a study was conducted by four organizations (NASA, Boeing, GE, and Goodrich) to compare impedance measurement methodologies.

During this study (Ref. 39), tests were conducted with liners made from the same parent materials as those used in the current study. To improve statistical confidence, a number of samples fabricated using the same manufacturing process were added to this database, and DC flow resistance measurements were conducted to reduce the discharge coefficient for each sample. The mean (0.771) and standard deviation (0.135) reported for this series of tests are used in the current investigation. The reader will note that the standard deviation on C_D is 17.5 percent of the mean value. This percent standard deviation is greater than that for any other input variable, by about a factor of 3 (see Table 6.2 and Table 6.3). It should also be noted that there are multiple methods in use to determine the discharge coefficient of a conventional liner. These methods tend to be paired with corresponding impedance prediction models, such that the discharge coefficients are only applicable to the paired impedance prediction model. Given the importance of the discharge coefficient in most impedance prediction models, it is our view that significant benefit could be gained by settling on a single methodology. In the absence of this consensus, the discharge coefficient provided in Reference 39 is used in all impedance prediction models that do not offer an explicit, independent method of calculation.

(7) Excitation level (*SPL*):

- (a) A reference microphone flush mounted in the NIT duct wall 6.35 mm (0.25 in.) from the surface of the liner is used to record the sound pressure level *SPL*.
- (b) A microphone mounted in the lower wall of the GIT at the “computational source plane” (101.6 mm (4 in.) upstream of the liner leading edge) is used to record the source *SPL*. Since the *SPL* is reset for each frequency of interest (in the NIT and GIT), this frequency dependence of the *SPL* variability is included in the current investigation. Thus, an independent set of means and standard deviations is used at each frequency (based on corresponding measurements in the NIT and GIT). Note the GIT computational domain used in the current investigation is of shorter axial extent than that typically reported. A problem in the test setup resulted in an *SPL* variation that is larger than that typically observed (± 0.5 dB) in this test apparatus.

6.5.2.3 Processing Input Parameter Uncertainty Through Impedance Prediction Models

A Monte Carlo approach was used to estimate the 95% confidence intervals for the impedance prediction models, which were compared with 95% confidence intervals derived from zero-order replication tests (Ref. 10) conducted in the NASA Langley test rigs (NIT and GIT). As mentioned earlier, between 8 and 14 tests were conducted in the NIT and GIT at each aeroacoustic set point of interest (i.e., at each

frequency, *SPL*, and Mach number). The frequency was assumed to be deterministic (i.e., $StDev = 0$), but all other parameters were assumed to vary about their respective means. Thirty-one simulations were then conducted for each impedance prediction code, with their respective inputs based on these Gaussian distributions for each parameter of interest. For example, 31 values of static pressure were randomly selected from the Gaussian distribution generated by the procedure described above. This process was used for all of the geometric and aeroacoustic parameters except the source excitation level (*SPL*). In order to capture the additional variability in the *SPL*, a set of 31 (1 per simulation) values of *SPL* was randomly selected from the *SPL* Gaussian distribution at each test frequency of interest (i.e., the *SPL* at each frequency was independent of that selected for all other frequencies). The impedance prediction codes were then used to perform simulations based on these inputs, for 100 Hz increments from 400 to 3000 Hz. The means and standard deviations of the predicted impedance at each test frequency were then used to compute 95% confidence intervals; comparisons of these prediction confidence intervals with the corresponding measurement confidence intervals are used to highlight capabilities and limitations of the existing processes.

6.6 Results and Discussion

A number of tests and model simulations were conducted to evaluate the measurement processes and impedance prediction models presented above. This section provides results of these evaluations.

6.6.1 Graphical Format and Interpretation

Monte-Carlo simulations performed on the impedance prediction models are used to compute means and 95% confidence intervals (CIs). Figure 6.6 provides an example of how these results are compared with those from statistical sampling generated by repeated impedance measurements. The graphic format described below is information intensive and is key to interpreting the results. This format is used for comparisons of measured and predicted results. A similar format is also used to describe comparisons of two measured results.

The graphic ordinate is in normalized impedance units (in Figure 6.6, resistance), and the abscissa is frequency in hertz. The shaded regions indicate the measured and predicted CIs. A red region, bounded by dotted lines, represents a measured CI. Correspondingly, a green region, bounded by dashed lines, represents a predicted CI. Solid red and green lines depict the mean values for the measured and predicted impedances, respectively. Regions where the measured and predicted CIs overlap are shaded yellow. Thus, perfect agreement between the measured and predicted impedances would result in coincident means and CIs. However, it should be noted that coincidence between measured and predicted means does not imply the absence of systematic error, but rather that the systematic errors of the measurements and prediction are exactly the same. These systematic errors can be zero, but do

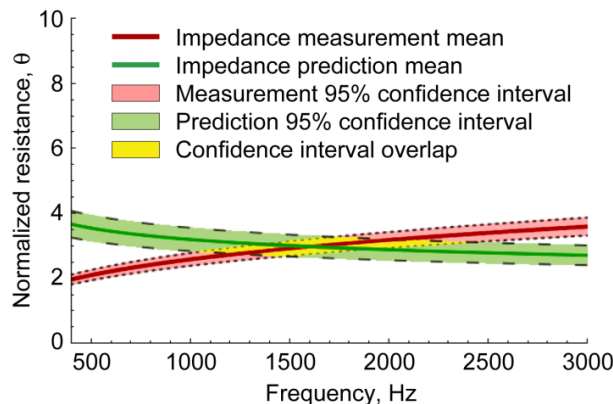


Figure 6.6.—Representative format for comparison of impedance prediction and measurement means and 95% confidence intervals.

not have to be. The reader should also note that measurements were taken in 100-Hz increments in the NIT and in 500-Hz increments in the GIT because data acquisition and processing is more labor and computation intensive for the GIT. The predictions were performed at 100-Hz increments.

In pursuit of the final goal to relate uncertainty analysis, as described here, to as-yet-unknown specification limits, the following language convention is adopted for comparing measurements with predictions. It is supposed that the prediction CIs are to be taken as the provisional or default specification limits, in the SPC sense. The objective is then to ascertain to what degree the prediction CIs subsume the measurement CIs, as would be the case if they were true specification limits. It is not known a priori how to parse systematic error between measurements and predictions. Thus, an out-of-compliance condition signifies that accuracy and precision of both the prediction and the measurement are to be scrutinized. Ultimately, both predictions and measurements should be independently validated to a level such that an out-of-compliance condition can be attributed to the liner fabrication process (assignable causes) at some stage prior to final product production. An important aspect of this approach to uncertainty is the inherent tradeoff between accuracy and precision to achieve compliance within specification limits.

6.6.2 Comparison of NIT and GIT Measurements With No Flow

In this section, we focus on the measurements conducted in the NIT and GIT. Comparisons between measured and predicted results are discussed in a subsequent section. For a local-reacting liner, there should be no difference between normal incidence impedance spectra measured in a normal incidence or grazing incidence environment. Thus, any differences between the impedances measured in the two test rigs are indicative of either systematic or random error. We begin with a discussion of the results in the vicinity of the zero reactance crossing point (i.e., the liner resonance), as POHC liners are generally most effective for frequencies near resonance.

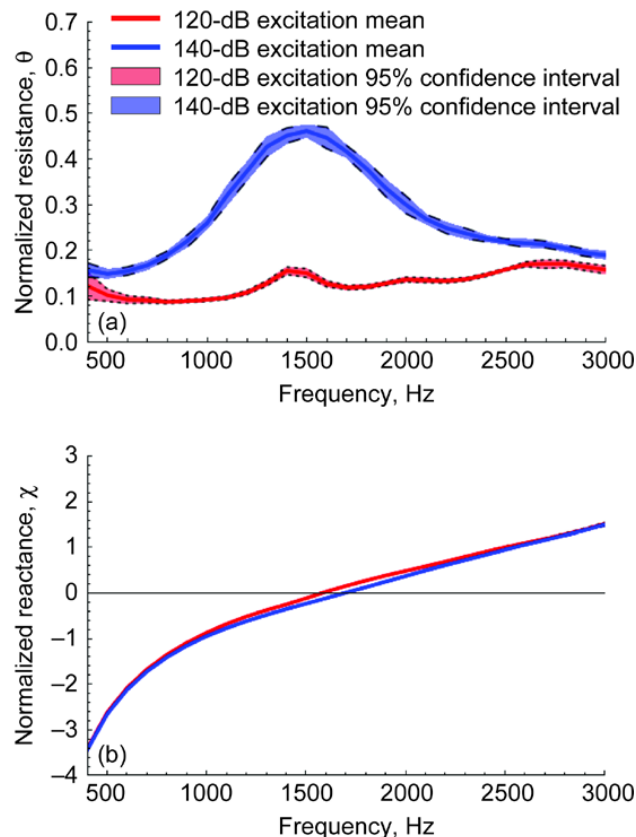


Figure 6.7.—Results from NIT impedance measurements with source excitation levels of 120 and 140 dB conducted at 100-Hz increments. (a) Resistance. (b) Reactance.

The NIT measurements for 120- and 140-dB excitations are shown in Figure 6.7. The resistance CIs (red and blue shading for 120 and 140 dB excitations, respectively) are very tightly centered on the measured means, with very modest CI growth at the low end of the frequency range. The resonance peak mean resistance increases from 0.16 to 0.45 with an excitation increase from 120 to 140 dB. For the reactance spectra, the measured CIs essentially collapse onto the means at the graphical resolution used here. Note that the reactance zero crossing occurs about 115 Hz above the peak resistance. Also, the mean resistance clearly increases at either end of the frequency range.

The corresponding GIT measurements for 120- and 140-dB excitations are provided in Figure 6.8. Very modest growth of the reactance CIs is noted, relative to those for the NIT, especially for the 120-dB excitation. The resistance CIs are noticeably greater across the entire frequency range for the GIT relative to the NIT. Also, in contrast with the very tight CIs for the NIT, the CIs for the lower excitation (120 dB) in the GIT are about 0.16 and 0.02 for 500 and 1000 Hz, respectively. The CIs for the remaining frequencies range from about 0.05 to 0.09, with no definite trend. For the higher excitation (140 dB), the CIs are generally less than 0.1, with

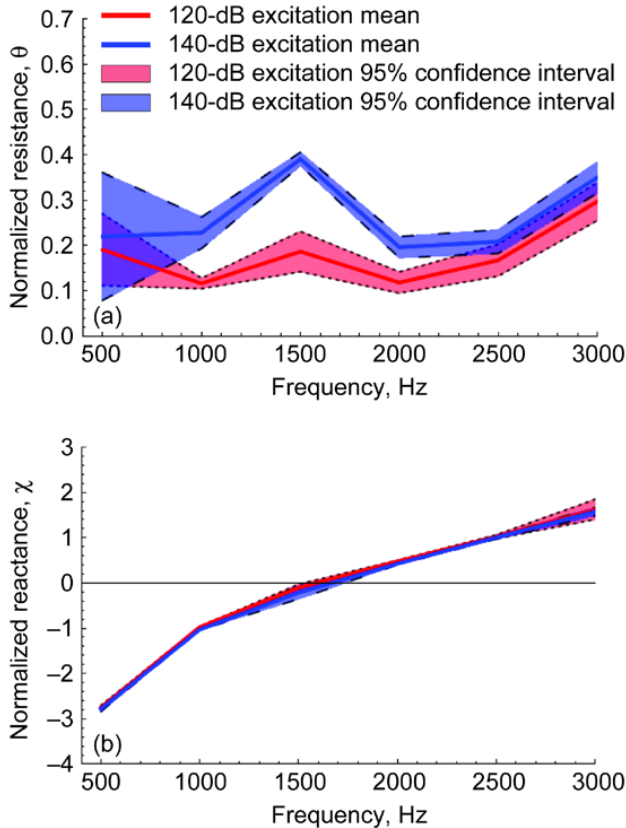


Figure 6.8.—Results from GIT impedance measurements with source excitation levels of 120 and 140 dB conducted at 500-Hz increments. (a) Resistance. (b) Reactance.

the exception of a CI of 0.28 at 500 Hz. The resonance mean resistance values of 0.14 and 0.38 for 120- and 140-dB excitations, respectively, compare with the corresponding values of 0.16 and 0.45 for the NIT. Also, increases in the resistance at the frequency extremes are more evident in the GIT results. The reactance zero-crossing frequencies measured in the GIT are very consistent with those observed from the NIT measurements. Also, there appears to be more separation between the reactance zero crossings and the peak resistances measured in the GIT than was the case for the NIT measurements. However, given the 500-Hz resolution of the GIT measurements, it is not clear whether this is truly the case.

These same results are presented in a different format in Figure 6.9 and Figure 6.10. Figure 6.9 presents comparisons of the NIT and GIT results for an excitation of 120 dB, while Figure 6.10 presents similar comparisons for an excitation of 140 dB. Because of the expanded scale of the graphical results, there appear to be substantial differences between the ranges of the resistance means measured with the two test rigs. In reality, the range are quite similar. For an excitation of 120 dB, the mean resistance ranges from 0.1 to 0.2 for the NIT measurements, and from 0.1 to 0.3 for the GIT measurements.

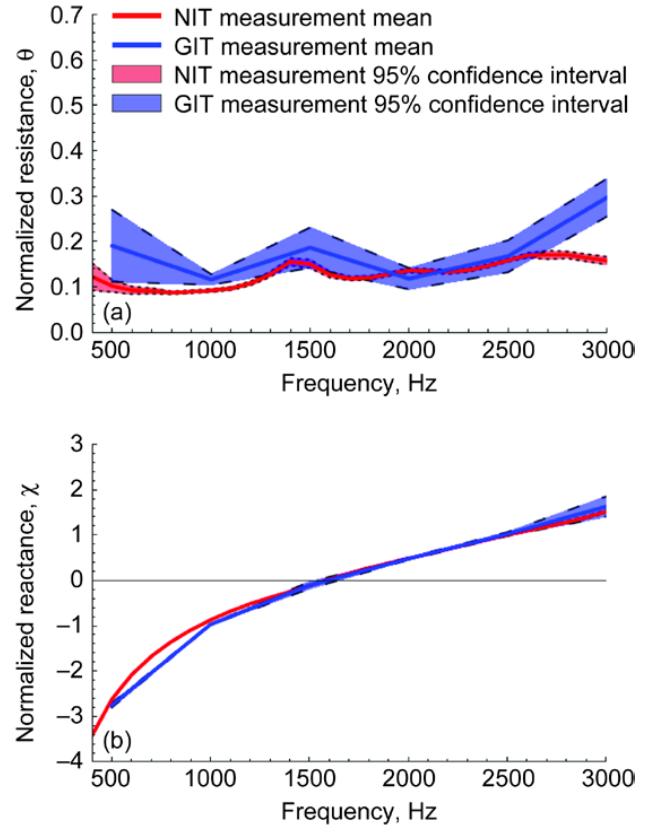


Figure 6.9.—Results from NIT and GIT impedance measurements with source excitation levels of 120 dB conducted at 100- and 500-Hz increments, respectively. (a) Resistance. (b) Reactance.

There is a slightly larger difference for an excitation of 140 dB, with the mean resistances measured in the NIT ranging from 0.1 to 0.5, while the corresponding results in the GIT range from 0.2 to 0.4.

6.6.3 Comparison of GIT Measurements With Flow

Impedance measurements acquired in the GIT with flow (see Figure 6.11) are reported at two centerline Mach numbers (0.3 and 0.475) and one excitation level (140 dB). These conditions were chosen as representative of the most realistic simulations of the aeroacoustic environment of full-scale aircraft engine nacelles. A comparison of Figure 6.10 and Figure 6.11 indicates a broadband increase in resistance with increasing Mach number, accompanied by a general flattening of the resistance spectra relative to the no-flow results in the vicinity of the reactance zero crossing (liner resonance). The mean resistances are approximately 0.5, 0.9, and 1.2 for centerline Mach numbers of 0.0, 0.3, and 0.475, respectively. Clearly, the effects of mean flow on the resistance spectra mask the resonance-related peak exhibited for no-flow at near 1500 Hz in the NIT.

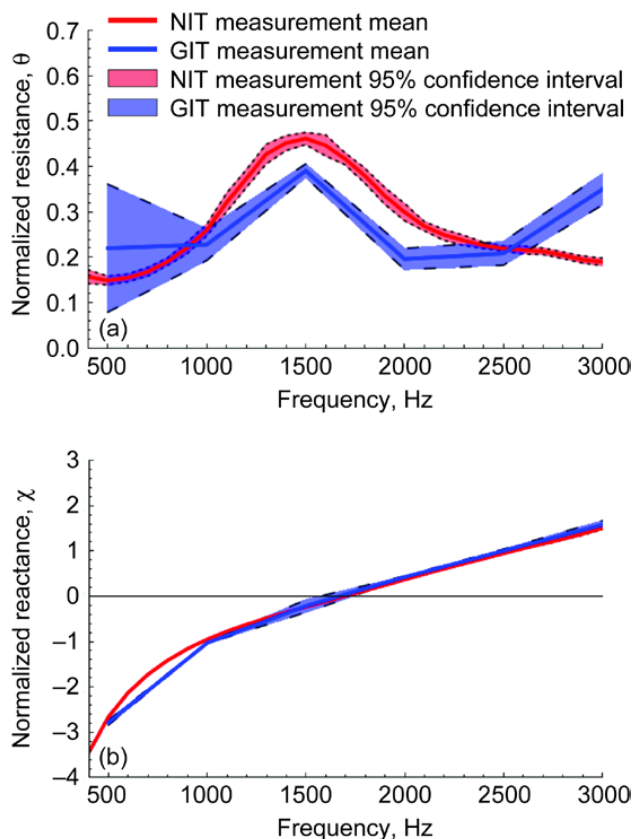


Figure 6.10.—Results from NIT and GIT impedance measurements with source excitation levels of 140 dB conducted at 100- and 500-Hz increments, respectively. (a) Resistance. (b) Reactance.

Significant variability is also evident in the mean resistance values across the frequency range. On the other hand, the reactance is less affected by mean flow. For frequencies near resonance, the reactance is virtually identical across the range of mean-flow velocities. However, the reactance is observed to increase with increasing mean flow at the lower frequencies, and to decrease with increasing mean flow at the higher frequencies. This results in a flattening of the reactance spectrum as the Mach number is increased. It is perhaps important to note that this flattening of the reactance at high excitation levels and grazing-flow velocities is a useful feature, in that it tends to make single-layer, POHC liners more viable for broadband turbofan noise attenuation.

In general, the resistance confidence intervals are relatively unchanged with flow (referring now to the ranges of the CIs, in contrast with their respective means). They tend to be very tight at the mid-range frequencies for a flow Mach number of 0.3, and somewhat greater at a flow Mach number of 0.475. They also show modest growth well away from resonance, especially toward the higher frequencies. Confidence intervals on the reactance nearly collapse on the mean values for a flow Mach number of 0.3 and are only slightly larger at a Mach number of 0.475.

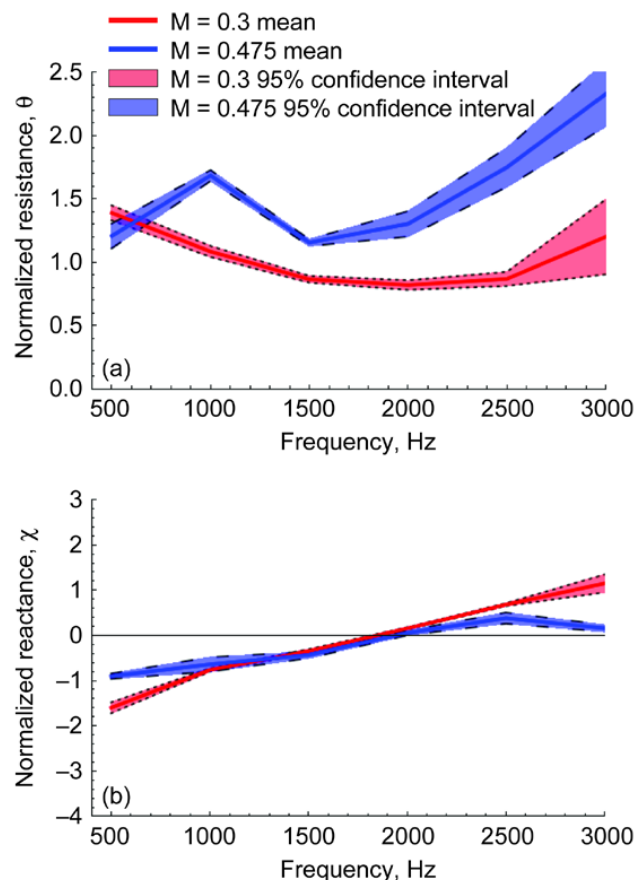


Figure 6.11.—Results from GIT impedance measurements with source excitation level of 140 dB conducted at 500-Hz increments for Mach numbers $M = 0.3$ and 0.475 . (a) Resistance. (b) Reactance.

6.6.4 Comparison of Predicted and Measured Results

This section presents comparisons of measured and predicted statistical parameters relevant to establishing the voice of the process with the “voice of the customer” with respect to the SPC paradigm. The main objective of the comparison is to demonstrate the shortfall in attaining an adequate voice of the process whereby a negotiation can happen between the end user (voice of the customer) and liner fabrication process (voice of the process).

6.6.4.1 Effects of Sample Size on Impedance Prediction Models

The reader will recall from Section 6.2 regarding statistical metrics that the computation of 95% confidence intervals on small samples involves the use of a coverage factor to account for the fact that small sample sizes generally deviate from the Gaussian behavior that is assumed to govern their parent population (Ref. 10). In the spirit of strict mathematical rigor, the application of a coverage factor to the small sample sizes, adopted for the prediction statistics to be consistent with the measurement statistics, violates the Gaussian distribution

assumption for the parent population. The possibility of a non-Gaussian predicted impedance distribution arises from the perforate nonlinearity incorporated into all four impedance prediction models. This concern is allayed via a Monte Carlo simulation, in which a large number of model predictions is used to determine the probability distribution associated with the underlying prediction model for a realistic set of Gaussian-distributed input parameters. In contrast, it was not possible to conduct a large number of measurements because of time and cost limitations. However, since the measured parameters do not vary over a large range, the “assumption” of Gaussian distribution was deemed acceptable. Of the impedance prediction models, the TP model was chosen for this more detailed coverage factor evaluation. The TP model was chosen because of its relative simplicity and straightforward algorithmic implementation of the model nonlinearity. This model was used to provide 10 000 simulations corresponding to the most nonlinear case included in this study, a target SPL of 140 dB and an average Mach number of 0.4. These simulations were conducted at 500-Hz increments from 500 to 3000 Hz. According to Reference 10, the coverage factor of 1.96 can be used for this large sample population; that is, 95 percent of the simulations should provide results that are within the mean ± 1.96 times the standard deviation. The mean and standard deviation for each of the six frequencies were computed, and the results from each of the 10 000 simulations were compared against this range. For these six frequencies, at least 95 percent of the acoustic resistances and reactances computed with the TP model were within this range. Thus, the use of the coverage factor to gain statistical results with small sample populations was deemed acceptable.

6.6.4.2 Order of Graphical Results

Comparisons between the measured and predicted impedance spectra are provided in the following sections. Each figure provides the results based on the following choices:

- (1) Prediction model: Two-Parameter (TP), Crandall Full-Solution (CF), Composite Empirical (CE), or Fluid Mechanical (FM)
- (2) Test rig: normal incidence tube (NIT) or grazing incidence tube (GIT)
- (3) Centerline Mach number: 0.0, 0.3, or 0.475
- (4) Source excitation level (SPL): 120 or 140 dB

In an attempt to add clarity to the graphical results, the figures are provided in the following order. First, comparisons are provided between the measured impedances and those predicted with the TP model. We begin with comparisons of the TP model with the NIT measurements, and follow with similar comparisons for the GIT measurements, with the centerline Mach number set to 0. Results are provided for each of the source excitation levels. Next, comparisons of the TP model with GIT measurements in the presence of mean flow are provided, for centerline Mach numbers of 0.3 and 0.475.

For these flow cases, only the 140 dB source excitation results are provided. This choice is made for the sake of brevity, as well as to focus attention on the test conditions that are most closely matched to those present in an aircraft engine nacelle (i.e., maximum SPL and M_{CL}). This sequence of graphical results is then repeated for the CF and CE impedance prediction models. Finally, since the FM model does not handle mean flow, the results for this model are only compared with measurements acquired in the NIT.

Instead of a detailed, figure-to-figure discussion of the model predictions and their comparisons with measured data, the trends of the predicted CIs (shaded green areas) and means (heavy green lines) are discussed in a general way with the aid of a perusal of all the relevant Figure 6.12 to Figure 6.31. Salient features are singled out for more detailed commentary. The discussion will close with remarks on model-to-model comparisons with the aid of Figure 6.32 to Figure 6.34. The reader is reminded that the figures follow the test parameter sequence previously indicated and that all predicted CIs and means are based upon 31 Monte Carlo simulations (large sample statistics) on the relevant prediction model.

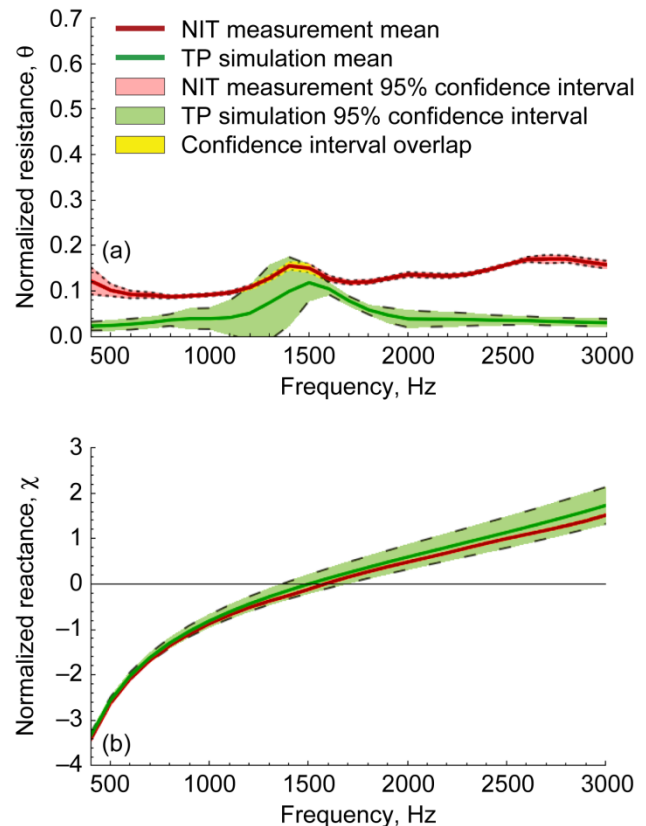


Figure 6.12.—Comparison of impedance results from 14 NIT measurements and 31 Two-Parameter model (TP) simulations with no flow and 120-dB source excitation level conducted at 100-Hz increments. (a) Resistance. (b) Reactance.

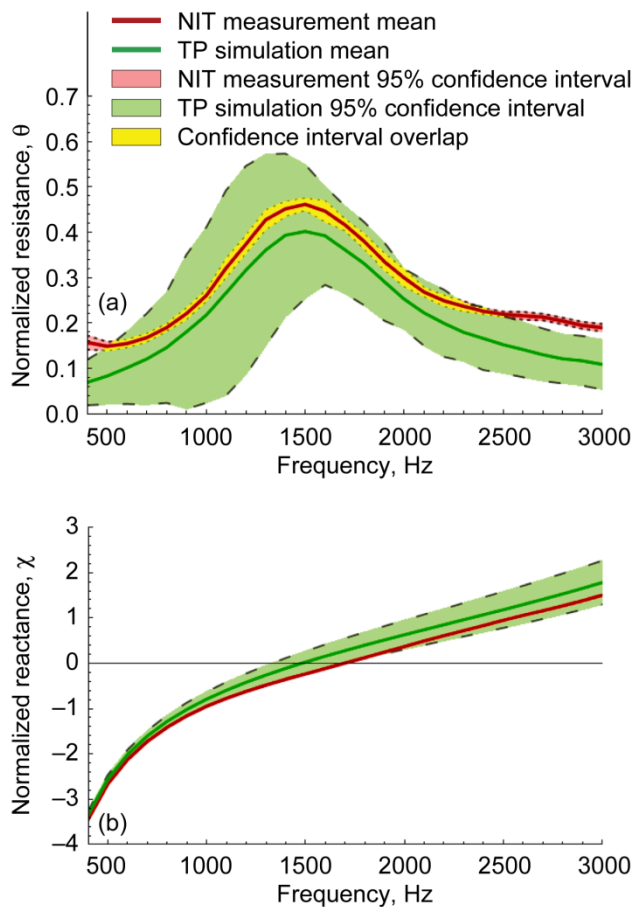


Figure 6.13.—Comparison of impedance results from 14 NIT measurements and 31 Two-Parameter model (TP) simulations with no flow and 140-dB source excitation level conducted at 100-Hz increments. (a) Resistance. (b) Reactance.

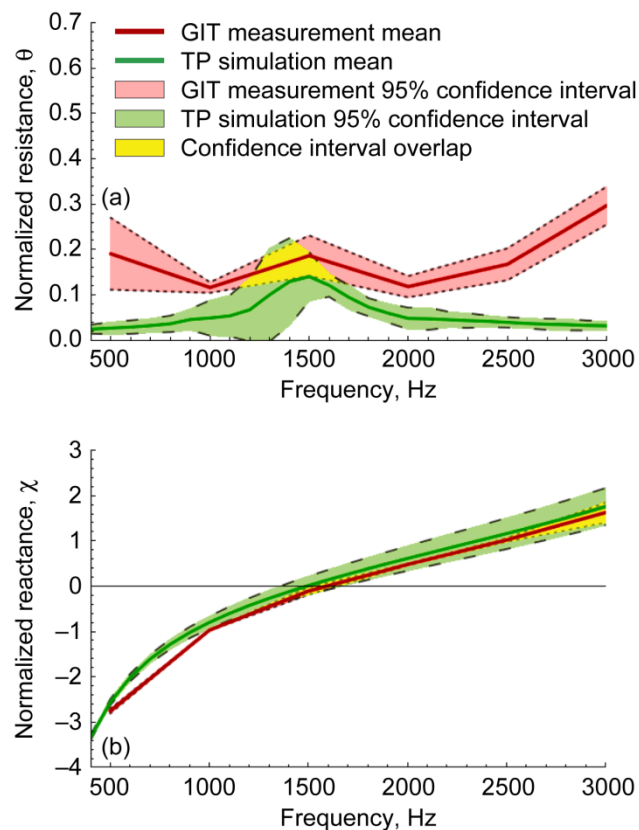


Figure 6.14.—Comparison of impedance results from 10 GIT measurements conducted at 500-Hz increments and 31 Two-Parameter model (TP) simulations conducted at 100-Hz increments with no flow and 120-dB source excitation level. (a) Resistance. (b) Reactance.

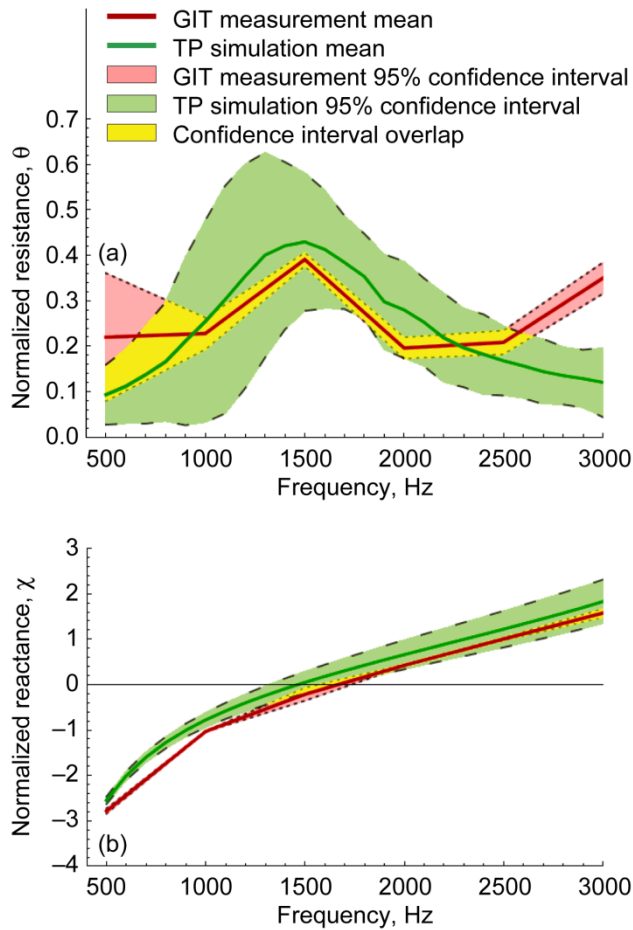


Figure 6.15.—Comparison of impedance results from 9 GIT measurements conducted at 500-Hz increments and 31 Two-Parameter model (TP) simulations conducted at 100-Hz increments with no flow and 140-dB source excitation level. (a) Resistance. (b) Reactance.

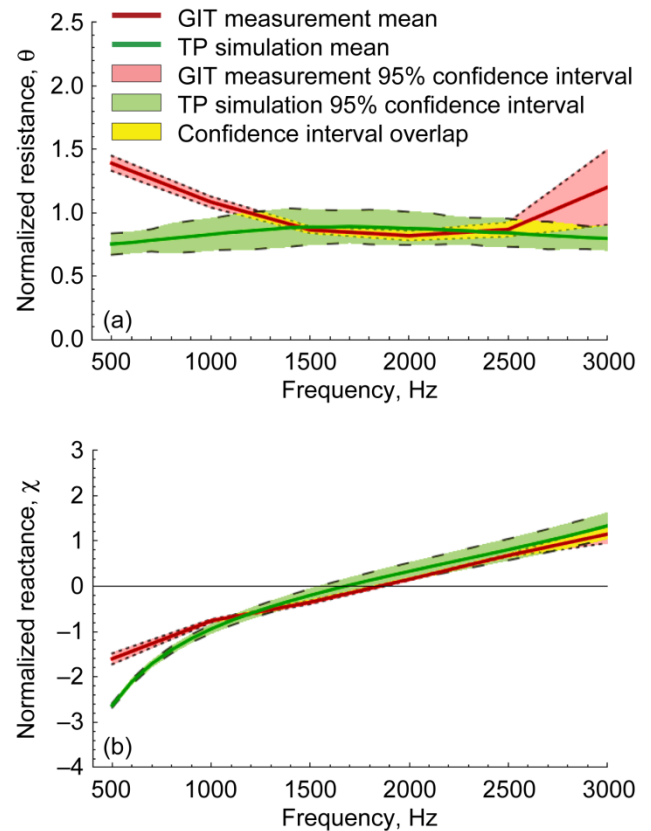


Figure 6.16.—Comparison of impedance results from 9 GIT measurements conducted at 500-Hz increments and 31 Two-Parameter model (TP) simulations conducted at 100-Hz increments with Mach number $M = 0.3$ and 140-dB source excitation level. (a) Resistance. (b) Reactance.

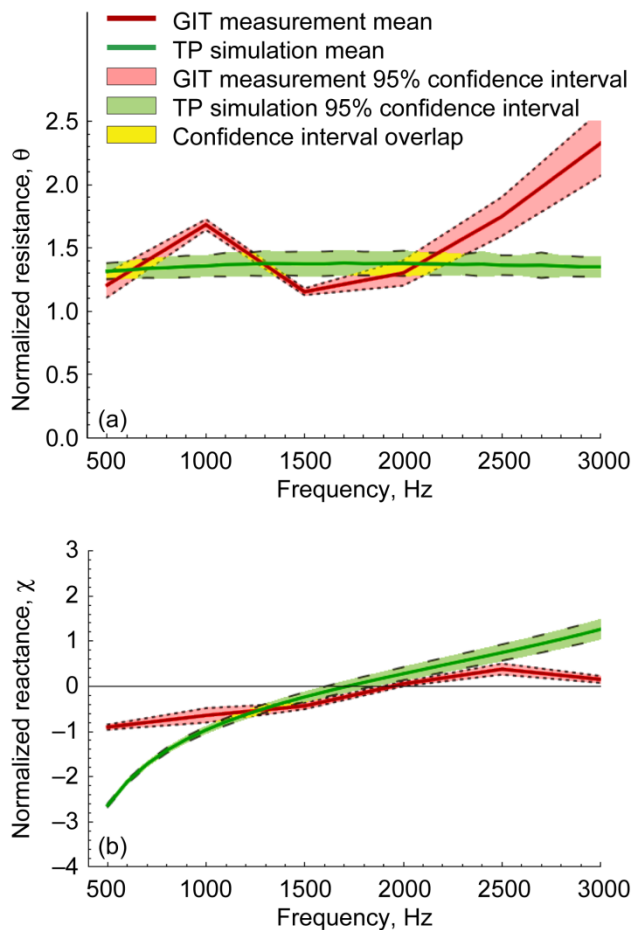


Figure 6.17.—Comparison of impedance results from 9 GIT measurements conducted at 500-Hz increments and 31 Two-Parameter model (TP) simulations conducted at 100-Hz increments with Mach number $M = 0.475$ and 140-dB source excitation level. (a) Resistance. (b) Reactance.

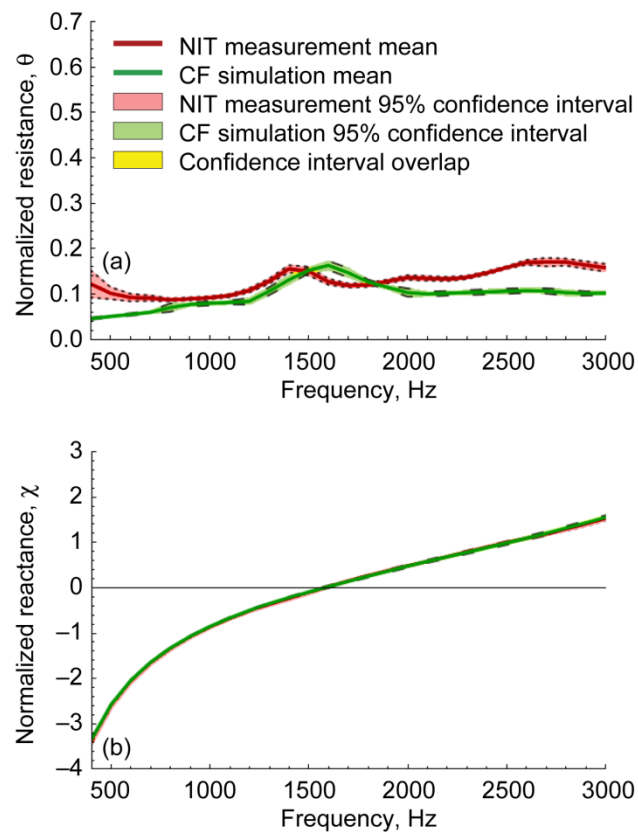


Figure 6.18.—Comparison of impedance results from 14 NIT measurements and 31 Crandall Full-Solution model (CF) simulations conducted at 100-Hz increments with no flow and 120-dB source excitation level. (a) Resistance. (b) Reactance.

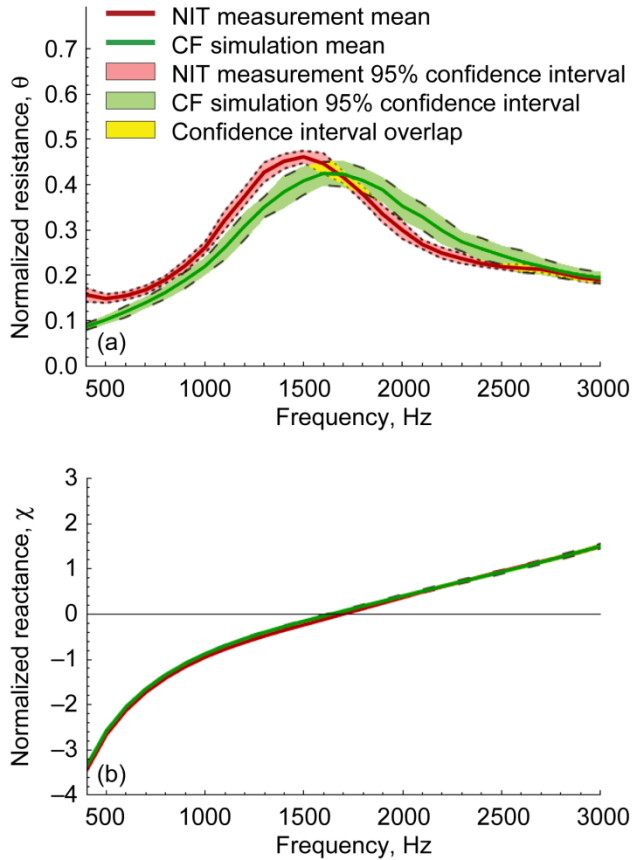


Figure 6.19.—Comparison of impedance results from 14 NIT measurements and 31 Crandall Full-Solution model (CF) simulations conducted at 100-Hz increments with no flow and 140-dB source excitation level. (a) Resistance. (b) Reactance.

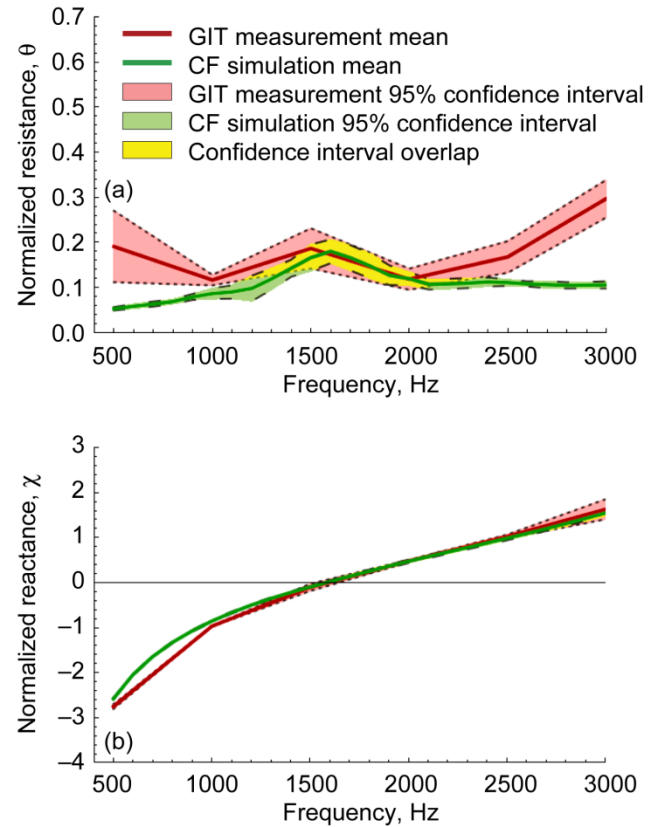


Figure 6.20.—Comparison of impedance results from 10 GIT measurements conducted at 500-Hz increments and 31 Crandall Full-Solution model (CF) simulations conducted at 100-Hz increments with no flow and 120-dB source excitation level. (a) Resistance. (b) Reactance.

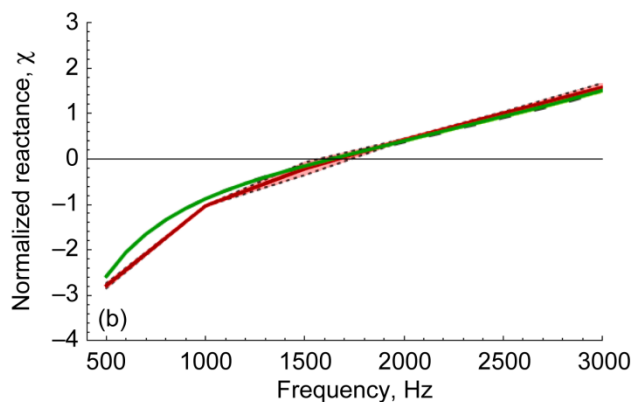
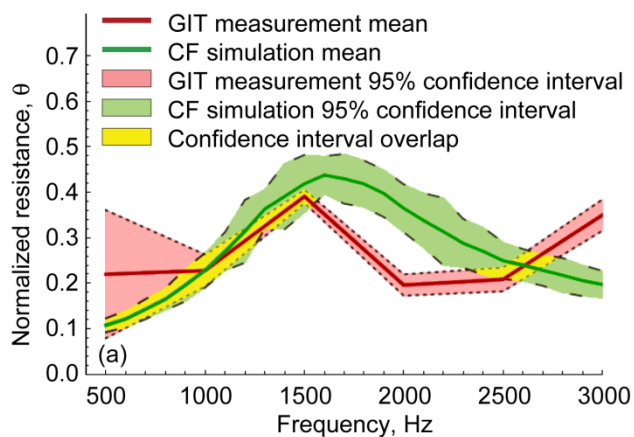


Figure 6.21.—Comparison of impedance results from 9 GIT measurements conducted at 500-Hz increments and 31 Crandall Full-Solution model (CF) simulations conducted at 100-Hz increments with no flow and 140-dB source excitation level. (a) Resistance. (b) Reactance.

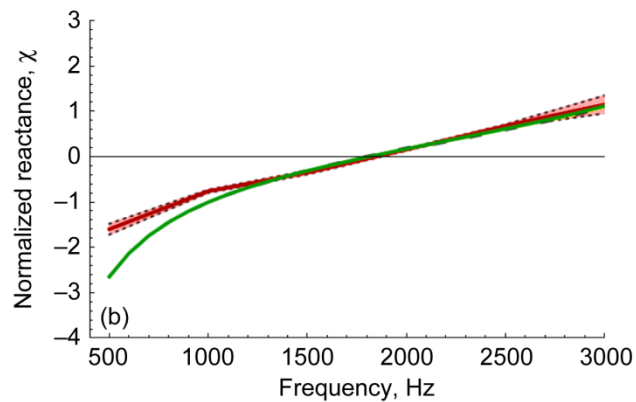
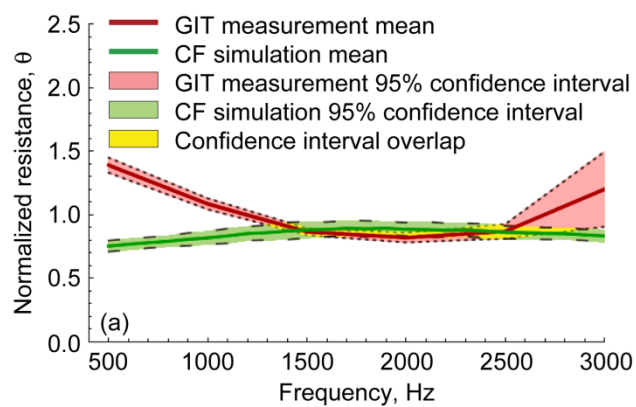


Figure 6.22.—Comparison of impedance results from 9 GIT measurements conducted at 500-Hz increments and 31 Crandall Full-Solution model (CF) simulations conducted at 100-Hz increments with Mach number $M = 0.3$ and 140-dB source excitation level. (a) Resistance. (b) Reactance.

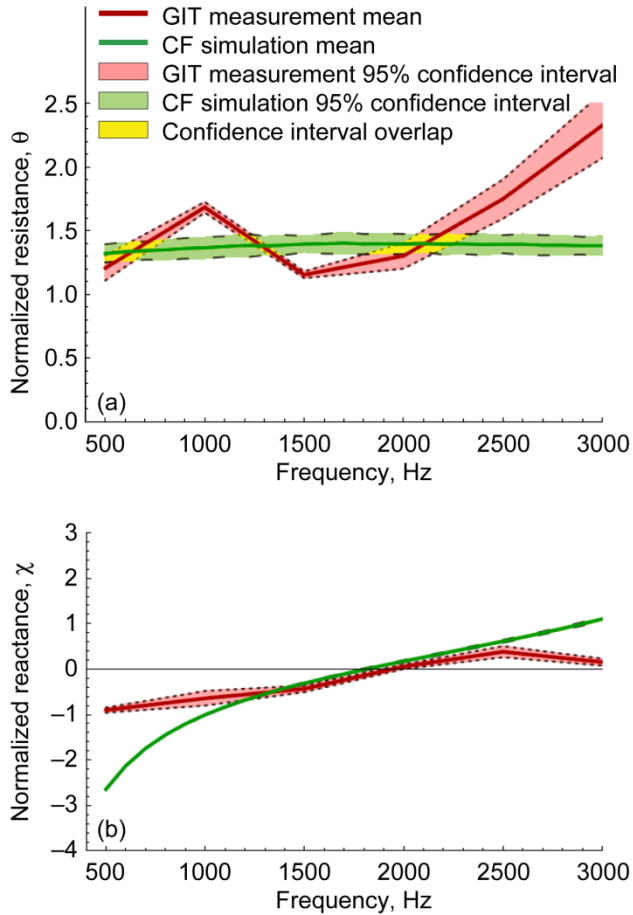


Figure 6.23.—Comparison of impedance results from 10 GIT measurements conducted at 500-Hz increments and 31 Crandall Full-Solution model (CF) simulations conducted at 100-Hz increments with Mach number $M = 0.475$ and 140-dB source excitation level. (a) Resistance. (b) Reactance.

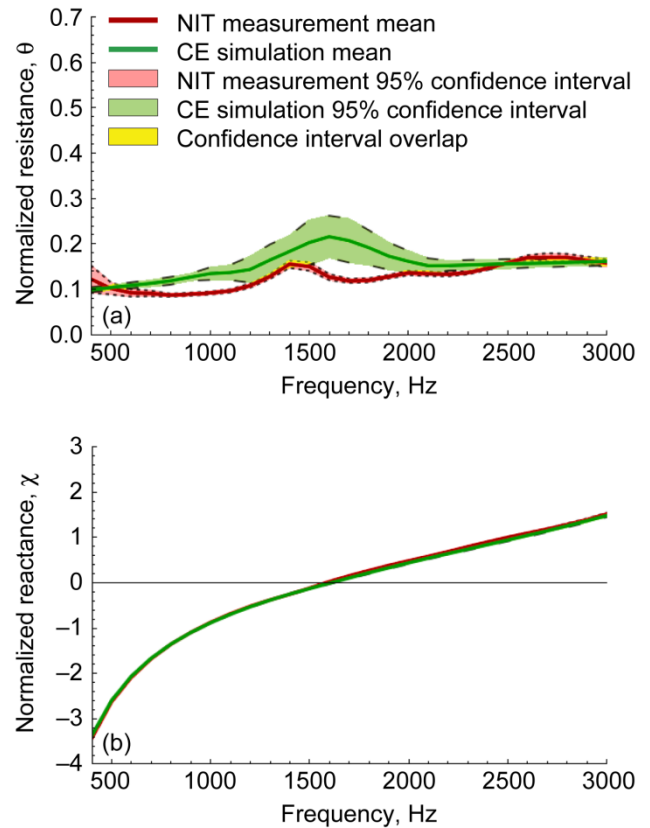


Figure 6.24.—Comparison of impedance results from 14 NIT measurements and 31 Composite Empirical model (CE) simulations conducted at 100-Hz increments with no flow and 120-dB source excitation level. (a) Resistance. (b) Reactance.

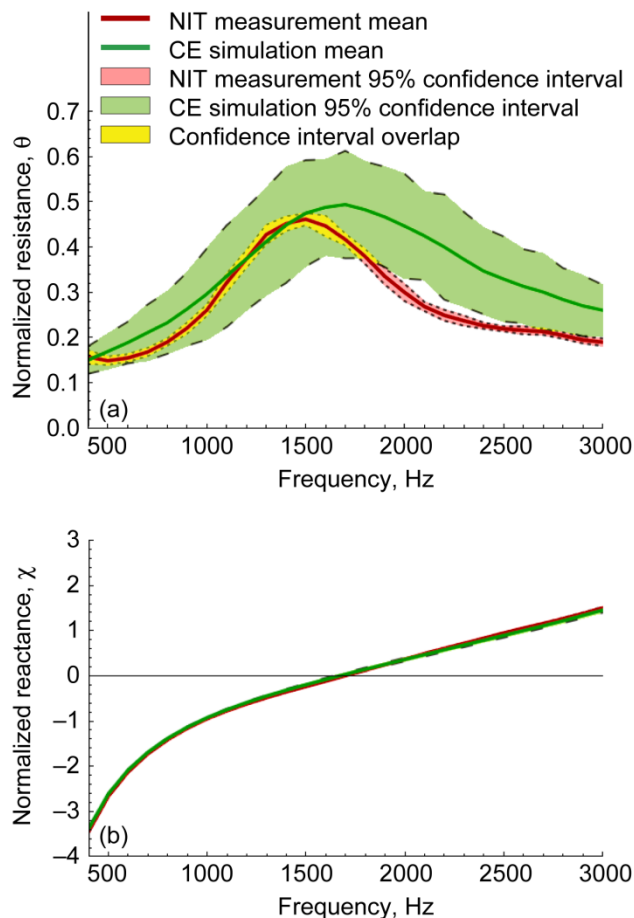


Figure 6.25.—Comparison of impedance results from 14 NIT measurements and 31 Composite Empirical model (CE) simulations conducted at 100-Hz increments with no flow and 140-dB source excitation level. (a) Resistance. (b) Reactance.

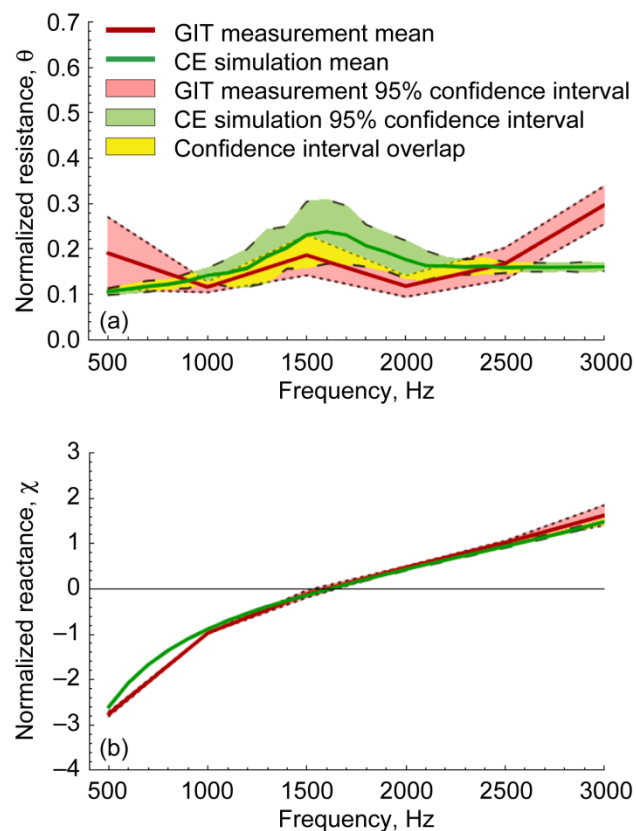


Figure 6.26.—Comparison of impedance results from 10 GIT measurements conducted at 500-Hz increments and 31 Composite Empirical model (CE) simulations conducted at 100-Hz increments with no flow and 120-dB source excitation level. (a) Resistance. (b) Reactance.

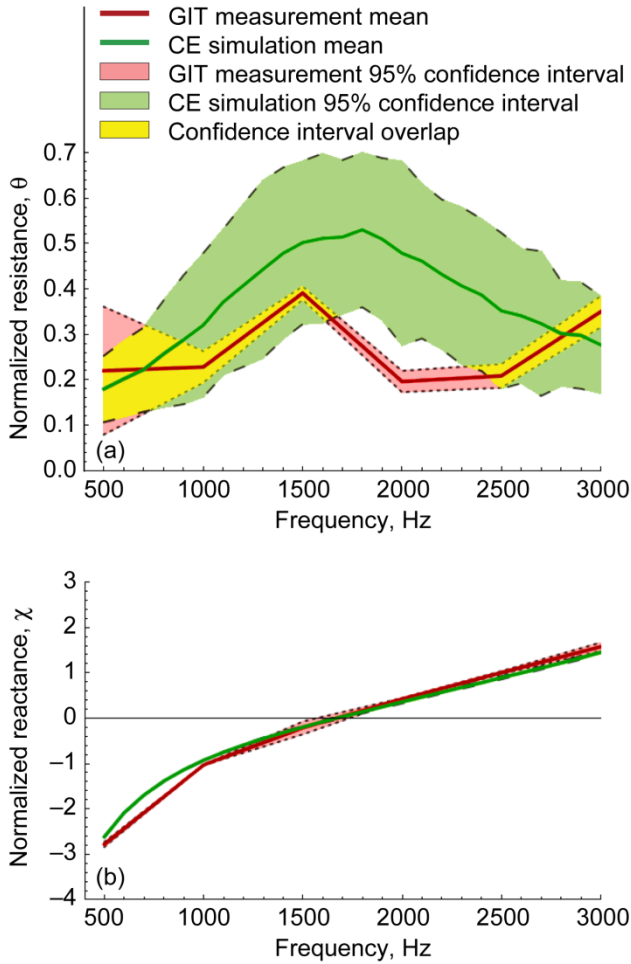


Figure 6.27.—Comparison of impedance results from 9 GIT measurements conducted at 500-Hz increments and 31 Composite Empirical model (CE) simulations conducted at 100-Hz increments with no flow and 140-dB source excitation level. (a) Resistance. (b) Reactance.

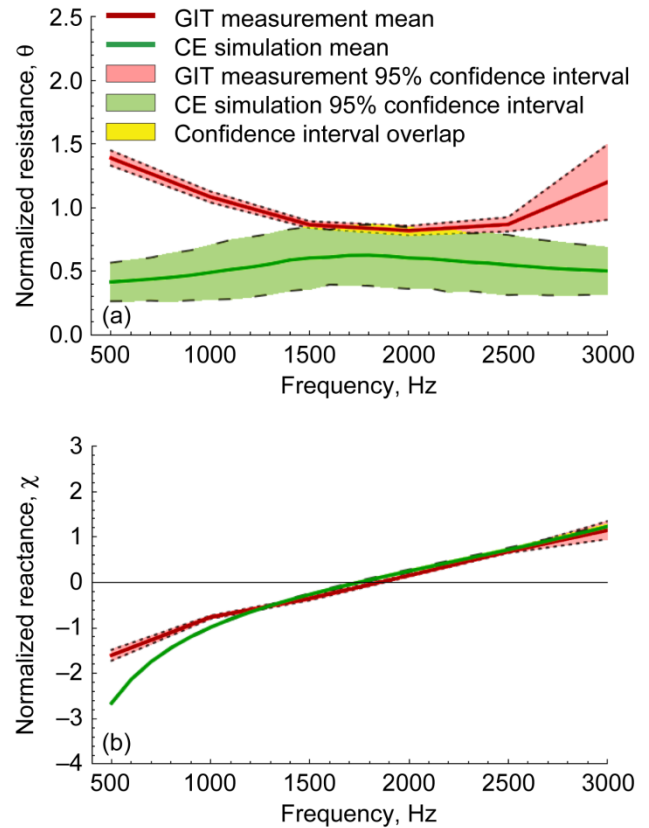


Figure 6.28.—Comparison of impedance results from 9 GIT measurements conducted at 500-Hz increments and 31 Composite Empirical model (CE) simulations conducted at 100-Hz increments with Mach number $M = 0.3$ and 140-dB source excitation level. (a) Resistance. (b) Reactance.

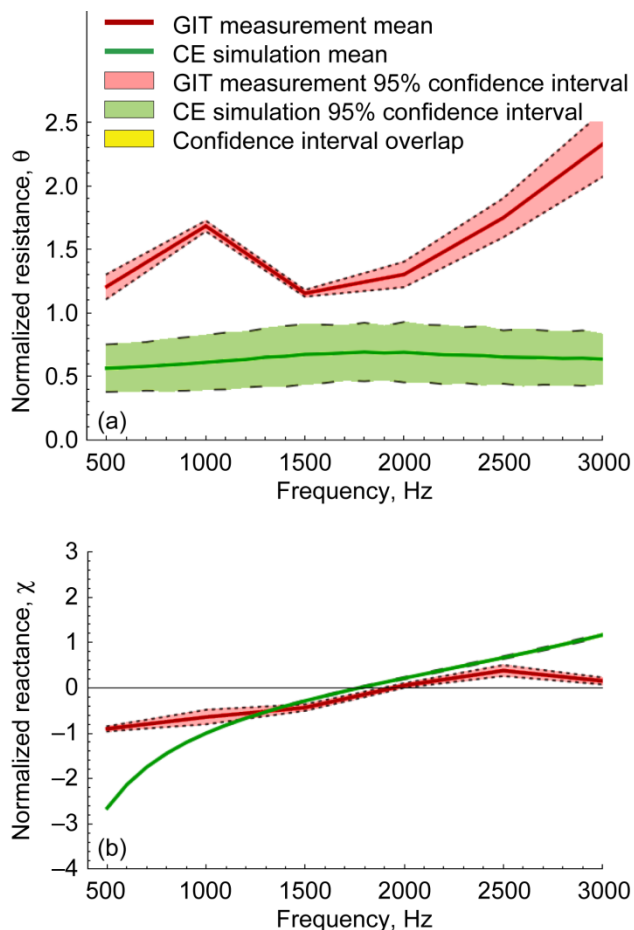


Figure 6.29.—Comparison of impedance results from 10 GIT measurements conducted at 500-Hz increments and 31 Composite Empirical model (CE) simulations conducted at 100-Hz increments with Mach number $M = 0.475$ and 140-dB source excitation level. (a) Resistance. (b) Reactance.

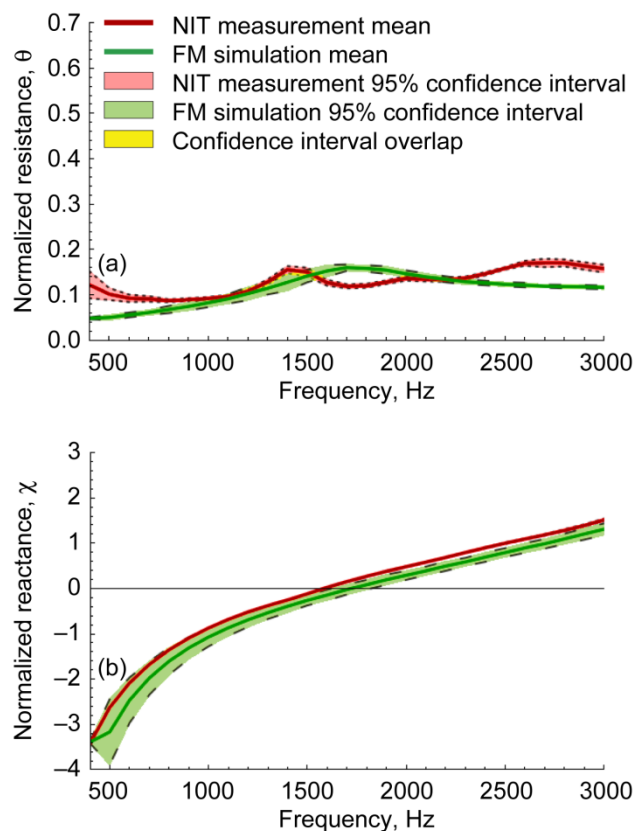


Figure 6.30.—Comparison of impedance results from 14 NIT measurements and 31 Fluid Mechanical model (FM) simulations conducted at 100-Hz increments with no flow and 120-dB source excitation level. (a) Resistance. (b) Reactance.

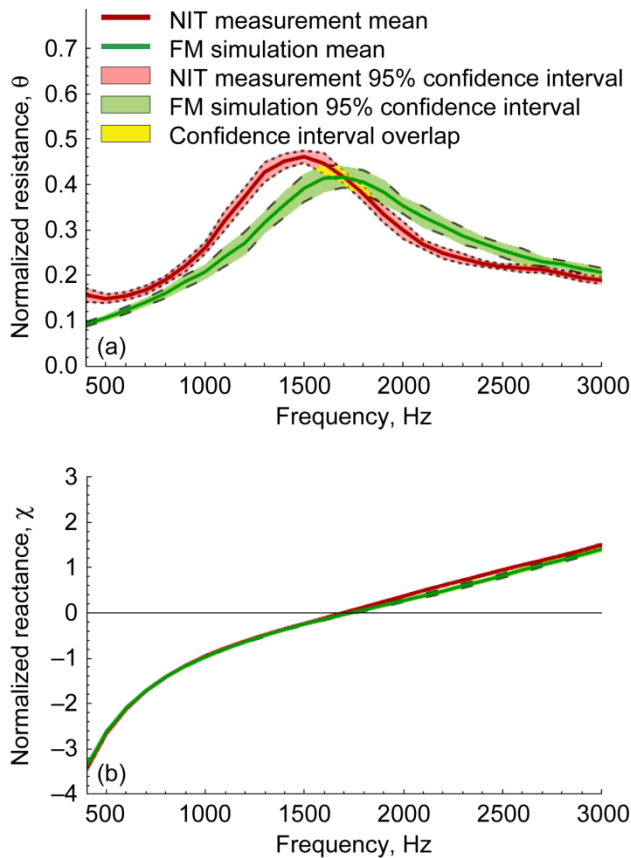


Figure 6.31.—Comparison of impedance results from 14 NIT measurements and 31 Fluid Mechanical model (FM) simulations conducted at 100-Hz increments with no flow and 140-dB source excitation level. (a) Resistance. (b) Reactance.

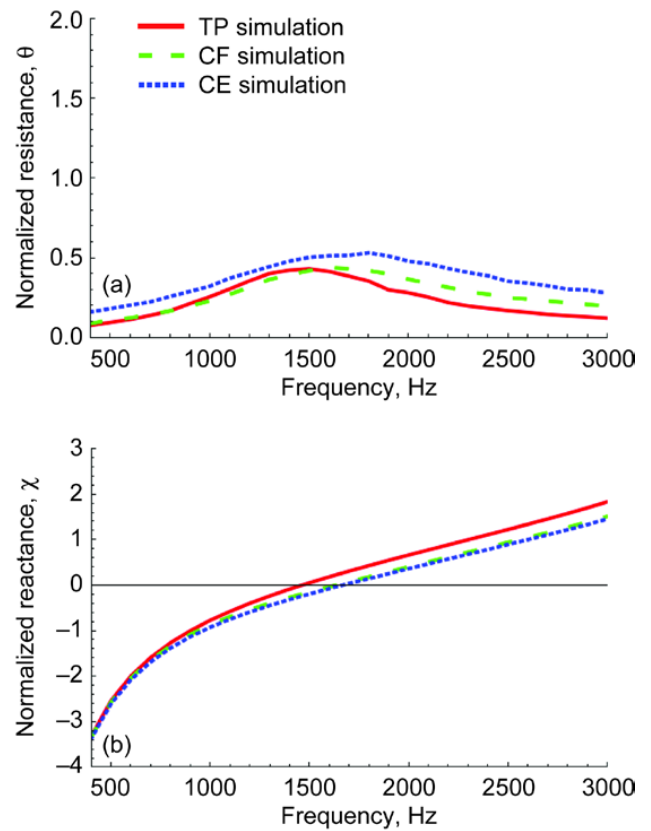


Figure 6.32.—Comparison of average impedance values from Two-Parameter model (TP), Crandall Full-Solution model (CF), and Composite Empirical model (CE) simulations conducted at 100-Hz increments with no flow and 140-dB source excitation level. (a) Resistance. (b) Reactance.

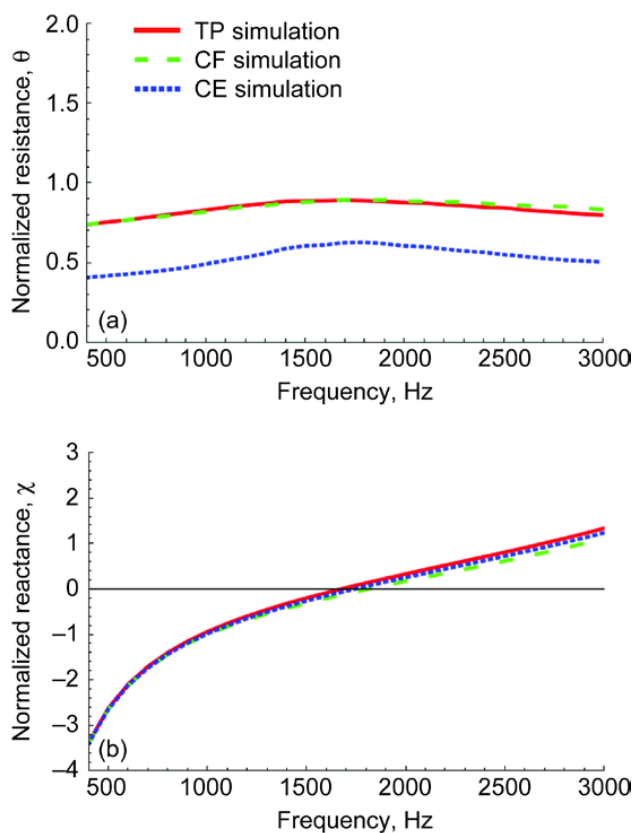


Figure 6.33.—Comparison of average impedance values from Two-Parameter model (TP), Crandall Full-Solution model (CF), and Composite Empirical model (CE) simulations conducted at 100-Hz increments with Mach number $M = 0.3$ and 140-dB source excitation level. (a) Resistance. (b) Reactance.

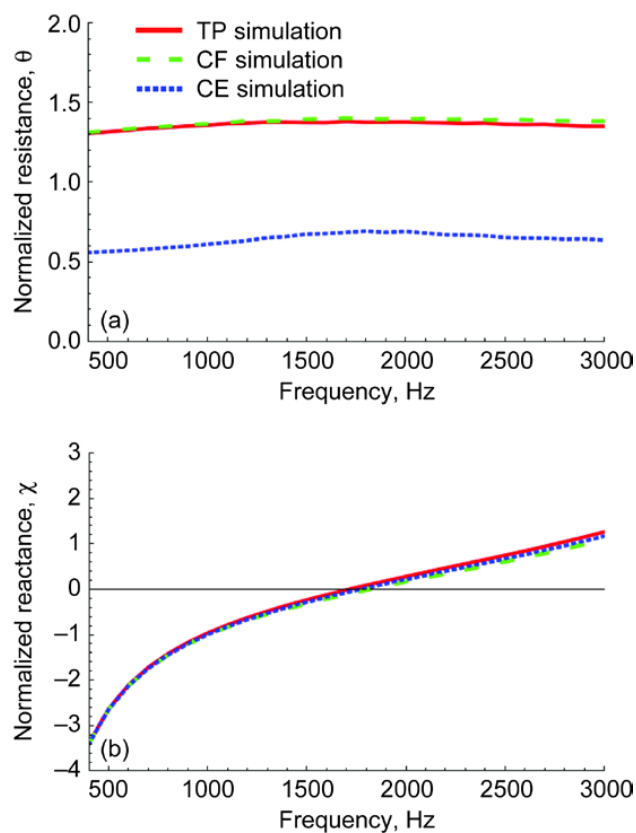


Figure 6.34.—Comparison of average impedance values from Two-Parameter model (TP), Crandall Full-Solution model (CF), and Composite Empirical model (CE) simulations conducted at 100-Hz increments with Mach number $M = 0.475$ and 140-dB source excitation level. (a) Resistance. (b) Reactance.

6.6.4.3 Results for $M_{CL} = 0.0$

At least for no flow, the presence of a peak resistance centered on the zero reactance crossing is a general feature of all the prediction models employed in this study, as is the monotonic decrease of resistance to either side of the peak resistance to the extremities of the test frequency range. This behavior serves as a context for further commentary on the measured impedance spectra. It arises from the absorption physics of a single-degree-of-freedom (SDOF) liner, because the facesheet experiences higher acoustically driven particle velocities in the vicinity of zero reactance. Thus, when exposed to a single, dominant tone, the peak resistance for an SDOF liner is a direct manifestation of the facesheet nonlinearity. As such, this is one reason to employ a test protocol utilizing a single tone at a time for prediction model validation.

When mean flow is present, the resistance peaks become greatly subdued because of a broadband increase in resistance. This results in a nearly uniform resistance spectrum that is still characterized by a broad peak resistance. With the addition of grazing-flow, boundary layer turbulence generates a random fluctuating fluid velocity through the facesheet that combines with the acoustically driven fluctuating velocity. These fluctuating velocities are assumed to combine on an energy basis, in a root-sum-squared sense, to create a broadband increase in resistance across the entire frequency spectrum. The empirical quantification of the grazing-flow “forcing potential” is a likely source of systematic error, as is the root-sum-squared assumption. Because of the assumed physics of the grazing-flow contribution, the liner resistance must still exhibit a single peak at the excitation frequency with a monotonic decrease on either side, however slight. In the limit of low acoustic rms velocity relative to that attributable to flow, the resistance becomes essentially uniform. Any departure of the means from this general behavior, in either the predicted or measured values, suggests the presence of systematic error in one or both. The reader will recall the discussion in Section 6.3.3, “Test Sample Size and Scale Implications,” in which a few potential sources of systematic error related to sample size effects are provided.

It is not known a priori how systematic errors, attributable to differences between prediction and measurement means, are to be parsed. Such parsing must be based on scrutinizing the physical basis for the model and measurement methodologies. Previous observations have indicated that, even in the absence of facesheet nonlinearity, the measured resistance of a single-layer liner exhibits a spike at its antiresonance frequencies, including a pseudo-antiresonance at 0 Hz. The width of this antiresonance can vary depending upon several factors, not yet well understood, and can influence the resistance well away from the antiresonance (Ref. 6). None of the models discussed here account for this effect, which the authors believe is responsible for a portion of the systematic error observed between predicted and measured resistances at the frequency range extremities.

To the graphical resolution provided in the enclosed figures, the peak resistance and the zero crossing of the reactance occur at essentially the same frequency for each of the impedance prediction models. However, the measured resistance peaks generally occur at frequencies approximately 50 to 100 Hz below their corresponding reactance zero crossings. The measured resistance peaks also tend to occur at lower frequencies than the corresponding predicted resistance peaks. An exception to this is shown in Figure 6.13 for a 140-dB excitation level in the NIT, where the measured and predicted (TP model) resistance peaks are nearly equal, but the measured zero reactance crossing is nearly 200 Hz greater than the predicted zero crossing. Other features of this figure are also noteworthy: First, the systematic error, shared between measurements and the TP model prediction, is roughly uniform across the entire frequency spectrum and never exceeds about 0.1. Second, the measurement resistance CIs cluster tightly on the means (pastel yellow region centered on red curve). However, the prediction CIs are relatively large and subsume the measurement CIs up to about 2500 Hz. Correspondingly, the shared reactance systematic error (i.e., the difference between the predicted and measured reactance mean values) increases with frequency and never exceeds about 0.4. The prediction reactance CIs also increase with frequency and generally subsume the measurement CIs, which collapse on their respective means.

The relative behavior of CIs and systematic errors in Figure 6.13 illustrates the potential of uncertainty analysis in the context of SPC. If the prediction CI limits are construed as specification limits (a default in the absence of actual customer specification limits), then the measurement process (yielding a combined systematic and random error, taken as a proxy for the voice of the process) is said to be in compliance with the specification limits when the specification limits (prediction CIs) subsume the voice of the process (measurement CIs). Focusing on resistance, this is the case in Figure 6.13 (excluding the lowest and highest frequencies where an out-of-compliance is evident). Clearly, both systematic error and prediction uncertainty are issues that need to be addressed in this proxy for SPC application to a liner fabrication process. The reader will recall that an out-of-compliance condition can be driven by an arbitrary combination of random and/or systematic error, as is the case in Figure 6.12, where a relatively large systematic error and relatively small random error drive the out-of-compliance condition at the low and high ends of the frequency range.

Attention was drawn above to the observation that the prediction CIs for resistance in Figure 6.13 were sufficiently large to subsume (for most of the frequency range) the combined systematic and random error associated with the measured resistance (the same is also true for reactance). It is of interest to note the large increase in the resistance CIs for the TP model prediction as the excitation level is increased from 120 to 140 dB (compare Figure 6.12 and Figure 6.13). It is also of interest to note that the peaks in lower and upper CI

limits differ by about 300 Hz. This observation is consistent with the zero-crossing of the CI limits associated with the reactance. The corresponding no-flow results for the other three models do not show this trend. Instead, the lower and upper bounds of the prediction resistance CIs are well aligned for each of the other models (see Figure 6.18 and Figure 6.19 for the CF model, Figure 6.24 and Figure 6.25 for the CE model, and Figure 6.30 and Figure 6.31 for the FM model). This misalignment of the prediction CI limits is an artifact of the TP model that is not yet fully understood.

It is also interesting to note that, whereas the peak in the prediction mean resistance for each model occurs at the frequency corresponding to the zero-crossing of the prediction mean reactance, the same is not true of the measured results. In fact, the peak in the measurement mean resistance often occurs at a frequency well below the zero-crossing of the measurement mean reactance, for many of the comparisons between predicted and measured results. The resulting misalignment between the predicted and measured resistance peaks exaggerates the differences between their corresponding CIs. In fact, if this misalignment of predicted and measured resistance peaks was removed (slide the measurement spectrum to the right in Figure 6.19), the prediction CIs would nearly subsume the measurement CIs.

Notwithstanding the systematic error evidenced by the differences between the prediction and measurement resistance mean values of Figure 6.19, the comparability of their trends and the ranges of their CIs illustrate a near-ideal distribution of systematic and random error suitable for applying the specification limit concept of the SPC paradigm as discussed earlier. The prediction reactance CIs for the CF model essentially collapse onto their respective reactance mean values for each of the conditions evaluated (all three Mach numbers and both excitation levels). This is also observed for the results with the CE model, with inputs based on measurements in the NIT (Figure 6.24 and Figure 6.25). In this case, the maximum resistance CI (maximum difference between the upper and lower bounds) increases from about 0.1 to 0.3 as the source excitation level is increased from 120 to 140 dB. For the FM model (see Figure 6.30 and Figure 6.31), the maximum resistance CI hovers at around 0.04 for both excitation levels.

6.6.4.4 Results for $M_{CL} > 0.0$

As previously noted, impedance means and CIs were measured and predicted for one excitation level (140 dB) and two flow Mach numbers (0.3 and 0.475). Both the TP model (Figure 6.16 and Figure 6.17) and the CF model (Figure 6.22 and Figure 6.23) predict measurement resistance means very well in the midfrequency range at the lower Mach number of 0.3, but suffer some separation from the measured results at the higher Mach number of 0.475. As was observed for the no-flow condition, the measurement mean resistances are generally higher than the prediction mean resistances at the frequency range extremes.

In all cases, the spans of the prediction CIs are relatively small, and yet they generally subsume the measurement CIs in the midfrequency range. However, there is clearly a divergence of measurement and prediction reactance means at the lowest frequencies for the lower Mach number of 0.3. This divergence grows for the higher Mach number of 0.475, for which a divergence also occurs at the highest frequencies. Again, the prediction reactance CIs vary substantially from model to model.

The above comparisons of prediction and measurement impedance means and CIs provide the framework for systematically identifying sources of systematic errors in both prediction models and measurements. The choice of a POHC assessment liner with conventional perforate geometry has demonstrated strengths and weaknesses of both the Langley measurement methodologies and the various predictive models considered. Clearly, it would appear there are systematic errors in both the measurement methodologies and the prediction models that warrant further study.

6.6.4.5 Effects of Impedance Measurement (Eduction) Methodology

Comparisons of the results provided above with those in Chapter 7, “Assessment of Acoustic Propagation and Radiation Codes for Locally Reacting Liners in Flow Ducts,” provide additional insight. It is interesting to note that the measurement impedance CI at a test condition tends to be inversely proportional to the prediction SPL attenuation CI. At first glance, this result appears counterintuitive and somewhat negative. Upon further review, it is noted that (at least for the test conditions evaluated in the current investigation) the prediction SPL attenuation CI tends to grow as the mean value increases (see Figure 7.8 in Chapter 7). In other words, at test conditions where a liner provides minimal attenuation (i.e., frequencies away from resonance), the prediction SPL attenuation CI is small, and the measurement impedance CI is large. Conversely, at test conditions where the prediction SPL CI is large, the measurement impedance CI is small. It should also be noted that these differences between the prediction SPL CI and the measurement impedance CI are accentuated by the choice of a single-layer configuration, since the attenuation is significantly larger at resonance for this liner geometry.

If the attenuation provided by an acoustic liner is low in a duct with a specified geometry, the impedance measurement process becomes less robust because large impedance changes produce small changes in attenuation. If this measured impedance were intended to be used only in ducts of the same geometry, this would be acceptable. However, the goal is to determine the impedance at each frequency of interest as accurately as possible. In order to improve the quality of the NASA Langley measurement process, it appears important that efforts be made to achieve sufficient attenuation at each test condition to minimize the size of the measurement impedance CI. Based on the results of the current

investigation, one approach that is currently being considered is to design test liners such that the resonance occurs near the frequency of interest. For those cases where the frequency range of interest is broad, this will require multiple liners to be tested. Each liner would be constructed with the same perforate facesheet material, but would have a cavity depth selected to “cover” a different portion of the frequency range. By combining the results from multiple liner tests, it is expected that the measurement impedance CI can be reduced to an acceptable range over the entire frequency range of interest.

6.6.4.6 Model-to-Model Comparisons

Model-to-model comparisons are shown in Figure 6.32 to Figure 6.34 for 140 dB excitation and grazing-flow Mach numbers of 0, 0.3, and 0.475. At zero flow, all of the models are in reasonably good agreement below the reactance zero-crossing frequency for the TP model. Above the zero-crossing frequency for the TP model, the agreement is not as good. The CE model forms an upper bound and the TP model forms a lower bound on the resistance spectra graphic of Figure 6.32. The spread in resistance above the reactance zero crossing averages about 0.2. Predicted reactance spectra are in excellent agreement for the CF and CE models. The TP model is the reactance spectrum outlier, with a positive divergence of about 0.4 from the CF and CE models at the highest frequency. This divergence gives rise to a delta in zero-crossing frequency between the TP and the (CF, CE) pair of nearly 200 Hz.

At a Mach number of 0.3, the predicted resistance spectra of the TP and CF models essentially coalesce. The CE model resistance is the outlier below the other two models, with a resistance delta of about 0.3 at the broad peak to about 0.32 at the lowest frequency. The small reactance spread on the three models is sufficient to generate a delta in the reactance zero crossing of about 80 Hz.

At a Mach number of 0.475, the trends for the 0.3 Mach number measurements are continued with the CE model now underpredicting resistance (relative to the TP and CF results) uniformly by about 0.7. Again, the reactance predictions virtually coalesce, to give a zero crossing delta of about 30 Hz (see Figure 6.34).

When compared with the near coalescence of the TP and CF predictions at flow Mach numbers of 0.3 and 0.475, the uniform discrepancies in predicted resistance spectra for the CE model of 0.3 and 0.7 are at first glance somewhat surprising. However, it should be recalled that the TP and CF models share several similarities, the most relevant being an identical model for the contribution of grazing flow to the resistance, the Rice-Heidelberg model. Thus, any difference between the TP and CF models is due to their respective no-flow model component contribution. Except for minor differences in empirical tweaking factors, the main difference in the TP and CF models is the way the viscous resistance is modeled. In the

TP model, the viscous resistance comes from a Hagen-Poiseuille type model for pipe flow. In the CF model, a frequency-dependent viscous resistance is derived from a full Navier-Stokes solution for oscillatory flow in a pipe. Differences in these two contributions would be expected to arise only for high frequencies and/or for large perforate thickness relative to hole diameter. That is assuredly not the case for the selected assessment liner, which has a t/d ratio close to unity. Thus, to understand the differences between the CE model and the other two models in the presence of mean flow, the physics underlying the Rice-Heidelberg resistance model and the empirical model for the boundary layer, turbulence-driven rms velocity through the perforate must be further analyzed.

In summary, the trends of the prediction and measurement resistance means are generally in agreement, while the details of how well the predicted values track the measurements differ from model to model. The bias error (with respect to measurements) for some models tends to be uniform, but is frequency-region selective for others. This frequency-region selective bias is generally excitation-level dependent. The prediction resistance CI spectra differ dramatically from model to model, but the corresponding reactance CI spectra are generally very tight. The sole exception to this is the TP model, which predicts CI growth with increasing frequency. The CIs grow with increasing excitation level for some of the models, but remain relatively constant for others. Those models for which the CIs grow with excitation level (especially through the resonance region) make explicit use of a discharge coefficient that, as mentioned previously, was characterized by a rather large standard deviation in the current investigation. A detailed input parameter sensitivity study was conducted with the TP model, which demonstrated a significant portion of the observed growth of prediction CIs is attributable to discharge coefficient uncertainty (Ref. 50).

6.7 Concluding Remarks and Recommendations

This chapter has provided the results of uncertainty analyses conducted by NASA Langley, cast in the statistical metrics of means and confidence intervals. This was done in anticipation of the usage of statistical process control (SPC) to predict out-of-compliance conditions for a target impedance spectrum during liner fabrication. These analyses have been conducted with four impedance prediction models, and the results have been compared with impedances measured in the NASA Langley normal incidence tube and grazing incidence tube. A number of findings have been highlighted by the current investigation. Some of the more salient ones include

1. A key focus of this document has been to propose an adaptation of the SPC paradigm to the production of an impedance target spectrum to within specifications defined by the customer. It offers a tool whereby the liner designer

negotiates a target design uncertainty with the customer. In SPC theory, the voice of the process is a sequence of component parameter measurements (e.g., flow resistance and hole geometry) prior to liner fabrication. A successful adaptation of the SPC paradigm to complying with the voice of the customer relies critically upon known accuracy and precision of the relevant impedance prediction models. This investigation is a first step toward this goal: systematic errors and uncertainties for four prediction models and two measurement processes have been compared. This exercise has demonstrated that much work remains to be done on both the predictive models and the measurement process in a grazing-flow environment.

2. Consistent trends are observed for the four impedance prediction models (Two-Parameter, Crandall Full-Solution, Composite Empirical, and Fluid Mechanical) in the absence of flow, and for the first three models in the presence of mean flow:

- a. The resistance increases with increasing mean flow.
- b. The reactance becomes flatter with increasing mean flow.
- c. The Two-Parameter and Crandall Full-Solution models produce very similar resistances, below the Composite Empirical resistances in the absence of mean flow and above the Composite Empirical resistances in the presence of mean flow (difference increases with increasing mean flow).

3. Confidence intervals for measured impedances tend to increase with increasing mean flow, and tend to be much larger for resistance than for reactance.

4. Differences between predicted and measured impedances generally increase with increases in mean-flow velocity.

5. Impedance prediction and sound pressure level (SPL) attenuation confidence intervals are inversely related. As the attenuation is reduced (at frequencies away from resonance), the impedance measurement process becomes less robust (since large impedance changes only produce small changes in attenuation). Correspondingly, these impedances become less critical (when applied in the current duct) at these frequencies of less attenuation. Differences between predicted and measured SPL attenuations are accentuated by the choice of a single-layer configuration, since the attenuation is significantly larger at resonance for this liner geometry.

This investigation has provided valuable insight with regards to impedance measurement and prediction methodologies and their shortcomings. The following items are recommended for further research, and will form the basis of continued liner physics research at NASA Langley:

1. Incorporate three-dimensional aeroacoustic effects into the impedance measurement (education) model, including
 - a. Nonuniform mean flow
 - b. Boundary-layer growth
 - c. Duct geometry

- d. Higher-order modes (at the source plane, upstream of the liner)

Plans are underway to implement two test ducts (50.8- by 63.5-mm (2- by 2.5-in.) and 152.4- by 381.0-mm (6- by 15-in.) cross sections) designed to evaluate each of these effects, both individually and jointly. It is expected that measurements in these ducts will provide data of increased fidelity that can in turn be used to improve current impedance prediction models.

2. Conduct tests with additional validation liners to exercise a wider range of impedance variability. These liners should be linear (independent of mean-flow velocity and source excitation level) and predictable from first principles. Liner segmentation should also be exploited to achieve impedance variability along the liner length, such that the ability of the impedance measurement methodology to account for axial impedance spectra changes that occur with conventional, nonlinear liners can be thoroughly evaluated.

3. Conduct tests with multiple samples of the same geometry, such that the effects of manufacturing repeatability can be properly assessed (i.e., application of SPC).

4. Conduct detailed sensitivity studies with each impedance prediction model, and with the impedance measurement methodology, to determine which parameters are of greatest importance to the final results. In the SPC paradigm, results from these studies would provide a measure of the voice of the process. They should also be used to guide future tests in the two test rigs mentioned above.

5. Extend the measurement range to higher mean-flow velocity, source excitation level, and frequency to more closely simulate the realistic aircraft engine nacelle environment. One of the new test ducts mentioned above is a grazing-flow impedance tube and is expected to support each of these goals. This test duct is expected to support up to Mach 0.6 flow, with source levels up to at least 150 dB for frequencies up to 3000 Hz. It will also support analysis at frequencies up to 6000 Hz, although initially at perhaps limited source SPLs.

6. Extend the evaluation to incorporate a broadband noise source into the impedance education method. Modern aircraft engines produce a combination of tones and broadband noise. As the tonal content has gradually been reduced, the importance of the broadband noise has increased. As such, there is a need to include both in future liner evaluations.

7. Extend the evaluation to include other liner types. These are expected to include multilayer perforate-over-honeycomb liners and extended-reaction liners, each of which provides increased broadband attenuation. Multilayer perforate-over-honeycomb liners are commonly used in current engine nacelles, and multiple extended-reaction liner concepts are currently being investigated.

8. Conduct studies to identify the sources of discrepancy between the various methods for including grazing-flow effects in the acoustic resistance prediction. This should include investigation of the effects of boundary layer profile on the measured impedance.

6.8 Acknowledgments

The authors extend sincere gratitude to Carol Harrison for the care in which she conducted extensive tests to generate the measurement database used in this investigation. They also

wish to express appreciation to Willie Watson for his assistance with the impedance reduction methodology, to Carl Gerhold and Martha Brown for their assistance with the impedance prediction models, and to Brian Howerton for his assistance with the measurement process.

Appendix A.—Nomenclature

A.1 Acronyms

ADP	Advanced Ducted Propulsor
CE	Composite Empirical model
CF	Crandall Full-Solution model
CHE	convected Helmholtz equation
CI	confidence interval
DC	direct current
FM	Fluid Mechanical model
GIT	grazing incidence tube
ISM	in situ method
LEE	linearized Euler equations
MMM	multimicrophone method
NIT	normal incidence tube
POHC	perforate-over-honeycomb core
rms	root-mean-squared
SDOF	single degree of freedom
SPC	statistical process control
SPL	sound pressure level
TMM	two-microphone method
TTM	T-tube method
TP	Two-Parameter model

A.2 Symbols

A	constant from Equation (6.3)
a	Hagen-Poiseuille laminar flow friction factor, empirical constant from Equation (6.5)
B	constant from Equation (6.3)
\mathcal{B}	model coefficient defined in Equation (6.30b)
C_D	perforate hole discharge coefficient
c	ambient speed of sound
\mathcal{D}	single hole orifice inertial length parameter defined by Equation (6.39)
d	liner facesheet hole diameter
F	function defined by Equation (6.23)
f	frequency
f_0	frequency parameter defined by Equation (6.41a)
H	duct height
\mathcal{H}	orifice nonlinear inertial length defined by Equation (6.38)
h	honeycomb cell depth
i	$\sqrt{-1}$
J_0	zeroth-order Bessel function of the first kind

J_1	first-order Bessel function of the first kind
\mathcal{K}	viscous loss parameter from Fluid Mechanical model (FM)
k	acoustic wavenumber
κ	end effect empirical constant
L	duct length
M	Mach number
\mathcal{M}	nondimensional curve fit parameter for \mathcal{H} defined by Equation (6.40a)
$Mean(^*)$	mean of parameter *
m, n	C_D -related nondimensional curve fit components
N	number of samples
\mathcal{N}	number of holes in perforated sheet
P	steady pressure
p	acoustic pressure
R	resistance
r	liner facesheet hole radius
S	nonlinear slope parameter
s	orifice separation distance
SPL	sound pressure level in decibels
$StDev(^*)$	standard deviation of parameter *
T	wavelength period
T_s	static temperature
t	liner facesheet thickness
V	steady fluid velocity
\mathcal{V}	nondimensional acoustic velocity parameter defined by Equation (6.40c)
v	acoustic velocity
$Var(^*)$	variance of parameter *
x	distance or direction of interest
z	model coefficient defined in Equation (6.33)
α	steady pressure loss coefficient due to viscosity in Equation (6.4)
β	steady pressure loss coefficient due to fluid inertia in Equation (6.4)
δ_1	boundary layer displacement thickness
δ_2	boundary layer momentum thickness
ε	coefficient for hole length end correction factor
ζ	normalized complex acoustic impedance
η	\mathcal{H} -related nondimensional curve fit components with subscripts 0 and 1
θ	normalized acoustic resistance

ρ	ambient fluid density
σ	perforate open area ratio (porosity)
τ	time
μ	ambient dynamic viscosity
χ	normalized acoustic reactance
ω	radial frequency

Subscripts:

<i>AC</i>	frequency dependent
<i>ac</i>	acoustic
<i>ave</i>	cross-sectional area averaged
<i>c</i>	column
<i>cav</i>	cavity
<i>C/L</i>	centerline
<i>DC</i>	frequency independent
<i>e</i>	exit end effects
<i>eff</i>	effective
<i>f</i>	steady flow
<i>fs</i>	facesheet
<i>gf</i>	grazing flow
<i>I</i>	inertial contribution
<i>Im</i>	imaginary part

<i>i</i>	entrance end effects
<i>inc</i>	incident
<i>L</i>	linear
<i>lin</i>	linear
<i>m</i>	mass
<i>me</i>	mass end effects
<i>NL</i>	nonlinear
<i>non</i>	nondimensional
<i>nonlin</i>	nonlinear
<i>pk</i>	peak
<i>R</i>	resistance
<i>res</i>	at resonant conditions
<i>ref</i>	reference
<i>r</i>	row
<i>Re</i>	real part
<i>rms</i>	root-mean-squared
<i>s</i>	static
<i>ss</i>	steady state
μ	viscous Stokes wave
ω	unsteady, or frequency dependent
0	frequency independent

References

1. Proceedings of the Aircraft Noise Symposium—Acoustical Duct Treatments for Aircraft. Invited tutorial papers presented at the 77th Meeting of the Acoustical Society of America, Philadelphia, PA, 1969.
2. The Boeing Company: Study and Development of Turbofan Nacelle Modifications to Minimize Fan-Compressor Noise Radiation. Volume IV—Flightworthy Nacelle Development, NASA CR-1714, 1971.
3. Elliott, David M.; and Dittmar, James H.: Some Acoustic Results From the NASA/Pratt and Whitney Advanced Ducted Propulsor Model. AIAA-2000-351, 2000.
4. Vaidya, P.G.; and Dean, P.D.: The State of the Art of Duct Acoustics. AIAA-1977-1279, 1977.
5. Syed, Asif Ali, et al.: Development of the Acousti-Cap Technology for Double-Layer Acoustic Liners in Aircraft Engine Nacelles. SAE 2007-01-3792, 2007.
6. Parrott, Tony; and Jones, Michael: Cascaded Perforates as One-Dimensional, Bulk Absorbers. AIAA-2006-2402, 2006.
7. Jones, Michael; and Parrott, Tony: Assessment of Bulk Absorber Properties for Multi-Layer Perforates in Porous Honeycomb Liners. AIAA-2006-2403, 2006.
8. Wheeler, Donald J.: Understanding Variation: The Key to Managing Chaos. Second ed., SPC Press, Knoxville, TN, 2000.
9. Wheeler, Donald J.: Beyond Capability Confusion. Second ed., SPC Press, Knoxville, TN, 2000.
10. Coleman, Hugh W.; and Steele, W. Glenn, Jr.: Experimentation and Uncertainty Analysis for Engineers. Second ed., Wiley, New York, NY, 1999.
11. Parrott, Tony L.; and Jones, Michael G.: Parallel-Element Liner Impedances for Improved Absorption of Broadband Sound in Ducts. Noise Control Eng. J., vol. 43, no. 6, 1995, pp. 183-195.
12. Schultz, Todd, et al.: Uncertainty Analysis of the Two-Microphone Method for Acoustic Impedance Testing. AIAA-2002-2465, 2002.
13. Parrott, Tony L.; Watson, Willie R.; and Jones, Michael G.: Experimental Validation of Two-Dimensional Shear-Flow Model for Determining Acoustic Impedance. NASA TP-2679, 1987.
14. Watson, Willie; and Jones, Michael: Comparison of a Convected Helmholtz and Euler Model for Impedance Education in Flow. AIAA-2006-2643, 2006.
15. Blackstock, David T.: Fundamentals of Physical Acoustics. Wiley, New York, NY, 2000.
16. Attenborough, Keith: Acoustical Characteristics of Porous Materials. Phys. Rep., vol. 82, no. 3, 1982, pp. 179-227.
17. Eversman, Walter, et al.: Design of Acoustic Linings for Ducts With Flow. J. Aircraft, vol. 9, no. 8, 1972, pp. 548-556.
18. Heidelberg, Laurence J.; Rice, Edward J.; and Homyak, Leonard: Experimental Evaluation of a Spinning-Mode Acoustic-Treatment Design Concept for Aircraft Inlets. NASA TP-1613, 1980.
19. Rice, E.J.: A Model for the Acoustic Impedance of a Perforated Plate Liner With Multiple Frequency Excitation. NASA TM-X-67950, 1971.
20. Parrott, T.L.; and Zorumski, W.E.: Nonlinear Acoustic Theory for Rigid Porous Materials. NASA-TN-D-6196, 1971.
21. Schultz, Todd; Cattafesta, Louis N., III; and Sheplak, Mark: Modal Decomposition Method for Acoustic Impedance Testing in Square Ducts. J. Acoust. Soc. Am., vol. 120, no. 6, 2006.
22. Dean, P.D.: An In Situ Method of Wall Acoustic Impedance Measurement in Flow Ducts. J. Sound Vib., vol. 34, no. 1, 1974, pp. 97-130.
23. Kraft, R.E., et al.: Acoustic Treatment Design Scaling Methods: Phase II Final Report. NASA/CR-2003-212428, 2003.
24. Tam, C.K.W., et al.: A Computational and Experimental Study of Slit Resonators. J. Sound Vib., vol. 284, nos. 3-5, 2005, pp. 947-984.
25. Dean, L.W., III; and Feder, E.: Analytical and Experimental Studies for Predicting Noise Attenuation in Acoustically Treated Ducts for Turbofan Engines. NASA CR-1373, 1969.
26. Standard Test Method for Impedance and Absorption of Acoustical Materials Using a Tube, Two Microphones and a Digital Frequency Analysis System. Annual Book of ASTM Standards 2000, ASTM E1050-08, vol. 04.06, 2000, pp. 962-972.
27. Jones, Michael G.; and Parrott, Tony L.: Evaluation of a Multi-Point Method for Determining Acoustic Impedance. Mech. Syst. Sig. Process., vol. 3, no. 1, 1989, pp. 15-35.
28. Jones, Michael G.; and Stiede, Patricia E.: Comparison of Methods for Determining Specific Acoustic Impedance. J. Acoust. Soc. Am., vol. 101, no. 5, 1997, pp. 2694-2704.
29. Watson, Willie R.; Tanner, Sharon E.; and Parrott, Tony L.: Optimization Method for Educing Variable-Impedance Liner Properties. AIAA J., vol. 36, no. 1, 1998, pp. 18-23.
30. Jones, Michael G., et al.: Comparison of Two Acoustic Waveguide Methods for Determining Liner Impedance. AIAA-2001-2266, 2001.
31. Watson, Willie R., et al.: Validation of a Numerical Method for Extracting Liner Impedance. AIAA J., vol. 34, no. 3, 1996, pp. 548-554.
32. Watson, Willie R., et al.: A Finite Element Propagation Model for Extracting Normal Incidence Impedance in Nonprogressive Acoustic Wave Fields. J. Comput. Acoust., vol. 125, no. 1, 1996, pp. 177-186.
33. Tijdeman, H.: On the Propagation of Sound Waves in Cylindrical Tubes. J. Sound Vib., vol. 39, no. 1, 1975, pp. 1-33.
34. Yuan, S.W.: Foundations of Fluid Mechanics. Prentice-Hall, Englewood Cliffs, NJ, 1967.
35. Green, Leon, Jr.; and Duwez, Pol: Fluid Flow Through Porous Metals. J. Appl. Phys., vol. 18, 1951, pp. 39-45.
36. Melling, T.H.: The Acoustic Impedance of Perforates at Medium and High Sound Pressure Levels. J. Sound Vib., vol. 29, no. 1, 1973, pp. 1-65.
37. Kraft, R.E.; Yu, J.; and Kwan, H.W.: Acoustic Treatment Design Scaling Methods. NASA/CR-1999-209120/VOL2, 1999.
38. Liu, Fei, et al.: A Multiple Degree of Freedom Electromechanical Helmholtz Resonator. J. Acoust. Soc. Am., vol. 122, no. 1, 2007, pp. 291-301.
39. Syed, Asif A., et al.: The Steady Flow Resistance of Perforated Sheet Materials in High Speed Grazing Flows. NASA/CR-2002-211749, 2002.
40. Guess, A.W.: Calculation of Perforated Plate Liner Parameters From Specified Acoustic Resistance and Reactance. J. Sound Vib., vol. 40, no. 1, 1975, pp. 119-137.
41. Hubbard, Harvey H., ed.: Aeroacoustics of Flight Vehicles: Theory and Practice. Volume 2: Noise Control. NASA RP-1258-VOL-2, 1991.
42. Ingard, U.: On the Theory and Design of Acoustic Resonators. J. Acoust. Soc. Am., vol. 25, 1953, pp. 1037-1061.

43. Yu, Jia; Ruiz, Marta; and Kwan, Hwa-Wan: Validation of Goodrich Perforate Liner Impedance Model Using NASA Langley Test Data. AIAA-2008-2930, 2008.
44. Premo, John: The Boeing Company, Seattle, WA, personal communication, 2007.
45. Hersh, A.S.; Walker, B.E.; and Celano, J.W.: Helmholtz Resonator Impedance Model, Part 1: Nonlinear Behavior. AIAA J., vol. 41, no. 5, 2003, pp. 795-808.
46. Hersh, A.S.; and Walker, B.: Effect of Grazing Flow on the Acoustic Impedance of Helmholtz Resonators Consisting of Single and Clustered Orifices; Final Report. NASA CR-3177, 1979.
47. Baumeister, K.J.: Orifice Resistance for Ejection Into a Grazing Flow. *Advances in Engineering Sciences*, NASA CP-2001, vol. 3, 1976, pp. 895-905.
48. Jones, Michael; Parrott, Tony; and Watson, Willie: Comparison of Acoustic Impedance Eduction Techniques for Locally-Reacting Liners. AIAA-2003-3306, 2003.
49. Jones, Michael; Watson, Willie; and Parrott, Tony: Benchmark Data for Evaluation of Aeroacoustic Propagation Codes With Grazing Flow. AIAA-2005-2853, 2005.
50. Jones, Michael; Parrott, Tony; and Watson, Willie: Uncertainty and Sensitivity Analyses of a Two-Parameter Impedance Prediction Model. AIAA-2008-2928, 2008.

Chapter 7—Assessment of Acoustic Propagation and Radiation Codes for Locally Reacting Liners in Flow Ducts

Willie R. Watson and Douglas M. Nark
National Aeronautics and Space Administration
Langley Research Center
Hampton, Virginia 23681

Summary

A suite of duct acoustic propagation and radiation codes is assembled, consisting of the four most commonly used NASA Langley Research Center codes, a code from academia, and three codes recently developed at Boeing. These codes support propagation through acoustically treated inlet and aft-fan ducts with locally reacting liners in the presence of irrotational or rotational mean flow, as well as radiation to the far field. Collectively, they are a representative cross section of the state of the art in the liner industry. This chapter reviews the basic assumptions, governing differential equations, acoustic boundary conditions, and numerical methods underlying the development of each code. An assessment of each code is then provided using the accuracy of the predicted attenuation, computational efficiency, and effects of input uncertainties as the primary metrics. Each assessment is performed on the same problem, same computer, and grid. Code results are compared with each other and to analytical and measured data.

Several primary conclusions are drawn from the assessment. First, wall clock time increases of an order of magnitude or more are observed for three-dimensional codes relative to the corresponding two-dimensional versions of the same codes. Second, of all codes in the suite the one based on the parabolic approximation is the most efficient but is of low fidelity. Third, predicted results from codes are in excellent agreement with exact analytical results for hard-wall ducts. Fourth, when liners are included, most codes compare well with each other and to analytical results except at a frequency where the attenuation is quite large. However, it is observed that results from one code in the suite tend to diverge from that of others at the higher Mach number. Fifth, attenuations predicted for a conventional perforate-over-honeycomb liner installed in the Langley “grazing incidence tube” compare well with measured attenuations for a plane wave source. As expected, the uncertainty (attenuation 95% confidence interval) is proportional to the amount of attenuation (i.e., small changes in the code inputs at a frequency where significant attenuation occurs result in sizable changes in attenuation). Finally, code results compare well to measurements in the Langley Research Center Curved Duct Test Rig for lower-order mode sources, but errors in the comparisons occur when higher-order modes are present.

The following items are recommended for further research, and are expected to form the basis for continuing code development at NASA: First, more efficient three-dimensional solvers should be incorporated into the three-dimensional propagation codes, such that these codes can be used to efficiently perform parameter studies and to model engine nacelles closer to full scale. A reduction in wall clock time by at least 2 to 3 orders of magnitude is desired. Second, many of the codes included in the current investigation were not initially designed to take advantage of current and future computer architectures. Where possible, these codes should be upgraded to take advantage of these architectures. Third, the effects of the mean boundary layer should be incorporated into the three-dimensional propagation codes to improve their fidelity. Finally, a parallel effort should be conducted to develop propagation codes for the evaluation of extended-reaction liners. It is expected that these propagation codes would be based on approaches described herein for locally reacting liners.

7.1 Introduction

High levels of engine noise radiated from modern turbofan engine nacelles, especially at approach and cutback conditions, threaten to curtail much needed growth in commercial air transportation systems both in the United States and abroad. Engine fan noise is acoustic energy generated at the fan or exit guide vanes of a turbofan engine. It radiates forward via the nacelle inlet duct and rearward by propagating through the aft nacelle duct and ambient shear layer, ultimately reaching observers on the ground. Fan noise from earlier versions of the turbofan engine was dominated by tones associated with the blade passage frequency and its harmonics; however, broadband noise has become an increasingly important component of fan noise from recent engines

incorporating increased fan bypass ratios and modified fan designs.

One of the most effective means for reducing levels of engine noise from commercial aircraft engines is the installation of acoustic treatment into the walls of the inlet and aft fan ducts. Such treatments significantly reduce radiated noise by attenuating both the inlet and aft duct noise as it propagates through the engine nacelle. Suitable aircraft noise prediction codes are required to optimally design the acoustic treatment for maximum attenuation within specified nacelle geometry. Some codes predict the attenuation achieved by the acoustic treatment within the nacelle, while others predict the amount of noise radiated to observers on the ground.

Noise prediction codes for aircraft nacelles are divided into potential and rotational flow codes. Each code has advantages

and disadvantages depending upon the problem being modeled, assumptions that are made, and computer facilities available to code users. At the current time, information available to users of these codes is often fragmented and incomplete. The purpose of this chapter is to assemble a number of noise propagation and radiation codes together under a single umbrella, to describe their basic assumptions, and to give an assessment of each code using predefined metrics. The codes detailed in this chapter represent a broad spectrum of approaches and are validated against a number of test configurations. The three primary metrics chosen for this assessment are (1) accuracy of the predicted attenuation, (2) computational efficiency, and (3) effects of input uncertainties on the predicted attenuations. Readers are assumed to have some background in vector calculus, fluid dynamics, aeroacoustics, numerical methods, computer science, and statistics. Although many duct propagation codes exist in the literature that are based on modal analysis, such codes are generally not applicable to the variable cross-sectional area distribution encountered in aircraft engine nacelles. Therefore, only the nonmodal duct propagation codes that can accommodate variable cross-sectional area distributions are considered in this chapter.

This chapter begins by presenting the basic assumptions, the governing differential equations, and duct boundary conditions for each of the two classes of flows. A description of the numerical method used to solve these equations is then presented for each code. Because considerable economy is often achieved by writing the equations in a vector format, a standard vector format is used throughout this chapter. Each of the three primary assessment metrics is evaluated (for each code) on the same problem, using identical grids, and on the same computer. Whenever appropriate, results are compared to measured data. The chapter closes with recommendations on necessary code improvements and suggestions for new models or approaches. A list of the symbols used in this chapter is given in Appendix A.

7.2 Statement of Problem

Figure 7.1 shows a sketch of a typical three-dimensional, finite length, nacelle duct geometry. The duct carries a nonuniform, subsonic mean flow that flows from left to right. A Cartesian coordinate system (x, y, z) is used, in which the axial coordinate is z and the two transverse coordinates are x and y . The source plane is defined to be at the fan face and as seen in Figure 7.2, is denoted by an imaginary plane Γ_s . Codes discussed in this chapter consider two types of acoustic propagation. For inlet propagation, the sound propagates upstream of the fan against the flow and exits the duct as shown in Figure 7.2(a). In this case, the duct termination is located at the entrance to the inlet and is denoted by the plane Γ_t . The second type of propagation is aft-duct propagation, in which the sound propagates downstream of the fan face and exits the duct via the aft-fan duct as shown in Figure 7.2(b). For aft propagation, the termination plane Γ_t is located

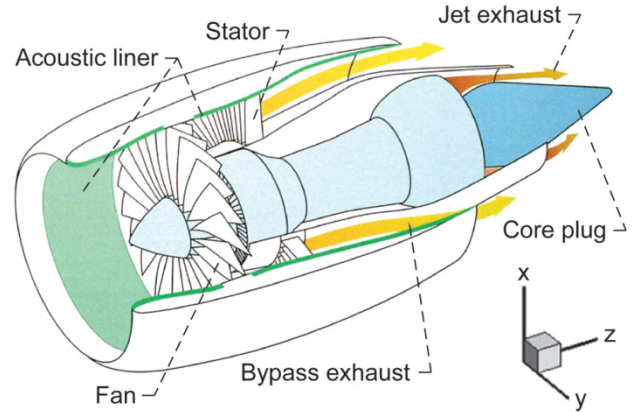


Figure 7.1.—Turbofan engine nacelle with acoustic liner.

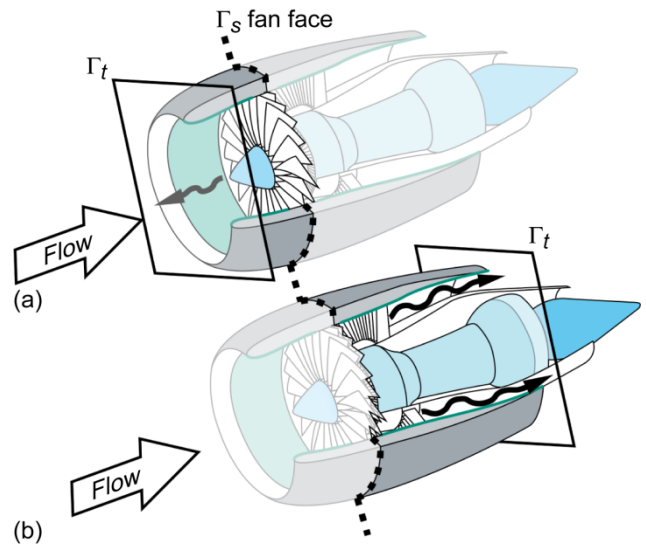


Figure 7.2.—Two types of acoustic propagation in flow ducts addressed in this chapter, showing source plane boundary Γ_s and termination plane boundary Γ_t . (a) Inlet propagation. (b) Aft-duct propagation.

downstream of the fan face in the exhaust duct. In both inlet and aft-duct propagation the computational volume is denoted by Ω , and the perimeter of the duct containing the physical duct walls will be denoted by Γ_w . Let the surface bounding Ω (for inlet or aft-duct propagation) be denoted by Γ , such that the union of Γ_s , Γ_t , and Γ_w is Γ :

$$\Gamma = \Gamma_s \cup \Gamma_t \cup \Gamma_w \quad (7.1)$$

Further, the perimeter of the duct is lined with acoustic material that is assumed to be locally reacting (i.e., acoustic waves propagate through it normal to the surface). The normalized acoustic impedance of the wall lining will be denoted by ζ . The wall impedance contains real and imaginary components (i.e., $\zeta = \Re[\zeta] + i\Im[\zeta]$) and is generally a function of wall location. Here $\Re[\dots]$ and $\Im[\dots]$ denote the real and

imaginary part of a complex quantity, respectively, and i denotes the unit imaginary number. The real component of the normalized impedance $\Re[\zeta]$ is the normalized resistance, and the imaginary component $\Im[\zeta]$ is the normalized reactance. Throughout this chapter, all impedances are normalized with respect to the characteristic impedance of the air flowing in the duct. The problem to be addressed is to describe the basic assumptions and give an assessment of available nonmodal duct propagation codes that predict the noise attenuated by the acoustic treatment in the inlet (see Figure 7.2(a)) or the aft duct (see Figure 7.2(b)). In addition, codes that predict the level of sound radiated to observers on the ground are also described.

7.3 Potential Flow Formulation

The basic assumption of potential flow is that the fluid in the duct is an ideal gas and the flow is reversible, adiabatic, and irrotational. These assumptions allow one to write a single, scalar wave equation that governs the sound field in the duct. The nonmodal potential flow codes discussed in this chapter compute a solution to this wave equation that satisfies the appropriate acoustic boundary conditions at the source plane, duct wall, and duct termination. The derivation of this wave equation and the relevant acoustic boundary conditions are presented in this section.

7.3.1 Governing Differential Equations

The starting point for the potential flow formulation is the equations that govern conservation of mass and momentum in the flow duct based on an assumption of adiabatic reversible flow (Ref. 1):

$$\frac{\partial \hat{p}}{\partial t} + (\hat{\mathbf{u}} \cdot \nabla) \hat{p} + \hat{p} \nabla \cdot \hat{\mathbf{u}} = 0 \quad (7.2)$$

$$\hat{p} \left[\frac{\partial \hat{\mathbf{u}}}{\partial t} + (\hat{\mathbf{u}} \cdot \nabla) \hat{\mathbf{u}} \right] + \nabla \hat{p} = 0 \quad (7.3)$$

where, ρ , \mathbf{u} , and p are the fluid density, fluid velocity vector, and fluid pressure, respectively. Further, the superscript $\hat{}$ denotes a total quantity, the boldface characters denote a vector quantity, t denotes dimensional time, and \bullet denotes the vector dot product. Throughout this chapter, the components of the fluid velocity vector \mathbf{u} in the x -, y -, and z -directions are referred to as “ u ,” “ v ,” and “ w ,” respectively. In addition to the assumptions that the flow is reversible and adiabatic, other assumptions used in deriving the equations governing conservation of mass (Eq. (7.2)) and momentum (Eq. (7.3)) are

- (1) The fluid is a continuum.
- (2) There are no effective gravity forces acting on the fluid.

Instead of using the full energy equation to close the system of equations, the much simpler isentropic relation for an ideal gas is assumed:

$$\hat{p} = C \hat{p}^\gamma \quad (7.4)$$

where C is a constant and γ is the ratio of the specific heat at constant pressure to that at constant volume.

7.3.2 The Linearized Acoustic Equations

The effects of acoustic perturbations within the flow are now determined by decomposing the flow into a time independent mean flow and a time-dependent acoustic perturbation

$$\hat{\rho} = \rho_0 + \tilde{\rho}, \quad \hat{p} = p_0 + \tilde{p}, \quad \hat{\mathbf{u}} = \mathbf{u}_0 + \tilde{\mathbf{u}} \quad (7.5)$$

where the mean (or steady-flow) quantities ρ_0 , p_0 and \mathbf{u}_0 are solutions to the steady form of Equations (7.2) and (7.3) and the perturbations, $\tilde{\rho}$, \tilde{p} and $\tilde{\mathbf{u}}$ are considered small with respect to the mean quantities. Substituting Equation (7.5) into Equations (7.2) and (7.3) allows the equations for mass and momentum continuity to be rewritten in terms of the perturbation variables

$$\begin{aligned} \frac{D\tilde{\rho}}{Dt} + \nabla \cdot (\rho_0 \tilde{\mathbf{u}}) + \tilde{\rho} \nabla \cdot \mathbf{u}_0 + NL1 \\ = - \left(\frac{D\rho_0}{Dt} + \rho_0 \nabla \cdot \mathbf{u}_0 \right) \end{aligned} \quad (7.6)$$

$$\begin{aligned} \rho_0 \frac{D\tilde{\mathbf{u}}}{Dt} + \rho_0 (\tilde{\mathbf{u}} \cdot \nabla) \mathbf{u}_0 + \tilde{\rho} \frac{D\mathbf{u}_0}{Dt} + \nabla \tilde{p} + NL2 \\ = - \left(\rho_0 \frac{D\mathbf{u}_0}{Dt} + \nabla p_0 \right) \end{aligned} \quad (7.7)$$

where the material derivative is taken following the mean flow

$$\frac{D}{Dt} = \frac{\partial}{\partial t} + \mathbf{u}_0 \cdot \nabla \quad (7.8)$$

and the nonlinear terms are

$$NL1 = \tilde{\rho} (\nabla \cdot \tilde{\mathbf{u}}) + (\tilde{\mathbf{u}} \cdot \nabla) \tilde{\rho} \quad (7.9)$$

$$\begin{aligned} NL2 = \tilde{\rho} \frac{\partial \tilde{\mathbf{u}}}{\partial t} + \rho_0 (\tilde{\mathbf{u}} \cdot \nabla) \tilde{\mathbf{u}} + \tilde{\rho} (\tilde{\mathbf{u}} \cdot \nabla) \mathbf{u}_0 \\ + \tilde{\rho} (\mathbf{u}_0 \cdot \nabla) \tilde{\mathbf{u}} + \tilde{\rho} (\tilde{\mathbf{u}} \cdot \nabla) \tilde{\mathbf{u}} \end{aligned} \quad (7.10)$$

Although Equations (7.6) and (7.7) are exact, the difficulty lies in the nonlinear terms. A considerable simplification can be realized by linearizing these equations about the steady flow. This is achieved by neglecting the nonlinear terms ($NL1 = NL2 \approx 0$) and recalling that the right-hand sides of Equations (7.6) and (7.7) are zero since the steady flow is the solution to the steady form of Equations (7.2) and (7.3). Thus, the exact equations for mass and momentum continuity are now approximated using much simpler equations that contain no nonlinear terms:

$$\frac{D\tilde{p}}{Dt} + \rho_0 \nabla \cdot \tilde{\mathbf{u}} + \tilde{p} \nabla \cdot \mathbf{u}_0 + (\tilde{\mathbf{u}} \cdot \nabla) \rho_0 = 0 \quad (7.11)$$

$$\rho_0 \frac{D\tilde{\mathbf{u}}}{Dt} + \rho_0 (\tilde{\mathbf{u}} \cdot \nabla) \mathbf{u}_0 + \tilde{p} \frac{D\mathbf{u}_0}{Dt} + \nabla \tilde{p} = 0 \quad (7.12)$$

In component form, a combination of the scalar Equation (7.11) along with the vector Equation (7.12) constitutes four equations in the five unknown perturbation variables \tilde{p} , \tilde{u} , \tilde{v} , and \tilde{w} . To close the system of equations, it is necessary to establish a relationship between \tilde{p} and \tilde{p} . This is achieved by linearizing Equation (7.4) to obtain

$$\tilde{p} = c_0^2 \tilde{p}, \quad c_0^2 = \gamma \frac{p_0}{\rho_0} \quad (7.13)$$

where c_0 is the speed of sound waves in the flow.

7.3.3 Derivation of Scalar Wave Equations

Potential flow follows from the assumption that the vorticity, $\nabla \times \tilde{\mathbf{u}}$, equals zero

$$\tilde{\mathbf{u}} = \nabla \tilde{\phi} \quad (7.14)$$

$$\tilde{p} = -\frac{\rho_0}{c_0^2} \frac{D\tilde{\phi}}{Dt} \quad (7.15)$$

where $\tilde{\phi}$ is the acoustic velocity potential. Substituting Equations (7.14) and (7.15) into the linearized continuity equation (Eq. (7.11)) and simplifying gives a single scalar equation on the acoustic velocity potential in a nonuniform flow:

$$-\frac{D}{Dt} \left[\frac{1}{c_0^2} \left(\frac{D\tilde{\phi}}{Dt} \right) \right] + \frac{1}{\rho_0} \nabla \cdot (\rho_0 \nabla \tilde{\phi}) = 0 \quad (7.16)$$

It is often desirable to solve for the acoustic pressure field in the presence of an assumed uniform mean flow. When the mean flow is uniform, it is convenient to express the scalar wave equation (Eq. (7.16)) as an equation on acoustic pressure. Such an approach is desirable because the acoustic pressure field is directly measurable in laboratory experiments and is therefore available for comparison with numerical computations. To begin, the linearized continuity equation (Eq. (7.11)) and momentum equations (Eq. (7.12)) for an assumed uniform mean flow imply that

$$\frac{1}{c_0^2} \frac{D\tilde{p}}{Dt} + \rho_0 \nabla \cdot \tilde{\mathbf{u}} = 0 \quad (7.17)$$

$$\rho_0 \frac{D\tilde{\mathbf{u}}}{Dt} = -\nabla \tilde{p} \quad (7.18)$$

Taking the material derivative of Equation (7.17) gives

$$\frac{1}{c_0^2} \frac{D^2 \tilde{p}}{Dt^2} + \rho_0 \frac{D}{Dt} (\nabla \cdot \tilde{\mathbf{u}}) = 0 \quad (7.19)$$

Now taking the divergence of Equation (7.18) gives

$$\rho_0 \nabla \cdot \left(\frac{D\tilde{\mathbf{u}}}{Dt} \right) = -\nabla^2 \tilde{p} \quad (7.20)$$

Recalling that the gradient operator commutes with the material derivative of the acoustic velocity field in a uniform flow,

$$\rho_0 \frac{D}{Dt} (\nabla \cdot \tilde{\mathbf{u}}) = \rho_0 \nabla \cdot \left(\frac{D\tilde{\mathbf{u}}}{Dt} \right) \quad (7.21)$$

and substituting Equation (7.21) into Equation (7.19) gives

$$\frac{1}{c_0^2} \frac{D^2 \tilde{p}}{Dt^2} + \rho_0 \nabla \cdot \left(\frac{D\tilde{\mathbf{u}}}{Dt} \right) = 0 \quad (7.22)$$

Now substituting Equation (7.20) into Equation (7.22) gives a scalar wave equation on the acoustic pressure for uniform mean flow,

$$\frac{1}{c_0^2} \frac{D^2 \tilde{p}}{Dt^2} = \nabla^2 \tilde{p} \quad (7.23)$$

It is noted that a second order wave equation on the acoustic pressure field is not derivable in three space dimensions for nonuniform mean flows.

7.3.4 Scalar Wave Equation in Frequency Domain

Time-harmonic (i.e., frequency domain) solutions to Equations (7.16) and (7.23) are sought so that

$$\begin{Bmatrix} \tilde{\phi} \\ \tilde{p} \end{Bmatrix} = \begin{Bmatrix} \phi \\ p \end{Bmatrix} e^{i\omega t}, \quad \text{where } i = \sqrt{-1} \quad (7.24)$$

where ω is the circular frequency and ϕ and p are now understood to be frequency dependent. It should be noted that the $+i\omega t$ sign convention is employed throughout this chapter unless explicitly stated otherwise. Substituting Equation (7.24) into Equation (7.23) gives the differential equation that governs the time-harmonic acoustic pressure field in a uniform flow,

$$\frac{1}{c_0^2} \frac{D^2 p}{Dt^2} = \nabla^2 p \quad (7.25)$$

Similarly, substituting Equation (7.24) into Equation (7.16) gives the differential equation for the time-harmonic acoustic potential in a nonuniform flow,

$$-\frac{D}{Dt} \left[\frac{1}{c_0^2} \left(\frac{D\phi}{Dt} \right) \right] + \frac{1}{\rho_0} \nabla \cdot (\rho_0 \nabla \phi) = 0 \quad (7.26)$$

where the material derivative in Equations (7.25) and (7.26) is now expressed in the frequency domain

$$\frac{D}{Dt} = i\omega + \mathbf{u}_0 \cdot \nabla \quad (7.27)$$

The single scalar wave equation for uniform (Eq. (7.25)) or nonuniform mean flow (Eq. (7.26)) may now be solved (subject to acoustic boundary conditions) to obtain the time-harmonic acoustic pressure or acoustic velocity potential. The appropriate acoustic boundary conditions for both scalar wave equations are the subject of the following subsection.

7.3.5 Acoustic Boundary Conditions

In the current subsonic flow problem, the linearized acoustic problem in three space dimensions requires one boundary condition at the source boundary and another at the duct termination. Codes that solve the uniform-flow, time-harmonic acoustic pressure equation (Eq. (7.25)) often have the time-harmonic acoustic pressure p_s specified directly at the source plane:

$$p = p_s \quad \text{along } \Gamma_s \quad (7.28)$$

Alternatively, the source plane acoustic pressure may be split into incident, p_{inc} , and reflected, p_{ref} , components with the incident component specified as the source plane condition

$$p_s = p_{\text{inc}} + p_{\text{ref}} \quad \text{along } \Gamma_s \quad (7.29)$$

In Equation (7.29) the reflected acoustic pressure p_{ref} is obtained as part of the solution procedure. The two approaches to acoustic source specification are generally driven by either the desire to support experimental facilities or to perform parameter studies. In experimental facilities, the sum of the incident and reflected source plane acoustic pressure p_s is measured and readily available for code input, and Equation (7.28) is therefore used as the source plane condition. However, in parameter studies, only the incident part of the source plane acoustic pressure p_{inc} is generally known (the reflected wave p_{ref} is a function of the liner impedance, duct termination, and geometry and cannot be known a priori), and Equation (7.29) is therefore implemented. Either method for specifying the source plane boundary condition (Eq. (7.28) or (7.29)) is mathematically correct and leads to an identical solution (provided other conditions are the same within Ω).

At the duct termination, a boundary condition is specified in the form of either an acoustic pressure, where the incident acoustic pressure is given as

$$p = p_{\text{inc}} + p_{\text{ref}} \quad \text{along } \Gamma_t \quad (7.30)$$

or as a termination boundary condition of the form

$$\frac{ic_0}{\omega} [\zeta_t] \{ \nabla p \cdot \mathbf{n} \} = \{ p \} \quad \text{along } \Gamma_t \quad (7.31)$$

One important point that can be easily overlooked is that the termination boundary condition defined by Equation (7.31) is a nonlocal condition. That is, the normal gradient of the acoustic pressure field at a point along the boundary depends upon the collective influence of the acoustic pressure field at all other points along the boundary. The square matrix $[\zeta_t]$ is the dimensionless node impedance matrix, \mathbf{n} is the outward unit normal vector to Γ_t , $\{p\}$ and $\{\nabla p \cdot \mathbf{n}\}$ are column vectors containing the acoustic pressure and its normal derivative at points along Γ_t . Further, when the exit boundary is discretized with N grid points, the dimensionless node impedance matrix is of order N , the vector $\{p\}$ is a column vector of length N that contains the acoustic pressure at the N grid points along Γ_t , and $\{\nabla p \cdot \mathbf{n}\}$ is a column vector of length N that contains the normal derivative of the acoustic pressure at the N grid points along Γ_t . The elements in the matrix $[\zeta_t]$ may be chosen so that the termination is modeled as reflecting or nonreflecting; the choice for elements in $[\zeta_t]$ will be discussed in more detail later when results are presented. A more detailed discussion of Equation (7.31) along with its derivation is given in Reference 2. It is also worth noting that Equation (7.30) is often used by codes in which only the incident wave p_{inc} is known. Equation (7.31), on the other hand, is used mostly by codes that support experimental facilities where the total pressure field (i.e., the sum of incident and reflected pressure field) and dimensionless node impedance matrix can be measured.

There has been considerable discussion in the literature during the past half century concerning the acoustic boundary condition for general surface shapes with mean flow. Myers (Ref. 3) resolved this controversy a quarter of a century ago and his boundary condition has been generally accepted as correct in modern duct acoustic literature. Thus, all codes discussed in this chapter employ the Myers boundary condition, which in its most general time-harmonic form is

$$-\rho_0 c_0 \mathbf{u} \cdot \mathbf{n} = -\frac{p}{\zeta} - \frac{\rho_0 c_0}{i\omega} (\mathbf{u}_0 \cdot \nabla) \left(\frac{p}{\rho_0 c_0 \zeta} \right) + \frac{p}{i\omega \zeta} \mathbf{n} \cdot \mathbf{n} \cdot \nabla (\mathbf{u}_0) \quad \text{on } \Gamma_w \quad (7.32)$$

It is noted that Equation (7.32) is restricted to locally reacting acoustic treatment and will not be valid for those absorbers that allow wave propagation through the material in directions parallel to the flow path. To write the impedance boundary condition (Eq. (7.32)) in terms of acoustic pressure in the presence of uniform flow, take the normal component of the linearized momentum equation (Eq. (7.18)) to obtain

$$\frac{D}{Dt}(-\rho_0 c_0 \mathbf{u} \bullet \mathbf{n}) = c_0 \nabla p \bullet \mathbf{n} \quad \text{in } \Omega \quad (7.33)$$

Substituting Equation (7.32) into Equation (7.33) and assuming a uniform flow gives

$$\frac{D}{Dt} \left[\frac{p}{\zeta} + \frac{\rho_0 c_0}{i\omega} (\mathbf{u}_0 \bullet \nabla) \left(\frac{p}{\rho_0 c_0 \zeta} \right) \right] = -c_0 \nabla p \bullet \mathbf{n} \quad \text{on } \Gamma_w \quad (7.34)$$

Equation (7.34) is the appropriate wall impedance boundary condition for the scalar pressure equation (Eq. (7.25)).

Returning now to solutions for the acoustic potential equation in nonuniform mean flow (Eq. (7.26)), we specify either the acoustic potential at the source plane

$$\phi = \phi_s \quad \text{along } \Gamma_s \quad (7.35)$$

or the source plane acoustic potential is split into an incident and reflected source plane potential

$$\phi = \phi_{\text{inc}} + \phi_{\text{ref}} \quad \text{along } \Gamma_s \quad (7.36)$$

with the incident source plane potential ϕ_{inc} specified and the reflected potential ϕ_{ref} obtained as part of the solution. Along the duct termination, a nonlocal boundary condition similar to Equation (7.31) is specified in the form

$$\frac{ic_0}{\omega} [\zeta_t] \{ \nabla \phi \bullet \mathbf{n} \} = \{ \phi \} \quad \text{along } \Gamma_t \quad (7.37)$$

The Myers boundary condition (Eq. (7.32)) is applied along the duct wall. When written in terms of the time-harmonic acoustic potential, this boundary condition is

$$\begin{aligned} -\nabla \phi \bullet \mathbf{n} = & \frac{1}{c_0 \zeta} \frac{D\phi}{Dt} + \left(\frac{\mathbf{M}_0 c_0}{i\omega} \bullet \nabla \right) \left(\frac{1}{c_0 \zeta} \frac{D\phi}{Dt} \right) \\ & - \frac{1}{i\omega c_0 \zeta} \frac{D\phi}{Dt} \mathbf{n} \bullet \mathbf{n} \bullet \nabla (c_0 \mathbf{M}_0) \end{aligned} \quad (7.38)$$

where the mean-flow Mach number vector, \mathbf{M}_0 is defined as

$$\mathbf{M}_0 = \frac{\mathbf{u}_0}{c_0} \quad (7.39)$$

7.4 Acoustic Liner Sound Attenuation

The acoustic intensity I at any axial plane can be evaluated using the Morfey expression (Ref. 4):

$$I = \frac{1}{2} \Re \left[p \mathbf{u}^* \bullet \mathbf{n} + \rho_0 (\mathbf{u}_0 \bullet \mathbf{u}) (\mathbf{u} \bullet \mathbf{n})^* + \frac{pp^*}{\rho_0 c_0^2} (\mathbf{u}_0 \bullet \mathbf{n}) + \frac{p^*}{c_0^2} (\mathbf{u}_0 \bullet \mathbf{u}) (\mathbf{u}_0 \bullet \mathbf{n}) \right] \quad (7.40)$$

where the asterisk superscript denotes the complex conjugate. Furthermore, the total acoustic power at the source or duct termination is the integral of the acoustic intensity across the cross section

$$E_s = \int_{\Gamma_s} I \, d\Gamma \quad (7.41)$$

$$E_t = \int_{\Gamma_t} I \, d\Gamma \quad (7.42)$$

and the decrease in decibels of the acoustic power from the source to the duct termination (i.e., the liner attenuation) can be written as

$$\Delta E = 10 \log_{10} \left(\frac{E_s}{E_t} \right) \quad (7.43)$$

It should be noted that ΔE represents that portion of the acoustic energy in decibels that is attenuated by the liner and does not propagate away from the duct exit to the far field. The goal of optimum liner design is to maximize the liner attenuation.

Unfortunately, the normal component of acoustic velocity, $\mathbf{u} \bullet \mathbf{n}$, needed to evaluate the acoustic intensity in Equation (7.40) is generally not available. In this situation, it is convenient to use the difference in the integrated (i.e., average) sound pressure level (SPL) between the source and duct termination ΔSPL as a measure of lining performance. This expression is

$$\Delta SPL = SPL_s - SPL_t \quad (7.44)$$

$$SPL_s = 10 \log_{10} \left(\frac{\int_{\Gamma_s} pp^* \, d\Gamma}{\int_{\Gamma_s} p_{\text{reference}}^2 \, d\Gamma} \right) \quad (7.45)$$

$$SPL_t = 10 \log_{10} \left(\frac{\int_{\Gamma_t} pp^* \, d\Gamma}{\int_{\Gamma_t} p_{\text{reference}}^2 \, d\Gamma} \right) \quad (7.46)$$

where SPL_s and SPL_t are the average SPLs at the source and duct termination, respectively, and $p_{\text{reference}}$ is a reference pressure usually taken as 20 μPa . Equation (7.44) is used throughout this chapter to compute the performance of the

wall lining when only the acoustic pressure is known (such as with experimental measurements). On the other hand, Equation (7.43) can be used when both the acoustic pressure and the normal component of acoustic velocity are known (such as in numerical simulations).

7.5 Potential Flow Computer Codes

Obtaining solutions to the potential flow scalar wave equation (Eq. (7.25) or Eq. (7.26)), when coupled with the appropriate source, termination, and wall impedance boundary condition, remains a formidable task. Exact solutions for arbitrary sources and mean flows have thus far not been found. However, the introduction of large-scale digital computers has allowed for numerical solutions to be obtained. These numerical solutions are essential for optimum design of noise-efficient aircraft. Over the past two decades, a number of computer codes have emerged for the numerical solution of these scalar wave equations when coupled to the appropriate boundary conditions. The remaining subsections discuss the various computer codes along with their salient features and limitations. There are four potential flow codes discussed in this chapter:

- (1) Quasi-three-dimensional uniform-flow code
- (2) Axially symmetric code
- (3) Three-dimensional uniform-flow code
- (4) Three-dimensional code with the parabolic approximation

Readers are reminded that the code descriptions presented in this chapter are intended as a review only and more technical details are provided on the quasi-three-dimensional code in Reference 5, the axially symmetric code in Reference 6, and the three-dimensional code with the parabolic approximation in Reference 7. Details of the three-dimensional uniform-flow code have not been published and are provided in this chapter for the first time. Each of these codes is discussed in the above order in the following subsections.

7.5.1 Quasi-Three-Dimensional Uniform-Flow Code

The quasi-three-dimensional approximation is applicable to duct geometries and flows for which the acoustic solution in one orthogonal direction (assumed to be the y direction in this chapter) is separable due to the fact that the sidewalls are both rigid and orthogonal to that direction. Quasi-three-dimensional acoustic analysis is restricted to a liner impedance that depends only on the axial coordinate z ($\zeta = \zeta(z)$), and mean velocity fields that have only a uniform axial component. Further, the mean static pressure, and mean static density are constant

$$\begin{aligned} v_0 &= 0 \\ u_0 &= 0 \\ w_0 &= \text{constant} \\ p_0 &= \text{constant} \\ \rho_0 &= \text{constant} \end{aligned} \quad (7.47)$$

so that the uniform-flow pressure equation (Eq. (7.25)) and acoustic pressure boundary conditions (Eqs. (7.28), (7.31), and (7.34)) may be used. Physically, the quasi-three-dimensional approximation is applicable to laboratory experiments conducted in constant-area, rectangular geometries such as grazing-flow impedance tubes where the mean-flow velocity is fairly low and boundary layer effects can be neglected.

The weighted residual approximate solution to Equation (7.25) requires that the time-harmonic acoustic pressure p be first approximated by a trial solution \bar{p} and that the resulting error in the governing differential equation (Eq. (7.25)) be minimized by requiring that it be orthogonal to a complete set of basis functions W_J ,

$$\int_{\Omega} \left[\frac{1}{c_0^2} \frac{D^2 \bar{p}}{Dt^2} - \nabla \cdot \nabla \bar{p} \right] W_J d\Omega = 0 \quad (7.48)$$

where $\frac{D}{Dt}$ is expressed in the frequency domain by Equation (7.27). The above formulation has the restriction that $\nabla \bar{p}$ must be continuous in Ω before \bar{p} can converge to p . This restriction can be relaxed by applying the Stokes theorem to Equation (7.48) so that the order of the highest derivatives are reduced. This results in the weak form

$$\begin{aligned} \int_{\Omega} \left[-k^2 \bar{p} W_J - 2ik(\mathbf{M}_0 \cdot \nabla \bar{p}) W_J \right. \\ \left. - (\mathbf{M}_0 \cdot \nabla W_J)(\mathbf{M}_0 \cdot \nabla \bar{p}) - (\nabla \bar{p}) \cdot (\nabla W_J) \right] d\Omega \\ = \int_{\Gamma} [\nabla \bar{p} - \mathbf{M}_0(\mathbf{M}_0 \cdot \nabla \bar{p})] \cdot \mathbf{n} W_J d\Gamma \end{aligned} \quad (7.49)$$

where \mathbf{M}_0 is the mean-flow Mach number vector defined in Equation (7.39) and the freespace wave number k is

$$k = \frac{\omega}{c_0} \quad (7.50)$$

Equation (7.49) is solved numerically using a quasi-three-dimensional, Galerkin finite element method with rectangular finite elements. A full discussion of the theory underlying the development of the finite element method may be found in Reference 8. The method as used here assumes that there are N nodes in the axial direction (i.e., the z -direction) and M nodes in the transverse direction (i.e., the x -direction) of the duct as shown in Figure 7.3. Because the solution in the spanwise direction (i.e., the y -direction) is separable and contains rigid sidewalls, it is expanded into a series of hard-wall duct modes. Thus, the finite element solution needs to be obtained only in the x,z -plane. A typical two-dimensional rectangular element $[I,J]$ is shown in Figure 7.4. Each element consists of four local node numbers labeled 1, 2, 3, and 4. Each element is considered to have length in z -direction

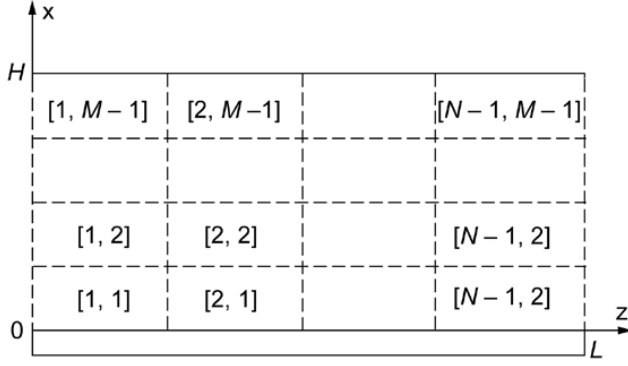


Figure 7.3.—Finite-element discretization of two-dimensional duct.

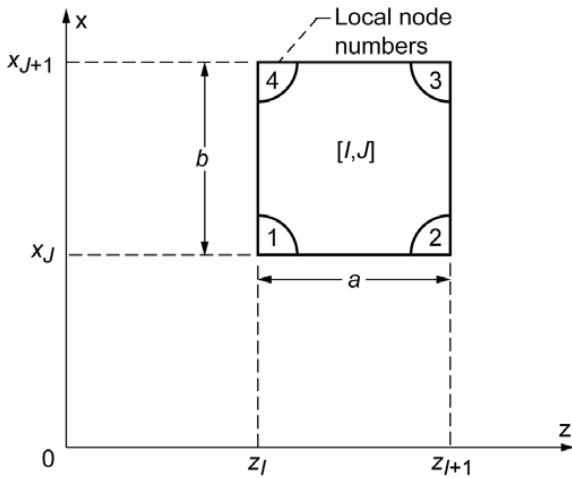


Figure 7.4.—Typical two-dimensional finite-element, $[I, J]$, and local node numbering system.

of $a = (z_{I+1} - z_I)$ and length in x -direction of $b = (x_{J+1} - x_J)$ as shown. The objective of the method is to obtain the unknown acoustic pressure and its derivatives at the nodes of each of the $(N-1) \times (M-1)$ elements.

Within each finite element, \bar{p} is represented as a linear combination of 16 cubic functions, $\mathcal{N}_1, \mathcal{N}_2, \mathcal{N}_3, \dots, \mathcal{N}_{16}$, which compose a complete set of basis functions:

$$\bar{p}(z, x, y) = \cos\left(\frac{m\pi y}{D}\right) \sum_{I=1}^{I=16} \mathcal{N}_I(z, x) \Phi_I \quad (7.51)$$

where D is the distance between the rigid sidewalls, and the node coefficients Φ_I are understood to depend on the hard-wall-mode order m . We use a Galerkin finite element method so that the set of weighting functions W_J equals the basis functions used in the expansion for \bar{p} :

$$W_J = \mathcal{N}_J(z, x) \cos\left(\frac{m\pi y}{D}\right) \quad (7.52)$$

The 16 two-dimensional basis functions \mathcal{N}_I and nodal parameters Φ_I are easily constructed from the products of the four cubic Hermite polynomial basis functions in the two coordinate directions,

$$\begin{aligned} f_1(z, a) &= 1 - 3\left(\frac{z}{a}\right)^2 + 2\left(\frac{z}{a}\right)^3 \\ f_2(z, a) &= z\left(\frac{z}{a} - 1\right)^2 \\ f_3(z, a) &= \left(\frac{z}{a}\right)^2 \left(3 - \frac{2z}{a}\right) \\ f_4(z, a) &= \left(\frac{z^2}{a}\right) \left(\frac{z}{a} - 1\right) \end{aligned} \quad (7.53)$$

and the requirement that $\nabla \bar{p}$ be continuous within each element and along inter-element boundaries

$$\begin{aligned} \mathcal{N}_1 &= f_1(z, a) f_1(x, b) \\ \mathcal{N}_2 &= f_2(z, a) f_1(x, b) \\ &\vdots \\ \mathcal{N}_{16} &= f_4(z, a) f_4(x, b) \end{aligned} \quad (7.54)$$

$$\begin{aligned} \Phi_1 &= \bar{p}(z_I, x_J) \\ \Phi_2 &= \frac{\partial \bar{p}(z_I, x_J)}{\partial z} \\ &\vdots \\ \Phi_{16} &= \frac{\partial^2 \bar{p}(z_I, x_{J+1})}{\partial z \partial x} \end{aligned} \quad (7.55)$$

The variable impedance $\zeta(z)$ is represented in a similar manner along each boundary element:

$$\begin{aligned} \frac{1}{\zeta(z)} &= \frac{1}{\zeta(z_I)} f_1(z, a) + \frac{1}{\zeta'(z_I)} f_2(z, a) \\ &+ \frac{1}{\zeta(z_{I+1})} f_3(z, a) + \frac{1}{\zeta'(z_{I+1})} f_4(z, a) \end{aligned} \quad (7.56)$$

where ζ' represents the derivative of ζ with respect to z . The importance of the choice of the trial solution and basis functions given in Equations (7.51) and (7.52) is that they satisfy the convergence and continuity requirements of the finite element method (Ref. 8). Thus by substituting Equations (7.51) to (7.56) into Equation (7.49) and setting the weighting function W_J to the basis function \mathcal{N}_J allows one to compute the contributions to the minimization of the total error from each individual element,

$$\begin{aligned} \sum_{\text{elements}} \int_{\Omega_e} [-k^2 \bar{p} \mathcal{N}_J - 2ik(\mathbf{M}_0 \cdot \nabla \bar{p}) \mathcal{N}_J \\ - (\mathbf{M}_0 \cdot \nabla \mathcal{N}_J)(\mathbf{M}_0 \cdot \nabla \bar{p}) - (\nabla \bar{p} \cdot \nabla \mathcal{N}_J)] d\Omega_e \quad (7.57) \\ = \sum_{\text{elements}} \int_{\Gamma_e} [\nabla \bar{p} - \mathbf{M}_0(\mathbf{M}_0 \cdot \nabla \bar{p})] \cdot \mathbf{n} \mathcal{N}_J d\Gamma_e \end{aligned}$$

where the sum in Equation (7.57) is carried out over all finite elements using the usual rules of finite element assembly. In Equation (7.57), Ω_e is now interpreted as the element volume and Γ_e is the surface that bounds the element volume. The surface integral on the right-hand side of Equation (7.57) produces no net contribution except at the source plane, at the duct termination, and along the perimeter of the duct. This occurs because, away from these boundaries, adjoining finite elements produce surface integral contributions on the right-hand side of Equation (7.57) that are equal in magnitude and opposite in direction. Effects of the wall impedance boundary condition is included in weak form at the element level by substituting the uniform-flow form of the Myers boundary condition (see Eq. (7.34))

$$\nabla \bar{p} \cdot \mathbf{n} = -[ik + (\mathbf{M}_0 \cdot \nabla)]^2 \left(\frac{\bar{p}}{ik\zeta} \right) \quad (7.58)$$

directly into the surface integral on the right-hand side of Equation (7.57). A similar procedure is used to implement the exit impedance boundary condition (Eq. (7.31)). Because of the orthogonality of the hard-wall duct modes, Equation (7.57) with appropriate substitution from Equation (7.58) will hold for each spanwise mode m so that it needs to be constructed only in the z, x -plane. Contributions to Equation (7.57) from a typical element $[I, J]$ are of the form $[S]\{\Phi\}$ where $[S]$ is a 16×16 complex matrix for each element $[I, J]$, and $\{\Phi\}$ is a 16×1 column vector containing the unknown acoustic pressure and its derivatives at the four nodes of the element. The coefficients in the local stiffness matrix, $[S]$, are computed in closed form using Mathematica (Ref. 9) intrinsic functions.

Assembly of the global equations for the computational domain is a basic procedure in the finite element method. Appropriate shifting of rows and columns is all that is required to add the local element matrix, $[S]$, directly into the global stiffness matrix. Assembling the elements for the entire domain results in a global matrix equation of the form:

$$[S_{\text{CH2D}}]\{\Phi\} = \{F_{\text{CH2D}}\} \quad (7.59)$$

where the global stiffness matrix $[S_{\text{CH2D}}]$ is a complex square matrix whose order is $4MN$, and $\{\Phi\}$ and $\{F_{\text{CH2D}}\}$ are $4MN \times 1$ column vectors. The vector $\{\Phi\}$ contains the nodal values of the unknown acoustic pressure and its derivatives at the nodes of the elements and $\{F_{\text{CH2D}}\}$ is the null vector.

It is necessary to apply the source pressure condition (Eq. (7.28)) to the system of Equations (7.59) before a unique solution can be obtained. Satisfying the noise source boundary

condition consists simply of constraining all nodal values of acoustic pressure and its derivative at the source plane Γ_s to the known value of source pressure, p_s , and its derivative. This procedure introduces nonzero elements into the first $4M$ components of the vector $\{F_{\text{CH2D}}\}$.

After implementation of source boundary condition, Equation (7.59) remains block tridiagonal. Much practical importance arises from this matrix structure, as it is convenient for minimizing storage and maximizing computational efficiency. Special matrix techniques exist for a solution of this structure. An unsymmetrical parallel sparse solver with equation reordering to minimize fill is used to decompose $[S_{\text{CH2D}}]$ into the products of a unit lower ($[L]$) and a unit upper ($[U]$) triangular matrices, and a nonsingular diagonal matrix ($[DD]$)

$$[S_{\text{CH2D}}] = [L][DD][U] \quad (7.60)$$

Equation (7.60) now decomposes into two triangular systems

$$[L]\{\bar{\Phi}\} = \{F_{\text{CH2D}}\} \quad (7.61)$$

$$[DD][U]\{\Phi\} = \{\bar{\Phi}\} \quad (7.62)$$

The sequential operations of forward and backward substitution are used to obtain the solution vector, $\{\Phi\}$. In this work, all computations are performed on a parallel computer and only the nonzero elements in $[S_{\text{CH2D}}]$ are stored and operated upon during the solution stage. The computer code developed for the solution of the convected Helmholtz uniform-flow equation following the aforementioned two-dimensional finite element approach with a direct solve strategy is referred to as the CH2DDS code in subsequent discussion.

7.5.2 Axially Symmetric Code

The axially symmetric code was developed in academia (Ref. 6), is written in cylindrical coordinates, and is termed axially symmetric because the nacelle geometry and the mean flow field in and around the nacelle are axially symmetric. Unlike the quasi-three-dimensional code that computes only the in-duct propagation, the axially symmetric code allows the noise field in the nacelle to radiate to the far field. The cylindrical coordinates are z , r , and θ , where the axial coordinate is z , the radial coordinate is r , and θ is the angular or circumferential coordinate. Acoustic solutions are sought in terms of the angular harmonics of a Fourier series with angular mode m . This reduces the acoustic solution to a two-dimensional problem in the z, r -plane. The inlet and aft radiation are treated similarly in the code. The exception is that the jet is included in the aft fan radiation by separating the interior and exterior flow outside the aft fan duct with a thin barrier created by disconnecting the interior and exterior domain. In what follows, a discussion of the inlet radiation code is performed in detail. Afterwards, we show how to include the effects of the jet in the formulation for aft radiation.

For inlet radiation, the sound fields in the duct and far field are extracted using a weighted residual formulation for which the acoustic potential is ϕ and the weighting functions are W_J . Thus, the weighted residual formulation of Equation (7.26) gives

$$\int_{\Omega} \frac{\rho_0}{c_0^2} \left[\frac{D}{Dt} \left(\frac{D\phi}{Dt} \right) - c_0^2 \nabla \cdot \nabla \phi \right] W_J d\Omega = 0 \quad (7.63)$$

where Ω consists of the entire domain (interior and exterior to the nacelle). Applying the Stokes theorem to Equation (7.63) and simplifying as shown above in the quasi-three-dimensional discussion gives the weak formulation

$$\begin{aligned} & \int_{\Omega} \frac{\rho_0}{c_0^2} \left[-\omega^2 \phi W_J + i\omega(\mathbf{u}_0 \cdot \nabla \phi) W_J - i\omega(\mathbf{u}_0 \cdot \nabla W_J) \phi \right. \\ & \quad \left. - (\mathbf{u}_0 \cdot \nabla W_J)(\mathbf{u}_0 \cdot \nabla \phi) - c_0^2 (\nabla \phi) \cdot (\nabla W_J) \right] d\Omega \\ & = \int_{\Gamma} \frac{\rho_0}{c_0^2} \left[-i\omega \mathbf{u}_0 \phi + c_0^2 \omega \nabla \phi - \mathbf{u}_0 (\mathbf{u}_0 \cdot \nabla \phi) \right] \cdot \mathbf{n} W_J d\Gamma \end{aligned} \quad (7.64)$$

Solutions are sought in cylindrical coordinates in terms of angular harmonics of the form

$$\begin{Bmatrix} W_J(z, r, \theta) \\ \phi(z, r, \theta) \end{Bmatrix} = \begin{Bmatrix} W_J^m(z, r) e^{im\theta} \\ \phi_m(z, r) e^{-im\theta} \end{Bmatrix} \quad (7.65)$$

and the gradient operators are defined as

$$\nabla W_J = \frac{\partial W_J}{\partial r} \mathbf{e}_r + \frac{im W_J}{r} \mathbf{e}_\theta + \frac{\partial W_J}{\partial z} \mathbf{e}_z \quad (7.66)$$

$$\nabla \phi_m = \frac{\partial \phi_m}{\partial r} \mathbf{e}_r - \frac{im \phi_m}{r} \mathbf{e}_\theta + \frac{\partial \phi_m}{\partial z} \mathbf{e}_z \quad (7.67)$$

where \mathbf{e}_r , \mathbf{e}_θ and \mathbf{e}_z , are unit vectors in the r -, θ -, and z -directions. The irrotational mean flow, \mathbf{u}_0 , is the gradient of the axially symmetric mean flow potential $\phi_0(r, z)$:

$$\mathbf{u}_0 = \nabla \phi_0 = \frac{\partial \phi_0}{\partial r} \mathbf{e}_r + \frac{\partial \phi_0}{\partial z} \mathbf{e}_z \quad (7.68)$$

Note that the factors $e^{\pm im\theta}$ cancel out of Equation (7.64) and the problem is reduced to one in two spatial coordinates r and z for each Fourier mode m .

In a steady, nonuniform flow field, Equation (7.64) is solved using a conventional Galerkin finite element method, where the weighting functions W_J are identical to the finite element basis functions. The finite element basis functions in this region (i.e., where the mean flow is nonuniform) are rectangular, eight noded, isoparametric serendipity elements (elements without interior nodes). Thus, a quadratic expression is used to approximate the acoustic potential within

each finite element. The near field (where the flow is nonuniform) is terminated on a boundary Γ_r , beyond which a single layer of far-field or infinite elements is used. An artificial baffle Γ_b formed by a ray from the origin is used to limit the domain. In the far field, Equation (7.64) is discretized using mapped wave envelope elements. The basis functions in the infinite elements are constructed to display the characteristics of the fundamental source solution at large distances from the source. The weighting functions in the far field are chosen so that the boundary integrals in Equation (7.64) have no contribution along Γ_r . The details of the mapped wave envelope implementation are rather lengthy and are discussed in further detail in Reference 6. The effects of the wall impedance and the sound source are included by substitution into the boundary integrals in Equation (7.64), just as in the quasi-three-dimensional formulation. Only the incoming waves are specified at the source plane (i.e., Eq. (7.36)), and the reflected portion of the solution is captured as part of the solution procedure.

Assembling the elements together leads to a linear matrix equation similar in form to Equation (7.59), but different in structure. The axially symmetric solver uses a frontal solver by Irons (Ref. 10) to solve this matrix equation. Modifications have been made to the original solver of Irons so that all direct-access inputs and outputs are eliminated in favor of active storage or sequential inputs and outputs. This has resulted in as much as 50 percent reduction in computation time, dependent mainly on available fast memory.

For the aft radiation code, the acoustic potential is discontinuous across the shear layer dividing the extended jet from the external flow. Therefore, elements above and below the shear layer have additional degrees of freedom on the shear layer boundaries that contain the acoustic particle displacement. Because the acoustic pressure and particle displacement are continuous across the shear layer, a penalty constraint in the form of a surface integral is added to the surface integrals on the right-hand side of Equation (7.64) to enforce the proper conditions across the shear layer. The penalty constraint simply modifies the coefficient matrix, $[S_{CH2D}]$. The computer code developed based on the aforementioned axially symmetric formulation with inlet or aft radiation is referred to as the CH2DIE code in subsequent discussion.

7.5.3 Three-Dimensional Uniform-Flow Code

The three-dimensional uniform-flow code makes assumptions similar to the quasi-three-dimensional formulation, with the exception that all four walls of the duct may be lined and the liner impedance is a function of both wall coordinates. Consequently, the solution in the y (or any other) dimension is not separable, and a fully three-dimensional model is required to compute the acoustic field.

The three-dimensional weighted residual approximate solution to Equation (7.25) in weak form is still given by Equation (7.49):

$$\begin{aligned} \int_{\Omega} [-k^2 \bar{p} W_J - 2ik(\mathbf{M}_0 \cdot \nabla \bar{p}) W_J \\ - (\mathbf{M}_0 \cdot \nabla W_J)(\mathbf{M}_0 \cdot \nabla \bar{p}) - (\nabla \bar{p}) \cdot (\nabla W_J)] d\Omega \quad (7.49) \\ = \int_{\Gamma} [\nabla \bar{p} - \mathbf{M}_0(\mathbf{M}_0 \cdot \nabla \bar{p})] \cdot \mathbf{n} W_J d\Gamma \end{aligned}$$

Here, Equation (7.49) is solved numerically using a three-dimensional Galerkin finite element method. The three-dimensional finite element method assumes that there are N nodes in the axial, or z -direction, M nodes in the x -direction, and Q nodes in the y -direction of the duct as shown in Figure 7.5. Brick elements with eight nodes are used in the analysis. A typical brick element, $[I, J, K]$, is shown in Figure 7.6. Each element consists of eight local node numbers labeled 1, 2, ..., 8. Each element is considered to have length $a = (z_{I+1} - z_I)$, height $b = (x_{J+1} - x_J)$ and width $d = (y_{K+1} - y_K)$ as shown. The objective of the three-dimensional method is to obtain the unknown acoustic pressure and its derivatives at the nodes of each of the $(N-1) \times (M-1) \times (Q-1)$ elements.

Within each element, \bar{p} is represented as linear combinations of 64 cubic functions, $\mathcal{N}_1, \mathcal{N}_2, \mathcal{N}_3, \dots, \mathcal{N}_{64}$ that compose a complete set of basis functions:

$$\bar{p}(z, x, y) = \sum_{I=1}^{I=64} \mathcal{N}_I(z, x, y) \Phi_I \quad (7.69)$$

A Galerkin finite element method is used so that the set of weighting functions W_J equals the basis functions:

$$W_J = \mathcal{N}_J(z, x, y) \quad (7.70)$$

The 64 three-dimensional basis functions \mathcal{N}_I and node coefficients Φ_I are easily constructed from the products of the four cubic Hermite polynomial basis functions (Eq. (7.53)) in the three coordinate directions and the requirement that \bar{p} and $\nabla \bar{p}$ be continuous within and along inter-element boundaries:

$$\begin{aligned} \mathcal{N}_1 &= f_1(z, a) f_1(x, b) f_1(y, d) \\ \mathcal{N}_2 &= f_2(z, a) f_1(x, b) f_1(y, d) \\ &\vdots \\ \mathcal{N}_{64} &= f_4(z, a) f_4(x, b) f_4(y, d) \end{aligned} \quad (7.71)$$

$$\begin{aligned} \Phi_1 &= \bar{p}(z_I, x_J, y_K) \\ \Phi_2 &= \frac{\partial \bar{p}(z_I, x_J, y_K)}{\partial z} \\ &\vdots \\ \Phi_{64} &= \frac{\partial^3 \bar{p}(z_I, x_{J+1}, y_{K+1})}{\partial z \partial x \partial y} \end{aligned} \quad (7.72)$$

The variable impedance ζ is represented in a similar manner for elements along Γ_w :

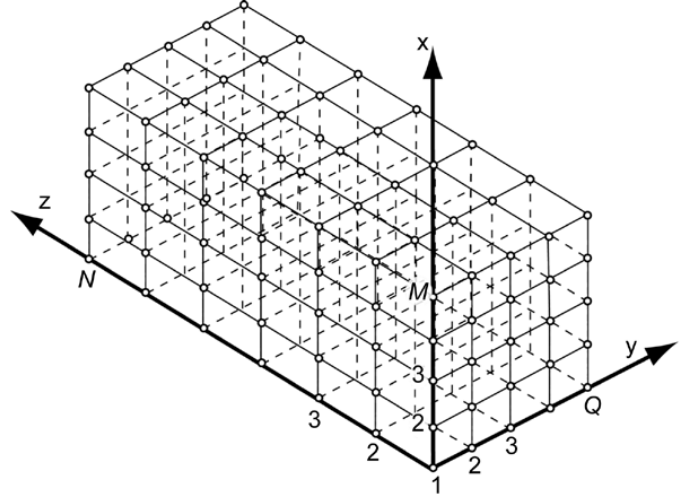


Figure 7.5.—Finite-element discretization of three-dimensional duct.

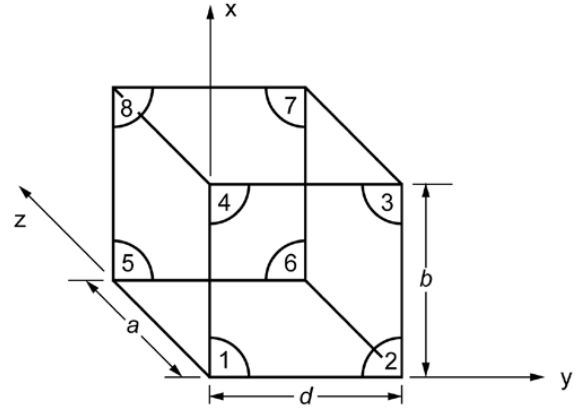


Figure 7.6.—Typical three-dimensional finite-element, $[I, J, K]$, and local node numbering system.

$$\frac{1}{\zeta} = \sum_{I=1}^{I=64} \mathcal{N}_I(z, x, y) \frac{1}{\zeta_I}, \text{ along } \Gamma_w \quad (7.73)$$

where ζ_I are values of the impedance function and its derivatives at nodes along Γ_w . Only 16 of the basis functions \mathcal{N}_I are nonzero along Γ_w .

Substituting Equations (7.69) to (7.73) into Equation (7.49) and setting the weighting function W_J to the basis functions allows one to compute the contributions to the minimization of the total error from each individual element as

$$\begin{aligned} \sum_{\text{elements}} \int_{\Omega} [-k^2 \bar{p} \mathcal{N}_J - 2ik(\mathbf{M}_0 \cdot \nabla \bar{p}) \mathcal{N}_J \\ - (\mathbf{M}_0 \cdot \nabla \mathcal{N}_J)(\mathbf{M}_0 \cdot \nabla \bar{p}) - (\nabla \bar{p}) \cdot (\nabla \mathcal{N}_J)] d\Omega \quad (7.74) \\ = \sum_{\text{elements}} \int_{\Gamma} [\nabla \bar{p} - \mathbf{M}_0(\mathbf{M}_0 \cdot \nabla \bar{p})] \cdot \mathbf{n} \mathcal{N}_J d\Gamma \end{aligned}$$

where the sum in Equation (7.74) is again carried out over all finite elements using the usual rules of finite element assembly. Effects of the wall impedance boundary condition are included in weak form at the element level by substituting the Myers boundary condition directly into the surface integral on the right-hand side of Equation (7.74):

$$\nabla \bar{p} \cdot \mathbf{n} = -[ik + (\mathbf{M}_0 \cdot \nabla)]^2 \left(\frac{p}{ik\zeta} \right) \quad (7.75)$$

A similar procedure is used to implement the duct termination boundary condition. Contributions to Equation (7.74) from a typical element $[I,J,K]$ are of the form $[S]\{\Phi\}$, where $[S]$ is a 64×64 complex square matrix for each element $[I,J,K]$, and $\{\Phi\}$ is a 64×1 column vector containing the unknown acoustic pressure and its derivatives at the eight nodes of the element. The coefficients in the local stiffness matrix $[S]$ are computed in closed form just as in the quasi-three-dimensional analysis.

Assembling the elements for the entire domain results in a matrix equation that is again of the form

$$[S_{\text{CH3D}}]\{\Phi\} = \{F_{\text{CH3D}}\} \quad (7.76)$$

where $[S_{\text{CH3D}}]$ is a complex, square, block tridiagonal matrix whose order is $8MNQ$, and $\{\Phi\}$ and $\{F_{\text{CH3D}}\}$ are $8MNQ \times 1$ column vectors. The vector $\{\Phi\}$ contains the nodal values of the unknown acoustic pressure and its derivatives at the nodes of the element, and $\{F_{\text{CH3D}}\}$ is the zero vector. The source plane boundary condition is introduced into Equation (7.76) by constraining the nodal degrees of freedom just as in the quasi-three-dimensional case. This introduces 4QM nonzero elements into $\{F_{\text{CH3D}}\}$. The same unsymmetrical parallel sparse solver used in the quasi-three-dimensional case is used to solve the fully three-dimensional system. However, the three-dimensional system has a much larger bandwidth. The computer code developed for the solution of the convected Helmholtz uniform-flow equation following the aforementioned three-dimensional finite element approach with a direct solver strategy is referred to as the “CH3DDS” code in subsequent discussion.

7.5.4 Three-Dimensional Code With Parabolic Approximation

A duct fan noise propagation and radiation code has been developed that utilizes a parabolic approximation to the convected Helmholtz equation (Ref. 11). The code is composed of five distinct modules: (1) input and output specification, (2) mean flow and acoustic grid generation, (3) background flow calculation, (4) duct acoustic propagation, and (5) acoustic radiation. The propagation module, which is the focus of this section, incorporates the work of Dougherty

(Refs. 7 and 12) and utilizes a parabolic approximation to the convected Helmholtz equation. This approach affords very efficient propagation calculations, thus allowing solutions for complex three-dimensional geometries to be handled with relatively low computational costs. This efficiency comes at the expense of reduced accuracy as the direction of propagation of an acoustic mode diverges from the preferred angle of the parabolic approximation. Additionally, loss of accuracy may occur when reflection of acoustic waves in the axial direction becomes important, as these effects are not captured in this formulation. Nevertheless, if appropriate care is taken to account for these limitations, this code can provide an efficient environment in which to perform three-dimensional propagation calculations. Thus, an additional aspect of this assessment is the continuation of a systematic study to identify a “working envelope” within which to use the various approaches to modeling duct propagation.

Although the parabolic approximation and general splitting technique were discussed in detail in previous work, a brief introduction is useful in understanding the approach. The full formulation is carried out in terms of the acoustic velocity potential ϕ and is based on the convected Helmholtz equation (Eq. 7.26). However, for simplicity, a rectangular duct is considered in which a steady mean-flow Mach number M_0 aligned with the duct z -axis is present. Thus, the initial governing equation of the analysis is the convected Helmholtz equation in the form

$$(1 - M_0^2) \frac{\partial^2 \phi}{\partial z^2} = -\nabla_{\perp}^2 \phi + \left(2ikM_0 + M_0 \frac{\partial M_0}{\partial z} \right) \frac{\partial \phi}{\partial z} - k^2 \phi \quad (7.77)$$

where ∇_{\perp}^2 is the transverse Laplacian defined as

$$\nabla_{\perp}^2 = \nabla_{\perp} \cdot \nabla_{\perp} = \frac{\partial^2}{\partial x^2} + \frac{\partial^2}{\partial y^2} \quad (7.78)$$

and an $e^{i\omega t}$ time dependence has again been assumed. As discussed by Dougherty (Ref. 12) and outlined by Coronos (Ref. 13), a derivation based on splitting the solution of the governing equation (Eq. 7.77) into “positive” and “negative” traveling waves is proposed. This general splitting may be represented as

$$\begin{Bmatrix} \phi^+ \\ \phi^- \end{Bmatrix} = [T(z)] \begin{Bmatrix} \phi \\ \frac{\partial \phi}{\partial z} \end{Bmatrix} \text{ or } \begin{Bmatrix} \phi \\ \frac{\partial \phi}{\partial z} \end{Bmatrix} = [T(z)]^{-1} \begin{Bmatrix} \phi^+ \\ \phi^- \end{Bmatrix} \quad (7.79)$$

where the splitting matrix $[T(z)]$ is arbitrary. Substitution of the general variable splitting (Eq. (7.79)) into the convected Helmholtz equation (Eq. (7.77)) leads to a coupled pair of differential equations for ϕ^{\pm} of the form

$$\begin{aligned}
 & (1 - M_0^2) \frac{\partial}{\partial z} \begin{Bmatrix} \phi^+ \\ \phi^- \end{Bmatrix} \\
 &= \left[(1 - M_0^2) \left(\frac{\partial T}{\partial z} \right) [T]^{-1} \right. \\
 & \quad \left. + [T] \begin{bmatrix} 0 & 1 - M_0^2 \\ -(\nabla_{\perp}^2 + k^2) & 2ikM_0 + M_0 \left(\frac{\partial M_0}{\partial z} \right) \end{bmatrix} [T]^{-1} \right] \begin{Bmatrix} \phi^+ \\ \phi^- \end{Bmatrix}
 \end{aligned} \quad (7.80)$$

Dougherty considered plane waves to produce a splitting of the form

$$\begin{Bmatrix} \phi \\ \frac{\partial \phi}{\partial z} \end{Bmatrix} = \begin{bmatrix} 1 & 1 \\ -ik & ik \\ 1 + M_0 & 1 - M_0 \end{bmatrix} \begin{Bmatrix} \phi^+ \\ \phi^- \end{Bmatrix} \quad (7.81)$$

Typically, at this point in the derivation, the terms that couple the equations for ϕ^{\pm} are neglected to produce a single parabolic equation for the “positive” or “negative” traveling wave.

The general formulation outlined by Dougherty considers a system of orthogonal, curvilinear coordinates (ξ_1, ξ_2, ξ_3) defined so that ξ_3 is aligned with the steady potential mean flow. Following the aforementioned splitting process and neglecting the off-diagonal terms in the resulting matrix equation gives the parabolic approximation

$$\frac{\partial \phi^+}{\partial \xi_3} = \frac{h_3 ik}{1 + M_0} \phi^+ - \frac{h_3}{2ik} \nabla_{\perp}^2 \phi^+ - \frac{1}{2h_1 h_2} \frac{\partial}{\partial \xi_3} (h_1 h_2) \phi^+ \quad (7.82)$$

where h_i is the element of length given by

$$h_i = \sqrt{\left(\sum_{j=1}^3 \frac{\partial x_j}{\partial \xi_i} \right)^2} \quad \text{for } i = 1, 2, 3 \quad (7.83)$$

The source boundary condition is given by

$$\phi^+ \Big|_{z=0} = \phi_{\text{inc}} \quad (7.84)$$

and the solution for ϕ^+ is marched from the source to the exit plane, where the source is taken to be a specified ϕ^+ distribution and no exit impedance is required, as ϕ^{\pm} coupling is not considered.

The effects of acoustic treatment on the duct walls are included by assuming locally reacting impedance surfaces, which are out of the flow. The acoustic pressure and the normal acoustic particle displacement are continuous across an

infinitely thin boundary layer. Denoting quantities within the duct interior with subscript “I” and those outside the infinitely thin boundary layer with subscript “II,” the impedance boundary condition may be written as

$$\pm \frac{1}{h_j} \frac{\partial \phi_{\text{II}}^+}{\partial \xi_j} = \frac{ik \phi_{\text{II}}^+}{\zeta} \quad (7.85)$$

where ϕ_{II}^+ is the acoustic velocity potential below the boundary layer, ζ is the normalized impedance, and the sign is negative for minimum ξ_j and positive for maximum ξ_j . The continuity of pressure condition leads to

$$\frac{D \phi_{\text{I}}^+}{Dt} = \frac{\partial \phi_{\text{II}}^+}{\partial t} \quad (7.86)$$

and the normal particle displacement condition leads to

$$\left(\frac{D}{Dt} \right)^{-1} (\nabla \phi_{\text{I}}^+ \cdot \mathbf{n}) = \left(\frac{\partial}{\partial t} \right)^{-1} (\nabla \phi_{\text{II}}^+ \cdot \mathbf{n}) \quad (7.87)$$

where the material and time derivatives in Equations (7.86) and (7.87) are expressed in the frequency domain. Eliminating ϕ_{II}^+ and neglecting derivatives of the Mach number in the direction of the flow leads to

$$\frac{\partial \phi^+}{\partial \xi_j} = \pm \frac{ik}{\zeta} \frac{h_j}{(1 + M_0)^2} \phi_{\text{I}}^+ \mp \frac{h_j M_0}{1 + M_0} \frac{\partial}{\partial \xi_3} \left(\frac{1}{\zeta} \right) \phi_{\text{I}}^+ \quad (7.88)$$

The code that implements the aforementioned parabolic approximation method without computing the far-field radiation is referred to as “CH3DPA.”

As mentioned above, the code suite also contains an acoustic radiation module for the prediction of far-field noise (Ref. 11). The approach is based on a time-domain integral representation of the solution of the Ffowcs Williams-Hawkings equation with penetrable data surfaces (FW- H_{pds}) (Refs. 14 and 15). Here, acoustic quantities and mean flow conditions are provided on a penetrable source surface. This surface is typically defined by extending the aforementioned in-duct propagation calculations a short distance beyond the inlet or exhaust planes for inlet or aft-fan cases, respectively. At the termination of the in-duct prediction domain, the necessary input information is transferred to the FW- H_{pds} domain for subsequent use in radiation predictions.

For aft-fan cases, the shear layer between the bypass flow and external stream can refract the sound waves radiated to the far field. Radiation results can be improved by including this effect as well as the reflection of the sound in the bypass region from the solid surface external to the bypass duct

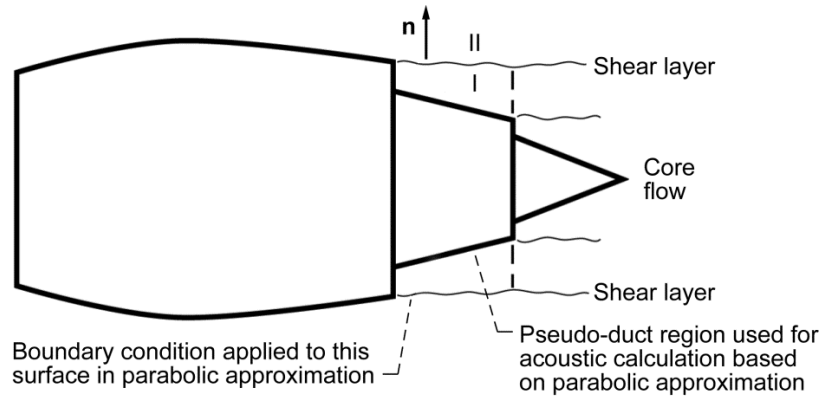


Figure 7.7.—Turbfan engine showing boundary regions of axisymmetric aft-fan geometry for parabolic approximation acoustic propagation and far-field radiation code FWH3D, where \mathbf{n} is unit vector normal to outer shear layer.

surrounding the core flow (see Figure 7.7). As described in Section 7.5.2, “Axially Symmetric Code,” this is taken into account in the axially symmetric finite element code by the inclusion of additional degrees of freedom on the shear layer boundaries that contain the acoustic velocity. For the base implementation described above, this effect is not taken into account. However, one possible method of modeling this effect has been proposed. It entails extending the bypass duct propagation calculation into a “pseudo-duct” beyond the exhaust plane. This pseudo-duct extends axially from the exhaust plane of the bypass duct to the trailing edge of the core cowl; its inner and outer radii are defined by the core cowl and shear layer, respectively, as indicated in Figure 7.7. Acoustic treatment may be included on the core cowl and an acoustic-liner-type boundary condition is applied to the shear layer surface.

Although presented previously in Reference 16, a brief review of this boundary condition may be useful. The development is based on the satisfaction of two conditions on the shear layer, which is assumed to be infinitely thin:

- (1) The particle displacement must be continuous across the shear layer.
- (2) The acoustic pressure must be continuous across the shear layer.

First, an expression relating the normal components of the acoustic velocity on the opposing sides of the shear layer is developed. Second, assuming that duct modal patterns persist within the shear layer flow region, an expression for the impedance on the external surface of the shear layer is derived. Finally, the impedance on the internal surface of the shear layer is given as

$$\zeta_I = \frac{(\mathbf{u}_{II} \cdot \mathbf{n})}{(\mathbf{u}_I \cdot \mathbf{n})} \zeta_{II} \quad (7.89)$$

where the subscripts I and II indicate the corresponding regions shown in Figure 7.7, \mathbf{u} is the acoustic velocity vector,

\mathbf{n} is the unit normal vector to the shear layer’s external surface, and ζ is the acoustic impedance. The computer code developed for the solution of the convected Helmholtz equation in three dimensions following the aforementioned parabolic approximation with the acoustic radiation module used to predict the far-field noise is referred to as the “FWH3D” code in subsequent discussion.

7.6 Rotational Flow Computer Codes

This section presents the governing differential equations, duct boundary conditions, and numerical methods for the suite of duct propagation models that allow for rotational flow. Four codes are discussed:

- (1) Two-dimensional code
- (2) Quasi-three-dimensional code
- (3) Axially symmetric code
- (4) Three-dimensional code

The quasi-three-dimensional code is based upon a finite element simulation of the linearized equations that govern conservation of mass and momentum for the fluid in the duct. Readers interested in more technical details concerning the quasi-three-dimensional code than presented in this chapter may consult (Ref. 17). The other three rotational flow codes were developed at Boeing with partial funding from NASA. Each of these three codes use a pseudo-time marching scheme to solve the linearized equations governing the conservation of mass and momentum either in two-dimensional, axially symmetric, or three-dimensional flows. More technical details on the pseudo-time marching codes are provided in (Refs. 18 and 19). In this section, the governing equations and boundary conditions for three-dimensional rotational flows are first presented. Next, we discuss the quasi-three-dimensional finite element code and its assumptions. Finally, we discuss the recently developed pseudo-time marching method that is used for the remaining three codes.

7.6.1 Governing Differential Equations and Boundary Conditions

The equations that govern conservation of mass and momentum in a flow duct with viscous effects are (Ref. 1)

$$\frac{\partial \hat{p}}{\partial t} + (\hat{\mathbf{u}} \cdot \nabla) \hat{p} + \hat{p} \nabla \cdot \hat{\mathbf{u}} = 0 \quad (7.2)$$

$$\hat{p} \left[\frac{\partial \hat{\mathbf{u}}}{\partial t} + (\hat{\mathbf{u}} \cdot \nabla) \hat{\mathbf{u}} \right] + \nabla \hat{p} - \nabla \cdot [\hat{\boldsymbol{\tau}}] = 0 \quad (7.90)$$

At this point, the assumptions and equations governing continuity of mass and momentum in the fluid are the same as those presented in Section 7.3, “Potential Flow Formulation,” except for the additional matrix, $[\hat{\boldsymbol{\tau}}]$, which is the shear stress tensor. Thus, Equation (7.90) is now the Navier-Stokes equation, which accounts for viscous effects.

Decomposing the flow into a time independent mean flow and a time dependent acoustic perturbation gives

$$\hat{p} = p_0 + \tilde{p}, \quad \hat{\mathbf{u}} = \mathbf{u}_0 + \tilde{\mathbf{u}}, \quad [\hat{\boldsymbol{\tau}}] = [\boldsymbol{\tau}_0] + [\tilde{\boldsymbol{\tau}}] \quad (7.91)$$

Substituting Equation (7.91) into Equations (7.2) and (7.90) allows the equations for mass and momentum continuity to be rewritten in terms of the perturbation variables

$$\begin{aligned} \frac{D\tilde{p}}{Dt} + \rho_0 \nabla \cdot \tilde{\mathbf{u}} + \tilde{p} \nabla \cdot \mathbf{u}_0 + (\tilde{\mathbf{u}} \cdot \nabla) \rho_0 \\ + NL1 = - \left[\frac{D\rho_0}{Dt} + \rho_0 \nabla \cdot \mathbf{u}_0 \right] \end{aligned} \quad (7.6)$$

$$\begin{aligned} \rho_0 \frac{D\tilde{\mathbf{u}}}{Dt} + \rho_0 (\tilde{\mathbf{u}} \cdot \nabla) \mathbf{u}_0 + \tilde{p} \frac{D\mathbf{u}_0}{Dt} + \nabla \tilde{p} \\ - \nabla \cdot [\tilde{\boldsymbol{\tau}}] + NL2 = - \left[\rho_0 \frac{D\mathbf{u}_0}{Dt} + \nabla p_0 - \nabla \cdot [\boldsymbol{\tau}_0] \right] \end{aligned} \quad (7.92)$$

and the nonlinear terms are

$$NL1 = \tilde{p} (\nabla \cdot \tilde{\mathbf{u}}) + (\tilde{\mathbf{u}} \cdot \nabla) \tilde{p} \quad (7.9)$$

$$\begin{aligned} NL2 = \tilde{p} \frac{\partial \tilde{\mathbf{u}}}{\partial t} + \rho_0 (\tilde{\mathbf{u}} \cdot \nabla) \tilde{\mathbf{u}} + \tilde{p} (\tilde{\mathbf{u}} \cdot \nabla) \mathbf{u}_0 \\ + \tilde{p} (\mathbf{u}_0 \cdot \nabla) \tilde{\mathbf{u}} + \tilde{p} (\tilde{\mathbf{u}} \cdot \nabla) \tilde{\mathbf{u}} \end{aligned} \quad (7.10)$$

By neglecting the nonlinear terms ($NL1 = NL2 \approx 0$) in Equations (7.6) and (7.92), and recalling that the right-hand side of Equations (7.6) and (7.92) are zero since the viscous mean flow is the solution to the steady form of Equations (7.2) and (7.90), the linearized form of the perturbation equations becomes

$$\frac{D\tilde{p}}{Dt} + \rho_0 \nabla \cdot \tilde{\mathbf{u}} + \tilde{p} \nabla \cdot \mathbf{u}_0 + (\tilde{\mathbf{u}} \cdot \nabla) \rho_0 = 0 \quad (7.11)$$

$$\rho_0 \frac{D\tilde{\mathbf{u}}}{Dt} + \rho_0 (\tilde{\mathbf{u}} \cdot \nabla) \mathbf{u}_0 + \tilde{p} \frac{D\mathbf{u}_0}{Dt} + \nabla \tilde{p} - \nabla \cdot [\tilde{\boldsymbol{\tau}}] = 0 \quad (7.93)$$

In order to close the system of equations, it is necessary to establish a relationship between \tilde{p} and $\tilde{\rho}$ and establish transport properties relating the coefficient of viscosity to the velocity field. Here, it is assumed that the disturbance takes place homentropically in an ideal gas, so that

$$\tilde{p} = c_0^2 \tilde{\rho}, \quad c_0^2 = \frac{\gamma p_0}{\rho_0} \quad (7.13)$$

Note that the homentropic relation (Eq. (7.13)) neglects the effects of viscous and heat conduction effects on the perturbations ($\nabla \cdot [\tilde{\boldsymbol{\tau}}] \approx 0$). This leads to a linear system of four perturbation equations in four unknown variables (often referred to as the “linearized Euler equations”):

$$c_0^2 \frac{D}{Dt} \left(\frac{\tilde{p}}{c_0^2} \right) + \gamma p_0 \nabla \cdot \tilde{\mathbf{u}} + \tilde{p} (\nabla \cdot \mathbf{u}_0) + c_0^2 \gamma (\tilde{\mathbf{u}} \cdot \nabla) \frac{p_0}{c_0^2} = 0 \quad (7.94)$$

$$\gamma p_0 \frac{D\tilde{\mathbf{u}}}{Dt} + \gamma p_0 (\tilde{\mathbf{u}} \cdot \nabla) \mathbf{u}_0 + \tilde{p} \left(\frac{D\mathbf{u}_0}{Dt} \right) + c_0^2 \nabla \tilde{p} = 0 \quad (7.95)$$

We now seek time-harmonic solutions to Equations (7.94) and (7.95) so that

$$\tilde{p} = p e^{i\omega t}, \quad \tilde{\mathbf{u}} = \mathbf{u} e^{i\omega t}, \quad i = \sqrt{-1} \quad (7.96)$$

where p and \mathbf{u} are now understood to be frequency dependent. Substituting Equation (7.96) into Equations (7.94) and (7.95) gives the following system of four equations in four unknown variables:

$$c_0^2 \frac{D}{Dt} \left(\frac{p}{c_0^2} \right) + \gamma p_0 \nabla \cdot \mathbf{u} + p \nabla \cdot \mathbf{u}_0 + c_0^2 \gamma (\mathbf{u} \cdot \nabla) \frac{p_0}{c_0^2} = 0 \quad (7.97)$$

$$\gamma p_0 \frac{D\mathbf{u}}{Dt} + \gamma p_0 (\mathbf{u} \cdot \nabla) \mathbf{u}_0 + p \frac{D\mathbf{u}_0}{Dt} + c_0^2 \nabla p = 0 \quad (7.98)$$

Equations (7.97) and (7.98) are referred to here as the “time-harmonic linearized Euler equations.” These equations can be solved uniquely to determine the perturbation variables, provided the appropriate boundary conditions are prescribed.

In the current subsonic flow problem, the linearized Euler equations in three space dimensions require three boundary

conditions at the inflow (i.e., the source boundary), one boundary condition at the outflow (i.e., the termination boundary), and a boundary condition at the acoustically lined wall. The wall impedance boundary condition remains the Myers time-harmonic boundary condition (Eq. (7.32)). Two implementations of the inflow and outflow boundary conditions are presented in this section. The first implementation (Ref. 17) specifies the acoustic pressure and the two transverse perturbation velocity components at the source boundary Γ_s :

$$\begin{Bmatrix} p \\ u \\ v \end{Bmatrix} = \begin{Bmatrix} p_s \\ u_s \\ v_s \end{Bmatrix} \text{ along } \Gamma_s \quad (7.99)$$

where p_s , u_s , and v_s are the known values of p , u , and v at points along Γ_s . Along the duct termination, a boundary condition of the form

$$\rho_0 c_0 [\zeta_t] \{w\} = \{p\} \text{ along } \Gamma_t \quad (7.100)$$

is specified. In Equation (7.100) $\{p\}$ and $\{w\}$ are vectors containing the values of p and w at nodes along Γ_t , and $[\zeta_t]$ is the normalized node impedance matrix that is either calculated from mode theory or measured. The second implementation of the boundary conditions (Ref. 18) splits p_s , u_s , and v_s into incident and reflected waves and specifies only the incident wave. The reflected wave is computed by invoking a non-reflecting boundary condition at the source plane. At the duct termination, a nonreflecting boundary condition is also specified, the details of which are discussed further in Reference 18.

7.6.2 Quasi-Three-Dimensional Code

The quasi-three-dimensional rotational flow code is applicable to duct geometries and flows for which the solution in one orthogonal direction (assumed to be the y-direction in this chapter) is separable, due to the fact that the sidewalls are both rigid and orthogonal to that direction. Quasi-three-dimensional analysis is valid only if the mean velocity field \mathbf{u}_0 does not have a component in the separable dimension and the other mean flow quantities are also independent of that dimension:

$$\begin{aligned} v_0 &= 0 \\ u_0 &= u_0(x, z) \\ w_0 &= w_0(x, z) \\ \rho_0 &= \rho_0(x, z) \\ p_0 &= p_0(x, z) \end{aligned} \quad (7.101)$$

For the solution to be separable (as required in the quasi-three-dimensional theory) the wall impedance must also be solely a function of the axial coordinate (i.e., $\zeta = \zeta(z)$). Further, the

quasi-three-dimensional theory is mostly applicable to laboratory experiments conducted in rectangular geometries such as grazing-flow impedance tubes. Therefore, the quasi-three-dimensional formulation is presented in Cartesian coordinates.

In the case of quasi-three-dimensional acoustics, the time-harmonic acoustic pressure and velocity field components are expanded into the following series of hard-wall duct modes:

$$p(z, x, y) = \sum_{m=0}^{m=\infty} p_m(x, z) \cos\left(\frac{m\pi y}{D}\right) \quad (7.102)$$

$$u(z, x, y) = \sum_{m=0}^{m=\infty} u_m(x, z) \cos\left(\frac{m\pi y}{D}\right) \quad (7.103)$$

$$v(z, x, y) = \sum_{m=1}^{m=\infty} v_m(x, z) \sin\left(\frac{m\pi y}{D}\right) \quad (7.104)$$

$$w(z, x, y) = \sum_{m=0}^{m=\infty} w_m(x, z) \cos\left(\frac{m\pi y}{D}\right) \quad (7.105)$$

where the hard-wall duct mode m takes on integer values and D is the distance between the parallel rigid duct walls. Substituting Equations (7.101) to (7.105) into Equations (7.97) and (7.98) and writing the resulting equations in component form yields the following system of four equations in four unknown variables for each m .

$$\{E\} = \begin{Bmatrix} E_p \\ E_u \\ E_v \\ E_w \end{Bmatrix} = \begin{Bmatrix} 0 \\ 0 \\ 0 \\ 0 \end{Bmatrix} \quad (7.106)$$

$$\begin{aligned} E_p &= i\omega p_m + c_0^2 \left[u_0 \frac{\partial}{\partial x} \left(\frac{p_m}{c_0^2} \right) + w_0 \frac{\partial}{\partial z} \left(\frac{p_m}{c_0^2} \right) \right] \\ &+ \gamma p_0 \left(\frac{\partial u_m}{\partial x} + \frac{m\pi}{D} v_m + \frac{\partial w_m}{\partial z} \right) + p_m \left(\frac{\partial u_0}{\partial x} + \frac{\partial w_0}{\partial z} \right) \\ &+ \gamma c_0^2 \left[u_m \frac{\partial}{\partial x} \left(\frac{p_0}{c_0^2} \right) + w_m \frac{\partial}{\partial z} \left(\frac{p_0}{c_0^2} \right) \right] \end{aligned} \quad (7.107)$$

$$\begin{aligned} E_u &= i\omega \gamma p_0 u_m + \gamma p_0 \left(u_0 \frac{\partial u_m}{\partial x} + w_0 \frac{\partial u_m}{\partial z} \right) \\ &+ \gamma p_0 \left(u_m \frac{\partial u_0}{\partial x} + w_m \frac{\partial u_0}{\partial z} \right) \\ &+ p_m \left(u_0 \frac{\partial u_0}{\partial x} + w_0 \frac{\partial u_0}{\partial z} \right) + c_0^2 \frac{\partial p_m}{\partial x} \end{aligned} \quad (7.108)$$

$$E_v = i\omega\gamma p_0 v_m + \gamma p_0 \left(u_0 \frac{\partial v_m}{\partial x} + w_0 \frac{\partial v_m}{\partial z} \right) + \frac{-m\pi c_0^2}{D} p_m \quad (7.109)$$

$$\begin{aligned} E_w = & i\omega\gamma p_0 w_m + \gamma p_0 \left(u_0 \frac{\partial w_m}{\partial x} + w_0 \frac{\partial w_m}{\partial z} \right) \\ & + \gamma p_0 \left(u_m \frac{\partial w_0}{\partial x} + w_m \frac{\partial w_0}{\partial z} \right) \\ & + p_m \left(u_0 \frac{\partial w_0}{\partial x} + w_0 \frac{\partial w_0}{\partial z} \right) + c_0^2 \frac{\partial p_m}{\partial z} \end{aligned} \quad (7.110)$$

The computational domain is divided into $N-1$ elements in the axial direction and $M-1$ elements in the x-direction, as shown in Figure 7.3. These elements need not be equally spaced. Within each element, each acoustic variable is expanded as a series

$$\begin{aligned} p &= \sum_{I=1}^4 \mathcal{N}_I p_I \\ u &= \sum_{I=1}^4 \mathcal{N}_I u_I \\ v &= \sum_{I=1}^4 \mathcal{N}_I v_I \\ w &= \sum_{I=1}^4 \mathcal{N}_I w_I \end{aligned} \quad (7.111)$$

where \mathcal{N}_I , p_I , u_I , v_I , and w_I are the basis functions and nodal values of p , u , v , and w , respectively, at local node I . Here the subscript m has been dropped for the sake of brevity and the basis functions \mathcal{N}_I are linear two-dimensional polynomials

$$\begin{aligned} \mathcal{N}_1 &= f_1(a, z) f_1(b, x) \\ \mathcal{N}_2 &= f_2(a, z) f_1(b, x) \\ \mathcal{N}_3 &= f_2(a, z) f_2(b, x) \\ \mathcal{N}_4 &= f_1(a, z) f_2(b, x) \\ f_1(a, z) &= 1 - \frac{z}{a} \\ f_2(a, z) &= \frac{z}{a} \end{aligned} \quad (7.112)$$

The variable impedance ζ and mean flow quantities are represented in similar series but the nodal values of these quantities are known.

The discrete equation system that governs the quasi-three-dimensional formulation is obtained by using a Galerkin finite element method to minimize the field residual error vector $\{E\}$. This is achieved by requiring that $\{E\}$ be orthogonal to each basis function \mathcal{N}_I . The contribution to the minimization

of the field error for each element is expressed in matrix form as

$$\int_0^b \int_0^a \{E\} \mathcal{N}_I dz dx = [S] \{\Phi\} \quad (7.113)$$

where $[S]$ is a 16×16 complex matrix for each element $[I, J]$ and $\{\Phi\}$ is a 16×1 column vector that contains the unknown acoustic pressures, axial acoustic velocities, and transverse acoustic velocities at the four nodes of the element. The coefficients in the local stiffness matrix, $[S]$, are computed in closed form. Appropriate shifting of rows and columns is all that is required to add the local element matrix $[S]$ directly into the global matrix $[S_{\text{LEE2D}}]$. This process leads to a set of linear matrix equations of the form

$$[S_{\text{LEE2D}}] \{\Phi\} = \{0\} \quad (7.114)$$

Here, the matrix $[S_{\text{LEE2D}}]$ is singular until boundary conditions are applied.

Before a nontrivial solution to Equation (7.114) can be obtained, the source, termination, and wall impedance boundary conditions must be imposed. Minimizing the boundary residual along the wall satisfies the wall impedance boundary condition

$$\begin{aligned} \sum_{\text{wall elements}} \int_{\Gamma_w} & \left[-\rho_0 c_0 \mathbf{u} \cdot \mathbf{n} + \frac{p}{\zeta} \right. \\ & \left. + \frac{\rho_0 c_0}{i\omega} (\mathbf{u} \cdot \nabla) \left(\frac{p}{\rho_0 c_0 \zeta} \right) \right] \mathcal{N}_I d\Gamma_w = 0 \end{aligned} \quad (7.115)$$

Equation (7.115) is rewritten as a matrix equation

$$[S_w] \{\Phi_w\} = \{0\}, \{\Phi_w\} = \begin{Bmatrix} \{p_w\} \\ \{u_w\} \end{Bmatrix} \quad (7.116)$$

where $\{p_w\}$ and $\{u_w\}$ are $2N \times 1$ vectors containing the values of the normal component of acoustic velocities and acoustic pressures at the $2N$ nodes along Γ_w . Here, $[S_w]$ is a complex $2N \times 4N$ matrix containing the values of the wall impedance ζ at the $2N$ nodes of Γ_w and $\{0\}$ is a null column vector of length $2N$. The discrete form of the wall impedance boundary condition (Eq. (7.116)) is imposed on Equation (7.115) as a set of constraints. Likewise, the sound source boundary condition (Eq. (7.99)) and duct termination boundary conditions (Eq. (7.100)) are implemented as constraints on Equation (7.114).

Imposing the wall impedance, sound source, and duct termination boundary condition into Equation (7.115) leads to a modified system of equations of the form

$$[S_{\text{LEE2D}}] \{\Phi\} = \{F_{\text{LEE2D}}\} \quad (7.117)$$

where $[S_{LEE2D}]$ is a complex, asymmetric matrix with an order of $4NM$, and $\{\Phi\}$ is a $4NM \times 1$ column vector that contains the nodal values of the unknown acoustic variables (p , u , v , and w) at the NM nodes of the duct. The vector $\{F_{LEE2D}\}$ is a $4NM \times 1$ column vector that contains source effects. Equation (7.117) is solved using a standard band solver to extract the solution vector $\{\Phi\}$. The computer code developed for the solution of the linearized Euler equations following the aforementioned two-dimensional finite element approach with a direct solve strategy is referred to as the "LEE2DDS" code in subsequent discussion.

7.6.3 Pseudo-Time Marching Codes

Pseudo-time marching codes have also been developed for solutions of the linearized Euler equations (Eqs. (7.97) and (7.98)) when coupled with the source, termination, and wall impedance (Eq. (7.32)) boundary conditions. The pseudo-time marching codes are available in three-dimensional, two-dimensional, or axially symmetric form. The starting point for the pseudo-time marching method is to rewrite Equations (7.97) and (7.98) in a compact vector format for either three-dimensional, two-dimensional, or axially symmetric flows. In three dimensions, the compact vector format at a location (x, y, z) is

$$\begin{aligned} -i\omega\{Q\} + [A]\left\{\frac{\partial Q}{\partial x}\right\} + [B]\left\{\frac{\partial Q}{\partial y}\right\} \\ + [C]\left\{\frac{\partial Q}{\partial z}\right\} + [D]\{Q\} = 0 \end{aligned} \quad (7.118)$$

$$\{Q\} = \begin{Bmatrix} p \\ u \\ v \\ w \end{Bmatrix}$$

where $[A]$, $[B]$, and $[C]$ are 4×4 matrices that contain mean flow effects and $[D]$ is a 4×4 matrix containing terms related to the gradient of the mean flow field. (See Ref. 18 for the definition of these matrices.) For axially symmetric flows in cylindrical coordinates (r, θ, z) with spinning modes of the form $e^{im\theta}$, the compact vector format is

$$\begin{aligned} -i\omega\{Q\} + [A]\left\{\frac{\partial Q}{\partial r}\right\} + [C]\left\{\frac{\partial Q}{\partial z}\right\} + [D]\{Q\} = 0 \end{aligned} \quad (7.119)$$

$$\{Q\} = \begin{Bmatrix} p \\ u \\ v \\ w \end{Bmatrix}$$

and for two-dimensional flows the vector format is

$$\begin{aligned} -i\omega\{Q\} + [A]\left\{\frac{\partial Q}{\partial x}\right\} + [C]\left\{\frac{\partial Q}{\partial z}\right\} + [D]\{Q\} = 0 \end{aligned} \quad (7.120)$$

$$\{Q\} = \begin{Bmatrix} p \\ u \\ v \end{Bmatrix}$$

For two-dimensional flows, $[A]$, $[C]$, and $[D]$ are 3×3 matrices. However, in axially symmetric and three-dimensional flows $[A]$, $[C]$, and $[D]$ are 4×4 matrices. Further, although the coefficients in these matrices are not explicitly written in this chapter, these coefficients are different in three-dimensional, two-dimensional, and axially symmetric flows.

Adding a pseudo-time derivative to the compact vector form of the linearized Euler equations gives in three dimensions,

$$\begin{aligned} \left\{\frac{\partial Q}{\partial \tau}\right\} = -i\omega\{Q\} + [A]\left\{\frac{\partial Q}{\partial x}\right\} + \\ [B]\left\{\frac{\partial Q}{\partial y}\right\} + [C]\left\{\frac{\partial Q}{\partial z}\right\} + [D]\{Q\} \end{aligned} \quad (7.121)$$

in axially symmetric flows,

$$\left\{\frac{\partial Q}{\partial \tau}\right\} = -i\omega\{Q\} + [A]\left\{\frac{\partial Q}{\partial r}\right\} + [C]\left\{\frac{\partial Q}{\partial z}\right\} + [D]\{Q\} \quad (7.122)$$

and in two-dimensional flows

$$\left\{\frac{\partial Q}{\partial \tau}\right\} = -i\omega\{Q\} + [A]\left\{\frac{\partial Q}{\partial x}\right\} + [C]\left\{\frac{\partial Q}{\partial z}\right\} + [D]\{Q\} \quad (7.123)$$

where τ is the pseudo-time variable. The pseudo-time derivative is introduced so that Equations (7.121) to (7.123) may be marched in pseudo-time until the solution is steady. Thus, the steady solution to Equations (7.121) to (7.123) is the solution to Equations (7.118) to (7.120). In the following, we describe the pseudo-time marching procedure only in three dimensions (see Eq. (7.121)), since its simplification to axially symmetric flows (Eq. (7.122)) and two-dimensional flows (Eq. (7.123)) is relatively straightforward.

To begin, Equation (7.121) is discretized in pseudo-time using a forward-Euler scheme:

$$\begin{aligned} \left\{\frac{Q^{n+1} - Q^n}{\Delta \tau}\right\} + i\omega\{Q^{n+1}\} = [A]\left\{\frac{\partial Q^n}{\partial x}\right\} + \\ [B]\left\{\frac{\partial Q^n}{\partial y}\right\} + [C]\left\{\frac{\partial Q^n}{\partial z}\right\} + [D]\{Q^n\} \end{aligned} \quad (7.124)$$

where n is the pseudo-time index, $\Delta\tau$ is the pseudo-time step, and the first term on the right-hand side of Equation (7.121) is treated implicitly. Equation (7.124) can then be written in a delta form

$$\{\Delta Q\} \left(\frac{1}{\Delta\tau} + i\omega \right) = -i\omega\{Q^n\} + [A] \left\{ \frac{\partial Q^n}{\partial x} \right\} + [B] \left\{ \frac{\partial Q^n}{\partial y} \right\} + [C] \left\{ \frac{\partial Q^n}{\partial z} \right\} + [D]\{Q^n\} \quad (7.125)$$

$$\Delta Q = Q^{n+1} - Q^n \quad (7.126)$$

Upon approximating the spatial derivatives and implementation of boundary conditions, Equation (7.125) can be marched iteratively in pseudo-time until the solution is steady (i.e., until $\{\Delta Q\} = \{0\}$) to achieve the frequency domain solution. The spatial gradients are approximated using a fourth-order optimized finite difference technique, referred to as the “dispersion-relation-preserving” (DRP) scheme (Ref. 20). The DRP scheme is a central difference approximation to the gradient in each coordinate direction that uses a seven-point stencil. The DRP scheme is especially designed to minimize dissipation and dispersion errors with a resolution of eight points per wavelength. At and near boundaries of the computational domain, the DRP central difference scheme requires points from outside the computational domain. This is avoided by switching to a fourth-order optimized one-sided difference at and near these boundaries. Further, an eighth-order filtering scheme is applied to prevent spurious waves from contaminating the solution domain, as the solution is advanced forward in pseudo-time. The source, liner, and duct termination boundary condition are inserted into the pseudo-time marching method by replacing each derivative (i.e., in these boundary conditions) by a fourth-order optimized one-sided difference. All of the intricate details involved in the implementation of the DRP scheme to the acoustic equations, as well as implementation of other acoustic boundary conditions (these are not considered in this text), are described in detail in Reference 18 and are not presented herein.

The three-dimensional, axially symmetric, and two-dimensional pseudo-time marching methods are implemented on a curvilinear mesh using uniform computational coordinates. Thus, solutions using arbitrary geometries are possible. In addition, the three-dimensional pseudo-time marching code uses a domain decomposition scheme that utilizes the message-passing interface (MPI) method to reduce wall clock time on parallel computers. The domain decomposition is only in the axial direction so that the other two dimensions are not parallelized. It should be noted that the two-dimensional and axially symmetric versions of the pseudo-time marching code available for this study are not currently parallelized. The computer codes developed for the solution of the linearized Euler equations in two-dimensions and three dimensions following the aforementioned pseudo-time approach with an

iterative solve strategy are referred to in subsequent discussion as the “LEE2DIS” and “LEE3DIS” codes, respectively.

7.7 Results and Discussion

This section provides an assessment of the potential and rotational flow codes discussed in this chapter. This assessment uses the accuracy of the predicted attenuation, the computational efficiency, and the effects of input uncertainties as its primary metrics. Code results are compared with each other and to analytical solutions when they are available. For duct configurations where analytical solutions are not available, code results are compared with measured data acquired in either the NASA Langley grazing incidence tube, the NASA Langley Curved Duct Test Rig, or the NASA Glenn Advanced Noise Control Fan Rig.

7.7.1 NASA Langley Grazing Incidence Tube Simulations

A number of the codes were run for a geometry corresponding to the NASA Langley Research Center grazing incidence tube (GIT). This geometry was chosen for the following reasons:

- (1) Experimental data was available to compare with code predictions.
- (2) A detailed description of the apparatus and its capabilities already exists in the literature (Ref. 21).
- (3) Currently, some of the codes only support a rectangular geometry.
- (4) The GIT is frequently used to deduce liner impedance (as discussed in detail in Chapter 6, “Uncertainty in Acoustic Liner Impedance Measurement and Prediction”) and the accuracy of the resulting impedance estimates is dependent upon the accuracy of the propagation model.

Sound and flow are directed in the same direction (only aft-duct propagation was modeled), and the centerline Mach numbers range from 0.0 to 0.5. Results are presented for six selected excitation frequencies (500, 1000, 1500, 2000, 2500, and 3000 Hz).

Results are presented for the following three lining configurations:

- (1) A hard-wall duct
- (2) An infinitely long duct for which the lower and two sidewalls are rigid, and the upper wall contains a uniform liner. The impedance values of the uniform liner were judiciously chosen so that they spanned the ranges of resistance and reactance observed for a number of liners tested in the GIT.
- (3) A 71.12-cm-long portion of a duct for which the lower wall and two sidewalls are rigid. The upper wall is also rigid, except for a 40.64-cm-long, uniformly treated section that is positioned 10.16 cm downstream of the source plane. The test liner was a conventional perforate-over-honeycomb material whose impedance was obtained from measurements in the

GIT. Because the upper wall of this duct incorporates a hard-wall section, followed by a soft-wall section, followed again with a hard-wall section, it is referred to as the “segmented liner” example in the following discussion.

7.7.1.1 Accuracy Assessment

The most important metric in assessing a propagation code is the accuracy of the predicted attenuation. To assess the accuracy of the predicted attenuation, two example problems were chosen for which the attenuation could be determined analytically. The first example problem tests the ability of the in-duct codes to predict the attenuation of a plane wave propagating through a hard-wall duct with flow. It is well known that a plane wave does not attenuate as it propagates along a hard-wall duct, and therefore the codes should predict zero attenuation. The second example problem tests the ability of each code to predict the finite attenuation of a cut-on mode in a softwall duct with a uniform lining. For this case, an exact value for the attenuation is obtained using mode theory.

In the first example problem, the hard-wall attenuations were simulated for nine different conditions obtained from three excitation frequencies (1000, 2000, and 3000 Hz) and three mean-flow Mach numbers (0.0, 0.3, and 0.5). For each simulation, the source was planar (i.e., $p_s = 1$) and the termination was nonreflecting (i.e., $[\zeta_r] = [I]$). Simulations were run at standard atmospheric conditions: the mean static pressure was 101325.0 N/m², density was 1.2 kg/m³, and temperature was 293.0 K.

Predicted sound pressure level (*SPL*) attenuations from Equation (7.44) for the three Mach numbers and three frequencies are presented in Table 7.1 for the hard-wall duct. The first column in the table gives the excitation frequency in Hertz, and the second column gives the attenuation in decibels (exactly 0 for a hard wall). The predicted in-duct attenuations are presented for six of the eight codes in the suite. Note that predicted hard-wall attenuations are for three potential flow and three rotational flow codes from the suite. The three

potential flow codes were the quasi-three-dimensional flow code (CH2DDS), the three-dimensional uniform-flow code (CH3DDS), and the three-dimensional code with the parabolic approximation (CH3DPA). The axially symmetric code (see Sec. 7.5.2) was used to compute radiated sound and therefore is not included in this comparison. The three rotational flow codes used to predict the in-duct attenuation were the quasi-three-dimensional rotational code (LEE2DDS), the two-dimensional rotational flow code (LEE2DIS), and the three-dimensional rotational flow code (LEE3DIS). The axially symmetric rotational flow code (see Sec. 7.6.3) was not run because the GIT is not an axially symmetric geometry. Table 7.1 shows that the predicted hard-wall attenuations from each of the six in-duct codes are in excellent agreement with the exact value of 0.

The second example tests the ability of each code to predict the finite attenuation of a cut-on mode in a softwall duct with a uniform lining. In this case, an exact value for the attenuation is obtained using mode theory. It is easily shown that the exact value of the *SPL* attenuation from Equation (7.44) for this configuration is

$$\Delta SPL = 20 \log_{10}(e) \Im[K_{m,n}L] \quad (7.127)$$

where $K_{m,n}$ is the axial propagation constant. The transverse wavenumber $\lambda_{m,n}$ satisfies the transcendental equation

$$ik\alpha_{m,n} = \zeta \lambda_{m,n} \tan(\lambda_{m,n}H) \quad (7.128)$$

where

$$k = \frac{\omega}{c_0} \quad (7.50)$$

$$\alpha_{m,n} = 1 - 2 \left(\frac{M_0 K_{m,n}}{k} \right) + \left(\frac{M_0 K_{m,n}}{k} \right)^2 \quad (7.129)$$

TABLE 7.1.—SOUND ATTENUATION IN DECIBELS COMPUTED FOR PLANE WAVE
IN HARD-WALL DUCT WITH NONREFLECTING TERMINATION
[For different values of mean-flow Mach number M_0 .]

Excitation frequency, Hz	Exact	Acoustic propagation code					
		CH2DDS	LEE2DDS	LEE2DIS	CH3DPA	CH3DDS	LEE3DIS
	M ₀ = 0.0						
1000	0.00	0.00	0.01	0.00	0.00	0.00	0.00
2000	0.00	0.00	0.02	0.00	0.00	0.00	0.00
3000	0.00	0.00	0.00	0.05	0.00	0.00	0.09
	M ₀ = 0.3						
1000	0.00	0.00	0.01	0.00	0.00	0.00	0.00
2000	0.00	0.00	0.01	0.00	0.00	0.00	0.00
3000	0.00	0.00	0.21	0.01	0.00	0.00	0.01
	M ₀ = 0.5						
1000	0.00	0.00	0.00	0.00	0.00	0.00	0.00
2000	0.00	0.00	0.02	0.00	0.00	0.00	0.00
3000	0.00	0.00	0.06	0.00	0.00	0.00	0.00

The $\lambda_{m,n}$ and axial propagation constant $K_{m,n}$ are related by the dispersion relation

$$\frac{K_{m,n}}{k} = \frac{M_0 \pm \sqrt{1 - (1 - M_0^2) \left[(m\pi/kD)^2 + (\lambda_{m,n}/k)^2 \right]}}{-(1 - M_0^2)} \quad (7.130)$$

The axial propagation constant $K_{m,n}$ is approximated by finding the roots of the transcendental equation (Eq. (7.128)). Note that for a given value of $\lambda_{m,n}$, the $K_{m,n}$ satisfying Equation (7.130) has two roots. Here, the root that corresponds to right-moving waves in the duct is chosen. It is easily shown that right-moving waves are identified as those waves for which the axial propagation constant $K_{m,n}$ has a zero or negative imaginary part and a positive real part. The method used to obtain the eigenvalues parallels the analytic continuation method discussed in Reference 22. However, we replace Mullers' iterative scheme (Ref. 23) with Stewart's adaptation of the Davidon-Fletcher-Powell method (Ref. 24) during the iteration phase of the analytic continuation method.

Attenuations due to a softwall were computed for 36 different conditions. These 36 conditions correspond to the same frequencies and Mach numbers as presented in Table 7.1. Four softwall impedances were used with each combination of Mach number and frequency. The sound source p_s was chosen to be the least attenuated mode in the duct, the termination was chosen to be nonreflecting (i.e., $[\zeta_r] = \zeta_{\text{exit}}[I]$), and the mean static pressure, density, and temperature were those at the standard atmospheric conditions used in the hard-wall simulations. Here, ζ_{exit} is the characteristic impedance for the least attenuated right-moving wave and was computed from the exact expression for the outgoing wave impedance:

$$\zeta_{\text{exit}} = \frac{k - M_0 K_{m,n}}{K_{m,n}} \quad (7.131)$$

Softwall attenuations predicted from CH2DDS, LEE2DDS, LEE2DIS, CH3DPA, and CH3DDS for the softwall duct with an anechoic (i.e., nonreflecting) termination and zero flow are compared to the exact attenuations in Table 7.2. The normalized resistance and reactance of the wall lining are given in the second and third columns, respectively, of the table. Recall that the sound source in this second example was a softwall duct mode. Results from LEE3DIS were not computed because the available version of LEE3DIS was designed to take source inputs in the form of hard-wall duct modes only. As shown in Table 7.2, CH2DDS, LEE2DDS, and CH3DDS are in excellent agreement with the exact results with one exception. Note that at 2000 Hz, LEE2DDS fails to predict the large attenuation of 143 dB when the impedance is $\zeta = 0.5 - 0.5i$. Attenuations predicted with LEE2DIS and CH3DPA are in good agreement with the exact attenuation except at the frequency and impedance corresponding to the peak attenuation of 143 dB. The failure of three of the codes

(LEE2DDS, LEE2DIS, and CH3DPA) to predict the peak attenuation of 143 dB was somewhat surprising and should be further investigated. Generally speaking, LEE2DIS and CH3DPA are slightly less accurate than the other three in-duct codes in the absence of flow. Given the parabolic approximation of the CH3DPA code, its performance is quite good.

Softwall attenuations predicted at Mach 0.3 and Mach 0.5 are also given in Table 7.2. Several high-Mach-number observations are noted. First, a significant reduction in the peak attenuation is observed at the higher Mach numbers (e.g., the highest attenuation is slightly more than 56 dB, compared with 143 dB at Mach 0.0). Second, CH2DDS, LEE2DDS, and CH3DDS are in excellent agreement with the exact results at each Mach number (note that LEE2DDS is in agreement with the exact attenuation now that the peak attenuation is much lower). Third, given the lower fidelity of the CH3DPA compared with the other codes, its predicted attenuation is still quite good, except at a few frequencies where wide-angle effects are more pronounced. Fourth, the attenuation of LEE2DIS is diverging from the exact attenuation and from the attenuation predicted by other codes as Mach number increases. This is an unexpected result, but may be due to use of the LEE2DIS plane-wave nonreflecting boundary condition. Recall that the exact attenuation (see the fourth column in Table 7.2) is computed assuming that the duct termination is nonreflecting. However, the LEE2DIS boundary condition that is used to predict the LEE2DIS attenuation will yield a nonreflecting termination only if the termination is located in a hard-wall section of duct. Because the duct termination was located in a softwall section of duct, this may explain the divergence of the LEE2DIS results.

7.7.1.2 Efficiency Assessment

Two important metrics often used to determine the efficiency of a computer code are wall clock time per central processing unit (CPU) and computer memory requirements. The suite of codes presented in this chapter solve a discrete set of acoustic equations using either a direct solve (e.g., CH2DDS, LEE2DDS, CH3DPA, or CH3DDS) or an iterative solve (e.g., LEE2DIS or LEE3DIS) strategy to compute the acoustic solution. The codes that are based on an iterative solve strategy were designed for computers with low memory (e.g., workstations and small clusters), whereas those that implement direct solve strategies are designed for high-memory machines (e.g., large clusters). Generally speaking, the wall clock time is not as important on low-memory machines because they are often under the control of a single user and there is little competition for CPU usage from other users. However, high-memory machines often support many users that compete for available wall clock time and CPUs. In this chapter, we choose to place focus on how these codes are used at Langley, where the most important metrics for deciding on the choice of a code are the wall clock time and number of CPUs. This occurs for three primary reasons:

TABLE 7.2.—SOUND ATTENUATION IN DECIBELS COMPUTED FOR LEAST ATTENUATED
MODE IN SOFT-WALL DUCT WITH NONREFLECTING TERMINATION
[For different values of mean-flow Mach number M_0 .]

Excitation frequency, Hz	Normalized resistance, $\Re[\zeta]$	Normalized reactance, $\Im[\zeta]$	Exact	Sound propagation code				
				CH2DDS	LEE2DDS	LEE2DIS	CH3DPA	CH3DDS
			$M_0 = 0.0$					
1000	0.50	-0.50	61.70	61.70	59.50	56.22	68.77	61.10
1000	0.50	0.50	50.00	50.00	49.80	48.32	43.15	49.50
1000	2.00	-0.50	24.60	24.60	24.40	24.90	25.73	24.30
1000	2.00	0.50	24.00	24.00	23.90	23.78	24.25	23.80
2000	0.50	-0.50	143.00	143.00	61.70	66.26	79.00	142.00
2000	0.50	0.50	19.30	19.30	19.20	19.19	35.52	19.10
2000	2.00	-0.50	26.50	26.50	26.30	28.33	25.39	26.20
2000	2.00	0.50	21.00	21.00	20.90	22.53	22.71	20.80
3000	0.50	-0.50	36.10	36.10	35.90	39.53	24.06	35.70
3000	0.50	0.50	10.30	10.30	10.20	14.18	8.35	10.20
3000	2.00	-0.50	26.40	26.40	26.30	31.01	27.63	26.10
3000	2.00	0.50	17.90	17.90	17.70	22.87	17.63	17.70
			$M_0 = 0.3$					
1000	0.50	-0.50	21.20	21.20	20.80	10.60	39.76	21.00
1000	0.50	0.50	44.10	44.10	44.10	16.94	29.85	43.70
1000	2.00	-0.50	13.70	13.70	13.60	15.81	15.57	13.50
1000	2.00	0.50	15.00	15.00	15.00	15.00	15.03	14.90
2000	0.50	-0.50	39.10	39.10	40.70	49.83	43.01	38.70
2000	0.50	0.50	19.20	19.20	19.30	19.02	24.90	19.00
2000	2.00	-0.50	15.20	15.20	15.10	21.53	15.31	15.00
2000	2.00	0.50	14.00	14.00	14.00	18.37	14.28	13.80
3000	0.50	-0.50	52.30	52.30	52.50	52.57	56.22	51.70
3000	0.50	0.50	11.50	11.50	11.70	15.68	9.78	11.40
3000	2.00	-0.50	15.80	15.80	15.80	26.46	16.73	15.60
3000	2.00	0.50	12.80	12.80	12.90	21.62	12.72	12.70
			$M_0 = 0.5$					
1000	0.50	-0.50	13.30	13.30	13.00	8.69	31.12	13.10
1000	0.50	0.50	38.90	39.00	39.10	15.83	25.53	38.50
1000	2.00	-0.50	9.93	9.93	9.87	13.50	12.05	9.83
1000	2.00	0.50	11.40	11.40	11.40	14.85	11.74	11.30
2000	0.50	-0.50	23.20	23.20	23.10	14.34	31.47	23.00
2000	0.50	0.50	18.50	18.50	18.70	15.22	20.48	18.30
2000	2.00	-0.50	11.10	11.10	11.10	9.66	11.63	11.00
2000	2.00	0.50	10.90	10.90	10.90	9.49	11.03	10.70
3000	0.50	-0.50	46.80	46.80	45.60	36.99	51.67	46.30
3000	0.50	0.50	11.60	11.60	11.90	16.16	9.80	11.40
3000	2.00	-0.50	11.60	11.60	11.60	24.40	12.44	11.50
3000	2.00	0.50	10.20	10.20	10.30	21.60	10.12	10.10

(1) codes are often run on a massively parallel computer within a multiuser environment where users must compete for both wall clock time and CPUs, (2) much emphasis is placed on impedance reduction, in which the selected propagation code must be run hundreds (sometimes thousands) of times to reduce the unknown impedance of a test liner, and (3) Langley is working toward the ability to model full-scale, large commercial engine nacelles with high-fidelity codes to get a quality prediction (high-fidelity codes require significantly more wall clock time and CPUs than low-fidelity codes). Again, it is reemphasized that other research organizations may utilize these codes for other reasons or may have different computing facilities that may dictate choosing different metrics for deciding on the choice of a code.

Each computer code was converted to the same operating system, and an attempt was made to compare wall clock time per CPU for each code. Assessment of wall clock time was conducted with the Columbia clusters. Each Columbia cluster is an Altix 3700 system that uses the Itanium2 processor by Madison and has a clock speed of 1.5 GHz. One thousand CPUs (each with 2 GB RAM, random-access memory) are available on each cluster. Unfortunately, some of the codes were designed to run only on sequential machines (e.g., CH3DPA and LEE2DDIS), while others were designed to run on parallel machines (e.g., CH2DDS, CH3DDS, LEE2DDS, and LEE3DIS). Further, many of the parallel codes scale poorly with the number of CPUs (e.g., CH2DDS, CH3DDS, and LEE2DDS), and others (e.g., LEE3DIS) have not been fully parallelized. Therefore, comparison of codes using wall clock time per CPU as a metric proved difficult. The decision was made, therefore, to run each code using the least amount of CPUs possible for a chosen grid, and to simply record the wall clock time for interested users.

A grid refinement study showed that all codes were converged on a uniform computational grid with 97 points in the axial and 21 points in the two transverse directions for all Mach numbers and frequencies. Thus, the three-dimensional and two-dimensional codes were run on uniform $97 \times 21 \times 21$ and 97×21 baseline grids, respectively. Table 7.3 gives the wall clock time on the baseline grid for three two-dimensional codes and three

three-dimensional codes. The six columns in the table correspond to (1) the code name, (2) the number of spatial dimensions considered by the code, (3) the governing differential equations that are solved by the code, (4) the type of numerical method used to solve the governing differential equations, (5) the minimum number of CPUs required for the grid, and (6) the wall clock time consumed (in seconds). Although the wall clock times are those necessary to obtain the solution in the hard-wall duct, there was almost no change when the wall was lined with acoustic material. Note that the wall clock time increases by a factor of 19 when the cubic finite element analysis (i.e., with a direct solve strategy) is increased from two-dimensional (CH2DDS) to three-dimensional (CH3DDS). When the pseudo-time marching code (i.e., with an iterative solve strategy) is increased from two-dimensional (LEE2DIS) to three-dimensional (LEE3DIS), the wall clock time increases by a factor of 26. As expected, the lowest fidelity three-dimensional code in the suite (CH3DPA, using the parabolic approximation) is the most time efficient of the three-dimensional codes. CH3DPA is observed to be more than 2 orders of magnitude faster than CH3DDS, and nearly 3 orders of magnitude faster than LEE3DIS.

7.7.1.3 Uncertainty Assessment

The first example problem contained a hard-wall configuration, while the second considered a uniform liner. In these two example problems, the inputs to the prediction codes were known exactly, and exact solutions for the attenuations were determined analytically for comparison with code predictions. In this section, a third example is presented for which the upper wall incorporates the segmented lining configuration. Unfortunately, exact values for the attenuation were not available for this configuration, and predicted attenuations were therefore compared to measured data. Additionally, because the code inputs must be measured, they were not known exactly, but were subject to measurement uncertainty. The measured attenuation values also carried uncertainty. Therefore, comparisons between measured and predicted attenuations are made on a statistical basis, and uncertainty bounds placed on both quantities. When taken in conjunction

TABLE 7.3.—WALL CLOCK TIME CONSUMED ON COLUMBIA CLUSTERS COMPUTING SOUND ATTENUATION WITH IN-DUCT CODES ON BASELINE GRID

Sound propagation code				Number of CPUs ^a	Wall clock time, s
Code name	Spatial dimensions	Governing differential equations	Numerical method		
CH2DDS	2	Convected Helmholtz	Cubic finite element	8	48
LEE2DDS	2	Linearized Euler	Linear finite element	8	60
LEE2DIS	2	Linearized Euler	Pseudo-time-stepping	1	210
CH3DPA	3	Convected Helmholtz	Parabolic approximation	1	7
CH3DDS	3	Convected Helmholtz	Cubic finite element	32	912
LEE3DIS	3	Linearized Euler	Pseudo-time-stepping	4	5400

^aNumber of central processing units (CPUs) on Columbia clusters used for sound attenuation calculations.

with Chapter 6, “Uncertainty in Acoustic Liner Impedance Measurement and Prediction,” these comparisons provide valuable insights into uncertainties expected from the impedance reduction process.

For this configuration, attenuation predictions were performed for a 140-dB plane-wave source in the GIT, in which the upper wall contains a 40.16-cm-long single-degree-of-freedom (SDOF) liner as described in Table 6.1 of Chapter 6. Results were acquired at three flow rates for frequencies ranging from 500 to 3000 Hz, in steps of 500 Hz. Data were acquired at each of these conditions at least eight times in order to allow for a small-sample statistical evaluation (Ref. 25). These tests were conducted at different times over a period of 1 year to minimize systematic errors due to atmospheric effects. Uncertainty intervals (95% confidence intervals) were computed for a number of parameters based on these measured results. The attenuation uncertainty intervals are represented as black squares in Figure 7.8 to Figure 7.12 (i.e., the separation between two black squares at a particular frequency represents the range of uncertainty in the measured attenuation). Similarly, uncertainty intervals for the following parameters were computed from these measurements in the GIT:

- (1) Source SPL
- (2) Average Mach number
- (3) Liner impedance
- (4) Exit impedance
- (5) Mean static pressure
- (6) Mean static temperature

Each of these parameters, which were used as inputs to the propagation codes, was assumed to be Gaussian distributed about their respective mean values.

Next, 31 simulations were conducted at each nominal test condition of interest (SPL , M_0 , and ζ) using a Monte Carlo approach. For each simulation, each input parameter was randomly selected from its respective Gaussian distribution, and the set of inputs was used with each of the propagation codes of interest. It should be noted that two of the codes (CH3DPA and LEE2DIS) could not take advantage of the measured exit impedance because they assumed anechoic terminations. Each simulation was run on the baseline grid discussed in the previous subsection.

Figure 7.8 to Figure 7.11 provide comparisons of measured and predicted attenuations (see Eq. (7.44)) when 31 simulations with each code were considered. The 95% confidence intervals for measurements and predictions are provided at each frequency of interest in each figure. The 95% confidence interval was the primary statistical metric of interest in this investigation, and the upper and lower bounds for each interval are represented by the same symbol in each figure. Essentially, this interval indicates that if another simulation were conducted, there is a 95-percent confidence that the resulting attenuation would fall between these limits. In general, the mean values of the simulations are observed to track the mean values of the measured data quite well.

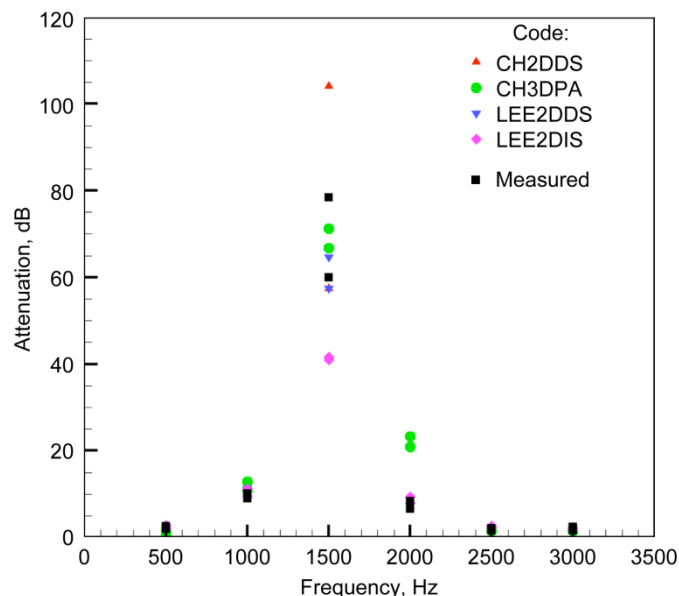


Figure 7.8.—Sound attenuation results from 8 grazing incidence tube (GIT) measurements and 31 simulations with each sound propagation code for liner 1, no flow, and source sound pressure level of 140 dB.

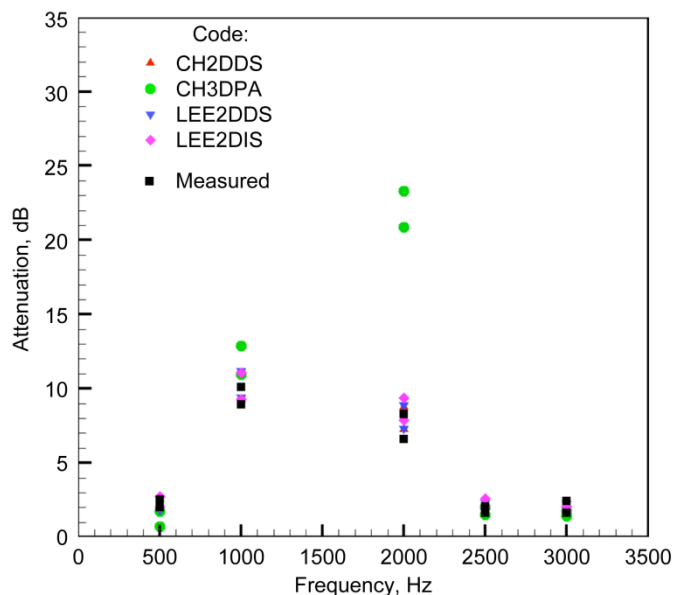


Figure 7.9.—Sound attenuation results from 8 grazing incidence tube (GIT) measurements and 31 simulations with each sound propagation code, resonance removed, for liner 1, no flow, and source sound pressure level of 140 dB.

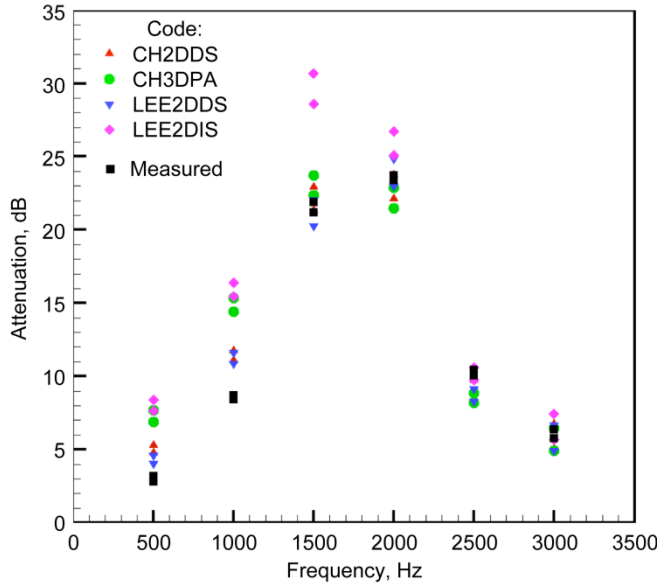


Figure 7.10.—Sound attenuation results from 8 grazing incidence tube (GIT) measurements and 31 simulations with each sound propagation code for liner 1, mean flow Mach number $M_0 = 0.25$, and source sound pressure level of 140 dB.

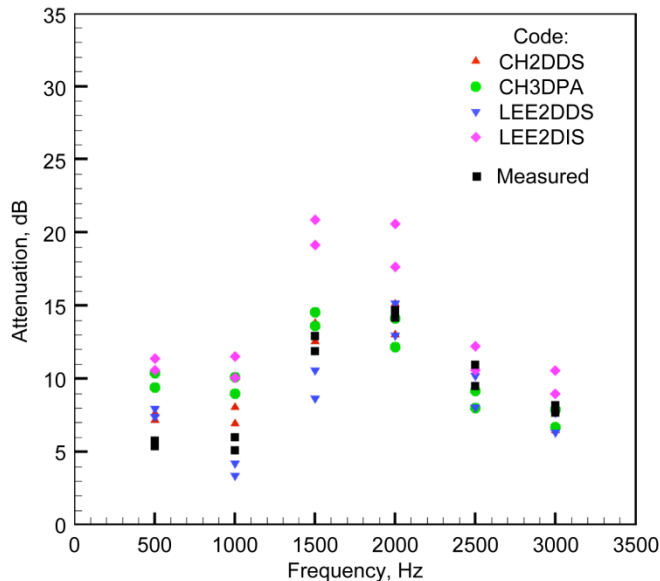


Figure 7.11.—Sound attenuation results from 8 grazing incidence tube (GIT) measurements and 31 simulations with each sound propagation code for liner 1, mean flow Mach number $M_0 = 0.40$, and source sound pressure level of 140 dB.

It should be noted that the propagation codes assumed a uniform-flow profile. Thus, it is expected that part of the reason for the differences in the mean predicted and measured attenuation values is the absence of the mean-flow boundary layer in the predictive methods. In addition, the resonant

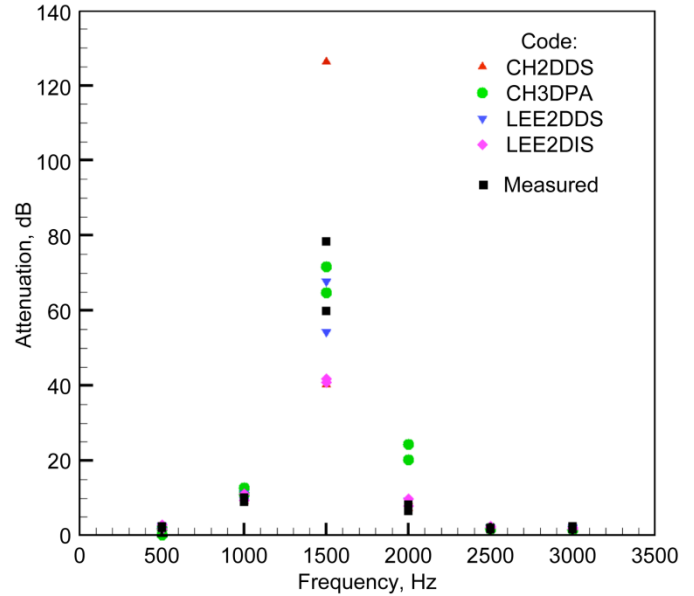


Figure 7.12.—Sound attenuation results from 8 grazing incidence tube (GIT) measurements and 6 simulations with each sound propagation code for liner 1, no flow, and source sound pressure level of 140 dB.

behavior of this SDOF liner is clearly evident at 1500 Hz in Figure 7.8 (no flow, $SPL = 140$ dB). The differences between predicted and measured SPL attenuations are accentuated at resonance because of the intrinsic behavior of single-layer liners. When one notes the levels of measured and predicted attenuation at 1500 Hz of at least 60 dB, these differences between predicted and measured results are of limited concern. Certainly, if a 40.64-cm-long liner provides greater than 60 dB (predicted or measured), it is performing quite well. It is anticipated that differences between predicted and measured attenuations would be significantly reduced for multilayer liners because the resonant behavior of such liners is a less dominant contributor to attenuation.

Because of the large confidence interval at resonance (1500 Hz) in Figure 7.8 (no flow, 140 dB), the attenuation scale is expanded in Figure 7.9 to more clearly show the results at the remaining frequencies. As expected, the confidence intervals grow as the mean-flow velocity is increased (see Figure 7.8 to Figure 7.11). Also, the confidence intervals for the measured data are observed to be less than for the predictive methods as Mach number increases. Figure 7.12 shows results for 6 simulations at Mach 0.0 with each code, for comparison with the 31 simulations shown in Figure 7.8. This information is also provided in tabular form in Table 7.4. Here, the mean attenuation and 95% confidence interval uncertainty (in dB) are given for the predicted attenuations when 31 and 6 simulations were considered. As described in Coleman and Steele (Ref. 25), the uncertainty values are the product of the Student's t factor and standard deviation σ in the predicted attenuation. As expected, the scatter (confidence interval) is observed to decrease as the number of simulations

TABLE 7.4.—GRAZING INCIDENCE TUBE MEAN SOUND ATTENUATION (μ) IN DECIBELS
AND 95% CONFIDENCE INTERVAL UNCERTAINTY VALUES ($t_n * \sigma$)^a
[For Liner 1, mean-flow Mach number $M_0=0.00$, and source sound pressure level = 140 dB.]

Excitation frequency, Hz	Sound propagation code							
	CH2DDS		LEE2DDS		LEE2DIS		CH3DPA	
	μ	$ t_n * \sigma $	μ	$ t_n * \sigma $	μ	$ t_n * \sigma $	μ	$ t_n * \sigma $
31 simulations ($t_n = 2.042$)								
500	2.22	0.35	2.16	0.35	2.36	0.35	1.22	0.52
1000	10.12	0.88	10.30	0.90	10.14	0.90	11.90	0.97
1500	80.78	23.35	61.02	3.64	41.27	0.31	68.99	2.21
2000	8.00	0.77	8.09	0.79	8.60	0.74	22.07	1.23
2500	1.91	0.29	2.01	0.29	2.29	0.27	1.76	0.24
3000	2.01	0.26	2.05	0.20	1.90	0.17	1.56	0.17
6 simulations ($t_n = 2.571$)								
500	2.11	0.56	2.05	0.57	2.26	0.58	1.05	0.84
1000	10.14	0.90	10.32	0.88	10.14	0.84	11.90	0.87
1500	83.18	43.00	60.98	6.80	41.25	0.39	68.17	3.40
2000	8.23	0.97	8.32	1.01	8.79	0.94	22.36	2.05
2500	1.91	0.35	2.00	0.31	2.33	0.20	1.80	0.18
3000	2.05	0.22	2.06	0.20	1.92	0.13	1.58	0.13

^a t_n is Student's t factor and σ is standard deviation.

is increased. This decrease in scatter with an increase in the number of simulations was observed for all conditions evaluated. It is noted that the Monte Carlo approach used herein has assumed that all input parameters were uncorrelated. In fact, this assumption is likely to be incorrect (i.e., some of the parameters may be correlated). If they are correlated, inclusion of this information would likely cause the uncertainty intervals to decrease.

7.7.2 NASA Langley Curved Duct Test Rig Simulations

To illustrate the progression of testing that may be performed in other facilities, a series of predictions was also carried out for the NASA Langley Curved Duct Test Rig (CDTR) (Ref. 26). The CDTR affords the opportunity to test the codes in a larger geometry than the GIT, and in an aeroacoustic environment for which the effects of higher-order propagating modes can be isolated and evaluated. Some insight into the potential use of the CDTR for impedance reduction may also be obtained from this study. Although a further uncertainty analysis is desirable, this was precluded by the availability of only one data set. As time was also limited, only the two codes (i.e., CH3DPA and CH2DDS) requiring the least wall clock time were considered. In addition to allowing investigation of higher-order mode effects, the CDTR is also intended to improve the understanding of the behavior of duct treatment in curved ducts. For example, the aft bypass duct flow path of aircraft engines is often curved to accommodate the engine core. Therefore, the design of the

CDTR allows the baseline straight rectangular design to be modified with horizontal offsets of up to one duct width, with the aim of determining whether use can be made of curvature to enhance liner performance. The test section cross section is rectangular in order to facilitate the design and manufacture of candidate duct liner configurations, and it is relatively large (scaled to between 25 and 50 percent of the bypass duct of most modern engines). Airflow through the duct is designed to be typical of bypass duct flow. In this subsection, attenuations measured with the straight CDTR configuration are compared with those predicted using the in-duct codes.

The CDTR test section modeled in each code is 38.10 cm high, 15.54 cm wide, and 197.36 cm long. A 81.28-cm-long test liner was inserted into the left sidewall so that the leading and trailing edges of the liner were located 58.29 and 57.81 cm from the source and termination planes, respectively. The right sidewall consists of another liner sample, which was covered with tape to simulate an acoustically hard wall. The test liner consists of an impervious backing sheet, a 2.8-cm-thick honeycomb core, and a perforate cover sheet (i.e., similar to the SDOF liner of the previous section). An illustrative test configuration is shown in Figure 7.13. Frequencies from 500 to 2400 Hz were generated upstream of the liner test section, and the relative amplitudes and phases at each of the acoustic drivers were chosen such that the (0,0), (1,0), or (0,1) mode was dominant. (Note: First index refers to vertical (parallel to the liner) mode and second index refers to the spanwise (perpendicular to the liner) mode.) The results provided here are for the “no flow” condition.

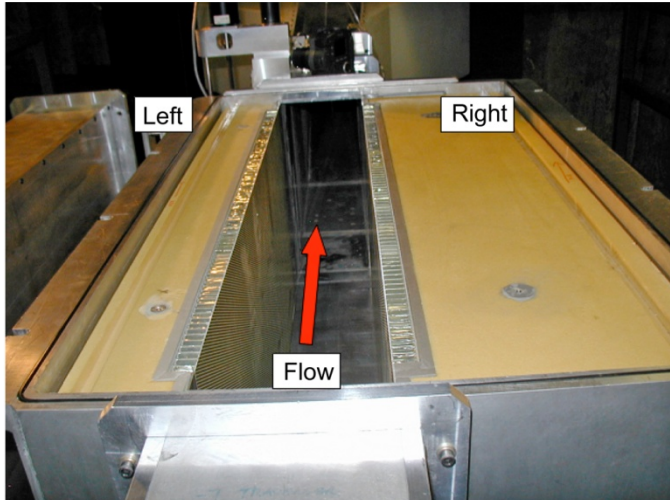


Figure 7.13.—Curved Duct Test Rig (CDTR) liner test section with straight liner installed, top removed, view looking downstream.

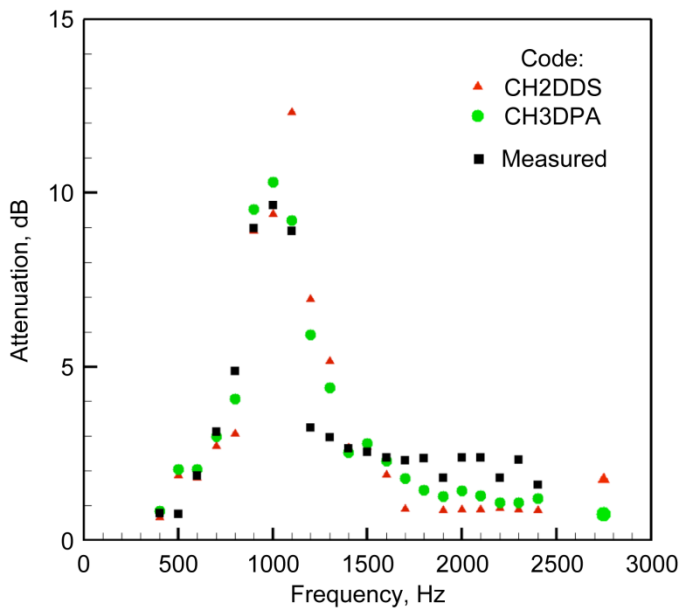


Figure 7.14.—Curved Duct Test Rig (CDTR) sound attenuation measured and predicted with two sound propagation codes; no flow, incident mode (0,0), and source sound pressure level of 130 dB.

A 51×1555 (spanwise and axial directions) evenly spaced grid was used to model the CDTR in CH2DDS, whereas the CH3DPA grid utilized 17, 33, and 81 points in the spanwise, vertical, and axial directions, respectively. Both CH3DPA and CH2DDS use the modal amplitudes and phases in the hard-wall section upstream of the liner as source input. These were obtained from acoustic pressures measured with flush-mounted microphones in the walls of the CDTR. The codes

also require the impedance of the test liner as input. The test liner impedance values were deduced from measurements in the GIT using a sample liner of the same design as that placed in the CDTR left sidewall. The CH3DPA assumes a nonreflecting termination, whereas CH2DDS uses the measured termination impedance to construct the node impedance matrix ($[\zeta_i]$). In the attenuation comparison to follow, the measured mode amplitudes in the hard-wall sections upstream and downstream of the liner were used to determine the acoustic pressure field present in the CDTR via modal expansion. The axial velocity needed to compute the intensity (Eq. (7.40)) was determined from this modal expansion. Similarly, the numerical solutions obtained from CH2DDS in the hard-wall sections of the duct upstream and downstream of the liner were decomposed into hard-wall duct modes, and the axial velocity was computed using this mode expansion. The CH3DPA code is formulated in terms of acoustic potential, from which the acoustic pressure and velocity may be directly computed. Based on the acoustic pressure and axial velocity field, Equation (7.43) was then used to compute both the measured and numerical values of attenuation. It is these quantities that are compared in this section.

Figure 7.14 compares the attenuation measured in the CDTR to that computed using the CH3DPA and CH2DDS computer codes with a plane-wave source. The plane wave had 130 dB incidence SPL and was isolated approximately 20 dB above all other modes. Discrepancies in measured and predicted attenuation are quite small except near the peak of the attenuation curve. An impedance variability study has been performed, and it has been observed that in the vicinity of the sharp attenuation peak, normalized deduced reactance changes of ± 0.1 lead to significantly different attenuations predicted by the in-duct codes. The effect of an error in the deduced impedance was barely noticeable at frequencies away from the frequency of peak attenuation. This behavior is very similar to that observed in the GIT results of Figure 7.8 and is due to the SDOF liner considered.

Until now, no results have been presented for sources other than plane waves. Figure 7.15 compares the measured and predicted attenuations for the first nonplanar mode to cut on (i.e., the (1,0) mode) in the CDTR. Again, the first index refers to the vertical-mode order (i.e., in the long dimension) and the second index refers to the spanwise-mode order (i.e., in the short dimension). This vertical mode was isolated at least 10 dB above all other propagating modes. As shown in Figure 7.15, the measured attenuation and that predicted by the in-duct codes are in very good agreement. Note that the attenuation for this nonplanar mode is observed to peak at approximately the same frequency as the plane-wave mode (between 1000 and 1100 Hz). It is not surprising that the shape of the attenuation spectrum for the (1,0) mode source would be similar to that for the (0,0) mode source, as the mode number in the direction normal to the liner is the same. At frequencies above 1500 Hz, the measured attenuation is slightly greater than the predictions, but by no more than 2 dB.

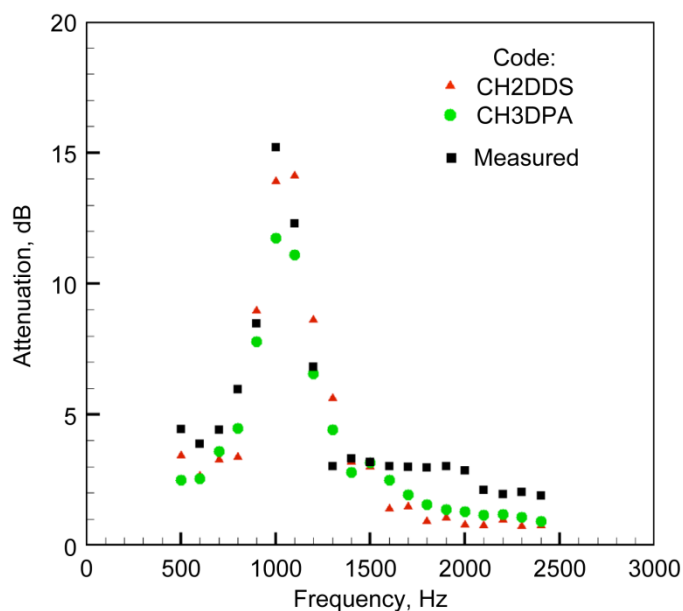


Figure 7.15.—Curved Duct Test Rig (CDTR) sound attenuation measured and predicted with two sound propagation codes; no flow, incident mode (1,0), and source sound pressure level of 130 dB.

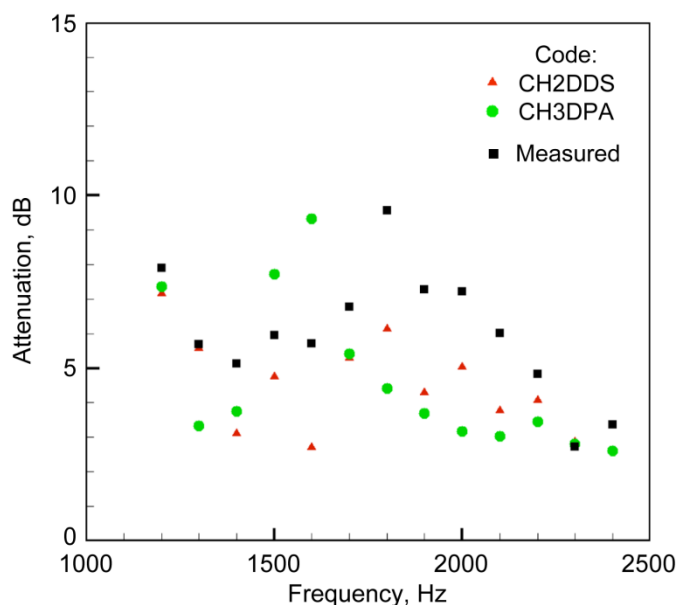


Figure 7.16.—Curved Duct Test Rig (CDTR) sound attenuation measured and predicted with two sound propagation codes; no flow, incident mode (0,1), and source sound pressure level of 130 dB.

For a source consisting of the spanwise mode closest to the plane-wave mode (i.e., the (0,1) mode), the attenuation does not show the same “peak-dominated” behavior, and the measured and in-duct code attenuations do not agree as well as for previous source specifications. This is the case in Figure 7.16, where the (0,1) mode was generated and isolated

at least 10 dB above other propagating modes in the CDTR. Although there is some similarity between the measured and predicted data trends, the magnitude of the predicted attenuation is approximately half of the measured values at frequencies above mode cut-on. Similar trends were observed when the (1,1) mode was isolated in the duct, although these results are not presented. Currently, indications are that the primary cause of the discrepancy is likely compliance of the taped right sidewall. This appears possible because the predicted attenuations, which assume a rigid sidewall, fall below the measured attenuations (except for the CH3DPA code at the frequencies of 1500 and 1600 Hz).

7.7.3 NASA Glenn Advanced Noise Control Fan Simulations

Section 7.7.1.3, “Uncertainty Assessment,” focused on in-duct attenuation prediction uncertainties based on input parameters, because it relates directly to the impedance modeling and education discussed in Chapter 6, “Uncertainty in Acoustic Liner Impedance Measurement and Prediction.” In many instances, efficient prediction of the far-field radiated noise is also of interest. In fact, it is an essential tool in assessing the community noise impact of low-noise concepts. Therefore, for completeness, example acoustic radiation predictions are presented that employ the approaches of Section 7.5.2, “Axially Symmetric Code,” and Section 7.5.4, “Three-Dimensional Code With Parabolic Approximation,” referred to here as “CH2DIE” and “FWH3D,” respectively. Currently, the FWH3D is connected to the in-duct results of CH3DPA. However, development is underway to allow for use with the CH2DDS, CH3DDS, and LEE2DDS propagation codes. It should also be noted that the pseudo-time marching codes described in Section 7.6.3 follow the FWH3D paradigm and implement a frequency-domain Ffowcs Williams-Hawkings formulation. However, predictions are not presented because of time constraints and the similarity with the FWH3D approach.

Predictions were made for the NASA Glenn Advanced Noise Control Fan (ANCF) rig, which is a low-speed fan testbed designed for noise reduction concept testing (Ref. 27). In addition to collection of far-field data, the ANCF allows for the insertion of a rotating microphone rake (Ref. 28) to measure the interaction modes of the ducted fan. Therefore, for selected test configurations, in-duct rotating rake measurements and far-field acoustics measurements may be obtained. A general schematic of the axisymmetric rig is presented in Figure 7.17.

The example cases considered are the by-product of calculations performed in conjunction with colleagues at the NASA Glenn Research Center. Based on rotating rake data, inlet and aft predictions were performed for the (2,0) mode at the blade-passing frequency (BPF) of 533 Hz. For the inlet case, the source mode was prescribed at an axial location of –30 cm (see Figure 7.17), with an amplitude of 6.27 Pa, phase of –121.6°, and duct Mach number of 0.130. Predictions were

obtained at 15 equally spaced locations on a 366-cm arc centered on the inlet plane origin. For the aft case, the source mode was prescribed at an axial location of 156 cm, with an amplitude of 8.14 Pa, phase of 2.3° , and duct Mach number of 0.175. Predictions were obtained at 15 equally spaced locations on a 457-cm arc centered on the exhaust plane origin. The proximity of the source location to the inlet or exhaust planes leads to the use of a short duct section for the internal propagation calculations, thereby minimizing the influence of any in-duct propagation errors. For the aft case, the CH2DIE predictions include shear layer modeling by default. For the FWH3D model, both aft-baseline and shear-layer-corrected predictions were performed. Illustrative internal and pseudo-duct meshes are shown in Figure 7.18 and are represented with white and green wireframe, respectively. Note that although the geometry is axisymmetric, the FWH3D calculations were performed over the fully three-dimensional geometry. Comparisons for the full prediction set are provided in Figure 7.19. Some of the discrepancy at large off-axis radiation angles may be due to differing extents to which the models are able to account for engine cowl shielding and edge effects. For the aft predictions, differences in nacelle trailing-edge thickness used in each model may also be the cause of some discrepancy in the peak levels. Note that for the

FWH3D aft results, inclusion of the shear-layer correction increases the peak directivity level and shifts its location forward. The comparisons are encouraging and provide motivation for the further use of the approaches. It is expected that recent ANCF data collected under the Engine Validation of Noise and Emissions Reduction Technology (EVNERT) task of the Quiet Aircraft Technology (QAT) Program will provide an excellent opportunity for further validation work.

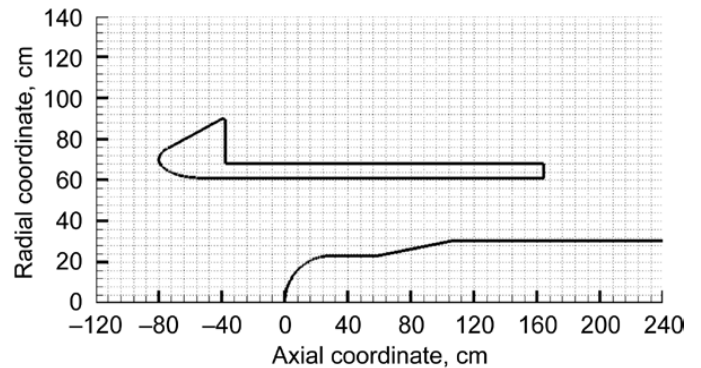


Figure 7.17.—NASA Glenn Advanced Noise Control Fan (ANCF) rig.

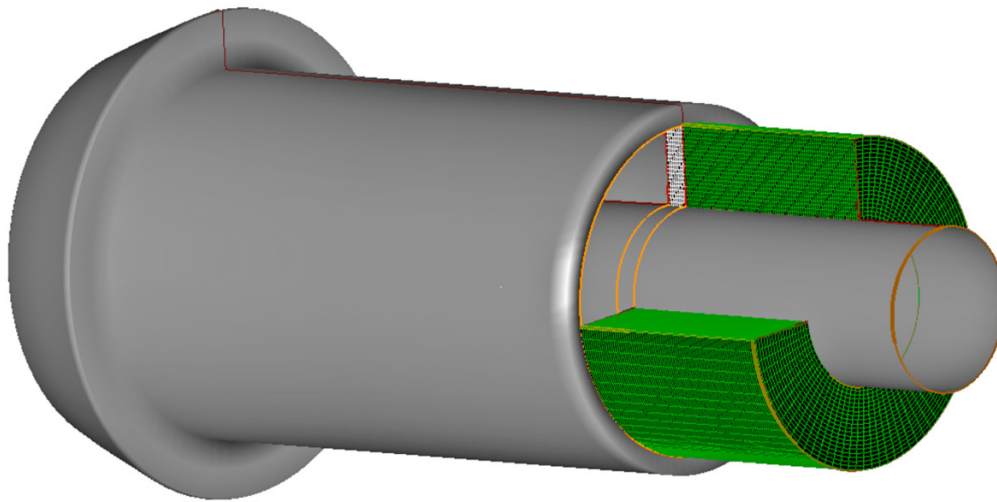


Figure 7.18.—Internal and pseudo-duct Advanced Noise Control Fan (ANCF) computational meshes.

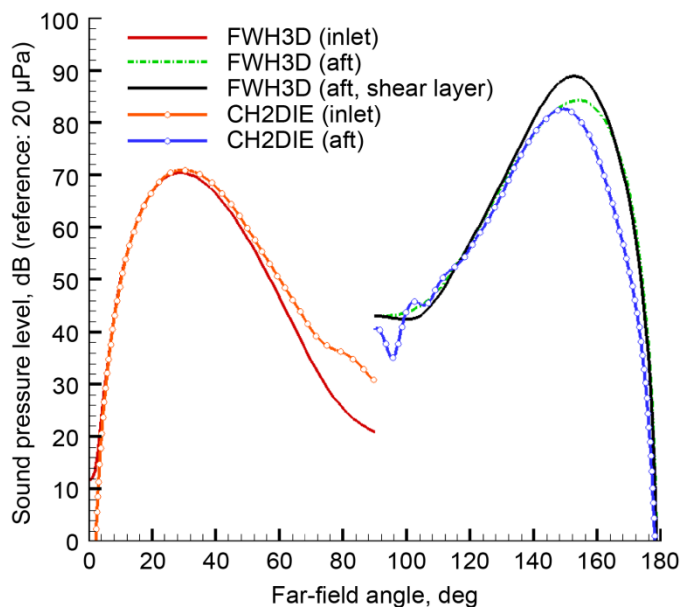


Figure 7.19.—Comparison of FWH3D and CH2DIE predictions of sound radiated from a duct for Active Noise Control Fan (ANCF); mode (2,0) and blade-passing frequency (BPF) = 533 Hz.

7.8 Concluding Remarks and Recommendations

This chapter has been used as a research umbrella, underneath which a suite of acoustic duct propagation and radiation codes has been gathered together for the first time. The suite consists of the most commonly used NASA Langley codes, a code from academia, and three codes recently developed at Boeing with partial NASA funding. These codes support propagation through acoustically treated inlet and aft-fan ducts in the presence of mean flow, as well as radiation to the far field. Collectively, they are believed to be a representative cross section of the state-of-art in the liner industry. The following is a brief summary of contributions provided in this chapter:

1. The basic assumptions underlying each code were quantified.
2. Each code was evaluated on the same massively parallel computer system (i.e., the Columbia clusters) using identical grids.
3. The predicted attenuations in a hard-wall duct were computed for nine combinations of frequencies and Mach numbers, and were compared to known values determined from analytical models.
4. The predicted attenuations (for each code) over a section of an infinitely long duct with a uniform impedance liner along the top wall were computed for 36 combinations of Mach number, frequency, and lining impedance, and were compared to values obtained from mode theory.

5. Attenuation measurements were made with a conventional perforate-over-honeycomb liner in the NASA Langley grazing incidence tube (GIT) and were compared to code predictions. Results were compared for a 140-dB incident sound pressure level for three flow rates and for source excitation frequencies from 500 to 3000 Hz in 500-Hz increments.

6. Limited code predictions were compared with attenuations measured in the NASA Langley Curved Duct Test Rig, which has a geometry closer to that of a full-scale engine than the GIT and allows for higher-order mode effects to be evaluated.

7. Example far-field acoustic predictions were conducted for the NASA Glenn Advanced Noise Control Fan Rig geometry.

The following primary conclusions have resulted from this investigation:

1. Increases in wall clock time of an order of magnitude or more are observed for three-dimensional codes relative to the corresponding two-dimensional versions of the same codes.
2. Attenuations predicted with each code are in excellent agreement with exact results for the hard-wall duct.
3. Attenuations predicted with the CH2DDS, LEE2DDS, CH3DDS, and CH3DPA codes over a portion of an infinitely long duct with uniform acoustic treatment compare well with results from mode theory for the 36 combinations of Mach number, frequency, and wall impedance used in this study. Of these four codes, the CH3DPA is considerably more time efficient and is only slightly less accurate. The LEE2DIS attenuation predictions compare well with mode theory at low Mach numbers, but tend to diverge from mode theory as the flow Mach number is increased.
4. Attenuations predicted for a conventional perforate-over-honeycomb liner installed in the GIT compare well with measured attenuations. As expected, the uncertainty (attenuation 95% confidence interval) is proportional to the amount of attenuation (i.e., small changes in the code inputs at a frequency where significant attenuation occurs will result in sizable changes in attenuation).
5. Attenuations were predicted with the CH3DPA and CH2DDS codes for planar and higher-order vertical modes (zero-order spanwise mode) in the CDTR. These predictions were based on liner impedances deduced for a similar liner in the GIT and are observed to agree well with measured attenuations.

This investigation has provided valuable insights with regards to strengths and weakness of several propagation codes. The following items are recommended for further research and are expected to form the basis for continuing code development at NASA Langley Research Center.

1. More efficient three-dimensional solvers should be incorporated into the three-dimensional propagation codes,

such that these codes can be used to efficiently perform parameter studies and to model engine nacelles closer to full scale. A reduction in wall clock time by at least 2 to 3 orders of magnitude is desired.

2. Many of the codes included in the current investigation were not initially designed to take advantage of current and future computer architectures. Where possible, these codes should be upgraded to take advantage of these architectures.

3. The effects of the mean boundary layer should be incorporated into the three-dimensional propagation codes to improve their fidelity.

4. If possible, the fidelity of the CH3DPA code should be increased (while maintaining its current efficiency). An ongoing effort is underway to develop a multipass version of this code, which is expected to significantly increase the fidelity of the results with minimal reductions in efficiency.

5. Discrepancies between attenuations measured in the CDTR and those predicted with the CH3DPA and CH2DDS codes, for sources with a dominant, higher-order spanwise mode, should be further evaluated. This should include an uncertainty analysis of the measurement and prediction processes for this duct geometry.

6. The divergence between LEE2DIS results and those computed with the other codes as the mean-flow Mach

number is increased should be further evaluated. Every indication is that the source of the discrepancy is the termination boundary condition.

7. Initial far-field prediction comparisons were encouraging, and it is expected that recent ACNF data collected under the QAT Program will be a source for further validation.

In addition, a parallel effort will be conducted to develop a propagation code for the evaluation of extended-reaction liners. It is expected that this code will be based on approaches described herein for evaluation of locally reacting liners.

7.9 Acknowledgments

The authors wish to express appreciation to Tony Parrott and Mike Jones for their time and input in connecting this effort to Chapter 6, “Uncertainty in Acoustic Liner Impedance Measurement and Prediction.” The authors also extend sincere gratitude to Carol Harrison for the care in which she conducted extensive tests to generate the measurement database used in this investigation. They also thank Carl Gerhold, Brian Howerton, and Martha Brown for their assistance in the measurement and impedance prediction processes.

Appendix A.—Nomenclature

A.1 Acronyms

ANCF	Advanced Noise Control Fan
BPF	blade-passing frequency
CDTR	Curved Duct Test Rig
CH2DDS	convected Helmholtz two-dimensional direct solver
CH2DIE	convected Helmholtz two-dimensional infinite element
CH3DDS	convected Helmholtz three-dimensional direct solver
CH3DPA	convected Helmholtz three-dimensional parabolic approximation
CPU	central processing unit
DRP	dispersion-relation-preserving
EVNERT	Engine Validation of Noise and Emissions Reduction Technology
FWH3D	Ffowcs Williams-Hawkings three-dimensional
FW-H _{pds}	Ffowcs Williams-Hawkings (equation) with penetrable data surfaces
GIT	grazing incidence tube
LEE2DDS	linearized Euler equations two-dimensional direct solver
LEE2DIS	linearized Euler equations two-dimensional iterative solver
LEE3DIS	linearized Euler equations three-dimensional iterative solver
MPI	message-passing interface
QAT	Quiet Aircraft Technology
RAM	random-access memory
SDOF	single degree of freedom
SPL	sound pressure level

A.2 Symbols

$[A], [B]$	matrices for constructing the linearized Euler equations
a	width of finite element
b	height of finite element
c	speed of sound
C	constant in Equation (7.4)
$[C], [D]$	matrices for constructing the linearized Euler equations
D	distance between two parallel rigid sidewalls
$[DD]$	diagonal matrix in decomposition of $[S]$
$\frac{D}{Dt}$	material derivative

d	length of a finite element
E	total acoustic power
$\{E\}$	error residual vector
\mathbf{e}	unit vector in cylindrical coordinate system
$\{F\}$	column vector containing source effects
f	linear or cubic polynomials
H	height of duct
h	arc length in a coordinate direction
I	acoustic intensity
$[I]$	identity matrix
i	unit imaginary number
$\Im[\dots]$	imaginary part of complex expression ...
K	axial propagation constant
k	freespace wave number
L	length of duct
$[L]$	lower triangular matrix in decomposition of $[S]$
M	number of nodes in transverse x-direction
M_0	uniform-flow Mach number
\mathbf{M}_0	Mach number vector
m	mode number
N	number of nodes in z-direction
\mathcal{N}	finite element basis function
n	pseudo-time index
\mathbf{n}	outward unit normal vector to Γ_t
$NL1$	nonlinear term from Equation (7.6) defined in Equation (7.9)
$NL2$	nonlinear term from Equation (7.7) defined in Equation (7.10)
p	fluid pressure
Q	number of nodes in the transverse y-direction of the duct
(r, θ, z)	cylindrical coordinates
$\Re[\dots]$	real part of complex expression ...
SPL	sound pressure level
$[S]$	finite element stiffness matrix
$[T(z)]$	splitting matrix
t_n	Student's t factor
t	time
$[U]$	upper triangular matrix in decomposition of $[S]$
u	scalar component of \mathbf{u} in x-direction
\mathbf{u}	particle velocity vector
v	scalar component of \mathbf{u} in y-direction
W	weighting function

w	scalar component of \mathbf{u} in z-direction	exit	exit
(x, y, z)	Cartesian coordinates	e	element
γ	ratio of specific heat at constant pressure to that at constant volume in fluid	I	index
λ	transverse wavenumber	inc	incident
ζ	normalized acoustic impedance of wall lining	J	index
θ	angular cylindrical coordinate	LEE2D	linearized Eulers equations, two-dimensional
Γ	surface bounding Ω ; union of Γ_s , Γ_t , and Γ_w	m	mode number
(ξ_1, ξ_2, ξ_3)	generalized curvilinear coordinates	n	mode number
ρ	fluid density	(r, θ, z)	cylindrical coordinate
σ	standard deviation	ref	reflected
τ	pseudo-time variable in rotational pseudo-time marching codes	reference	reference
$[\boldsymbol{\tau}]$	shear stress tensor	s	source
Φ	node coefficients	t	duct termination
ϕ	acoustic velocity potential	w	duct walls
ω	circular frequency	0	mean or steady flow
Ω	computational volume	I	inner region
∇	gradient vector	II	outer region
Subscripts:		Superscripts:	
b	baffle	\sim	an acoustic or perturbation quantity
CH2D	convected Helmholtz equation, two-dimensional	(\quad)	a trial solution
CH3D	convected Helmholtz equation, three-dimensional	\wedge	a total fluid quantity
		$+$	positive traveling
		$-$	negative traveling
		$*$	complex conjugate

References

1. White, Frank M.: *Viscous Fluid Flow*. McGraw-Hill, New York, NY, 1974.
2. Zorumski, W.E.; Watson, W.R.; and Hodge, S.L.: A Nonlocal Computational Boundary Condition for Duct Acoustics. *J. Comput. Acoust.*, vol. 3, no. 1, 1995, pp. 15–26.
3. Myers, M.K.: On the Acoustic Boundary Condition in the Presence of Flow. *J. Sound Vib.*, vol. 71, no. 3, 1980, pp. 429–434.
4. Morfey, C.L.: Acoustic Energy in Non-Uniform Flows. *J. Sound Vib.*, vol. 14, no. 2, 1971, pp. 159–170.
5. Watson, Willie; Jones, Michael; and Parrott, Tony: A Quasi-3-D Theory for Impedance Eduction in Uniform Grazing Flow. *AIAA–2005–2848*, 2005.
6. Eversman, Walter: *Turbofan Acoustic Propagation and Radiation*. Final Report, NASA NAG3–2109, 2000.
7. Dougherty, Robert P.: A Wave-Splitting Technique for Nacelle Acoustic Propagation. *AIAA–1997–1652*, 1997.
8. Desai, C.S.; and Abel, John Fredrick: *Introduction to the Finite Element Method: A Numerical Method for Engineering Analysis*. Van Nostrand Reinhold Co., New York, NY, 1972.
9. Wolfram Research, Inc.: *Mathematica*, Version 6.0, Champaign, IL, 2007.
10. Irons, Bruce M.: A Frontal Solution Program for Finite Element Analysis. *Int. J. Numer. Methods Eng.*, vol. 2, 1970, pp. 5–32.
11. Nark, Douglas, et al.: The Development of the Ducted Fan Noise Propagation and Radiation Code CDUCT-LaRC. *AIAA–2003–3242*, 2003.
12. Dougherty, Robert: A Parabolic Approximation for Flow Effects on Sound Propagation in Nonuniform, Softwall, Ducts. *AIAA–1999–1822*, 1999.
13. Coronas, J.: Bremmer Series that Correct Parabolic Approximations. *J. Math. Anal. Appl.*, vol. 50, 1975, pp. 361–372.
14. Brentner, Kenneth S.; and Farassat, F.: Analytical Comparison of the Acoustic Analogy and Kirchhoff Formulation for Moving Surfaces. *AIAA J.*, vol. 36, no. 8, 1998, pp. 1379–1386.
15. Farassat, F.: Derivation of Formulations 1 and 1A of Farassat. *NASA/TM–2007–214853*, 2007.
16. Nark, Douglas; and Farassat, Fereidoun: CDUCT-LaRC Status—Shear Layer Refraction and Noise Radiation. *AIAA–2006–2587*, 2006.
17. Watson, Willie R., et al.: Impedance Eduction in the Presence of Shear Flow. *AIAA–2001–2263*, 2001.
18. Lan, Justin; and Breard, Cyrille: Development and Validation of a 3D Linearized Euler Solver. *AIAA–2006–2585*, 2006.
19. Lan, Justin; and Breard, Cyrille: Validation of 3D Acoustic Propagation Code With Analytical and Experimental Results. *AIAA–2005–2901*, 2005.
20. Tam, C.K.W.; and Webb, J.C.: Dispersion-Relation-Preserving Finite-Difference Schemes for Computational Acoustics. *J. Comput. Phys.*, vol. 107, no. 2, 1993, pp. 262–281.
21. Watson, W.; Jones, M.; and Parrott, T.: Validation of an Impedance Eduction Method in Flow. *AIAA J.*, vol. 37, no. 7, 1999, pp. 818–824.
22. Snider, Royce Wayne: *Attenuation Predictions for Segmented Liners in Supersonic Flow*. M.S. Thesis, George Washington University, 1993.
23. Muller, David E.: A Method for Solving Algebraic Equations Using an Automatic Computer. *Mathematical Tables and Other Aids to Computation*, Vol. X, no. 56, 1956, pp. 208–215.
24. Stewart, G.W., III: A Modification of Davidon's Minimization Method to Accept Difference Approximations of Derivatives. *JACM*, vol. 14, no. 1, 1967, pp. 72–83.
25. Coleman, Hugh W.; and Steele, W. Glenn, Jr.: *Experimentation and Uncertainty Analysis for Engineers*. Second ed., Wiley, New York, NY, 1999.
26. Gerhold, Carl; Cabell, Randolph; and Brown, Martha: Development of an Experimental Rig for Investigation of Higher Order Modes in Ducts. *AIAA–2006–2637*, 2006.
27. Sutliff, Daniel L., et al.: Baseline Acoustic Levels of the NASA Active Noise Control Fan Rig. *AIAA–1996–1745*, 1996.
28. Sutliff, Daniel L.: Rotating Rake Turbofan Duct Mode Measurement System. *NASA/TM–2005–213828*, 2005.

Chapter 8—Jet Noise Prediction

James E. Bridges and Abbas Khavaran
National Aeronautics and Space Administration
Glenn Research Center
Cleveland, Ohio 44135

Craig A. Hunter
National Aeronautics and Space Administration
Langley Research Center
Hampton, Virginia 23681

Summary

An assessment exercise investigated three jet noise prediction methods that are in NASA's possession: an empirically based model and two models based on the acoustic analogy theory. The assessment started by identifying a suite of jet flows covering a wide range of nozzle geometries, bypass ratios, flow speeds, temperatures, and flight speeds. The data from far-field acoustic measurements, and for some cases advanced flow measurements, were assembled. The accuracy of the measured data was established by comparing measured data taken in different facilities, using different measurement techniques, and documented by different authors. In addition, comparisons of measured data were made with analytical results. This determined experimental uncertainty bands about the acoustic data and established the uncertainty in the input flow solutions used in the acoustic analogy noise prediction codes. Finally, the results of the prediction codes were directly compared with far-field acoustic data, with the error being directly computed and compared over the entire range of jet flows for all codes. From this overview, recommendations for future improvements in jet noise prediction methods are made.

The empirical code assessed was the Stone Jet Noise module (ST2JET) contained within the Aircraft Noise Prediction Program (ANOPP) Level 25 aircraft noise prediction code. This code predicts both jet mixing noise and shock-associated noise. It is well documented and represents the state of the art in acoustic prediction codes where virtual sources are associated with various aspects of noise generation and are combined to predict the noise spectral directivity for a given jet plume. A total of 265 jet noise cases were run on the ST2JET code, with run times of the order of fractions of a second apiece and with no additional input beyond simple geometric and flow parameters. Considering that the internally mixed nozzle systems are approximated two different ways by the code, 408 runs were actually performed and analyzed here.

Two acoustic analogy jet noise prediction codes were also evaluated. These codes predict the jet mixing noise, but not the shock-associated noise component. Fewer cases were examined with the acoustic analogy prediction codes because these methods require substantially more resources, typically an external Reynolds-averaged Navier-Stokes (RANS) solution to the jet plume, followed by numerical processing of the plume data for source strength as well as the propagation effects, integrated over the entire jet plume. The cases evaluated do span much of the parameter space but much more sparsely than in the empirical model.

All predictions were compared against experimental data from the NASA Glenn Research Center jet noise rigs. Far-field noise data were themselves validated against other high-quality published jet noise datasets. In addition, a large amount of flow-field data was obtained using the NASA facility, which was required to validate the RANS solutions that were used as input for the acoustic analogy codes. The flow-field data were also validated against available published data. The cross-facility comparisons were used, in conjunction with component analysis, to establish the experimental uncertainty of the data.

Neither empirical nor acoustic analogy models predicted the overall acoustic power of subsonic axisymmetric nozzle flows to within the experimental uncertainty for all cases. The empirical code ANOPP did not predict the spectral directivity within experimental uncertainty for most cases, having systematic disagreements at high frequencies especially at downstream angles. Consequently, the projected effective perceived noise level (EPNL) values were off by several decibels for sample cases studied, an intolerable situation in practice, where EPNL values need to be known to within fractions of a decibel. However, for axisymmetric jets, the ANOPP code was more robust than the acoustic analogy codes, and produced a consistent level of error for a broad range of jet flows. The acoustic analogy code JeNo v1.0 predicted noise spectral directivity to within experimental uncertainty for subsonic cold jets, but deviated when either the jet speed approached or exceeded the speed of sound or the jet temperature was elevated. JeNo did capture the impact of nonaxisymmetric jets with azimuthal periodicity greater than 4, but did not capture the azimuthal directivity effect from low-order asymmetries such as offset nozzles. The acoustic analogy code Jet3D was able to predict the noise level and the spectral content of high-speed hot jets at forward and side angles, but incorrectly predicted the noise level and its peak frequency at aft angles. The Jet3D code did not predict cold jets very well, missing both the spectral shape and the peak frequency.

8.1 Introduction

When jet aircraft were first introduced, observers were awed by their potential for high levels of thrust as well as the incredible sound levels they generated. The level of effort to tame this source of noise quickly elevated from an engineering problem to a full research topic as it became clear that the major source of the tremendous noise was not the vibrating surfaces as envisioned by classical acoustics and noise engineering, but the turbulent mixing of the exhaust plume. Thus understanding the noise generation mechanism in the absence of solid surfaces became the primary problem in jet noise. Considerable resources have been devoted to the topic, and many research papers have been written on the subject, yet aeronautical engineers acknowledge that prediction of jet noise remains a highly empirical art compared to other engineering disciplines. Unlike solid mechanics and computational fluid dynamics (CFD), where complex designs have benefited strongly from the advent of the computer, the same is not true in aeroacoustics. The problem may be attributed to the complicated and poorly understood relationship between turbulence and noise and our limited ability to accurately compute certain turbulence parameters.

Jet noise is a byproduct of turbulent flow, a nearly negligible fraction of the flow energy as the thrust of the aircraft engine converts from steady kinetic energy to unsteady fluid motion and heat via viscous dissipation. Since turbulence remains difficult to robustly quantify, jet noise is equally difficult to predict. Empirical relations have yielded certain scaling laws for simple exhaust geometries. Yet first-principle theoretical approaches have not benefited from the same level of success, and have often been frustrating to researchers in the field. For basic engineering work, empirical methods (e.g., programmed interpolations between measured cases) remain at the forefront, with occasional unpleasant surprises, especially when subtle changes in the flow produce unexpected noise changes.

Many years of research have finally produced relative success in implementing the acoustic analogy models in jet noise prediction using Reynolds-averaged Navier-Stokes (RANS) code flow solutions as input. Such methods make an attempt to define a closed-form relationship for certain statistical parameters of interest in turbulence, such as space-time correlations, preferably in compliance with available data. Since statistical measurements are often carried out under restrictive flow conditions due to lab and instrumentation limits, it is not uncommon for such models to be pushed beyond their intended envelope and include assumptions that are true only at limited or special cases. Parameters not available in the data bank may also rely solely on the physical intuition of the researcher. But how well do these methods predict the spectral directivity of jet noise over a broad range of jet flow conditions, and how successful are they in transforming predictions of the turbulent kinetic energy into predictions of jet noise? These are questions to be answered, quantitatively, in this assessment.

This chapter will introduce jet noise prediction codes that were available in the assessment exercise. These codes are discussed briefly, and references are provided for more in-depth discussions of their development and modeling details. Sample runs illustrate the sensitivity of each code relative to input parameters. The CFD code Wind-US, which generated the mean flow and turbulence information for the acoustic analogy codes is also discussed briefly with an overview of the validation work that puts an error bar on the input to the acoustic analogy codes. Next, experimental data sources are introduced and details of the measurement systems are given. This information is used to determine the uncertainties in both acoustic predictions and the CFD input to the acoustic codes. A set of metrics is then established by which the predictions and experimental results are compared, and the results of each code are catalogued. The chapter closes with a summary of each code's performance and an overview of the state of the art in jet noise prediction. Appendix A lists the acronyms and symbols used in this chapter.

8.2 Discussion of Codes

Jet noise predictive codes fall into three categories:

- (1) Empirical—based on scaling laws and interpolations on measured data
- (2) Acoustic analogy—based on a RANS solution to the mean flow and turbulence
- (3) Direct—based on direct numerical solution to the set of Navier-Stokes equations

The first category describes the majority of codes used in practice today, whether they are simple interpolations across existing corporate databases, such as the ESDU method (Ref. 1), or more complicated schemes that attempt to subdivide the jet into a number of noise sources depending on the geometric details and operating conditions of each jet, such as the Stone jet method (Ref. 2). The latter code is currently contained within the NASA Aircraft Noise Prediction Program (ANOPP) code (Ref. 3). These codes typically require as input parameters some description of the flow condition such as velocity and temperature plus geometric parameters such as nozzle areas, extension lengths, and perhaps hydraulic perimeter in the case of enhanced mixing devices. Empirical codes are quick to run and are typically suitable for large systems studies where thousands of evaluations of overall system noise and performance may have to be carried out to find an optimal design space with less emphasis on the details.

Codes in the second category attempt to make use of formulations such as acoustic analogy theories that describe the transfer of energy from turbulence to noise. Typically these codes require as input a RANS CFD solution for the mean velocities, temperatures, turbulent kinetic energy, and length and time scales. Models are proposed for the space-time correlations of noise generating turbulent eddies in the jet, and

subsequently the noise produced from each volume element is propagated through the inhomogeneous acoustic medium to the far-field observer. As long as the statistical properties of turbulence are correctly incorporated into the source model, the acoustic analogy approaches are expected to provide the noise estimate using a superposition of noise emitted from independent correlation volume elements that comprise the jet. Details of the source correlations as related to velocity-velocity or velocity-temperature fluctuations at two points separated in space and time are still unresolved, and it is not uncommon to see some important source terms discarded due to lack of data for validation and/or the inability of the RANS solvers to provide the required input parameters. Aside from the generation mechanism associated with the source, propagation of sound through the non-uniform base flow also poses computational challenges in a general three-dimensional jet. Even in the relatively subtle axisymmetric jets, effects such as scattering of sound by turbulence are completely overlooked and the effects on the sound propagation are attributed only to non-uniformities in mean velocity and temperature.

Codes in the third category compute the time-dependent turbulent flow directly, resolving scales of motion as small as permitted by the grid density and computer storage capacity. In large eddy simulations (LES), the smaller scales (subgrid scale terms) are modeled, and the Navier Stokes equations are filtered for the larger scales that are considered as sources of jet noise. Consequently, predicted noise levels tend to be much lower at high frequency compared to data. In principle, one should be able to compute the pressure fluctuations directly along with other variables of interest. Because our interest is usually the far field, computationally it is advantageous if the flow calculation is stopped outside the hydrodynamic domain and matched with an acoustic solution to propagate to a far-field observer point. This type of calculation as exemplified by LES requires massive computational resources and is still in its infancy. For these reasons, this category of predictive code is not considered in the present assessment exercise.

8.2.1 Empirical Prediction Tool: Stone Jet Noise Module (ST2JET) Within ANOPP

The purpose of the NASA Aircraft Noise Prediction Program ANOPP is to predict noise from aircraft, accounting for the effects of the aircraft characteristics, its engines, its operations, and the atmosphere, in an attempt to meet noise certification rules. During certification exercises, the aircraft follows an arbitrary flight path in the presence of an observer on the ground. Throughout this operation, various noise sources on the aircraft emit noise with defined power, directional, and spectral distribution characteristics, all of which may depend on time. Noise propagates through the atmosphere subject to the atmospheric attenuations, and reaches to the vicinity of the observer. The observer receives noise signals from the direct ray as well as ground reflection.

A complete background on ANOPP is given in Chapter 2, “Aircraft System Noise Prediction.”

The ST2JET module is based on the semi-empirical model developed by J.R. Stone of Modern Technologies Corporation (Ref. 4). The method was developed from data with bypass ratios ranging from 5.0 to 14.9 obtained from free-jet facilities at NASA Glenn and NASA Langley Research Centers as well as the anechoic free-jet facilities at Lockheed Martin Corporation and General Electric Company. The ST2JET module is an update to the older STNJET module in ANOPP and extends the ANOPP jet noise prediction capability to higher bypass ratio engines for a full range of nozzle configurations including jets with inverted velocity profiles. The jet mixing noise and broadband shock noise components (associated with supersonic jets) also include corrections for forward flight effects.

The components of jet mixing noise are inner stream mixing noise, outer stream mixing noise, and merged stream mixing noise. The inner stream mixing noise (intermediate-scale mixing noise) is a mid- to high-frequency-range noise source generated by the shear between the primary jet stream and either the secondary jet stream or the ambient air for a circular single-stream jet. The outer stream mixing noise (small-scale mixing noise) is relatively high-frequency noise generated by the small-scale turbulent mixing near the nozzle exit. The merged mixing noise (large-scale mixing noise) is the lowest frequency noise source generated by the mixing of the large-scale coherent structures in the jet with the ambient flow well downstream of the nozzle exit. Nozzles with center plugs have an additional plug separation noise component caused by the flow disturbance at the tip of the center plug. The plug separation noise is a high-frequency component associated with the primary stream. The method also includes procedures for computing nozzle exit perimeter suppression effects, such as might be found with chevrons, tabs, chutes, or other exit suppression devices that do not separate the flow stream. These effects are applied to the three mixing noise components.

Broadband shock noise is evaluated for supersonic shock-containing jets in the primary and/or the secondary stream. Co-annular nozzles with a center plug but without exit perimeter suppression devices are treated as a special case. For such nozzle configurations, if both streams are supersonic and the secondary stream total pressure is greater than the primary stream total pressure, the outer stream shock noise is replaced with the downstream merged shock noise. Otherwise shock noise is predicted using the outer stream shock component only.

8.2.1.1 Description of Input Parameters

The ST2JET module requires nozzle flow properties and geometric dimensions of the nozzle. The nozzle exit flow parameters can be provided by the “Jet Noise Parameters Module” within ANOPP or specified by the user directly. The main input parameters are nozzle diameters at exit and throat

of core and bypass streams, plus temperature and jet velocity for both streams as well as the flight Mach number.

8.2.1.2 Description of Output and Options Used

The ST2JET prediction method combines the component noise from sources described above into a single 1/3-octave band spectrum at each polar angle. The output is a table of the mean-square acoustic pressure as a function of frequency, polar directivity angle as measured from jet inlet axis, and azimuthal directivity angle when the noise field is not axisymmetric. Jet exhaust noise from circular nozzles is independent of the azimuthal directivity angle; however, it is tabulated as a constant function of azimuthal angle so that the output table is compatible with other noise tables generated by ANOPP. For the definition of these angles, see Figure 2.3 in Chapter 2, “Aircraft System Noise Prediction.”

In this assessment exercise, only the ST2JET source module was invoked, and the main ANOPP code was used to propagate the sound to a set of observers at the same far-field locations and frequencies as the experimental measurement. In cases involving simulated forward flight, ANOPP output as expressed in a fixed-observer frame of reference was post-processed, and transformed to “infinite wind tunnel” coordinates with the observer moving with the source, essentially removing the Doppler shift from the data. In all cases, 1/3-octave data from ANOPP were imported into the NASA Glenn digital acoustic data system (DADS) where it was converted to narrowband power spectral density for later manipulation. The frequency f was normalized using nozzle diameter D (based on total area) and jet velocity U (ideally expanded), and expressed as a Strouhal number $St = fD/U$. The sound spectral density was also integrated over each 1/3-octave frequency band for smooth presentation of data.

8.2.2 Acoustic Analogy Prediction Tools

Flow-induced noise, in principle, is associated with small pressure fluctuations that radiate at the speed of sound from a turbulent flow to a distant observer. Rather than solving the governing fluid dynamic equations directly from a noise-generating region to the far field, an equivalent problem may be posed in the form of an inhomogeneous wave equation. Subsequently, a solution is written in closed form as a convolution of the source with an appropriate Green’s function as is done in classical acoustics. Lighthill’s second-order wave equation (Ref. 5 and 6) is the simplest form of the acoustic analogy because its Green’s function, at any frequency of interest, is that of the reduced Helmholtz equation. A successful implementation of this particular analogy is rather difficult because of the complexity of the source term and the simplifying assumption required to model the source. Other variants of the wave operator were later proposed that place less demand on the source but also require a more complicated Green’s function. Lilley’s third-order wave equation (Ref. 7) is an example of such an analogy where flow effects such as source convection and mean-flow refraction are explicitly

described by the operator part of the equation. A practical implementation of any acoustic analogy involves several steps: (1) computation of a nonradiating base flow, (2) modeling of the source term(s), and (3) computation of the Green’s function. In general, step (1) is achieved by considering the base flow as the mean flow computed by a RANS solver. A two-equation turbulence model is also used to evaluate the turbulent kinetic energy and its dissipation rate as needed for the source modeling. Step (3) in general, is computationally intensive and in some instances high- or low-frequency analytical approximations to the Green’s function are sufficient and computationally efficient.

A formal solution to any acoustic analogy model may be written as

$$p'(\mathbf{x}, t) = \int_{-\infty}^{\infty} d\tau \int_{\mathbf{y}} G(\mathbf{x}, t | \mathbf{y}, \tau) q(\mathbf{y}, \tau) d\mathbf{y} \quad (8.1)$$

where p' denotes the fluctuations in pressure p at the observer location \mathbf{x} and at time t ; q is the source intensity per unit volume at source location \mathbf{y} at the time of emission τ , and G is the relevant Green’s function. Following the computation of the autocorrelation function

$$\overline{p^2}(\mathbf{x}, \tau) = \frac{1}{2\mathcal{T}} \int_{-\mathcal{T}}^{\mathcal{T}} p'(\mathbf{x}, t) p'(\mathbf{x}, t + \tau) dt \quad (8.2)$$

the Fourier transform is used to compute the acoustic spectrum

$$\overline{P^2}(\mathbf{x}, \omega) = \frac{1}{2\pi} \int_{-\infty}^{\infty} \overline{p^2}(\mathbf{x}, \tau) e^{i\omega\tau} d\tau \quad (8.3)$$

where \mathcal{T} denotes some large but finite time and ω is the radian frequency. The two acoustic analogy tools described next, Jet3D and JeNo v1.0, use Lighthill’s and Lilley’s formulations, respectively.

8.2.2.1 Jet3D

The Jet3D code (Ref. 8) is based on a straightforward application of Lighthill’s Acoustic Analogy (Ref. 5 and 6) in three dimensions. Manipulating the equations of motion, a second-order, inhomogeneous wave equation is derived,

$$\frac{\partial^2 p'}{\partial t^2} - c_{\infty}^2 \frac{\partial^2 p'}{\partial x_j^2} = \frac{\partial^2 T_{ij}}{\partial x_i \partial x_j} \quad (8.4)$$

where $T_{ij} = \rho u_i u_j + (p - c_{\infty}^2 \rho) \delta_{ij} - \sigma_{ij}$ is the Lighthill stress tensor, u_i is the fluid velocity vector, c_{∞} is the ambient speed of sound, ρ is the fluid density, p is pressure, δ_{ij} is the Kronecker delta, and σ_{ij} is the viscous stress tensor. In the far field, pressure and density fluctuations are related by $p' = c_{\infty}^2 \rho'$. The source term

$$q(\mathbf{y}, \tau) = \frac{\partial^2 T_{ij}(\mathbf{y}, \tau)}{\partial y_i \partial y_j} \quad (8.5)$$

and the corresponding Green's function

$$G(\mathbf{x}, t | \mathbf{y}, \tau) = \frac{\delta(t - \tau - R/c_\infty)}{4\pi R} \quad (8.6)$$

where the distance between the source and receiver $R = |\mathbf{x} - \mathbf{y}|$. Substituting Equations (8.5) and (8.6) into Equation (8.1) formally solves for the far-field pressure p' . In deriving the acoustic analogy, Lighthill cast the complicated nonlinear jet noise problem into a simple analogy within the scope of classical acoustics; the flow field and complex flow-acoustic interactions (such as source convection and mean-flow refraction) in a real jet are replaced by a fictitious volume source distribution of acoustic quadrupoles radiating into a uniform ambient medium with a free-space Green's function. This formulation makes the calculation of propagation a simple matter, but puts weight on modeling of the source terms to accommodate for flow-sound interaction. In practice, the viscous stress σ_{ij} is neglected because of its small contribution, and the entropy source term $(p - c_\infty^2 \rho)$ is also neglected in unheated jets, although it could potentially become significant in heated jets. Of note in this assessment, the source modeling does not include the impact of the entropy source term; rather, the source is represented by the Reynolds stress term $\rho u_i u_j$. Specific details of the implementation of the Lighthill theory in

the Jet3D code can be found in Chapter 9, "Propulsion Airframe Aeroacoustic Interactions."

Early validation of Jet3D was done using the Yamamoto et al. dataset (Ref. 9). Noise predictions were made for a heated Mach number $M = 1.4$ jet issuing from a convergent-divergent nozzle, exit diameter 13.7 cm (5.4 in.), operating at its design nozzle pressure ratio of 3.18, with a jet total temperature of approximately 956 K (1720 °R). The Jet3D noise predictions were made for 13 observer locations along a 12-m (40-ft) radius arc (approximately 88 nozzle diameters) centered on the nozzle exit. For each observer, 1/3-octave band frequency sound pressure levels (SPLs) were computed over bands from 50 Hz to 80 kHz.

For this assessment exercise, Jet3D was run using RANS CFD input from the Wind-US CFD code (Ref. 10). This led to some concern since Jet3D was calibrated using the PAB3D CFD code (Ref. 11). As a cross check, two of the nine cases listed in Table 8.1 were recomputed using Jet3D with RANS input from the PAB3D code. As expected, using the different flow solutions from the RANS codes caused differences in the computed noise spectra. Also, one of the cases was repeated with a higher resolution grid, but the changes in noise prediction were minimal. Figure 8.1 illustrates the differences in a typical computed flow solution by comparing the predicted turbulent kinetic energy from the PAB3D and Wind-US codes with particle image velocimetry (PIV) data from the same facility as the noise data were acquired. Figure 8.2 shows the impact on the predicted noise when using two different computed flow solutions for the conditions of case 037 from Table 8.1.

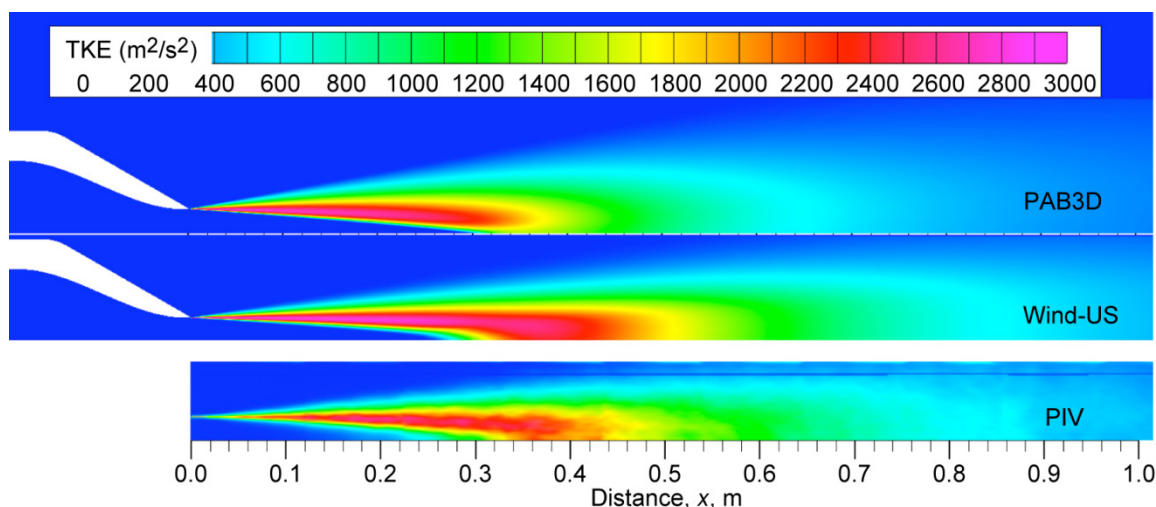


Figure 8.1.—Turbulent kinetic energy (TKE) contours downstream from a nozzle. Comparison of predictions from different CFD codes, PAB3D and Wind-US, and experimental particle image velocimetry (PIV) data.

TABLE 8.1.—ASSESSMENT CASES FOR JET3D
PREDICTIONS OF JET NOISE SPECTRA^a

Case	M	Axial geometry	M _a	T _{s,r}	nozid
003	0.51	Convergent ↓ C-D	0.500	0.955	SMC000
007	0.98		0.902	0.842	SMC015
022	0.37		0.492	1.767	
025	0.68		0.901	1.770	
027	1.01		1.330	1.759	
034	0.30		0.484	2.624	
037	0.56		0.901	2.702	
040	0.92		1.483	2.703	
268	1.40		2.20	2.530	

^aNomenclature for table headings:

M	ideally expanded Mach number
Axial geometry	indicates if nozzle was convergent or convergent-divergent (C-D)
M _a	acoustic Mach number, U/c_∞
T _{s,r}	static temperature ratio, T_s/T_∞
nozid	nozzle identification

8.2.2.2 JeNo v1.0

JeNo v1.0 (hereafter referred to as “JeNo”) is also an embodiment of an acoustic analogy. Unlike the Jet3D code that follows the Lighthill analogy, JeNo follows a third-order convective wave equation associated with Lilley (Ref. 7). When this equation is linearized about a unidirectional transversely sheared mean flow, it may be expressed as

$$L\Pi = q(\mathbf{x}, t) \quad (8.7)$$

where $\Pi = (p/p_o)^\gamma - 1$ is the pressure variable, p_o is the mean pressure, and $p = p' + p_o$. Since the ratio p'/p_o is very small compared to 1 (on the order of 10^{-5}), the dominating term in the series expansion of the pressure variable Π becomes $\Pi \approx p'/\gamma p_o$ where γ is the specific heat ratio of air. The operator L depends on the convective derivative $D/Dt = \partial/\partial t + u_o \partial/\partial x_1$, where u_o is the mean axial velocity, and x_1 is the streamwise direction

$$L \equiv \frac{D}{Dt} \left(\frac{D^2}{Dt^2} - \frac{\partial}{\partial x_j} \left(c_o^2 \frac{\partial}{\partial x_j} \right) \right) + 2c_o^2 \frac{\partial u_o}{\partial x_j} \frac{\partial^2}{\partial x_1 \partial x_j} \quad (8.8)$$

and the source term may be written as

$$q(\mathbf{x}, t) = \frac{D}{Dt} \frac{\partial \xi_j}{\partial x_j} - 2 \frac{\partial u_o}{\partial x_j} \frac{\partial \xi_j}{\partial x_1} \quad (8.9)$$

where

$$\xi_j \equiv \frac{\partial}{\partial x_i} (1 + \Pi) u'_i u'_j + (\gamma - 1) h' \frac{\partial \Pi}{\partial x_j} \quad (8.10)$$

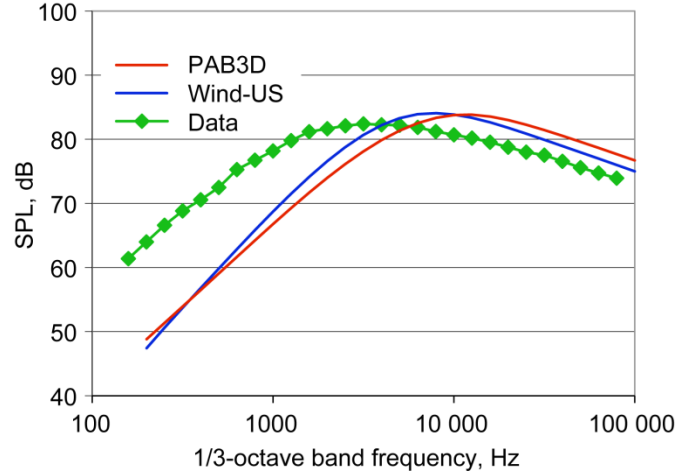


Figure 8.2.—Comparison of sound pressure levels (SPLs) predicted by Jet3D for a jet from a converging nozzle using input from different CFD codes, PAB3D and Wind-US, and experimental data. Case 037 from Table 8.1. Inlet angle $\theta = 90^\circ$.

Lilley’s formulation of the wave equation accounts for both the convection effect and the refraction of the sound that is caused by gradients in the jet mean velocity u_o and sound speed c_o . Here u'_i is a fluctuating velocity vector and h' is enthalpy fluctuations in the flow. The entropy source term that was associated with the $(p - c_o^2 \rho)$ term in Lighthill’s acoustic analogy is now written in a more transparent form by using the energy equation. As seen above, this source relates to fluctuations in temperature through h' . When a nonradiating base flow is additionally subtracted from the governing equations, as described by Goldstein’s generalized acoustic analogy (Ref. 12), this source is shown to depend on fluctuations in total enthalpy. A full derivation of the theory behind JeNo, development of the propagator and source modeling is provided in References 13 and 14.

In axisymmetric jets, the reduced form of the wave operator (Eq. (8.8)) at any frequency ω becomes the second-order, self-adjoint, compressible Rayleigh equation. Once the radial distribution of the mean velocity and temperature are specified, this equation is solved numerically at each frequency of interest to obtain the Green’s function, $G(\mathbf{x}|\mathbf{y};\omega)$. For comparison, the corresponding Green’s function in Lighthill’s acoustic analogy is simply the Fourier transform of Equation (8.6); that is, $G(\mathbf{x}|\mathbf{y};\omega) = \exp(i\omega R/c_\infty)/(4\pi R)$.

As in Jet3D, JeNo does not model the enthalpy-related term in its source model and approximates the source term as

$$q(\mathbf{x}, t) \approx \frac{D}{Dt} \frac{\partial^2 (u'_i u'_j)}{\partial x_i \partial x_j} - 2 \frac{\partial u_o}{\partial x_j} \frac{\partial^2 (u'_i u'_j)}{\partial x_1 \partial x_j} \quad (8.11)$$

To include the enthalpy-related source term, dedicated RANS solvers are needed to provide the variance in total enthalpy as an additional input parameter to the noise code. Such solvers are currently under development and will not be discussed here. The source volume integration (dy) in Equation (8.1) may be subdivided into a composite of ring volume elements if the jet is axisymmetric. Nonaxisymmetric jets, however, pose additional difficulties, and in general five linear equations need to be solved in generalized three-dimensional coordinates for the five components of a vector Green's function. Such a vector function should be able to address the azimuthal variation of the sound field in both polar θ and azimuthal directions ϕ in unconventional (nonaxisymmetric) jets. A more practical type of computation currently employed in JeNo is a so-called 2.5-dimensional approximation that extends the axisymmetric Green's function to a three-dimensional jet. Such an approximation allows for the variation in source strength in the azimuthal direction, but convolves that with a Green's function that is calculated along a specified azimuthal plane. For example, in the “line-of-sight” approach the Green's function is calculated along a

predefined azimuthal plane, referred to as the “line of sight,” while the source density is allowed to change azimuthally as the volume integration is carried out. An alternative 2.5-dimensional approximation evaluates the Green's function at the same azimuthal plane as the source (i.e., $\phi = \phi^s$) and computes a new Green's function at each azimuthal plane using the corresponding flow profile into the second-order compressible Rayleigh equation. This method resembles some form of azimuthal averaging of the sound field and is referred to as the “line-of-source” approximation.

Calibration constants for source amplitude, length scale, and time scale were determined for the best fit with a Mach 0.51 unheated jet. Two of these constants work with the input turbulent kinetic energy and dissipation rate to set the local time- and length-scales. Subsequently, these parameters show sensitivity with respect to the specific RANS solver as well as the particular turbulence model within a single flow solver. For example, Figure 8.3 shows the spectral density computed by the JeNo code at 90° and 150° using the Wind-US RANS code to compute the flow for a cold jet with an acoustic Mach number of 0.5 with three different turbulence models: the

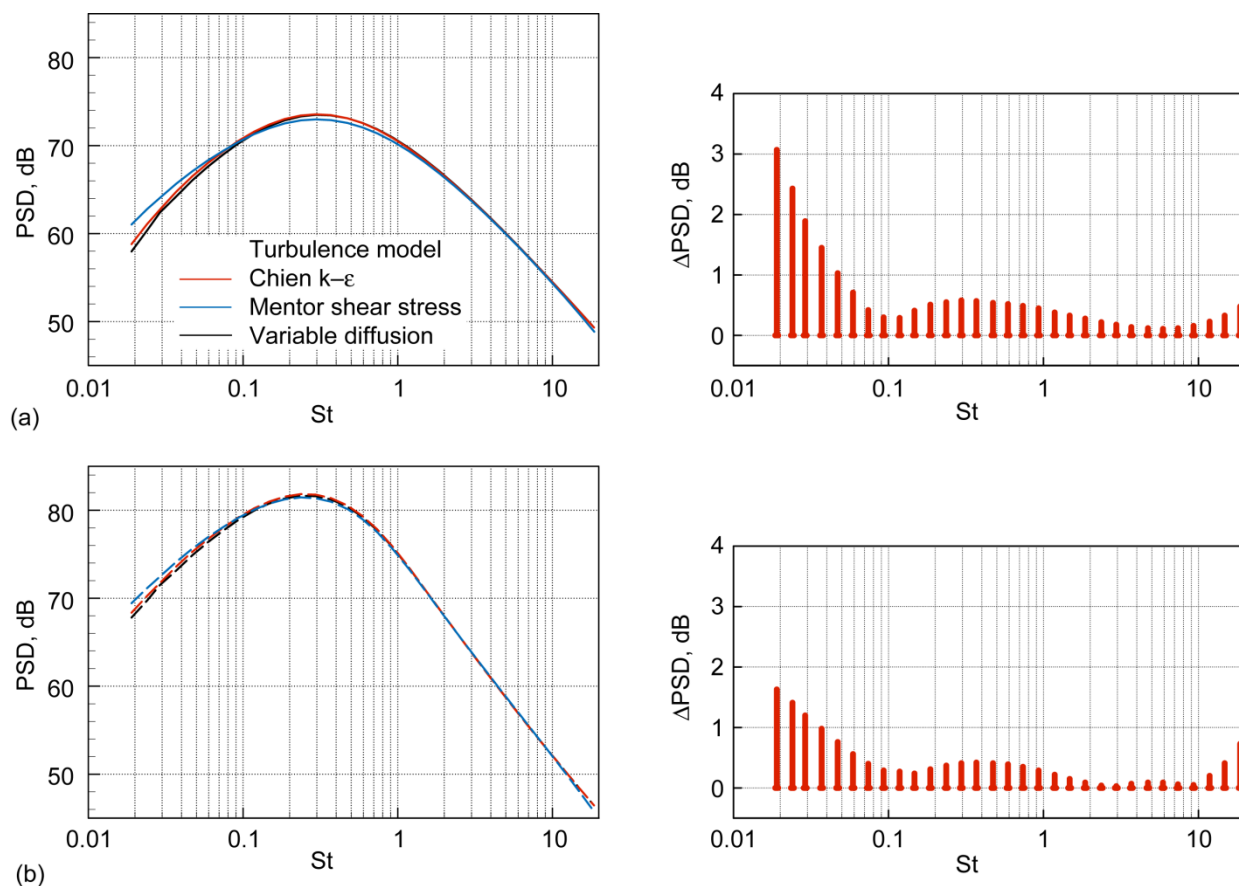


Figure 8.3.—Power spectral density (PSD) versus Strouhal number St of cold jet, acoustic Mach number $M_a = 0.5$, predicted by JeNo using RANS input with three turbulence models; and largest difference Δ between predictions. (a) Inlet angle $\theta = 90^\circ$. (b) $\theta = 150^\circ$.

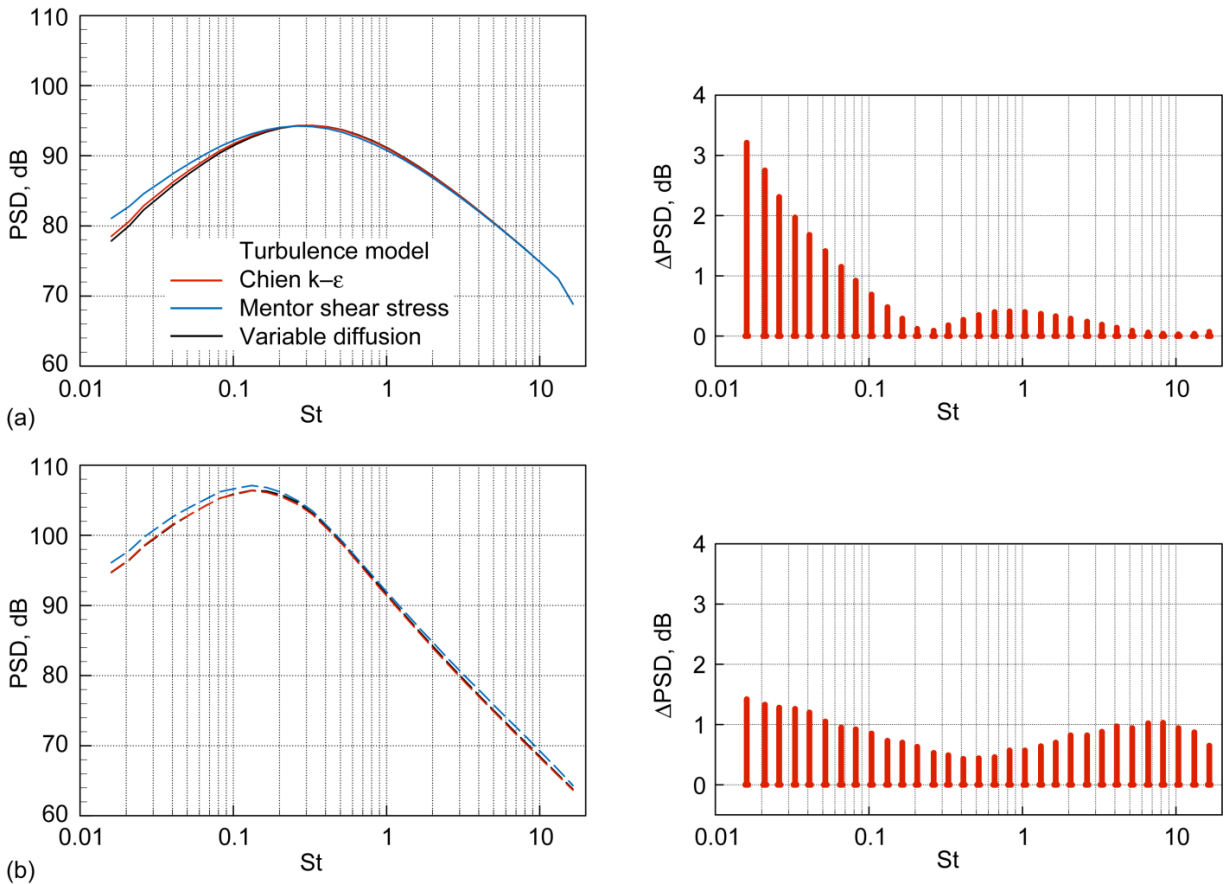


Figure 8.4.—Power spectral density (PSD) versus Strouhal number St of cold jet, acoustic Mach number $M_a = 0.9$, predicted by JeNo using RANS input with three turbulence models; and largest difference Δ between predictions. (a) Inlet angle $\theta = 90^\circ$. (b) $\theta = 150^\circ$.

standard Chien $k-\epsilon$ model, Mentor shear stress transport (SST) model, and the variable diffusion model. The details of each model, and sample velocity and turbulence comparisons, are examined in Georgiadis et al. (Ref. 15). Noise predictions that use the solutions from the same RANS solver but with the three turbulence models are in close agreement, and the largest differences are at the lower frequencies. The difference in decibels is computed between the largest and smallest spectral value at each frequency among the three predicted spectral densities. Figure 8.4 shows a similar set of results for a cold jet with a 0.9 acoustic Mach number.

An alternative uncertainty assessment is shown for JeNo predictions in Figure 8.5, using flow input from two different RANS solvers. Here the flow-field simulation is achieved using identical grids and similar turbulence models (standard Chien $k-\epsilon$ model) but different flow solvers, Wind-US (Ref. 10) and Craft (Ref. 16). Parameter Δ measures the difference in decibels between the JeNo predicted overall sound pressure levels (OASPLs)—Wind-US minus Craft—and should be related to numerical algorithm and convergence criteria in each flow simulation.

The effect of the turbulent kinetic energy on the predicted OASPL directivity is shown in Figure 8.6. The input level of turbulent kinetic energy has been intentionally modified by ± 10 percent to show that it could have a 3.5- to 5.0-dB impact on the predicted noise level.

8.2.3 Reynolds-Averaged Navier-Stokes (RANS) Tool: Wind-US

Input to acoustic analogy jet noise prediction codes consist of the grid file, the mean-flow parameters, plus turbulent kinetic energy k and its dissipation rate ϵ . Prior to evaluating the acoustic codes' predictive capability, it was critical to assess the accuracy of the flow field. The degree to which the CFD predictions impact the accuracy of the acoustic predictions is determined once we know the noise code sensitivities to errors in the input flow parameters. As shown in the descriptions of the Jet3D and JeNo codes, the mean-flow parameters such as mean Mach number (velocity and temperature) could affect the propagation portion of the acoustic solution whereas parameters such as density, turbulent kinetic

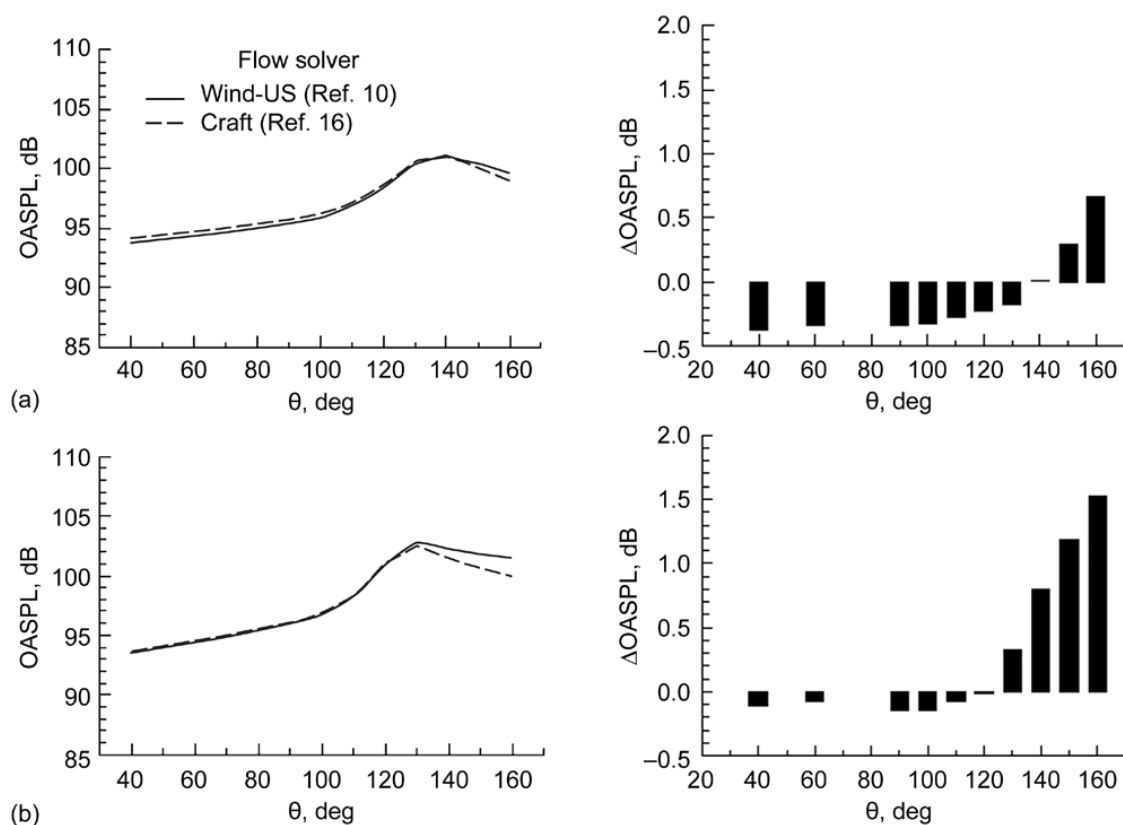


Figure 8.5.—Overall sound pressure level (OASPL) predicted by JeNo for jets at changing inlet angle θ using two different RANS code flow solutions; difference Δ in predictions is (Wind-US – Craft).
(a) Acoustic Mach number $M_a = 0.5$. (b) $M_a = 0.9$.

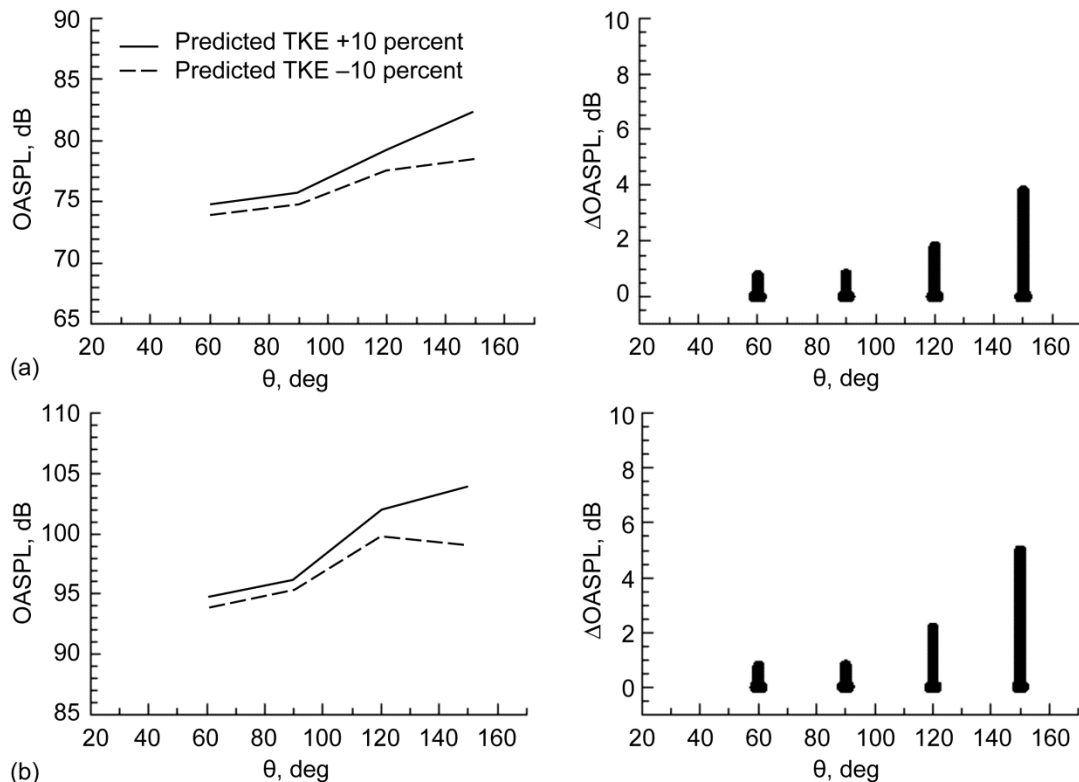


Figure 8.6.—Overall sound pressure level (OASPL) predicted by JeNo for cold jets at changing inlet angle θ with ± 10 percent change in RANS code turbulent kinetic energy (TKE); and difference Δ in predictions. (a) Acoustic Mach number $M_a = 0.5$. (b) $M_a = 0.9$.

energy, and dissipation rate affect the predicted source strength. Mean velocity and temperature and turbulent velocity have been measured for validation purposes. However, dissipation is very difficult to measure, and the quantity labeled as dissipation in most CFD codes is more a surrogate factor than a physically realizable quantity. Thus it is difficult to validate the dissipation fields from various CFD codes, and indeed this parameter is observed to vary most between different flow solvers. Hence (1) noise prediction codes were mostly evaluated using the CFD code on which they had been calibrated, and (2) only mean velocity and turbulent kinetic energy were directly compared with experimental data.

Jet3D has been used mostly with the flow solver PAB3D, and JeNo has been calibrated using the code Wind-US. Both codes are available to United States concerns and are open to researchers working to improve and modify the turbulence models and other aspects of the codes. A great deal of documentation exists for these codes and will not be repeated here. An in-depth analysis of the suitability of different turbulence models was carried out by Georgiadis et al. (Ref. 15) and should be referred to. Note that all CFD predictions for jet noise assessment were performed using the Mentor SST turbulence model.

Shown in Figure 8.7 are the predicted turbulent kinetic energy distributions—in normalized form as \sqrt{k}/U —for the 5.1-cm (2-in.) convergent nozzle operated at the conditions listed as cases 003, 007, and 040 in Table 8.1 corresponding to acoustic Mach numbers of 0.50, 0.90, and 1.48, respectively. The first two jets are unheated, and the last jet is at exit static temperature ratio of $T_{s,r} = 2.70$. Favorable agreement with the PIV measurements are observed in the turbulence levels, as well as the shortening of the core length due to the heat—which is the product of a faster jet spread and improved mixing.

8.3 Identification of Test Programs

In large part, jets chosen for the assessment were selected from datasets that had well-known uncertainties in noise measurement. First, the idiosyncrasies of the facilities, such as internal rig noise, anechoic character, and microphone placements, must be known. Issues such as sample time, accuracy of the set point over the duration of sampling, stability of the air supply controls, transfer functions of the signal conditioning equipment, calibration procedures and policies all can play a role and produce subtle changes in the data. A very significant factor that has noticeable impact on

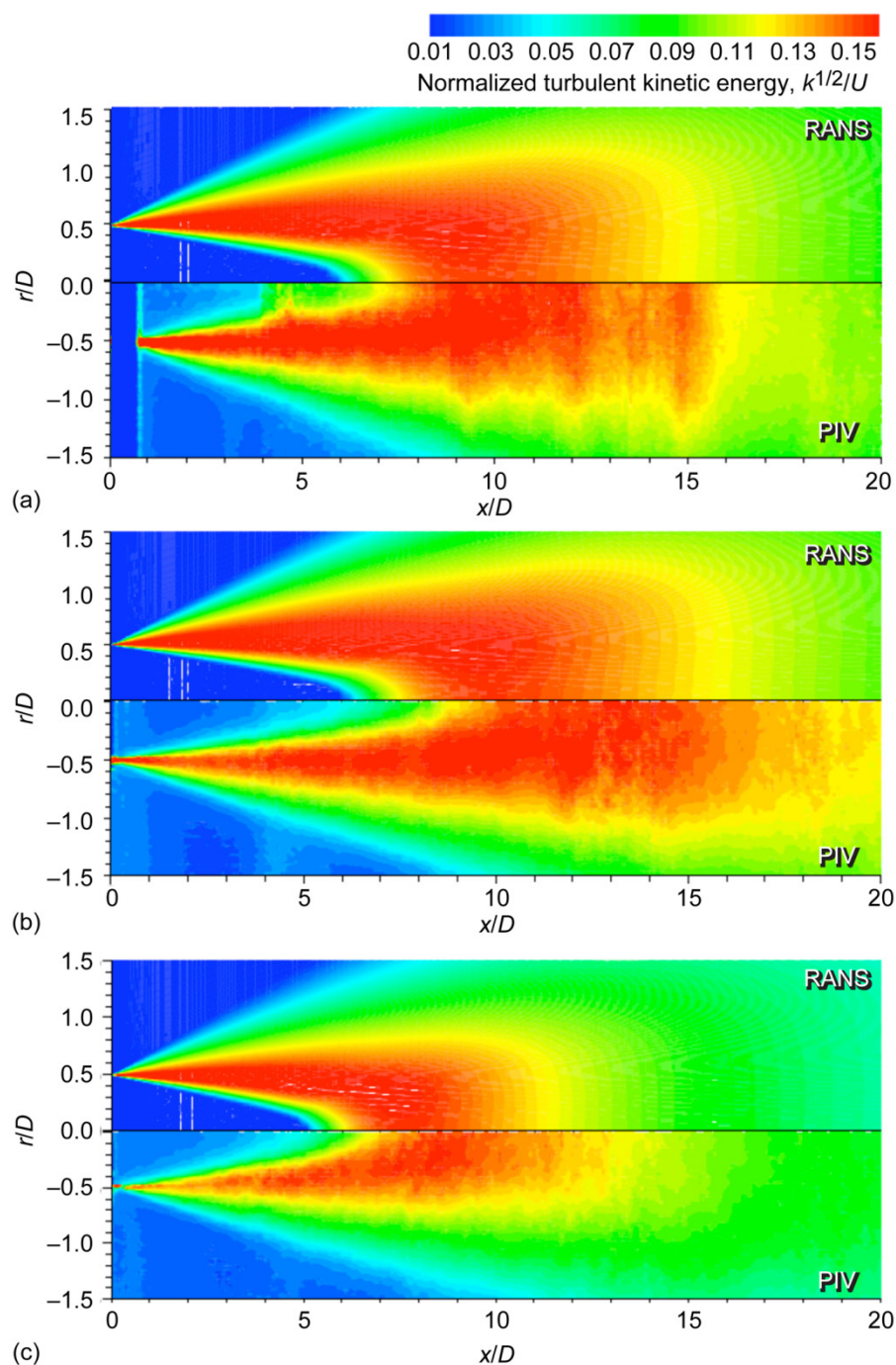


Figure 8.7.—Distribution of normalized turbulent kinetic energy (TKE) for 5-cm convergent nozzle; here, r is radial coordinate and x is axial distance, normalized over nozzle diameter D . Wind-US Reynolds-averaged Navier-Stokes (RANS) predictions and particle image velocimetry (PIV) measurements. (a) Acoustic Mach number $M_a = 0.5$ unheated jet (case 003, Table 8.1). (b) $M_a = 0.9$ unheated jet (case 007). (c) $M_a = 1.48$ heated jet (case 040).

the jet noise spectrum is whether the boundary layer at the nozzle exit is turbulent or laminar. Accuracy of ambient conditions during noise measurements and proper correction for atmospheric attenuation must also be documented.

To properly evaluate the acoustic predictions, input parameters as predicted with the CFD codes had to be evaluated against data. This implied a comprehensive measurement of parameters such as mean velocity and turbulent kinetic energy at a wide range of temperatures and velocities of interest—in addition to the far-field noise for each jet. Very few datasets exist containing both turbulence and noise, especially in hot and/or supersonic flows.

Over the years from 2002 to 2009, such a dataset has been compiled at NASA Glenn to be used in guiding prediction and validation efforts. Substantial effort has gone into quantifying the internal rig noise, electronic noise sources, and in comparing measurements of both flow and noise with highly qualified facilities that do not have the capability to measure both flow and noise. Both single- and dual-flow jet rigs were utilized with cross-rig comparisons used to reassure rig-independent measurements. Comparisons of single-stream jets were carried out against results from Boeing's Low-Speed Aeroacoustic Facility jet rig, where the quality of the facility has been well documented. To validate dual-stream results, the test nozzles for several separate-flow configurations were tested at NASA Langley's Low Speed Aeroacoustic Wind Tunnel to ensure that the internal rig noise was well understood and removed from data prior to the assessment exercise.

8.4 Jet Noise Case Taxonomy

To parameterize the jet noise cases of interest, the following jet parameters were considered:

- Bypass ratio (BPR)
- Mach number (M = ideally expanded value computed using nozzle pressure ratio and total temperature)
- Acoustic Mach number (M_a = ideally expanded jet velocity/sound speed at ambient temperature)
- Static temperature ratio ($T_{s,r}$ = ideally expanded static temperature/ambient temperature)
- Total temperature ratio ($T_{t,r}$ = total temperature/ambient temperature)
- Flight Mach number (M_{fl} = flight speed/ambient sound speed)
- Convergent and convergent-divergent (C-D) nozzles
- Internally and externally mixed nozzles
- Azimuthal base periodicity (m)

With this selection of parameters, taxonomy was established according to Table 8.2. Essentially, the cases include single-stream jets (BPR at 0) that are subsonic with convergent nozzles (Configuration A, axisymmetric, and Configuration B with chevrons) and supersonic with convergent-divergent nozzles (Configuration C). Different internal splitters changed the BPRs from 0.2 to 1.0 and 3.0 (Configurations D, E, and F, respectively) for both subsonic and supersonic conditions. At BPRs of 5 and 8 (Configurations G and H) the data were obtained from an internally mixed nozzle test with axisymmetric splitter, and with strongly mixed lobed mixer and an externally mixed separate flow nozzle. At BPRs of 11 and above (Configuration I) all the data were acquired at externally mixed, separate-flow nozzle systems with two different area ratios. Several of the jet conditions with externally mixed nozzle systems at BPRs 5 and above have datasets with and without forward flight.

8.5 Description of Facilities

Single-stream data primarily came from measurements on the Small Hot Jet Acoustic Rig (SHJAR, Figure 8.8). The SHJAR, located in the Aero-Acoustic Propulsion Laboratory (AAPL, Figure 8.9) at the NASA Glenn Research Center in Cleveland, Ohio, was developed to test jet-noise-reduction concepts at a low technology readiness level (TRL 1 to 3) and at minimum expense. As a jet-noise testing rig, the SHJAR was designed to minimize rig noise sources, incorporating the work of Viswanathan (Ref. 19) and Ahuja (Ref. 20) to achieve this goal. The rig is a single-flow jet rig that used 1034-kPa (150-psi) air supplied by several remotely located compressors. The maximum mass flow rate was 2.7 kg/s (6 lbm/s) and the maximum temperature air was 700 °C (1300 °F). A hydrogen-burning combustor, permitting a large range of temperatures, provided the heat. The air passed through a baffled muffler, followed by a settling chamber before reaching the nozzle. Two valves, a large main valve and a small vernier valve, controlled the rate of airflow, providing precise control over the entire range of operating conditions. Nozzle sizes from 2.5 to 7.6 cm (1 to 3 in.) in diameter were supported, although most data for this assessment was acquired using a 5.1-cm (2-in.) nozzle. The AAPL, which houses the SHJAR, is an 18.3-m (60-ft) radius geodesic dome lined with sound absorbing wedges that reduce sound reflection at all frequencies above 200 Hz. The jet exhaust is directed outside through a large door. An extensive study of the acoustic properties of the SHJAR rig and its validation are given in Brown and Bridges (Ref. 21).

TABLE 8.2.—TAXONOMY OF TEST CASES FOR ASSESSMENT OF JET NOISE PREDICTION CODES^a

Configuration	BPR	M	Geometry		M_a	$T_{s,r}$	Data source ^b
			Axial	Azimuthal			
A	0	0.3 to 1.0	Convergent	$m = 0$	0.35 to 1.5	0.85 to 2.7	SHJAR, Ref. 17, Ref. 18
B	0	0.5 to 1.0	Convergent	$m = 6$	0.5 to 1.3	0.85 to 2.6	SHJAR
C	0	1.2 to 1.8	C-D	$m = 0$	1.0 to 2.4	0.6 to 2.7	SHJAR, Ref. 17
D	0.2	0.6 to 1.0	Internal, convergent	$m = 0$	0.8 to 1.5	0.8 to 2.9	SDF07
		1.0 to 2.0		$m = 0$	1.0 to 2.4	1.0 to 2.9	SDF07
		1.2 to 21.8	Internal, C-D	$m = 0$	1.4 to 2.4	1.0 to 2.3	SDF07
E	1	0.6 to 1.0	Internal, convergent	$m = 0$	0.8 to 1.5	0.8 to 2.9	SDF07
		1.0 to 2.0		$m = 0$	0.9 to 2.4	0.8 to 2.3	SDF07
		1.2 to 2.0	Internal, C-D	$m = 0$	1.4 to 2.4	1.0 to 2.3	SDF07
F	3	0.6 to 1.0	Internal, convergent	$m = 0$	0.9 to 1.5	0.9 to 2.9	SDF07
		1.0 to 2.0		$m = 0$	1.0 to 2.4	0.8 to 2.3	SDF07
G	5	0.6 to 1.0	Internal, convergent	$m = 0$	0.9 to 1.7	2.5 to 3.1	LDIM05
		0.6 to 0.9		$m = 8$	0.9 to 1.7	2.6 to 3.1	LDIM05
		0.6 to 0.9		$m = 20$	0.9 to 1.6	2.6 to 3.1	LDIM05
		0.8 to 1.1	External, convergent	$m = 0$	1.0 to 1.6	1.8 to 2.4	HFXF07
H	8	0.6 to 1.0	Internal, convergent	$m = 0$	0.9 to 1.7	2.5 to 3.1	LDIM05
		0.8 to 0.9		$m = 8$	1.27 to 1.4	2.8 to 3.0	LDIM05
		0.8 to 0.9		$m = 20$	1.3 to 1.4	2.8 to 3.0	LDIM05
		0.7 to 0.8	External, convergent	$m = 0$	0.7 to 1.0	2.1 to 2.3	HFXF07
I	11	0.7	External, convergent	$m = 0$	0.9	2.3 to 2.4	HFXF07
	14	0.7		$m = 0$	0.8 to 0.9	2.4	HFXF07

^aNomenclature for table headings:

BPR is bypass ratio. Values in table are approximate.

C-D is convergent-divergent.

M is ideally expanded Mach number; for dual stream flows, it is the higher M.

m is azimuthal base periodicity.

M_a is acoustic Mach number, U/c_∞ .

$T_{s,r}$ is static temperature ratio, T_s/T_∞ .

^bData sources are listed in Section 8.6, “Description of Test Hardware for Data Sources.”

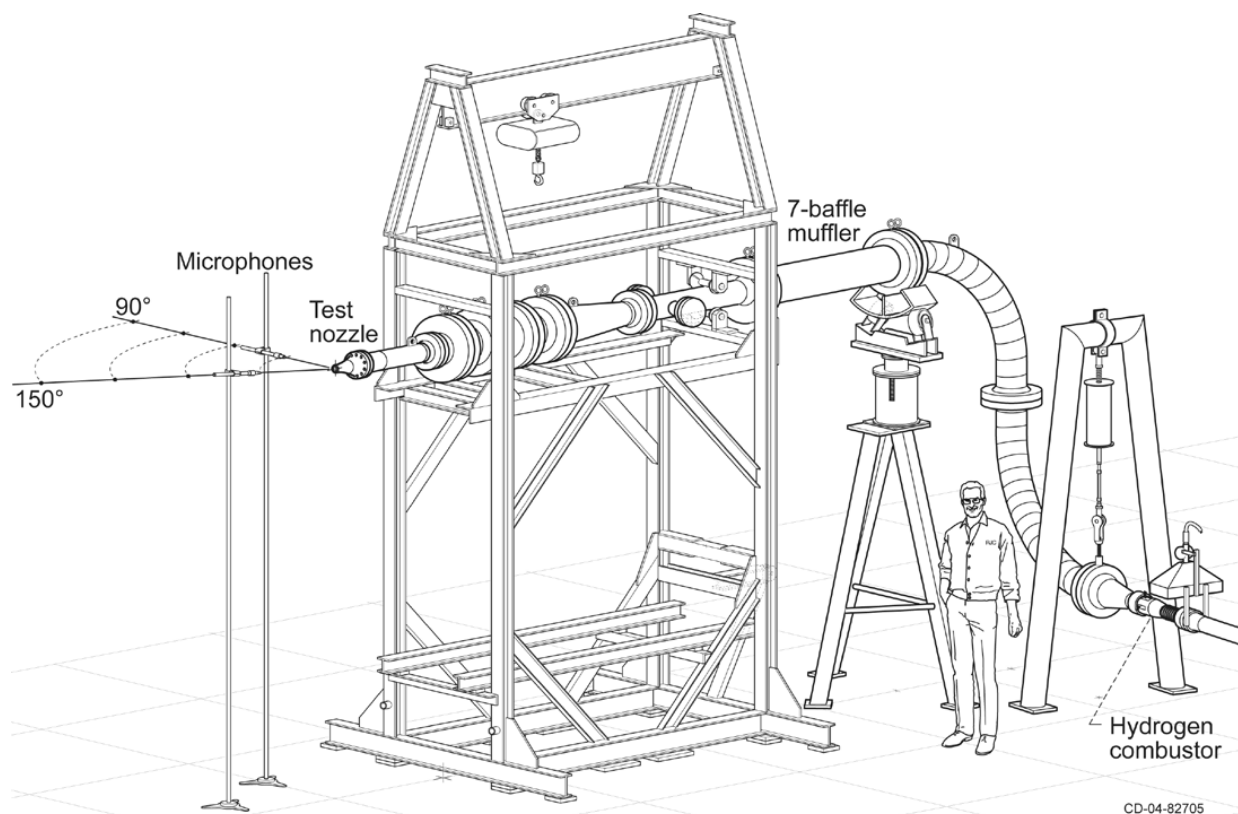


Figure 8.8.—Small Hot Jet Acoustic Rig (SHJAR).

For dual-stream test cases, data were acquired using the High Flow Jet Exit Rig (HFJER), which supplied air to the nozzle model at conditions similar to an aircraft engine. The HFJER sat at the exit of the Nozzle Acoustic Test Rig (NATR, Figure 8.9), a 1.3-m (53-in.) free-jet that provided the forward flight airflow around the nozzle at speeds up to Mach 0.35. The NATR sat in the middle of the AAPL mentioned above. A cutaway view of the HFJER is shown in Figure 8.10. Capabilities of the facilities are detailed in Reference 22. The use of NATR's simulated forward flight conforms to industry standard practice, such as General Electric's Cell 41 facility in Evandale, Ohio, and Boeing's larger Low-Speed Aeroacoustic Facility in Seattle, Washington.

8.6 Description of Test Hardware for Data Sources

All data used in this assessment were acquired within NASA-sponsored test programs over the period 2004 to 2007. Each data source is identified with a particular test set facility, and is intended to address a subset of cases, loosely grouped by BPR, illustrated in Table 8.2.

8.6.1 SHJAR

Most single-stream jet data acquired with nozzles attached to the SHJAR used the SMCxxx series model system. Originally conceived as a model system for parametric testing of chevron nozzles, its modular design allowed for a large number of nozzle concepts to be mounted such as chevrons and convergent-divergent nozzles in addition to the baseline axisymmetric convergent nozzle SMC000 (see Figure 8.11 and Figure 8.12).

Examples of nonaxisymmetric nozzles are SMC001, SMC005, and SMC006, each with six chevrons of identical dimensions except for the bending shape of the chevrons that determines the degree to which the chevron penetrates the flow (see Figure 8.12). For fully expanded supersonic jets, a family of five single-flow convergent-divergent nozzles was designed applying the method of characteristics (Ref. 23), each nozzle flow reaching a full expansion at the exit at a specified design Mach number M_d . Figure 8.13 shows the cross section of the convergent-divergent nozzle SMC014 with the lowest M_d of 1.18. All five single-flow convergent-divergent nozzles are identified in Table 8.3.

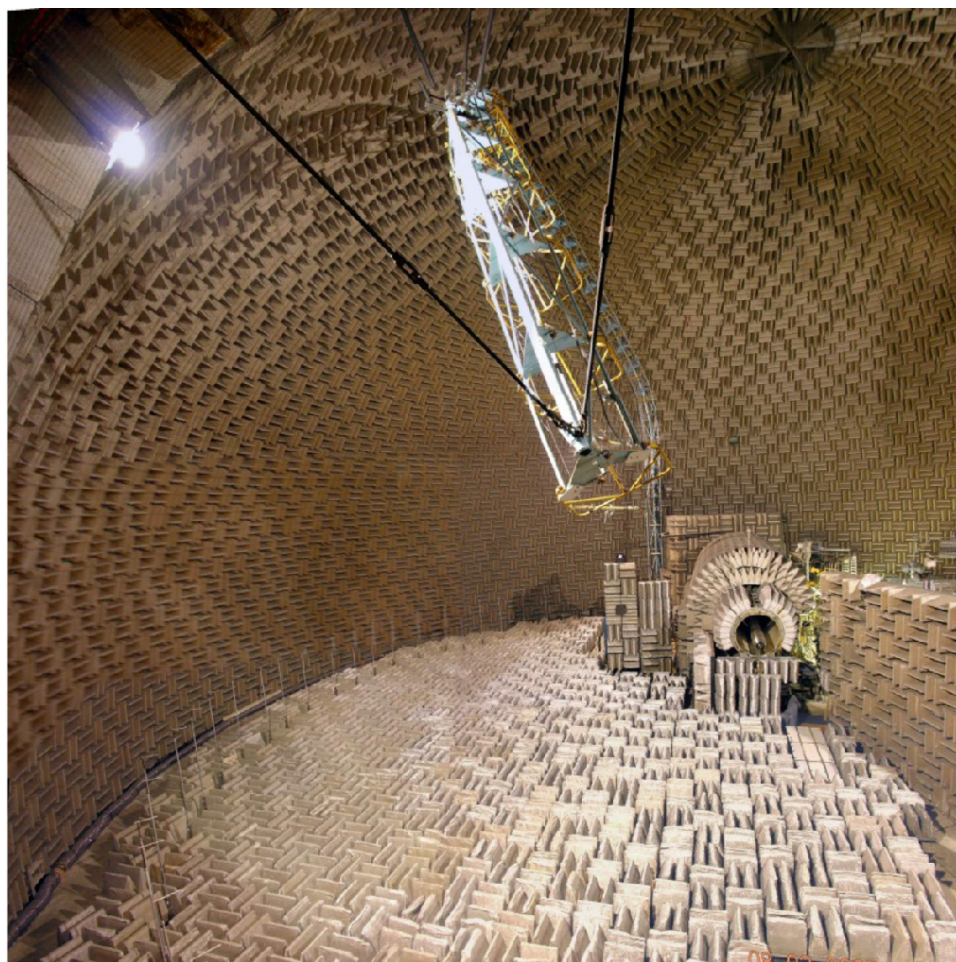


Figure 8.9.—Inside Aero-Acoustic Propulsion Laboratory (AAPL), showing Nozzle Acoustic Test Rig (NATR) and overhead far-field microphone array used in NATR acoustic testing.

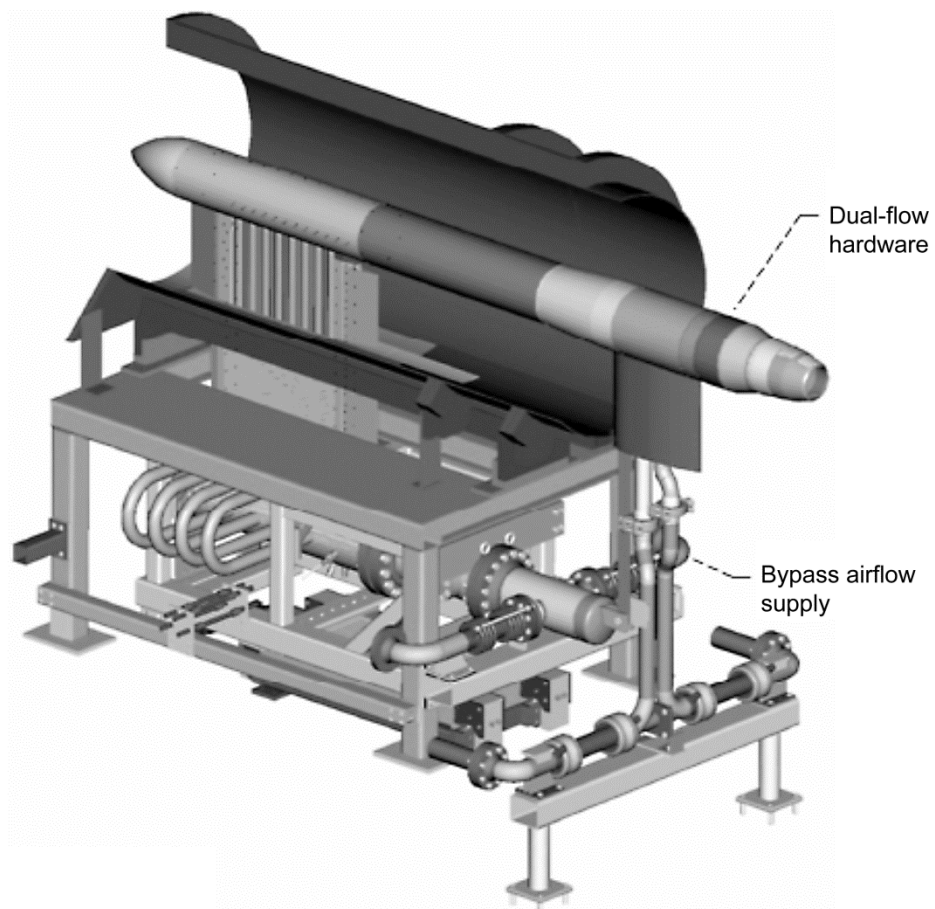


Figure 8.10.—High Flow Jet Exit Rig (HFJER) in dual-flow mode.

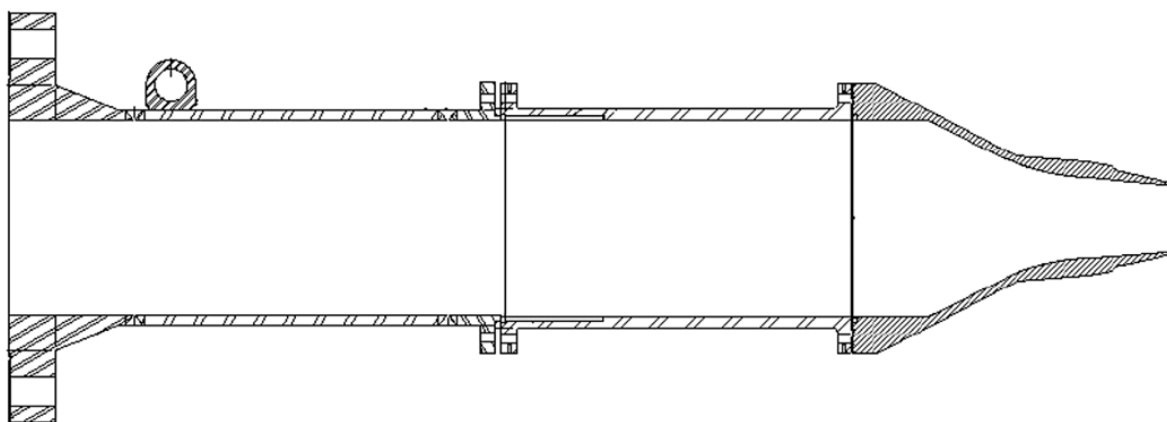


Figure 8.11.—SHJAR nozzle system with SMC000 nozzle attached.

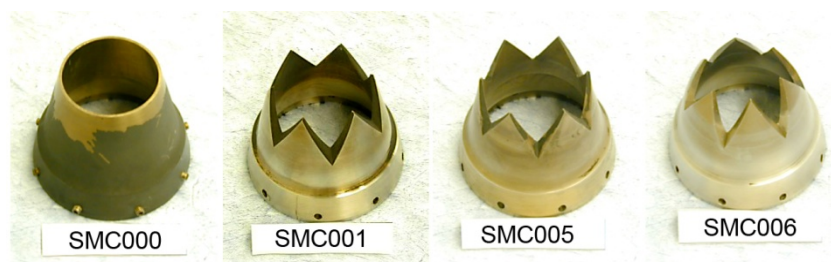


Figure 8.12.—SHJAR nozzles used in this jet noise assessment.

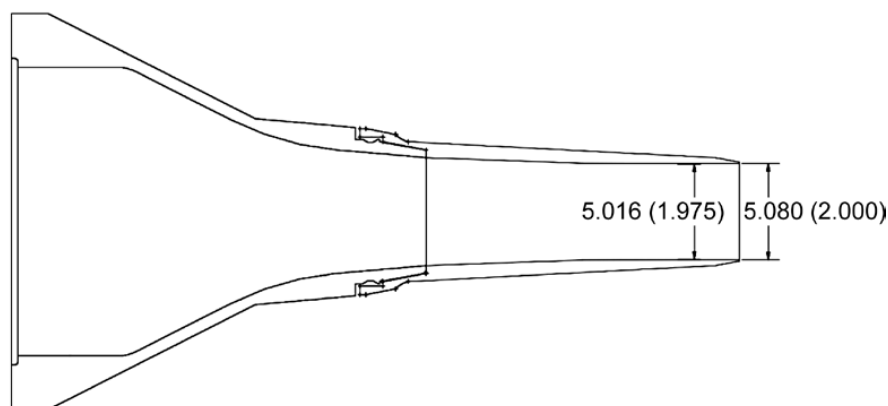


Figure 8.13.—Convergent-divergent nozzle SMC014, design Mach number $M_d = 1.18$. Dimensions are in centimeters (inches).

TABLE 8.3.—DESIGN MACH NUMBERS OF SINGLE-FLOW CONVERGENT-DIVERGENT NOZZLES
[Used for SHJAR jet noise measurements.]

Nozzle	Design Mach number, M_d
SMC014	1.18
SMC015	1.4
SMC016	1.5
SMC017	1.66
SMC018	1.8

8.6.2 Supersonic Dual-Flow Hardware (Test Program SDF07)

For dual flows, several different exhaust systems were employed. The family of models from the supersonic dual-flow tests SDF07 (see Table 8.2) featured internally mixed flows with variable bypass ratios. A series of splitters were fabricated which, when coupled with a special contraction section, produced four secondary to primary area ratios ranging from 0.2 to 2.0, designated as S1 to S3 in Figure 8.14, and with a convergent nozzle exhaust (C4) of diameter 10.2-cm (4-in.). To obtain fully expanded, dual flows, a series of convergent divergent nozzles with exit diameter of 10.2 cm

were fabricated. The method of characteristics (Ref. 23) was used to design these nozzles for the fully expanded Mach numbers of 1.18, 1.4, 1.5, 1.6, 1.8, and 2.0. An example of a dual stream nozzle with area ratio of 0.2 (splitter configuration S1), and convergent-divergent exhaust at design Mach number of 1.18 (M_8) is shown in Figure 8.15. Between variations in splitters to give area ratios and variations in nozzles to give different fully expanded Mach numbers, a wide range of supersonic and subsonic jet flows were obtained from approximate bypass ratio 0.2 to 4.7.

8.6.3 Long Duct Internal Mixer Hardware (Test Program LDIM05)

Examples of dual-flow nozzles with internal mixing from nonaxisymmetric splitters, both lobed mixers and chevrons, are shown in Figure 8.16. The nozzle system designated 5000.00 had a convergent common nozzle and an axisymmetric splitter with plug sized to produce flows of roughly bypass ratio 5. In nozzle 5001.04 the splitter of 5000.00 is replaced with a chevron mixer having 6 outward and 6 inward chevrons, and in nozzle 5002.02 it is replaced with a lobed mixer having 20 deep lobes. Nozzles designated as 8000.00, 8001.04, and 8002.02 followed the same convention, but with a larger plug to produce a bypass ratio of approximately 8.

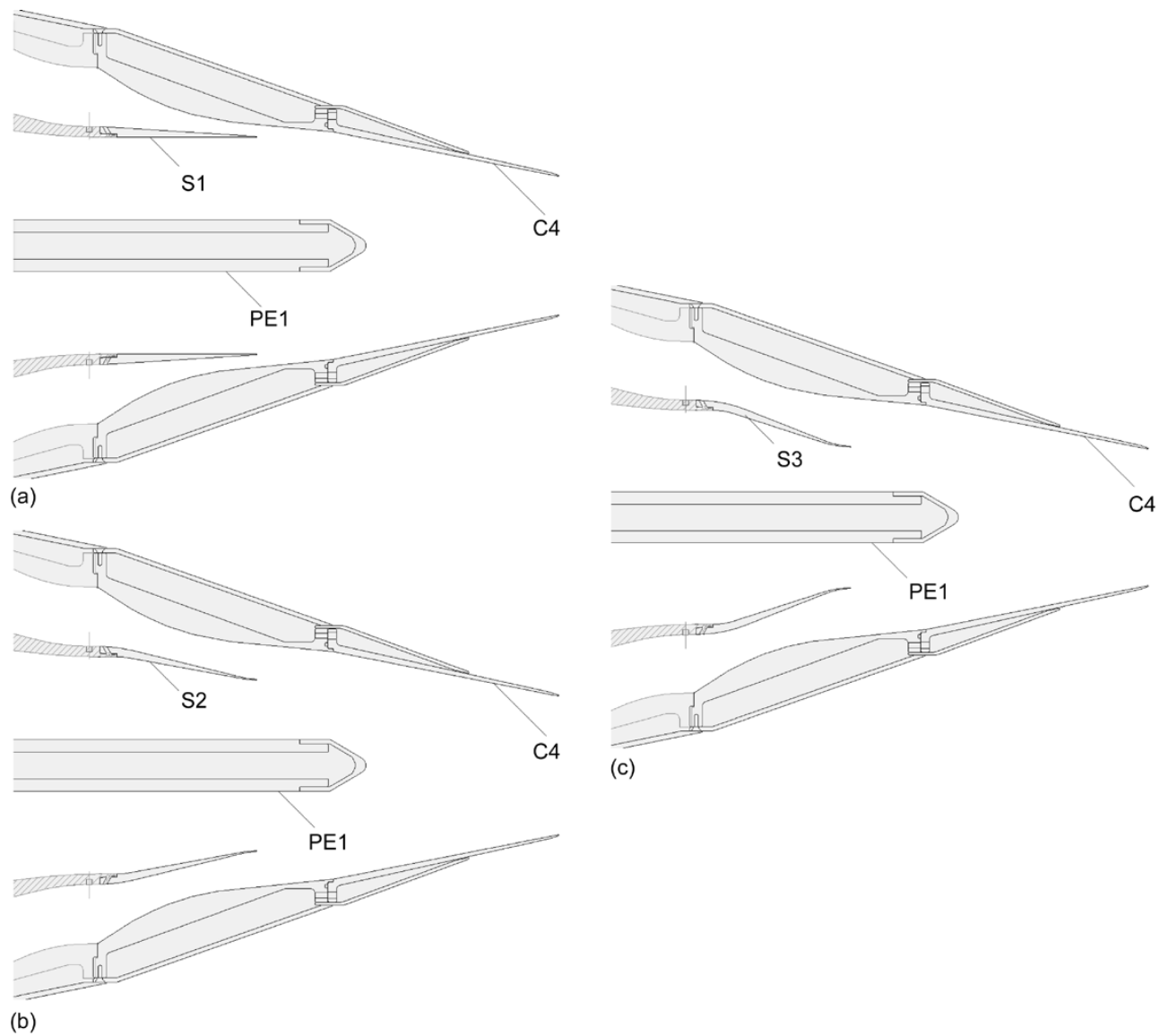


Figure 8.14.—Internally mixed, axisymmetric, dual-flow exhaust system with convergent nozzle and different bypass ratios (BPRs). S1 to S3 are splitters, PE1 is center plug, and C4 is convergent nozzle. (a) Nozzle C4S1PE1, BPR = 0.2. (b) Nozzle C4S2PE1, BPR = 1. (c) Nozzle C4S3PE1, BPR = 3.

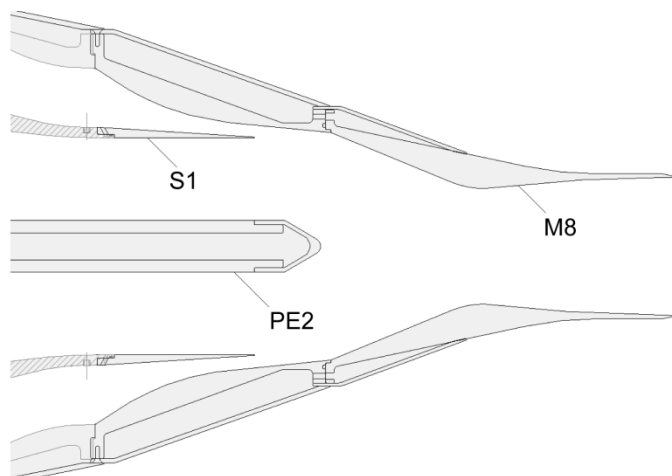


Figure 8.15.—Internally mixed, axisymmetric, dual-flow exhaust system with convergent-divergent nozzle M8 shown with bypass ratio (BPR) = 0.2, splitter S1. PE2 is center plug.

8.6.4 High-Flow Cross-Facility Hardware (Test Program HFXF07)

Externally mixed exhaust systems, both with internal plugs and external plugs, had fan nozzle diameters of 24.4 cm (9.6 in.) and different core nozzles and plugs to achieve bypass ratios from 5 to roughly 14. Figure 8.17 gives the cross-sectional views of the four separate flow nozzles tested in the High Flow Cross-Facility Test (HFXF07). The data used in this assessment were acquired at the NASA APL, but most of the nozzles and test conditions were also run at NASA Langley Jet Noise Laboratory, hence the designation of cross-facility test.

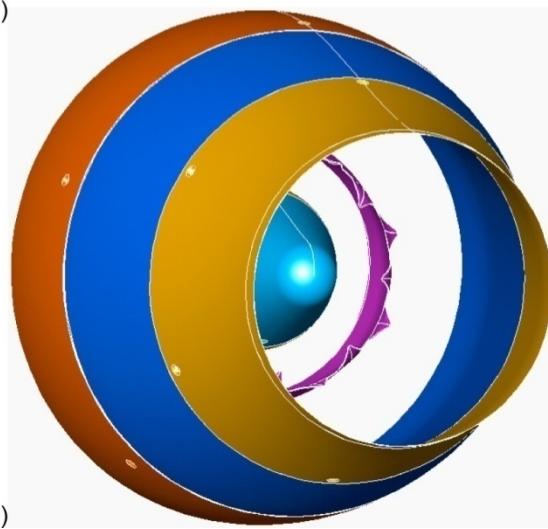
8.7 Details of Measurements, Sensors, Transducers, and Placement

Acoustic measurements on SHJAR were recorded by an array of 24 microphones placed on an arc with a radius of 2.54 m (100 in.) at 5° intervals from 50° to 165° measured from the inlet. The microphones were Brüel & Kjær (B&K) 1/4-in. microphones (model 4939, with a B&K Model 2670 preamp), used without grid caps and pointed at the nozzle exit. To minimize reflection from the microphone stands, six stands—each holding four microphones—were used. On the HFJER, a similar arc array was deployed, with a nominal radius of 13.7 m (45 ft). On HFJER, the microphones were located on 1.9-cm (0.75-in.) pipe-frame carts, which were located on a track across the ceiling of the NATR (see Figure 8.9).

A DataMAX Instrumentation Recorder (RC Electronics Inc.) simultaneously recorded data from all microphones, using a 90-kHz low-pass filter to limit the bandwidth (at 200 kHz sample rate). B&K Nexus amplifiers provided



(a)



(b)

Figure 8.16.—Internally mixed, dual-flow exhaust system with convergent nozzle and nonaxisymmetric splitters. (a) Lobed. (b) Chevron.

the signal conditioning. Eight seconds of data were recorded at each point. The high-frequency response of the Nexus amplifiers and DataMAX recorder had been documented using a white noise generator. When a 100-kHz signal from a white noise generator was directly input into the DataMAX, the recorded signal had a 1-dB down point at 63 kHz compared to 70 kHz for the signal generator itself. When the white noise first passed through the Nexus amplifier, the recorded signal was further decreased above 74 kHz. In practice the trusted bandwidth was closer to 75 kHz than the 90 kHz set on the recorder itself.

To record flow conditions during the acoustic data acquisition, a facility computer called ESCORT recorded variables such as rig temperatures, pressures, and mass flows, as well as ambient temperature, pressure, and humidity. The ESCORT averaged the data over the same time that the acoustic record was recorded, giving one value per variable per acoustic data point.

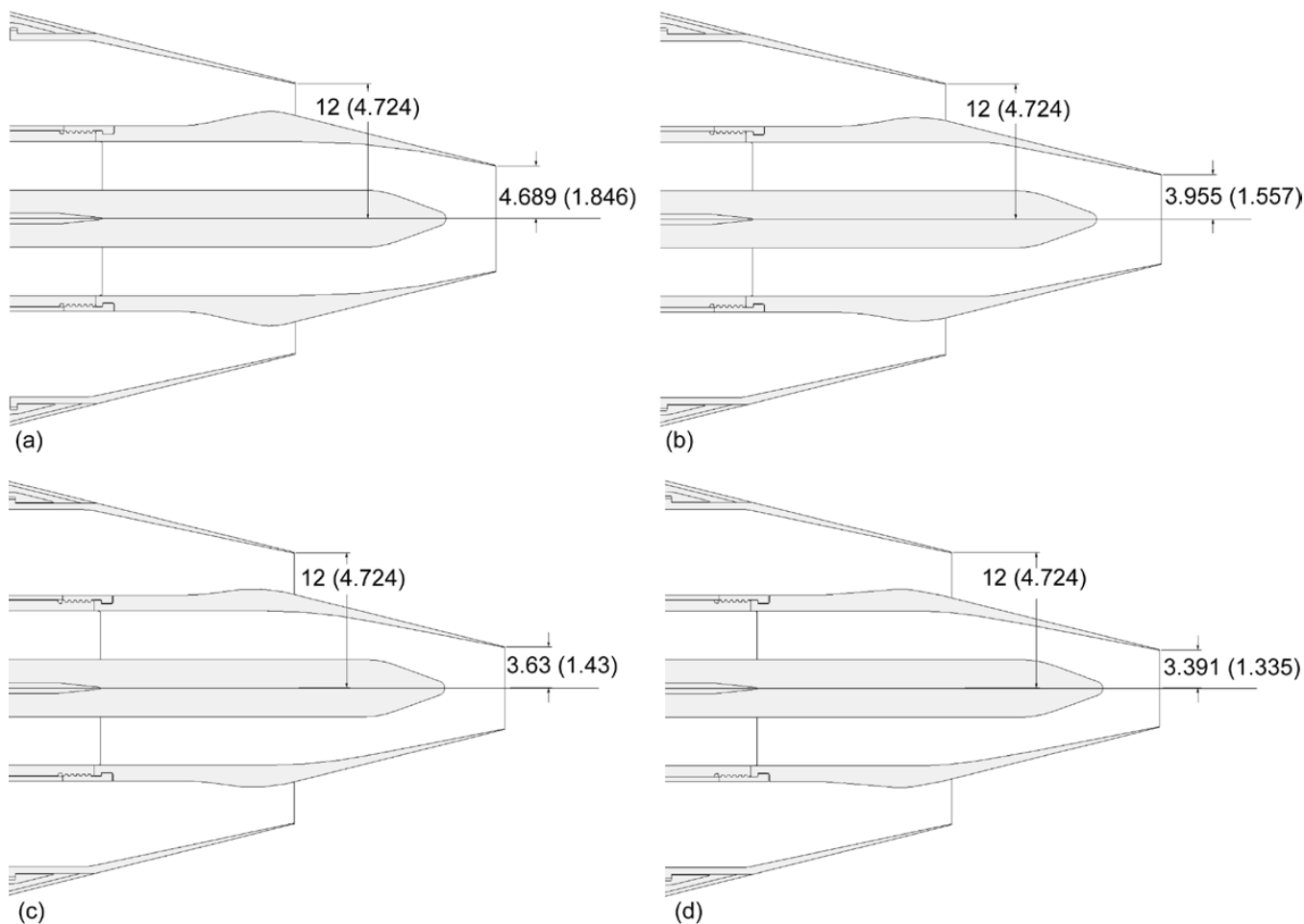


Figure 8.17.—Externally mixed dual-flow exhaust systems. Dimensions are in centimeters (inches). (a) Nozzle PAA5. (b) Nozzle PAA8. (c) Nozzle PAA11. (d) Nozzle PAA14.

8.8 Acoustic Data Collection and Processing

The far-field microphone data were processed in a series of procedures given below:

(1) Time series were multiplied by amplification factors from the variable gain Nexus signal conditioners and by the calibration factor determined by in situ recording of the B&K pistonphone.

(2) Fourier transforms were computed using fast Fourier transform algorithms and 10th-order Kaiser-Bessel windowing on 16384-point records with 50 percent overlapping.

(3) Background noise, measured immediately before the data set was acquired, was subtracted, and any frequency band within 3 dB of the background was flagged and was not considered for future processing and final plotting. Note that for conditions with simulated forward flight the background noise included the noise of the large free jet.

(4) Data were corrected for microphone spectral response characteristics based on the manufacturer's documentation of

each individual microphone obtained during calibration performed within 1 year of the test.

(5) Data were converted to a 0.3-m (1-ft) lossless condition using the ANSI S1.26–1995 standard atmospheric corrections (Ref. 24).

(6) Data have been reported as lossless, and scaled to an arc distance of 100*D* based on the nozzle diameter *D*. Note that scaling the sound amplitude to a distance based on a constant number of nozzle diameters is mathematically identical to scaling the data to a common nozzle size.

(7) The frequency is normalized as Strouhal number when multiplied by the factor [(nozzle diameter)/(jet velocity)]. The spectra are also normalized and stored as power spectral density per Strouhal number.

(8) Power spectral density was later integrated over 1/3-octave bands, using a method consistent with the IEC 1260:1995 standard (Ref. 25)—specifically an ideal 1/3-octave filter, for presentation and comparison.

(9) For those datasets involving forward-flight simulation (free-jet operation), corrections for the refraction of sound through the free-jet shear layer were made using the method documented in NASA CR–3056 (Ref. 26). The method is

equivalent to the technique commonly referred to as “Amiet’s method” when the source location is taken to be at the nozzle exit for all frequencies. This step was carried out prior to corrections for atmospheric attenuation.

Processing of the far-field acoustic data to correct for the refraction of sound is handled differently at different facilities because of differences in philosophy in handling the distributed, directional sources of the jet plume. However, all facilities can, and have, used the Amiet’s correction method as used in this chapter. There is still substantial concern about the relationship between model-scale acoustic data obtained in this manner and the full-scale flight data, but the resolution of this problem is beyond the scope of this chapter.

8.9 Identifying Uncertainties in Acoustic Data

The procedure established to identify and eliminate external and background noise sources addressed the issue of data accuracy. This section will address the precision of the measured jet noise data using two methods. First, direct analysis of the primary sources of precision error, using manufacturers specifications, gives the worst-case error band. Second, data points recorded during different test programs but using the same nozzle and jet condition are considered to establish the actual precision observed under complete test conditions.

8.9.1 Measurement Uncertainties

The measurement uncertainties were determined by identifying the sources of uncertainty that affect the data and then averaging the data. The results of this analysis are shown in Table 8.4 with the following descriptions for the sources of uncertainty:

(1) Measurement of atmospheric conditions, which feed the calculation of atmospheric attenuation. This turns out to be a rather small error, ~ 0.1 dB, because the measurement uncertainties of 0.6 °C (1 °F) and 2 percent relative humidity only impact the highest frequencies; that is, the last few 1/3-octave bands.

(2) Location of the microphones. Using gyro-stabilized laser alignment tools allows microphones to be positioned to within 1.3 cm out of 250 cm (0.5 in. out of 100 in.) on the SHJAR and a comparable 2.5 cm out of 15 m (1 in. out of 50 ft) on the HFJER. This translates into 0.04 dB uncertainty.

(3) Accuracy of the jet flow condition settings and maintaining them during data acquisition. The test procedure in both SHJAR and HFJER maintained a 0.5 percent tolerance on the jet velocity. Transducers were calibrated to assure this tolerance level, which translated into noise uncertainty of ± 0.17 dB.

(4) Pistonphone calibration, a value that is easily determined from the manufacturer’s specifications. Note that most calibrators have a higher uncertainty than the 4220 pistonphone.

(5) Spectral calibration that relates the microphone response from 250 Hz, where the pistonphone signal is generated, to all the other frequencies. The calibration laboratory that provides this spectral response also includes the uncertainty. Values shown are typical for the indicated frequencies.

(6) Averaging of the spectral data.

Using chi-square analysis on 1/3-octave bands, which are the result of many narrowband estimates of power spectral density, the biggest uncertainty appears at the low-frequency end, where relatively few narrowbands are available for integration and statistical analysis. Here, at a 90% confidence interval, the uncertainty for the roughly 450-sample measurement (5 narrow bands with 90 ensembles each) is ± 0.33 dB. As each 1/3-octave band picks up 1.25 times as many samples as a previous band, the error estimated within a decade is of the order of ± 0.1 dB. The cumulative uncertainty, as shown in Table 8.4 at three representative frequencies, is 0.66 dB at the lower 1/3-octave frequency bands, reduces to 0.46 dB by the mid-frequency bands, and rises to 0.60 dB at the highest frequency bands.

8.9.2 Experimental Uncertainties

A final and larger source of uncertainty in jet noise measurements emerges when jet flows are scaled from experimental model size (order of centimeters) to that of the application size (order of meters). The imperfect scaling of nozzle lip thickness to jet diameter, internal and external boundary layer properties, and core turbulence intensities are but a few of the documented scaling parameters that cause jet rig experiments to differ from aircraft engines.

In addition, variations in jet noise facilities, especially subtle aspects such as flow collectors, entrainment air, size of free stream in simulated flight experiments, and distance from microphones to jet contribute to the so-called site-related errors. When uncertainties are added together it is no surprise that people who have compared experimental facilities have also experienced a renewed sense of humility considering many challenges present in measuring the true source of jet noise. Several excellent references have examined these issues in detail (Refs. 18 to 21, and 27) and the lessons shared in those efforts have been observed in this work. Comparison with measurements from alternative facilities also provides some level of confidence in one’s own data quality, and helps to establish an overall measure of experimental uncertainty. Assuming compliance with best practices, this uncertainty represents an estimate of noise measurement errors due to hardware, data processing, corrections, and so forth in two nominally identical jets at two different facilities.

TABLE 8.4.—ANALYSIS OF UNCERTAINTY IN MEASURED JET NOISE SPECTRA

Measurement uncertainty, <i>e</i> , dB				Basis for determining uncertainty
Source	Nominal frequency, Hz			
	300	3000	30 000	
Atmospheric attenuation	0.00001	0.001	0.1	±0.56 °C (1 °F), ±2 percent relative humidity
Distance	0.04	0.04	0.04	±1.3-cm (0.5-in.) error in 254 cm (100 in.)
Setpoint	0.17	0.17	0.17	±0.5-percent error in jet velocity <i>U</i>
Pistonphone	0.15	0.15	0.15	B&K 4220 specification
Spectral calibration	0.0	0.01	0.16	B&K calibration laboratory specification
1/3- octave-band averaging	0.33	0.1	0.01	Chi-squared analysis of 1/3 octave integration at 90 percent confidence. Lowest 1/3-octave band has 450 measurements (5 narrowbands with 90 ensembles each). Each higher frequency band has 1.25 more measurements than previous band, resulting in less uncertainty.
- or -				
Narrow-band averaging	0.61	0.61	0.61	Chi-squared analysis of 194-average narrow band at 90 percent confidence
Total ^a	0.66	0.45	0.60	1/3-octave SPL (dB)
	0.92	0.93	1.13	Narrowband power spectral density (dB)

^aTotal uncertainty is summed according to $10\log_{10}\left[1 + \sum(10^{e/10} - 1)\right]$.

As an example, consider three well-documented datasets acquired 30 years apart. The far-field spectra of Tanna (Ref. 17) and Viswanathan (Ref. 18) are reproduced in Figure 8.18, and are compared with the current SHJAR dataset (shown in blue) at 90° for three unheated jets at acoustic Mach numbers of $M_a = 0.50, 0.70$, and 0.90 . The data from SHJAR fit to within 1 dB of the other two facilities, mostly splitting the difference, but exhibits lower amplitude at the highest frequencies where rig noise is most commonly observed. There is some concern that the Tanna dataset may have been improperly corrected for atmospheric attenuation at the highest frequencies due to the inaccurate methods utilized at the time. There is also concern that the Tanna and SHJAR datasets may contain some additional high-frequency noise due to low-Reynolds-number effects (i.e., smaller diameter nozzles compared with those tested by Viswanathan). That said, the variation observed between the SHJAR data and the other datasets is less than 1 dB below a Strouhal number of 0.40 and less than 2 dB above this number.

Similar comparisons are also carried out at heated conditions. Figure 8.19 and Figure 8.20 compare the data of Tanna and that of the current SHJAR dataset at three different temperature ratios, and at acoustic Mach numbers of $M_a = 0.5$ and 0.90 respectively. As documented in Reference 28, there are concerns regarding the relatively low Reynolds numbers of some heated jets (below 500 000 for $M_a = 0.5$ jets), which may have an impact on SHJAR data at Strouhal numbers

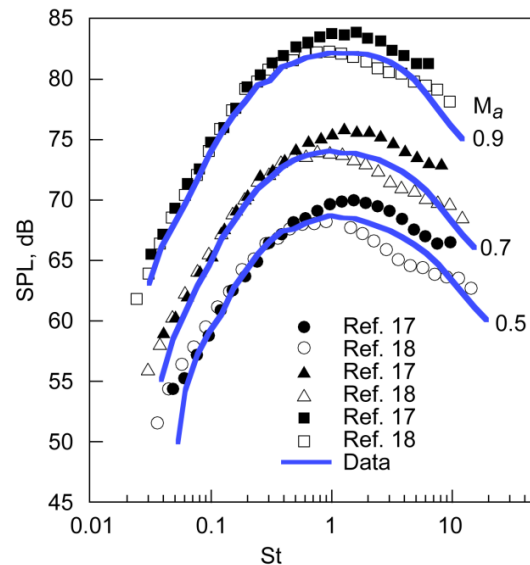


Figure 8.18.—Sound pressure level (SPL) versus Strouhal number *St* at inlet angle $\theta = 90^\circ$ for different jet acoustic Mach numbers M_a . Comparison of results from current SHJAR experimental data, Reference 17, and Reference 18.

above 5.0. However, the discrepancies in SHJAR measurements are within 2 dB, and at 150° the results agree within less than 1 dB—better than expected considering measurement uncertainties!

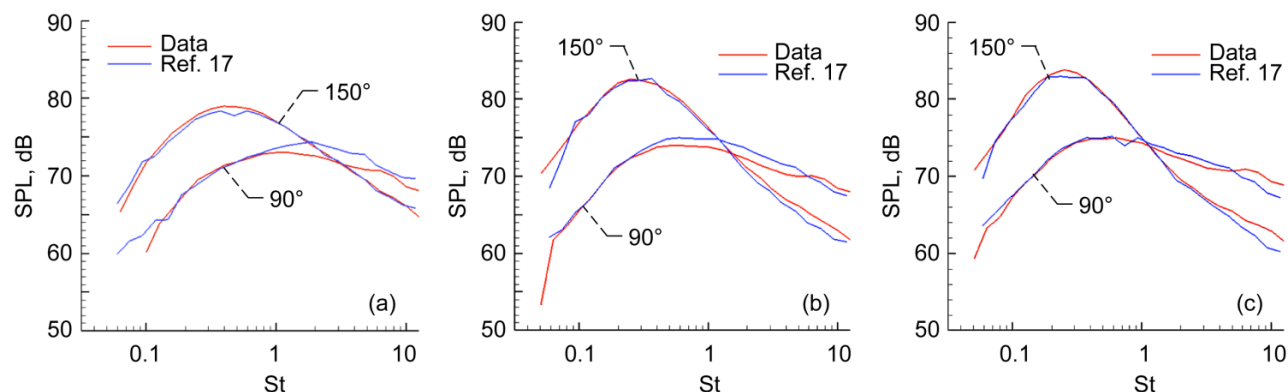


Figure 8.19.—Sound pressure level (SPL) versus Strouhal number St at jet acoustic Mach number $M_a = 0.5$ for inlet angles $\theta = 90^\circ$ and 150° . Comparison of values from current SHJAR experimental data and Reference 17. (a) Static temperature ratio $T_{s,r} = 0.86$ (cold). (b) $T_{s,r} = 1.76$. (c) $T_{s,r} = 2.27$.

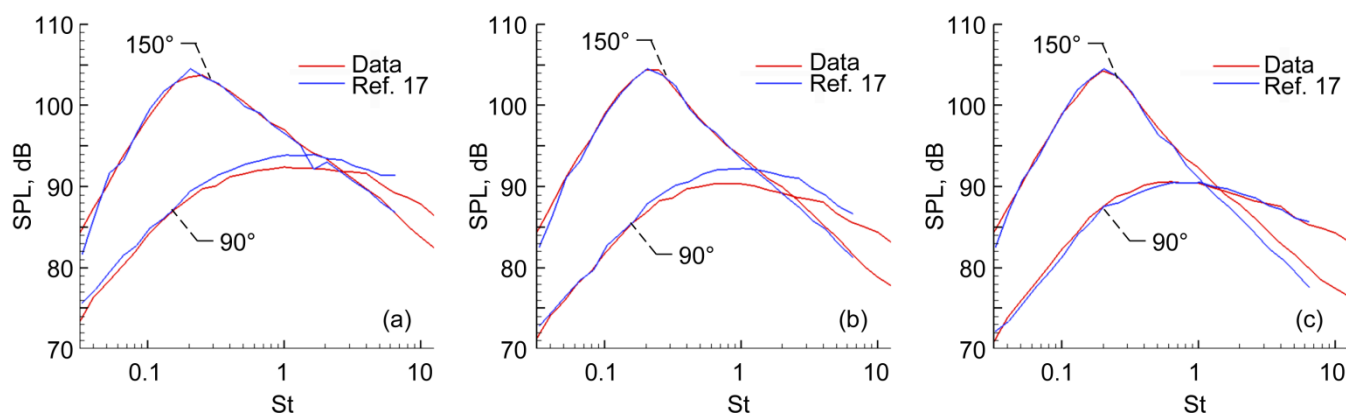


Figure 8.20.—Sound pressure level (SPL) versus Strouhal number St at jet acoustic Mach number $M_a = 0.9$ for inlet angles $\theta = 90^\circ$ and 150° . Comparison of values from current SHJAR experimental data and Reference 17. (a) Static temperature ratio $T_{s,r} = 0.86$ (cold). (b) $T_{s,r} = 1.76$. (c) $T_{s,r} = 2.27$.

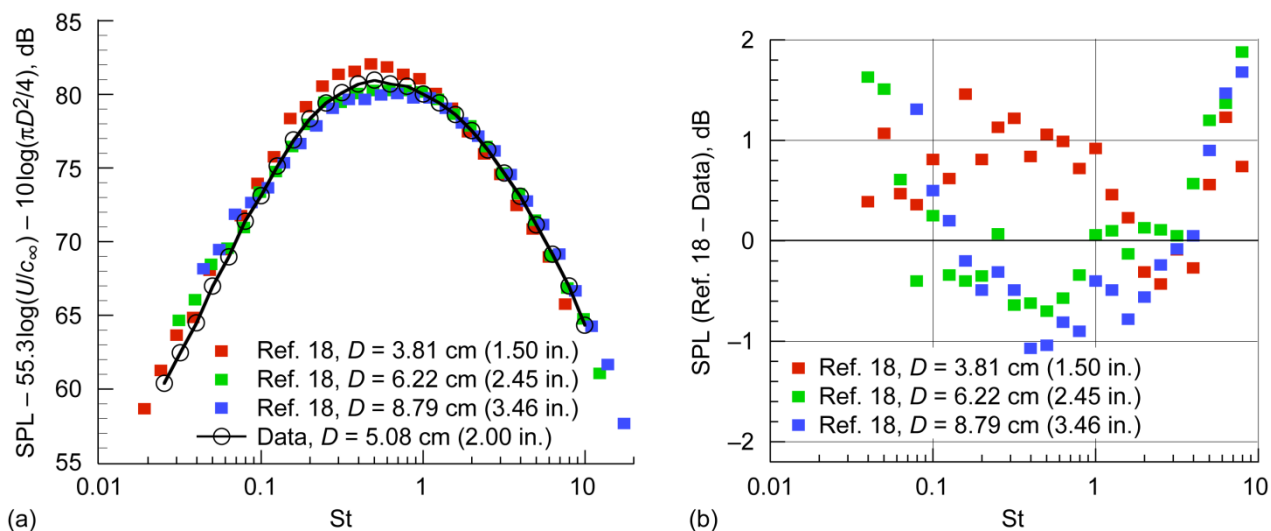


Figure 8.21.—Hot jet sound pressure level (SPL) normalized to standard day at 4.6 m (15 ft) versus Strouhal number St for different nozzle diameters D at inlet angle $\theta = 90^\circ$, Mach number $M = 0.7$, and total temperature ratio $T_{t,r} = 3.2$. (a) Comparison of values from current SHJAR experimental data and Reference 18. (b) Difference between values of Reference 18 and SHJAR data.

Reference 18 provides several interesting test cases to demonstrate the scale independence in hot jets. Figure 8.21(a) shows the 90° noise measurements in a Mach 0.70 heated jet at a total temperature ratio of 3.20 using three different jet diameters of 3.81, 6.22, and 8.79 cm (1.50, 2.45, and 3.46 in.) (in Ref. 18). This data is compared with the present jet data after SHJAR measurements were normalized to conditions specified in Reference 18. The level of agreement is a testimony to the quality of SHJAR data compared to other high-quality jet rigs. Shown in Figure 8.21(b) are delta dB noise difference between SHJAR data and the three jets examined in Reference 18. The difference is roughly 1.0 dB except at very high frequencies. This is the best one would hope; an expected difference closer to 2 dB, as demonstrated in the earlier Tanna comparisons, and will be adopted in the following assessment exercise as the experimental uncertainty for a 1/3-octave SPL spectrum.

8.10 Flow Data Collection and Processing

To properly validate the acoustic analogy noise prediction codes, the flow solutions used as input to these codes had to be validated as well. From analysis of the code's sensitivities it seems that the most critical flow parameters for acoustic accuracy are mean and turbulent velocities predicted by the RANS solver. To measure these quantities in hot, high-speed jets, PIV was deployed in the same facility and rigs where the acoustic measurements were made. Details of the PIV implementation are provided in Reference 29. The major issues related to data quality are also explained in this reference. Not all 265 jets considered in the assessment exercise have flow measurements available, but a substantial number have and those were used to assess the accuracy of the CFD predictions, and hence the input to the acoustic analogy prediction tools.

8.10.1 Stereoscopic PIV System

Flow datasets used in validating the RANS solutions were obtained using stereoscopic PIV. In this configuration, shown in Figure 8.22, the cameras are located on opposite sides of the light sheet. This arrangement is suitable for streamwise (axial-plane) measurements. The system consisted of a dual-head pulsed Nd:YAG laser (Continuum Surelite III) operating at 508 nm (2×10^{-5} in.), which generated a 400 mJ per pulse pair of light sheets defining the measurement plane orientation. The light-sheet-forming optics consisted of a spherical lens with a 1200-mm (47.2-in.) focal length followed by two cylindrical lenses, -75- and -40-mm (-3- and -1.6-in.) focal length.

Each laser pulse was synchronized with a pair of 2048- by 2048-pixel cross-correlation cameras (Redlake Megaplug ES 4.0) viewing the laser sheet at oblique angles. Image frame pairs from each camera were obtained by straddling adjacent frame exposures. PCI (peripheral component interconnect) frame grabbers were used to acquire and stream the image

data directly to disk in 200 image-pair sequences (for each camera). Image acquisition occurred at a nominal camera frame rate of ~5 Hz. Each camera and PCI board was connected to individual dual-processor 3.1-GHz Pentium computers, configured in a master-slave mode of operation. The entire system was controlled using NASA-developed PIV image acquisition software PIVACQ (Ref. 30).

Two Nikon 105-mm (4-in.) f/2.5 lenses were used with 2× teleconverters. An f/5.6 setting was preferred in this case because of the enhanced light collection from the particle forward-scattering orientation. The cameras were positioned approximately 1.8 m from the measurement plane, roughly 45° from vertical as shown in Figure 8.22. The cameras and lenses were adjusted to satisfy the Scheimpflug condition for stereo viewing of a plane; the angle between the camera lens and image planes was below 5°.

Since the AAPL is open to the environment during testing, the SHJAR could not be operated in complete darkness. To accommodate this situation, optical backdrops for the cameras were provided. These darkened camera backgrounds were positioned such that they were aligned with each camera view behind the measurement plane. The backgrounds were offset a suitable distance to minimize any influence on the ambient seeded flow distribution.

The complete stereo digital PIV system (Ref. 30), including all cameras and backdrops, data acquisition computers, laser hardware, and optics, was rigidly mounted on a large axial traverse located downstream of the nozzle exit plane. The travel range of the traverse was approximately 2.5 m (8.2 ft), with a positioning accuracy of 1.0 mm (0.04 in.). Rezeroing of the traverse to coincide with the trailing edge of individual chevron nozzles was aided by the installation of a calibration target, required in stereo PIV, on a fixture secured to the traverse. This enabled highly repeatable cross- and axial-flow measurement plane locations with numerous chevron nozzle

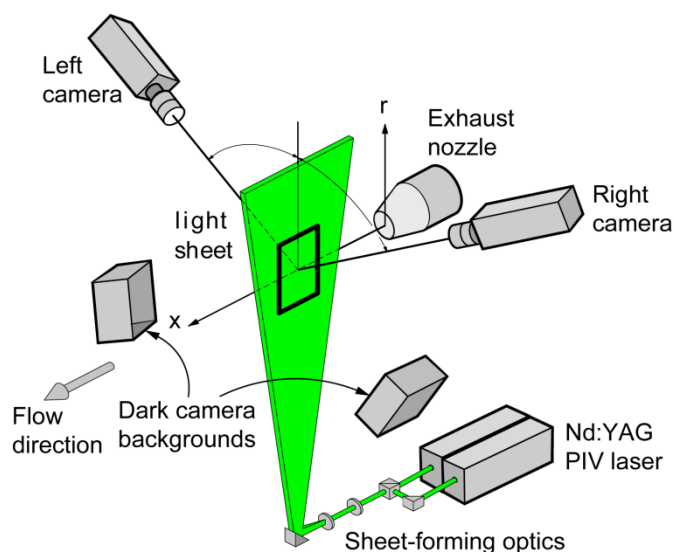


Figure 8.22.—Experimental arrangement for axial-flow stereo particle image velocimetry (PIV) measurements.

configuration changes. Following a cold start-up, the entire test rig experiences axial growth when operating at elevated-temperature set points. Thus, a rezeroing adjustment of the transverse rig was required and performed by optical means, using the current camera nozzle views to reference known chevron trailing edge tip locations at the nozzle exit planes.

8.10.2 Optical Calibration and Verification

Each camera was oriented at a certain angle with respect to the laser sheet to obtain a stereo view of the measurement plane. Because of the incorporation of the Scheimpflug condition, magnification factors between the image and object planes are variable due to perspective distortion. In order to combine camera measurements from both views into a single, three-component velocity vector map in the fluid plane, camera calibrations were required. The three-dimensional in situ calibration procedure as outlined by Soloff et al. (Ref. 31) was performed.

Prior to each day's collection of test runs, both cameras were precalibrated at the same time using the existing optical setup and the introduction of a calibration target into the measurement plane. The target was positioned in the same orientation, and at the same location, as the laser light sheet. A commercial dual-sided, four-plane target manufactured by TSI Incorporated was used. The identically sized target, also with marker locations on 10-mm centers, in this case was fixed, with its centerline positioned along the nozzle jet axis centerline during calibration image acquisition. Both "A" and "B" light sheets were centered on the target, with the thinner "A" sheet precisely aligned and centered within the wider "B" sheet. Polynomial mapping functions were determined using the known marker locations in the fluid and the recorded locations in the image planes to uniquely characterize the camera to fluid mapping functions for particle displacement (Ref. 29). Polynomial mapping orders of 2 and 1 were selected for mapping the displacement components in the laser light sheet plane and normal to the laser light sheet plane, respectively.

In this calibration verification procedure, particle images from each camera illuminated by the same laser pulse are warped to the fluid plane using the existing calibration equations. If the laser light sheet were of zero thickness and the calibration perfectly accurate, the particle images from each camera would map to the same location in the warped images. By using cross-correlation processing (the same processing used to measure the flow velocity) to measure the displacements in the warped images, a target-to-light sheet alignment error can be determined. All measured warped pixel displacements are assumed to be caused by errors in the axial location of the calibration target due to an x-axis translation and/or out-of-measurement-plane tilt (see Figure 8.22). This information reveals the actual position of the target relative to the light sheet and permits the finding of a best-fit solution through an iteration procedure to correct the calibration target position marker locations in the fluid coordinate system.

8.10.3 Three-Dimensional Vector Processing

Velocity vector maps for each camera were computed (in the image planes) from the image pairs using NASA-developed PIVPROC software (Ref. 30). The software utilizes conventional multipass PIV cross-correlation processing algorithms and incorporates error detection based on image correlation signal-to-noise ratio. First-pass interrogation region sizes of 64 by 64 pixels on 32-pixel centers and final-pass interrogation region sizes of 32 by 32 pixels on 16-pixel centers were used to process image pairs from the cameras in both stereo configurations.

After processing the images acquired by each camera, the pixel displacement data from the left and right views were combined to obtain the three-component velocity vector field at the measurement plane in the fluid. The equations that govern the transformation of the image plane data to the object plane are those given following the verified calibration procedures noted above. The software used to perform these operations was developed in-house to permit execution via command line processing. Some notable features include the ability to perform bicubic vector interpolation of the neighboring vector data in the image plane prior to being mapped back into the fluid space, as well as the ability to calculate three-dimensional vectors in the fluid on arbitrarily defined rectangular grids of any size—useful for nonsquare correlation region processing.

As the u -, v -, and w -components of each three-dimensional flow velocity vector are computed using a linear least-squares fit (singular value decomposition) of the left and right two-dimensional vector, a residual error is found by substituting each solution back into the least-squares equations. The total residual error for each vector is given as the square root of the sum of these residual errors squared. This error, given in pixels, is indicative of the total mismatch between left and right vectors. A residual pixel threshold of 0.5 pixels was specified for validating the solution vector. For the cross-flow configuration, solutions exceeding this threshold indicate the v -components of velocity between the two vectors differed by more than 0.5 pixel.

Ensemble averaging of the 200 individual vector maps was performed to obtain statistical information at each measurement plane. The averaging procedure incorporated both hard velocity cutoff limits and Chauvenet's criterion for data outlier removal (Ref. 30). This ensemble averaging was also performed using in-house developed software, with any three-dimensional vector data that exceeded the residual pixel threshold (0.5 pixels) being excluded from the ensemble averaging procedures.

8.10.4 Flow Seeding

As is typical in all PIV applications, quality flow seeding was an essential factor in obtaining high-accuracy results. Because of the elevated operating temperatures, a refractory seed material was required for the core jet flow. The flow seeding material utilized was $\sim 0.5\text{-}\mu\text{m}$ ($\sim 2 \times 10^{-5}$ in.) powdered

alumina particles. This material, contained within a pH-adjusted ethanol solution, was delivered to the core flow upstream of the flow conditioning screens. Uniform dispersion was provided by a pair of air-assisted, atomizing nozzles. As determined from a particle frequency response analysis, the core flow particles were expected to be able to accurately follow the jet flows over the complete range of nozzle operating conditions considered in this test program.

The ambient air was seeded with $\sim 0.2 \mu\text{m}$ ($\sim 8 \times 10^{-6}$ in.) mineral oil droplets produced by a commercial smoke generator. This ambient smoke system was located in a partially enclosed rig support structure upstream of the nozzle. Entrainment of the particles around the nozzles was aided by the use of two circulating fans. This provided a very low velocity (< 5 m/s, or < 16 ft/s) airstream surrounding the nozzle core jet flows. The performance of this flow seeding arrangement has been previously applied to PIV measurements with successful results (Ref. 29).

8.11 Identifying Uncertainties in Flow Measurements

Beyond internal calibrations and checks on data quality, the PIV results were compared with data obtained with conventional measurement techniques to estimate experimental uncertainties. Similar to acoustic results, comparisons with measurements made at other facilities using other measurement techniques give a more complete determination of overall experimental error. Measurements made in a cold

$M_a = 0.50$ jet using PIV were compared with the same facility data using conventional hotwire anemometry as well as data obtained elsewhere using laser Doppler velocimetry (LDV) (Ref. 32). The results are displayed in Figure 8.23 as PIV for conventional PIV data, TRPIV for time-resolved PIV, hotwire, and LDV data. While the mean velocity agreement between the LDV and PIV is to within a few percent, the turbulence levels differ by as much as 10 percent (the hotwire turbulence measurements agree better with the PIV). At a higher acoustic Mach number of $M_a = 0.90$, which is beyond the functionality range of the hotwire anemometry, the LDV data was compared with two PIV datasets taken a year apart, denoted as PIV(T3) and PIV(T4). As seen in Figure 8.24, the difference in mean velocities is less than 5 percent. The root-mean-squared (rms) velocities agree within 5 to 10 percent. Finally, to evaluate the accuracy of PIV data in a high-speed hot jet, the PIV data is compared with LDV data for nearly comparable jets at $M_a = 0.90$ and $T_{s,r} = 2.7$ for the PIV tests and at $M_a = 0.78$ and $T_{s,r} = 2.7$ for the LDV tests (see Figure 8.25). Discrepancies in the centerline velocity decay appear mostly well past the end of the potential core, leading to concerns about the equivalence of the two jet flows rather than differences in the measurement techniques. The rms values as a percentage of jet exit velocity agree much better to within 5 percent, except for a limited segment near the ending of the potential core—and subsequent internal examination of the PIV data based on the particle images confirmed data to be somewhat questionable.

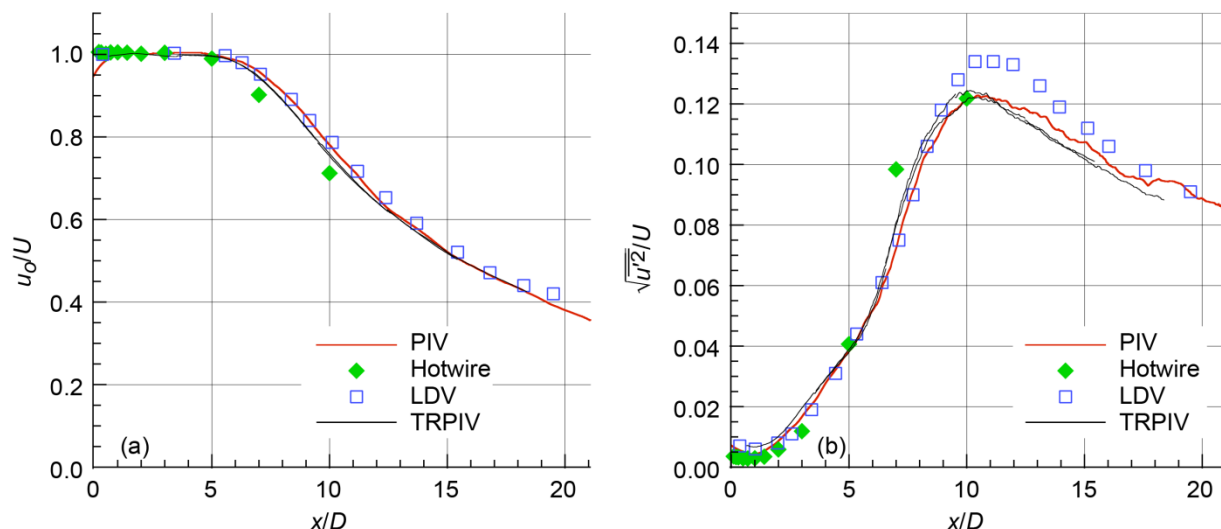


Figure 8.23.—Axial velocity of cold jet, acoustic Mach number $M_a = 0.5$, measured along centerline x/D using conventional particle image velocimetry (PIV), time-resolved PIV (TRPIV), laser Doppler velocimetry (LDV), and hotwire anemometry. (a) Normalized mean axial velocity, u_0/U . (b) Normalized root-mean-squared fluctuating axial velocity, $\sqrt{u'^2}/U$.

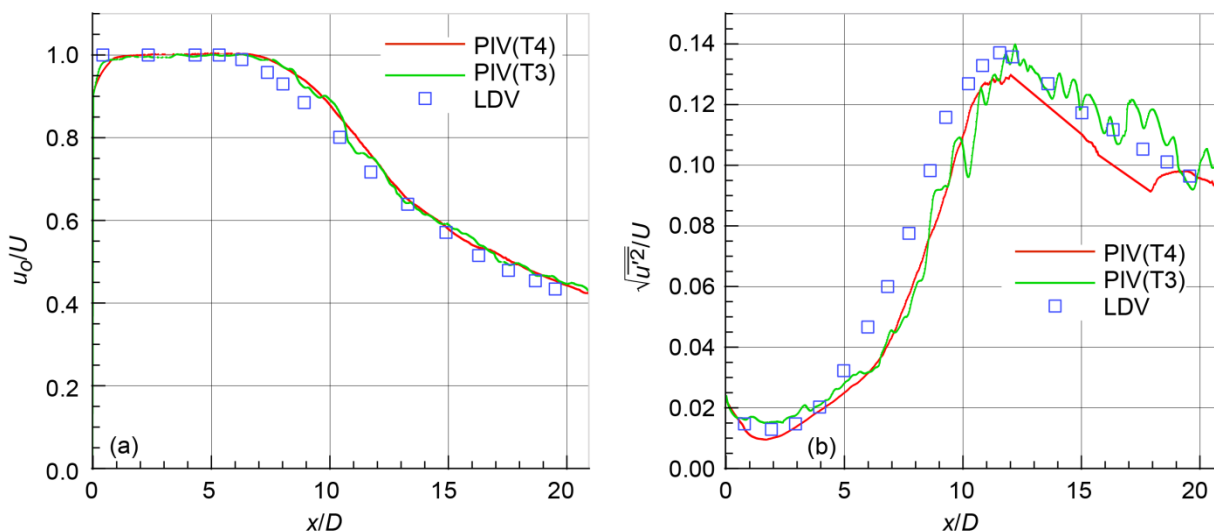


Figure 8.24.—Axial velocity of cold jet, static temperature ratio $T_{s,r} = 0.84$ and acoustic Mach number $M_a = 0.9$, measured along centerline x/D using particle image velocimetry (PIV) and laser Doppler velocimetry (LDV). T3 and T4 designate PIV measurements taken 1 year apart. (a) Normalized mean axial velocity u_o/U .

(b) Normalized root-mean-squared fluctuating velocity $\sqrt{u'^2}/U$.

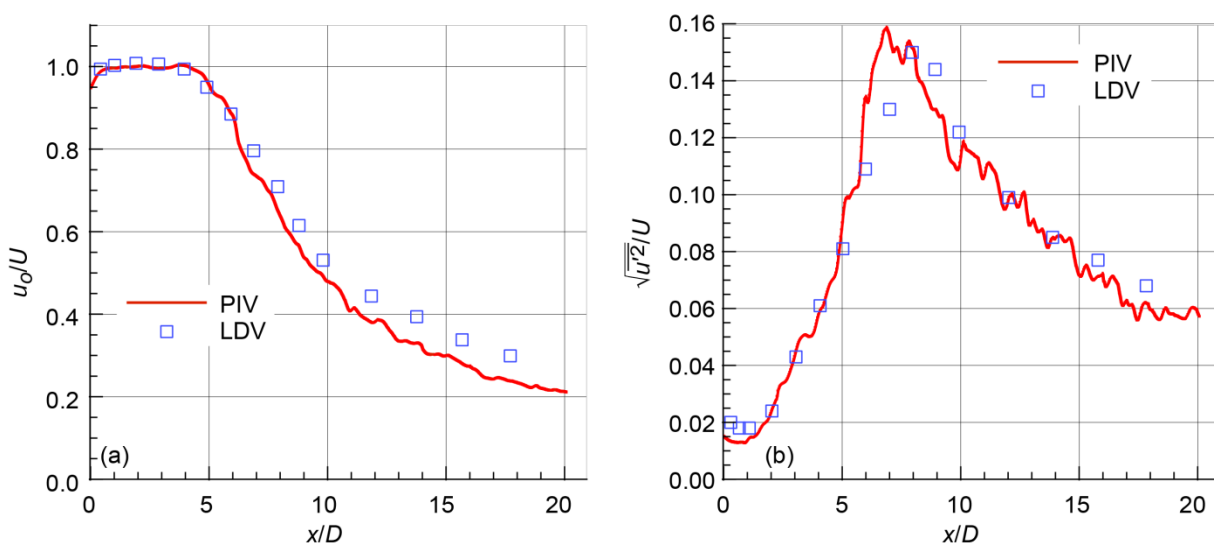


Figure 8.25.—Axial velocity of hot jet measured along centerline x/D using particle image velocimetry (PIV) (static temperature ratio $T_{s,r} = 2.7$ and acoustic Mach number $M_a = 0.9$) and laser Doppler velocimetry (LDV) ($T_{s,r} = 2.7$ and $M_a = 0.78$). (a) Normalized mean axial velocity u_o/U . (b) Normalized root-mean-squared fluctuating velocity $\sqrt{u'^2}/U$.

Assumptions regarding flow axisymmetry or location of the jet centerline could also lead to additional subtle errors. This is especially true in the case of dual-stream jets with a hot core flow as documented by Birch et al. (Ref. 33). In the referenced work, azimuthal variations of 12 percent in turbulence intensity were observed in nominally axisymmetric separate flow nozzles. Much of the CFD validation in the present chapter was achieved with single-stream jets where such azimuthal variations are much less important. Typically when

measurements are carried out along the opposite mixing planes in a single-stream jet, the turbulence intensities agree to within experimental error. Validating CFD results in dual-stream jets requires much more care. Adding a fixed known asymmetry such as a pylon is likely to reduce the error introduced by the sensitivity of the dual-stream jet to asymmetries.

From above comparisons, we estimate that the mean and rms velocity measurements are accurate to within 3 and

5 percent, respectively. While this puts the uncertainty near 10 percent for the turbulent kinetic energy, it is noted that most RANS solvers do not come this close to the measured data.

8.12 Metrics

In all cases and for all codes, 1/3-octave spectral directivity comparisons were made. For simplicity, only two spectra, at polar angles of either 90° and 150° or 90° and 130° from the inlet axis, are shown in plots. All spectra have been normalized to power spectra versus Strouhal number, removing atmospheric attenuation, to the condition of an observer at 100 jet diameters. First, the predictions were compared with the data in standard overlay plots for the two angles, and then the difference between the prediction and the data was plotted as a function of Strouhal number St . This second plot contains dashed lines representing the upper and lower uncertainty band of the experimental data. If the difference lies within these lines, the prediction is projected as within experimental uncertainty.

Similarly, to judge the ability of the codes to predict the OASPL directivity, the predicted and measured spectra are integrated within the frequency range $0.05 < St < 30$. Again, the predicted and measured OASPL directivities are plotted together, and their difference is examined in relation to experimental uncertainty bars.

To help summarize the data collection, the average μ and variance σ^2 of error Δ in the OASPL between ANOPP predictions and experimental data were computed over a jet sample case at N polar angles (24 polar angles θ , 50° to 165° in 5° increments)

$$\Delta_i \equiv OASPL_{ANOPP} - OASPL_{expt} \quad \text{at } \theta = \theta_i \quad (8.12)$$

$$\mu = \frac{1}{N} \sum_{i=1}^N \Delta_i \quad (8.13a)$$

$$\sigma^2 = \frac{1}{N} \sum_{i=1}^N (\Delta_i - \mu)^2 \quad (8.13b)$$

The average error μ gives an indication of how close the prediction comes to the data in overall sound power, and the variance σ^2 (or its square root σ , the standard deviation) of the error in OASPL could be interpreted as the ability to predict directivity. It is possible for the error in predicting OASPL to average to zero even if the prediction has the wrong directivity. In this case the standard deviation of the error would be nonzero. Conversely, the standard deviation could be very small if the prediction were correct in directivity but wrong in overall sound power. Combined, these two metrics give a strong insight into the accuracy of the prediction compared with the experiment. Distilling the voluminous data from all the cases into these two metrics helps spot trends across all cases.

Another significant measure of great interest to practicing engineers in jet noise is the effective perceived noise level (EPNL). This metric is tied to the scale of the jet and weighs frequency bands near 2000 Hz full-scale much more heavily than the typical peak of jet noise. To get a feel for the error in EPNL, all cases were transformed to a 1-m- (3.3-ft-) diameter nozzle in level flight at 0.28 Mach number and an altitude of 500 m (1640 ft). This parameter penalizes codes that do well in capturing the peak jet noise but do not perform as well at off-peak high frequencies.

8.13 Description of Presentation Format for Acoustic Data

Because of the large volume of the illustrations, it was important to choose a legend consistent throughout the presentations. A typical illustration, such as Figure 8.26, consists of 1/3-octave SPL spectra at two inlet angles (such as $\theta = 90^\circ$ and 150°). Figure 8.26(a) examines the predictions (lines) versus measurements (symbols). The difference between prediction and data is compared with the experimental uncertainty bars (dashed lines) in Figure 8.26(b). The uncertainty band labeled “Measurement” is the uncertainty of the measurement at the facility, and that marked as “Experimental” represents the variation observed between facilities for nominally the same experiment. To provide an assessment over a broad range of angles, Figure 8.26(c) examines the OASPL directivity (i.e., the integrated spectrum at each angle). This figure also serves as a “typical” spectral result for many of the shock-free flows. Because it encompasses measurement uncertainty, only experimental uncertainty will be plotted in the prediction and measurement comparisons and labeled as “Uncertainty.”

Without getting into the specifics of the jet that Figure 8.26 represents, it is seen that the predicted spectra agree with the experimental data relatively well in the peak amplitude and the peak frequency, but then fall too sharply and depict a second hump at $St = 10$. The experimental data, on the other hand, show steady high frequency decay at both angles. This pattern is observed in many ANOPP spectral predictions and represents a consistent error in the source modeling.

Using the jet noise component controls for the ST2JET module, it is possible to turn various sources on and off to discern the origin of this high-frequency hump. The three spectral components in a shock-free jet, as predicted by ANOPP, are labeled as “Inner Stream,” “Outer Stream,” and “Merged Stream,” intended to model jet noise from different scales of turbulence associated with three shear layers due to bypass-core, ambient-bypass, and the fully merged regions, respectively. These components are shown separately in Figure 8.27. The suspect high-frequency hump at Strouhal number 10 is identified as part of the “Outer Stream,” which points to the source modeling deficiencies in the ambient-bypass mixing region.

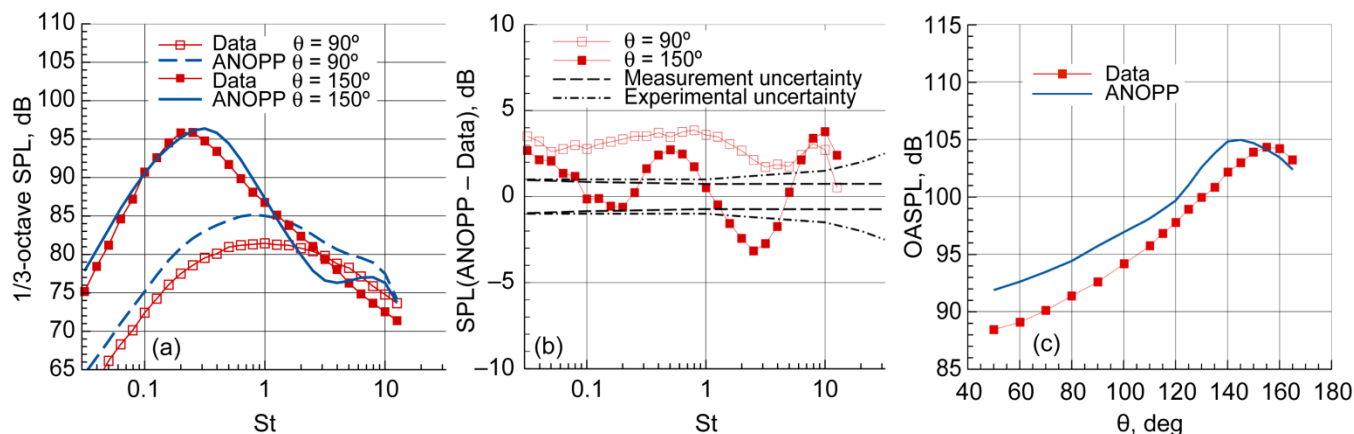


Figure 8.26.—Typical results for jet noise directivity analyses. (a) 1/3-octave sound pressure level (SPL) versus Strouhal number St for two inlet angles θ from SHJAR experimental data and ANOPP predictions. (b) Difference between predicted and measured SPL, with uncertainty bands. (c) Overall sound pressure level (OASPL) as function of θ .

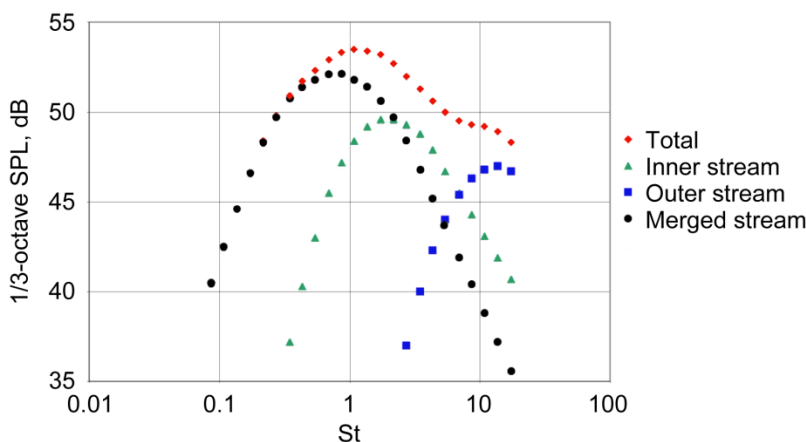


Figure 8.27.—Example of source noise component and total spectra computed by ANOPP for a shock-free jet at inlet angle $\theta = 90^\circ$. 1/3-octave sound pressure level (SPL) versus Strouhal number St .

8.14 Empirical Code Assessment Results

The only empirical model available during this assessment exercise was the jet noise routine within the ANOPP code. Section 8.2.1 briefly outlined the origin of the ST2JET module. This section examines sample cases in an attempt to provide a direction for future improvements.

8.14.1 Case Listing

Table 8.7 in Appendix B details nine jet configurations (identified alphabetically as A through I) considered in the ANOPP ST2JET assessment exercise. These configurations encompass a broad range of operating conditions (jet temperature and velocity) in both subsonic and supersonic jets. In addition to the convergent nozzles, a number of single-stream convergent-divergent nozzles were also designed to generate shock-free jets at exhaust Mach numbers shown in Table 8.3.

Aside from single stream jets, dual stream nozzles were also examined with a BPR as high as 14.

8.14.2 Overall Results

Figure 8.28 to Figure 8.30 are an attempt to distill the results for the 265 cases listed in Table 8.7 into a few figures that answer the question, “How well does ANOPP predict jet noise?” The metrics used are defined in Equation (8.13). Figure 8.28 shows the average difference μ in the OASPL between ANOPP and experiments, and is essentially a measure of how well ANOPP predicts the total noise of the jet. First, with the exception of configuration B, which represents convergent nozzles with chevron mixers, it appears that ANOPP predicted the OASPL to within a few decibels and within experimental uncertainty for most configurations. Second, given that the jet velocity generally increases with case number within each configuration group, it

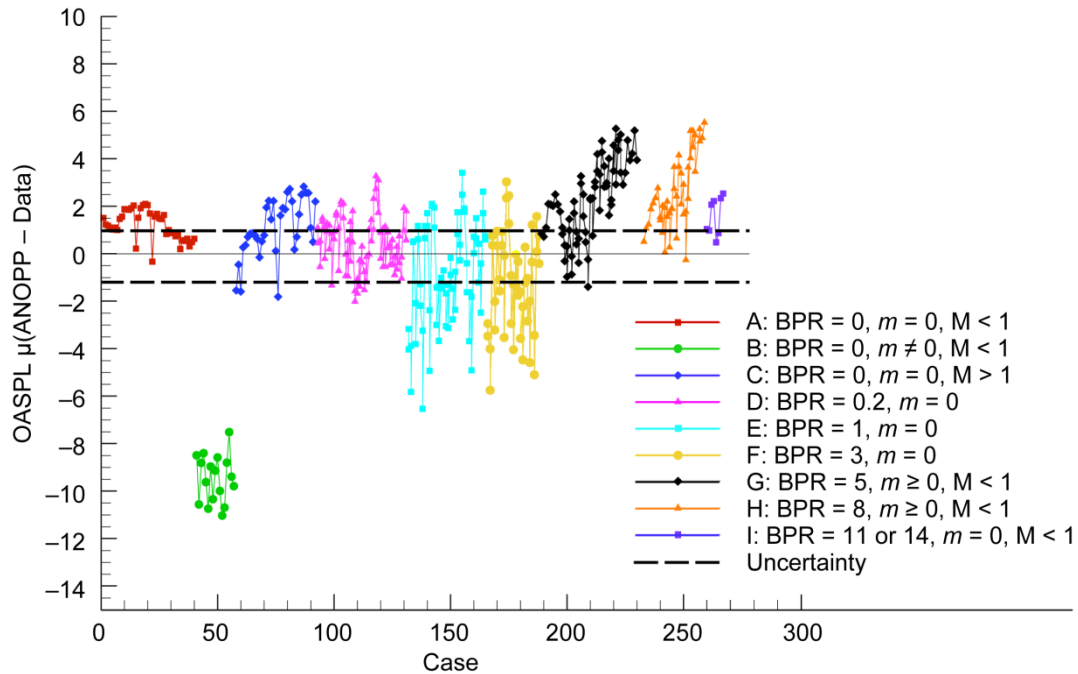


Figure 8.28.—Average error μ in overall sound pressure level (OASPL) between ANOPP predictions and experimental data for all ANOPP assessment cases listed in Table 8.7 (Appendix B), grouped in configurations A through I with corresponding bypass ratio (BPR), azimuthal periodicity m , and Mach number M .

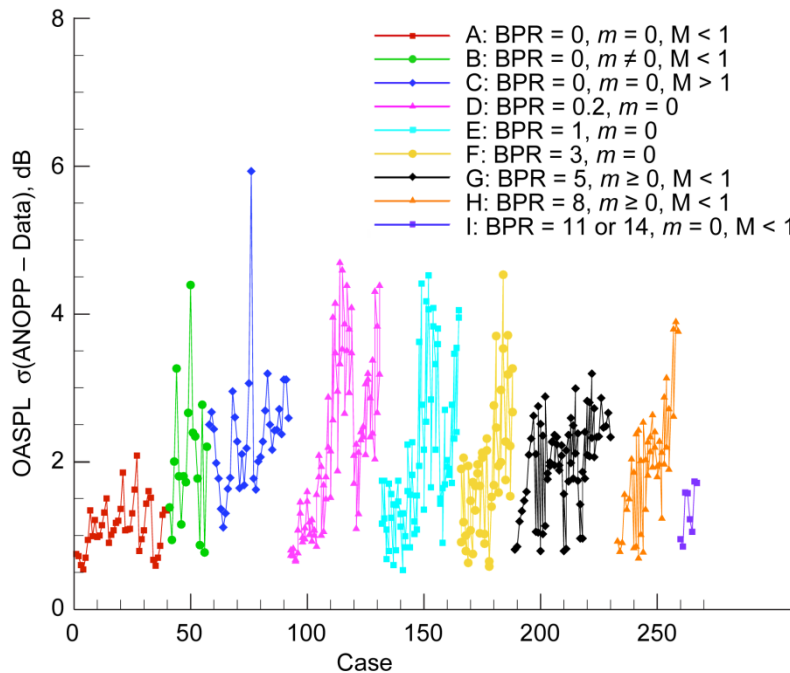


Figure 8.29.—Standard deviation σ about the average overall sound pressure level (OASPL) error between ANOPP predictions and experimental data for all ANOPP assessment cases listed in Table 8.7 (Appendix B), grouped in configurations A through I with corresponding bypass ratio (BPR), azimuthal periodicity m , and Mach number M .

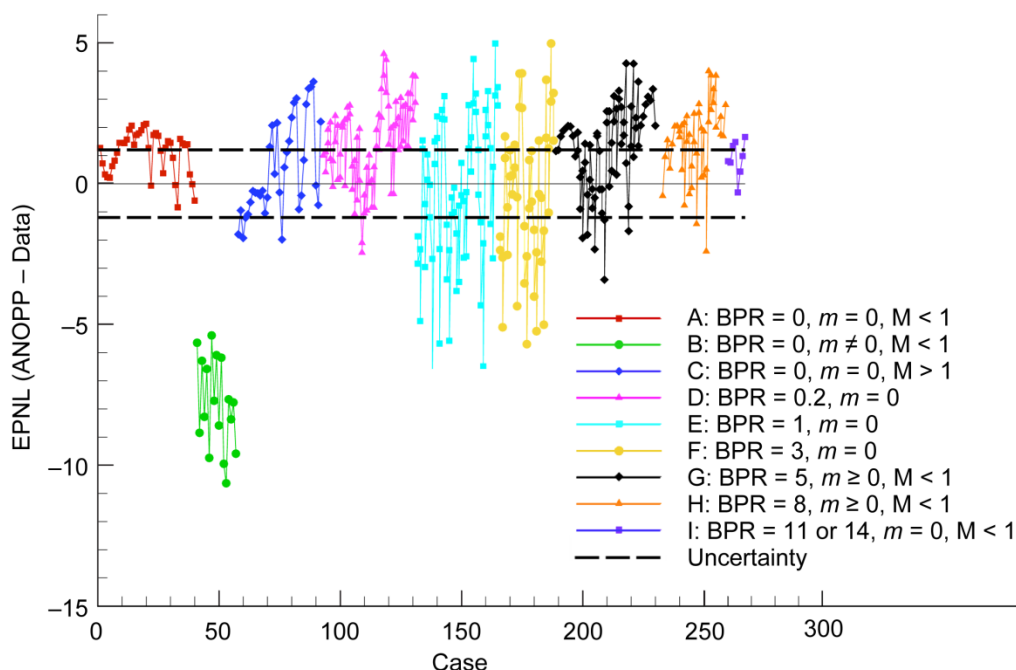


Figure 8.30.—Difference in effective perceived noise level (EPNL) between ANOPP predictions and experimental data for all ANOPP assessment cases listed in Table 8.7 (Appendix B), grouped in configurations A through I with corresponding bypass ratio (BPR), azimuthal periodicity m , and Mach number M .

appears that ANOPP tends to do a better job of predicting OASPL at lower speeds. Third, configuration groups E and F have less accuracy because most of these cases were shock-containing jets where the noise prediction was dominated by the prediction of broadband shock noise. Apparently the broadband shock noise prediction code is less accurate than the mixing noise code that dominates in most jet noise predictions.

To assess how well ANOPP predicted the directivity in OASPL, the standard deviation σ of the difference in OASPL over the polar angles is plotted in Figure 8.29. The discrepancy in predicting directivity is similar across all configurations, even configuration B in which predictions credited the chevrons with much more reduction of sound power than was measured but properly predicted the directivity. As in the average error μ , the overall upward trend in σ with increasing case number within each configuration points to a decline in the prediction quality with increasing jet speed.

Figure 8.30 is similar to Figure 8.28, but measures the average difference in the EPNL between predictions and data assuming an arbitrary nozzle area of 0.7854 m^2 (1217 in.^2) flown at Mach 0.28 in level flight of 500 m (1640 ft) altitude. The EPNL of predictions shows slightly less discrepancy with data compared to predictions of OASPL shown in Figure 8.28; however, this assessment is dependent upon scale factor. Looking across all configurations the predicted EPNL generally matches the measured EPNL within 2 EPNdB.

Results comparing measured and predicted 1/3-octave spectra and OASPL directivities for a representative subset of 265 cases appear in Figure 8.60 to Figure 8.103 in Appendix C.

8.15 Acoustic Analogy Code Assessment Results: Jet3D

In the Jet3D code, computation of the jet mixing noise is carried out according to Lighthill's acoustic analogy as described in Section 8.2.2, "Acoustic Analogy Prediction Tools." The spectral density of the far-field noise is evaluated following Equation (8.3) using the source and the Green's function as defined in Section 8.2.2.1. The Wind-US CFD solver (Ref. 10) supplied the RANS solution files for cases shown here.

8.15.1 Case Listing

The acoustic analogy code Jet3D was assessed at single-flow subsonic, and shock-free supersonic jet conditions listed in Table 8.1. The table represents only a limited subset of the full assessment matrix (cases listed in Table 8.7). This was partially due to the relatively large resources—gridding and CFD computation—required for each test case. In addition, Jet3D is not equipped with modeling tools to evaluate broadband shock associated noise hence none of the shock-containing jets were included.

8.15.2 Discussion of Jet3D Results

Of nine single-stream axisymmetric cases examined with Jet3D, the first two (003 and 007) represent unheated subsonic jets. These presented the least agreeable Jet3D performances, with OASPL overpredictions that exceeded above 10.0 dB at most angles (Figure 8.31 and Figure 8.32). This was partially due to the fact that the code was originally calibrated around hot jets and the heat-related sources were also considered as small and dismissed as a source. Subsequently, it was anticipated to see improved predictions at heated conditions. The next six cases present heated jets at a static temperature ratio ranging from 1.76 to 2.70. At the highest temperature, the overpredictions diminished to an average of ~5.0 dB above measurements, but the peak frequency was off by as much as a full octave as seen in Figure 8.33 to Figure 8.38. The last

example (case 268) was a shock-free supersonic jet at Mach 1.40. This case (see Figure 8.39) presented the best performance of the Jet3D in terms of the OASPL directivity; however, the details of the spectrum were not correct, and the spectral peak at 130° was off by ~0.80 of a full octave below measured data. This was the case for which Jet3D had been calibrated in Reference 8.

In general, Jet3D did better at low-Mach-number heated conditions. Given that the usual approximation of the Lighthill stress tensor neglects enthalpy related terms as a source, it was not surprising to see prediction inconsistencies across temperatures.

It is noted that the prediction shortfalls were not related to the particular CFD solver or the grid-density, as sensitivity to both were explored earlier in the discussion of Jet3D code in Section 8.2.2.1 (Figure 8.2).

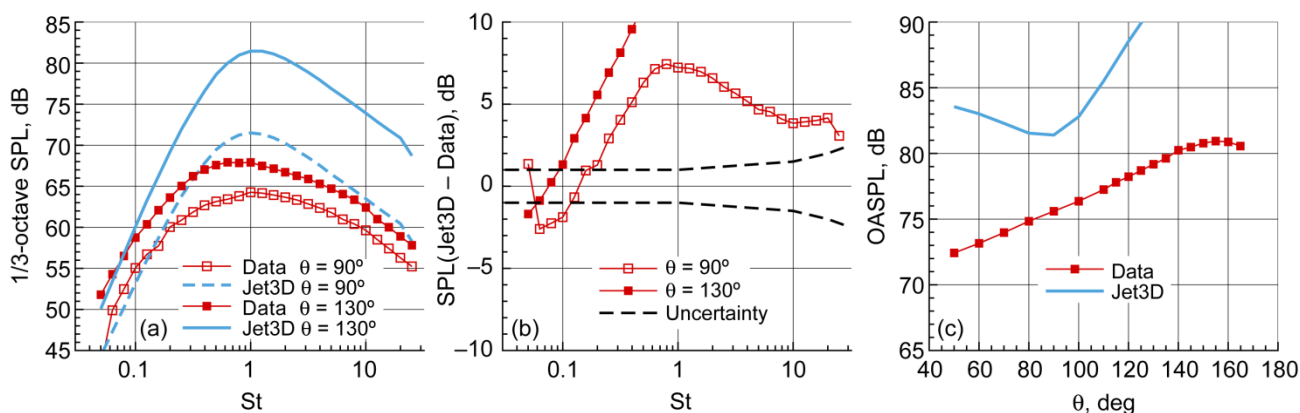


Figure 8.31.—Assessment of Jet3D jet noise predictions. Case 003 (see Table 8.1) for convergent, axisymmetric nozzle: bypass ratio (BPR) = 0, Mach number $M = 0.51$, acoustic Mach number $M_a = 0.5$, and static temperature ratio $T_{s,r} = 0.955$. Comparison between Jet3D predictions and SHJAR experimental data. (a) 1/3-octave sound pressure level (SPL) versus Strouhal number St for inlet angles $\theta = 90^\circ$ and 130° . (b) Difference in SPL values, with uncertainty. (c) Overall sound pressure level (OASPL) as function of θ .

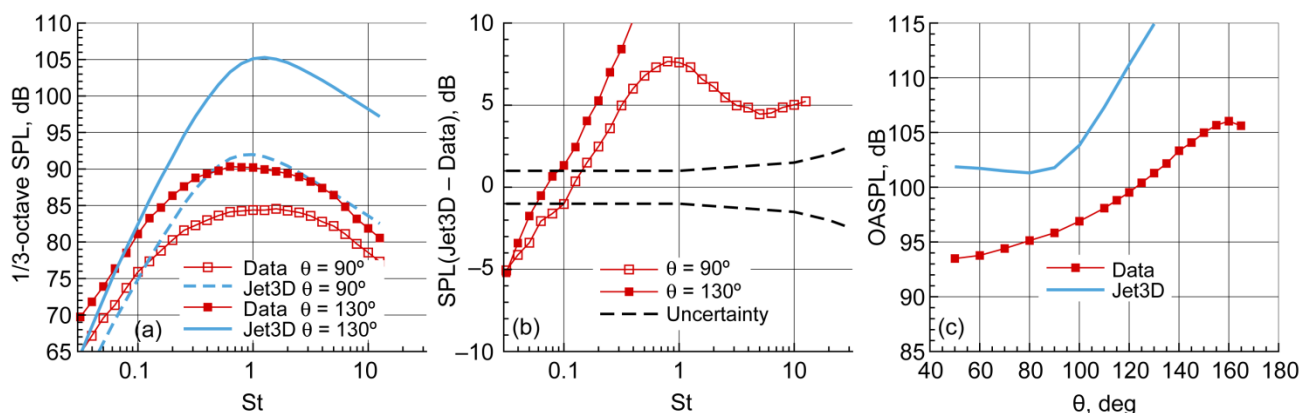


Figure 8.32.—Assessment of Jet3D jet noise predictions. Case 007 (see Table 8.1) for convergent, axisymmetric nozzle: bypass ratio (BPR) = 0, Mach number $M = 0.98$, acoustic Mach number $M_a = 0.902$, and static temperature ratio $T_{s,r} = 0.842$. Comparison between Jet3D predictions and SHJAR experimental data. (a) 1/3-octave sound pressure level (SPL) versus Strouhal number St for inlet angles $\theta = 90^\circ$ and 130° . (b) Difference in SPL values, with uncertainty. (c) Overall sound pressure level (OASPL) as function of θ .

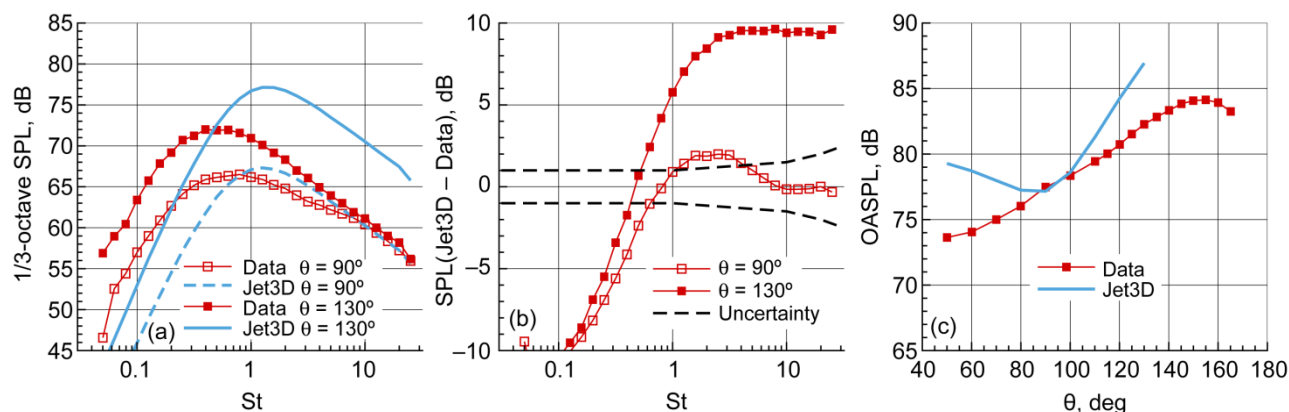


Figure 8.33.—Assessment of Jet3D jet noise predictions. Case 022 (see Table 8.1) for convergent, axisymmetric nozzle: bypass ratio (BPR) = 0, Mach number $M = 0.37$, acoustic Mach number $M_a = 0.492$, and static temperature ratio $T_{s,r} = 1.767$. Comparison between Jet3D predictions and SHJAR experimental data. (a) 1/3-octave sound pressure level (SPL) versus Strouhal number St for inlet angles $\theta = 90^\circ$ and 130° . (b) Difference in SPL values, with uncertainty. (c) Overall sound pressure level (OASPL) as function of θ .

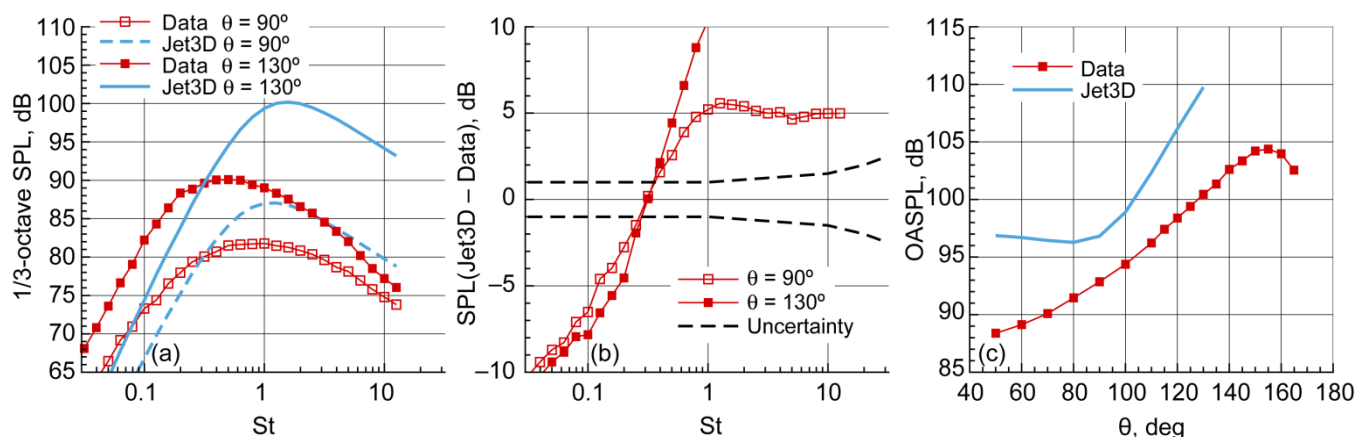


Figure 8.34.—Assessment of Jet3D jet noise predictions. Case 025 (see Table 8.1) for convergent, axisymmetric nozzle: bypass ratio (BPR) = 0, Mach number $M = 0.68$, acoustic Mach number $M_a = 0.901$, and static temperature ratio $T_{s,r} = 1.77$. Comparison between Jet3D predictions and SHJAR experimental data. (a) 1/3-octave sound pressure level (SPL) versus Strouhal number St for inlet angles $\theta = 90^\circ$ and 130° . (b) Difference in SPL values, with uncertainty. (c) Overall sound pressure level (OASPL) as function of θ .

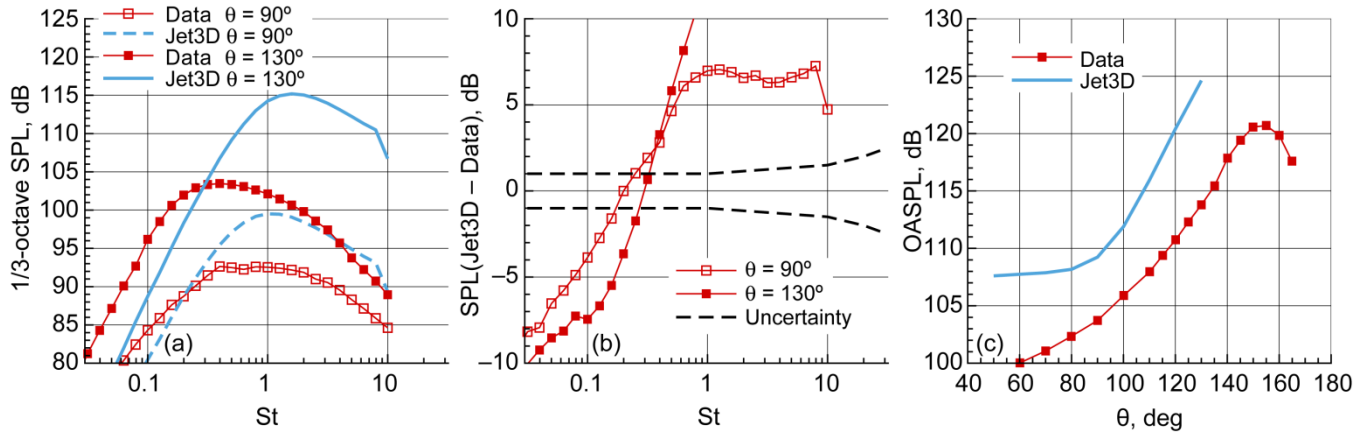


Figure 8.35.—Assessment of Jet3D jet noise predictions. Case 027 (see Table 8.1) for convergent, axisymmetric nozzle: bypass ratio (BPR) = 0, Mach number $M = 1.01$, acoustic Mach number $M_a = 1.33$, and static temperature ratio $T_{s,r} = 1.759$. Comparison between Jet3D predictions and SHJAR experimental data. (a) 1/3-octave sound pressure level (SPL) versus Strouhal number St for inlet angles $\theta = 90^\circ$ and 130° . (b) Difference in SPL values, with uncertainty. (c) Overall sound pressure level (OASPL) as function of θ .

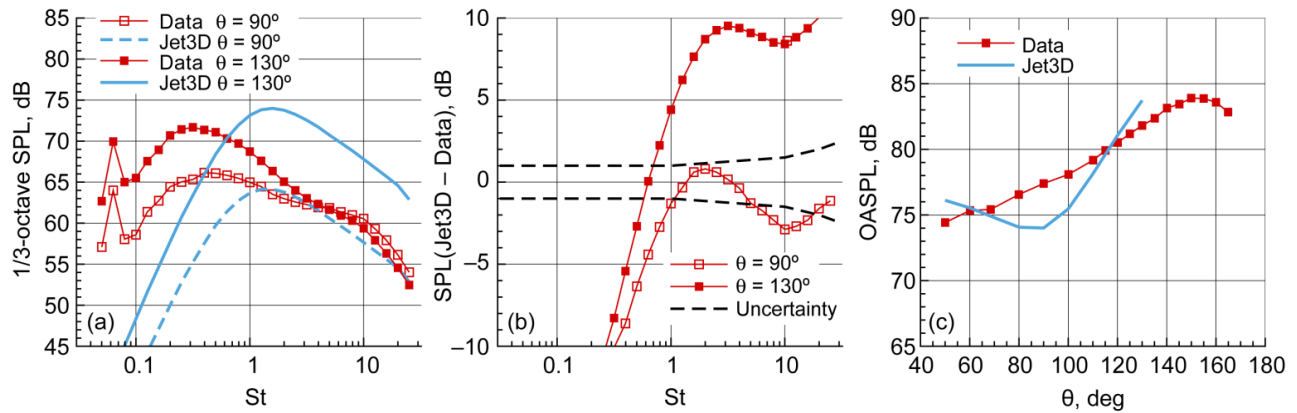


Figure 8.36.—Assessment of Jet3D jet noise predictions. Case 034 (see Table 8.1) for convergent, axisymmetric nozzle: bypass ratio (BPR) = 0, Mach number $M = 0.3$, acoustic Mach number $M_a = 0.484$, and static temperature ratio $T_{s,r} = 2.624$. Comparison between Jet3D predictions and SHJAR experimental data. (a) 1/3-octave sound pressure level (SPL) versus Strouhal number St for inlet angles $\theta = 90^\circ$ and 130° . (b) Difference in SPL values, with uncertainty. (c) Overall sound pressure level (OASPL) as function of θ .

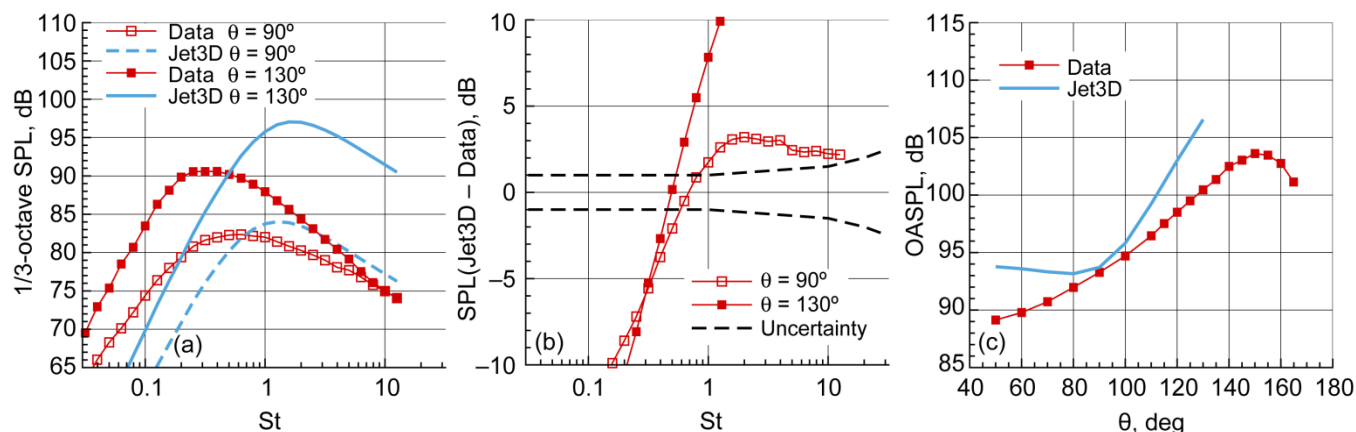


Figure 8.37.—Assessment of Jet3D jet noise predictions. Case 037 (see Table 8.1) for convergent, axisymmetric nozzle: bypass ratio (BPR) = 0, Mach number $M = 0.56$, acoustic Mach number $M_a = 0.901$, and static temperature ratio $T_{s,r} = 2.702$. Comparison between Jet3D predictions and SHJAR experimental data. (a) 1/3-octave sound pressure level (SPL) versus Strouhal number St for inlet angles $\theta = 90^\circ$ and 130° . (b) Difference in SPL values, with uncertainty. (c) Overall sound pressure level (OASPL) as function of θ .

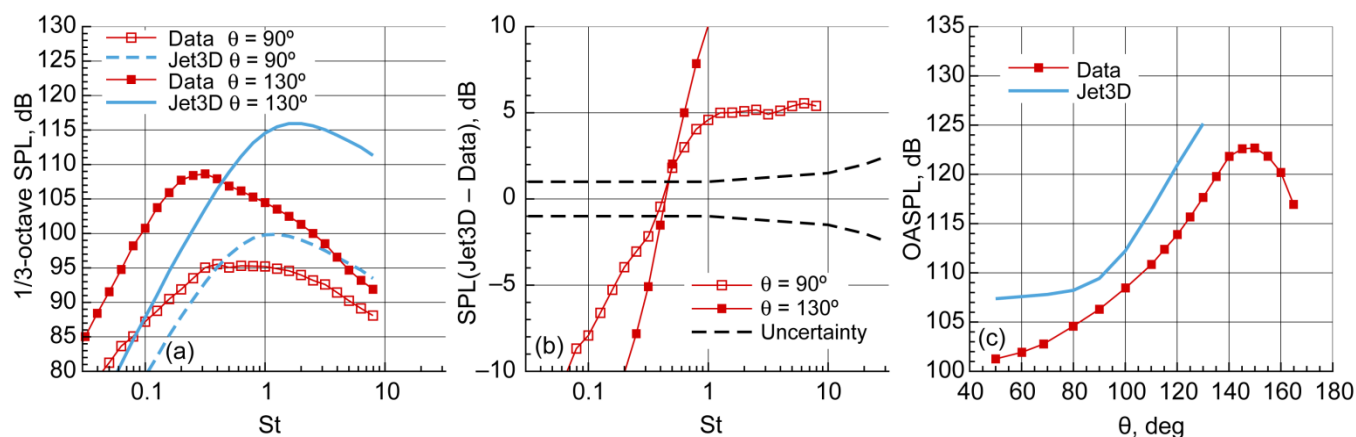


Figure 8.38.—Assessment of Jet3D jet noise predictions. Case 040 (see Table 8.1) for convergent, axisymmetric nozzle: bypass ratio (BPR) = 0, Mach number $M = 0.92$, acoustic Mach number $M_a = 1.483$, and static temperature ratio $T_{s,r} = 2.703$. Comparison between Jet3D predictions and SHJAR experimental data. (a) 1/3-octave sound pressure level (SPL) versus Strouhal number St for inlet angles $\theta = 90^\circ$ and 130° . (b) Difference in SPL values, with uncertainty. (c) Overall sound pressure level (OASPL) as function of θ .

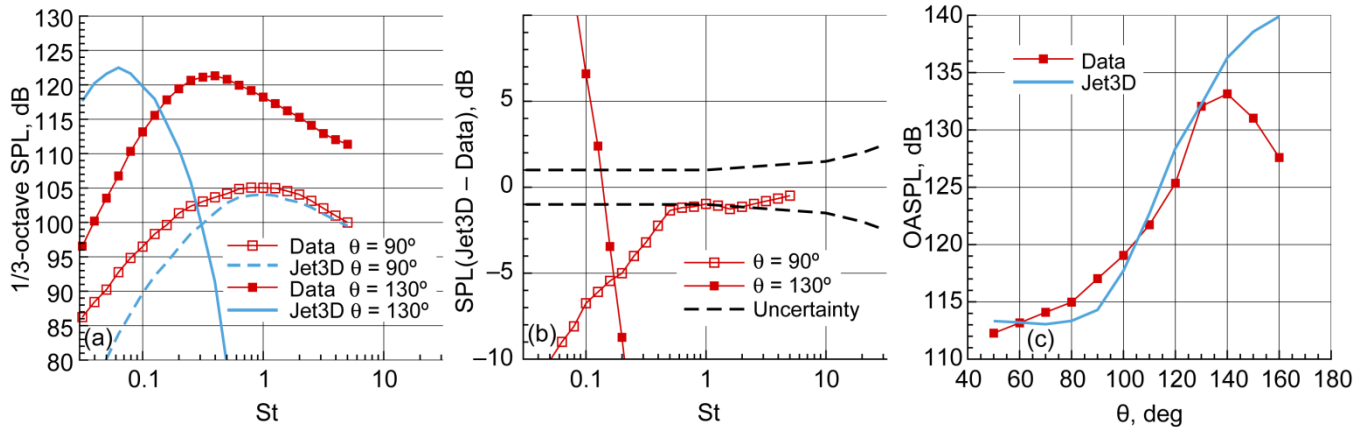


Figure 8.39.—Assessment of Jet3D jet noise predictions. Case 268 (see Table 8.1) for convergent-divergent, axisymmetric nozzle: bypass ratio (BPR) = 0, Mach number $M = 1.4$, acoustic Mach number $M_a = 2.2$, and static temperature ratio $T_{s,r} = 2.53$. Comparison between Jet3D predictions and SHJAR experimental data. (a) 1/3-octave sound pressure level (SPL) versus Strouhal number St for inlet angles $\theta = 90^\circ$ and 130° . (b) Difference in SPL values, with uncertainty. (c) Overall sound pressure level (OASPL) as function of θ .

8.16 Acoustic Analogy Code Assessment Results: JeNo v1.0

In JeNo, computations of the turbulent mixing noise are carried out according to Lilley's acoustic analogy, and the spectral density of the far-field noise is evaluated following Equation (8.3) using the source and the Green's function as defined in Section 8.2.2.2. The version considered in the assessment exercise (i.e., JeNo v1.0) does not address the heat-related sources that are associated with enthalpy fluctuation in a jet. Consequently, source term q relates to second rank velocity tensors as shown in Equation (8.11). Aside from differences in their source modeling, the major difference between the two acoustic analogy codes Jet3D and JeNo is their Green's functions. While Jet3D used a free space Green's function, JeNo solves the second-order compressible Rayleigh equation numerically at each frequency and at each source location (Ref. 13). The Wind-US CFD solver (Ref. 10) supplied the RANS solution files for cases shown here.

8.16.1 Case Listing

The acoustic analogy code JeNo v1.0 was assessed only on a subset of the full assessment matrix. These consist of 13 axisymmetric, convergent and convergent-divergent nozzles as listed in Table 8.5, plus additional cases with nonaxisymmetric geometries as listed in Table 8.6. JeNo is not presently equipped with modeling tools to evaluate the broadband shock associated noise hence none of the shock-containing jets were included in the list.

TABLE 8.5.—ASSESSMENT MATRIX FOR JeNo v1.0
PREDICTIONS OF JET NOISE SPECTRA—
AXISYMMETRIC GEOMETRIES^a


Case	M	Axial geometry	M_a	$T_{s,r}$	nozid
003	0.51	Convergent ↓ C-D ↓	0.500	0.955	SMC000
007	0.98		0.902	0.842	↓ SMC014
022	0.37		0.492	1.767	
025	0.68		0.901	1.770	
027	1.01		1.330	1.759	
034	0.30		0.484	2.624	
037	0.56		0.901	2.702	
040	0.92		1.483	2.703	
059	1.172		1.047	0.797	
068	1.394	C-D ↓	1.191	0.730	SMC015
075	1.497		1.251	0.699	SMC016
083	1.659		1.342	0.654	SMC017
090	1.784		1.403	0.619	SMC018

^aNomenclature for table headings:

M	ideally expanded Mach number
Axial geometry	indicates if nozzle was convergent or convergent-divergent (C-D)
M_a	acoustic Mach number, U/c_∞
$T_{s,r}$	static temperature ratio, T_s/T_∞
nozid	nozzle identification

TABLE 8.6.—ASSESSMENT MATRIX FOR JeNo v1.0 PREDICTIONS OF JET NOISE SPECTRA—NONAXISYMMETRIC GEOMETRIES^a

Case	Geometry		M	M_a	$T_{s,r}$	nozid
	Axial	Azimuthal				
042	Convergent	$m = 6$	0.972	0.902	0.837	SMC001

Geometry		BPR	M	Core		Bypass		M_{fl}	nozid
Axial	Azimuthal			M_a	$T_{t,r}$	M_a	$T_{t,r}$		
Separate flow 	Axisymmetric	2.84	0.82	0.888	1.004	0.701	1.001	0.28	5000
	Fan-wedge	2.43	0.83	0.901	1.002	0.711	0.999	0.28	520x
	Axisymmetric	2.09	0.73	0.909	1.039	0.530	0.999	0.0	5000
	S-duct	2.04	0.73	0.904	1.003	0.527	1.006	0.0	50Sx

^aNomenclature for table headings:

BPR	bypass ratio
M	ideally expanded Mach number; for dual stream, mass averaged
Axial geometry	indicates convergent or externally mixed separate flow
Azimuthal geometry	indicates nozzle is axisymmetric or defined as shown in Figure 8.40, or single stream, azimuthal base periodicity m
M_a	acoustic Mach number U/c_∞
$T_{s,r}$	static temperature ratio T_s/T_∞
$T_{t,r}$	total temperature ratio T_t/T_∞ , for dual stream cases
M_{fl}	flight Mach number
nozid	nozzle identification

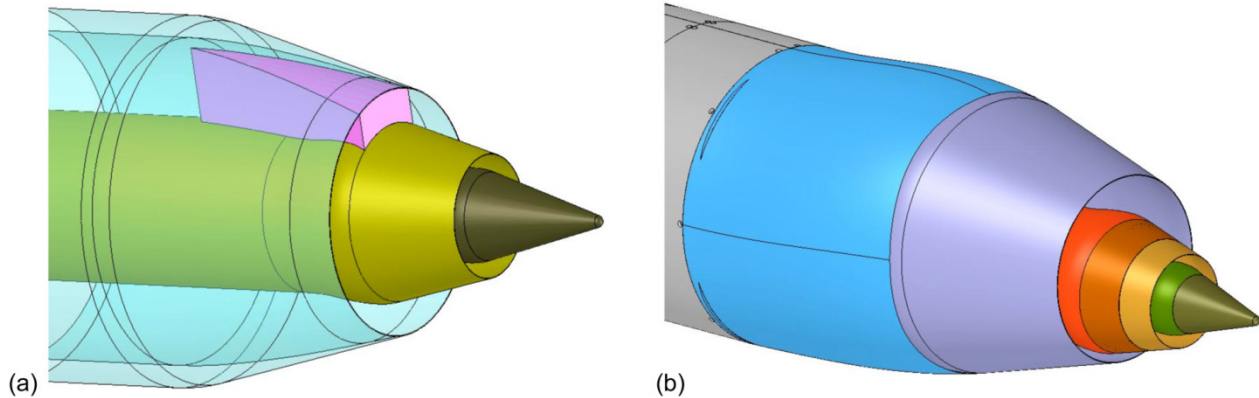


Figure 8.40.—Nozzles with offset stream technology used to assess the JeNo v1.0 code jet noise prediction capability. (a) Fan-wedge. (b) S-duct.

8.16.1.1 Axisymmetric Jets

Cases listed in Table 8.5 are made up of seven unheated, and six heated jets. Unheated cases consist of two subsonic jets at acoustic Mach numbers of 0.50 and 0.90 (cases 003 and 007), and five supersonic flows at ideally expanded Mach numbers from 1.17 to 1.78 (cases 059, 068, 075, 083, and 090). An additional six heated cases (022, 025, 027, 034, 037, and 040) were also considered with static temperature ratios from 1.76 to 2.70 to highlight the shortcomings in hot jet predictions and needed future improvements. The RANS solutions were generated using the Wind-US code and the Mentor SST turbulence model as discussed previously in Sections 8.2.2.2 and 8.2.3. Upstream nozzle conditions were

specified in terms of plenum total temperature ratio and the nozzle pressure ratio in computing the CFD solutions, however, only the external flow downstream of the nozzle exit plane was integrated in noise computations.

8.16.1.2 Nonaxisymmetric Jets

One of the main promises of the RANS-based acoustic analogy models is their ability to predict the variations in noise generation due to subtle changes in the nozzle geometry and jet flow. One obvious and historically productive geometrical change has been azimuthal variations in the nozzle lip geometry (i.e., lobed mixers, chevrons, and pylons). The ability of the codes to predict the impact on noise of

alterations to nozzle axisymmetry is almost as useful as their ability to predict the absolute jet noise itself. A tool that could predict noise modification due to geometric changes is satisfactory for engineering quieter nozzles.

8.16.1.2.1 Chevron Nozzles

Chevron nozzles have the potential to reduce jet noise at its peak directivity angle near the downstream jet axis with minimal benefit or even slight noise increase along the sideline. They are designed with the premise that the strengthened axial vorticity generated by the chevrons would decay the centerline velocity faster, enhance mixing, and help reduce the core length. Chevron nozzle SMC001 was a litmus test case that examined the ability of RANS-based acoustic analogy codes to capture noise trends in nonaxisymmetric configurations. This particular nozzle design (see Figure 8.12) consists of six identical chevrons at 5° penetration angle, and with an effective nozzle exit diameter of 5.1 cm (2 in.). The details of the geometry and its aeroacoustics performance compared to the base nozzle as well as alternative chevron designs are discussed in Reference 34. For the purpose of this assessment, only one operating condition was considered (case 042, Table 8.6).

8.16.1.2.2 Offset Nozzles

The offset streams are designed primarily in dual-flow nozzles in an attempt to modify the fan stream and to divert the core-fan shear noise in a favorable direction away from an observer on the ground. These designs usually result in a noise increase in the opposite direction. Two offset-stream concepts are discussed here (Figure 8.40): (1) the “fan-wedge” design places a 20° wedge in the fan stream with the wedge tip

pointing upstream and (2) the “S-duct” design shifts the flow centerlines to create 5 percent offset while allowing for the two streams to remain parallel at the jet exit. Both designs create a relatively thicker flow with less turbulence on one side relative to the opposite side (Ref. 35) when compared to the flow of the dual stream geometry without offset or fan-wedge. The operating conditions for the two concepts are very similar (see Table 8.6). This operating condition was chosen to have similar velocity gradients as many commercial aviation jet cycles but with a cold core flow, knowing that the JeNo code was not calibrated for hot jets. The Wind-US RANS solver provided the mean flow and turbulence for offset nozzles as well as the base configuration.

8.16.2 Discussion of JeNo v1.0 Results

Figure 8.41 to Figure 8.53 show comparisons of measured data and predicted results for the cases listed in Table 8.5 and Table 8.6.

The subsonic cold jet comparisons (cases 003 and 007) are very good, generally within the experimental uncertainty (Figure 8.41 and Figure 8.42). The hot jet cases (Figure 8.43 to Figure 8.48) are off by as much as 10 dB, depending upon the jet speed. The discrepancy is always an underprediction, and gets worse with increased heating, and the aft angle has an incorrect peak frequency at the highest speeds (cases 027 and 040). On the other hand, the supersonic cold jet predictions (cases 059, 068, 075, 083, and 090) are not too bad, typically within 5 dB of data (Figure 8.49 to Figure 8.53). This was not surprising, as this version of JeNo was expected to do relatively well in the unheated jet cases. The discrepancies are mostly at aft angles and become more prominent at higher supersonic speeds.

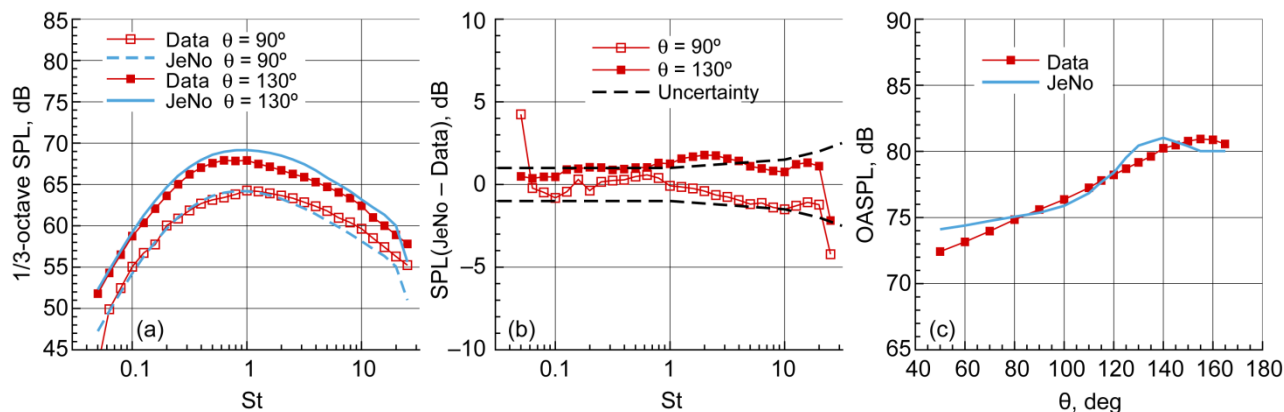


Figure 8.41.—Assessment of JeNo v1.0 jet noise predictions. Case 003 (see Table 8.5) for convergent, axisymmetric nozzle: bypass ratio (BPR) = 0, Mach number $M = 0.51$, acoustic Mach number $M_a = 0.5$, and static temperature ratio $T_{s,r} = 0.955$. Comparison between JeNo predictions and SHJAR experimental data. (a) 1/3-octave sound pressure level (SPL) versus Strouhal number St for inlet angles $\theta = 90^\circ$ and 130° . (b) Difference in SPL values, with uncertainty. (c) Overall sound pressure level (OASPL) as function of θ .

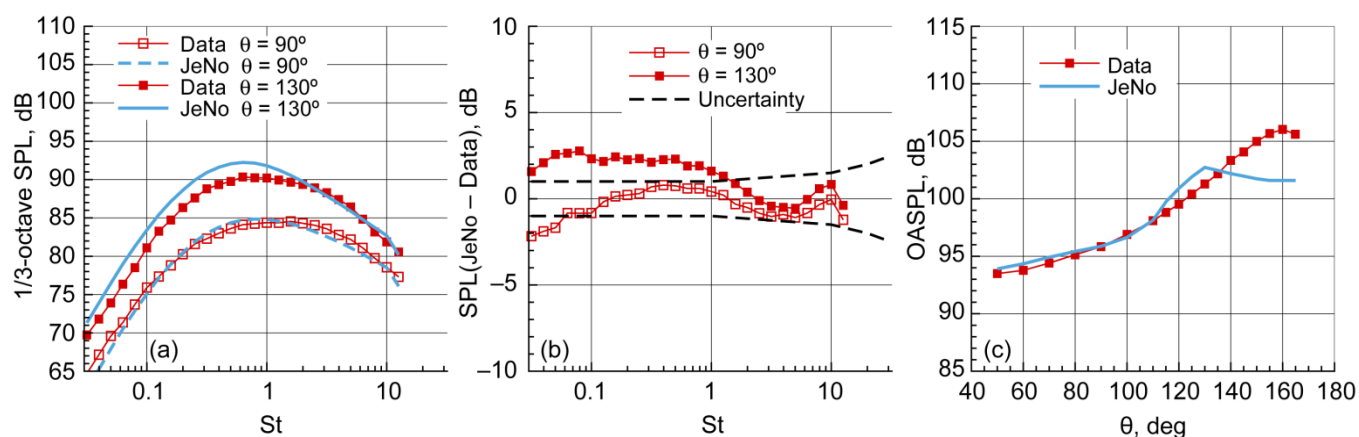


Figure 8.42.—Assessment of JeNo v1.0 jet noise predictions. Case 007 (see Table 8.5) for convergent, axisymmetric nozzle: bypass ratio (BPR) = 0, Mach number $M = 0.98$, acoustic Mach number $M_a = 0.902$, and static temperature ratio $T_{s,r} = 0.842$. Comparison between JeNo predictions and SHJAR experimental data. (a) 1/3-octave sound pressure level (SPL) versus Strouhal number St for inlet angles $\theta = 90^\circ$ and 130° . (b) Difference in SPL values, with uncertainty. (c) Overall sound pressure level (OASPL) as function of θ .

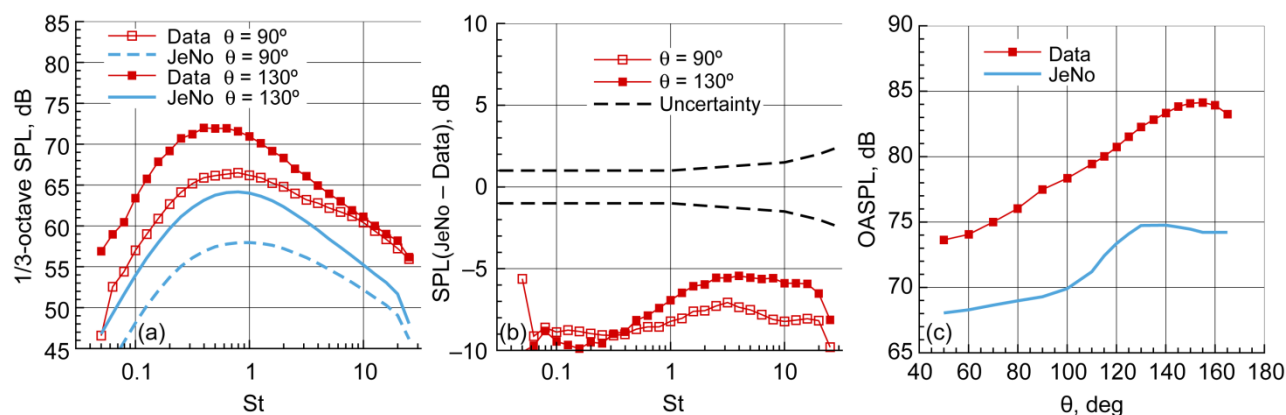


Figure 8.43.—Assessment of JeNo v1.0 jet noise predictions. Case 022 (see Table 8.5) for convergent, axisymmetric nozzle: bypass ratio (BPR) = 0, Mach number $M = 0.37$, acoustic Mach number $M_a = 0.492$, and static temperature ratio $T_{s,r} = 1.767$. Comparison between JeNo predictions and SHJAR experimental data. (a) 1/3-octave sound pressure level (SPL) versus Strouhal number St for inlet angles $\theta = 90^\circ$ and 130° . (b) Difference in SPL values, with uncertainty. (c) Overall sound pressure level (OASPL) as function of θ .

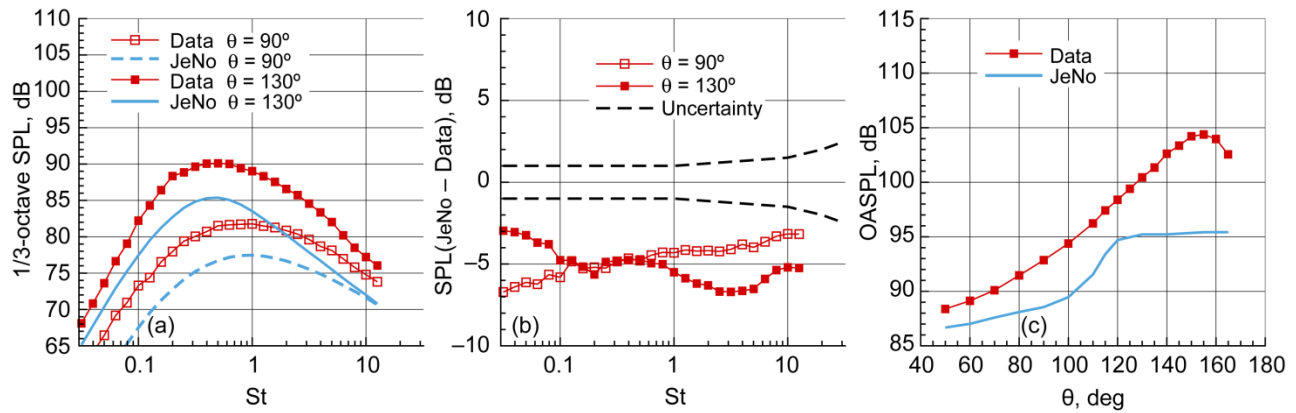


Figure 8.44.—Assessment of JeNo v1.0 jet noise predictions. Case 025 (see Table 8.5) for convergent, axisymmetric nozzle: bypass ratio (BPR) = 0, Mach number $M = 0.68$, acoustic Mach number $M_a = 0.901$, and static temperature ratio $T_{s,r} = 1.77$. Comparison between JeNo predictions and SHJAR experimental data. (a) 1/3-octave sound pressure level (SPL) versus Strouhal number St for inlet angles $\theta = 90^\circ$ and 130° . (b) Difference in SPL values, with uncertainty. (c) Overall sound pressure level (OASPL) as function of θ .

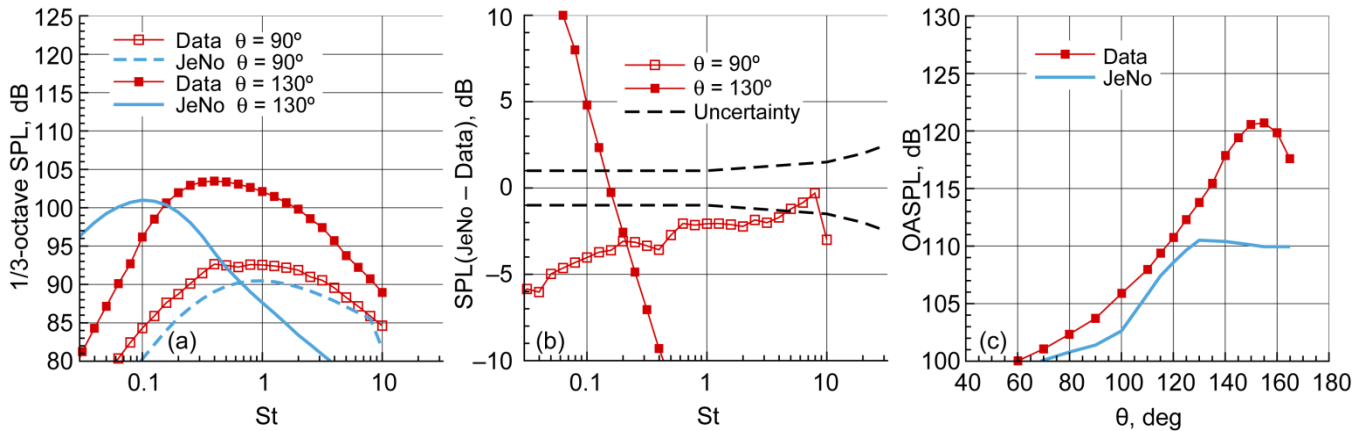


Figure 8.45.—Assessment of JeNo v1.0 jet noise predictions. Case 027 (see Table 8.5) for convergent, axisymmetric nozzle: bypass ratio (BPR) = 0, Mach number $M = 1.01$, acoustic Mach number $M_a = 1.33$, and static temperature ratio $T_{s,r} = 1.759$. Comparison between JeNo predictions and SHJAR experimental data. (a) 1/3-octave sound pressure level (SPL) versus Strouhal number St for inlet angles $\theta = 90^\circ$ and 130° . (b) Difference in SPL values, with uncertainty. (c) Overall sound pressure level (OASPL) as function of θ .

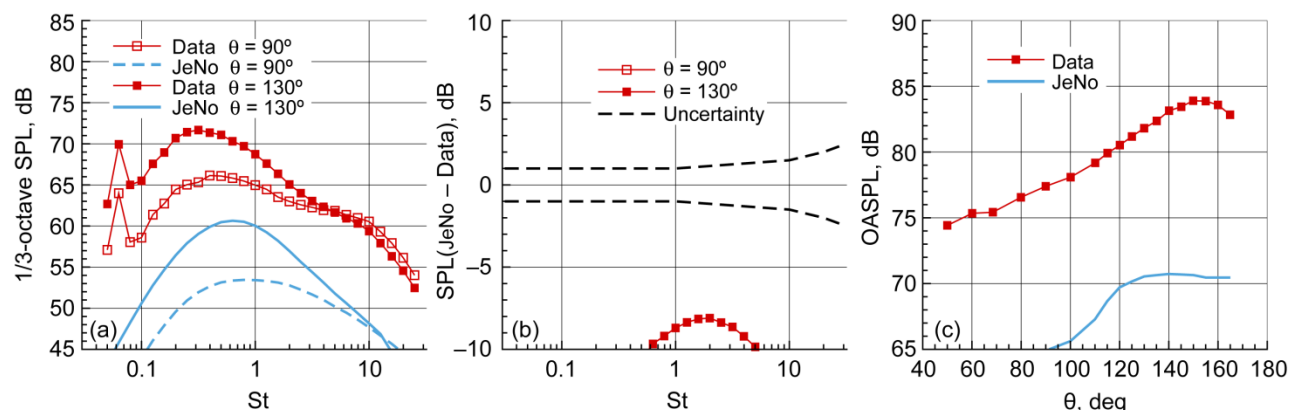


Figure 8.46.—Assessment of JeNo v1.0 jet noise predictions. Case 034 (see Table 8.5) for convergent, axisymmetric nozzle: bypass ratio (BPR) = 0, Mach number $M = 0.3$, acoustic Mach number $M_a = 0.484$, and static temperature ratio $T_{s,r} = 2.624$. Comparison between JeNo predictions and SHJAR experimental data. (a) 1/3-octave sound pressure level (SPL) versus Strouhal number St for inlet angles $\theta = 90^\circ$ and 130° . (b) Difference in SPL values, with uncertainty. (c) Overall sound pressure level (OASPL) as function of θ .

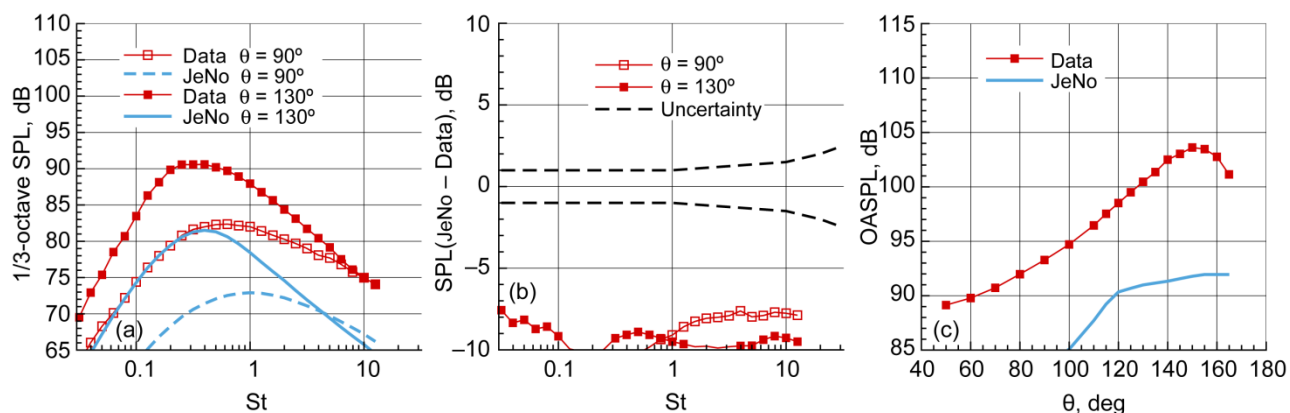


Figure 8.47.—Assessment of JeNo v1.0 jet noise predictions. Case 037 (see Table 8.5) for convergent, axisymmetric nozzle: bypass ratio (BPR) = 0, Mach number $M = 0.56$, acoustic Mach number $M_a = 0.901$, and static temperature ratio $T_{s,r} = 2.702$. Comparison between JeNo predictions and SHJAR experimental data. (a) 1/3-octave sound pressure level (SPL) versus Strouhal number St for inlet angles $\theta = 90^\circ$ and 130° . (b) Difference in SPL values, and uncertainty. (c) Overall sound pressure level (OASPL) as function of θ .

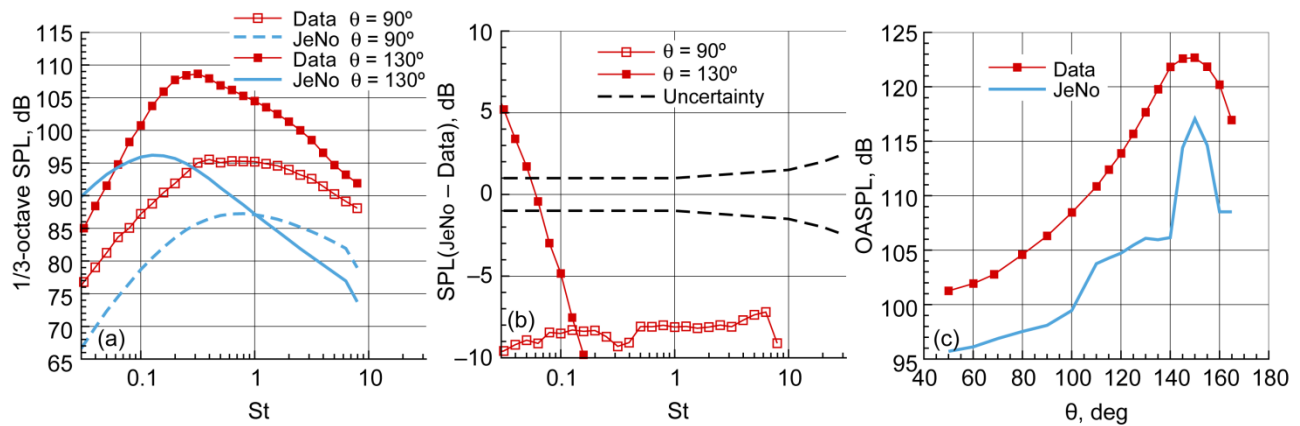


Figure 8.48.—Assessment of JeNo v1.0 jet noise predictions. Case 040 (see Table 8.5) for convergent, axisymmetric nozzle: bypass ratio (BPR) = 0, Mach number $M = 0.92$, acoustic Mach number $M_a = 1.483$, and static temperature ratio $T_{s,r} = 2.703$. Comparison between JeNo predictions and SHJAR experimental data. (a) 1/3-octave sound pressure level (SPL) versus Strouhal number St for inlet angles $\theta = 90^\circ$ and 130° . (b) Difference in SPL values, with uncertainty. (c) Overall sound pressure level (OASPL) as function of θ .

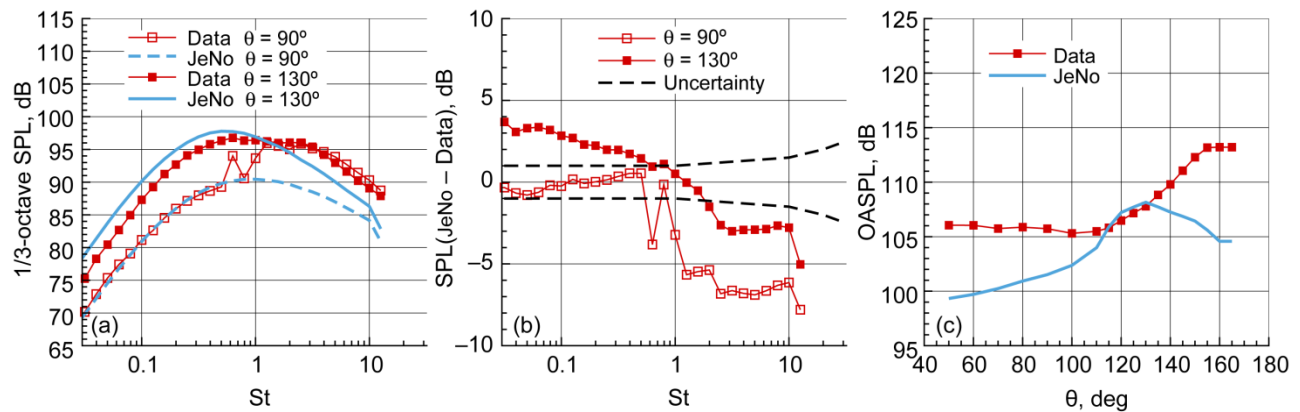


Figure 8.49.—Assessment of JeNo v1.0 jet noise predictions. Case 059 (see Table 8.5) for convergent-divergent, axisymmetric nozzle: bypass ratio (BPR) = 0, Mach number $M = 1.172$, acoustic Mach number $M_a = 1.047$, and static temperature ratio $T_{s,r} = 0.797$. Comparison between JeNo predictions and SHJAR experimental data. (a) 1/3-octave sound pressure level (SPL) versus Strouhal number St for inlet angles $\theta = 90^\circ$ and 130° . (b) Difference in SPL values, with uncertainty. (c) Overall sound pressure level (OASPL) as function of θ .

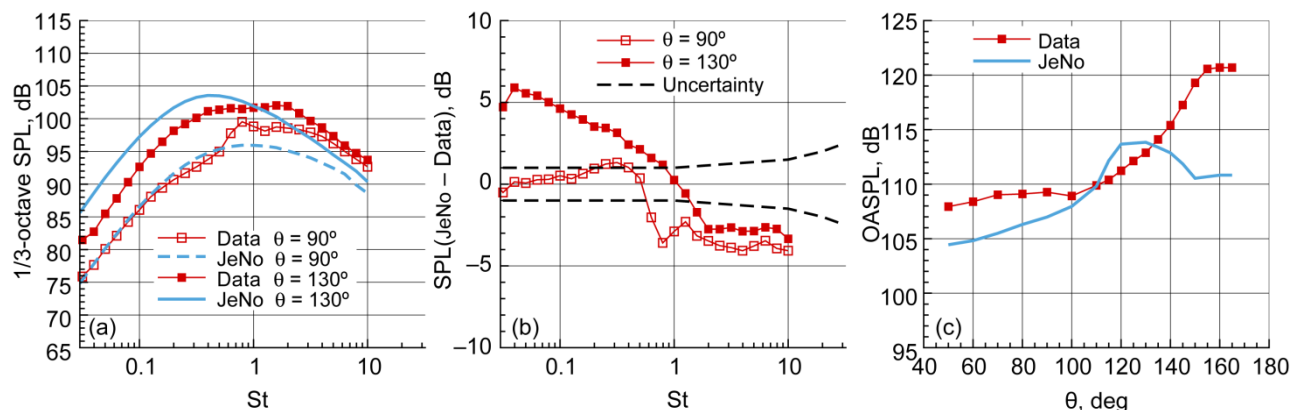


Figure 8.50.—Assessment of JeNo v1.0 jet noise predictions. Case 068 (see Table 8.5) for convergent-divergent, axisymmetric nozzle: bypass ratio (BPR) = 0, Mach number $M = 1.394$, acoustic Mach number $M_a = 1.191$, and static temperature ratio $T_{s,r} = 0.73$. Comparison between JeNo predictions and SHJAR experimental data. (a) 1/3-octave sound pressure level (SPL) versus Strouhal number St for inlet angles $\theta = 90^\circ$ and 130° . (b) Difference in SPL values, with uncertainty. (c) Overall sound pressure level (OASPL) as function of θ .

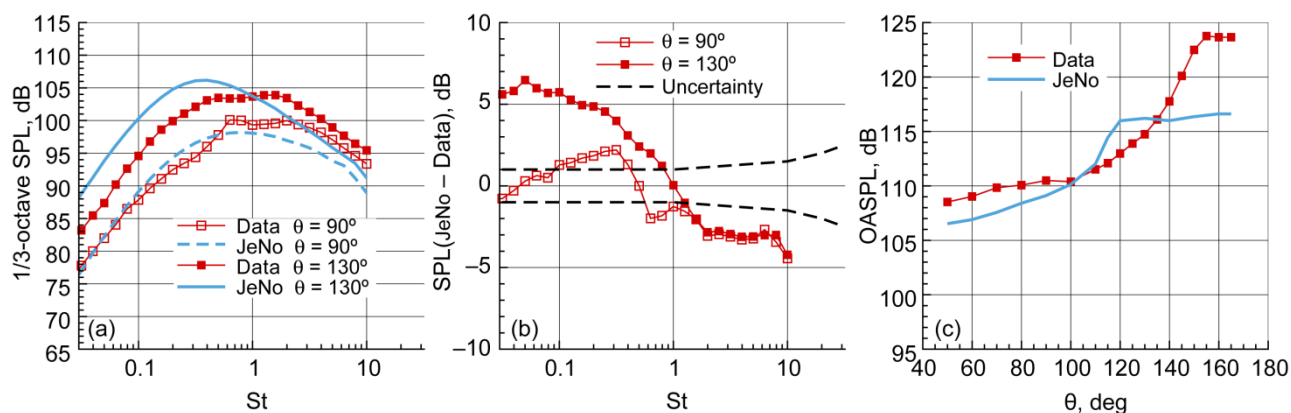


Figure 8.51.—Assessment of JeNo v1.0 jet noise predictions. Case 075 (see Table 8.5) for convergent-divergent, axisymmetric nozzle: bypass ratio (BPR) = 0, Mach number $M = 1.497$, acoustic Mach number $M_a = 1.251$, and static temperature ratio $T_{s,r} = 0.699$. Comparison between JeNo predictions and SHJAR experimental data. (a) 1/3-octave sound pressure level (SPL) versus Strouhal number St for inlet angles $\theta = 90^\circ$ and 130° . (b) Difference in SPL values, with uncertainty. (c) Overall sound pressure level (OASPL) as function of θ .

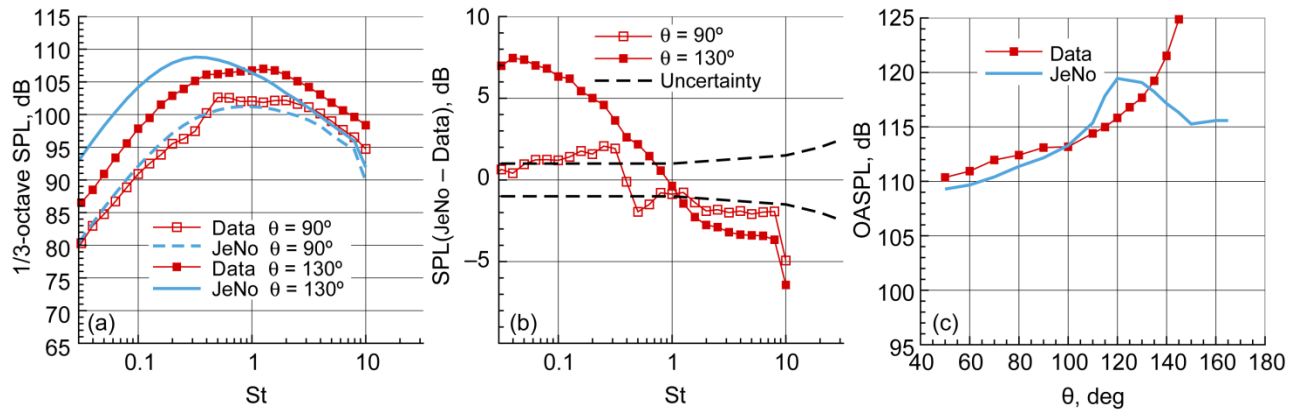


Figure 8.52.—Assessment of JeNo v1.0 jet noise predictions. Case 083 (see Table 8.5) for convergent-divergent, axisymmetric nozzle: bypass ratio (BPR) = 0, Mach number $M = 1.659$, acoustic Mach number $M_a = 1.342$, and static temperature ratio $T_{s,r} = 0.654$. Comparison between JeNo predictions and SHJAR experimental data. (a) 1/3-octave sound pressure level (SPL) versus Strouhal number St for inlet angles $\theta = 90^\circ$ and 130° . (b) Difference in SPL values, with uncertainty. (c) Overall sound pressure level (OASPL) as function of θ .

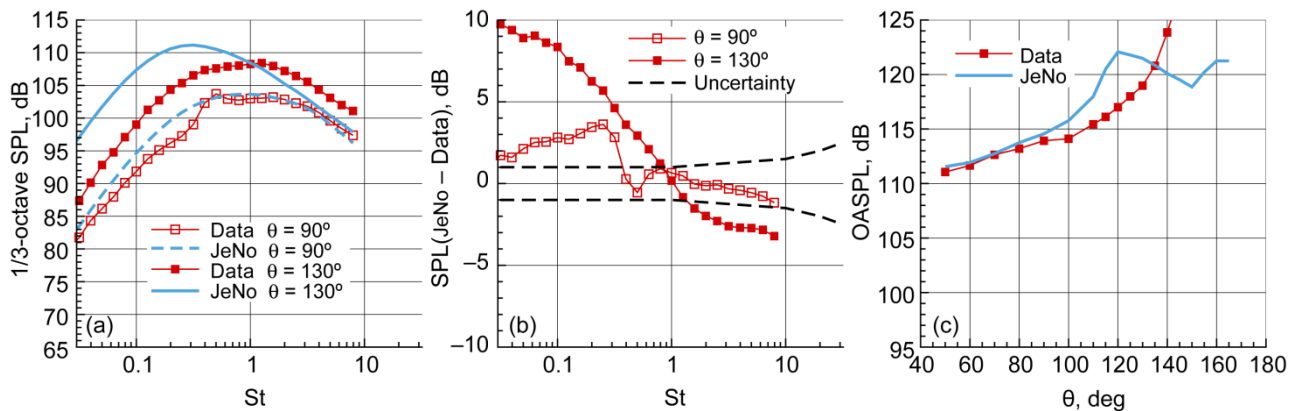


Figure 8.53.—Assessment of JeNo v1.0 jet noise predictions. Case 090 (see Table 8.5) for convergent-divergent, axisymmetric nozzle: bypass ratio (BPR) = 0, Mach number $M = 1.784$, acoustic Mach number $M_a = 1.403$, and static temperature ratio $T_{s,r} = 0.619$. Comparison between JeNo predictions and SHJAR experimental data. (a) 1/3-octave sound pressure level (SPL) versus Strouhal number St for inlet angles $\theta = 90^\circ$ and 130° . (b) Difference in SPL values, with uncertainty. (c) Overall sound pressure level (OASPL) as function of θ .

The 130° spectra peaked at a lower frequency relative to measurements and showed a deficit in noise level at all speeds. One might conclude that the parallel flow assumption in the Green's function predicts a larger cone of silence near the downstream jet axis. Spreading jets are expected to generate a much shallower zone of silence as seen in measured data.

The presence of residual shock noise—a noise generation mechanism not modeled in the code—is also quite visible in the experimental spectra. This accounts for some of the “underprediction” at the upstream angles, meaning that in reality the mixing noise predictions may be quite better than what data projects at such angles. Still, the aft angle predictions were not as good.

In carrying out the source volume integration in axisymmetric jets, JeNo considers the source as a superposition of ring volume elements. Radial distributions of the axial mean velocity and temperature are used to evaluate the Green's function at each frequency. As pointed out in Section 8.2.2.2, rather than solving for the five components of a vector Green's function, propagation effects in nonaxisymmetric geometries are treated with a more robust approach using either the line-of-sight or the line-of-source method. These methods, also referred to as 2.5-dimensional approximation, allow for the azimuthal variation of the source strength in such jets; however, the Green's function is evaluated along a user-defined azimuthal plane.

A single-stream chevron nozzle represents the first example of such nonaxisymmetric nozzle concepts. Figure 8.54 shows the power spectral density (PSD) in an SMC001 nozzle with six chevrons (see Figure 8.12 for geometry). JeNo predictions in a 2.5-dimensional approximation are shown with the line of sight placed either at the chevron tip or its valley. The spectra are compared with both measured data and prediction for a base axisymmetric geometry (no chevrons). The differences between the two lines of sight emerge primarily at aft angles. At 150°, significantly more high frequency noise is projected when the line of sight is placed at the chevron tip compared to the chevron valley. The reality may be somewhere between these two extremes. This is illustrated in Figure 8.55 when the 2.5-dimensional concept is carried out using line-of-source model. Such an approximation removes any azimuthal dependency from the final result and resembles some form of azimuthal averaging of the sound field. Measurements show

that the sound field for a six-chevron nozzle is nearly axisymmetric.

Computational study of the offset nozzle designs (Ref. 36), and experimental results (Refs. 37 and 38), indicate that modifications in the fan stream could provide noise benefits on one side of a separate flow jet at the expense of increased noise on the opposite side. A qualitative assessment of such concepts is shown here using the 2.5-dimensional approximation and the line-of-sight method. Figure 8.56 shows JeNo predictions for the S-duct concept. Lossless spectra are shown on an arc at 24.46 m (80.24 ft) at 90° and 150° inlet angles, respectively, with the line-of-sight placed either along the thick or thin sides of the fan flow. Experimental data are also shown separately in Figure 8.56(b). Measures of noise benefit (reduction), or penalty (increase) at 150° between the base geometry and the thick side of S-duct concept are shown separately in Figure 8.57(a) and (b) as the decibel difference between the thick side spectrum and the baseline, axisymmetric spectrum for the predictions and the experimental data, respectively. A positive delta dB indicates noise penalty. The task of error analysis may be accomplished if the error band is defined as the difference between the trends suggested by Figure 8.57(a) and (b), as seen in part (c). A similar error band is shown at 90° in part (d).

An assessment of the fan-wedge concept is presented in Figure 8.58. In this exercise, the spectra are shown along the opposing sides using two lines of sight separated by 180°, and are compared with the base geometry operating at a similar condition. Again 90° and 150° power spectral density predictions are presented and similar data illustrations are also provided for comparison. The delta dB difference in noise between the two sides of the fan-wedge concept at 150° inlet angle is shown in Figure 8.59(a), with similar representation of the experimental data in Figure 8.59(b). An error band that displays the difference between the two is shown in Figure 8.59(c), and an additional error band at 90° inlet angle is also seen in Figure 8.59(d).

A realistic assessment of the three-dimensional effects, as indicated earlier, requires a full three-dimensional propagation Green's function. The present exercise shows that the 2.5-dimensional concept and extension of the axisymmetric Green's function to three-dimensional jets is rather successful in capturing the observed trends.

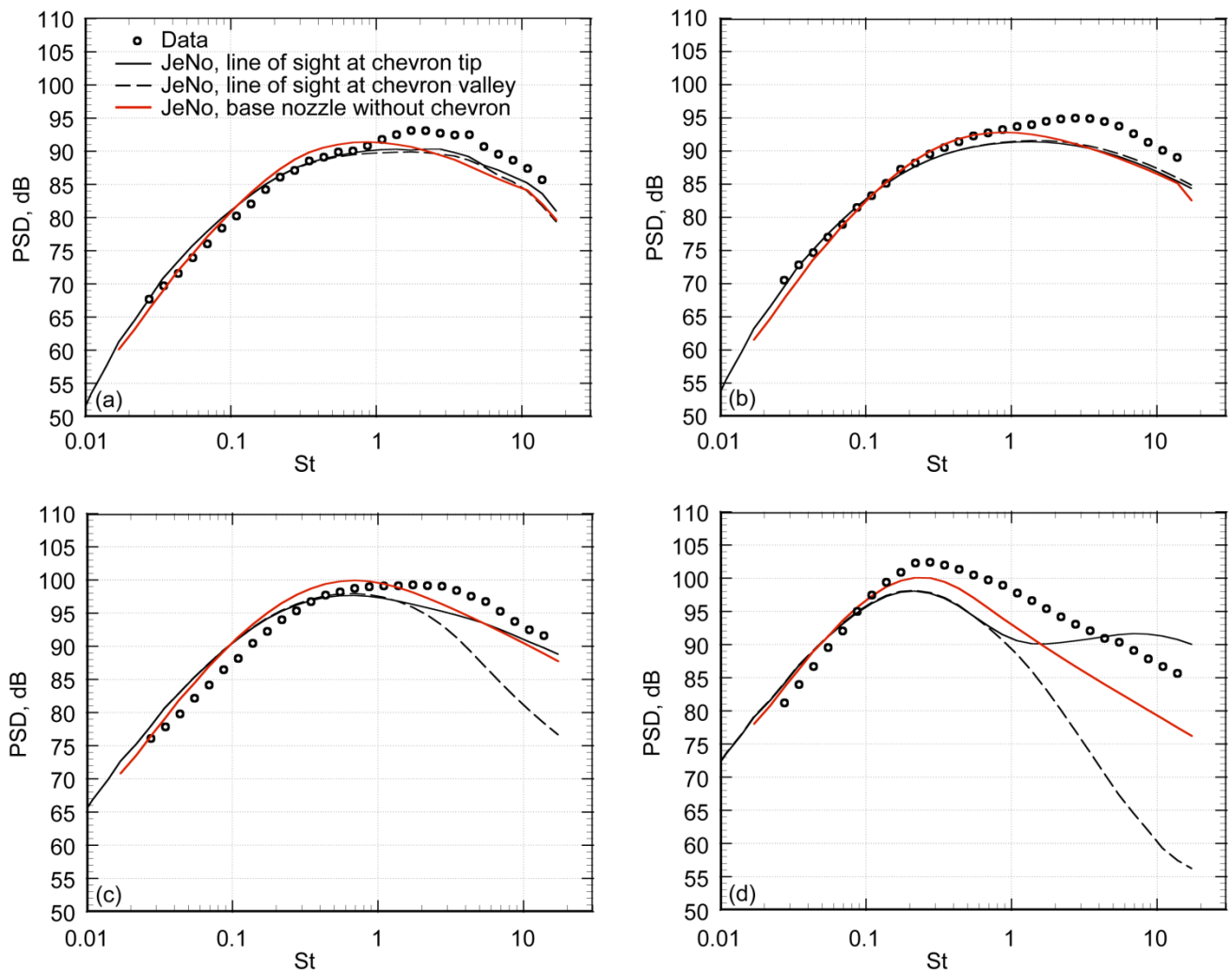


Figure 8.54.—Comparison of lossless power spectral density (PSD) of jet noise versus Strouhal number St at different inlet angles θ on a $40D$ arc. NATR data and JeNo v1.0 predictions. (a) $\theta = 60^\circ$. (b) $\theta = 90^\circ$. (c) $\theta = 130^\circ$. (d) $\theta = 150^\circ$.

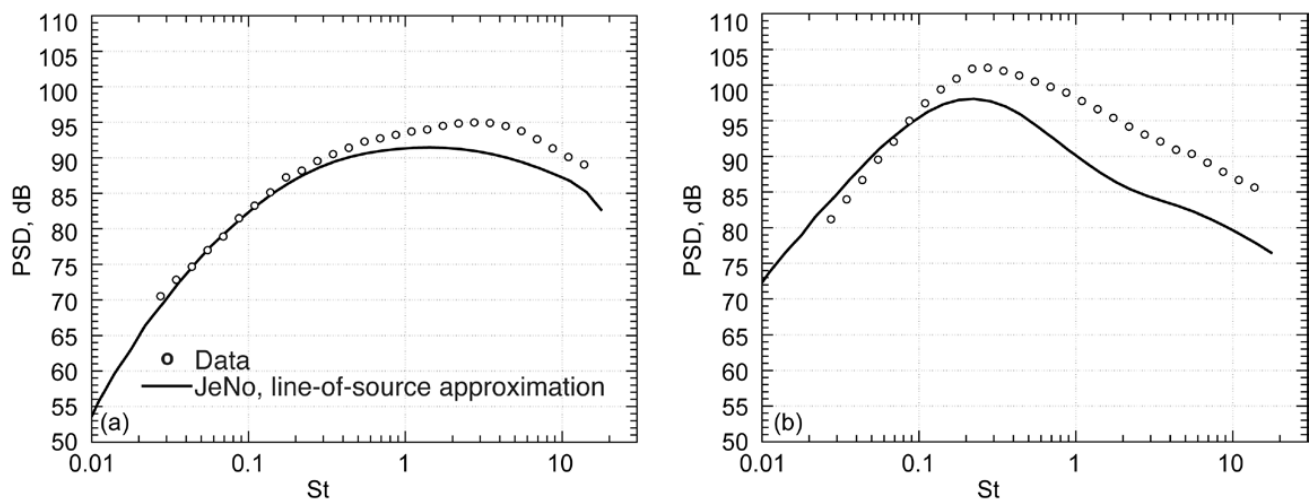


Figure 8.55.—Comparison of lossless power spectral density (PSD) for offset nozzle versus Strouhal number St at different inlet angles θ on a $40D$ arc. NATR data and JeNo v1.0 predictions. (a) $\theta = 90^\circ$. (b) $\theta = 150^\circ$.

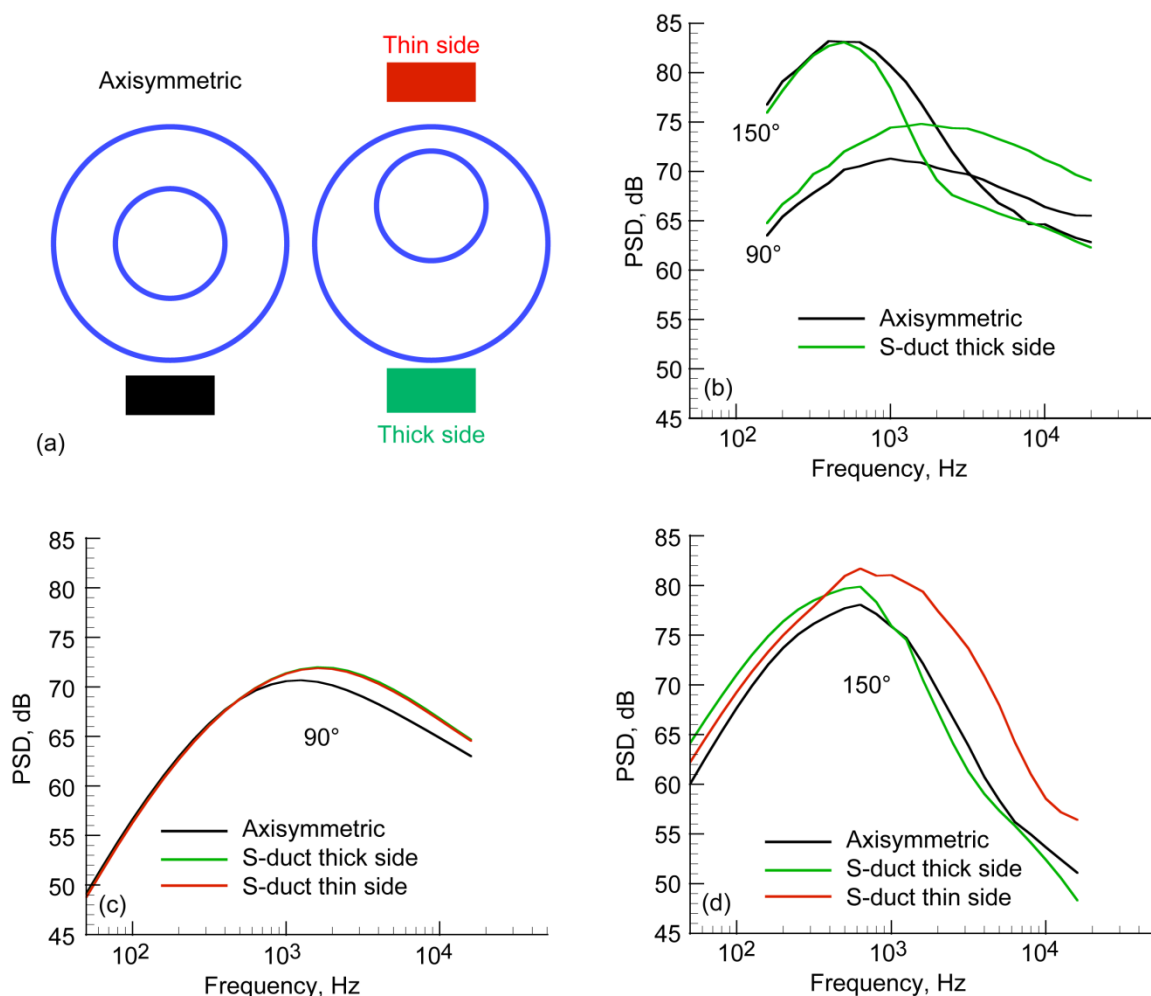


Figure 8.56.—Comparison of lossless power spectral density (PSD) for offset S-duct nozzle and axisymmetric geometry (see Table 8.6 and Figure 8.40(b)) at different inlet angles θ on $40D$ arc. (a) Nozzle geometries. (b) NATR experimental data, $\theta = 90^\circ$ and 150° . (c) JeNo v1.0 predictions at 90° using 2.5-dimensional approximation with line-of-sight method. (d) JeNo v1.0 predictions at 150° using 2.5-dimensional approximation with line-of-sight method.

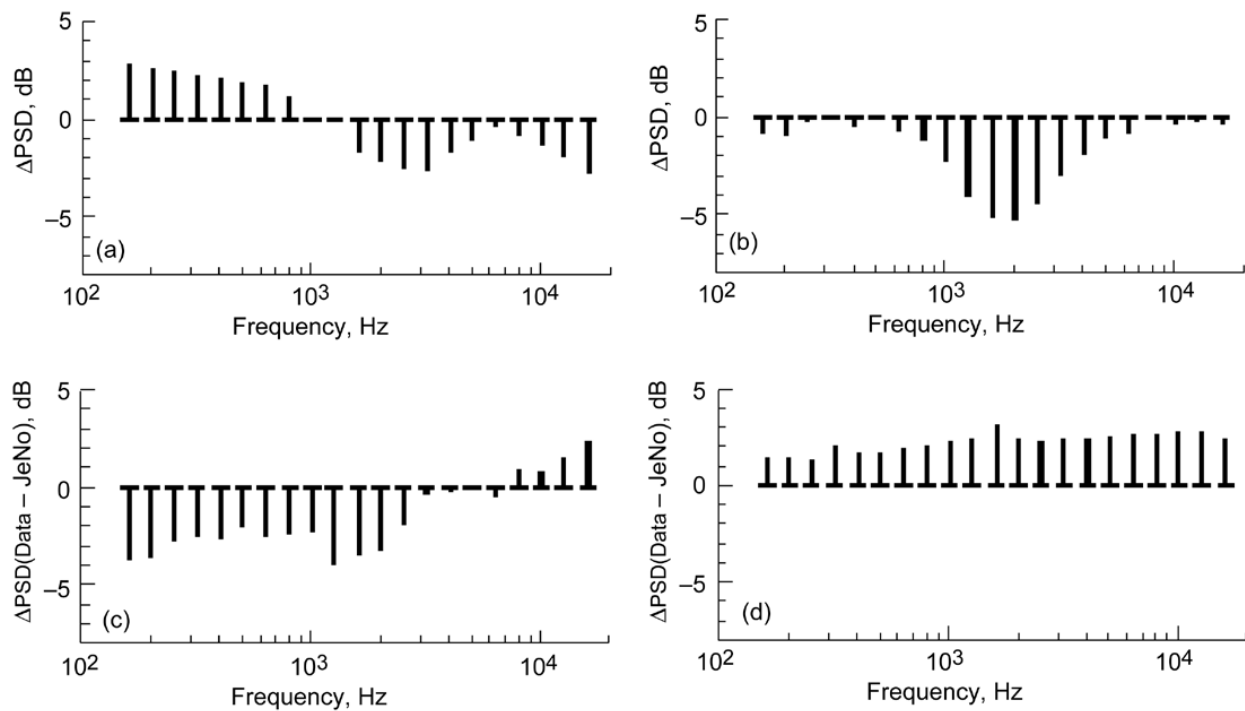


Figure 8.57.—Difference Δ between power spectral density (PSD) measured on thick side of S-duct nozzle and axisymmetric nozzle. (a) JeNo v1.0 prediction at inlet angle $\theta = 150^\circ$. (b) NATR experimental data at $\theta = 150^\circ$. (c) Error estimate at $\theta = 150^\circ$; difference between NATR data and prediction. (d) Error estimate at $\theta = 90^\circ$.

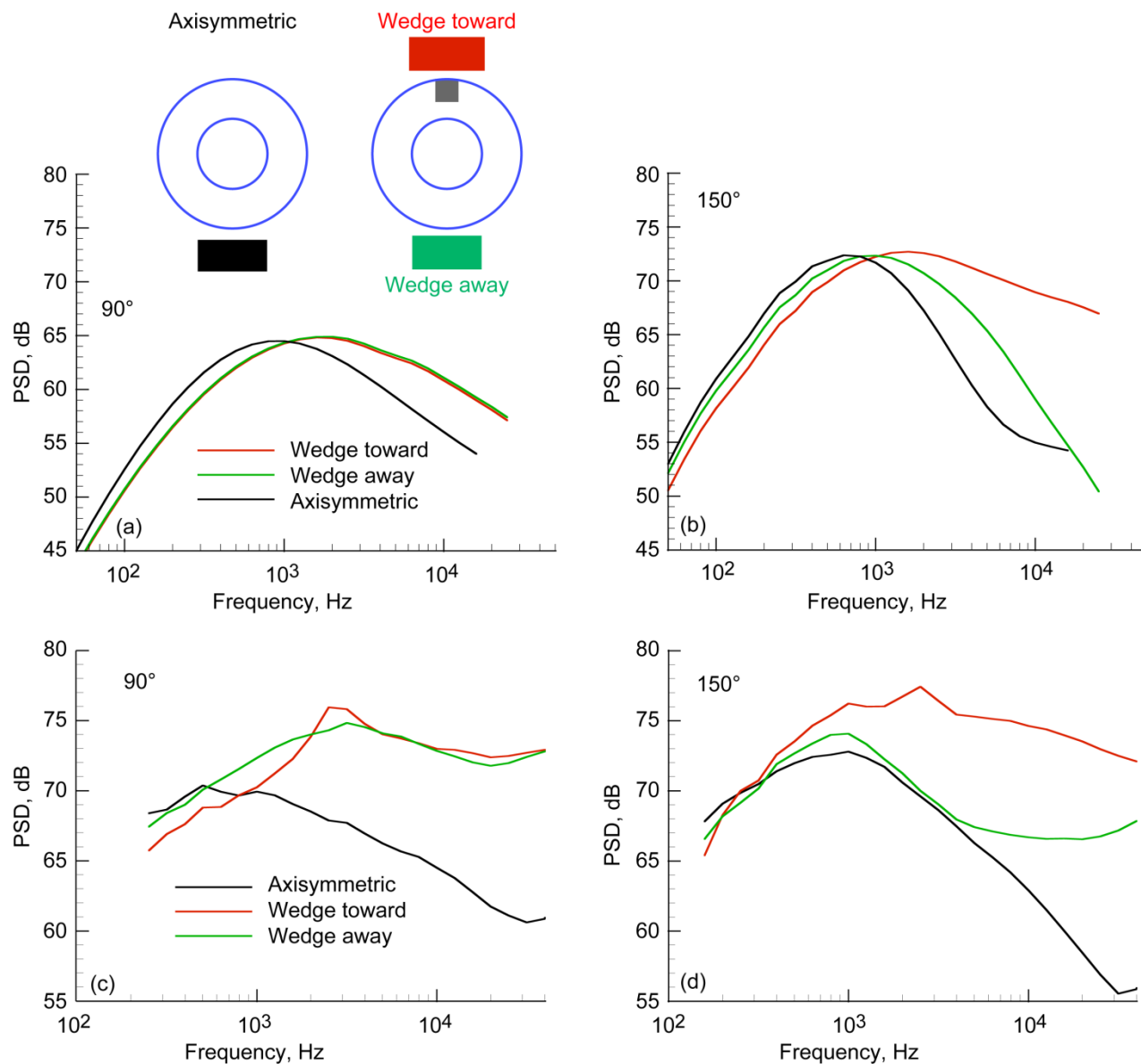


Figure 8.58.—Lossless power spectral density (PSD) for offset fan-wedge nozzle and axisymmetric geometry (see Table 8.6 and Figure 8.40(a)) at different inlet angles θ on 24.46-m (80.24-ft) arc. (a) Nozzle geometries. (b) NATR experimental data. (c) JeNo v1.0 predictions at $\theta = 90^\circ$ using 2.5-dimensional approximation with line-of-sight method. (d) JeNo v1.0 predictions at $\theta = 150^\circ$ using 2.5-dimensional approximation with line-of-sight method.

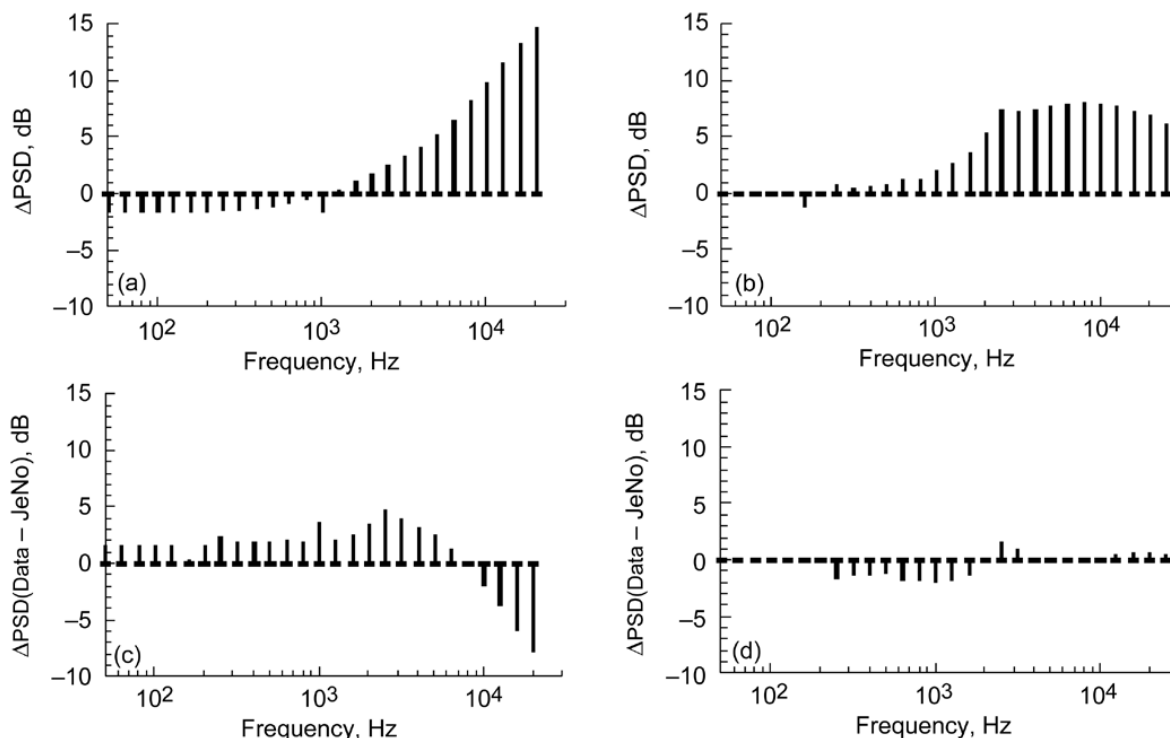


Figure 8.59.—Difference Δ between power spectral density (PSD) measured on thick (quiet) and thin (noisy) sides of fan-wedge nozzle and axisymmetric nozzle. (a) JeNo v1.0 prediction at inlet angle $\theta = 150^\circ$. (b) NATR experimental data at $\theta = 150^\circ$. (c) Error estimate at $\theta = 150^\circ$; difference between NATR data and prediction. (d) Error estimate at $\theta = 90^\circ$.

8.17 Conclusions

Neither empirical nor acoustic analogy models predicted overall acoustic power of subsonic axisymmetric nozzle flows within experimental uncertainty for all cases examined in this assessment exercise. The empirical code ANOPP did not predict spectral directivity within experimental uncertainty for most cases, and displayed systematic errors leading to spectral disagreement at high frequencies, especially at downstream angles. Sample-case EPNL predictions were off by several decibels, an intolerable situation in practice where EPNL values need to be known to within fractions of a decibel. However, for axisymmetric jets, the ANOPP code was more robust than the acoustic analogy codes, and displayed a consistent level of error—slightly overpredicting the peak and displaying an erroneously large amplitude at high frequency near the Strouhal number 10.0—for a broad range of jet flows. At 150° the prediction was very good except for this high-frequency component.

The acoustic analogy code JeNo v1.0 predicted noise spectral directivity to within experimental uncertainty for subsonic cold jets, but deviated when either jet speed approached the speed of sound or the jet temperature was elevated. Also, JeNo did capture the impact of nonaxisymmetric jets with azimuthal periodicity greater than 4, but did not capture the azimuthal

directivity effect from low-order asymmetries such as offset nozzles.

The acoustic analogy code Jet3D was able to predict the noise and spectral content from a high-speed hot jet at forward and side angles, but incorrectly predicted noise and peak frequency at angles in the aft arc. Jet3D did not predict cold jets very well, missing the spectral shape, peak frequency, and amplitude.

8.17.1 Empirical Code

1. The Stone Jet Noise module (ST2JET) contained within ANOPP was applicable to a wide range of flow conditions, predicting OASPLs only slightly outside of experimental uncertainty for most axisymmetric jets.

2. The error in the prediction first became apparent in OASPL directivity, where the aft angle noise was predicted to change more radically with angle than the data supports. Spectrally, the main problem was with a predicted high-frequency noise component, the “outer stream mixing noise” from the ambient-bypass mixing region, which caused a high-frequency hump in the spectra not observed in the data.

3. The model for predicting the impact of chevrons did not successfully predict the noise produced by an external chevron nozzle, overpredicting the noise reduction by 15 dB or so.

8.17.2 Acoustic Analogy Codes

Both acoustic analogy codes suffered from their inability to predict the jet mixing noise consistently across heated and unheated jet conditions.

8.17.2.1 JeNo v1.0

1. The JeNo version 1.0 code predicted noise from cold, shock-free jets within experimental uncertainty at both broadside and aft angles.

2. As jet speed increased past the sonic speed, the broadside spectra maintained their accuracy; however, the aft angle spectra displayed inaccurate peak frequency and amplitude.

3. As jet temperature increased, underpredictions in noise amplitude emerged at both broadside and aft angles. Since JeNo v1.0 does not contain enthalpic sources, this was expected.

4. Predicted far-field noise from nonaxisymmetric nozzles with azimuthal-mode order greater than 4 was axisymmetric and consistent with data. Jets with low-order asymmetries and nonaxisymmetric noise field, such as offset streams, pylons, or rectangular nozzles were not predicted well. Ideally, a full three-dimensional calculation of the Green's function is required in three-dimensional jets. This capability was not available in JeNo v1.0.

8.17.2.2 Jet3D

1. The Jet3D code predicted noise for cold, shock-free jets that differed from the experimental data by 5 dB or more in peak amplitude at broadside angles. Spectral shape was grossly incorrect for these cases.

2. As temperature increased, overpredictions diminished to an average of 5 dB above measurements, but the peak frequency was off by a significant margin.

3. Jet3D did predict jet noise within experimental uncertainty for high-speed hot jets at broadside angles. At a total temperature ratio above 2 and jet velocity exceeding twice the ambient sound speed, the broadside spectra were within experimental uncertainty, although aft angle noise amplitudes were in error by 10 dB or more.

8.17.3 Recommendations

1. The empirical jet noise prediction code ST2JET within ANOPP Level 25 should be used for high-speed, system-level design studies with the understanding that it produces results only accurate to within 2 decibels in EPNL. The ANOPP code could be improved using the current database if the predicted noise accuracy is not satisfactory for system studies.

2. Both acoustic analogy codes JeNo v1.0 and Jet3D need to include additional source terms associated with unsteady temperature (i.e., enthalpy related sources).

3. Both acoustic analogy codes—especially Jet3D—need improved directivity factors. To improve JeNo v1.0 it may be necessary to examine the significance of source noncompactness in high-speed jets. Relaxing the parallel flow assumption in favor of a spreading jet could also improve predictions at small aft angles.

4. A three-dimensional vector Green's function is required as a propagator to correctly predict the propagation of sound from unconventional nozzle geometries.

Appendix A.—Nomenclature

A.1 Acronyms

AAPL	Aero-Acoustic Propulsion Laboratory
ANOPP	Aircraft Noise Prediction Program
B&K	Brüel & Kjær
BBSN	broadband shock-associated noise
BPR	bypass ratio
C-D	convergent-divergent
CFD	computational fluid dynamics
DADS	digital acoustic data system
EPNL	effective perceived noise level
HFJER	High Flow Jet Exit Rig
LDV	laser Doppler velocimetry
LES	large eddy simulations
NATR	Nozzle Acoustic Test Rig
NPR	nozzle pressure ratio
OASPL	overall sound pressure level
PCI	peripheral component interconnect
PIV	particle image velocimetry
RANS	Reynolds-averaged Navier-Stokes
rms	root-mean-squared
SHJAR	Small Hot Jet Acoustic Rig
SPL	sound pressure level
SST	shear stress transport
TKE	turbulent kinetic energy
TRL	technology readiness level
TRPIV	time-resolved PIV

A.2 Symbols

c	speed of sound
D	nozzle diameter
f	frequency
G	Green's function
h	enthalpy
i	unit imaginary number
k	turbulent kinetic energy
L	linear differential operator, Eq. (8.8)
M	Mach number
m	azimuthal base periodicity
N	number of polar angles
P	Fourier transform of p
p	pressure
q	source term
R	distance between source and receiver

r	radial coordinate
St	Strouhal number
T	temperature
\mathcal{T}	large period of integration
t	time
T_{ij}	Lighthill stress tensor
U	fully expanded jet velocity
u, v, w	components of flow velocity vector
x	axial direction
\mathbf{x}	observer spatial position vector
\mathbf{y}	source spatial position vector
γ	specific heat ratio of air
Δ	error (difference between measurements and predictions)
δ	Dirac delta function
δ_{ij}	Kronecker delta
ε	turbulent kinetic energy dissipation rate
θ	polar (or inlet) angle
μ	average error, Eq (8.13a)
Π	pressure variable in Eq. (8.7)
ρ	fluid density
σ_{ij}	viscous stress tensor
σ^2	variance, Eq. (8.13b)
τ	time of emission
ϕ	azimuthal angle
ω	radian frequency
$\overline{(\quad)}$	mean value

Subscripts:

a	acoustic
ANOPP	predicted with ANOPP code
d	design
expt	experimental value
fl	flight
o	mean
r	ratio
s	static
t	total
∞	ambient

Superscripts:

s	source
$'$	fluctuating

Appendix B.—Jet Configurations Tested in NASA-Sponsored Test Programs

Details of the operating conditions for nine test categories are identified as configurations A through I. Tests were carried out at NASA Glenn Research Center over a period of four years (2004 to 2007), and extensive aerodynamic and noise data have been compiled to guide model development and validation efforts.

Nomenclature for the table:

BPR	bypass ratio
M	ideally expanded Mach number; for dual stream flows, it is the higher M
Axial geometry	indicates if nozzle was convergent or convergent-divergent (C-D) or if it was internally or externally mixed

Azimuthal geometry	azimuthal base periodicity, indicates nozzle was axisymmetric ($m = 0$) or had lobes or chevrons
M_a	acoustic Mach number U/c_∞
$T_{s,r}$	static temperature ratio T_s/T_∞
$T_{t,r}$	total temperature ratio T_t/T_∞ ; for dual stream cases
M_{fl}	flight Mach number
nozid	nozzle identification

TABLE 8.7.—TEST CASE IDENTIFIER WITHIN EACH CONFIGURATION
(a) Configuration A: BPR = 0, convergent axisymmetric nozzles, hot subsonic flow^a

Case	M	Geometry		M_a	$T_{s,r}$	M_{fl}	nozid
		Axial	Azimuthal				
001	0.35	Convergent	$m = 0$	0.350	0.980	0	SMC000
002	0.41			0.401	0.972	0	SMC000
003	0.51			0.500	0.955	0	SMC000
004	0.62			0.601	0.932	0	SMC000
005	0.74			0.701	0.906	0	SMC000
006	0.85			0.799	0.877	0	SMC000
007	0.98			0.902	0.842	0	SMC000
008	0.80			0.798	1.001	0	SMC000
009	0.90			0.897	0.997	0	SMC000
010	0.55			0.599	1.202	0	SMC000
011	0.64			0.701	1.198	0	SMC000
012	0.73			0.799	1.204	0	SMC000
013	0.82			0.899	1.203	0	SMC000
014	0.91			1.001	1.203	0	SMC000
015	0.33			0.399	1.431	0	SMC000
016	0.42			0.502	1.430	0	SMC000
017	0.50			0.599	1.430	0	SMC000
018	0.59			0.698	1.428	0	SMC000
019	0.67			0.802	1.428	0	SMC000
020	0.75			0.897	1.428	0	SMC000
021	0.99			1.185	1.426	0	SMC000
022	0.37			0.492	1.767	0	SMC000
023	0.53			0.698	1.764	0	SMC000
024	0.61			0.801	1.768	0	SMC000
025	0.68			0.901	1.770	0	SMC000
026	0.89			1.184	1.771	0	SMC000
027	1.01			1.330	1.759	0	SMC000
028	0.47			0.699	2.267	0	SMC000
029	0.54			0.801	2.272	0	SMC000
030	0.60			0.899	2.269	0	SMC000
031	0.78			1.158	2.270	0	SMC000
032	0.89			1.329	2.263	0	SMC000
033	0.99			1.483	2.277	0	SMC000
034	0.30			0.484	2.624	0	SMC000
035	0.43			0.700	2.707	0	SMC000
036	0.49			0.800	2.699	0	SMC000
037	0.56			0.901	2.702	0	SMC000
038	0.73			1.187	2.695	0	SMC000
039	0.82			1.329	2.704	0	SMC000
040	0.92			1.483	2.703	0	SMC000

^aSee the beginning of this appendix for definitions of table columns.

TABLE 8.7.—Continued.
(b) Configuration B: BPR = 0, convergent chevron nozzles, hot subsonic flow^a

Case	M	Geometry		M_a	$T_{s,r}$	M_{fl}	nozid
		Axial	Azimuthal				
041	0.50	Convergent	$m = 6$	0.499	0.958	0	SMC001
042	0.972			0.902	0.837	0	SMC001
043	0.668			0.881	1.752	0	SMC001
044	1.006			1.320	1.734	0	SMC001
045	0.551			0.883	2.639	0	SMC001
046	0.827			1.308	2.576	0	SMC001
047	0.506	Convergent	$m = 6$	0.494	0.953	0	SMC005
048	0.972			0.893	0.844	0	SMC005
049	0.674			0.884	1.740	0	SMC005
050	1.008			1.325	1.743	0	SMC005
051	0.549			0.879	2.649	0	SMC005
052	0.823			1.304	2.585	0	SMC005
053	0.977	Convergent	$m = 6$	0.898	0.844	0	SMC006
054	0.673			0.885	1.745	0	SMC006
055	1.006			1.320	1.736	0	SMC006
056	0.555			0.891	2.651	0	SMC006
057	0.828			1.309	2.571	0	SMC006

^aSee the beginning of this appendix for definitions of table columns.

TABLE 8.7.—Continued.

(c) Configuration C: BPR = 0, convergent-divergent axisymmetric nozzles, hot supersonic flow^a

Case	M	Geometry		M_a	$T_{s,r}$	M_{fl}	nozid
		Axial	Azimuthal				
058	1.174	C-D	$m = 0$	1.178	1.007	0	SMC014
059	1.172			1.047	0.797	0	SMC014
060	1.170			1.171	1.003	0	SMC014
061	1.171			1.401	1.436	0	SMC014
062	1.172			1.469	1.578	0	SMC014
063	1.177			1.554	1.759	0	SMC014
064	1.175			1.663	2.032	0	SMC014
065	1.170			1.746	2.271	0	SMC014
066	1.169			1.828	2.509	0	SMC014
067	1.174			1.897	2.693	0	SMC014
068	1.394	C-D	$m = 0$	1.191	0.730	0	SMC015
069	1.381			1.381	0.998	0	SMC015
070	1.392			1.489	1.145	0	SMC015
071	1.384			1.826	1.757	0	SMC015
072	1.384			2.058	2.262	0	SMC015
073	1.384			1.652	1.430	0	SMC015
074	1.395			2.132	2.397	0	SMC015
075	1.497	C-D	$m = 0$	1.251	0.699	0	SMC016
076	1.484			1.485	1.002	0	SMC016
077	1.488			1.657	1.242	0	SMC016
078	1.482			1.773	1.436	0	SMC016
079	1.501			1.841	1.510	0	SMC016
080	1.484			1.966	1.771	0	SMC016
081	1.488			2.134	2.090	0	SMC016
082	1.538			2.268	2.218	0	SMC016
083	1.659	C-D	$m = 0$	1.342	0.654	0	SMC017
084	1.666			1.484	0.793	0	SMC017
085	1.658			1.657	0.999	0	SMC017
086	1.659			1.983	1.433	0	SMC017
087	1.656			2.191	1.767	0	SMC017
088	1.789	C-D	$m = 0$	2.136	1.429	0	SMC018
089	1.786			2.359	1.760	0	SMC018
090	1.784			1.403	0.619	0	SMC018
091	1.785			1.403	0.618	0	SMC018
092	1.779			1.778	0.999	0	SMC018

^aSee the beginning of this appendix for definitions of table columns.

TABLE 8.7.—Continued.

(d) Configuration D: BPR = 0.2, axisymmetric internally mixed nozzles, hot flow^a
 [Coplanar and fully mixed approximations.]

Case	M	Geometry		Core		Bypass		M_{β}	nozid
		Axial	Azimuthal	M_a	$T_{t,r}$	M_a	$T_{t,r}$		
093	0.6	Internal splitter, convergent	$m = 0$	0.902	2.450	0.607	1.088	0.0	C4S1PE1
094	0.6			1.001	3.038	0.611	1.099	0.0	C4S1PE1
095	0.8			0.898	1.433	0.758	1.010	0.0	C4S1PE1
096	0.8			1.197	2.576	0.780	1.072	0.0	C4S1PE1
097	0.9			0.834	1.002	0.835	1.008	0.0	C4S1PE1
098	0.9			1.197	2.078	0.853	1.045	0.0	C4S1PE1
099	0.9			1.498	3.293	0.874	1.094	0.0	C4S1PE1
100	1			0.906	0.988	0.910	0.995	0.0	C4S1PE1
101	1			1.000	1.200	0.979	1.149	0.0	C4S1PE1
102	1			1.500	2.724	0.944	1.068	0.0	C4S1PE1
103	1.05			1.051	1.221	1.031	1.173	0.0	C4S1PE1
104	1.05			1.184	1.546	0.955	1.006	0.0	C4S1PE1
105	1.18			1.400	1.748	1.071	1.023	0.0	C4S1PE1
106	1.18			1.601	2.296	1.083	1.044	0.0	C4S1PE1
107	1.18			1.801	2.910	1.094	1.071	0.0	C4S1PE1
108	1.18			2.000	3.592	1.110	1.102	0.0	C4S1PE1
109	1.4			1.400	1.392	1.188	1.003	0.0	C4S1PE1
110	1.5			1.503	1.455	1.262	1.026	0.0	C4S1PE1
111	1.5			1.799	2.087	1.268	1.035	0.0	C4S1PE1
112	1.5			2.004	2.578	1.274	1.044	0.0	C4S1PE1
113	1.6			1.603	1.513	1.310	1.013	0.0	C4S1PE1
114	1.6			1.803	1.916	1.322	1.031	0.0	C4S1PE1
115	1.6			2.406	3.393	1.346	1.065	0.0	C4S1PE1
116	1.8			1.801	1.650	1.415	1.017	0.0	C4S1PE1
117	1.8			2.402	2.917	1.441	1.053	0.0	C4S1PE1
118	2			1.999	1.794	1.511	1.026	0.0	C4S1PE1
119	2			2.401	2.581	1.523	1.042	0.0	C4S1PE1
120	1.18	Internal splitter, C-D	$m = 0$	1.401	1.750	1.061	1.004	0.0	M2S1PE2
121	1.18			1.603	2.291	1.067	1.016	0.0	M2S1PE2
122	1.18			1.808	2.916	1.073	1.030	0.0	M2S1PE2
123	1.4			1.399	1.397	1.176	0.987	0.0	M4S1PE2
124	1.5			1.504	1.463	1.236	0.988	0.0	M5S1PE2
125	1.5			1.804	2.097	1.245	1.002	0.0	M5S1PE2
126	1.5			2.008	2.595	1.257	1.019	0.0	M5S1PE2
127	1.6			1.601	1.516	1.286	0.979	0.0	M6S1PE2
128	1.6			1.805	1.925	1.294	0.989	0.0	M6S1PE2
129	1.6			2.407	3.398	1.334	1.054	0.0	M6S1PE2
130	1.8			1.801	1.647	1.421	1.027	0.0	M8S1PE2
131	1.8			2.402	2.913	1.441	1.055	0.0	M8S1PE2

^aSee the beginning of this appendix for definitions of table columns.

TABLE 8.7.—Continued.
(e) Configuration E: BPR = 1, axisymmetric internally mixed nozzles, hot flow^a
[Coplanar and fully mixed approximations.]

Case	M	Geometry		Core		Bypass		M_{fl}	nozid
		Axial	Azimuthal	M_a	$T_{t,r}$	M_a	$T_{t,r}$		
132	0.6	Internal splitter, convergent	$m = 0$	0.902	2.449	0.576	1.001	0.0	C4S2PE1
133	0.6			1.003	3.052	0.582	1.011	0.0	C4S2PE1
134	0.8			0.900	1.429	0.748	0.985	0.0	C4S2PE1
135	0.8			1.201	2.573	0.748	0.992	0.0	C4S2PE1
136	0.9			0.829	0.983	0.824	0.977	0.0	C4S2PE1
137	0.9			1.203	2.078	0.829	0.991	0.0	C4S2PE1
138	0.9			1.508	3.293	0.839	1.009	0.0	C4S2PE1
139	1			0.902	0.978	0.899	0.976	0.0	C4S2PE1
140	1			0.998	1.195	1.003	1.209	0.0	C4S2PE1
141	1			1.503	2.726	0.909	0.995	0.0	C4S2PE1
142	1.05			0.939	0.978	0.937	0.976	0.0	C4S2PE1
143	1.05			1.180	1.540	0.948	0.990	0.0	C4S2PE1
144	1.18			1.605	2.300	1.070	1.022	0.0	C4S2PE1
145	1.18			1.805	2.910	1.068	1.022	0.0	C4S2PE1
146	1.4			1.404	1.397	1.191	1.006	0.0	C4S2PE1
147	1.5			1.504	1.456	1.252	1.012	0.0	C4S2PE1
148	1.5			1.799	2.084	1.241	0.991	0.0	C4S2PE1
149	1.5			2.000	2.572	1.256	1.014	0.0	C4S2PE1
150	1.6			1.604	1.515	1.312	1.013	0.0	C4S2PE1
151	1.6			1.803	1.916	1.298	0.992	0.0	C4S2PE1
152	1.6			2.406	3.384	1.339	1.055	0.0	C4S2PE1
153	1.8			1.805	1.655	1.420	1.026	0.0	C4S2PE1
154	1.8			2.403	2.911	1.442	1.056	0.0	C4S2PE1
155	2			2.006	1.808	1.521	1.041	0.0	C4S2PE1
156	2			2.401	2.581	1.530	1.053	0.0	C4S2PE1
157	1.18	Internal splitter, C-D	$m = 0$	1.404	1.754	1.057	0.995	0.0	M2S2PE2
158	1.18			1.605	2.305	1.059	1.003	0.0	M2S2PE2
159	1.18			1.806	2.919	1.063	1.009	0.0	M2S2PE2
160	1.4			1.402	1.402	1.184	1.000	0.0	M4S2PE2
161	1.5			1.502	1.461	1.240	0.995	0.0	M5S2PE2
162	1.5			1.800	2.094	1.244	1.003	0.0	M5S2PE2
163	1.5			2.003	2.589	1.248	1.009	0.0	M5S2PE2
164	2			2.003	1.802	1.496	1.006	0.0	MTS2PE2
165	2			2.403	2.580	1.500	1.012	0.0	MTS2PE2

^aSee the beginning of this appendix for definitions of table columns.

TABLE 8.7.—Continued.
 (f) Configuration F: BPR = 3, convergent axisymmetric internally mixed nozzles, hot flow^a
 [Coplanar and fully mixed approximations.]

Case	M	Geometry		Core		Bypass		M_{fl}	nozid
		Axial	Azimuthal	M_a	$T_{t,r}$	M_a	$T_{t,r}$		
166	0.6	Internal splitter	$m = 0$	0.896	2.439	0.573	0.977	0.0	C4S3PE1
167	0.6			1.000	3.057	0.579	0.992	0.0	C4S3PE1
168	0.8			0.902	1.435	0.760	1.024	0.0	C4S3PE1
169	0.8			1.194	2.568	0.746	0.981	0.0	C4S3PE1
170	0.9			0.857	1.057	0.835	0.998	0.0	C4S3PE1
171	0.9			1.202	2.082	0.826	0.977	0.0	C4S3PE1
172	1			0.925	1.031	0.912	0.999	0.0	C4S3PE1
173	1			1.497	2.726	0.907	0.983	0.0	C4S3PE1
174	1.05			0.960	1.025	0.951	0.999	0.0	C4S3PE1
175	1.05			1.183	1.541	0.940	0.977	0.0	C4S3PE1
176	1.18			1.603	2.290	1.071	1.023	0.0	C4S3PE1
177	1.18			1.801	2.903	1.072	1.024	0.0	C4S3PE1
178	1.4			1.399	1.389	1.176	0.982	0.0	C4S3PE1
179	1.5			1.502	1.452	1.237	0.984	0.0	C4S3PE1
180	1.5			1.805	2.095	1.262	1.025	0.0	C4S3PE1
181	1.5			2.000	2.573	1.263	1.028	0.0	C4S3PE1
182	1.6			1.601	1.515	1.295	0.990	0.0	C4S3PE1
183	1.6			1.804	1.919	1.322	1.032	0.0	C4S3PE1
184	1.6			2.402	3.377	1.332	1.046	0.0	C4S3PE1
185	1.8			1.800	1.649	1.400	0.998	0.0	C4S3PE1
186	1.8			2.412	2.931	1.410	1.010	0.0	C4S3PE1
187	2			1.987	1.805	1.483	1.009	0.0	C4S3PE1
188	2			2.385	2.589	1.487	1.012	0.0	C4S3PE1

^aSee the beginning of this appendix for definitions of table columns.

TABLE 8.7.—Continued.
(g) Configuration G: BPR = 5, convergent internally or externally mixed nozzles, hot flow^a

Case	M	Geometry		Core		Bypass		M _{fl}	nozid
		Axial	Azimuthal	M _a	T _{t,r}	M _a	T _{t,r}		
Externally mixed									
189	0.80	Separate flow	m = 0	0.956	2.327	0.791	1.112	0.0	PAA5
190	0.87			1.120	2.482	0.871	1.146	0.0	PAA5
191	0.93			1.265	2.663	0.935	1.182	0.0	PAA5
192	0.80			0.959	2.335	0.790	1.113	0.1	PAA5
193	0.87			1.119	2.481	0.866	1.142	0.1	PAA5
194	0.93			1.264	2.662	0.938	1.182	0.1	PAA5
195	0.88			1.119	2.506	0.878	1.161	0.2	PAA5
196	0.94			1.272	2.676	0.940	1.190	0.2	PAA5
197	0.94			1.268	2.670	0.938	1.186	0.3	PAA5
Coplanar and fully mixed approximations									
198	0.6	Internal splitter	m = 0	0.886	2.691	0.674	1.258	0.0	5000.00
199				1.343	3.119	0.885	1.250	0.0	5000.00
200				1.637	3.543	0.984	1.302	0.0	5000.00
201				1.248	3.013	0.904	1.249	0.0	5000.00
202				1.401	3.176	0.872	1.249	0.0	5000.00
203				0.894	2.687	0.675	1.254	0.3	5000.00
204				1.334	3.055	0.879	1.230	0.3	5000.00
205				1.637	3.548	0.987	1.302	0.3	5000.00
206				1.245	3.015	0.906	1.254	0.3	5000.00
207				1.530	3.322	0.993	1.252	0.3	5000.00
208				1.407	3.184	0.878	1.256	0.3	5000.00
209		Internal chevron	m = 8	1.662	3.487	0.977	1.254	0.3	5000.00
210				0.913	2.790	0.690	1.309	0.0	5001.04
211				1.614	3.455	0.973	1.270	0.0	5001.04
212				0.908	2.790	0.687	1.306	0.3	5001.04
213				1.375	3.260	0.906	1.309	0.3	5001.04
214				1.651	3.596	0.992	1.317	0.3	5001.04
215				1.271	3.132	0.926	1.309	0.3	5001.04
216				1.406	3.202	0.878	1.260	0.3	5001.04
217				Internal deep scalloped lobes	m = 20	0.901	2.765	0.682	1.294
218		1.637	3.546			0.985	1.300	0.0	5002.02
219		0.906	2.762			0.681	1.290	0.3	5002.02
220		1.366	3.214			0.902	1.294	0.3	5002.02
221		1.633	3.540			0.986	1.303	0.3	5002.02
222		1.269	3.111			0.919	1.294	0.3	5002.02
223		1.429	3.297			0.893	1.297	0.3	5002.02
Externally mixed									
224		Separate flow	m = 0	1.037	2.130	1.165	1.050	0.1	PAA5
225				1.037	2.130	1.295	1.050	0.1	PAA5
226				1.037	2.390	1.487	1.050	0.1	PAA5
227				1.126	2.260	1.200	1.170	0.1	PAA5
228				1.126	2.260	1.335	1.170	0.1	PAA5
229				1.126	2.390	1.487	1.170	0.1	PAA5
230				1.126	2.460	1.566	1.170	0.1	PAA5

^aSee the beginning of this appendix for definitions of table columns.

TABLE 8.7.—Continued.

(h) Configuration H: BPR = 8, convergent internally or externally mixed nozzles, hot subsonic flow^a

Case	M	Geometry		Core		Bypass		M _{fl}	nozid
		Axial	Azimuthal	M _a	T _{t,r}	M _a	T _{t,r}		
Externally mixed									
233	0.68	Separate flow	m = 0	0.688	2.231	0.667	1.059	0.01	PAA8
234	0.76			0.859	2.356	0.746	1.078	0.01	PAA8
235	0.82			1.002	2.447	0.812	1.114	0.01	PAA8
236	0.68			0.690	2.238	0.665	1.057	0.10	PAA8
237	0.76			0.858	2.350	0.744	1.078	0.10	PAA8
238	0.82			1.002	2.455	0.814	1.115	0.10	PAA8
239	0.82			1.010	2.455	0.816	1.116	0.20	PAA8
Coplanar and fully mixed approximations									
240	0.6	Internal splitter	m = 0	0.912	2.773	0.686	1.296	0.0	8000.00
241				1.366	3.211	0.902	1.296	0.0	8000.00
242				1.637	3.549	0.988	1.307	0.0	8000.00
243				1.272	3.118	0.920	1.294	0.0	8000.00
244				1.428	3.286	0.891	1.295	0.0	8000.00
245				0.879	2.608	0.664	1.222	0.24	8000.00
246				1.328	3.043	0.878	1.222	0.24	8000.00
247				1.642	3.559	0.990	1.307	0.24	8000.00
248				1.225	2.937	0.892	1.220	0.24	8000.00
249				1.563	3.450	1.013	1.301	0.24	8000.00
250				1.387	3.096	0.863	1.220	0.24	8000.00
251				1.695	3.620	0.996	1.302	0.24	8000.00
252		Internal chevron	m = 8	1.371	3.225	0.900	1.294	0.0	8001.04
253				1.371	3.237	0.906	1.300	0.24	8001.04
254				1.271	3.114	0.919	1.296	0.24	8001.04
255				1.426	3.295	0.891	1.296	0.24	8001.04
256		Internal deep scalloped lobes	m = 20	1.375	3.240	0.906	1.305	0.0	8002.02
257				1.376	3.254	0.906	1.309	0.24	8002.02
258				1.267	3.135	0.926	1.306	0.24	8002.02
259				1.434	3.323	0.894	1.304	0.24	8002.02

^aSee the beginning of this appendix for definitions of table columns.

TABLE 8.7.—Concluded.

(i) Configuration I: BPR = 11+, convergent externally mixed nozzles, hot subsonic flow^a

Case	BPR	M	Geometry		Core		Bypass		M_{fl}	nozid
			Axial	Azimuthal	M_a	$T_{t,r}$	M_a	$T_{t,r}$		
260	11	0.74	Separate flow	$m = 0$	0.867	2.425	0.734	1.085	0.00	PAA11
261		0.75			0.881	2.579	0.736	1.084	0.01	PAA11
262		0.75			0.861	2.425	0.735	1.082	0.10	PAA11
263		0.75			0.873	2.568	0.738	1.083	0.10	PAA11
264	14	0.70	Separate flow	$m = 0$	0.757	2.468	0.686	1.072	0.01	PAA14
265		0.69			0.853	2.534	0.683	1.074	0.01	PAA14
266		0.69			0.751	2.464	0.684	1.073	0.10	PAA14
267		0.69			0.859	2.530	0.686	1.071	0.10	PAA14

^aSee the beginning of this appendix for definitions of table columns.

Appendix C.—ANOPP Jet Noise Predictions and Comparison With Data

A selective number of jet cases from each of the nine configurations listed in Table 8.7 in Appendix B were assessed with the empirical code ANOPP. Jet noise predictions and comparisons with measured data are shown in Figure 8.60 to Figure 8.103.

Studying the sound pressure level (SPL) and overall SPL (OASPL) plots for each case in detail bears out the overall observations made in the plots of OASPL error shown in Figure 8.28 and Figure 8.29. Looking at details in the spectra at broadside (90°) and peak angles (150°) reveals trends that could be investigated in future generations of the ANOPP ST2JET code.

For configurations with internally mixed exhaust systems two approximations were used within ANOPP to predict the radiated noise: (1) configurations assuming coplanar nozzle flow (fully unmixed streams), which are denoted by a “C” in their case numbers, and (2) configurations assuming fully mixed flow at the nozzle exit, which are denoted by an “F” in their case numbers. The few dual-stream jet examples with external mixing are denoted by an “N” in their case numbers.

Details shown in the following illustrations—spectral plots at broadside (90°) and peak (150°) inlet angles as well as the OASPL directivity—examine the ANOPP code performance at different jet conditions for nine jet configurations listed in Table 8.7. The goal is to equip researchers with a guide in their attempt for the future improvements of the ANOPP ST2JET code.

Figure 8.60 to Figure 8.67 apply to Configuration A from Table 8.7 in Appendix B: single-stream, convergent axisymmetric nozzles. The details of the operating conditions for these eight jets can also be found in Table 8.5 under case numbers 003 through 040, respectively.

The comparisons show that ANOPP does fairly well at 90° , often slightly overpredicting the peak and displaying an erroneously large amplitude at high frequency near the Strouhal number 10.0. At 150° the prediction is very good except for this high-frequency component.

Configuration B covers subsonic single-flow jets with six equally spaced chevrons at the nozzle lip. Two examples are presented in Figure 8.68 and Figure 8.69 at Mach numbers of 0.972 and 0.828, and static temperature ratios of 0.837 and 2.571, respectively. These examples exhibit a major weakness of the ANOPP prediction method—in spectral shape and noise amplitude—with the OASPL directivity underpredictions of 10.0 dB or more throughout the angle range. The relevant module in the ANOPP code is calibrated to predict noise reduction produced by chevrons in separate flow nozzle configurations. Apparently, the module performs poorly when chevrons are placed on the external nozzle, such as internally mixed nozzle configurations. In order to model the impact of the chevrons on the exhaust noise, ANOPP correlates the hydraulic diameter of the chevron to the jet equivalent diameter. Examination of the parameter space demonstrated that this may be an inappropriate parameter. For instance,

nozzles used within Configuration B had identical hydraulic diameters but different penetration—a parameter that certainly impacts noise but is not present in the prediction model.

Within the next grouping, Configuration C, five convergent-divergent (C-D) nozzles are considered. The operating conditions for these axisymmetric supersonic jets are detailed in Table 8.5 under case 059 through case 090. The design Mach number for each nozzle is also given in Table 8.3. Noise predictions and comparisons with data are shown in Figure 8.70 to Figure 8.74. The key question here was to examine the code’s ability to predict the jet mixing noise at high speeds. It should be noted that experimental data were not entirely shock-free, even though pressure ratios were set to their design values for the respective nozzles. Subsequently, broadband shock-associated noise (BBSN) was present in the spectra especially at upstream angles. Some of the ANOPP underpredictions in the OASPL at angles less than 100° could be attributed to the experimental data especially at lower Mach numbers where BBSN was relatively stronger. As for the spectral shapes at two angles of 90° and 150° , the peak amplitude was in good agreement with data and showed improvement with increased Mach number. However, the spectral decay at high frequency and near the downstream angles produced a dual peak feature, a shortfall also witnessed in subsonic jets.

Configuration D deals with internally mixed jets at very low bypass ratio, such as those associated with military aircraft. Because the flow is very similar to single-flow axisymmetric jets, ANOPP predictions are expected to be similar in quality to those in single stream nozzles. Two sample cases are illustrated here, both at a bypass ratio of 0.20. Since the core flow is supersonic, a shock noise module within ANOPP was invoked to predict the BBSN, and a sum of mixing and shock noise components is shown at each angle. As pointed out earlier, ANOPP provides two different source models for internally mixed jets, leading to a total of four comparisons in Figure 8.75 to Figure 8.78. Internally mixed jets can be treated either as fully mixed (designation “F” in the case number) single-stream jets, substituting in the fully mixed flow conditions, or can be treated as a co-flow nozzle with no internal mixing (designation “C” in the case number). For these low-bypass ratio jets the difference between the two models is insignificant because the bypass stream contributes very little to the fully mixed jet conditions. The main difference is in the predicted high-frequency noise associated with the higher speed outer shear layer when the fully mixed approximation is used. ANOPP missed predicting the peak spectra of higher temperature jets at downstream angles, overpredicting the levels by 5 to 10 dB. In addition, supersonic shock-containing jets were strongly underpredicted at high frequencies.

Configuration E also covers internally mixed jets, with bypass ratios near unity. Two examples are shown in Figure 8.79 to Figure 8.82. As before, two source models were

implemented in each example; the co-flow approximation produced better results probably because the amount of internal mixing is negligible. The peak frequency of the broadband shock noise was not accurately predicted over the range of conditions. The noise spectra from low-speed high-temperature jets were not predicted well either.

Configuration F was similar to Configuration E, but at a higher BPR of 3. Two examples are presented in Figure 8.83 to Figure 8.86 using two different models available in ANOPP. Prediction issues were similar to those cases under Configuration E. In general, low-supersonic jets were not well predicted, mostly because of mistakes in predicting the broadband shock associated noise.

Configuration G covers BPR 5 dual stream convergent axisymmetric nozzles. Five cases are presented—the first and last cases represent externally mixed flows “N”; while the remaining three cases are internally mixed streams, and are examined using both unmixed coplanar “C” and the fully mixed “F” approximation models available within ANOPP. These are shown in Figure 8.87 to Figure 8.94. Since the ST2JET code within ANOPP was originally calibrated for jets similar to this configuration, the predicted results were also the best among all dual flow configurations. For the internally mixed jets, both approximations give surprisingly similar results—often missing the experimental data by similar

margins. As before, the peak frequency of the broadband shock noise was poorly predicted.

Within Configuration H, one axisymmetric, separate-flow nozzle and three internally mixed convergent nozzles at BPR 8 are presented: (1) axisymmetric splitter, (2) mixer with eight equally spaced chevrons, and (3) mixer with 20 lobes. Each case was examined using two available approximation models within ANOPP for a total of seven illustrations as seen in Figure 8.95 to Figure 8.101. Since both streams were at subsonic Mach numbers (~ 0.81 for the core and ~ 0.85 for the bypass), and the code had been calibrated against subsonic cases matching these conditions, expectations were high for success. These expectations were largely met in axisymmetric nozzles as seen in Figure 8.96 and Figure 8.97, and discrepancies were mostly at the high frequency. The chevron- and lobed-mixer predictions did not fare as well and overpredictions as large as 7.0 dB were observed at aft angles near 140° . These latter jets also included a flight Mach number $M_{fl} = 0.24$.

Configuration I examines the largest bypass ratio in separate-flow axisymmetric nozzles at BPR of 11 and 14. At these large bypass ratios the unheated, subsonic, outer stream is expected to dominate the flow and noise; subsequently, predictions resembled the cold subsonic single-flow cases of Configuration A. Two examples are shown in Figure 8.102 and Figure 8.103 at $M_{fl} = 0.10$.

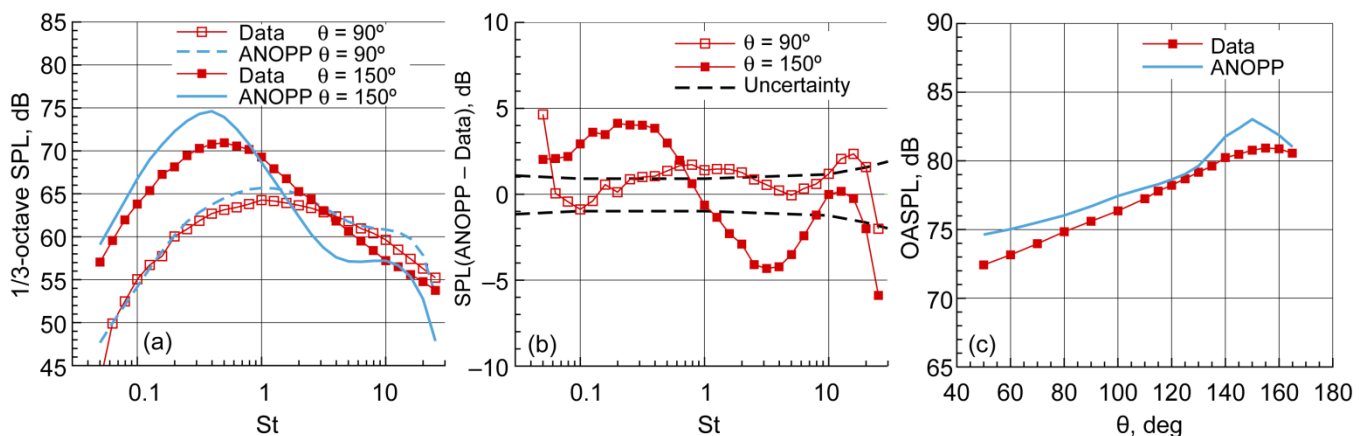


Figure 8.60.—Assessment of ANOPP ST2JET jet noise predictions (Table 8.7, Appendix B). Configuration A case 003 for convergent, axisymmetric nozzle: bypass ratio (BPR) = 0, Mach number $M = 0.51$, acoustic Mach number $M_a = 0.5$, and static temperature ratio $T_{s,r} = 0.955$. Comparison between ANOPP predictions and SHJAR experimental data. (a) 1/3-octave sound pressure level (SPL) versus Strouhal number St for inlet angles $\theta = 90^\circ$ and 150° . (b) Difference in 1/3-octave SPL values, with uncertainty. (c) Overall sound pressure level (OASPL) as function of θ .

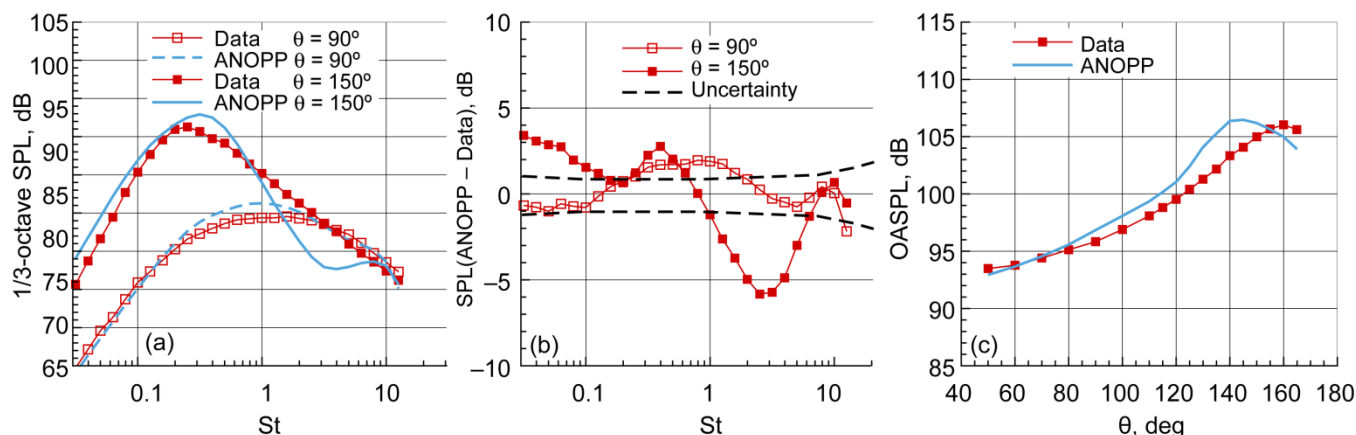


Figure 8.61.—Assessment of ANOPP ST2JET jet noise predictions (Table 8.7, Appendix B). Configuration A case 007 for convergent, axisymmetric nozzle: bypass ratio (BPR) = 0, Mach number $M = 0.98$, acoustic Mach number $M_a = 0.902$, and static temperature ratio $T_{s,r} = 0.842$. Comparison between ANOPP predictions and SHJAR experimental data. (a) 1/3-octave sound pressure level (SPL) versus Strouhal number St for inlet angles $\theta = 90^\circ$ and 150° . (b) Difference in 1/3-octave SPL values, with uncertainty. (c) Overall sound pressure level (OASPL) as function of θ .

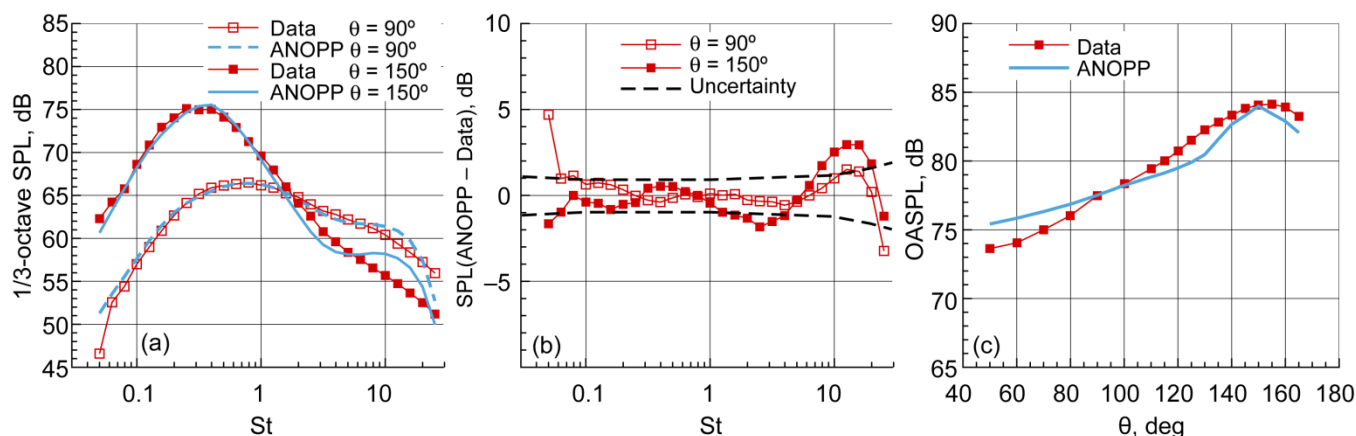


Figure 8.62.—Assessment of ANOPP ST2JET jet noise predictions (Table 8.7, Appendix B). Configuration A case 022 for convergent, axisymmetric nozzle: bypass ratio (BPR) = 0, Mach number $M = 0.37$, acoustic Mach number $M_a = 0.492$, and static temperature ratio $T_{s,r} = 1.767$. Comparison between ANOPP predictions and SHJAR experimental data. (a) 1/3-octave sound pressure level (SPL) versus Strouhal number St for inlet angles $\theta = 90^\circ$ and 150° . (b) Difference in 1/3-octave SPL values, with uncertainty. (c) Overall sound pressure level (OASPL) as function of θ .

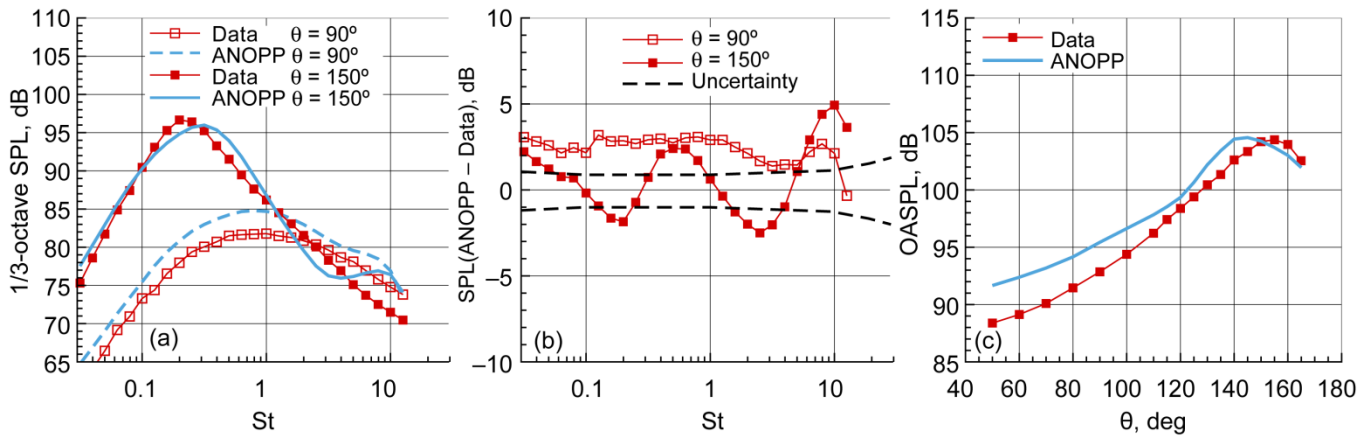


Figure 8.63.—Assessment of ANOPP ST2JET jet noise predictions (Table 8.7, Appendix B). Configuration A case 025 for convergent, axisymmetric nozzle: bypass ratio (BPR) = 0, Mach number $M = 0.68$, acoustic Mach number $M_a = 0.901$, and static temperature ratio $T_{s,r} = 1.77$. Comparison between ANOPP predictions and SHJAR experimental data. (a) 1/3-octave sound pressure level (SPL) versus Strouhal number St for inlet angles $\theta = 90^\circ$ and 150° . (b) Difference in 1/3-octave SPL values, with uncertainty. (c) Overall sound pressure level (OASPL) as function of θ .

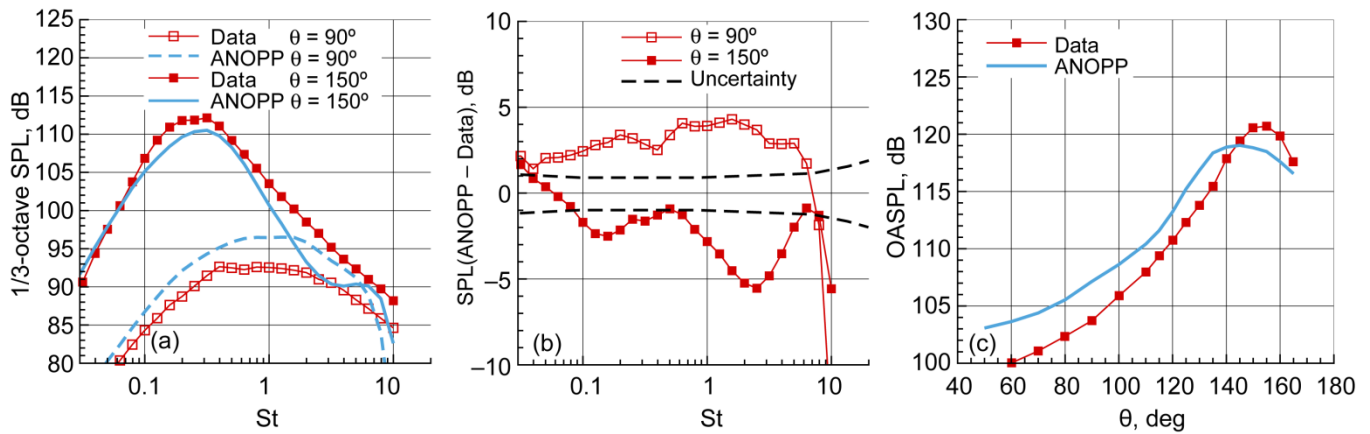


Figure 8.64.—Assessment of ANOPP ST2JET jet noise predictions (Table 8.7, Appendix B). Configuration A case 027 for convergent, axisymmetric nozzle: bypass ratio (BPR) = 0, Mach number $M = 1.01$, acoustic Mach number $M_a = 1.33$, and static temperature ratio $T_{s,r} = 1.759$. Comparison between ANOPP predictions and SHJAR experimental data. (a) 1/3-octave sound pressure level (SPL) versus Strouhal number St for inlet angles $\theta = 90^\circ$ and 150° . (b) Difference in 1/3-octave SPL values, with uncertainty. (c) Overall sound pressure level (OASPL) as function of θ .

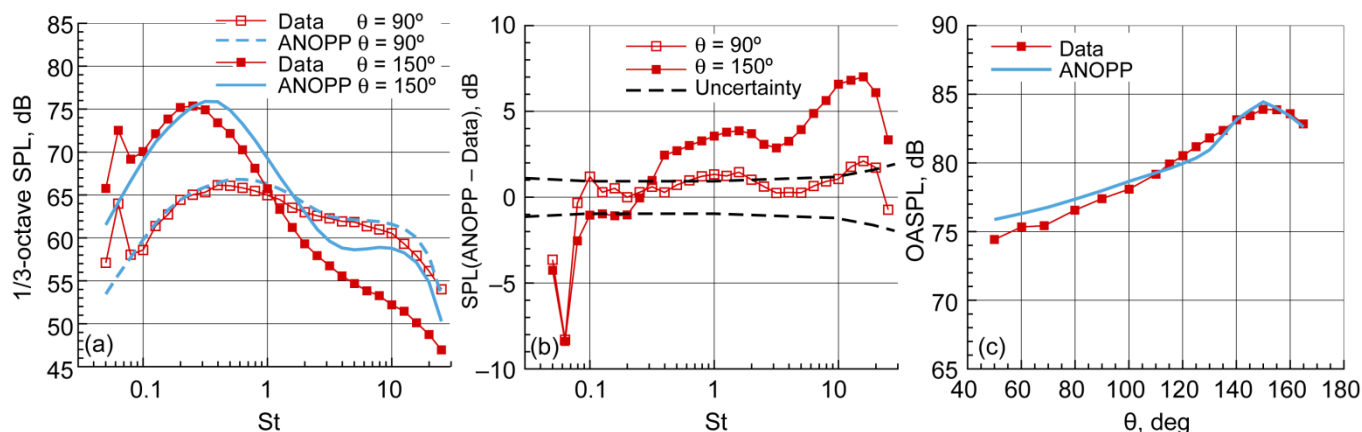


Figure 8.65.—Assessment of ANOPP ST2JET jet noise predictions (Table 8.7, Appendix B). Configuration A case 034 for convergent, axisymmetric nozzle: bypass ratio (BPR) = 0, Mach number $M = 0.3$, acoustic Mach number $M_a = 0.484$, and static temperature ratio $T_{s,r} = 2.624$. Comparison between ANOPP predictions and SHJAR experimental data. (a) 1/3-octave sound pressure level (SPL) versus Strouhal number St for inlet angles $\theta = 90^\circ$ and 150° . (b) Difference in 1/3-octave SPL values, with uncertainty. (c) Overall sound pressure level (OASPL) as function of θ .

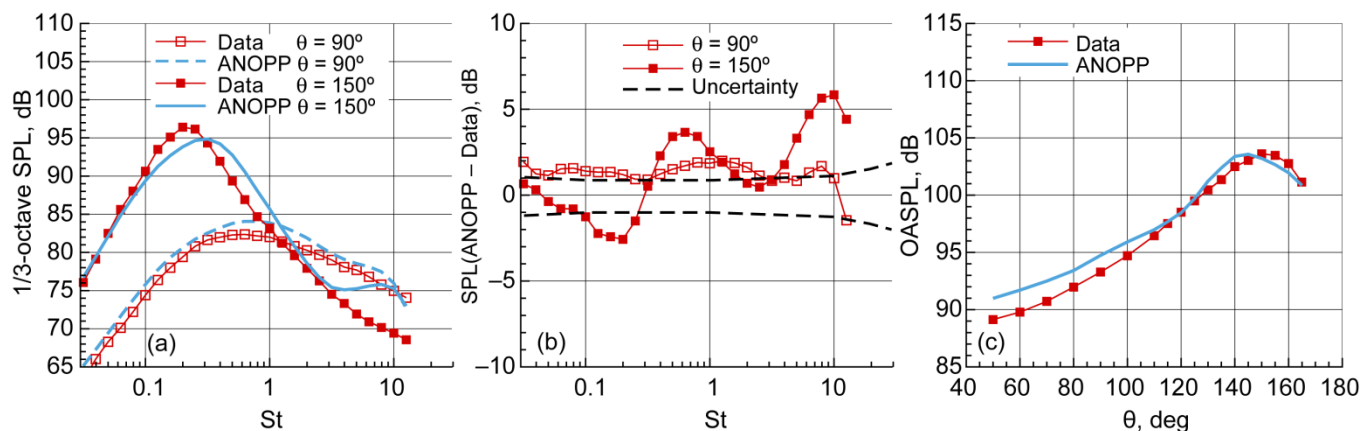


Figure 8.66.—Assessment of ANOPP ST2JET jet noise predictions (Table 8.7, Appendix B). Configuration A case 037 for convergent, axisymmetric nozzle: bypass ratio (BPR) = 0, Mach number $M = 0.56$, acoustic Mach number $M_a = 0.901$, and static temperature ratio $T_{s,r} = 2.702$. Comparison between ANOPP predictions and SHJAR experimental data. (a) 1/3-octave sound pressure level (SPL) versus Strouhal number St for inlet angles $\theta = 90^\circ$ and 150° . (b) Difference in 1/3-octave SPL values, with uncertainty. (c) Overall sound pressure level (OASPL) as function of θ .

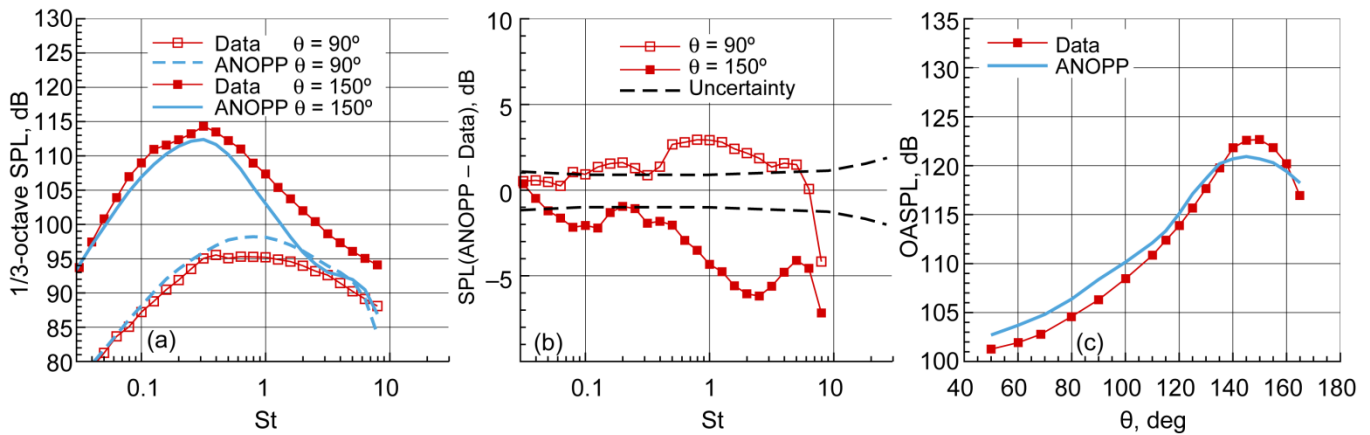


Figure 8.67.—Assessment of ANOPP ST2JET jet noise predictions (Table 8.7, Appendix B). Configuration A case 040 for convergent, axisymmetric nozzle: bypass ratio (BPR) = 0, Mach number $M = 0.92$, acoustic Mach number $M_a = 1.483$, and static temperature ratio $T_{s,r} = 2.703$. Comparison between ANOPP predictions and SHJAR experimental data. (a) 1/3-octave sound pressure level (SPL) versus Strouhal number St for inlet angles $\theta = 90^\circ$ and 150° . (b) Difference in 1/3-octave SPL values, with uncertainty. (c) Overall sound pressure level (OASPL) as function of θ .

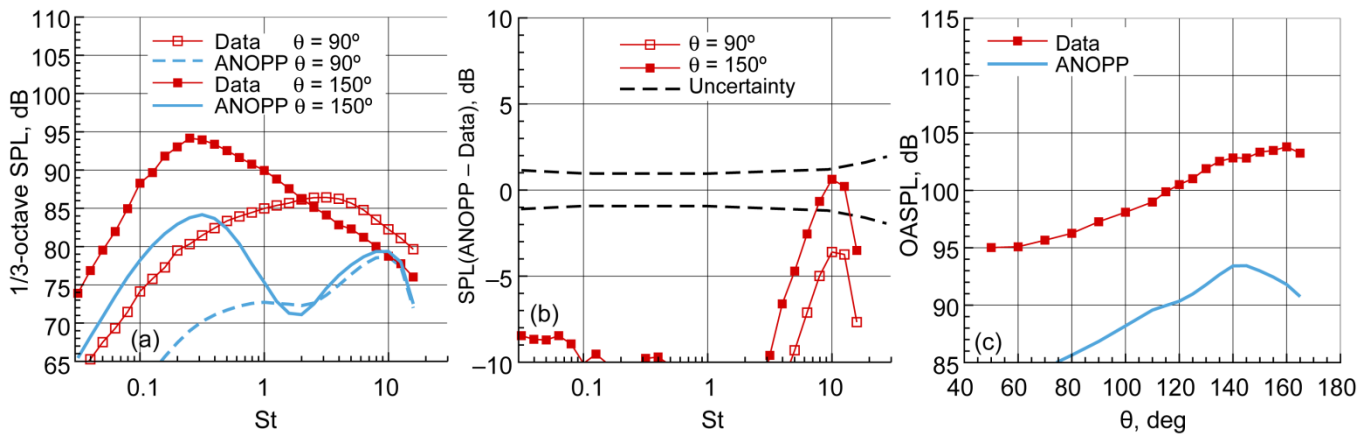


Figure 8.68.—Assessment of ANOPP ST2JET jet noise predictions (Table 8.7, Appendix B). Configuration B case 042 for convergent, azimuthal periodicity $m = 6$ nozzle: bypass ratio (BPR) = 0, Mach number $M = 0.972$, acoustic Mach number $M_a = 0.902$, and static temperature ratio $T_{s,r} = 0.837$. Comparison between ANOPP predictions and SHJAR experimental data. (a) 1/3-octave sound pressure level (SPL) versus Strouhal number St for inlet angles $\theta = 90^\circ$ and 150° . (b) Difference in 1/3-octave SPL values, with uncertainty. (c) Overall sound pressure level (OASPL) as function of θ .

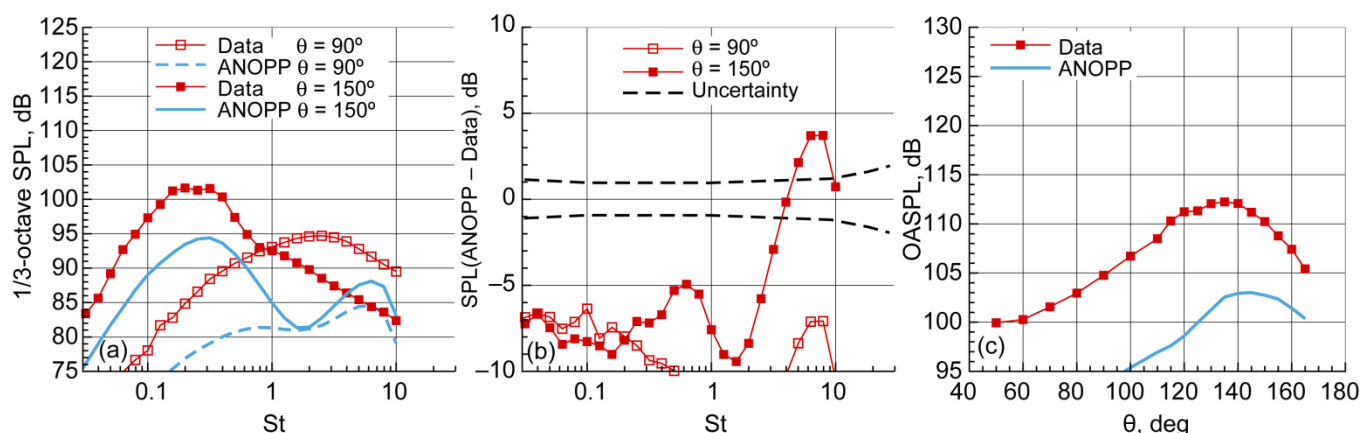


Figure 8.69.—Assessment of ANOPP ST2JET jet noise predictions (Table 8.7, Appendix B). Configuration B case 057 for convergent, azimuthal periodicity $m = 6$ nozzle: bypass ratio (BPR) = 0, Mach number $M = 0.828$, acoustic Mach number $M_a = 1.309$, and static temperature ratio $T_{s,r} = 2.571$. Comparison between ANOPP predictions and SHJAR experimental data. (a) 1/3-octave sound pressure level (SPL) versus Strouhal number St for inlet angles $\theta = 90^\circ$ and 150° . (b) Difference in 1/3-octave SPL values, with uncertainty. (c) Overall sound pressure level (OASPL) as function of θ .

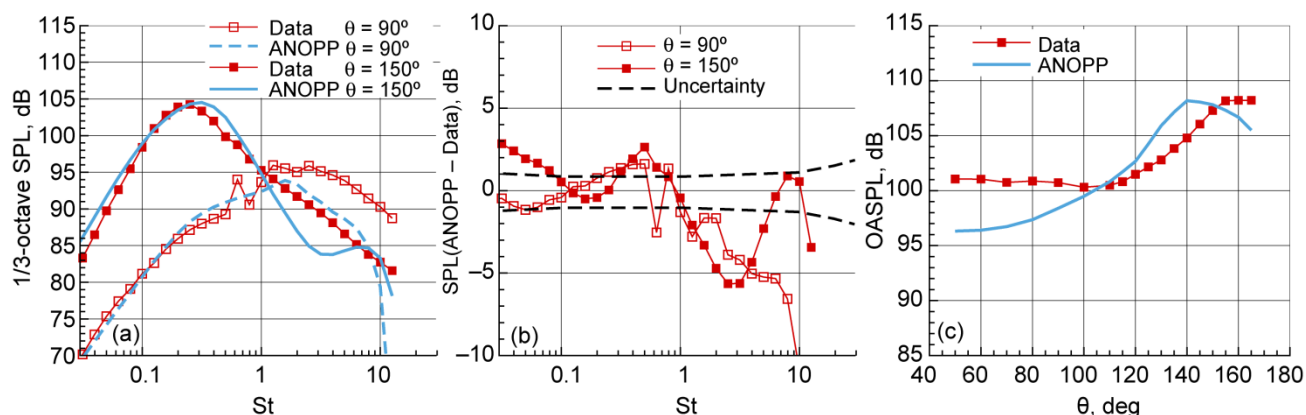


Figure 8.70.—Assessment of ANOPP ST2JET jet noise predictions (Table 8.7, Appendix B). Configuration C case 059 for convergent-divergent, axisymmetric nozzle: bypass ratio (BPR) = 0, Mach number $M = 1.72$, acoustic Mach number $M_a = 1.047$, and static temperature ratio $T_{s,r} = 0.797$. Comparison between ANOPP predictions and SHJAR experimental data. (a) 1/3-octave sound pressure level (SPL) versus Strouhal number St for inlet angles $\theta = 90^\circ$ and 150° . (b) Difference in 1/3-octave SPL values, with uncertainty. (c) Overall sound pressure level (OASPL) as function of θ .

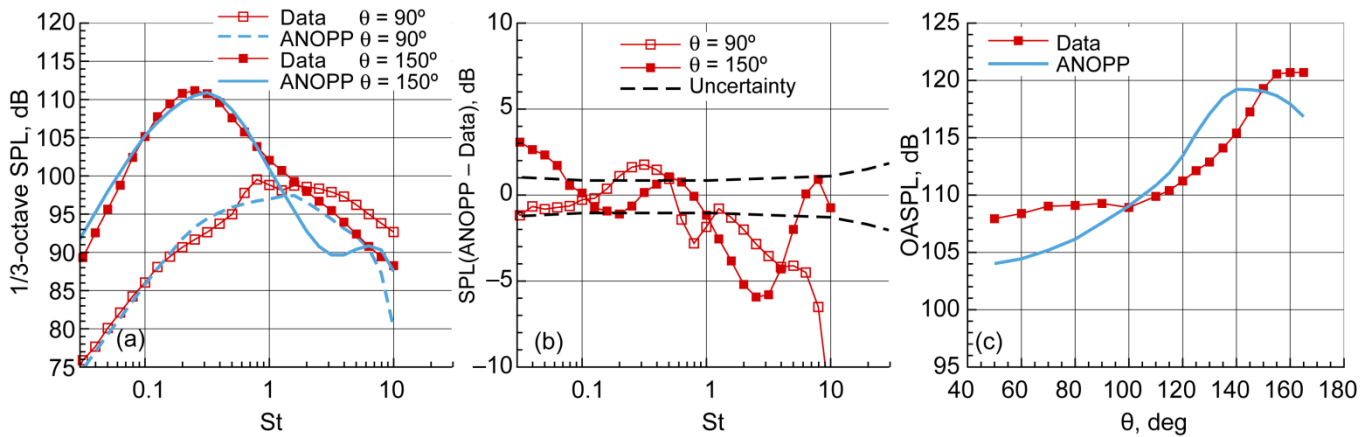


Figure 8.71.—Assessment of ANOPP ST2JET jet noise predictions (Table 8.7, Appendix B). Configuration C case 068 for convergent-divergent, axisymmetric nozzle: bypass ratio (BPR) = 0, Mach number $M = 1.394$, acoustic Mach number $M_a = 1.191$, and static temperature ratio $T_{s,r} = 0.73$. Comparison between ANOPP predictions and SHJAR experimental data. (a) 1/3-octave sound pressure level (SPL) versus Strouhal number St for inlet angles $\theta = 90^\circ$ and 150° . (b) Difference in 1/3-octave SPL values, with uncertainty. (c) Overall sound pressure level (OASPL) as function of θ .

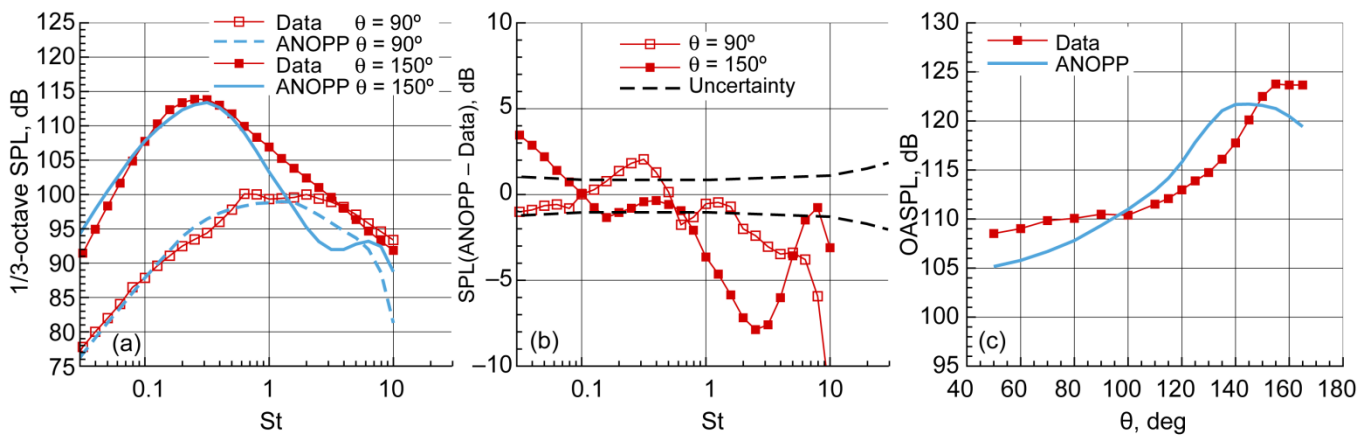


Figure 8.72.—Assessment of ANOPP ST2JET jet noise predictions (Table 8.7, Appendix B). Configuration C case 075 for convergent-divergent, axisymmetric nozzle: bypass ratio (BPR) = 0, Mach number $M = 1.497$, acoustic Mach number $M_a = 1.251$, and static temperature ratio $T_{s,r} = 0.699$. Comparison between ANOPP predictions and SHJAR experimental data. (a) 1/3-octave sound pressure level (SPL) versus Strouhal number St for inlet angles $\theta = 90^\circ$ and 150° . (b) Difference in 1/3-octave SPL values, with uncertainty. (c) Overall sound pressure level (OASPL) as function of θ .

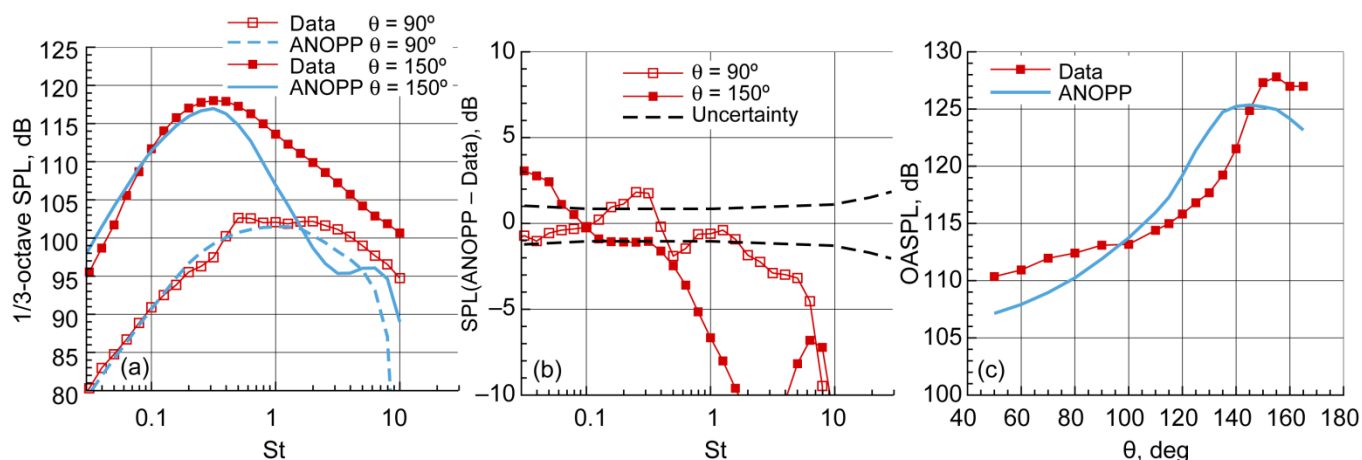


Figure 8.73.—Assessment of ANOPP ST2JET jet noise predictions (Table 8.7, Appendix B). Configuration C case 083 for convergent-divergent, axisymmetric nozzle: bypass ratio (BPR) = 0, Mach number $M = 1.659$, acoustic Mach number $M_a = 1.342$, and static temperature ratio $T_{s,r} = 0.654$. Comparison between ANOPP predictions and SHJAR experimental data. (a) 1/3-octave sound pressure level (SPL) versus Strouhal number St for inlet angles $\theta = 90^\circ$ and 150° . (b) Difference in 1/3-octave SPL values, with uncertainty. (c) Overall sound pressure level (OASPL) as function of θ .

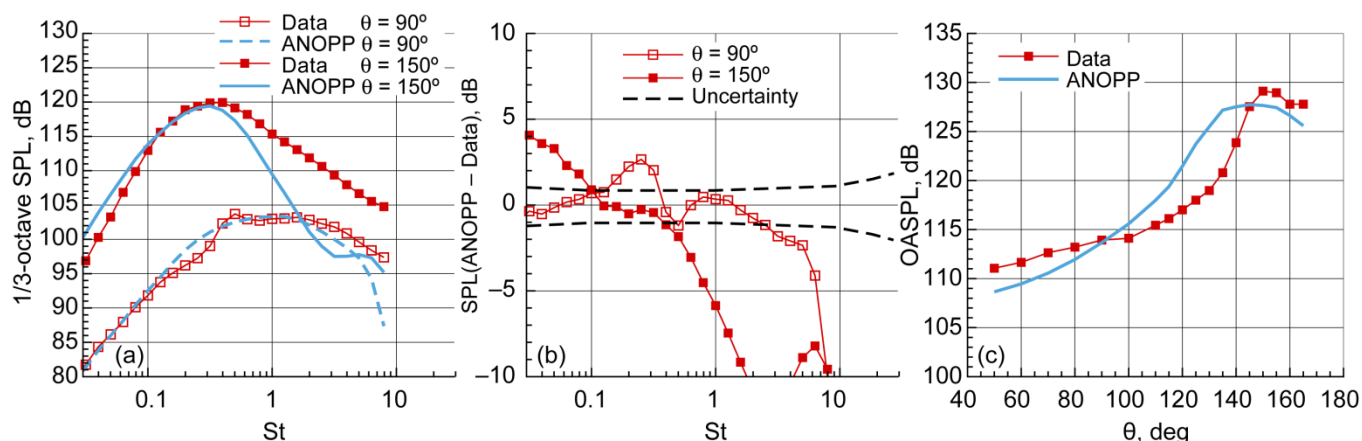


Figure 8.74.—Assessment of ANOPP ST2JET jet noise predictions (Table 8.7, Appendix B). Configuration C case 090 for convergent-divergent, axisymmetric nozzle: bypass ratio (BPR) = 0, Mach number $M = 1.784$, acoustic Mach number $M_a = 1.403$, and static temperature ratio $T_{s,r} = 0.619$. Comparison between ANOPP predictions and SHJAR experimental data. (a) 1/3-octave sound pressure level (SPL) versus Strouhal number St for inlet angles $\theta = 90^\circ$ and 150° . (b) Difference in 1/3-octave SPL values, with uncertainty. (c) Overall sound pressure level (OASPL) as function of θ .

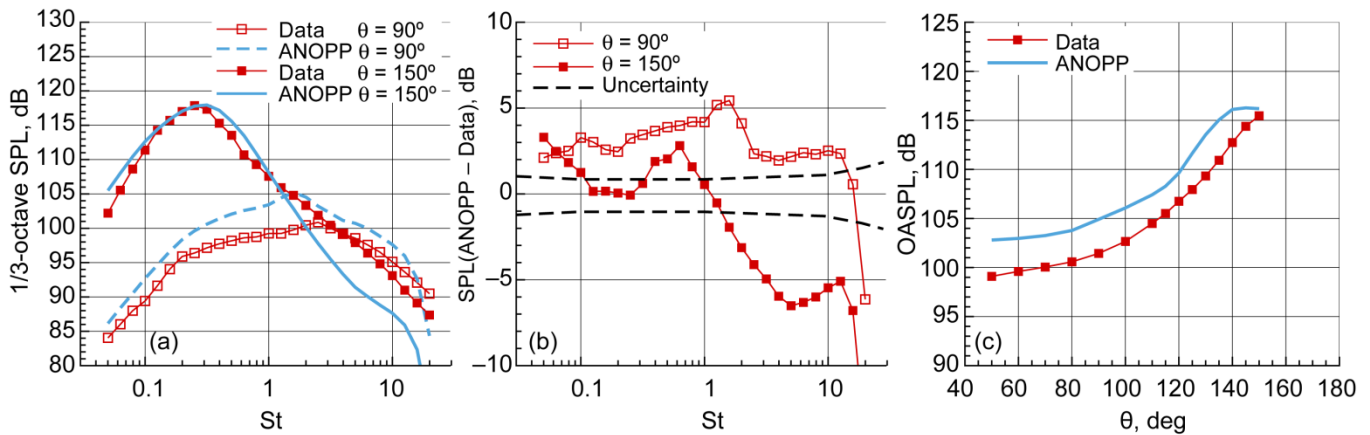


Figure 8.75.—Assessment of ANOPP ST2JET jet noise predictions (Table 8.7, Appendix B). Configuration D case 104C for internally mixed, convergent, axisymmetric nozzle: bypass ratio (BPR) = 0.2 and flight Mach number $M_{fl} = 0$. For core, acoustic Mach number $M_a = 1.184$ and stagnation temperature ratio $T_{t,r} = 1.546$. For bypass, $M_a = 0.955$ and $T_{t,r} = 1.006$. Comparison between ANOPP predictions with coplanar approximation and NATR experimental data. (a) 1/3-octave sound pressure level (SPL) versus Strouhal number St for inlet angles $\theta = 90^\circ$ and 150° . (b) Difference in 1/3-octave SPL values, with uncertainty. (c) Overall sound pressure level (OASPL) as function of θ .

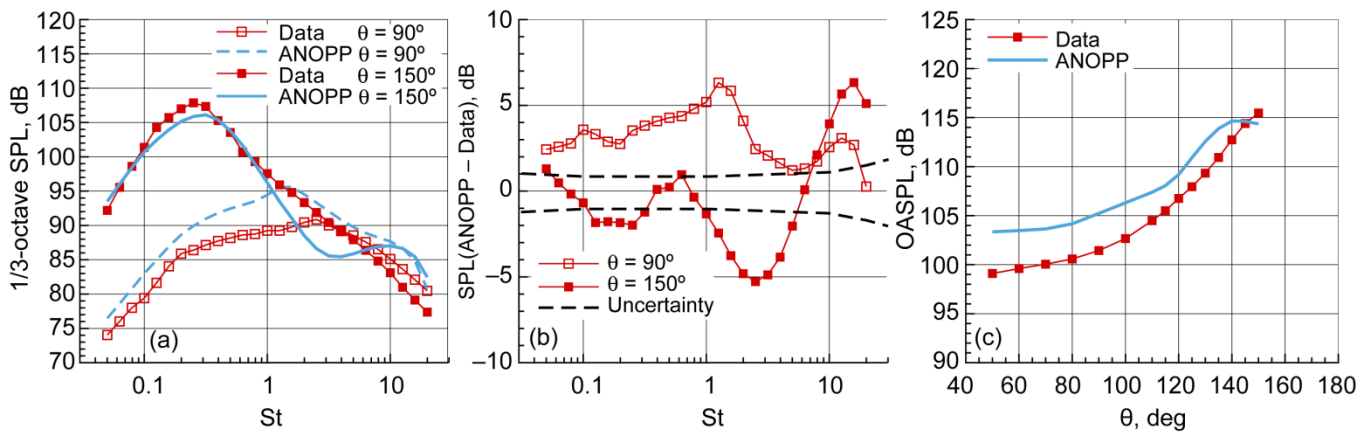


Figure 8.76.—Assessment of ANOPP ST2JET jet noise predictions (Table 8.7, Appendix B). Configuration D case 104F for internally mixed, convergent, axisymmetric nozzle: bypass ratio (BPR) = 0.2 and flight Mach number $M_{fl} = 0$. For core, acoustic Mach number $M_a = 1.184$ and stagnation temperature ratio $T_{t,r} = 1.546$. For bypass, $M_a = 0.955$ and $T_{t,r} = 1.006$. Comparison between ANOPP predictions with fully mixed approximation and NATR experimental data. (a) 1/3-octave sound pressure level (SPL) versus Strouhal number St for inlet angles $\theta = 90^\circ$ and 150° . (b) Difference in 1/3-octave SPL values, with uncertainty. (c) Overall sound pressure level (OASPL) as function of θ .

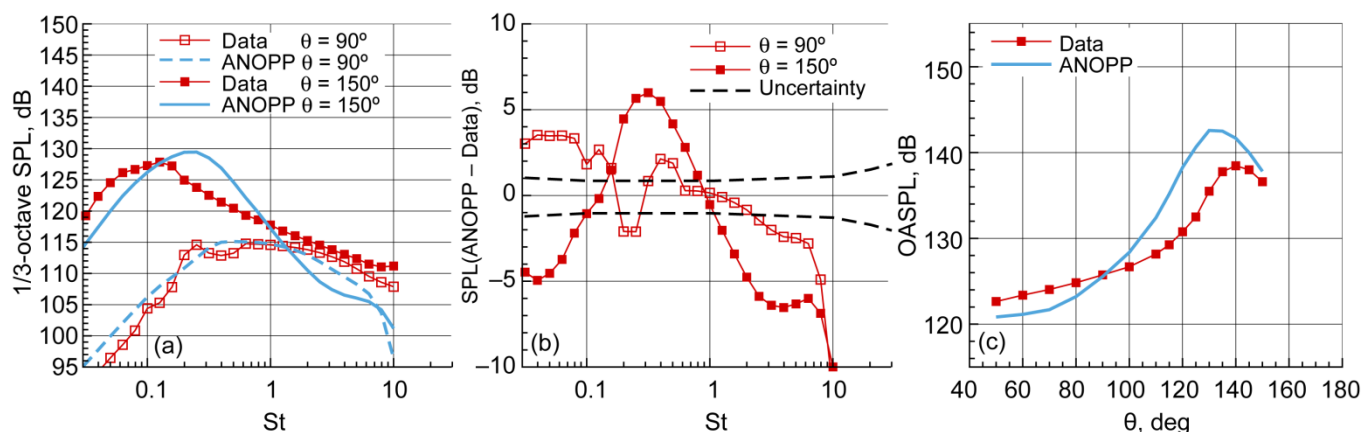


Figure 8.77.—Assessment of ANOPP ST2JET jet noise predictions (Table 8.7, Appendix B). Configuration D case 119C for internally mixed, convergent, axisymmetric nozzle: bypass ratio (BPR) = 0.2 and flight Mach number $M_{fl} = 0$. For core, acoustic Mach number $M_a = 2.401$ and stagnation temperature ratio $T_{t,r} = 2.581$. For bypass, $M_a = 1.523$ and $T_{t,r} = 1.042$. Comparison between ANOPP predictions with coplanar approximation and NATR experimental data. (a) 1/3-octave sound pressure level (SPL) versus Strouhal number St for inlet angles $\theta = 90^\circ$ and 150° . (b) Difference in 1/3-octave SPL values, with uncertainty. (c) Overall sound pressure level (OASPL) as function of θ .

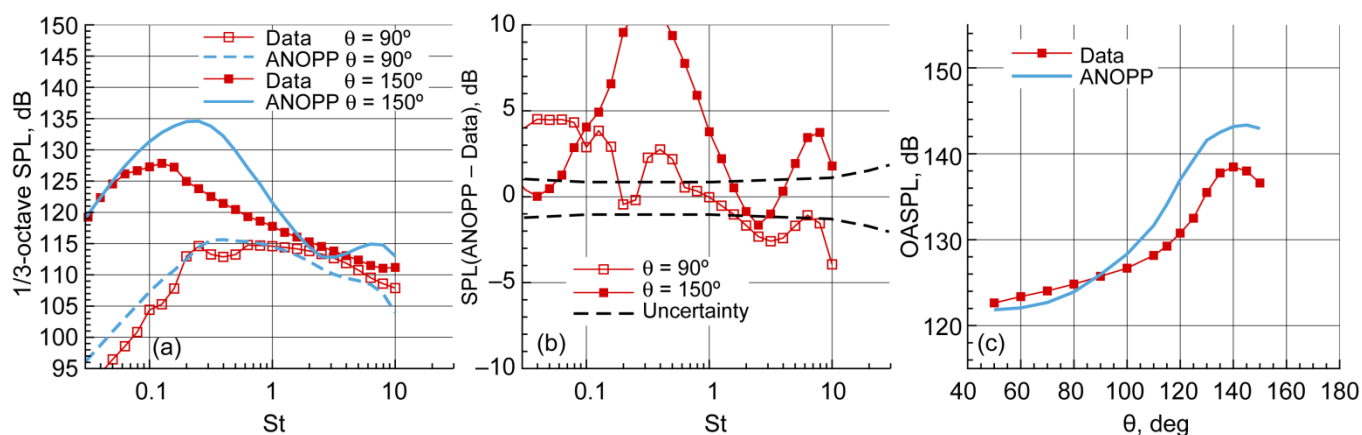


Figure 8.78.—Assessment of ANOPP ST2JET jet noise predictions (Table 8.7, Appendix B). Configuration D case 119F for internally mixed, convergent, axisymmetric nozzle: bypass ratio (BPR) = 0.2 and flight Mach number $M_{fl} = 0$. For core, acoustic Mach number $M_a = 2.401$ and stagnation temperature ratio $T_{t,r} = 2.581$. For bypass, $M_a = 1.523$ and $T_{t,r} = 1.042$. Comparison between ANOPP predictions with fully mixed approximation and NATR experimental data. (a) 1/3-octave sound pressure level (SPL) versus Strouhal number St for inlet angles $\theta = 90^\circ$ and 150° . (b) Difference in 1/3-octave SPL values, with uncertainty. (c) Overall sound pressure level (OASPL) as function of θ .

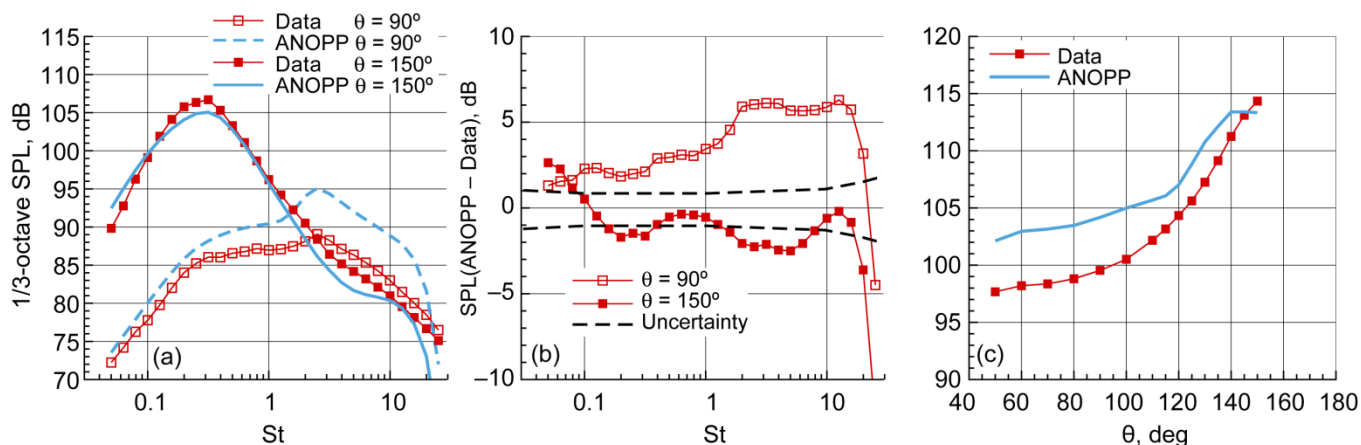


Figure 8.79.—Assessment of ANOPP ST2JET jet noise predictions (Table 8.7, Appendix B). Configuration E case 143C for internally mixed, convergent, axisymmetric nozzle: bypass ratio (BPR) = 1 and flight Mach number $M_{fl} = 0$. For core, acoustic Mach number $M_a = 1.18$ and stagnation temperature ratio $T_{t,r} = 1.54$. For bypass, $M_a = 0.948$ and $T_{t,r} = 0.99$. Comparison between ANOPP predictions with coplanar approximation and NATR experimental data. (a) 1/3-octave sound pressure level (SPL) versus Strouhal number St for inlet angles $\theta = 90^\circ$ and 150° . (b) Difference in 1/3-octave SPL values, with uncertainty. (c) Overall sound pressure level (OASPL) as function of θ .

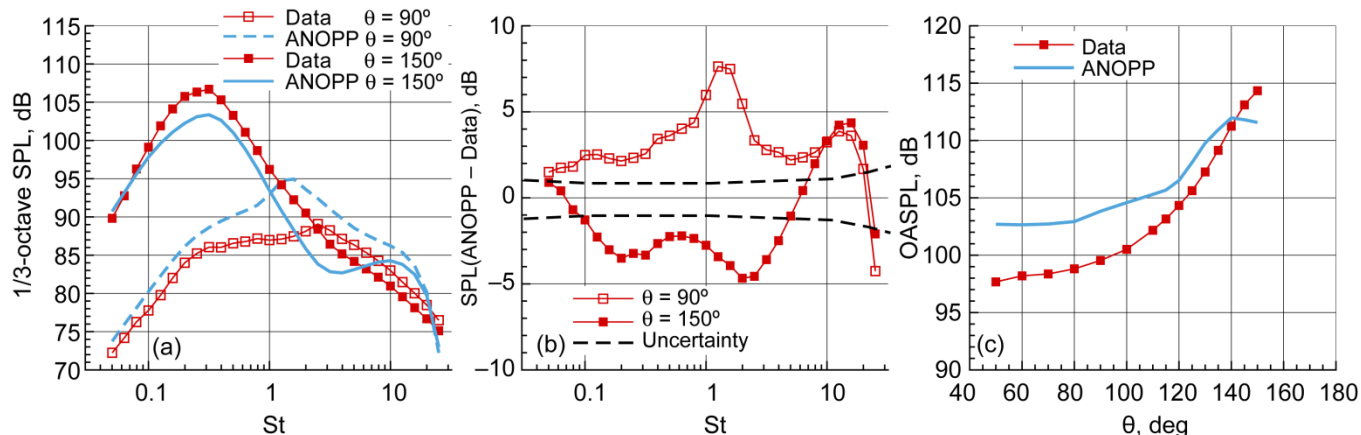


Figure 8.80.—Assessment of ANOPP ST2JET jet noise predictions (Table 8.7, Appendix B). Configuration E case 143F for internally mixed, convergent, axisymmetric nozzle: bypass ratio (BPR) = 1 and flight Mach number $M_{fl} = 0$. For core, acoustic Mach number $M_a = 1.18$ and stagnation temperature ratio $T_{t,r} = 1.54$. For bypass, $M_a = 0.948$ and $T_{t,r} = 0.99$. Comparison between ANOPP predictions with fully mixed approximation and NATR experimental data. (a) 1/3-octave sound pressure level (SPL) versus Strouhal number St for inlet angles $\theta = 90^\circ$ and 150° . (b) Difference in 1/3-octave SPL values, with uncertainty. (c) Overall sound pressure level (OASPL) as function of θ .

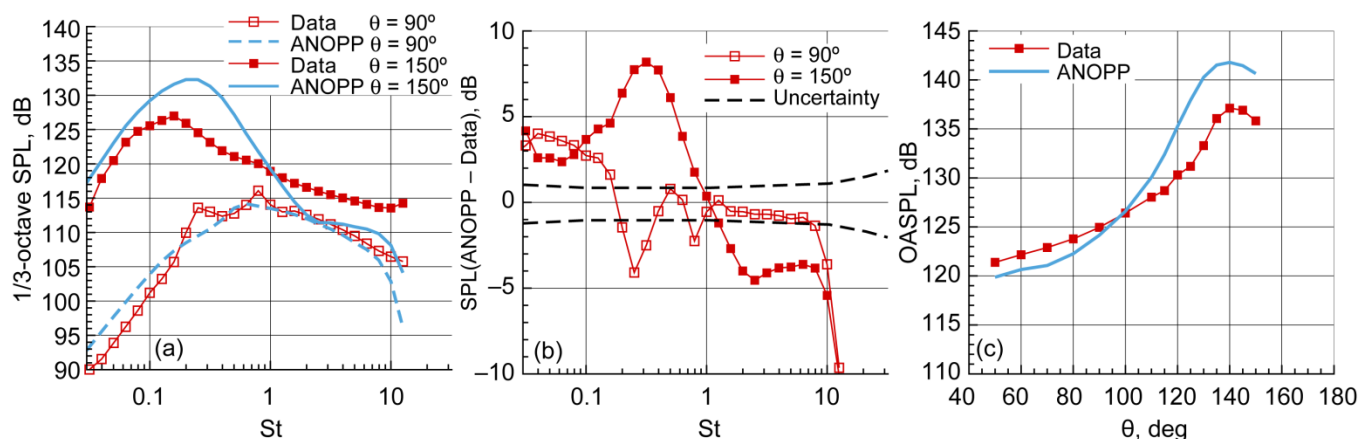


Figure 8.81.—Assessment of ANOPP ST2JET jet noise predictions (Table 8.7, Appendix B). Configuration E case 156C for internally mixed, convergent, axisymmetric nozzle: bypass ratio (BPR) = 1 and flight Mach number $M_{fl} = 0$. For core, acoustic Mach number $M_a = 2.401$ and stagnation temperature ratio $T_{t,r} = 2.581$. For bypass, $M_a = 1.53$ and $T_{t,r} = 1.053$. Comparison between ANOPP predictions with coplanar approximation and NATR experimental data. (a) 1/3-octave sound pressure level (SPL) versus Strouhal number St for inlet angles $\theta = 90^\circ$ and 150° . (b) Difference in 1/3-octave SPL values, with uncertainty. (c) Overall sound pressure level (OASPL) as function of θ .

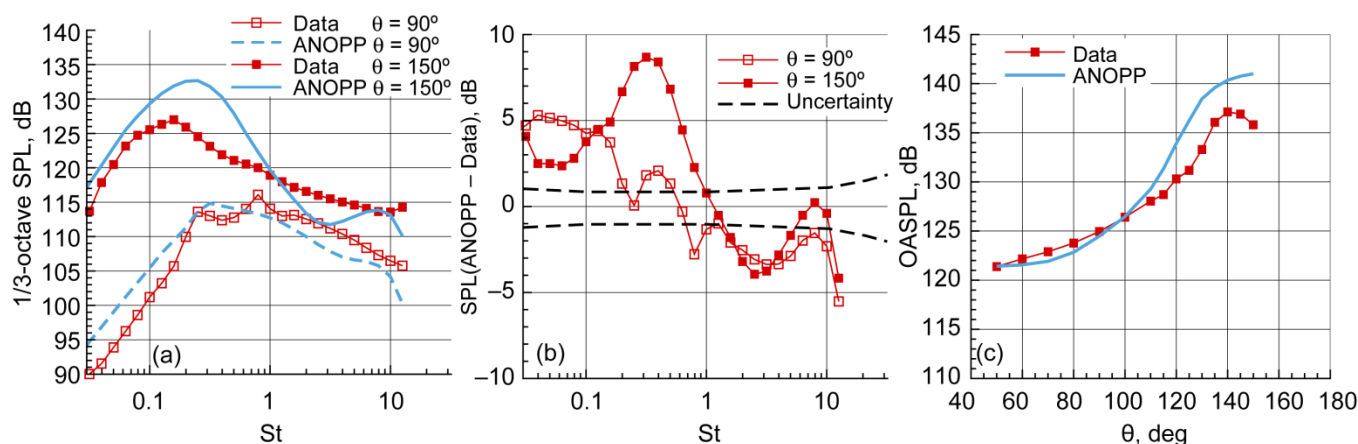


Figure 8.82.—Assessment of ANOPP ST2JET jet noise predictions (Table 8.7, Appendix B). Configuration E case 156F for internally mixed, convergent, axisymmetric nozzle: bypass ratio (BPR) = 1 and flight Mach number $M_{fl} = 0$. For core, acoustic Mach number $M_a = 2.401$ and stagnation temperature ratio $T_{t,r} = 2.581$. For bypass, $M_a = 1.53$ and $T_{t,r} = 1.053$. Comparison between ANOPP predictions with fully mixed approximation and NATR experimental data. (a) 1/3-octave sound pressure level (SPL) versus Strouhal number St for inlet angles $\theta = 90^\circ$ and 150° . (b) Difference in 1/3-octave SPL values, with uncertainty. (c) Overall sound pressure level (OASPL) as function of θ .

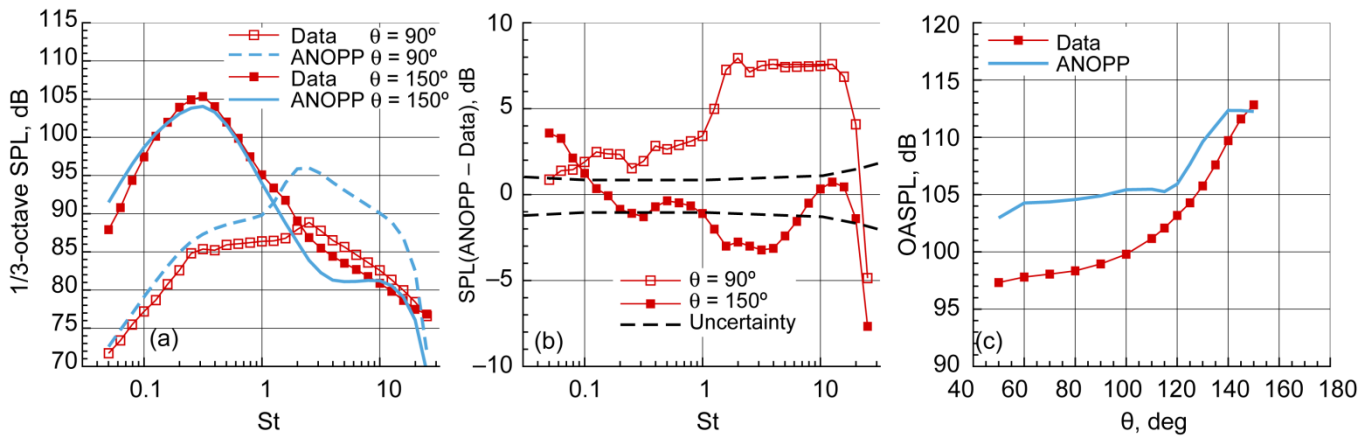


Figure 8.83.—Assessment of ANOPP ST2JET jet noise predictions (Table 8.7, Appendix B). Configuration F case 175C for internally mixed, convergent, axisymmetric nozzle: bypass ratio (BPR) = 3 and flight Mach number $M_{ij} = 0$. For core, acoustic Mach number $M_a = 1.183$ and stagnation temperature ratio $T_{t,r} = 1.541$. For bypass, $M_a = 0.94$ and $T_{t,r} = 0.977$. Comparison between ANOPP predictions with coplanar approximation and NATR experimental data. (a) 1/3-octave sound pressure level (SPL) versus Strouhal number St for inlet angles $\theta = 90^\circ$ and 150° . (b) Difference in 1/3-octave SPL values, with uncertainty. (c) Overall sound pressure level (OASPL) as function of θ .

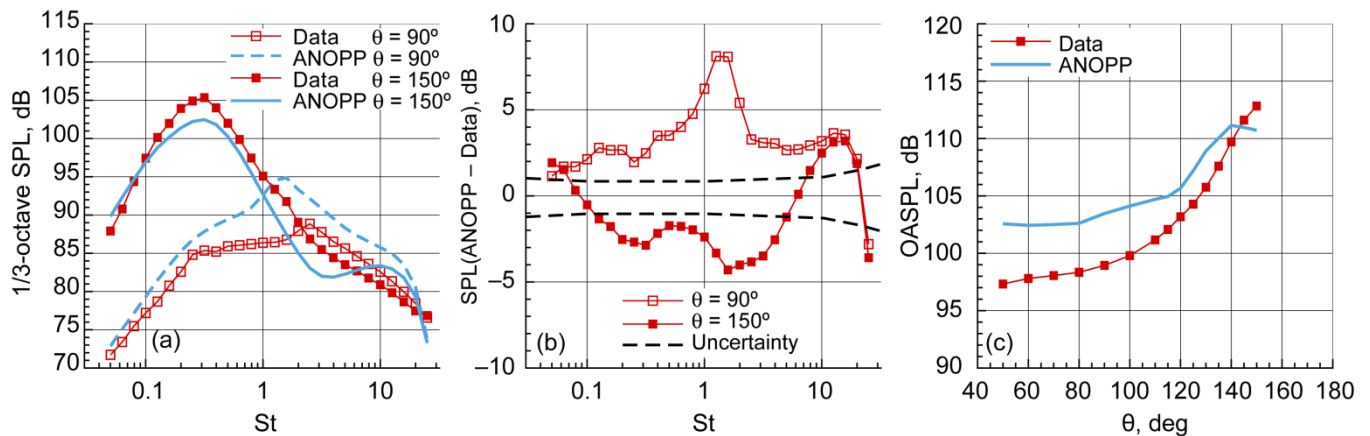


Figure 8.84.—Assessment of ANOPP ST2JET jet noise predictions (Table 8.7, Appendix B). Configuration F case 175F for internally mixed, convergent, axisymmetric nozzle: bypass ratio (BPR) = 3 and flight Mach number $M_{ij} = 0$. For core, acoustic Mach number $M_a = 1.183$ and stagnation temperature ratio $T_{t,r} = 1.541$. For bypass, $M_a = 0.94$ and $T_{t,r} = 0.977$. Comparison between ANOPP predictions with fully mixed approximation and NATR experimental data. (a) 1/3-octave sound pressure level (SPL) versus Strouhal number St for inlet angles $\theta = 90^\circ$ and 150° . (b) Difference in 1/3-octave SPL values, with uncertainty. (c) Overall sound pressure level (OASPL) as function of θ .

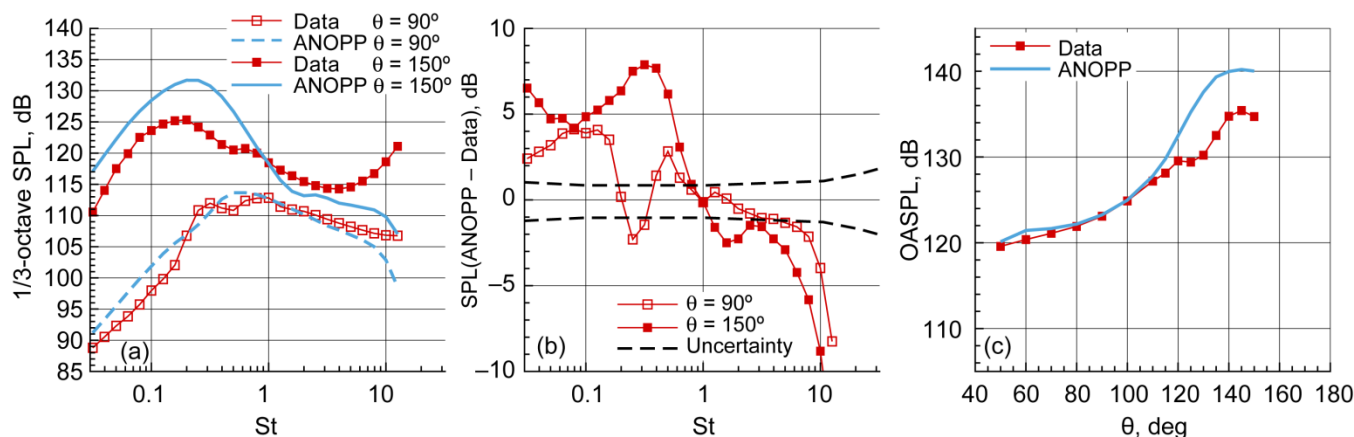


Figure 8.85.—Assessment of ANOPP ST2JET jet noise predictions (Table 8.7, Appendix B). Configuration F case 188C for internally mixed, convergent, axisymmetric nozzle: bypass ratio (BPR) = 3 and flight Mach number $M_{\theta} = 0$. For core, acoustic Mach number $M_a = 2.385$ and stagnation temperature ratio $T_{t,r} = 2.589$. For bypass, $M_a = 1.487$ and $T_{t,r} = 1.012$. Comparison between ANOPP predictions with coplanar approximation and NATR experimental data. (a) 1/3-octave sound pressure level (SPL) versus Strouhal number St for inlet angles $\theta = 90^\circ$ and 150° . (b) Difference in 1/3-octave SPL values, with uncertainty. (c) Overall sound pressure level (OASPL) as function of θ .

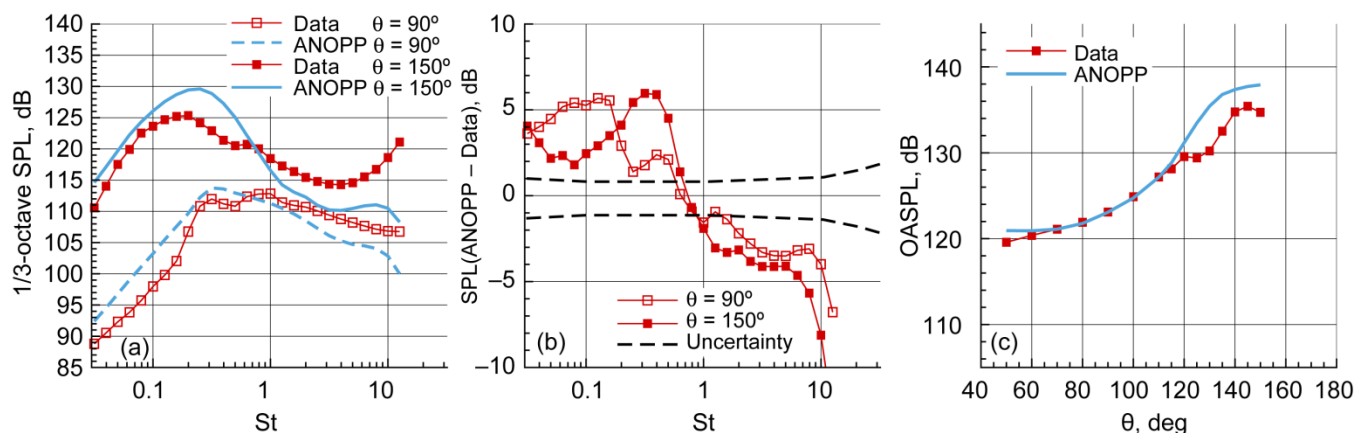


Figure 8.86.—Assessment of ANOPP ST2JET jet noise predictions (Table 8.7, Appendix B). Configuration F case 188F for internally mixed, convergent, axisymmetric nozzle: bypass ratio (BPR) = 3 and flight Mach number $M_{\theta} = 0$. For core, acoustic Mach number $M_a = 2.385$ and stagnation temperature ratio $T_{t,r} = 2.589$. For bypass, $M_a = 1.487$ and $T_{t,r} = 1.012$. Comparison between ANOPP predictions with fully mixed approximation and NATR experimental data. (a) 1/3-octave sound pressure level (SPL) versus Strouhal number St for inlet angles $\theta = 90^\circ$ and 150° . (b) Difference in 1/3-octave SPL values, with uncertainty. (c) Overall sound pressure level (OASPL) as function of θ .

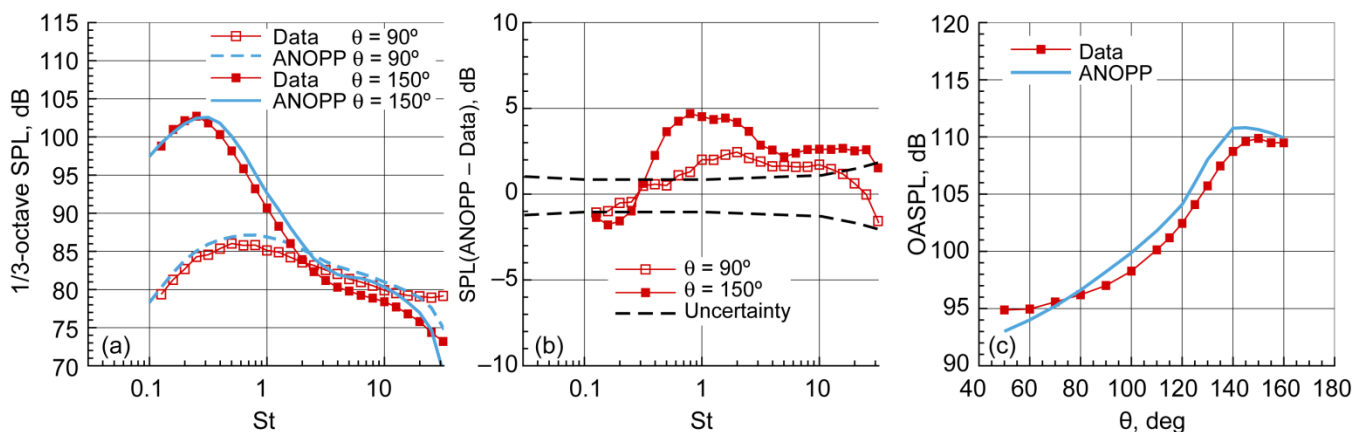


Figure 8.87.—Assessment of ANOPP ST2JET jet noise predictions (Table 8.7, Appendix B). Configuration G case 191N for externally mixed, convergent, axisymmetric nozzle: bypass ratio (BPR) = 5 and flight Mach number $M_\infty = 0$. For core, acoustic Mach number $M_a = 1.265$ and stagnation temperature ratio $T_{t,r} = 2.663$. For bypass, $M_a = 0.935$ and $T_{t,r} = 1.822$. Comparison between ANOPP predictions and NATR experimental data. (a) 1/3-octave sound pressure level (SPL) versus Strouhal number St for inlet angles $\theta = 90^\circ$ and 150° . (b) Difference in 1/3-octave SPL values, with uncertainty. (c) Overall sound pressure level (OASPL) as function of θ .

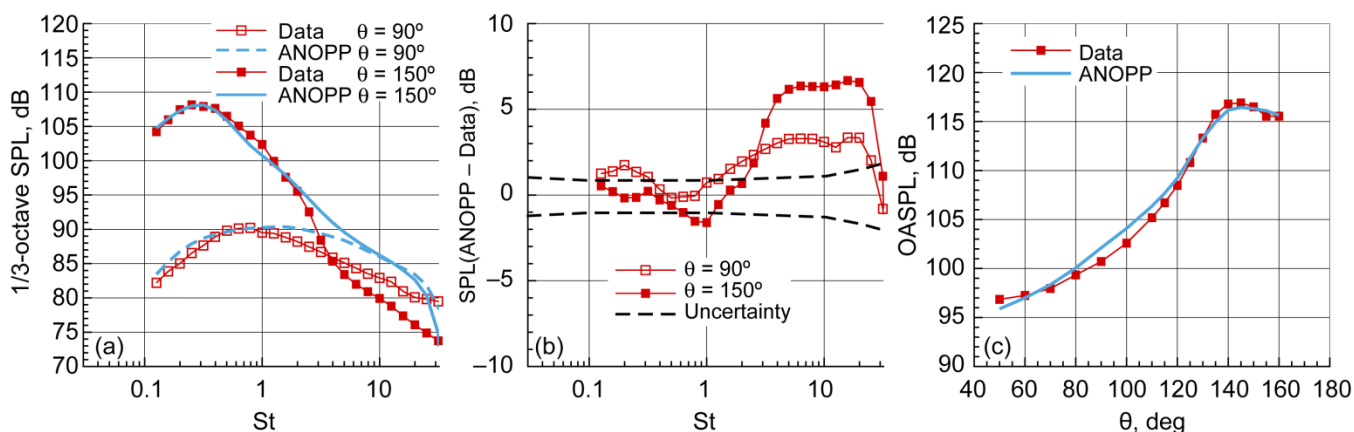


Figure 8.88.—Assessment of ANOPP ST2JET jet noise predictions (Table 8.7, Appendix B). Configuration G case 200C for internally mixed, convergent, axisymmetric nozzle: bypass ratio (BPR) = 5 and flight Mach number $M_\infty = 0$. For core, acoustic Mach number $M_a = 1.637$ and stagnation temperature ratio $T_{t,r} = 3.543$. For bypass, $M_a = 0.984$ and $T_{t,r} = 1.302$. Comparison between ANOPP predictions with coplanar approximation and NATR experimental data. (a) 1/3-octave sound pressure level (SPL) versus Strouhal number St for inlet angles $\theta = 90^\circ$ and 150° . (b) Difference in 1/3-octave SPL values, with uncertainty. (c) Overall sound pressure level (OASPL) as function of θ .

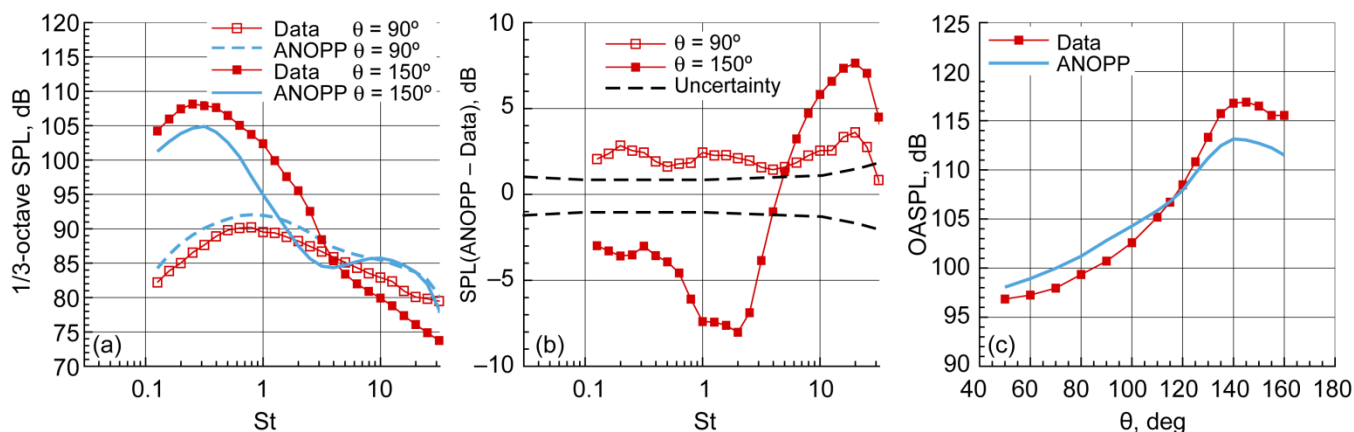


Figure 8.89.—Assessment of ANOPP ST2JET jet noise predictions (Table 8.7, Appendix B). Configuration G case 200F for internally mixed, convergent, axisymmetric nozzle: bypass ratio (BPR) = 5 and flight Mach number $M_{fl} = 0$. For core, acoustic Mach number $M_a = 1.637$ and stagnation temperature ratio $T_{t,r} = 3.543$. For bypass, $M_a = 0.984$ and $T_{t,r} = 1.302$. Comparison between ANOPP predictions with fully mixed approximation and NATR experimental data. (a) 1/3-octave sound pressure level (SPL) versus Strouhal number St for inlet angles $\theta = 90^\circ$ and 150° . (b) Difference in 1/3-octave SPL values, with uncertainty. (c) Overall sound pressure level (OASPL) as function of θ .

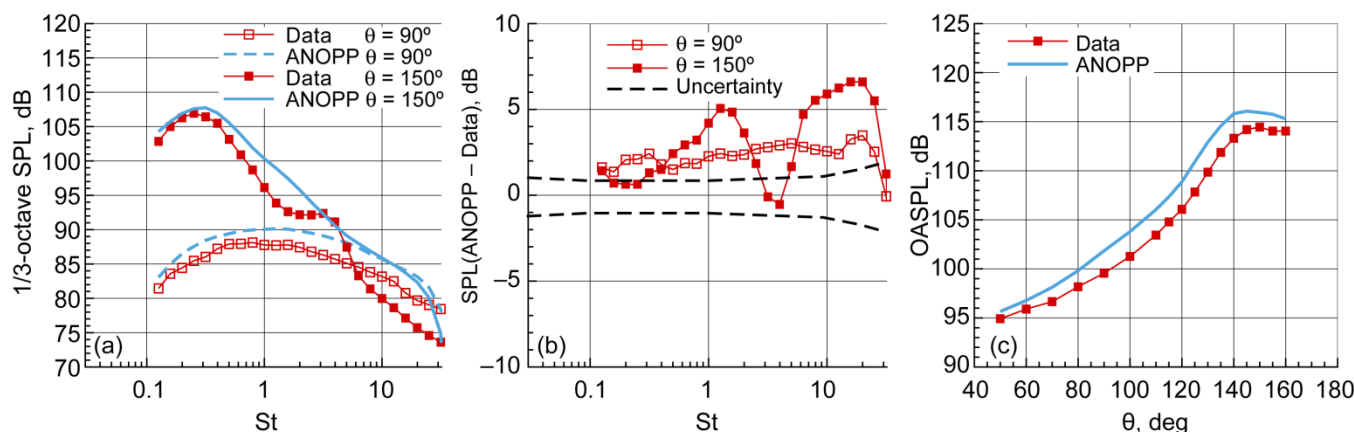


Figure 8.90.—Assessment of ANOPP ST2JET jet noise predictions (Table 8.7, Appendix B). Configuration G case 211C for internally mixed, chevron, azimuthal periodicity $m = 8$ nozzle: bypass ratio (BPR) = 5 and flight Mach number $M_{fl} = 0$. For core, acoustic Mach number $M_a = 1.614$ and stagnation temperature ratio $T_{t,r} = 3.455$. For bypass, $M_a = 0.973$ and $T_{t,r} = 1.27$. Comparison between ANOPP predictions with coplanar approximation and NATR experimental data. (a) 1/3-octave sound pressure level (SPL) versus Strouhal number St for inlet angles $\theta = 90^\circ$ and 150° . (b) Difference in 1/3-octave SPL values, with uncertainty. (c) Overall sound pressure level (OASPL) as function of θ .

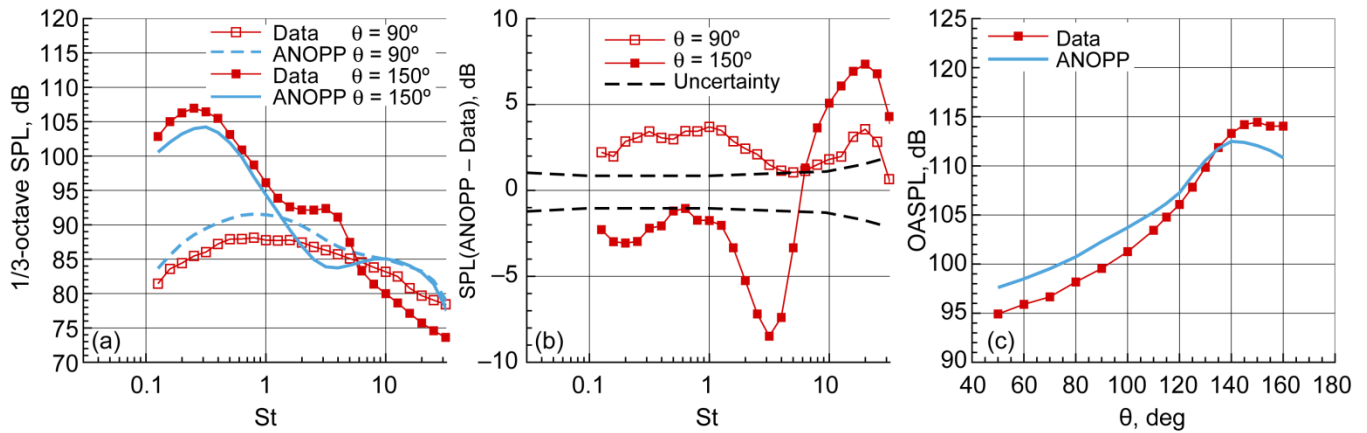


Figure 8.91.—Assessment of ANOPP ST2JET jet noise predictions (Table 8.7, Appendix B). Configuration G case 211F for internally mixed, chevron, azimuthal periodicity $m = 8$ nozzle: bypass ratio (BPR) = 5 and flight Mach number $M_{fl} = 0$. For core, acoustic Mach number $M_a = 1.614$ and stagnation temperature ratio $T_{t,r} = 3.455$. For bypass, $M_a = 0.973$ and $T_{t,r} = 1.27$. Comparison between ANOPP predictions with fully mixed approximation and NATR experimental data. (a) 1/3-octave sound pressure level (SPL) versus Strouhal number St for inlet angles $\theta = 90^\circ$ and 150° . (b) Difference in 1/3-octave SPL values, with uncertainty. (c) Overall sound pressure level (OASPL) as function of θ .

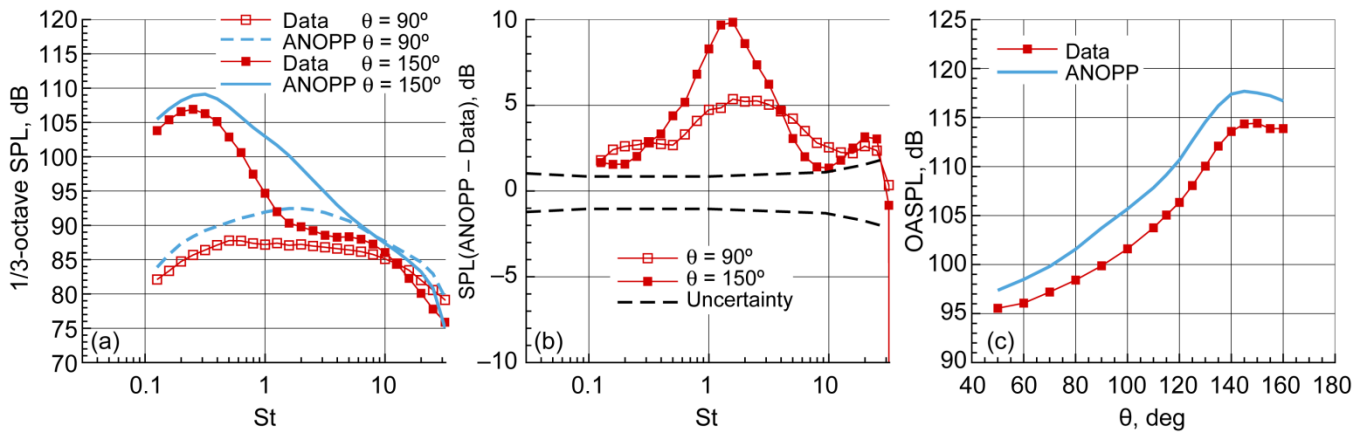


Figure 8.92.—Assessment of ANOPP ST2JET jet noise predictions (Table 8.7, Appendix B). Configuration G case 218C for internally mixed, lobed, azimuthal periodicity $m = 20$ nozzle: bypass ratio (BPR) = 5 and flight Mach number $M_{fl} = 0$. For core, acoustic Mach number $M_a = 1.637$ and stagnation temperature ratio $T_{t,r} = 3.546$. For bypass, $M_a = 0.985$ and $T_{t,r} = 1.3$. Comparison between ANOPP predictions with coplanar approximation and NATR experimental data. (a) 1/3-octave sound pressure level (SPL) versus Strouhal number St for inlet angles $\theta = 90^\circ$ and 150° . (b) Difference in 1/3-octave SPL values, with uncertainty. (c) Overall sound pressure level (OASPL) as function of θ .

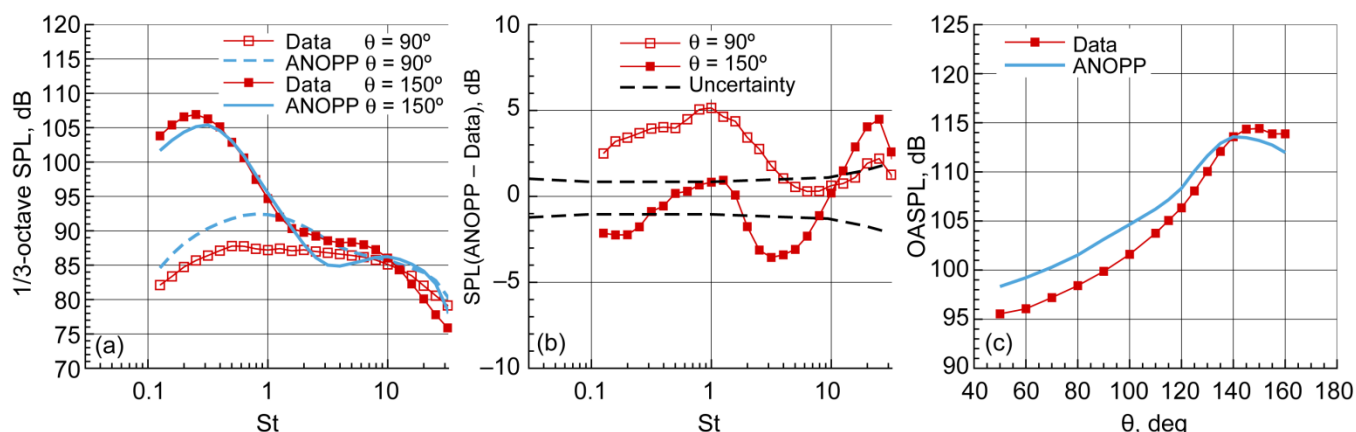


Figure 8.93.—Assessment of ANOPP ST2JET jet noise predictions (Table 8.7, Appendix B). Configuration G case 218F for internally mixed, lobed, azimuthal periodicity $m = 20$ nozzle: bypass ratio (BPR) = 5 and flight Mach number $M_{fl} = 0$. For core, acoustic Mach number $M_a = 1.637$ and stagnation temperature ratio $T_{t,r} = 3.546$. For bypass, $M_a = 0.985$ and $T_{t,r} = 1.3$. Comparison between ANOPP predictions with fully mixed approximation and NATR experimental data. (a) 1/3-octave sound pressure level (SPL) versus Strouhal number St for inlet angles $\theta = 90^\circ$ and 150° . (b) Difference in 1/3-octave SPL values, with uncertainty. (c) Overall sound pressure level (OASPL) as function of θ .

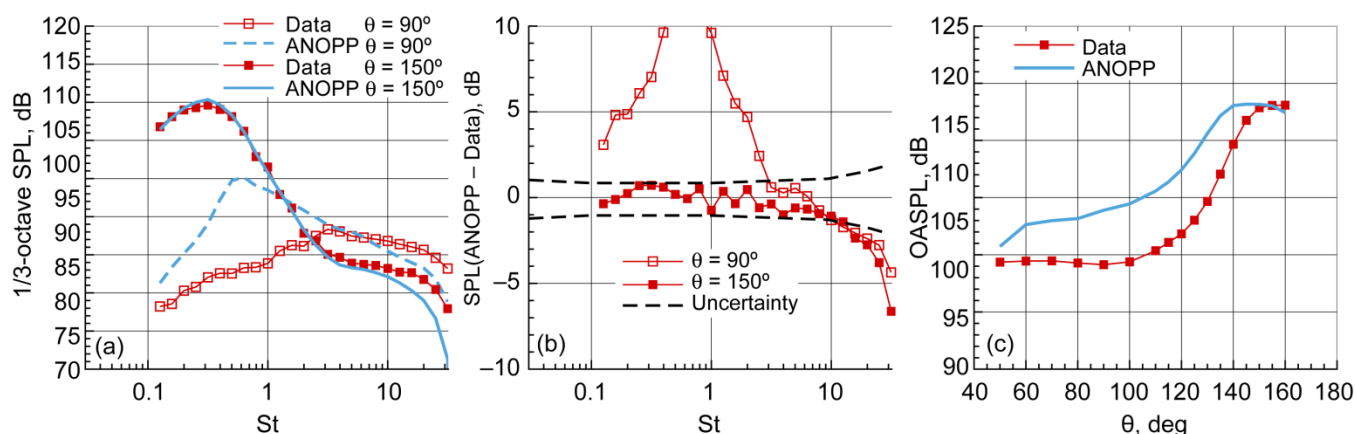


Figure 8.94.—Assessment of ANOPP ST2JET jet noise predictions (Table 8.7, Appendix B). Configuration G case 230N for externally mixed, convergent, axisymmetric nozzle: bypass ratio (BPR) = 5 and flight Mach number $M_{fl} = 0.1$. For core, acoustic Mach number $M_a = 1.126$ and stagnation temperature ratio $T_{t,r} = 2.46$. For bypass, $M_a = 1.566$ and $T_{t,r} = 1.17$. Comparison between ANOPP predictions and NATR experimental data. (a) 1/3-octave sound pressure level (SPL) versus Strouhal number St for inlet angles $\theta = 90^\circ$ and 150° . (b) Difference in 1/3-octave SPL values, with uncertainty. (c) Overall sound pressure level (OASPL) as function of θ .

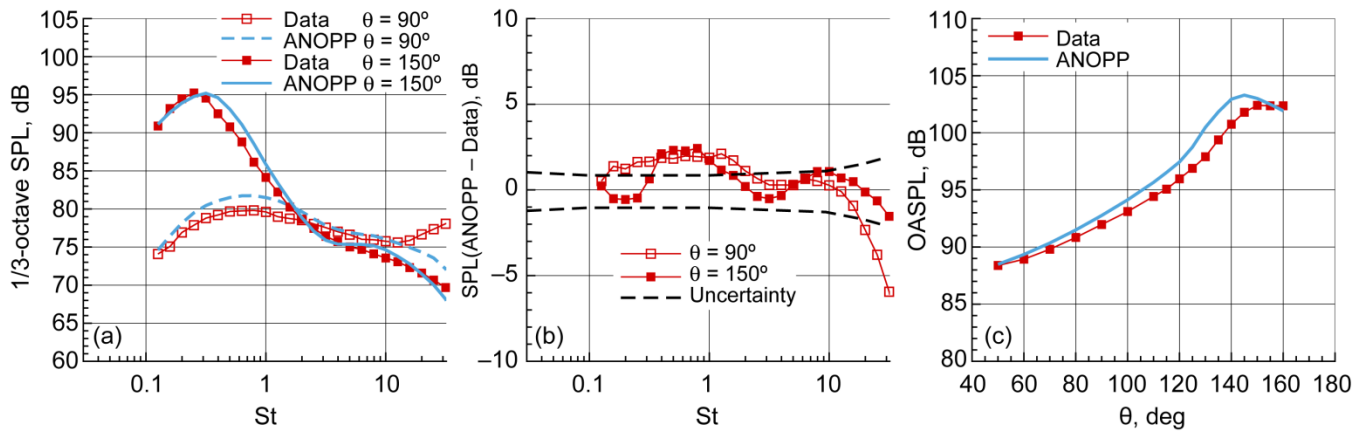


Figure 8.95.—Assessment of ANOPP ST2JET jet noise predictions (Table 8.7, Appendix B). Configuration H case 235N for externally mixed, convergent, axisymmetric nozzle: bypass ratio (BPR) = 8 and flight Mach number $M_\infty = 0.01$. For core, acoustic Mach number $M_a = 1.002$ and stagnation temperature ratio $T_{t,r} = 2.447$. For bypass, $M_a = 0.812$ and $T_{t,r} = 1.114$. Comparison between ANOPP predictions and NATR experimental data. (a) 1/3-octave sound pressure level (SPL) versus Strouhal number St for inlet angles $\theta = 90^\circ$ and 150° . (b) Difference in 1/3-octave SPL values, with uncertainty. (c) Overall sound pressure level (OASPL) as function of θ .

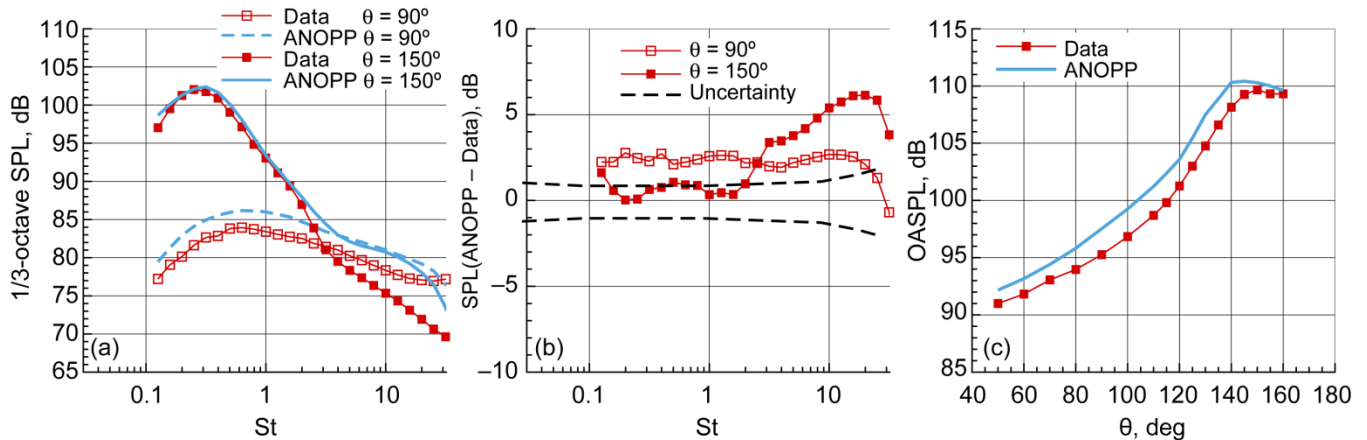


Figure 8.96.—Assessment of ANOPP ST2JET jet noise predictions (Table 8.7, Appendix B). Configuration H case 241C for internally mixed, convergent, axisymmetric nozzle: bypass ratio (BPR) = 8 and flight Mach number $M_\infty = 0$. For core, acoustic Mach number $M_a = 1.366$ and stagnation temperature ratio $T_{t,r} = 3.211$. For bypass, $M_a = 0.902$ and $T_{t,r} = 1.296$. Comparison between ANOPP predictions with coplanar approximation and NATR experimental data. (a) 1/3-octave sound pressure level (SPL) versus Strouhal number St for inlet angles $\theta = 90^\circ$ and 150° . (b) Difference in 1/3-octave SPL values, with uncertainty. (c) Overall sound pressure level (OASPL) as function of θ .

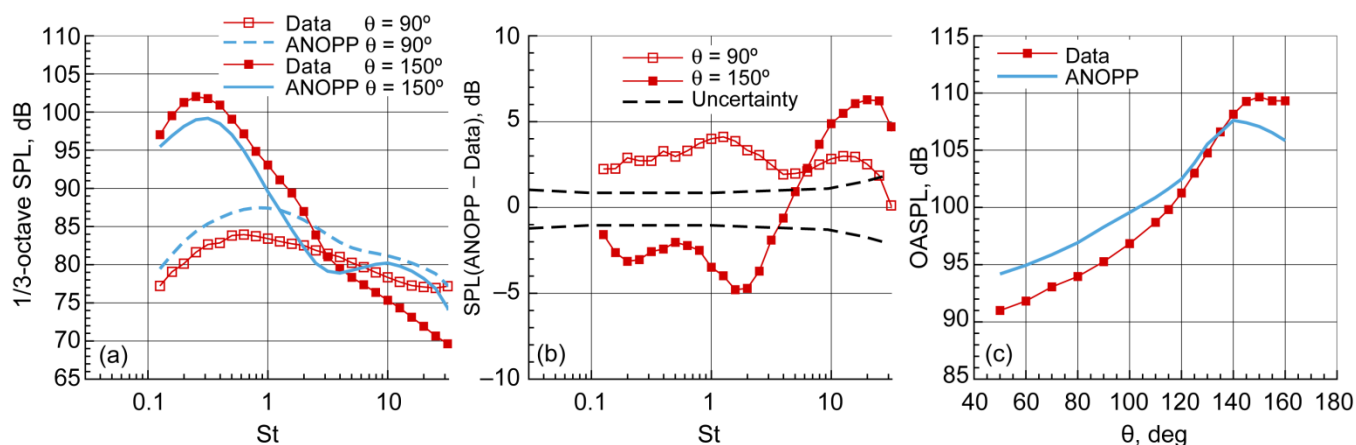


Figure 8.97.—Assessment of ANOPP ST2JET jet noise predictions (Table 8.7, Appendix B). Configuration H case 241F for internally mixed, convergent, axisymmetric nozzle: bypass ratio (BPR) = 8 and flight Mach number $M_{\theta} = 0$. For core, acoustic Mach number $M_a = 1.366$ and stagnation temperature ratio $T_{t,r} = 3.211$. For bypass, $M_a = 0.902$ and $T_{t,r} = 1.296$. Comparison between ANOPP predictions with fully mixed approximation and NATR experimental data. (a) 1/3-octave sound pressure level (SPL) versus Strouhal number St for inlet angles $\theta = 90^\circ$ and 150° . (b) Difference in 1/3-octave SPL values, with uncertainty. (c) Overall sound pressure level (OASPL) as function of θ .

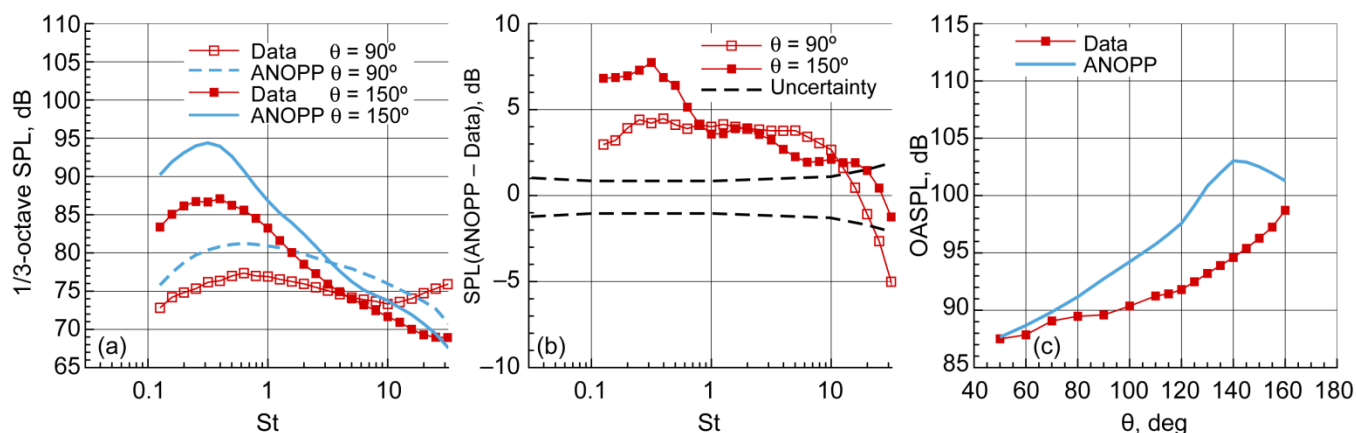


Figure 8.98.—Assessment of ANOPP ST2JET jet noise predictions (Table 8.7, Appendix B). Configuration H case 253C for internally mixed, chevron, azimuthal periodicity $m = 8$ nozzle: bypass ratio (BPR) = 8 and flight Mach number $M_{\theta} = 0.24$. For core, acoustic Mach number $M_a = 1.371$ and stagnation temperature ratio $T_{t,r} = 3.237$. For bypass, $M_a = 0.906$ and $T_{t,r} = 1.3$. Comparison between ANOPP predictions with coplanar approximation and NATR experimental data. (a) 1/3-octave sound pressure level (SPL) versus Strouhal number St for inlet angles $\theta = 90^\circ$ and 150° . (b) Difference in 1/3-octave SPL values, with uncertainty. (c) Overall sound pressure level (OASPL) as function of θ .

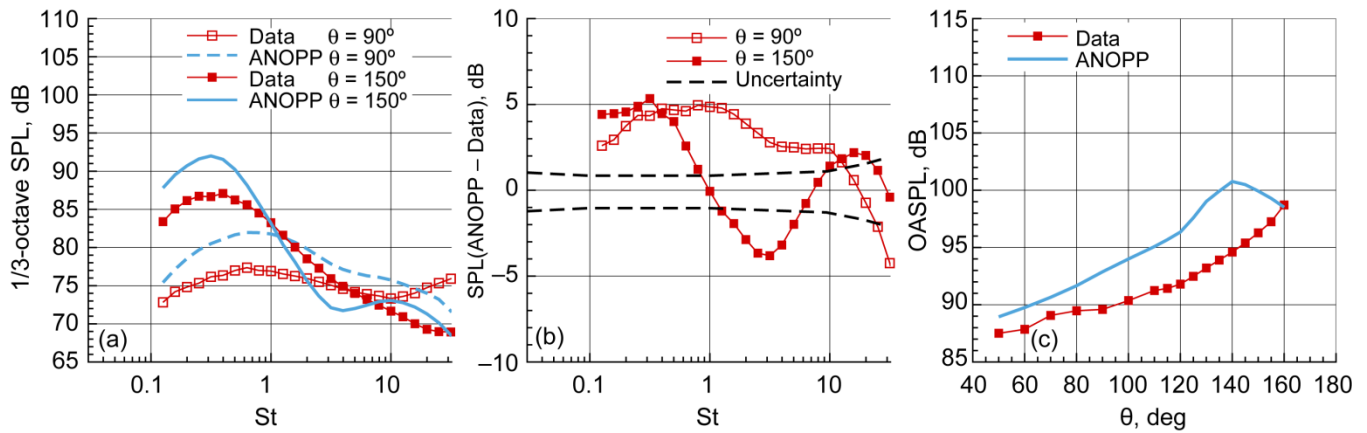


Figure 8.99.—Assessment of ANOPP ST2JET jet noise predictions (Table 8.7, Appendix B). Configuration H case 253F for internally mixed, chevron, azimuthal periodicity $m = 8$ nozzle: bypass ratio (BPR) = 8 and flight Mach number $M_{II} = 0.24$. For core, acoustic Mach number $M_a = 1.371$ and stagnation temperature ratio $T_{t,r} = 3.237$. For bypass, $M_a = 0.906$ and $T_{t,r} = 1.3$. Comparison between ANOPP predictions with fully mixed approximation and NATR experimental data. (a) 1/3-octave sound pressure level (SPL) versus Strouhal number St for inlet angles $\theta = 90^\circ$ and 150° . (b) Difference in 1/3-octave SPL values, with uncertainty. (c) Overall sound pressure level (OASPL) as function of θ .

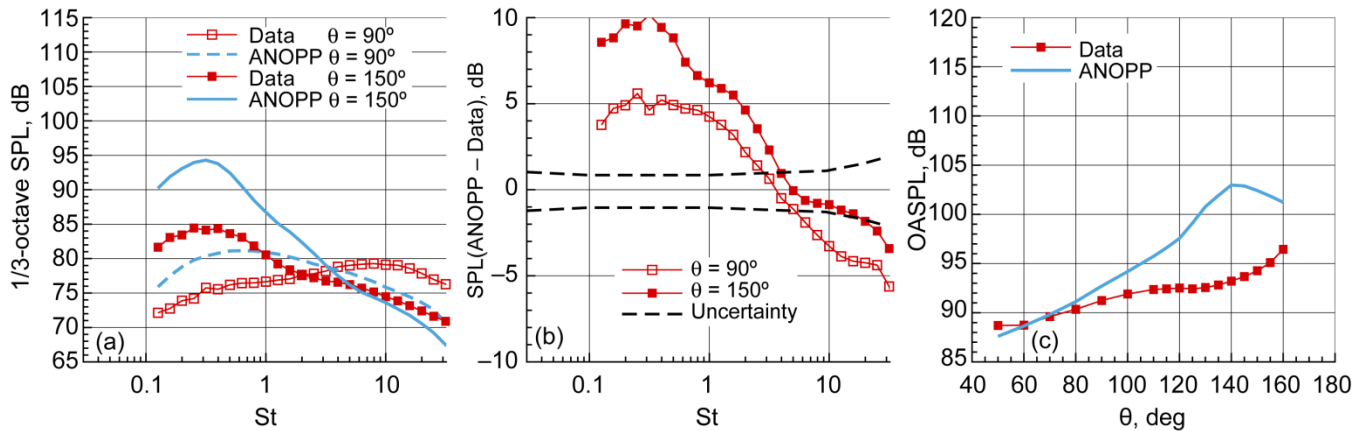


Figure 8.100.—Assessment of ANOPP ST2JET jet noise predictions (Table 8.7, Appendix B). Configuration H case 257C for internally mixed, lobed, azimuthal periodicity $m = 20$ nozzle: bypass ratio (BPR) = 8 and flight Mach number $M_{II} = 0.24$. For core, acoustic Mach number $M_a = 1.376$ and stagnation temperature ratio $T_{t,r} = 3.254$. For bypass, $M_a = 0.906$ and $T_{t,r} = 1.309$. Comparison between ANOPP predictions with coplanar approximation and NATR experimental data. (a) 1/3-octave sound pressure level (SPL) versus Strouhal number St for inlet angles $\theta = 90^\circ$ and 150° . (b) Difference in 1/3-octave SPL values, with uncertainty. (c) Overall sound pressure level (OASPL) as function of θ .

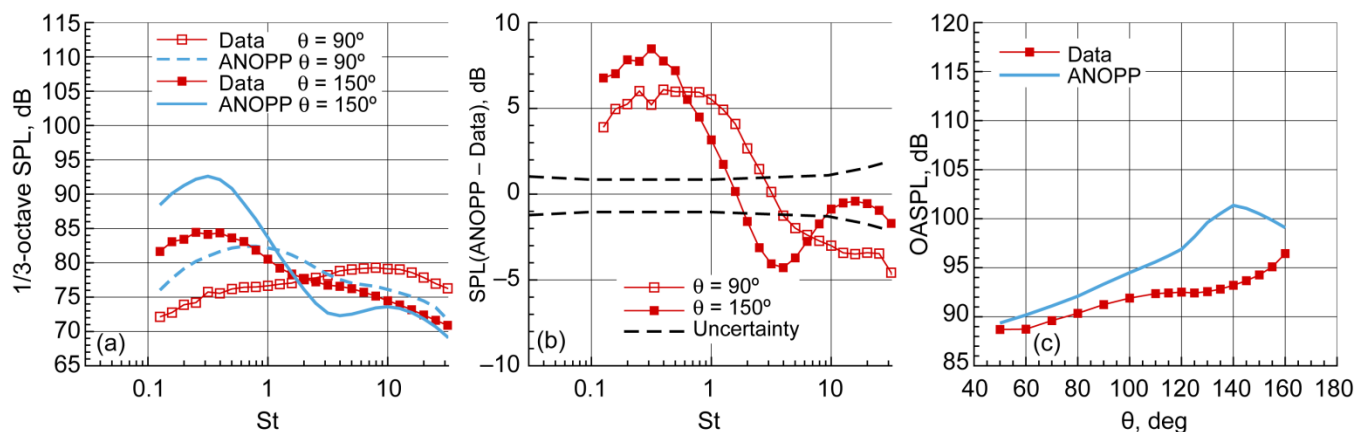


Figure 8.101.—Assessment of ANOPP ST2JET jet noise predictions (Table 8.7, Appendix B). Configuration H case 257F for internally mixed, lobed, azimuthal periodicity $m = 20$ nozzle: bypass ratio (BPR) = 8 and flight Mach number $M_{fl} = 0.24$. For core, acoustic Mach number $M_a = 1.376$ and stagnation temperature ratio $T_{t,r} = 3.254$. For bypass, $M_a = 0.906$ and $T_{t,r} = 1.309$. Comparison between ANOPP predictions with fully mixed approximation and NATR experimental data. (a) 1/3-octave sound pressure level (SPL) versus Strouhal number St for inlet angles $\theta = 90^\circ$ and 150° . (b) Difference in 1/3-octave SPL values, with uncertainty. (c) Overall sound pressure level (OASPL) as function of θ .

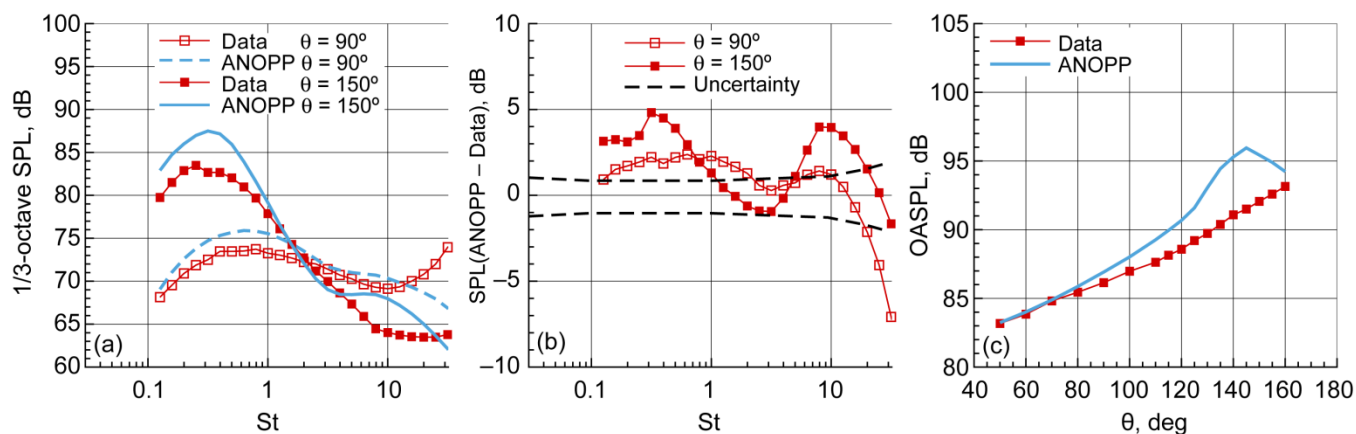


Figure 8.102.—Assessment of ANOPP ST2JET jet noise predictions (Table 8.7, Appendix B). Configuration I case 263N for externally mixed, convergent, axisymmetric nozzle: bypass ratio (BPR) = 11 and flight Mach number $M_{fl} = 0.1$. For core, acoustic Mach number $M_a = 0.873$ and stagnation temperature ratio $T_{t,r} = 2.568$. For bypass, $M_a = 0.738$ and $T_{t,r} = 1.083$. Comparison between ANOPP predictions and NATR experimental data. (a) 1/3-octave sound pressure level (SPL) versus Strouhal number St for inlet angles $\theta = 90^\circ$ and 150° . (b) Difference in 1/3-octave SPL values, with uncertainty. (c) Overall sound pressure level (OASPL) as function of θ .

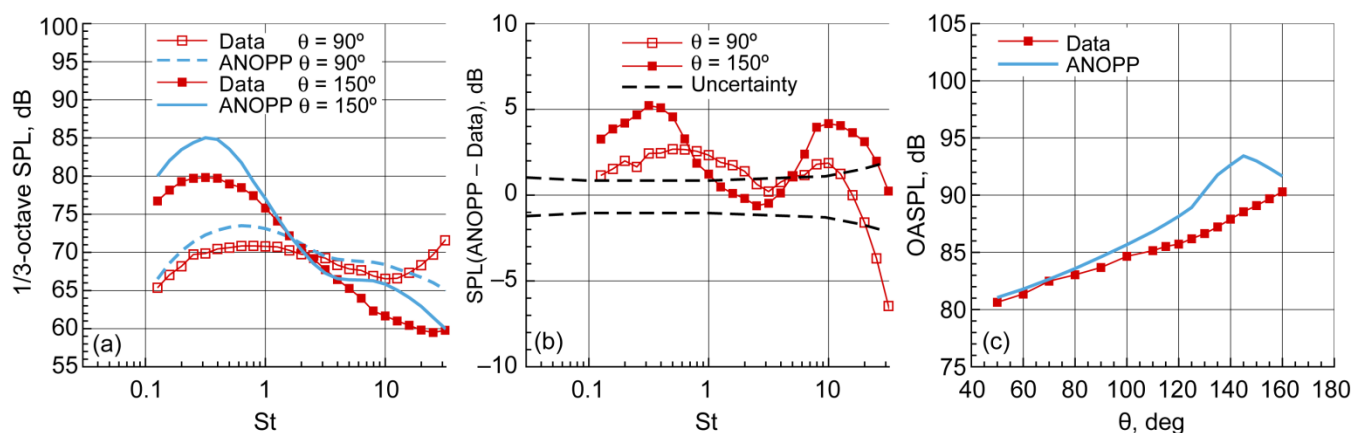


Figure 8.103.—Assessment of ANOPP ST2JET jet noise predictions (Table 8.7, Appendix B). Configuration I case 267N for externally mixed, convergent, axisymmetric nozzle: bypass ratio (BPR) = 14 and flight Mach number $M_H = 0.1$. For core, acoustic Mach number $M_a = 0.859$ and stagnation temperature ratio $T_{t,r} = 2.53$. For bypass, $M_a = 0.686$ and $T_{t,r} = 1.071$. Comparison between ANOPP predictions and NATR experimental data. (a) 1/3-octave sound pressure level (SPL) versus Strouhal number St for inlet angles $\theta = 90^\circ$ and 150° . (b) Difference in 1/3-octave SPL values, with uncertainty. (c) Overall sound pressure level (OASPL) as function of θ .

References

1. Engineering Sciences Data Unit: ESDU Aircraft Noise Series. April 2000.
2. Stone, James R., et al.: Jet Noise Modeling for Suppressed and Unsuppressed Aircraft in Simulated Flight. NASA/TM—2009-215524, 2009.
3. Zorunski, W.E.: Aircraft Noise Prediction Program Theoretical Manual. NASA TM—83199, pts. 1 and 2, 1982.
4. Stone, James; Krejsa, Eugene; and Clark, Bruce: Semi-Empirical Model for Coannular Nozzle Component Noise Extraction and Correlation Including the Effects of Noise Reduction Devices. AIAA—2003—1060, 2003.
5. Lighthill, M.J.: On Sound Generated Aerodynamically. 1. General Theory. Proc. Royal Soc. London Series A, vol. 211, no. 1107, 1952, pp. 564–587.
6. Lighthill, M.J.: On Sound Generated Aerodynamically. 2. Turbulence as a Source of Sound. Proc. R. Soc. London, Ser. B, vol. 222, no. 1148, 1954, pp. 1–32.
7. Lilley, G.M.: On the Noise From Jets, Proceedings of Noise Mechanisms, AGARD CP—131, 1973.
8. Hunter, Craig A.: An Approximate Jet Noise Prediction Method Based on Reynolds-Averaged Navier-Stokes Computational Fluid Dynamics Simulation. D.Sc. Thesis, George Washington University, 2002.
9. Yamamoto, K., et al.: Experimental Investigation of Shock-Cell Noise Reduction for Single-Stream Nozzles in Simulated Flight, Comprehensive Data Report. NASA CR—168234, vols. 1–3, 1984.
10. Nelson, C.C.; and Power, G.D.: CHSSI Project CFD-7: The NPARC Alliance Flow Simulation System. AIAA—2001—594, 2001.
11. Abdol-Hamid, Khaled, S., et al.: PAB3D: Its History in the Use of Turbulence Models in the Simulation of Jet and Nozzle Flows. AIAA—2006—489, 2006.
12. Goldstein, M.E.: A Generalized Acoustic Analogy. J. Fluid Mech., vol. 488, 2003, pp. 315–333.
13. Khavaran, Abbas; Bridges, James; and Georgiadis, Nicholas: Prediction of Turbulence-Generated Noise in Unheated Jets. Part 1: JeNo Technical Manual (Version 1.0), NASA/TM—2005-213827, 2005.
14. Khavaran, Abbas; Wolter, John D.; and Koch, L. Danielle: Prediction of Turbulence-Generated Noise in Unheated Jets. Part 2: JeNo Users' Manual (Version 1.0), NASA/TM—2009-213827/PART2, 2009.
15. Georgiadis, Nicholas; Yoder, Dennis; and Engblom, William: Evaluation of Modified Two-Equation Turbulence Models for Jet Flow Predictions. AIAA J., vol. 44, no. 12, 2006, pp. 3107–3114.
16. Dash, S.M., et al.: Recent Advances in Jet Flowfield Simulation: Part I—Steady Flows. AIAA—1993—4390, 1993.
17. Tanna, H.K.; Dean, P.D.; and Burrin, R.H.: The Generation and Radiation of Supersonic Jet Noise. Final Technical Report, AFAPL—TR—76—65—VOL—3, 1976.
18. Viswanathan, K.: Aeroacoustics of Hot Jets. J. Fluid Mech., vol. 516, 2004, pp. 39–82.
19. Viswanathan, K.: Jet Aeroacoustic Testing: Issues and Implications. AIAA J., vol. 41, no. 9, 2003, pp. 1674–1689.
20. Ahuja, K.K.: Designing Clean Jet-Noise Facilities and Making Accurate Jet-Noise Measurements. International J. Aeroacoustics, vol. 2, nos. 3 and 4, 2003, pp. 371–412.
21. Brown, Clifford; and Bridges, James: Acoustic Efficiency of Azimuthal Modes in Jet Noise Using Chevron Nozzles. AIAA—2006—2645, 2006.
22. Soeder, Ronald H.; Wnuk, Stephen P.; and Loew, Raymond A.: Aero-Acoustic Propulsion Laboratory Nozzle Acoustic Test Rig User Manual. NASA/TM—2006-212939, 2006. Available from the Center for AeroSpace Information.
23. Thompson, Phillip, A.: Compressible Fluid Dynamics (Advanced Engineering Series), McGraw Hill, 1972.
24. Acoustical Society of America: Calculation of the Absorption of Sound by the Atmosphere. ANSI/ASA S1.26—1995 (R2009), 2010.
25. International Electrotechnical Commission: Electroacoustics Octave-Band and Fractional-Octave-Band Filters. International Standard IEC 1260, First ed., 1995.
26. Ahuja, K.K.; Tester, B.J.; and Tanna, H.K.: The Free Jet as a Simulator of Forward Velocity Effects on Jet Noise. NASA CR—3056, 1978.
27. Viswanathan, K.; and Clark, L.T.: Effect of Nozzle Internal Contour on Jet Aeroacoustics. Intl. J. Aeroacoustics, vol. 3, no. 2, 2004, pp. 103–135.
28. Brown, Cliff; and Bridges, James: Small Hot Jet Acoustic Rig Validation. NASA/TM—2006-214234, 2006.
29. Opalski, Anthony; Wernet, Mark; and Bridges, James: Chevron Nozzle Performance Characterization Using Stereoscopic DPIV. AIAA—2005—444, 2005.
30. Wernet, Mark P.: Fuzzy Logic Enhanced Digital PIV Processing Software. NASA/TM—1999-209274, 1999.
31. Soloff, S.M.; Adrian, R.J.; and Liu, Z.-C.: Distortion Compensation for Generalized Stereoscopic Particle Image Velocimetry. Meas. Sci. Technol., vol. 8, no. 12, 1997, pp. 1441–1454.
32. Ahuja, K.K., et al.: Tone-Excited Jet: Theory and Experiments; Final Report. NASA CR—3538, 1982.
33. Birch, Stanley, et al.: An Experimental Study of Flow Asymmetry in Co-Axial Jets. AIAA—2005—2845, 2005.
34. Bridges, James; and Brown, Clifford: Parametric Testing of Chevrons on Single Flow Hot Jets. AIAA—2004—2824, 2004.
35. Brown, Clifford; Bridges, James; and Henderson, Brenda: Offset Stream Technologies Test—Summary of Results. AIAA—2007—3664, 2007.
36. Dippold, Vance; Foster, Lancert; and Wiese, Michael: Computational Analyses of Offset Stream Nozzles for Noise Reduction. AIAA—2007—3589, 2007.
37. Papamoschou, Dimitri: Parametric Study of Fan Flow Deflectors for Jet Noise Suppression. AIAA—2005—2890, 2005.
38. Zaman, Khairul: Noise- and Flow-Field of Jets From an Eccentric Coannular Nozzle. AIAA—2004—5, 2004.

Chapter 9—Propulsion Airframe Aeroacoustic Interactions

Craig A. Hunter and Russell H. Thomas
National Aeronautics and Space Administration
Langley Research Center
Hampton, Virginia 23681

Summary

State-of-the-art propulsion airframe aeroacoustic interaction experiments and prediction methods constitute important first steps leading towards the development of more comprehensive methods. Preliminary experiments have been done on the jet-pylon interaction and acoustic scattering in a static environment. While useful, these experiments have lacked many of the key interaction effects that occur in realistic environments. In the future, there will be a need for aircraft system level experiments (including fuselage, wing, high-lift system, etc.) with important parameters included such as angle of attack, and with more thorough far-field acoustic source characterization and flow-field data.

Prediction methods for propulsion airframe aeroacoustics (PAA) are lacking even a basic empirical or semi-empirical basis suitable for system noise tools. Higher fidelity methods have made progress in the area of PAA flow interactions focused on jet-pylon interaction. The future of propulsion airframe aeroacoustics methods is aimed at simulating the full aircraft configuration with flow interaction and acoustic scattering effects.

9.1 Introduction

Relative to other areas of aircraft acoustics, there has been too little research focused on the aeroacoustic effects of propulsion airframe integration, distinguished by the term “propulsion airframe aeroacoustics” (PAA). From a technology development point of view, this has largely been the result of limited prediction method capabilities, limited computational resources, and the more complex experimental approaches required to address fully integrated systems requiring full-scale flight experiments.

In general, the aeroacoustic effects related to propulsion airframe integration, or PAA effects, can be classified in various ways. The following classification begins with a fundamental division of PAA effects into those effects having to do with flow interaction and those having to do with acoustic propagation. However, it is important to remember that in many cases these are not entirely unrelated issues. With these two fundamental divisions, the classification can be extended to the next level. For flow interaction the next important division concerns the flow direction: upstream or inlet, and downstream or exhaust. Since turbomachinery and jet noise sources have different characteristics, acoustic propagation effects are more importantly divided along noise sources. The next lowest level of the classification tree is composed of identifying interactions between general engine and airframe components. And finally, some specific interactions are given along with key parameters. This classification tree is shown in Figure 9.1 and represents a general way of identifying and organizing PAA effects. However, at the same time, it is not meant to imply that these effects can necessarily be studied or addressed separate from the aircraft system as a whole.

Flow interaction effects are caused by the flow field of one component interacting with another specifically because of the location or orientation of installation. An example of this is the

influence of the engine mounting pylon on the core jet exhaust flow. The influence of the pylon creates flow features in the jet that are not present in an isolated jet. These features are then also influenced by aircraft attitude. Another example is the possible interaction of the fan or core jet exhaust flow with an extended flap and its flow; for example, with the typical engine-under-wing configuration. These types of flow interaction effects from installation can create new acoustic sources, or they can modify existing acoustic sources already associated with components.

Acoustic propagation effects arise when noise generated from various components propagates and interacts either with structures or with flow features created by flow over the airframe and propulsion device. The acoustic propagation of fan noise along the exhaust duct, for example, is altered by the presence of the bifurcator and pylon. Furthermore, the fan noise propagation can be scattered off deployed flaps compared to propagation of fan noise in isolation. Reflection of jet noise off of the underside of the wing for the typical engine-under-wing configuration is another example. Acoustic propagation effects are unlikely to create new noise sources specifically due to installation effects; however, these effects can conceivably modify existing component noise sources. An example of this modification could be reflected jet noise interacting with jet noise sources.

Overviews of PAA effects and some recent research can be found in References 1 to 3.

Acronyms and symbols used in this chapter are listed in Appendix A.

9.2 Experiments

There are several experiments that have been performed specifically as PAA studies in recent years as part of research by NASA and partners. The 2002 Pylon Effects test was conducted in the NASA Langley Research Center Jet Noise

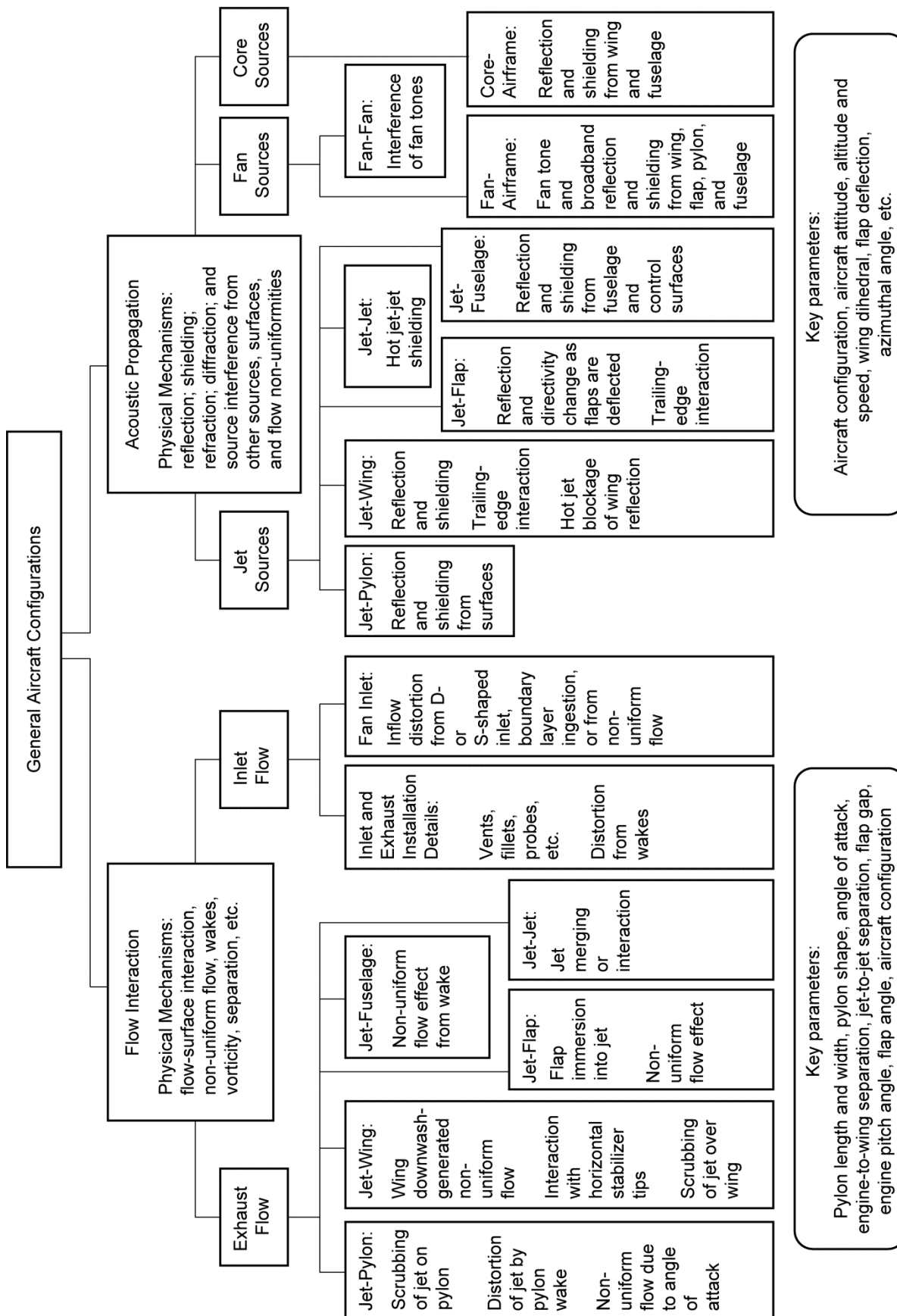


Figure 9.1.—Propulsion airframe acoustics (PAA) classification tree.

Laboratory and provided basic mean-flow-field and acoustic far-field data for a jet-pylon interaction study (Ref. 4). The 2004 NASA-Boeing PAA experiment in the Boeing Low-Speed Aeroacoustic Facility (LSAF) was an extensive experiment involving nozzle, pylon, and flap-trailing-edge modifications and effects (Refs. 5 to 8). As part of the same partnership, there was a PAA element to the Boeing-led Quiet Technology Demonstrator 2 (QTD2) flight test project (Ref. 9). Finally, specifically in the area of acoustic shielding, the 2003 blended wing body (BWB) acoustic shielding experiment was conducted using a broadband point source to document the shielding of the BWB airframe under static conditions; this is described together with predictions in Reference 10.

In general, more complex aircraft-system-level experiments, such as the 2004 NASA-Boeing LSAF PAA experiment and the QTD2 flight experiment, include the realistic PAA effects but are too complex for PAA prediction methods that are available to date. The 2002 Pylon Effects experiment with its limitation to the interaction of jet and pylon was used as the primary validation of the Jet3D prediction code, and that code and experiment are described in the following sections and are the focus of this chapter.

9.2.1 Pylon Effects Experiment

The experiments reported here were carried out at NASA Langley's Jet Noise Laboratory (JNL) and were concluded by the summer of 2002. The purpose was to provide an experimental database of acoustic and mean-flow surveys of a basic building block of propulsion airframe integration, the jet-pylon interaction. The components of the experiment consisted of the jet engine simulator, the Low Speed Aeroacoustic Wind Tunnel, and the model hardware.

The experimental investigation of jet-pylon effects included separate flow and chevron nozzles of bypass ratio (BPR) 5 and 8. These experiments measured the mean-flow quantities of pressure and temperature and acoustic effects. The mean-flow

measurements were reported in Reference 11, and the full report of the acoustic measurements has been reported in Reference 4. The models corresponded to an approximate "full scale to model scale" factor of 9. Operating conditions representing those from a typical subsonic aircraft at approach to takeoff were tested at wind tunnel free-jet Mach numbers of 0.1, 0.2, and 0.28. An eight-chevron nozzle and a pylon were primary configuration variables. In addition, two orientations of the chevrons relative to the pylon were tested. The effect of the pylon and the azimuthal directivity were investigated for the baseline nozzles and the chevron nozzles.

9.2.2 Experimental Facility

The jet engine simulator (JES) is installed in the NASA Langley Low Speed Aeroacoustic Wind Tunnel (LSAWT) as shown in Figure 9.2 to produce two streams and accurately simulate engine nozzle systems. The JES has two propane-fired sudden expansion burners to heat fan and core nozzle streams separately. Each stream can flow air up to a maximum of 7.7 kg/s (17 lbm/s). In addition, each stream has an electric pre-heater for low temperature operation and for burner stability. Airflow is straightened before transitioning to the nozzle. The JES is equipped with a six-component load cell for thrust measurements, although that capability was not used in this experiment. Airflow is measured by critical venturi meters in each stream. Airflow pressure and temperature rakes are positioned just upstream of the nozzle contraction to measure nozzle conditions.

The LSAWT is a continuous-flow in-draft wind tunnel that provides a free jet surrounding the JES exhaust flow. The free jet is produced by a 0.44-m² (4.7-ft²) nozzle. As shown in Figure 9.2, the JES is positioned in the free-jet nozzle and test section as it was configured in 2002. Wind tunnel speed can be varied from a Mach number of 0.1 up to 0.32. For this experiment the wind tunnel free jet was run at three Mach numbers: 0.1, 0.2, and 0.28.

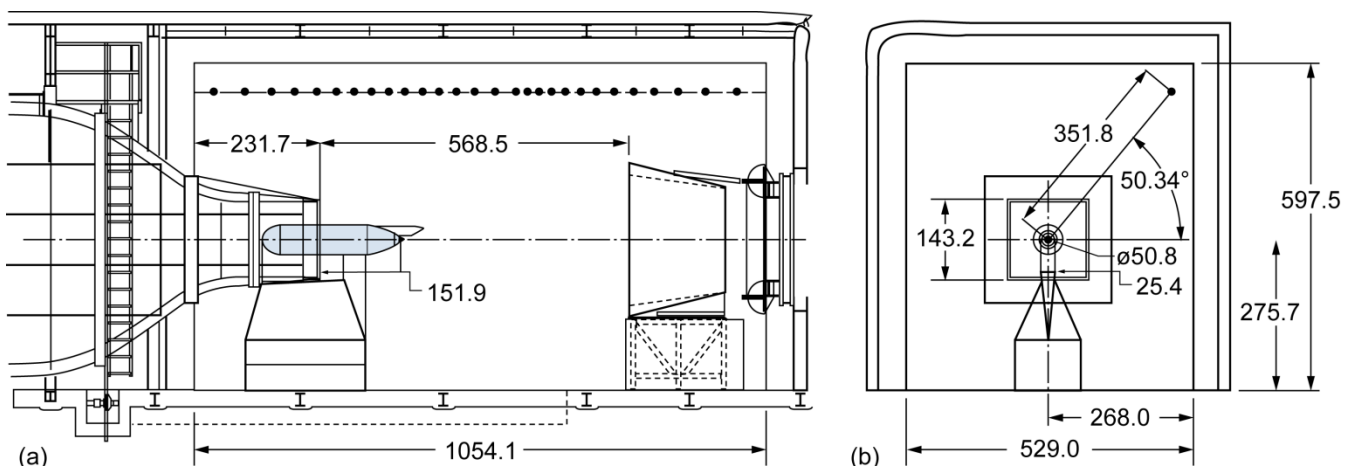


Figure 9.2.—NASA Langley's Low Speed Aeroacoustic Wind Tunnel (LSAWT). Dimensions are in centimeters. (a) Side view of test section with flow from left to right. (b) End view looking upstream with microphone array in upper right-hand side.

The test section has anechoic treatment from fiberglass wedges with a cutoff frequency of 250 Hz. Dimensions of the test cell, measured from tip to tip of the wedges is 10.4 m long by 5.2 m high by 5.2 m wide (34 by 17 by 17 ft). The downstream flow collector regulates flow recirculation in the test cell. Both the wind tunnel nozzle and the flow collector are acoustically treated to minimize reverberations.

9.2.3 Model Design and Experimental Configurations

The baseline configurations are two separate flow nozzles with BPR 5 and 8, each with an external plug. The nozzle and pylon design are from a nozzle study performed by McDonnell Douglas (now Boeing) in 1996 and represent a generic design of conventional nozzles for commercial subsonic transports. The baseline nozzle is modified by attaching a pylon and/or chevrons to the core nozzle; the fan nozzle remains the same for both BPR 5 and 8. The higher bypass ratio is achieved by reducing the diameter of the core nozzle from 12.8 to 11.9 cm (5.04 to 4.70 in.).

Chevrons are a noise-reduction technology that is rapidly being applied to newer engine nozzles, and since the pylon is an integral part of the nozzle, core and fan chevrons were tested with and without a pylon at both bypass ratios. On the baseline nozzles, when fan and core chevrons were installed, the orientation of the core and fan chevrons relative to each other was tested. When a pylon was installed, two orientations of the core chevrons relative to the pylon were tested. These two orientations occur when a chevron trough is aligned with the pylon centerline and again when a chevron tip is aligned with the pylon centerline.

The chevrons were designed for the core nozzle using guidelines similar to those used in studies during the NASA Advanced Subsonic Technology (AST) program. The chevrons were designed to penetrate into the core flow by approximately the estimated thickness of the boundary layer for the BPR 5 nozzle. For the BPR 8 nozzle the core chevrons did not penetrate the core flow. The trailing edge of the baseline nozzle is chosen to correspond to the midpoint of the chevron axial length.

Since the pylon clearly creates a nonaxisymmetric geometry, azimuthal angle was also variable in the experimental matrix. Three azimuthal angles were tested, including an orientation corresponding to a flyover (90°), a sideline or takeoff angle (34°), and a third angle at 0° that is normal to the line from the microphones to the nozzle centerline. To achieve the different azimuthal angles the microphones remain fixed and the model with pylon was rotated.

The pylon in these configurations has a diverging angle of 1.5° for the shelf of the pylon that the core flow follows. The junction of the core nozzle with chevrons and the pylon shelf is simply the result of a separate chevron and pylon design combined with no added design feature for the junction. A typical nozzle configuration used in this experiment is shown in Figure 9.3. This picture shows the BPR 5 nozzle with a baseline fan nozzle, and an eight-chevron core nozzle with a chevron tip aligned with the pylon. The pylon was added to the same baseline fan nozzle. Therefore, the fan nozzle area for a configuration with a pylon is less than the fan nozzle area for a baseline configuration. As will be described in sections below, the reduced area, for the same nozzle flow condition, means less fan area and less thrust.

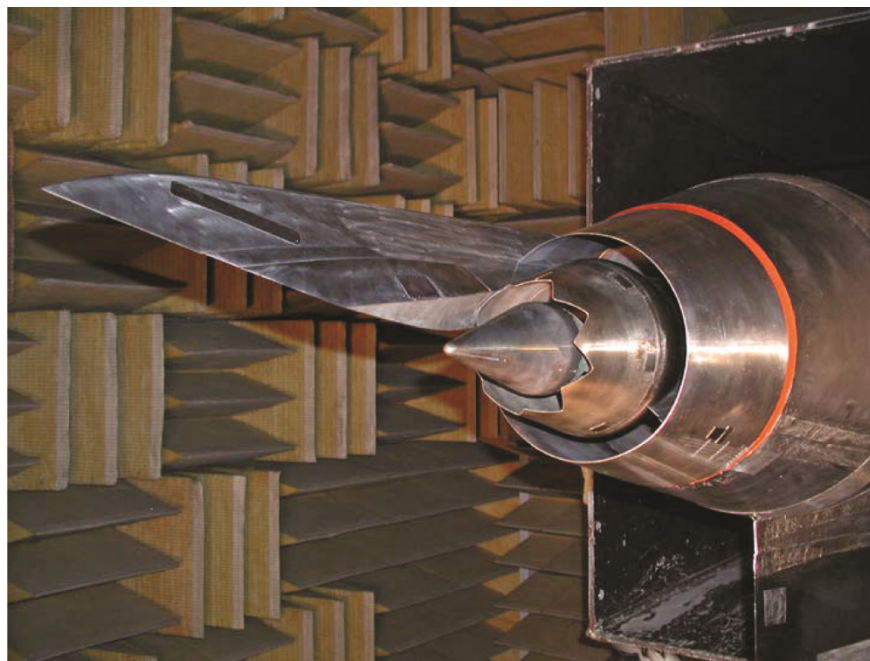


Figure 9.3.—Bypass ratio 5 nozzle with eight-chevron core nozzle and baseline fan nozzle installed in the jet engine simulator (JES) in the LSAWT.

Table 9.1 summarizes the total nozzle areas for both BPR 5 and 8 baseline and pylon configurations. The model-scale area at cold (room-temperature) conditions are based on measurements of the nozzles and are of the area normal to the inner surface at the exit of the nozzle as opposed to an area in the vertical plane at the exit. During the experiment, the nozzle operates at elevated temperatures, and thermal expansion causes the nozzle system dimensions to change slightly. The dimensions under hot operating conditions are not measured, but are estimated based on the known thermal expansion coefficients. These estimated areas under hot operating conditions are also shown in Table 9.1. The pylon has an axial split line that allows for thermal growth between the core and fan nozzles. The gap between the two parts of the pylon is typically less than 0.1 cm (0.04 in.) and is sealed to prevent air leakage. Chevron nozzles were assumed to have the same exit area as the corresponding baseline nozzle. Also in Table 9.1 are the scale factors (based on hot areas) used for processing of the acoustic data as will be described later.

Flow was varied by the nozzle operating conditions and the wind tunnel Mach numbers of 0.1, 0.2, and 0.28. Since the wind tunnel is open to the atmosphere, the ambient temperature and pressure fluctuate with prevailing conditions. However, the ambient temperature turned out to be

remarkably stable during the course of the experiment and only varied by about ± 5.6 K (± 10 °R) from day to day.

Detailed geometry modifications were also tested, including a fillet on the pylon-core nozzle body junction and an extended pylon. Not all of the results of the modifications are reported here since the general conclusions are not altered.

9.2.4 Nozzle Operating Conditions

The nozzle operating conditions for BPR 5 (see Table 9.2) were taken from the same AST study that produced the original hardware design for the baseline nozzles. These operating conditions have been used previously in a study of high-BPR jet noise during the AST program (Ref. 12). The BPR 8 operating conditions used in the experiment were updated to reflect more realistic conditions but were not used in the prediction method validation phase. The same operating conditions were used whether the configuration had a pylon or not, and therefore the nozzle exit conditions were also the same. As described in the discussion of Table 9.1, this meant that for a given baseline-to-pylon configuration comparison the fan area was different and therefore the actual thrust of the pylon configuration was less. As will be discussed in the next section, the acoustic data were scaled differently in order to allow an acoustic comparison on an equal thrust basis.

TABLE 9.1.—SEPARATE-FLOW NOZZLE MODEL AREAS FOR BOTH COLD AND HOT CONDITIONS AND SCALE FACTORS USED FOR ACOUSTIC DATA PROCESSING

Bypass ratio	Pylon	Test point	Cold model fan area, cm ² (in. ²)	Cold model core area, cm ² (in. ²)	Total cold model nozzle area, cm ² (in. ²)	Estimated total hot model area, cm ² (in. ²)	Scale factor	Full size total area, cm ² (in. ²)
5	Yes	15	173.4 (26.87)	69.35 (10.75)	242.7 (37.62)	240.2 (37.23)	9.00	19455.6 (3015.63)
5	No	15	186.1 (28.84)	69.35 (10.75)	255.4 (39.59)	253.0 (39.21)	8.77	19456.4 (3015.75)
8	Yes	5	194.0 (30.07)	48.80 (7.56)	242.8 (37.63)	241.5 (37.43)	9.72	22815.0 (3536.33)
8	No	5	208.5 (32.32)	48.80 (7.56)	257.3 (39.88)	256.1 (39.69)	9.44	22815.0 (3536.33)

TABLE 9.2.—BYPASS RATIO (BPR) 5 NOZZLE OPERATING CONDITIONS^a

Condition	Test point	Fan				Core				BPR	Estimated mixed velocity, m/s (ft/s)
		NPR	T_o , °R	Estimated velocity, m/s (ft/s)	Estimated flow rate, kg/s (lb/s)	NPR	T_o , °R	Estimated velocity, m/s (ft/s)	Estimated flow rate, kg/s (lb/s)		
Approach	1	1.27	582	207 (680)	4.16 (9.16)	1.15	1190	228 (749)	0.68 (1.51)	6.07	210 (690)
	2	1.39	596	244 (802)	4.92 (10.84)	1.24	1240	288 (944)	0.90 (1.98)	5.47	251 (824)
Cutback	5	1.51	612	276 (904)	5.53 (12.18)	1.33	1300	337 (1107)	1.03 (2.28)	5.34	285 (936)
	12	1.63	629	303 (993)	6.03 (13.3)	1.445	1390	394 (1294)	1.18 (2.61)	5.1	318 (1042)
Takeoff	15	1.75	647	327 (1072)	6.46 (14.25)	1.56	1491	447 (1466)	1.30 (2.87)	4.97	347 (1138)

^aNPR is nozzle pressure ratio.

T_o is stagnation temperature.

9.2.5 Acoustic Data Processing

Acoustic data were collected with a 28-microphone sideline array located 3.52 m (11.54 ft) from the centerline axis of the model. Microphones were 0.64 cm (0.25 in.) in diameter, operated with the grid caps removed, and calibrated with a pistonphone and electrostatic calibrator before and after the test. Acoustic data was processed using both General Electric Company (GE) and NASA procedures and using different shear-layer corrections. In general, although there are differences in the results from the different processing, the conclusions concerning changes between configurations are not altered. Therefore, data presented in this paper uses the GE process with the Amiet (Ref. 13) point-source model for the shear layer correction. Acoustic data shown in subsequent sections are processed to 1/3-octave bands and include corrections for the microphone calibration, wind tunnel background noise, a Doppler shift to the spectral data, and atmospheric absorption to acoustic standard day conditions using the Shields and Bass methodology (Ref. 14). The data were scaled to the full-scale engine size using the varying scale factors of Table 9.1, and extrapolated to a distance of 543.2 m (1782 ft), typical of certification. This corresponds to an altitude of 304.8 m (1000 ft) and a ground sideline distance of 449.9 m (1476 ft). After the model-scale data were transformed to full scale, the effective perceived noise level (EPNL) was calculated by simulating an aircraft flyover at Mach 0.28 and using the procedure described in Reference 15.

The repeatability of the acoustic measurements is approximately ± 0.4 dB. Most of the test points were repeated several times. For the PNL and EPNL plotted here as a function of operating condition, a linear fit is made through all available data points so differences between configurations can be made with more confidence by considering the trends demonstrated by all points along the operating line.

The model-scale nozzles are of almost identical total area as seen in Table 9.1. This implies less thrust from the nozzles with a higher BPR. To make comparisons meaningful, the acoustic results were scaled to achieve equivalent ideal thrust at the takeoff condition. This would, in theory, allow either of the two BPR nozzles to power the same aircraft with other practical issues ignored. This also means that for an equivalent ideal thrust, the mixed-jet velocity of each BPR nozzle will not necessarily be the same. With a scale factor of 9 fixed for the BPR 5 baseline nozzle, different scale factors were calculated for the BPR 5 nozzle with a pylon, the BPR 8 baseline, and the BPR 8 nozzle with a pylon. This allows for the acoustic data to be scaled to a representative full scale at equivalent ideal thrust.

9.3 Prediction Method Overview

The PAA prediction methods are grouped in several categories in parallel with the prior classification of PAA effects. An efficient tool and one suited to current system noise prediction methods would be an empirical or semi-empirical method

based primarily on experimental data. With the appropriate benchmark experiment, it would be possible to develop such an empirical or semi-empirical model for integration in a system noise prediction method like NASA's Aircraft Noise Prediction Program (see Chapter 2). Many parameters could be included in such a model addressing installation effects; however, no such comprehensive model has been developed in NASA efforts yet. Moving to higher fidelity methods, for PAA effects of the flow interaction type involving primarily jet and pylon, wing, and flap interaction, for example, methods based on computational fluid dynamics (CFD) exist using a flow solver (PAB3D, USM3D, etc.) in combination with a noise prediction code like Jet3D. For PAA effects of the acoustic interaction type there are a number of methods in various stages of development and use such as methods based on ray tracing, energy elements, or boundary elements, the latter being used in the NASA-sponsored acoustic scattering code described in Reference 10 together with comparison with the 2003 BWB acoustic scattering experiment.

9.4 Jet3D

Jet3D (Ref. 16) is based on a straightforward application of Lighthill's Acoustic Analogy (LAA) in three dimensions, solved and manipulated (according to Ffowcs Williams, Ref. 17) to give the far-field acoustic pressure p correlation as a function of spatial observer position \mathbf{x} and time delay τ :

$$\langle p^2 \rangle(\mathbf{x}, \tau) = \frac{1}{16\pi^2 c_\infty^4} \int_{\text{jet}} \hat{r}_i \hat{r}_j \hat{r}_m \hat{r}_n \int_{-\infty}^{\infty} \frac{\partial^4}{\partial \tilde{\tau}^4} \langle T_{ij} T'_{mn} \rangle d\boldsymbol{\zeta} d\mathbf{z} \quad (9.1)$$

where c_∞ is the ambient speed of sound, \hat{r}_i are components of the acoustic radius unit vector, C is the jet convection factor, C_∞ is the flight convection factor, r is the magnitude of the acoustic radius, $\tilde{\tau}$ is the time delay in the moving frame, T_{ij} is the Lighthill stress tensor, T'_{mn} is the stress tensor at a different spatial position, $\boldsymbol{\zeta}$ is the moving frame separation vector, and \mathbf{z} is the moving frame source position vector. Here $T_{ij} = (p - c_\infty^2 \rho) \delta_{ij} - \sigma_{ij} + \rho u_i u_j$ where ρ is the density of air, δ_{ij} is the Kronecker delta function, σ_{ij} is the viscous stress tensor, and u_i are components of the total velocity; quantities inside integrals are to be evaluated at a retarded time and corresponding position. The indices i, j, m , and n are integers that vary from 1 to 3. Developed over 50 years ago (Refs. 18 and 19), this elegant theory unified the fields of aerodynamics and acoustics. In deriving the acoustic analogy, Lighthill cast the complicated nonlinear jet noise problem into a simple analogy with classical acoustics; the flow field and complex flow-acoustic interactions (such as sound wave convection and refraction) in a real jet are replaced by a fictitious volume source distribution of acoustic quadrupoles radiating into a uniform ambient medium.

By formulating the jet noise problem into an equivalent linear acoustics problem, LAA makes it possible to handle complex three-dimensional flows and arbitrary nozzle configurations with ease, thus making it a good choice for PAA applications. Compared to other methods based on non-linear acoustic propagation and convected wave equation formulations, simplifying jet flow assumptions are not needed in LAA, and complicated ray-tracing or flow-acoustic interaction models are not required. The tradeoff, of course, is that LAA places a much heavier burden on source modeling, since the sources themselves produce analogous “propagation” effects through temporal and spatial phasing.

This leads to the chief difficulty in implementing LAA over the past 50+ years: the tacit assumption that the mean-flow and fluctuating turbulent fields in a jet—namely, components of the Lighthill stress tensor T_{ij} —are known. Full knowledge of the jet flow field would be equivalent to a full solution of the Navier-Stokes equation, which remains elusive to this day. However, advances in computational fluid dynamics have closed the gap quite a bit. The fidelity and quality of information available in a Reynolds-averaged Navier-Stokes (RANS) CFD simulation has improved to the point where it is now possible to develop better models and make educated assumptions about any remaining unknowns.

The source-to-observer conventions in Jet3D’s LAA implementation are shown in Figure 9.4, where effects of both aircraft motion (at Mach number M_∞) and source convection (at Mach number M_c) are included. All Mach numbers are relative to a fixed observer, and are based on the ambient speed of sound c_∞ . It is important to note the relationship between source motion and convection: because acoustic sources in a jet (essentially convecting turbulent eddies) have a finite lifetime, they possess a convective effect and Doppler shift that goes according to the convection Mach number M_c , but retarded time effects come in mainly through motion of the aircraft. Thus, the retarded time position of sources depends primarily on the flight Mach number M_∞ . Following the illustration in Figure 9.4, the geometric observer radius r^* and geometric observer angle θ^* can be used to give the effective acoustic radius r and observer angle θ at the retarded time (results shown assume subsonic M_∞):

$$r = \frac{-M_\infty r^* \cos \theta^* + \sqrt{M_\infty^2 (r^* \cos \theta^*)^2 + (1 - M_\infty^2) r^{*2}}}{(1 - M_\infty^2)} \quad (9.2)$$

$$\theta = \cos^{-1} \left[\frac{r^*}{r} \cos \theta^* - M_\infty \right] \quad (9.3)$$

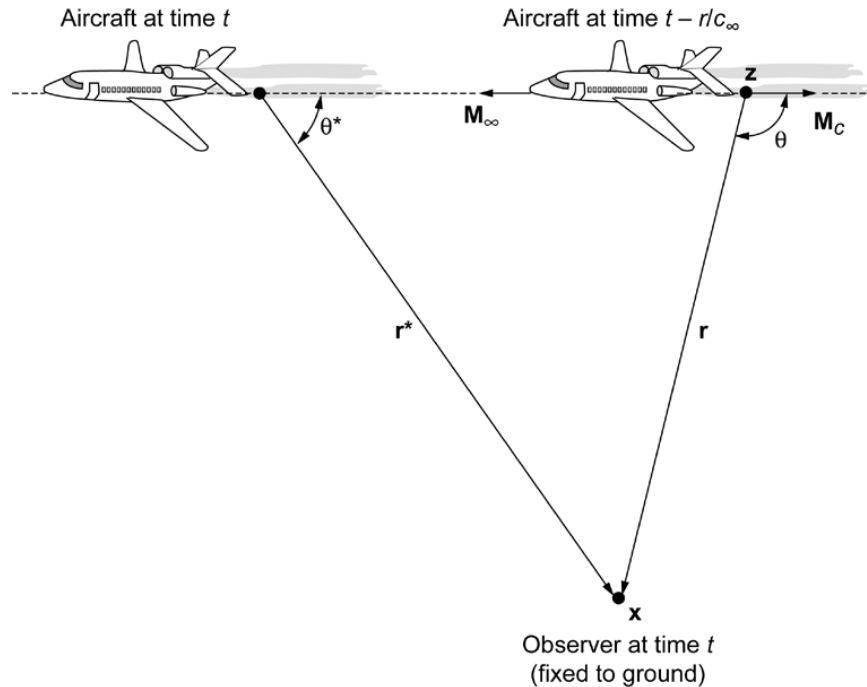


Figure 9.4.—Source-to-observer conventions in Jet3D’s implementation of Lighthill’s Acoustic Analogy (LAA).

By following Lighthill's assumption that the stress tensor can be approximated as $T_{ij} \sim \rho u_i u_j$, breaking velocities out into mean and fluctuating components $u_i(\mathbf{z}, t) = V_i(\mathbf{z}) + v_i(\mathbf{z}, t)$, and assuming that density is only a function of space (i.e., $\rho(\mathbf{z}, t) \approx \rho(\mathbf{z})$) the two-point time-delayed correlation of the Lighthill stress tensor becomes

$$\frac{\partial^4}{\partial \tilde{\tau}^4} \langle T_{ij} T'_{mn} \rangle = \rho \rho' \frac{\partial^4}{\partial \tilde{\tau}^4} \left[4V_j V'_n \langle v_i v'_m \rangle + \langle v_i v_j v'_m v'_n \rangle \right] \quad (9.4)$$

Note that odd terms involving triple correlations of the form $\langle v_i v'_m v'_n \rangle$ have been dropped, on the assumption that they would integrate to zero under the correlation integral. Of the two remaining terms, the first is known as the "shear noise" term, since it arises from interactions between turbulent and mean-flow velocities. The second term is the "self noise" term, as it arises from interactions between the turbulent velocities themselves. Under the assumption that the joint probability distribution of turbulent velocities is normal, the quadruple self noise correlation can be expanded into the product of double correlations as shown by Batchelor (Ref. 20):

$$\langle v_i v_j v'_m v'_n \rangle = \langle v_i v_j \rangle \langle v'_m v'_n \rangle + \langle v_i v'_m \rangle \langle v_j v'_n \rangle + \langle v_i v'_n \rangle \langle v_j v'_m \rangle \quad (9.5)$$

From this point onward, implementation of the Lighthill theory in Jet3D centers on the modeling of two-point space-time correlations for shear and self noise terms. Mean-flow correlations for velocity and density are modeled using a Taylor series expansion, written in terms of local mean-flow gradients and the separation vector between the two points of the mean-flow correlation:

$$V'_n \sim V_n + \zeta_k \frac{\partial V_n}{\partial z_k} \quad (9.6)$$

$$\rho' \sim \rho + \zeta_k \frac{\partial \rho}{\partial z_k} \quad (9.7)$$

where $k = 1, 2$, and 3 to carry out a dot product.

Turbulent velocity correlations are separated into space and time factors and modeled using the local one-point correlation (related to the Reynolds stress tensor) and a combination of Gaussian-type exponential functions and quadratic functions:

$$\langle v_i v'_m \rangle = \langle v_i v_m \rangle R(\mathbf{z}, \boldsymbol{\zeta}) g(\mathbf{z}, \tilde{\tau}) \quad (9.8)$$

where

$$R(\mathbf{z}, \boldsymbol{\zeta}) = \left[1 - \frac{1}{\mu^2} \left(\frac{\zeta_1^2}{\ell_1^2} + \frac{\zeta_2^2}{\ell_2^2} + \frac{\zeta_3^2}{\ell_3^2} \right) \right] \exp \left\{ -\pi \left(\frac{\zeta_1^2}{\ell_1^2} + \frac{\zeta_2^2}{\ell_2^2} + \frac{\zeta_3^2}{\ell_3^2} \right) \right\} \quad (9.9)$$

$$g(\mathbf{z}, \tilde{\tau}) = \exp \left\{ -\tilde{\tau}^2 / \tau_0^2 \right\} \quad (9.10)$$

$$\tilde{\tau} = \tau / C \quad (9.11)$$

and C is defined in Equation (9.18). Here, τ_0 is a characteristic time scale of turbulence

$$\tau_0 = \alpha_\tau \frac{k}{\varepsilon} \quad (9.12)$$

where k is the turbulent kinetic energy (TKE) per unit mass and ε is its dissipation rate, and ℓ_1 , ℓ_2 , and ℓ_3 are characteristic length scales of turbulence

$$\ell_1 = \alpha_L \frac{\langle v_1^2 \rangle^{3/2}}{\varepsilon} \quad (9.13a)$$

$$\ell_2 = \alpha_L \frac{\langle v_2^2 \rangle^{3/2}}{\varepsilon} \quad (9.13b)$$

$$\ell_3 = \alpha_L \frac{\langle v_3^2 \rangle^{3/2}}{\varepsilon} \quad (9.13c)$$

The specific form of the correlation functions is not so important, as discussed in Reference 21, as long as the spatial correlation function is integrable in $\boldsymbol{\zeta}$ and the temporal correlation function is amenable to Fourier transforms. Generally, any reasonable correlation function can be used and calibrated to give good results, with the majority of noise prediction accuracy and correct spectrum shape depending on the CFD solution.

For the correlation functions given above, early calibration work determined fixed values for the correlation calibration constant μ and the time scale calibration constant α_τ of 0.735 and 0.15, respectively. Over the past 7 years, values of the length scale calibration constant α_L between 0.3 and 0.34 have been used to predict noise for a wide range of nozzle configurations and flow conditions.

After carrying out tensor products with $\hat{r}_i \hat{r}_j \hat{r}_m \hat{r}_n$, and putting everything together, the acoustic pressure correlation can be written as

$$\langle p^2 \rangle(\mathbf{x}, \tau) = \underbrace{\langle p^2 \rangle(\mathbf{x}, \tau)}_{\text{shear}} + \underbrace{\langle p^2 \rangle(\mathbf{x}, \tau)}_{\text{self}} \quad (9.14)$$

where

$$\underbrace{\langle p^2 \rangle(\mathbf{x}, \tau)}_{\text{shear}} = \frac{1}{16\pi^2 c_\infty^4} \int_{\text{jet}} \frac{4\rho V_r \langle v_r v_r \rangle}{C_\infty C^5 r^2} G(\mathbf{x}, \tilde{\tau}) \int_{-\infty}^{\infty} \underbrace{F(\mathbf{z}, \boldsymbol{\zeta})}_{\text{shear}} d\boldsymbol{\zeta} d\mathbf{z} \quad (9.15a)$$

$$\langle p^2 \rangle_{\text{self}}(\mathbf{x}, \tau) = \frac{1}{16\pi^2 c_\infty^4} \int_{\text{jet}} \frac{2\rho \langle v_r v_r \rangle^2}{C_\infty C^5 r^2} G(\mathbf{x}, \tilde{\tau})_{\text{self}} \int_{-\infty}^{\infty} F(\mathbf{z}, \zeta)_{\text{self}} d\zeta d\mathbf{z} \quad (9.15b)$$

$$V_r = \hat{r}_j V_j \quad (9.16)$$

$$\langle v_r v_r \rangle = \hat{r}_i \hat{r}_m \langle v_i v_m \rangle \quad (9.17)$$

and the various functions are defined in Reference 16. The remaining analysis is straightforward but tedious, so the reader is referred to Reference 16 for details. In summary, the following steps are carried out:

- (1) The ζ correlation integrals are evaluated analytically.
- (2) A Fourier transform is applied to obtain the spectral density of the mean-square acoustic pressure.
- (3) The spectral density is integrated over a frequency band to obtain the mean-square acoustic pressure spectrum in that band.

The remaining \mathbf{z} integration over the jet is evaluated numerically. Thus, the Jet3D noise prediction algorithm is based on the volume integration over a set of equations giving the band-integrated acoustic pressure correlation spectrum for the shear and self noise. The integration is carried out for each volume element in a discretized jet flow field using data obtained from a CFD solution. Within the integration routine, turbulent Reynolds stresses are computed using one of several linear or nonlinear anisotropic models (Ref. 16), atmospheric absorption effects are calculated with the Shields and Bass attenuation model (Ref. 14), mean-flow gradients are computed with a finite volume scheme (Ref. 16), and local convection Mach number (M_c) is modeled empirically using correlated data trends from the classic Davies experiment (Ref. 22). The present formulation of Jet3D uses the Ribner/Ffowcs Williams (Ref. 23) jet convection factor

$$C = \left[(1 - M_c \cos \theta)^2 + \alpha_c^2 M_c^2 \right]^{1/2} \quad (9.18)$$

where $\alpha_c = 0.58$, along with the $C_\infty = |1 + M_\infty \cos \theta|$ forward flight convection factor.

Jet3D is written in FORTRAN 77/90/95 with dynamic memory allocation, and is easily ported across numerous computing platforms. The main algorithms in Jet3D are vectorized to take advantage of compiler optimizations and vector processing on certain architectures. Jet3D also

implements a low-level multiprocessing capability, where noise for multiple observers can be computed in parallel. Generally, noise predictions require on the order of 2 to 10 minutes per observer for the types of PAA applications discussed in this chapter. In addition to a prediction mode, Jet3D can be run in one of several diagnostic modes to output noise source maps for follow-on analysis.

9.4.1 Guidelines for Applying Jet3D

As alluded to above, the basic burden for noise prediction quality and accuracy falls on the CFD solution. Ultimately, the distribution of noise sources in a CFD solution determines sound pressure level (SPL) spectrum shape far more than the modeling assumptions in Jet3D. This leads to a few important guidelines:

- (1) The CFD grid should extend at least 30 jet diameters downstream for subsonic jets, and 40 to 50 diameters downstream for supersonic jets. Jet3D noise source maps can be used to verify that desired low-frequency sources are being captured within the computational domain.

- (2) Grid resolution around nozzle lips is critical to resolving high-frequency noise sources and predicting the correct high-frequency spectrum shape. On the order of 40 grid points across each boundary layer and 20 grid points across a nozzle lip are required to resolve this region and ensure suitable transition from nozzle boundary layer flows to shear layer flows.

- (3) Grid density should be fanned out from nozzle lips to cover developing shear layer regions. On the order of 40 grid points across a shear layer is appropriate. See Figure 9.5 for an example of this topology.

- (4) Whenever possible, CFD solutions should be compared with experimental mean-flow and turbulence data to ensure that the CFD-predicted jet flow field is valid and reasonable (i.e., correct potential core length, proper turbulence levels, etc.). Issues in the CFD solution should be resolved before proceeding to noise prediction.

- (5) RANS turbulence models have known deficiencies in predicting the correct potential core length for heated jets. In general, mixing is underpredicted and the jet potential core is too long (by several nozzle diameters), resulting in an incorrect mean flow and turbulence field. Proper steps should be taken to avoid this problem, using a correction such as the one suggested by Abdol-Hamid et al. (Ref. 24). This correction increases the mixing rate in the hot part of a jet flow with a minimally invasive modification to turbulent eddy viscosity. The correction is implemented in a way that is equally valid for wall-bounded and free shear flows, which is important for installed jet simulations of interest to PAA.

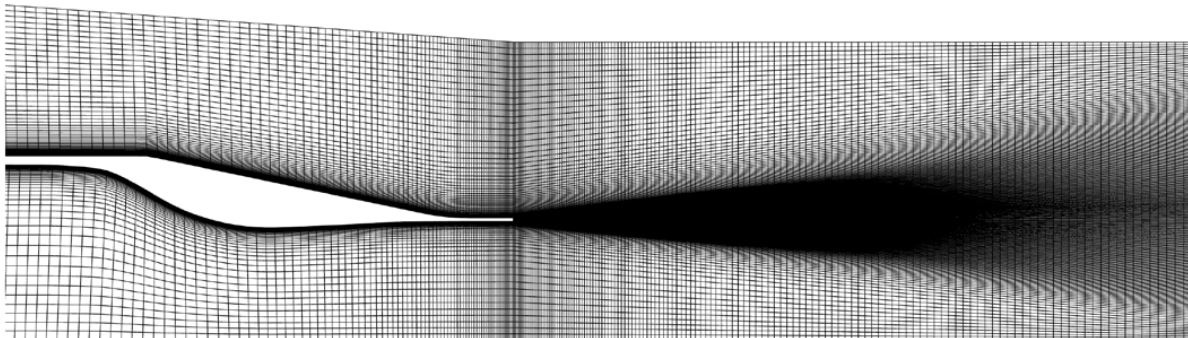


Figure 9.5.—Recommended shear layer grid topology for CFD predictions of jet flow.

In addition to these CFD guidelines, a few acoustic guidelines are worth noting:

(1) Observers must be at least 50 nozzle diameters from the nozzle exit to truly be in the far field of Jet3D's implementation of LAA.

(2) Best predictions are from 0° to 100° inlet angle. Predictions beyond a 110° inlet angle are generally not reliable, because of shortcomings in the Jet3D implementation of LAA (terms neglected in the Lighthill stress tensor).

(3) Noise analysis should begin with an observer at an inlet angle of 90°, where jet noise is least affected by convection and refraction effects and noise sources in Jet3D take on their simplest form. If the results at 90° do not correlate with the measured spectrum, the CFD solution should be analyzed for problems and deficiencies before proceeding to other observer angles.

9.4.2 Sensitivity to Input Settings

Most of the input settings for Jet3D are based on nozzle operating conditions and acoustic data reduction conventions. Of the various calibration constants in Jet3D, all have been frozen except for the spatial correlation constant α_L , which generally varies between 0.3 and 0.34 for most cases. Using the equations for predicted SPL from Reference 16, the sensitivity to α_L can be computed:

$$\frac{\partial \text{SPL}}{\partial \alpha_L} = \frac{30}{\alpha_L \ln 10} \approx \frac{13.029}{\alpha_L} \quad (9.19)$$

More simply, the change in SPL for a change in α_L is

$$\Delta \text{SPL} = 30 \log \left(1 + \frac{\Delta \alpha_L}{\alpha_L} \right) \quad (9.20)$$

Thus, the SPL changes by –1 dB for a –7.39 percent change in α_L , or it changes by 1 dB for a 7.98 percent change in α_L . The α_L constant can be used to calibrate noise prediction results to experimental data (most appropriately done at 90° observer angle) by shifting the SPL spectrum up or down as needed.

The effect of varying α_L is shown in Figure 9.6 and Figure 9.7, based on cases discussed in Reference 25. Figure 9.6 shows Jet3D predictions at a 90° observer angle for a baseline round BPR 5 dual-stream nozzle, and Figure 9.7 shows the same prediction for a BPR 5 nozzle with a pylon.

9.4.3 Applications

Early validation of Jet3D was done using the Yamamoto et al. dataset (Ref. 26). Noise predictions were made for a heated convergent-divergent nozzle with an exit diameter of 13.7 cm (5.4 in.) operating at its design nozzle pressure ratio (NPR) of 3.18, a Mach number of 1.4, and a jet stagnation temperature T_o of approximately 955.6 K (1720 °R). Jet3D noise predictions were made for 13 observer locations along a 40-ft-radius arc (approximately 88 nozzle diameters) centered on the nozzle exit. For each observer, 1/3-octave band frequency SPL was computed over bands from 50 Hz to 80 kHz.

Results from one of the validation cases, with a static free stream, are shown in Figure 9.8 and Figure 9.9. Jet3D did a reasonable job predicting SPL for inlet angles of 40° to 100°, but shows a frequency shift for inlet angles beyond 100°. This is due to flow acoustic interaction effects as the observer nears the jet axis. These interactions are not adequately handled in the present form of Jet3D, because of the neglect of terms from the Lighthill stress tensor. Overall sound pressure level (OASPL) results in Figure 9.9 are slightly more forgiving, showing decent OASPL prediction to an inlet angle of about 130°.

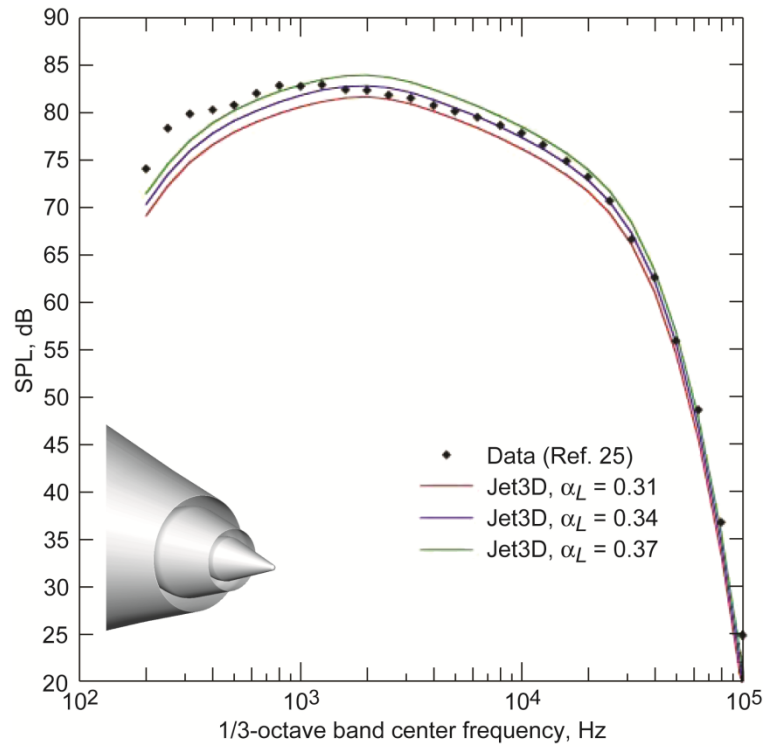


Figure 9.6.—Effect of varying spatial correlation constant α_L on Jet3D predictions of sound pressure level (SPL) for baseline round bypass ratio 5 dual-stream nozzle.

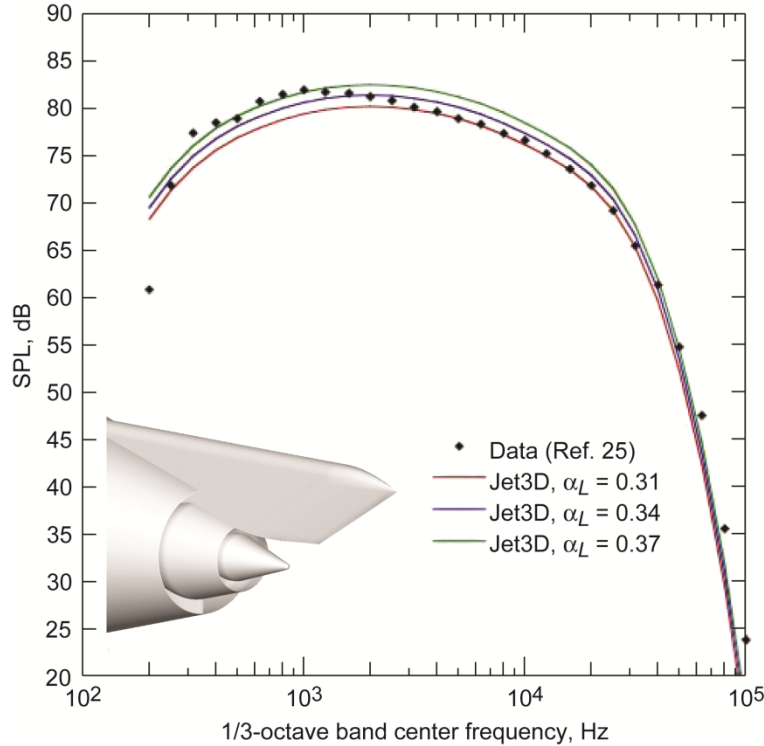


Figure 9.7.—Effect of varying spatial correlation constant α_L on Jet3D predictions of sound pressure level (SPL) for baseline round bypass ratio 5 dual-stream nozzle with pylon.

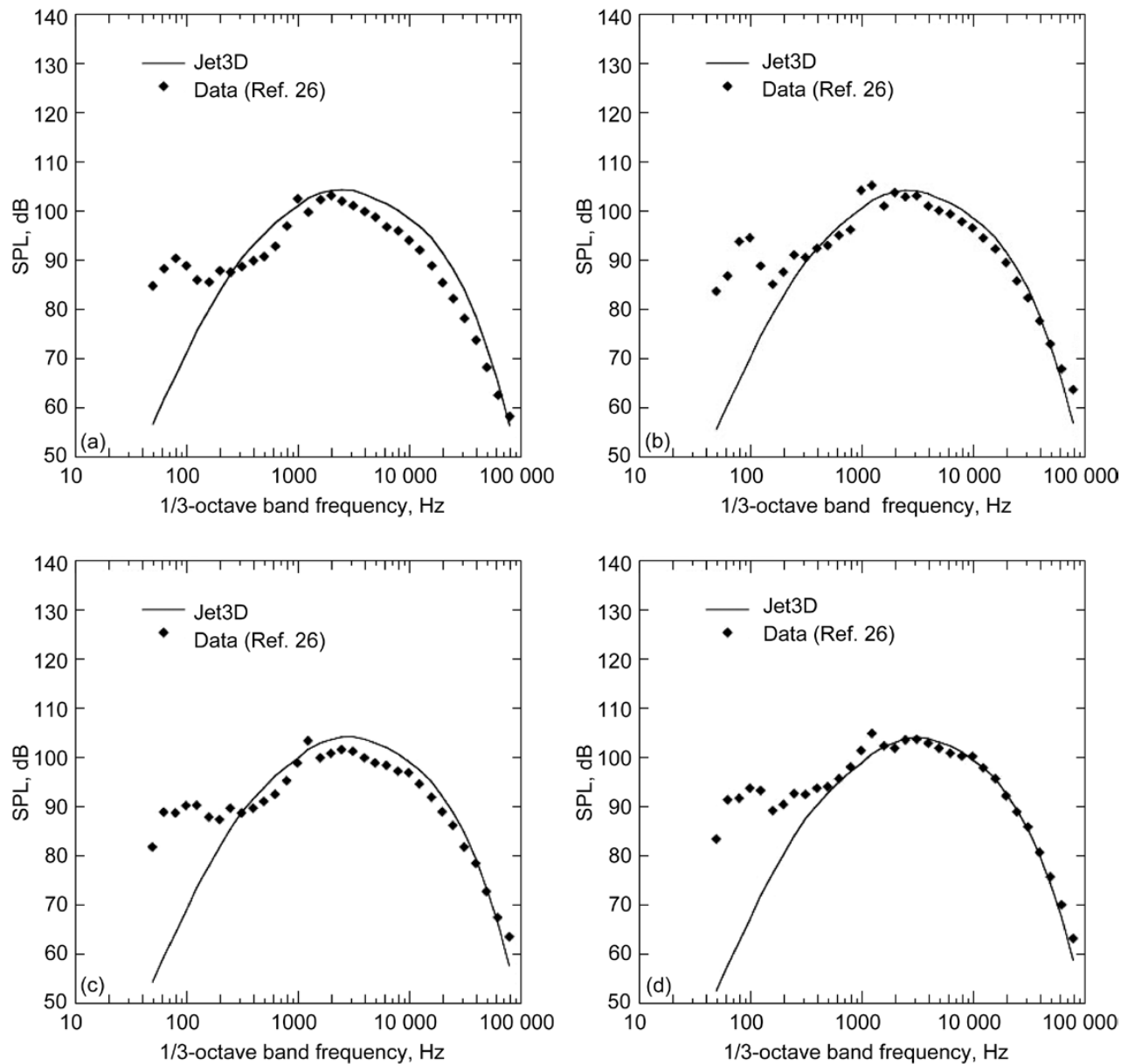


Figure 9.8.—Comparison of measured data and Jet3D predictions of sound pressure level (SPL) for convergent-divergent nozzle (jet stagnation temperature $T_o \approx 955.6$ K (1720 °R), nozzle pressure ratio NPR = 3.18, and Mach number 1.4). Jet3D noise predictions are made at 13 observer locations (inlet angles). (a) 40°. (b) 50°. (c) 60°. (d) 70°.

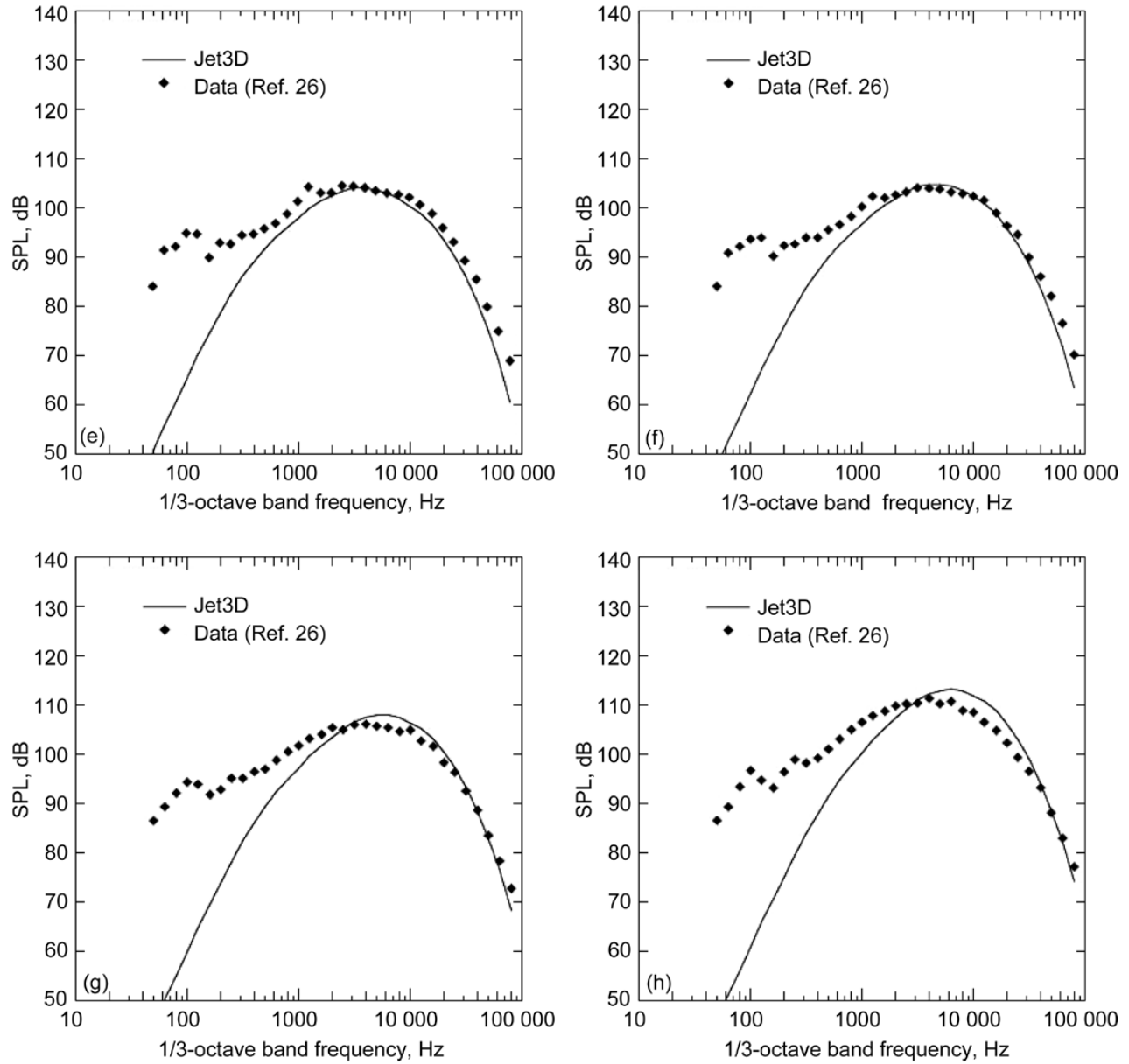


Figure 9.8.—Continued. (e) 80°. (f) 90°. (g) 100°. (h) 110°.

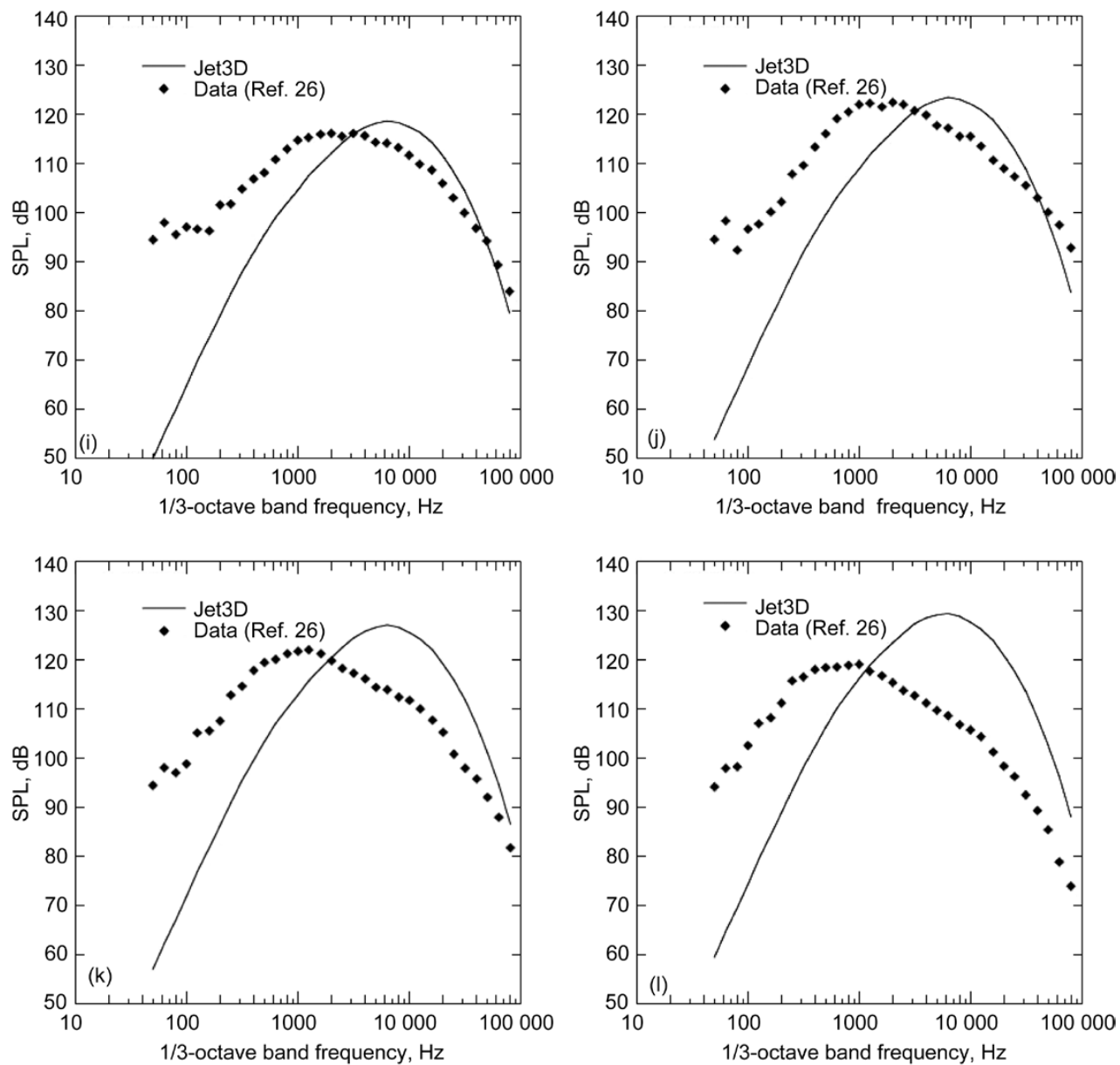


Figure 9.8.—Continued. (i) 120°. (j) 130°. (k) 140°. (l) 150°.

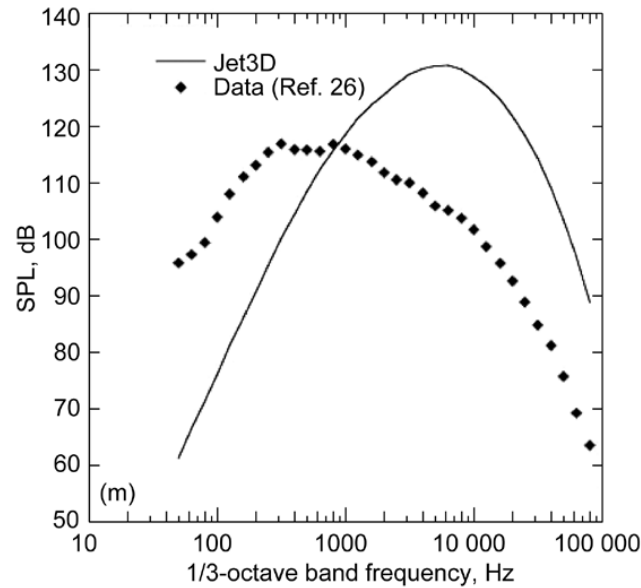
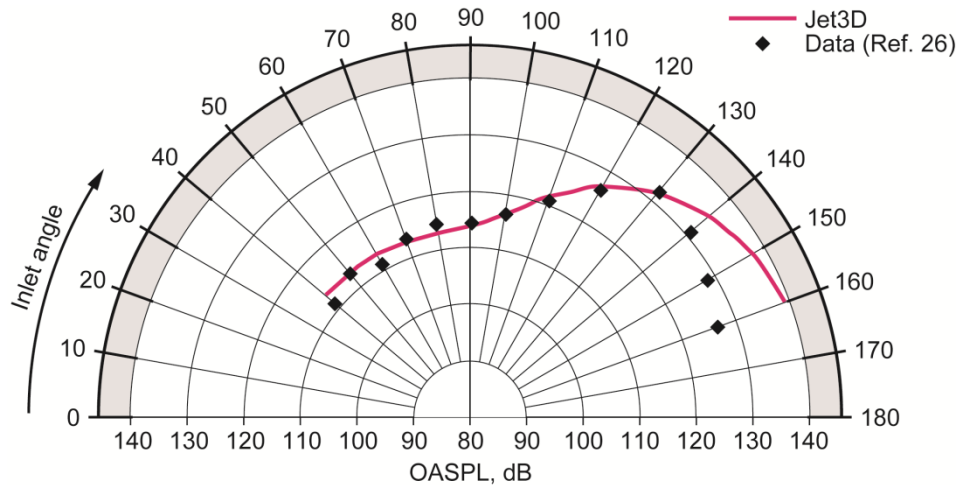


Figure 9.8.—Concluded. (m) 160°.


 Figure 9.9.—Comparison of measured data and Jet3D predictions of overall sound pressure level (OASPL) as function of inlet angle for convergent-divergent nozzle at jet stagnation temperature T_o of approximately 955.6 K (1720 °R) operating at its design nozzle pressure ratio (NPR) of 3.18 and Mach number of 1.4.

The first PAA application of Jet3D (Ref. 25) focused on dual-stream BPR 5 nozzles, shown in Figure 9.10 (baseline round nozzle, configuration 1) and Figure 9.11 (pylon nozzle, configuration 6). The primary interest was in using Jet3D to examine the pylon installation effect, later covered in more detail in Reference 27. Jet3D noise predictions were compared to experimental acoustic data obtained in the LSAWT at

NASA Langley's Jet Noise Laboratory (JNL), for nozzle configurations operating at the takeoff cycle point (core nozzle: NPR = 1.56 and T_o = 827.8 K (1490 °R); fan nozzle: NPR = 1.75 and T_o = 359 K (646 °R)) with a free-stream Mach number of 0.28. Each 1/9-scale nozzle has a nominal core exit diameter of D = 12.8 cm (5.04 in.).

For SPL comparisons, Jet3D noise predictions were made at 24 observer locations along a $100D$ -radius arc, at inlet angles ranging from 52° to 148° . At each observer point, 1/3-octave band frequency spectrum SPL were computed over center frequencies ranging from 200 Hz to 100 kHz. Additional sideline predictions were made at full scale (scale factor 9.0) and fed through JNL data processing routines to come up with EPNL predictions.

The SPL predictions for configuration 1 are shown in Figure 9.12, and predictions for configuration 6 are shown in Figure 9.13. Predictions are compared with JNL model-scale data (with standard deviation of ± 0.47 dB) at observer inlet angles of 52° , 62° , 69° , 78° , and 88° in the inlet arc, and inlet angles of 98° , 109° , 121° , 127° , 134° , 141° , and 148° in the jet arc. For both configurations, Jet3D predictions are in good to excellent agreement with JNL data in the inlet arc, but the agreement progressively deteriorates in the jet arc past about 121° , again, where flow-acoustic interaction issues come into play. The EPNL predictions for full-scale nozzle systems are compared with data in Figure 9.14. For both configurations, Jet3D predictions are within the ± 0.36 dB standard deviation for the EPNL determined from the JNL measurements. Furthermore, Jet3D properly captures the effect of the pylon (due in part to the reduced thrust of that configuration), predicting 0.69 EPNdB noise reduction.

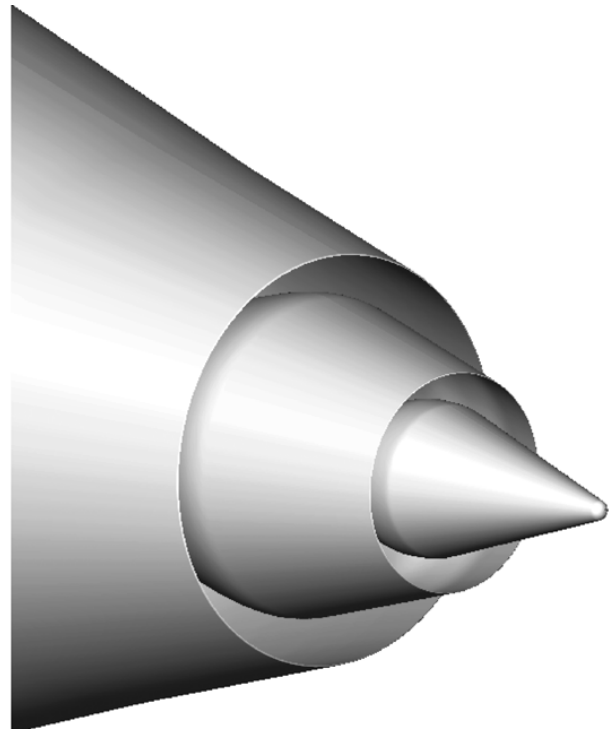


Figure 9.10.—Baseline separate-flow nozzle of BPR 5, configuration 1, for Jet3D jet noise prediction.

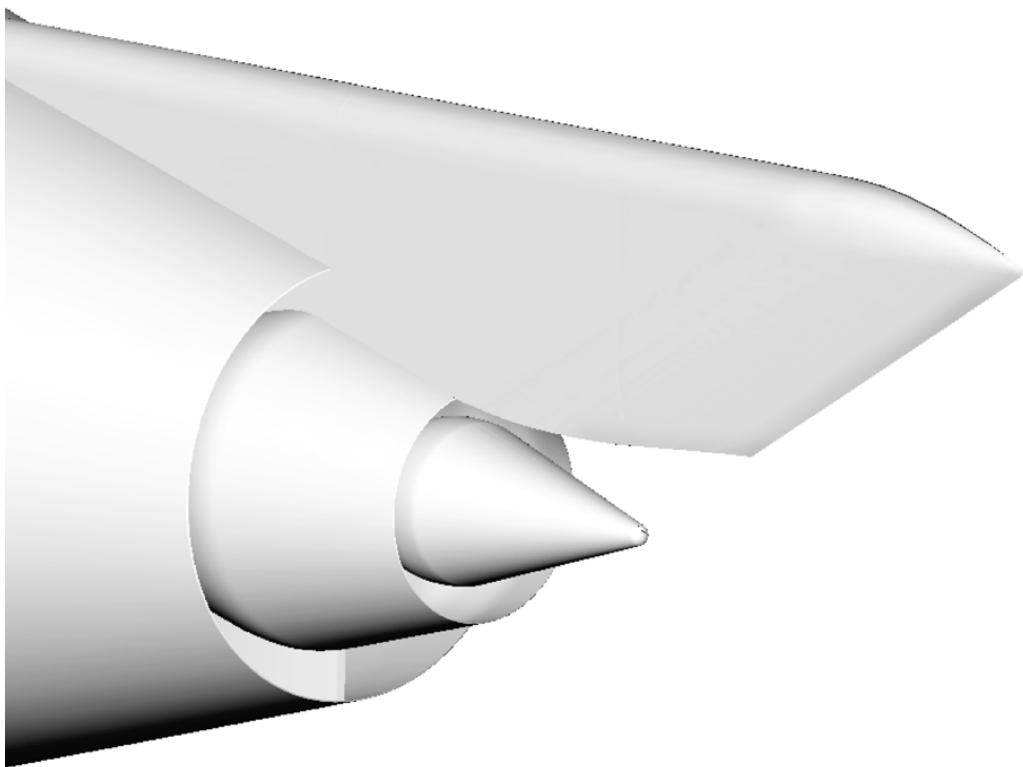


Figure 9.11.—Baseline separate-flow nozzle of BPR 5 with pylon, configuration 6, for Jet3D jet noise prediction.

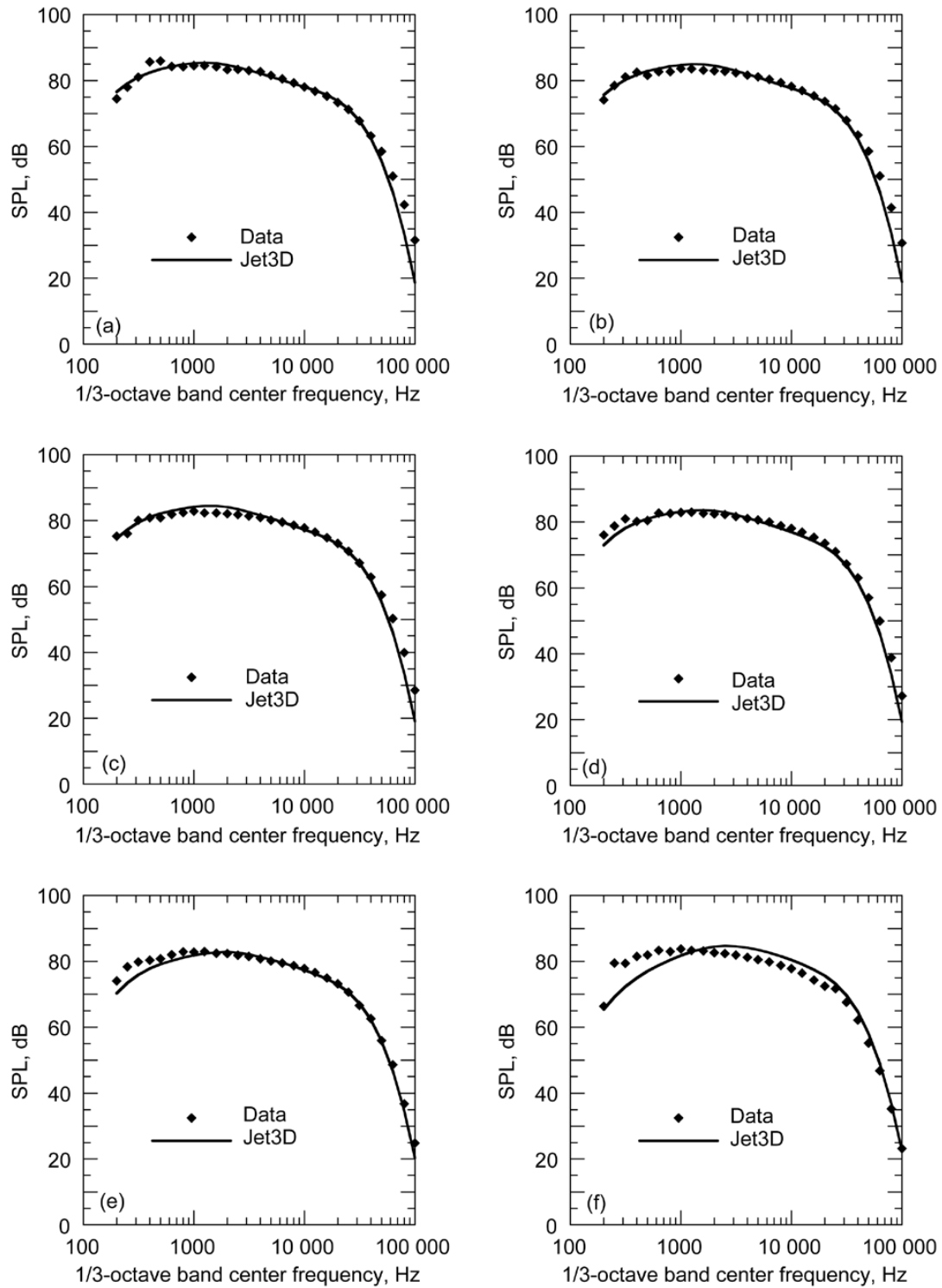


Figure 9.12.—Comparison of measured data and Jet3D predictions of sound pressure level (SPL) for baseline separate-flow nozzle of BPR 5, configuration 1, at different observer locations (inlet angles). From Reference 25. (a) 52°. (b) 62°. (c) 69°. (d) 78°. (e) 88°. (f) 98°.

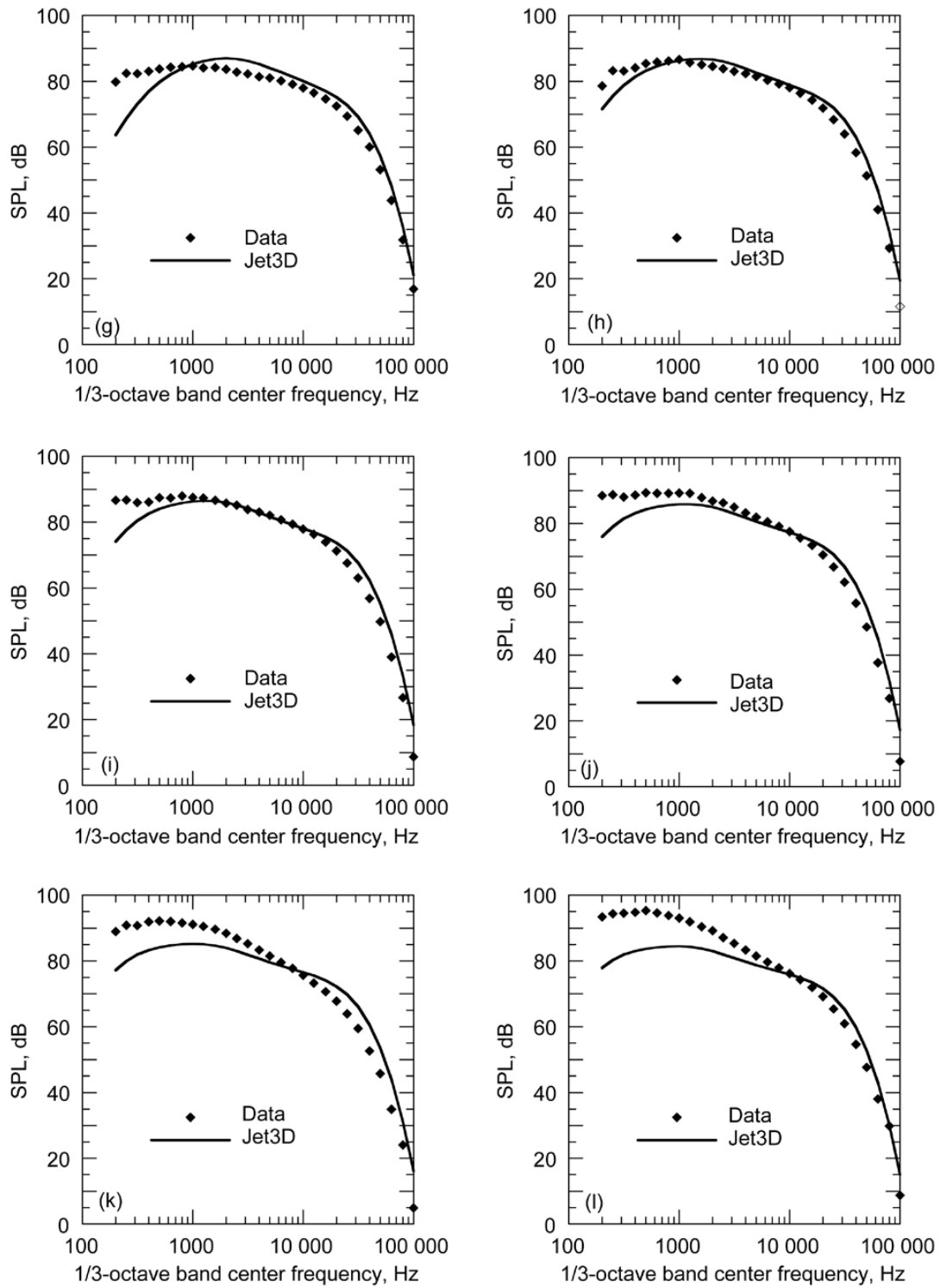


Figure 9.12.—Concluded. (g) 109°. (h) 121°. (i) 127°. (j) 134°. (k) 141°. (l) 148°.

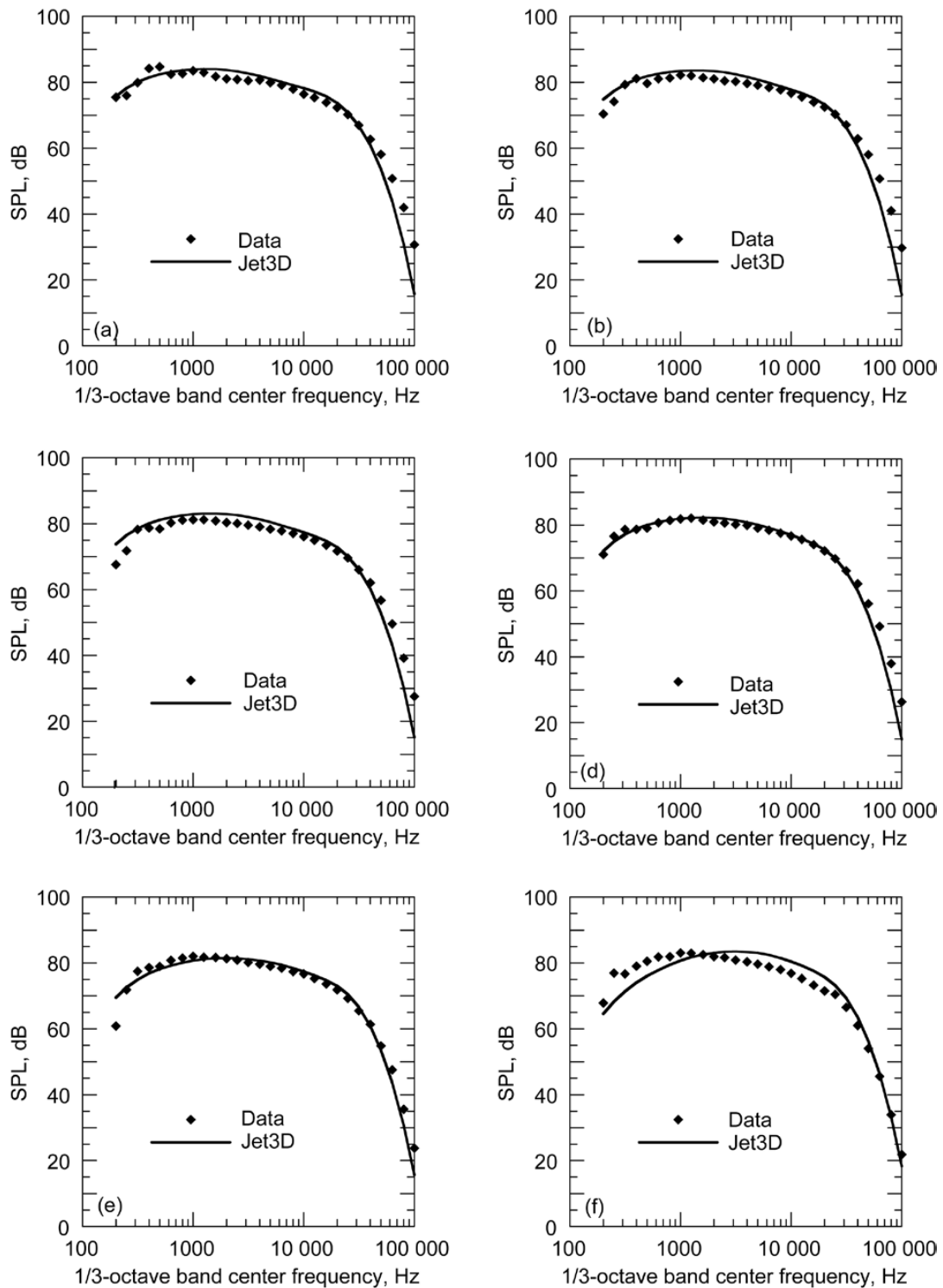


Figure 9.13.—Comparison of measured data and Jet3D predictions of sound pressure level (SPL) for baseline separate-flow nozzle of BPR 5 with pylon, configuration 6, at different observer locations (inlet angles). From Reference 25. (a) 52°. (b) 62°. (c) 69°. (d) 78°. (e) 88°. (f) 98°.

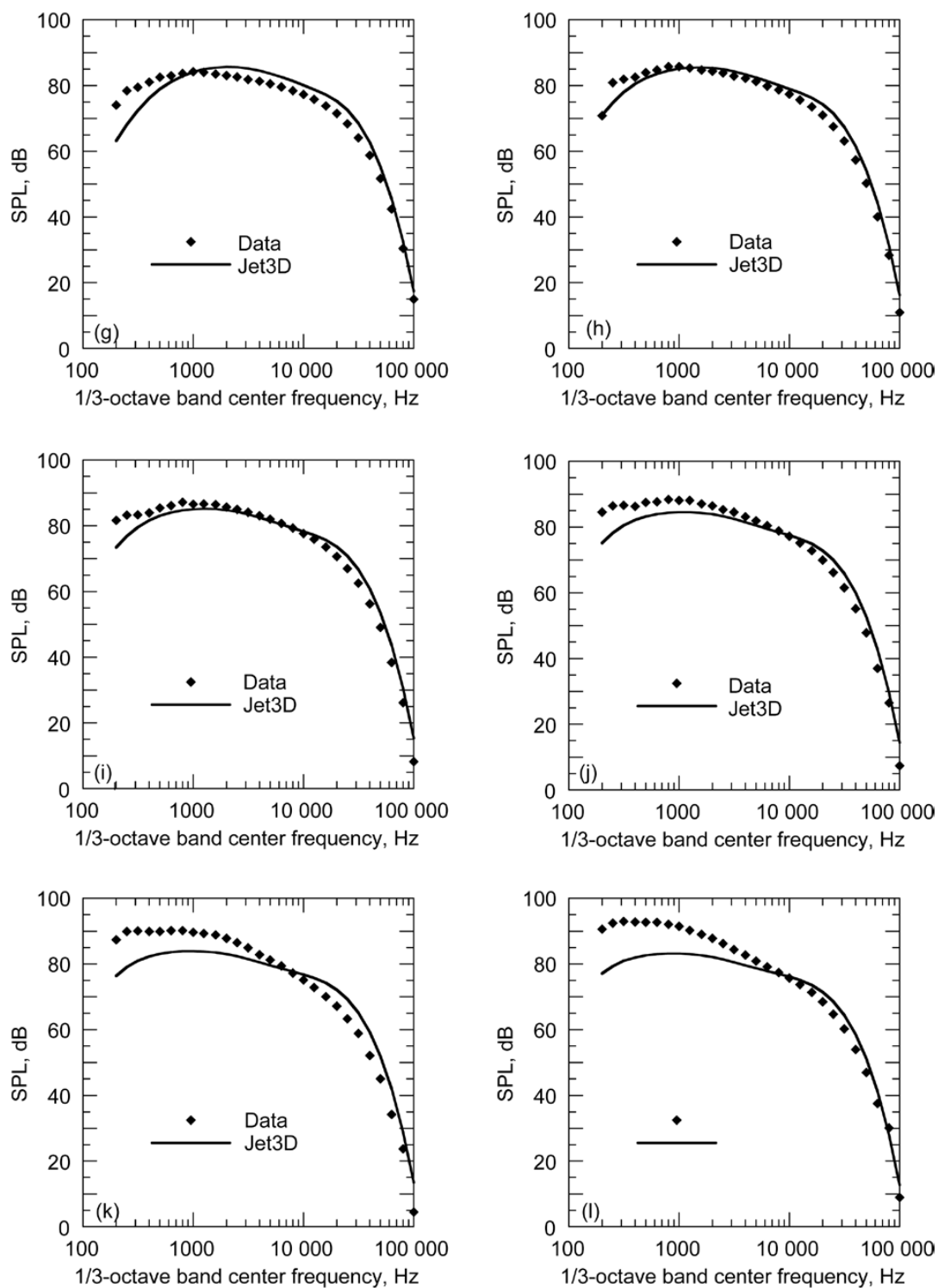


Figure 9.13.—Concluded. (g) 109°. (h) 121°. (i) 127°. (j) 134°. (k) 141°. (l) 148°.

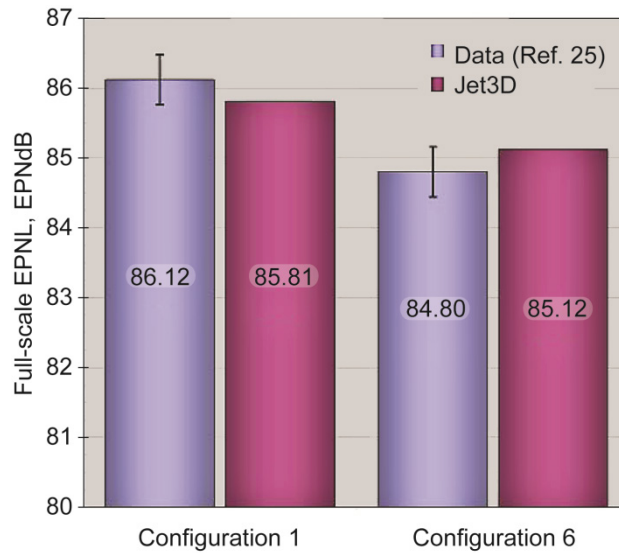


Figure 9.14.—Comparison of measured data and Jet3D predictions of effective perceived noise level (EPNL) for full-scale separate-flow nozzle of BPR 5, both configuration 1 and configuration 6 (with pylon). Standard deviation in data is ± 0.36 EPNdB.

9.4.4 Jet3D Challenges

Two challenges face Jet3D, the first being the poor aft arc prediction seen in previous examples. Past about 110° inlet angle, Jet3D SPL predictions are generally missing the experimental data in both amplitude and frequency. As mentioned previously, this is due to incomplete modeling of the Lighthill stress tensor in Jet3D—that is, the neglect of terms other than $\rho u_i u_j$ —in combination with the two-point space-time correlation formulation. Unfortunately, it is not practical to fix this modeling issue as long as RANS–CFD is used for flow input; however, ad hoc aft-arc corrections have been somewhat successful on a case-by-case basis.

For a more permanent, long-term improvement, Jet3D will transition to using data from nonaveraged simulations including large eddy simulation (LES), direct numerical simulation (DNS), and partially-averaged Navier-Stokes (PANS). Of these methods, PANS holds the most promise because it combines the affordability of RANS with the higher fidelity of LES and DNS. With any of these methods, the Lighthill stress tensor will be computed directly, with minimal need for approximations and modeling, and no need for two-point correlations.

The other challenge facing Jet3D is midfrequency SPL overprediction in dual-stream core-fan nozzles. This has been traced back to CFD overprediction of turbulent kinetic energy (TKE) near the end of the annular fan stream’s potential core and is present in solutions from a wide range of RANS solvers and turbulence models. The localized boost in TKE results in a

corresponding increase in noise sources and a 5- to 6-dB spike in SPL around 1600 to 3000 Hz (model scale). Presently, the problem is addressed on a case-by-case basis (using experimental data for guidance) by smoothing or filtering the TKE-spike portion of the CFD solution and its corresponding noise sources.

Going forward, the midfrequency overprediction problem is being investigated as a turbulence modeling issue. Though RANS turbulence modeling is not entirely appropriate near the end of a jet potential core, it is hoped that some improvement can be made. Early indications suggest that the TKE overprediction may be due to inflow turbulence initialization, with low initial levels resulting in higher-than-normal TKE growth at the end of the fan’s annular potential core.

9.5 Future PAA Experimental and Prediction Development

In addition to the underlying challenges of the noise source components (jet, fan, airframe, etc.), propulsion airframe aeroacoustics interaction experiments face many challenges to develop more comprehensive prediction methodologies.

One challenge involves the need for a benchmark PAA experiment on the prolific engine-under-wing configuration. This experiment would include variation of the major parameters from pylon length (jet-wing spacing), pylon thickness, jet exhaust plane to flap trailing-edge spacing, flap settings, nozzle types (conventional and chevron), and so

forth. Detailed acoustic and flow-field measurements would be required to provide the complete documentation that is missing to date. Both polar and azimuthal far-field acoustic measurements would be necessary with phased-array measurements. Flow-field measurements should include both surface pressures as well as mean-flow and turbulence measurements at key locations where the jet exhaust interacts with the flap and wing downwash. A comprehensive experiment of this type, at large scale (3 percent or larger) with high-fidelity geometry, does not appear to be available in the literature.

For the engine-under-wing configuration there should also be an experimental documentation of the fan noise reflection from the wing and fuselage. Clearly, for unconventional configurations that mount engines on top of the wing and fuselage, documentation of the shielding and reflection of propulsion noise sources, both fan and jet, is key. This includes parameters like forward flight effects and angle of attack. The flow interactions of such unconventional configurations should be investigated particularly on configurations that require highly integrated propulsion systems with embedded engines.

Future challenges for PAA prediction methods cover almost the full range because of the early state of development of methods that are focused on predictions of this kind. The PAA predictions must move toward predictions of the complete aircraft configuration because of the complex geometries required and the basic fact that it is only with the full aircraft configuration that the multiple flow and acoustic PAA effects are present. This overall challenge drives the needs for multiple improvements in prediction capabilities starting with issues of a fundamental nature including the improved RANS turbulence models, the use of time-dependent flow information for acoustic predictions, and the deployment of fast, efficient, flexible unstructured grid generation methods and CFD solutions.

On the way to this full aircraft configuration PAA prediction, the next major step will likely be the prediction of the jet-flap interaction for the engine-under-wing configuration. Including the nozzle, pylon, wing, and deployed flaps at relevant angle-of-attack, this problem will require significant effort just to obtain time-dependent flow-field solutions. These solutions must include aeroacoustics-relevant refinements such as off-body grid adaptation to noise-producing shear layers downstream of the jet-flap interaction. The flow-field solution is, of course, the essential prerequisite to the eventual CFD-based noise prediction.

Ultimately, the prediction method for jet-flap interaction will probably require the Jet3D approach described above, including the time-dependent flow field, to accurately predict the multiple jet and jet-airframe interactions sources present in the jet-flap interaction problem. Once this prediction capability for jet-flap interaction is in place for the engine-under-wing configuration, it will probably represent the basic capability needed for a flow-interaction PAA prediction method usable for more general configurations. For a less computationally intensive approach using a RANS flow-field solution, it remains to be seen how well such methods can do on the jet-flap interaction problem.

For the full PAA prediction capability, flow-interaction PAA effects prediction (such as three-dimensional jet-pylon and jet-flap interactions) will have to be linked to acoustic propagation and interaction, shielding, and reflection prediction. The needs for acoustic scattering prediction are focused in the foreseeable future on increasing the frequency range, including the effects of the mean nonuniform flow field, and on the computational resource and efficiency issues resulting from complex configuration geometry.

Finally, with such a flow and acoustic interaction PAA prediction capability, the overall requirement will be to integrate these methods into an effective aircraft system noise prediction tool.

Appendix A.—Nomenclature

A.1 Acronyms

AST	Advanced Subsonic Technology
BPR	bypass ratio
BWB	blended wing body
CFD	computational fluid dynamics
DNS	direct numerical simulation
EPNL	effective perceived noise level
GE	General Electric Company
JES	jet engine simulator
JNL	Jet Noise Laboratory
LAA	Lighthill's Acoustic Analogy
LES	large eddy simulation
LSAF	Low-Speed Aeroacoustic Facility
LSAWT	Low Speed Aeroacoustic Wind Tunnel
NPR	nozzle pressure ratio
OASPL	overall sound pressure level
PAA	propulsion airframe acoustics
PANS	partially-averaged Navier-Stokes
PNL	perceived noise level
QTD2	Quiet Technology Demonstrator 2
RANS	Reynolds-averaged Navier-Stokes
SPL	sound pressure level
TKE	turbulent kinetic energy

A.2 Symbols

c	local speed of sound
C	jet convection factor
C_∞	flight convection factor
D	core nozzle diameter
g	temporal correlation function, $g = g(\tilde{\tau})$
k	turbulent kinetic energy (TKE) per unit mass
ℓ_1, ℓ_2, ℓ_3	turbulence length scales
M	Mach number
p	acoustic pressure
\mathbf{r}	acoustic radius vector, $\mathbf{r} = \mathbf{x} - \mathbf{z}$
r	magnitude of acoustic radius \mathbf{r}
$\hat{\mathbf{r}}$	acoustic radius unit vector, $\hat{\mathbf{r}} = \mathbf{r}/r$

R	spatial correlation function
SPL	sound pressure level
t	time
T	temperature
T_{ij}	Lighthill stress tensor
u_i	total velocity vector component
v_i	turbulent velocity vector component
V_i	mean flow velocity vector component
$\langle v_i v_m \rangle$	one-point turbulent velocity correlation
$\langle v_i v'_m \rangle$	two-point turbulent velocity correlation
\mathbf{x}	fixed observer position vector
\mathbf{z}	moving frame source position vector
α_c	jet convection factor parameter
α_L	length scale calibration constant
α_τ	time scale calibration constant
δ_{ij}	Kronecker delta function
ε	dissipation rate of k
$\boldsymbol{\zeta}$	moving frame separation vector
θ	observer angle from jet axis
μ	correlation calibration constant
ρ	density
σ_{ij}	viscous stress tensor
τ	time delay in observer frame
$\tilde{\tau}$	moving frame time delay, $\tilde{\tau} = t/C$
τ_0	characteristic time scale of turbulence

Subscripts:

c	convection
o	stagnation
∞	ambient or free-stream conditions

Superscripts:

$*$	geometric observer
$'$	denotes spatial change for variable in a two-point correlation

References

1. Elkoby, Ronen: Full-Scale Propulsion Airframe Aeroacoustics Investigation. AIAA-2005-2807, 2005.
2. Thomas, R.H.; and Hill, G.A.: Challenges and Opportunities for Noise Reduction Through Advanced Aircraft Propulsion Airframe Integration and Configurations. Presented at the 8th ASC-CEAS Workshop on Aeroacoustics of New Aircraft and Engine Configurations, Budapest, Hungary, 2004.
3. Thomas, Russell H.: Aeroacoustics of Propulsion Airframe Integration: Overview of NASA's Research. Presented at the NOISE-CON 2003 Conference, NOISE-CON 2003 Paper 105, Cleveland, OH, 2003.
4. Thomas, Russell; and Kinzie, Kevin W.: Jet-Pylon Interaction of High Bypass Ratio Separate Flow Nozzle Configurations. AIAA-2004-2827, 2004.
5. Mengle, Vinod, et al.: Reducing Propulsion Airframe Aeroacoustic Interactions With Uniquely Tailored Chevrons: 1. Isolated Nozzles. AIAA-2006-2467, 2006.
6. Mengle, Vinod, et al.: Reducing Propulsion Airframe Aeroacoustic Interactions With Uniquely Tailored Chevrons: 2. Installed Nozzles. AIAA-2006-2434, 2006.
7. Mengle, Vinod, et al.: Reducing Propulsion Airframe Aeroacoustic Interactions With Uniquely Tailored Chevrons: 3. Jet-Flap Interaction. AIAA-2006-2435, 2006.
8. Mengle, Vinod, et al.: Flaperon Modification Effect on Jet-Flap Interaction Noise Reduction for Chevron Nozzles. AIAA-2007-3666, 2007.
9. Nesbitt, Eric, et al.: Flight Test Results for Uniquely Tailored Propulsion Airframe Aeroacoustic Chevrons: Community Noise. AIAA-2006-2438, 2006.
10. Reimann, Craig; Tinetti, Ana; and Dunn, M.: Noise Prediction Studies for the Blended Wing Body Using the Fast Scattering Code. AIAA-2005-2980, 2005.
11. Massey, Steven, et al.: Computational and Experimental Flow-field Analyses of Separate Flow Chevron Nozzles and Pylon Interaction. AIAA-2003-3212, 2003.
12. Posey, Joe W., et al.: Jet Noise From Ultrahigh Bypass Turbofan Engines. Presented at the 143rd Meeting of the Acoustical Society of America, Pittsburgh, PA, 2002.
13. Amiet, R.K.: Refraction of Sound by a Shear Layer. AIAA-1977-54, 1977.
14. Shields, F.D.; and Bass, H.E.: Atmospheric Absorption of High Frequency Noise and Application to Fractional-Octave Bands; Final Report. NASA CR-2760, 1977.
15. Harris, Cyril M.: Handbook of Acoustical Measurements and Noise Control. McGraw-Hill, New York, NY, 1991.
16. Hunter, Craig A.: An Approximate Jet Noise Prediction Method Based on Reynolds-Averaged Navier-Stokes Computational Fluid Dynamics Simulation. D.Sc. Thesis, George Washington University, 2002.
17. Ffowcs Williams, J.E.: The Noise From Turbulence Convected at High Speed. *Philos. Trans. R. Soc. London, Ser. A*, vol. 255, 1963, pp. 469-503.
18. Lighthill, M.J.: On Sound Generated Aerodynamically: I. General Theory. *Proc. Royal Soc. London Series A*, vol. 211, 1952, pp. 564-587.
19. Lighthill, M.J.: On Sound Generated Aerodynamically: II. Turbulence as a Source of Sound. *Proc. R. Soc. London, Ser. A*, vol. 222, 1954, pp. 1-32.
20. Batchelor, George Keith: *The Theory of Homogeneous Turbulence*. Cambridge University Press, Cambridge, England, 1953.
21. Farassat, F.; Doty, Michael; and Hunter, Craig: The Acoustic Analogy—A Powerful Tool in Aeroacoustics With Emphasis on Jet Noise Prediction. AIAA-2004-2872, 2004.
22. Davies, P.O.A.L.; Fisher, M.J.; and Barratt, M.J.: The Characteristics of the Turbulence in the Mixing Region of a Round Jet. *J. Fluid Mech.*, vol. 15, no. 3, 1963, pp. 337-367.
23. Ribner, H.S.: The Generation of Sound by Turbulent Jets. *Advan. Appl. Mech.*, vol. 8, 1964, pp. 103-182.
24. Abdol-Hamid, Khaled, et al.: Temperature Corrected Turbulence Model for High Temperature Jet Flow. AIAA-2003-4070, 2003.
25. Hunter, Craig; and Thomas, Russell: Development of a Jet Noise Prediction Method for Installed Jet Configurations. AIAA-2003-3169, 2003.
26. Yamamoto, K., et al.: Experimental Investigation of Shock-Cell Noise Reduction for Single-Stream Nozzles in Simulated Flight, Comprehensive Data Report. NASA CR-168234, vols. 1-3, 1984.
27. Massey, Steven, et al.: Computational Analysis of a Chevron Nozzle Uniquely Tailored for Propulsion Airframe Aeroacoustics. AIAA-2006-2436, 2006.

REPORT DOCUMENTATION PAGE				Form Approved OMB No. 0704-0188	
<p>The public reporting burden for this collection of information is estimated to average 1 hour per response, including the time for reviewing instructions, searching existing data sources, gathering and maintaining the data needed, and completing and reviewing the collection of information. Send comments regarding this burden estimate or any other aspect of this collection of information, including suggestions for reducing this burden, to Department of Defense, Washington Headquarters Services, Directorate for Information Operations and Reports (0704-0188), 1215 Jefferson Davis Highway, Suite 1204, Arlington, VA 22202-4302. Respondents should be aware that notwithstanding any other provision of law, no person shall be subject to any penalty for failing to comply with a collection of information if it does not display a currently valid OMB control number.</p> <p>PLEASE DO NOT RETURN YOUR FORM TO THE ABOVE ADDRESS.</p>					
1. REPORT DATE (DD-MM-YYYY) 01-07-2012		2. REPORT TYPE Technical Paper		3. DATES COVERED (From - To)	
4. TITLE AND SUBTITLE Assessment of NASA's Aircraft Noise Prediction Capability				5a. CONTRACT NUMBER	
				5b. GRANT NUMBER	
				5c. PROGRAM ELEMENT NUMBER	
6. AUTHOR(S) Dahl, Milo, D.				5d. PROJECT NUMBER	
				5e. TASK NUMBER	
				5f. WORK UNIT NUMBER WBS 561581.02.08.03.18.03	
7. PERFORMING ORGANIZATION NAME(S) AND ADDRESS(ES) National Aeronautics and Space Administration John H. Glenn Research Center at Lewis Field Cleveland, Ohio 44135-3191				8. PERFORMING ORGANIZATION REPORT NUMBER E-15800	
9. SPONSORING/MONITORING AGENCY NAME(S) AND ADDRESS(ES) National Aeronautics and Space Administration Washington, DC 20546-0001				10. SPONSORING/MONITOR'S ACRONYM(S) NASA	
				11. SPONSORING/MONITORING REPORT NUMBER NASA/TP-2012-215653	
12. DISTRIBUTION/AVAILABILITY STATEMENT Unclassified-Unlimited Subject Category: 71 Available electronically at http://www.sti.nasa.gov This publication is available from the NASA Center for AeroSpace Information, 443-757-5802					
13. SUPPLEMENTARY NOTES					
14. ABSTRACT A goal of NASA's Fundamental Aeronautics Program is the improvement of aircraft noise prediction. This document provides an assessment, conducted from 2006 to 2009, on the current state of the art for aircraft noise prediction by carefully analyzing the results from prediction tools and from the experimental databases to determine errors and uncertainties and compare results to validate the predictions. The error analysis is included for both the predictions and the experimental data and helps identify where improvements are required. This study is restricted to prediction methods and databases developed or sponsored by NASA, although in many cases they represent the current state of the art for industry. The present document begins with an introduction giving a general background for and a discussion on the process of this assessment followed by eight chapters covering topics at both the system and the component levels. The topic areas, each with multiple contributors, are aircraft system noise, engine system noise, airframe noise, fan noise, liner physics, duct acoustics, jet noise, and propulsion airframe aeroacoustics.					
15. SUBJECT TERMS Noise prediction; Aircraft noise; Engine noise; Computer simulation; Sensitivity analysis; Statistical analysis; Accuracy; Acoustic ducts; Acoustic attenuation					
16. SECURITY CLASSIFICATION OF:			17. LIMITATION OF ABSTRACT UU	18. NUMBER OF PAGES 392	19a. NAME OF RESPONSIBLE PERSON STI Help Desk (email: help@sti.nasa.gov)
a. REPORT U	b. ABSTRACT U	c. THIS PAGE U			19b. TELEPHONE NUMBER (include area code) 443-757-5802

